



# Making and breaking chemical bonds with light : synthesis and mechanisms

Corentin Bellanger

## ► To cite this version:

Corentin Bellanger. Making and breaking chemical bonds with light : synthesis and mechanisms. Catalysis. Université Paul Sabatier - Toulouse III, 2023. English. NNT : 2023TOU30155 . tel-04390705

**HAL Id: tel-04390705**

**<https://theses.hal.science/tel-04390705>**

Submitted on 12 Jan 2024

**HAL** is a multi-disciplinary open access archive for the deposit and dissemination of scientific research documents, whether they are published or not. The documents may come from teaching and research institutions in France or abroad, or from public or private research centers.

L'archive ouverte pluridisciplinaire **HAL**, est destinée au dépôt et à la diffusion de documents scientifiques de niveau recherche, publiés ou non, émanant des établissements d'enseignement et de recherche français ou étrangers, des laboratoires publics ou privés.



# THÈSE

**En vue de l'obtention du  
DOCTORAT DE L'UNIVERSITÉ DE TOULOUSE  
Délivré par l'Université Toulouse 3 - Paul Sabatier**

---

**Présentée et soutenue par  
Corentin BELLANGER**

Le 21 juillet 2023

**Formation et rupture de liaisons chimiques par action de la  
lumière visible: Synthèse et études mécanistiques**

---

Ecole doctorale : **SDM - SCIENCES DE LA MATIERE - Toulouse**

Spécialité : **Chimie Moléculaire**

Unité de recherche :

**LHFA - Laboratoire Hétérochimie Fondamentale et Appliquée**

Thèse dirigée par  
**Sami LAKHDAR**

Jury

**M. Guillaume BERIONNI**, Rapporteur  
**Mme Estelle METAY**, Rapporteuse  
**Mme Laurence GRIMAUD**, Examinatrice  
**M. Eric MANOURY**, Examineur  
**M. Sami LAKHDAR**, Directeur de thèse



## Remerciements

Il est toujours particulier de rédiger des remerciements, signe irréfutable qu'une page se tourne. Ainsi se terminent donc trois années dédiées à la recherche, en quête d'une meilleure compréhension du monde extérieur.

Merci avant tout au jury qui a accepté de porter un regard critique sur mes travaux. Merci à Guillaume Berionni et Estelle Metay pour leur lecture attentive du manuscrit en qualité de rapporteurs. Merci à Laurence Grimaud d'avoir accepté d'être examinatrice de cette thèse, et de l'avoir commentée avec franchise et bienveillance. Enfin, merci à Eric Manoury d'avoir endossé le rôle de président de ce jury avec joie et intérêt.

Sami, je ne saurais te remercier suffisamment par les quelques mots que je dépose dans ce manuscrit. Je sais combien ma décision de ne pas poursuivre dans la recherche te rend amer, et je sais aussi combien ton soutien a été inébranlable au cours de ce doctorat jalonné d'épreuves, et combien il le restera. Je poursuis mon chemin en portant en mon cœur tout ce que tu as pu y déposer, notamment l'écoute attentive de mes questionnements rarement épuisés et le respect fondamental de la santé, physique et mentale, que tu portes à ton entourage. Au sein de l'aventure exigeante qu'est la recherche, tu as su garder l'humain au cœur de tes considérations. C'est un défi que je crois d'autant plus difficile à tenir dans le contexte du monde en crise qu'est le nôtre, que dans celui d'une époque où l'avenir semble tout tracé. Merci d'avoir été là. Sans toi, je ne serais assurément pas allé au bout de cette thèse.

Isabelle, quel plaisir et quelle chance de t'avoir rencontrée. J'ai tellement apprécié dialoguer avec toi. La science est intéressante, la relation à l'autre est essentielle. Tu as toujours été là pour me remonter le moral et me montrer la face positive de la pièce, que j'avais parfois du mal à trouver. Savoir que j'allais passer la journée avec toi et qu'on pourrait discuter était un vrai moteur le matin, pour m'aider à me lever. Et... Merci pour le thé. J'en ai encore chaud au cœur.

Je remercie toutes celles et ceux qui ont participé de près ou de loin à ces travaux. Je pense ici aux doctorants (Avissek, Van, Saïf, David, Luca, Ugo, Alejandro, Rosa, Aymeric, Maryne, Cyril, Emile ...), aux post-docs (Valentin, Enrico, Nere, Idir, Soukaina...), à la plateforme technique, logistique et administrative (Saloua, Romaric, Isabelle F., Olivier V., Julien, Olivier Thillaye, Florence, Miguel, Maryse... sans vous un labo ça ne tourne pas !), aux chercheurs et enseignants (Eddy Maerten, Marie Boutignon, Montserrat Gomez, Eric Benoist, Nans Roques, Frédéric Guillen...), et aux stagiaires aussi (Aziz, Nour...). Je m'excuse sincèrement auprès de celles et ceux dont je n'ai pas cité le nom.

Je voudrais remercier plus personnellement certaines personnes. A commencer par toi Valentin. Je ne cache pas qu'après avoir passé plusieurs mois seul dans l'équipe, ta seule arrivée m'aurait fait du bien. Mais la réalité est que j'ai trouvé un grand frère quand je t'ai rencontré. Tu as su me guider, me supporter, m'écouter, me conseiller, tout en restant sincère, léger ; en assumant aussi



quand tu étais saoulé. Lorsque tous mes repères s'écroulaient je voyais que pour toi ça tenait bon, et ça me donnait confiance. Je suis si content que tu sois papa aujourd'hui, je vous embrasse fort tous les trois.

Je souhaite aussi te remercier Romaric, car tu as su repérer et reconnaître ma sensibilité, en prendre soin, et rester orienté vers l'essentiel dans un milieu où il est facile de se laisser dépasser. Merci beaucoup aussi pour les efforts que tu as déployés dans le projet sur les cyanoarènes... j'ai rarement vu telles rigueur et précision expérimentales !

Avisek, merci infiniment d'avoir rejoint l'équipe et porté la suite du projet sur le phosphirane... ce n'était pas facile, et tu m'as bien sauvé la mise sur ce coup-là ! Quel plaisir de t'avoir rencontré ! Luca, c'était génial de faire du judo avec toi, de sentir une rigueur scientifique solide pendant nos échanges, et aussi un cœur ouvert pour recevoir les remous intérieurs et les baisses de moral. Un véritable ami.

J'ai aussi été amené à voyager de Toulouse à Grenoble pour effectuer une partie de cette thèse, où j'ai été chaleureusement accueilli au Département de Chimie Moléculaire par Cyrille Costentin, Marie-Noëlle Collomb, Sylvie Chardon, Jérôme Fortage, Rana Deeba et Mélanie Guyot. Merci pour votre accueil, pour les discussions scientifiques et personnelles, la simplicité, et l'attention que vous avez su avoir à mon égard. Je vous en suis très reconnaissant.

Je remercie nos partenaires de l'URCOM du Havre, Vincent Dalla, Catherine Taillier, Sébastien Comesse et Mohammad Ahmad pour le projet ANR DePhi et les discussions scientifiques.

Avant de clore le chapitre des études scolaires, je souhaite enfin remercier Stéphane Perrio, qui a été mon mentor durant toutes les années d'études supérieures, qui m'a donné accès au laboratoire dès la première année de licence, et qui m'a surtout apporté son amour de la chimie avec toute la pédagogie du monde !

Merci à ma famille, bien évidemment... Papa, maman, vous avez toujours voulu pour moi ce qui me rendait heureux, peu importe que je sois chercheur ou éboueur. Merci à mes deux frères, mes belles sœurs, et mes nièces, vous apportez beaucoup d'amour dans ma vie et il n'y a rien de plus essentiel. Baptiste, je réalise que j'ai encore loupé ton anniversaire d'une journée alors que j'écris ce texte, on ne change pas les bonnes habitudes... !

Coline, merci d'être apparue comme ça, à l'improviste, pendant cette thèse. La vie a beau ne pas être facile tous les jours, un sens est apparu depuis notre rencontre. Coïncidence ou non, j'ai depuis ce jour le sentiment de vivre au plus près de la vérité.

Merci à Richard Feynman, Erwin Schrödinger, Edgar Morin, Albert Camus, Jiddu Krishnamurti et David Bohm d'avoir foulé cette terre avant moi, et d'avoir participé à redonner vie à une part de moi que je croyais asséchée.

*“Vivre demande en fait beaucoup d'amour, un fort penchant pour le silence, une grande simplicité, énormément d'expérience ; il faut avoir un esprit capable de penser de manière très lucide, et qui ne soit pas sous le joug des préjugés ou des superstitions, de l'espoir ou de la peur.” – Jiddu Krishnamurti*

## **Summary in English**

This manuscript, entitled “Making and breaking bonds with visible light: Synthesis and mechanisms”, covers the development of new synthetic procedures and their mechanistic investigations. It is divided into five chapters.

The first chapter is a general introduction on the definition of visible-light and the history of photochemistry.

Chapter II discloses the progress made in the challenging quaternarization of phosphiranes and the C-centered ring opening of phosphiranium salts. Extensive knowledge of the phosphorus-containing three-membered rings reactivity, namely phosphirane and phosphiranium salts, is lacking. We show that the formation of free electrophilic carbenes by visible-light irradiation of the corresponding aryldiazoacetates and their reactivity with 1-mesitylphosphirane allows the formation of phosphiranium ylides. The reactivity of the previously unknown phosphiranium ylides is explored in the presence of pronucleophiles bearing an acidic hydrogen to provide the selective carbon centered ring opening products by efficient ring strain release. Thiophenols and carboxylic acids were successfully used as reaction partners and afforded a wide scope with good yields and moderate diastereoselectivities. The experimental methodology was optimized to allow isolation and characterization of the products by oxidizing the phosphine resulting from the ring opening to a phosphine oxide. This study is finally complemented by DFT calculations to support a reasonable reaction mechanism. A pathway in good agreement with experimental observations was calculated and showed the importance of the ring strain release as the driving force of the reaction.

Chapter III focuses on donor-acceptor cyanoarenes, which are widely used photocatalysts in photoredox catalysis. Examples from the literature showing the super-reducing abilities of cyanoarenes radical anions to reduce aryl chlorides are discussed in the literature. However, the use of amines as sacrificial electron donors is not chemically innocent and further investigations were required. One way to complement this study is by electrochemically reducing the cyanoarenes. In chapter III, we show that the electrochemical generation of donor-acceptor cyanoarenes' radical anion is a clean and efficient method. The study of their photophysical properties in the presence and absence of chlorobenzene provided different results compared to a previous literature report and add more data to the current debate on the ability of radical anions to act as super-reducing agents. Part of this chapter is devoted to the study of the interaction between the strong Lewis acid  $B(C_6F_5)_3$  and donor-acceptor cyanoarenes. The

coordination induces important structural and photophysical modifications. An electrochemical study shows that the coordination of the reduced cyanoarene to the same Lewis acid is favored but that the resulting adduct is unstable and leads to the decomposition of the Lewis acid.

Chapter IV addresses the challenging cleavage of the fluorine-carbon bond in aryl fluorides. If these molecules are successfully provided an extra electron by electron transfer, the carbon-fluorine bond is known to be able to dissociate to provide the fluoride anion as well as the corresponding aryl radical. This step requires strong reducing agents, and only few of them are reported in the literature. The visible light-mediated germanylation of aryl fluorides is reported with a particular focus on the super-reducing properties of the triphenylgermyl anion's excited state. By simply combining readily available fluoro-arenes with germanes in the presence of a base and under blue irradiation, tetraarylgermanes were synthesized in reasonable to good yield. Experimental and theoretical investigations have been undertaken and a reasonable reaction mechanism is discussed.

Finally, chapter V gives a general conclusion to the manuscript by summarizing the different results obtained and the outlooks for each chapter.

## **Résumé en Français**

Ce manuscrit est intitulé « Formation et rupture de liaisons chimiques par action de la lumière visible : Synthèses et études mécanistiques ». Il est divisé en cinq chapitres. Le premier est une introduction générale sur la définition de la lumière visible et de l'histoire de la photochimie.

Le chapitre II présente les progrès effectués dans la quaternarisation des phosphiranes et de l'ouverture de cycle C-centrée des sels de phosphiranium. La connaissance de la réactivité du cycle phosphoré à trois chaînons, à savoir les phosphiranes et les sels de phosphiranium, est actuellement limitée. Dans ce chapitre, nous présentons que la réaction entre des carbènes électrophiles libres avec le 1-mésitylphosphirane produit des ylures de phosphiranium. La réactivité des ylures de phosphiranium, jusqu'ici inconnus, est explorée en présence de nucléophiles protiques qui, après déprotonation par le carbone de l'ylure, s'engagent dans une ouverture C-centrée du sel de phosphiranium généré. Les thiophénols et les acides carboxyliques ont été utilisés avec succès en tant que partenaires réactionnels et ont démontré l'applicabilité de la méthode par un scope important, de bons rendements, et des diastéréosélectivités modérées. La méthodologie expérimentale a été optimisée pour permettre l'isolement et la caractérisation des produits par oxydation des phosphines résultant de l'ouverture de cycle en oxydes de phosphine. Cette étude est finalement complétée par des calculs DFT afin de soutenir un mécanisme raisonnable. A chemin en bonne adéquation avec les observations expérimentales a été calculé et a montré l'importance déterminante du relâchement de la tension de cycle.

Le chapitre III se concentre sur les cyanoarènes donneur-accepteur, largement utilisés en tant que photocatalyseurs en catalyse photoredox. Des résultats récents ont montré la capacité de l'état excité de leur radicaux anions à réduire les chlorures d'aryles. Cependant, l'utilisation d'amine sacrificielle de la méthode n'est pas chimiquement innocente et de plus amples études sont nécessaires. Dans ce chapitre, nous montrons que la génération électrochimique des radicaux anions des cyanoarènes donneur-accepteur est une méthode efficace. L'étude de leurs propriétés photophysiques en présence et absence de chlorobenzène a fourni des résultats différents de la littérature précédente et ajoutent de nouvelles données au débat sur la capacité des radicaux anions à agir en tant que super-réducteurs. Une partie de ce chapitre est dédiée à l'étude de l'interaction entre les cyanoarènes donneur-accepteur et l'acide de Lewis  $B(C_6F_5)_3$ . Leur coordination induit d'importants changements structuraux et photophysiques. Une étude électrochimique montre que les cyanoarènes dans leur état réduit se coordonnent favorablement

au  $\text{B}(\text{C}_6\text{F}_5)_3$  mais que l'adduit qu'ils forment est instable et conduit à la décomposition de l'acide de Lewis.

Le chapitre IV présente la découverte de propriétés super-réductrices de l'état excité de l'anion du triphénylgermane. Celles-ci sont appliquées à la germanylation de différents fluorures d'aryle et suivie d'une étude théorique pour proposer un mécanisme raisonnable. Un transfert d'électron depuis l'état excité de l'anion du triphénylgermane vers le fluorure d'aryle conduit à la rupture de la liaison carbone-fluor et fournit un anion fluorure et un radical aryle. Ce radical aryle se recombine avec le radical du triphénylgermane pour fournir les ayles germanylés d'intérêt.

Enfin, le chapitre V fournit une conclusion générale au manuscrit en résumant les différents résultats obtenus ainsi que les perspectives de chaque chapitre.

## Table of content

Chapter I: General introduction .....	9
1. Light and life .....	10
2. Light and chemistry.....	14
3. Thesis overview .....	21
4. References .....	22
Chapter II: Exploration of the reactivity of free 1-mesitylphosphirane: Visible-light mediated quaternarization and ring opening .....	25
1. Introduction .....	26
2. Results and discussions.....	46
2.1. Phosphirane synthesis .....	46
2.2. Estimating phosphirane nucleophilicity and Lewis basicity .....	48
2.3. Phosphiranium ylides and phosphiranium salts: exploration of a new phosphirane quaternarization method .....	53
2.4. Reactivity of sterically hindered phosphiranium salts .....	61
2.5. Reactivity of phosphiranium ylides: A regioselective C-centered ring opening .....	65
2.6. Computational studies .....	83
3. Conclusion.....	105
4. Experimental section .....	106
5. References .....	113
Chapter III: Donor-acceptor cyanoarenes as powerful organic photocatalysts .....	121
1. Donor-acceptor cyanoarenes : General introduction.....	122
1.1. Cyanoarenes in materials science .....	128
1.2. Biomedical applications.....	134
2. Donor-acceptor cyanoarenes general properties: A first approach.....	135
2.1. Structure, geometry, and orbitals .....	135
2.2. Excited states multiplicity and lifetimes .....	140
2.3. Redox potentials .....	142
2.4. Table of selected D-A cyanoarenes properties.....	152
3. Donor-acceptor cyanoarenes as efficient organic photocatalysts: A broad applicability .....	153
3.1. Electron transfer .....	157
3.2. Energy transfer .....	174
3.3. Combined electron and energy transfers .....	176
4. Donor-acceptor cyanoarenes radical anions .....	177
4.1. Excited states multiplicity and lifetimes : The lifetime debate .....	177
4.2. Photocatalyst stability : Degradation pathways and incognito active species.....	180

5. Results and discussions.....	181
5.1. 3CzEPAIPN and 3CzEPAIPN $\bullet^-$ .....	182
5.1.1. Characterization.....	182
5.1.2. Excited state lifetime measurement by time-correlated single-photon counting (TCSPC).....	192
5.1.3. Chlorobenzene quenching experiments .....	196
5.1.4. 3CzEPAIPN radical anion isolation .....	199
5.1.5. Impact of the D-A cyanoarenes coordination to the B(C <sub>6</sub> F <sub>5</sub> ) <sub>3</sub> Lewis acid.....	200
5.2. Other D-A cyanoarenes .....	211
6. Conclusion.....	216
7. Experimental section .....	218
8. References .....	231
Chapter IV: Visible-light mediated germanylation of aryl fluorides: Synthetic and mechanistic insights .....	245
1. Introduction .....	246
2. Results and discussions.....	253
2.1. Optimization of the visible-light induced germanylation of fluoro-arenes reaction conditions .....	253
2.2. Application of the methodology to a scope of fluoro-arenes .....	255
2.3. Mechanism of the reaction: DFT investigation.....	260
3. Conclusion.....	264
4. Experimental section .....	265
5. References .....	279
Chapter V: General conclusion .....	283
Résumé détaillé en Français.....	287

# ***Chapter I:***

## ***GENERAL INTRODUCTION***



## 1. Light and life

The different projects presented in this manuscript are linked by a common interest for the interaction between light and organic molecules for the formation of carbon-heteroatom and carbon-carbon bonds.

What is light?

When we talk about light, we commonly mean *visible light*.

For early humans, daylight was what allowed to evolve in relative safety compared to the dangers that arise from darkness at night. The control of fire was a decisive breakthrough for mankind evolution as it allowed both light and heat to be manipulated at will.

From a modern scientific point of view, when not only fire but light itself was controlled in light-emitting-devices, visible light is an electromagnetic radiation whose wavelength is comprised between *ca.* 400 and 750 nanometers.

From a physics point of view, the elementary particle associated with light is the photon. Photons, which exhibit wave-particle duality, are perceived by the human eye when their energy ranges between 1.65 (red) and 3.10 eV (violet).

From a biology point of view, the mechanism of color perception is triggered by light absorption of three different types of cells present in the eye, which transform the electromagnetic radiation into electrical signals transmitted to the brain by the optic nerve.

From a chemistry point of view, the active species in these cells are iminium ions engaged in photochemical process.<sup>1</sup>

Figure I-1 purposely displays the electromagnetic spectrum associated with light in wavelength (nm) and the related energy (eV) and wavenumber ( $\text{cm}^{-1}$ ) units, three types of units commonly encountered in photochemistry. The overall electromagnetic radiation spectrum spans from  $10^{-14}$  to  $10^6$  eV ( $10^8$  to  $10^{-12}$  m) and covers radio waves, microwaves, infrared, visible light, ultraviolet, X-rays and gamma rays.

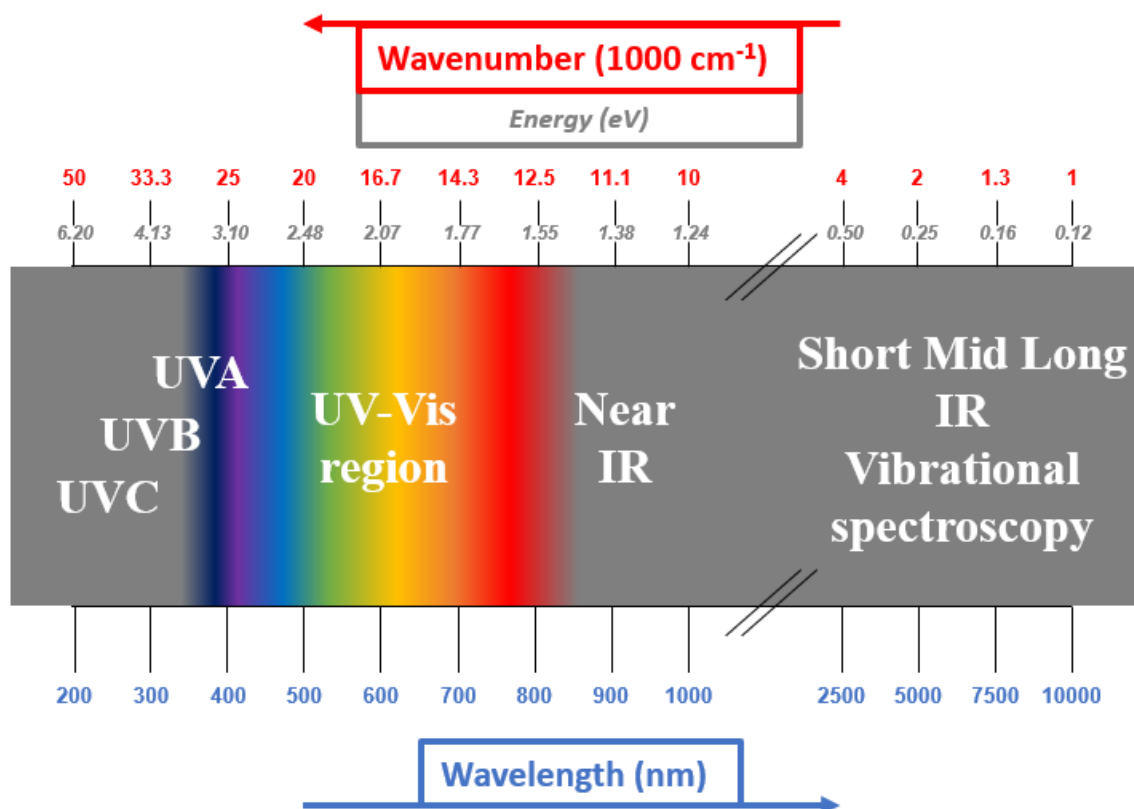


Figure I-1: Electromagnetic spectrum from ultraviolet to infrared with wavelength, wavenumber, and energy units.

Most of life as we know it involves the UV-Vis-IR region. Visible light is the narrowest region of the overall electromagnetic spectrum. With its neighboring electromagnetic radiations ultraviolet (UV) and infrared (IR), they compose the solar radiation spectrum.<sup>a</sup>

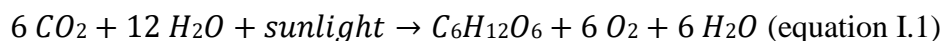
On the one hand, ultraviolet radiations are highly energetic and tend to cleave the molecules they interact with.<sup>2</sup> Bees can see ultraviolet radiations as their vision ranges from 300 to 600 nm, which allows them to find nectar more effectively.<sup>3</sup>

The low energy infrared radiations, on the other hand, are related to molecular motions/vibrations, and therefore, heat. Pit-vipers, often mentioned by Richard Feynman in his lectures,<sup>b</sup> can see in the infrared region thanks to an extra organ between their eyes and nostrils that allows them to detect the heat generated by mammals and birds.<sup>4</sup> These examples give an idea of what the world would look like if the human vision range would step just tens of nanometers outside the narrow visible spectrum.

<sup>a</sup> Information taken from <http://photobiology.info/Visser-Rolinski.html>

<sup>b</sup> Richard Feynman interview sample available at <https://www.youtube.com/watch?v=egB9p5ZbrEg>

Visible light is obviously not limited to vision. Its upmost importance is without the shadow of a doubt its involvement in photosynthesis. This *ca.* 2.4 billion years old process is at the foundation of sunlight energy storage inside matter on Earth. The extremely simplified global reaction (equation I.1) consists in the transformation of carbon dioxide and water into sugars and oxygen by visible light mediation.



Interestingly, in the first step of the process (the Kok cycle, Figure I-2), the consecutive storage of the energy of four photons is required to achieve the challenging four-electron oxidation of water (equation I.2).<sup>5</sup>

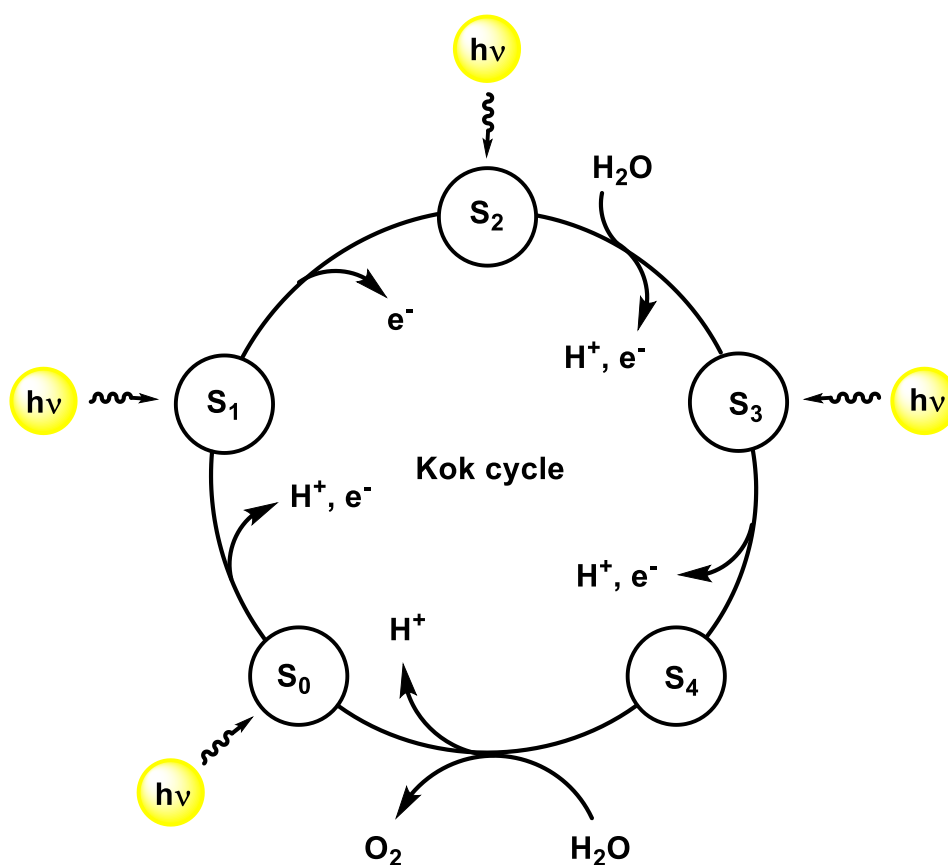
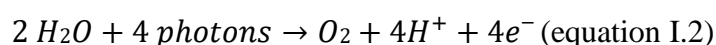


Figure I-2: Kok cycle for the oxidation of water in the photosynthesis process. S<sub>0</sub> to S<sub>4</sub> represent different complex association of molecules.

Furthermore, Earth can be considered a closed system where a fixed number of atoms undergoes transformations that manifest in various fashions.<sup>6</sup> The only input that allows life to sustain through photosynthesis is sunlight.

Finally, in this clumsy attempt at introducing light, two fundamental quantum physics equations must be mentioned. The first one is the Planck-Einstein (equation I.3).

$$E = \frac{hc}{\lambda} = hc\bar{\nu} = h\nu \text{ (equation I.3)}$$

This equation states that the energy of a photon is proportional to its frequency. The celerity of photons in vacuum ( $c$ , 299,792,458 m.s<sup>-1</sup>) along with Planck's constant ( $h$ , 6.626.10<sup>-34</sup> J.s), which is at the foundation of the quantized vision of our world, are the two parameters which connect energy and frequency in this statement. The meaning of this equation regarding the wave-behavior of photons is always a source of a mixed feeling of surprise and inspiration. 1933 Nobel Prize winner Erwin Schrödinger stated in his lecture "Our Conception of Matter"<sup>c</sup>: *"If you finally ask me: "Well, what are these corpuscles, really?" I ought to confess honestly that I am almost as little prepared to answer that as to tell where Sancho Panza's second donkey came from."*<sup>7</sup>

In equation (I.3), the more relevant wavenumber ( $\bar{\nu} = \frac{1}{\lambda}$ ), which is proportional to the energy, is often used instead of the wavelength.

Using the wavenumber as a scale for electromagnetic waves makes more sense in the way that a difference of **50 nm** between **200 and 250 nm** or **600 and 650 nm** is not energetically equivalent, since  $\Delta\lambda$  (**50 nm** in both cases) has no direct correlation with  $\Delta E$  (**1.239 eV** vs **0.156 eV**). However,  $\Delta\bar{\nu}$  (**10,000** vs **1,282**) is proportional to  $\Delta E$  (equation I.4):

$$\Delta E = \frac{hc}{\lambda_1} - \frac{hc}{\lambda_2} = hc \times \left( \frac{1}{\lambda_1} - \frac{1}{\lambda_2} \right) = hc \times \Delta\bar{\nu} \text{ (equation I.4)}$$

Figure I-1 provides the correspondence between wavenumber and wavelength. A change of scale is used to include the range of vibrational spectroscopy (between *ca.* 1000 and 4000 cm<sup>-1</sup>). Low energy vibrations (between *ca.* 300 and 1000 cm<sup>-1</sup>) as well as rotational vibrations (*ca.* 1-10 cm<sup>-1</sup>) are not displayed on this qualitative graph. Obviously, the wavenumber can be set as the reference increasing from left to right, which implies that the wavelength would decrease in the same direction since wavelength and wavenumber are inversely proportional.

The second fundamental equation is the energy-mass equivalence relationship (equation I.5).

$$E = mc^2 \text{ (equation I.5)}$$

The celerity of photons once again plays an important role in this equation, which states that energy and mass are equivalent. This equation implies that the conservation of mass is not true

<sup>c</sup> in Geneva in 1952

anymore for small systems, that systems in their resting state possess an enormous amount of energy due to their mass, and that energy and matter can interconvert. It is difficult to find the words to express how mind-blowing these statements are. The celerity of light acts once again as a universal constant.

It is difficult to find a better conclusion to this short introduction than the one elegantly expressed by Nobel Prize winner Ahmed Zewail in an interview in 2014 (Nobel Prize in Chemistry in 1999 for his work on ultrafast spectroscopy):

*“Light is life, it’s as simple as that.”*

## 2. Light and chemistry

Photochemistry, the field of science that studies the effects of light on chemical transformations, can be traced back to 1912 with a visionary publication from Giacomo Ciamician, famous for setting his lab benches on the rooftop of the university of Bologna.<sup>8</sup> “The future of photochemistry” already addressed in 1912 the problem of the limits of our world, its high dependence on fossil solar energy, and the need to better understand and use radiant solar energy. He envisioned that mankind, being in a hurry compared to natural processes, would attempt to mimic photosynthesis, master it, optimize it, and make use of artificial photosynthesis on an industrial scale. In the midst of the current effervescence around photochemistry, it is important to recall that it is a recent field of study (*ca.* a century old). It is also important to note that photochemistry affords reactivities that are inaccessible by thermal activation.

A milestone was reached when Jablonski proposed a diagram in 1933 (Figure I-3, left) to explain experimental observations of phosphorescence.<sup>9</sup> He proposed a transition from the F level (singlet state  $S_1$  today, at the origin of fluorescence) to the M level (triplet state  $T_1$  today, at the origin of phosphorescence) which then decayed radiatively. This diagram was further improved and Jablonski-Perrin diagrams are now a standard tool for photoscientists to schematize light interaction with matter (Figure I-3, right).<sup>10</sup>

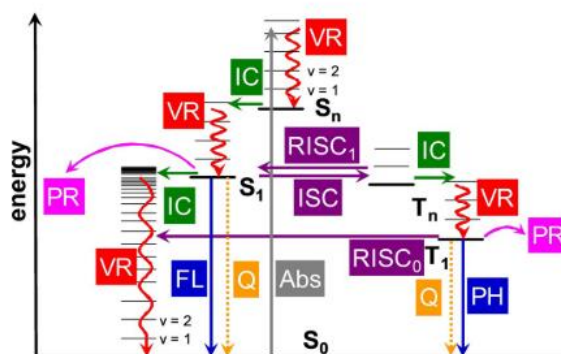
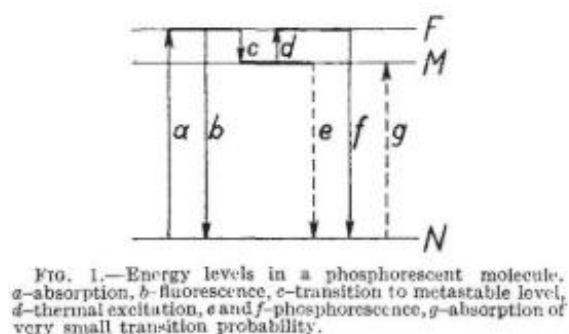


Figure I-3: First Jablonski diagram (left) and recent improved version (right). Reproduced with permission from references 9 (Copyright 1933 Nature Publishing Group) and 10 (Copyright 2021 Wiley-VCH GmbH).

One should not confuse energy state diagrams and molecular orbital (MO) diagrams (Figure I-4). The former represents the different ground and excited energy levels of a molecule, while MO diagrams display the frontier occupied and vacant orbitals of a molecule (respectively highest occupied molecular orbital HOMO and lowest unoccupied molecular orbital LUMO).

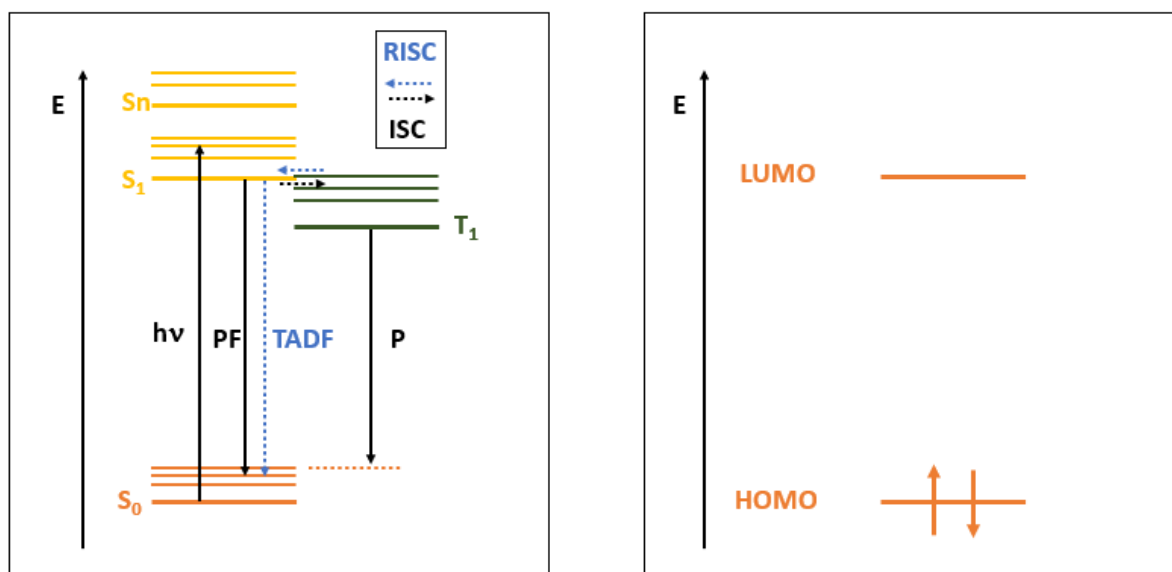


Figure I-4: Simple Jablonski diagram (left) and frontier molecular orbital (right). PF: prompt fluorescence. TADF: thermally activated delayed fluorescence. P: phosphorescence. ISC: intersystem crossing. RISC: reverse intersystem crossing.

The absorption of a photon by a molecule can trigger an electronic excitation, i.e., the electronic distribution within the molecule is modified. One should consider the excited state of the molecule as a new molecular entity with completely different properties.

Each state has closely spaced vibrational energy levels, populated according to a Boltzmann distribution depending on temperature  $T$  and the energy difference between each vibrational level  $\Delta E_{\text{vib}}$  (equation I.5).

$$N_1/N_0 = \exp(-\Delta E_{\text{vib}}/(k_B T)) \text{ (equation I.5)}$$

At room temperature, the lowest vibrational level ( $v=0$ ) is almost the only one populated. On a Jablonski diagram, the lowest vibrational levels are typically depicted in thick lines while higher vibrational levels are depicted in thin lines. In organic photochemistry, the two most common spin states are singlet ( $S=0$ , no unpaired electron, multiplicity  $2S+1 = 1$ ) and triplet ( $S=1$ , two unpaired electrons, multiplicity  $2S+1 = 3$ ). After light excitation, the molecule reaches an excited state  $S_n$  which may relax to the most stable  $S_1$  excited state. From  $S_1$ , prompt fluorescence (PF) or intersystem crossing (ISC) can occur. ISC involves a change in the spin of one electron, affording the triplet state. From this triplet state, phosphorescence (P) or reverse intersystem crossing (RISC) can occur. When RISC is followed by emission from the singlet state, so-called thermally activated delayed fluorescence (TADF) is observed with longer lifetimes than prompt fluorescence. Both singlet and triplet states can also decay non-radiatively through thermal deactivation (e.g. heat dissipation through vibration, or collisions with the environment). Figure I-5 shows a little more complexity with a cut of the potential energy surfaces (PES) and the vibrational wavefunctions.

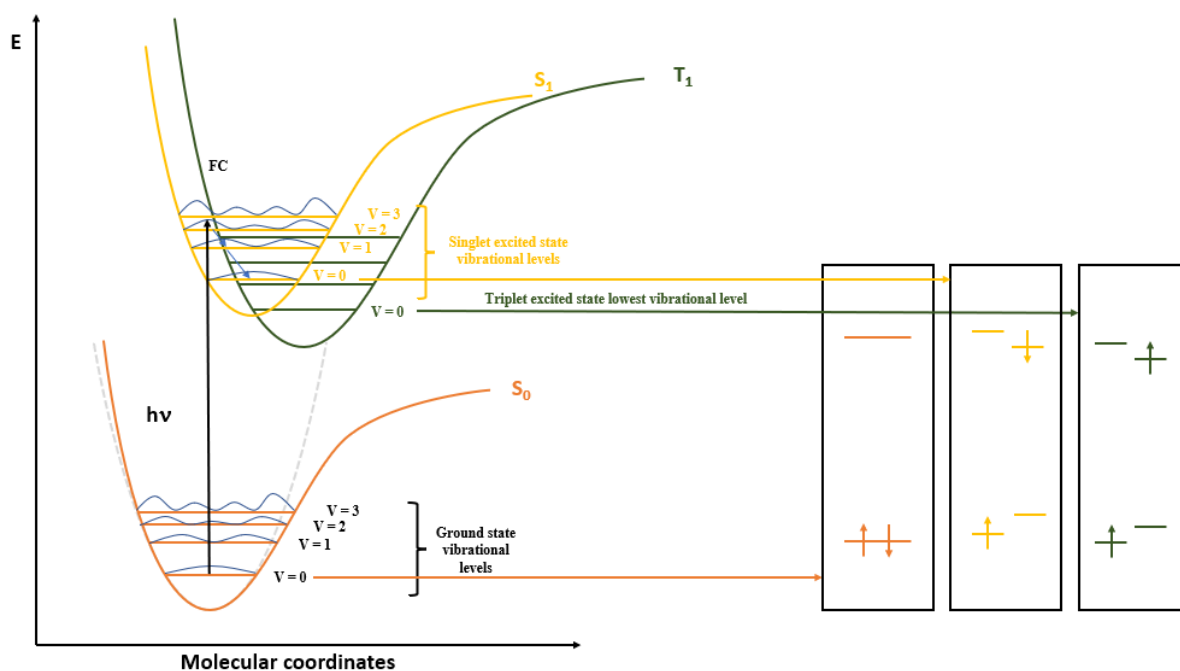


Figure I-5: Schematic potential energy curves and MO diagram for the frontier orbitals of the  $S_0$ ,  $S_1$  and  $T_1$  states ( $S_n$  and  $T_n$  states can be involved in the processes but are not shown)

The Franck-Condon principle states that the nuclear configuration of a molecule is static on the timescale of an electronic transition. Therefore, electronic transitions occur “vertically” (black arrow in Figure I-5) from  $S_0$  ( $v=0$ ) to the vibrational level of  $S_n$  (here,  $S_1$ ) that provides the highest vibrational wavefunction overlap (as an example,  $v=2$  in Figure I-5). The probability for an electronic transition to take place takes into account the minimal internal reorganization and the highest vibrational wavefunction overlap.

The timescales of the processes that take place after light absorption are key factors in understanding the photoreactivity of molecules (table I-1). They range from ultrafast (between  $10^{-15}$  s (fs) and  $10^{-12}$  s (ps), e.g. absorption and vibrational relaxation) to fast ( $10^{-9}$  s (ns), e.g. fluorescence) and slow ( $10^{-6}$  s ( $\mu$ s) to  $10^{-3}$  (s) e.g. phosphorescence).<sup>1</sup>

Table I-1: Time scales of photophysical processes

Process	Time scale (s)
Photon absorption	$10^{-15}$
Vibrational relaxation	$10^{-13}$ - $10^{-12}$
Internal conversion	$10^{-12}$ - $10^{-6}$
Intersystem crossing ( $S \rightarrow T$ )	$10^{-12}$ - $10^{-6}$
Intersystem crossing ( $T \rightarrow S$ )	$10^{-9}$ - $10^1$
Fluorescence	$10^{-9}$ - $10^{-7}$
Phosphorescence	$10^{-6}$ - $10^{-3}$

Light absorption may lead to unimolecular radiative processes (fluorescence or phosphorescence) or non-radiative processes such as structure modifications (intramolecular cycloaddition, isomerization, bond dissociation etc.). For instance, the photoisomerization of stilbene (either from the pure E or Z isomer) yields the same mixture of isomers (Figure I-6) where the Z form is favored (93%) in the photostationary state (PSS). Even if irradiation is maintained, proportions will stay the same.<sup>11</sup>

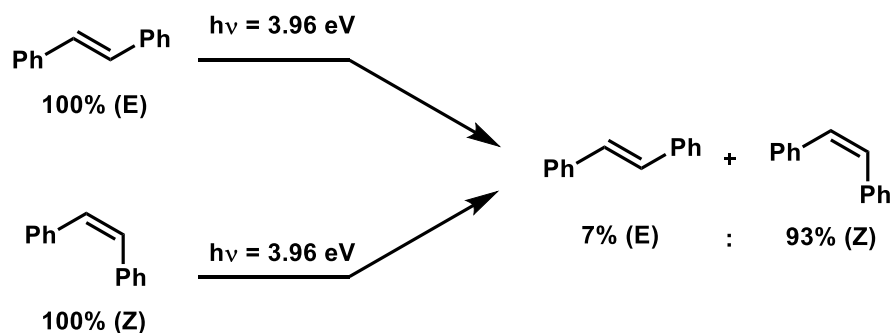


Figure I-6: Isomerization of both isomers of stilbene under UV light irradiation and resulting photostationary state.



We focus here on organic photochemistry, which was mostly triggered by UV irradiation until 2008 and was renewed by the groups of Yoon, MacMillan and Stephenson through visible-light photoredox catalysis.<sup>12–14</sup> In photocatalysis, the photocatalyst first absorbs light to reach its excited state and becomes able to engage in intermolecular non-radiative processes that are not accessible to its ground state.

There are two main modes of action for photocatalysts (PC, Figure I-7) : Electron transfer (ET, photoredox) and energy transfer (EnT, photocatalysis).

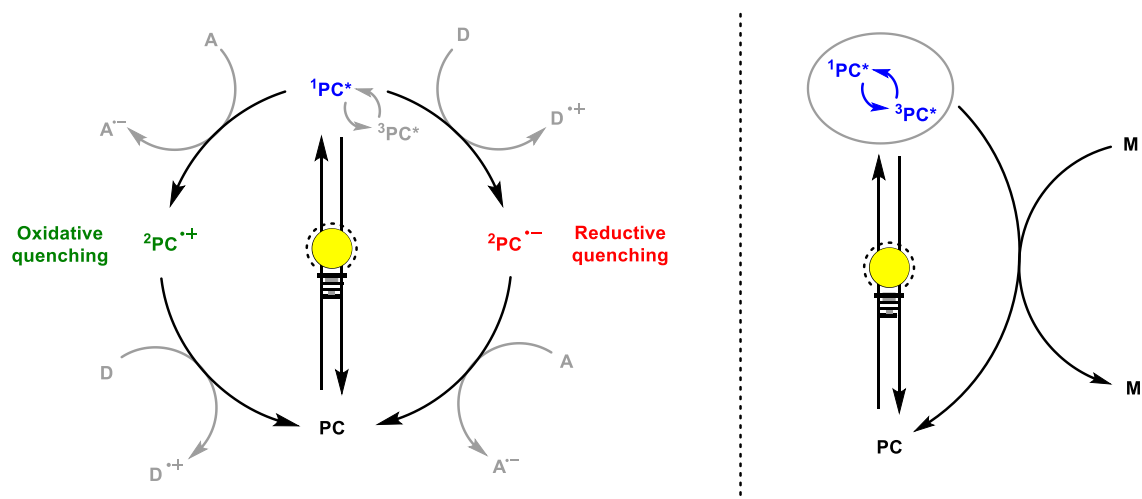


Figure I-7: Oxidative and reductive photoredox cycles (left) and energy transfer (right). A: electron acceptor. D: electron donor. M: molecule

In photoinduced electron transfer (PET), the photocatalyst can either be oxidized in the first step (oxidative quenching) or reduced (reductive quenching). The electron is either given to an electron acceptor (A) or taken from an electron donor (D) in the medium. This methodology is widely applied for the generation of radicals. Energy transfers can occur according to two mechanisms. The first one is Förster resonance energy transfer (FRET, Figure I-8). It occurs over long distances (the molecules do not need to be in close contact) and is the result of a dipole-dipole interaction between two molecules.

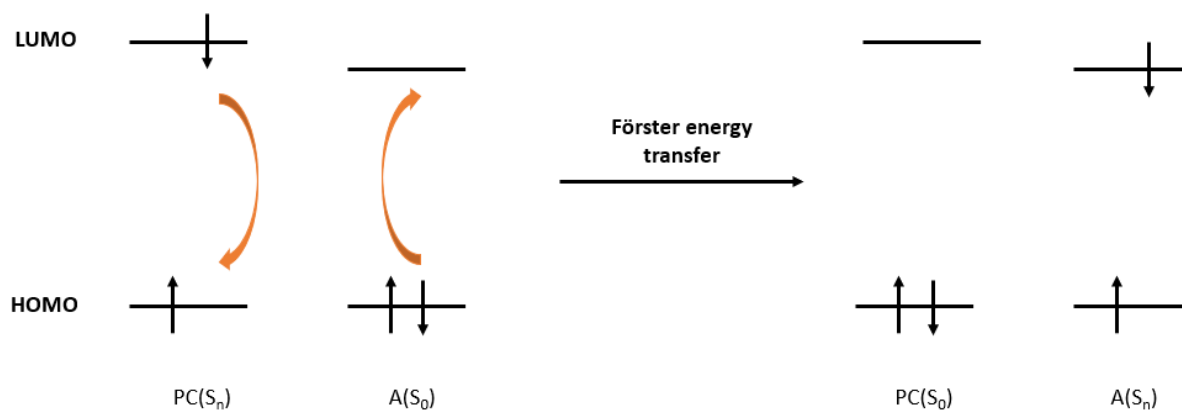


Figure I-8: Förster energy transfer mechanism from the excited state of a photocatalyst to a suitable energy acceptor.

The second one is Dexter energy transfer (Figure I-9) where there is a two-electrons exchange that requires an overlap of the orbitals. Both singlet-singlet and triplet-triplet energy transfer are accessible with this mechanism.

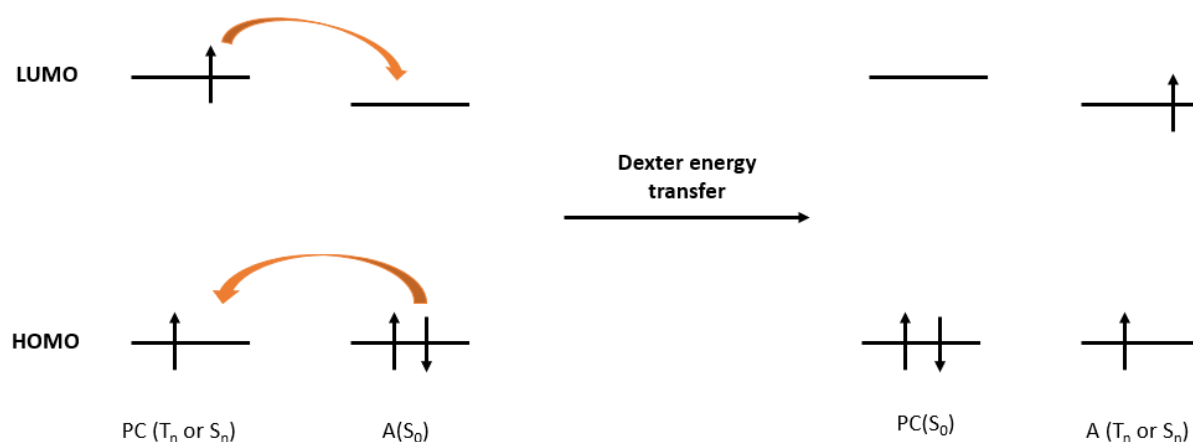


Figure I-9: Dexter energy transfer mechanism from the excited state of a photocatalyst to a suitable energy acceptor.

The main properties of interest for a photocatalyst are its absorbance ( $\lambda_{\text{max,abs}}$ ), the energy level and nature of its excited state(s) (singlet/triplet, local/charge transfer...) as well as their lifetimes ( $\tau$ ), and the redox potentials of both ground and excited states. In Nicewicz's 2016 review on organic photoredox chemistry,<sup>15</sup> ten families of organic photocatalysts were reported, some of which are illustrated here in table I-2.

Table I-2: Selected examples of organic photocatalysts structures and properties

Photocatalyst	$\lambda_{\text{max,abs}}$ (nm)	$\Delta E_{0,0}^{S1}$ (eV)	$\Delta E_{0,0}^{T1}$ (eV)	$\tau_{\text{PF}}$ (ns)	$E_{\text{PC/PC}^{\bullet-}}$ (V)	$E_{\text{PC}^{\bullet+}/\text{PC}}$ (V)
	335 <sup>a</sup>	3.22	3.00	0.008	-1.72	+2.39
	422	2.90	1.81	14.9	-0.91	/
	425	2.67	1.94	6	-0.49	/

All values given in MeCN unless noted otherwise. Potential values given against SCE.

<sup>a</sup>In MeOH

The redox potentials of the photocatalyst excited states can be estimated as follows (where  $\Delta E_{0,0}$  is the energy difference between the zeroth vibrational levels of the ground state and the lowest excited state, estimated as the intersection of absorbance and emission spectra) (equations I.6 and I.7):

$$E_{PC^*/PC^{\bullet-}} = E_{PC/PC^{\bullet-}} + \Delta E_{0,0} \text{ (equation I.6)}$$

$$E_{PC^{\bullet+}/PC^*} = E_{PC^{\bullet+}/PC} - \Delta E_{0,0} \text{ (equation I.7)}$$

The use of visible light to trigger chemical transformations in mild conditions has shown tremendous applicability and is still developing quickly to this day. The understanding of the underlying photophysical and photochemical mechanisms remains essential for the development of this field.

### 3. Thesis overview

Light-induced transformations are a key part in each chapter of this thesis work.

In chapter II, the chemistry of the phosphorus-containing three-membered rings, namely phosphirane and phosphiranium salts, is investigated. More specifically, formation of free electrophilic carbenes by visible light irradiation of the corresponding aryldiazoacetates and their reactivity with 1-mesitylphosphirane is disclosed. The reactivity of the resulting product, which we have named a phosphiranium ylide, is explored in the presence of nucleophiles bearing an acidic hydrogen to provide the selective carbon centered ring opening products by efficient ring strain release. This experimental study is finally complemented by DFT calculations to support a reasonable reaction mechanism.

Chapter III focuses on donor-acceptor cyanoarenes, which are widely used photocatalysts in photoredox catalysis. The activity of their radical anions as potent super-reducing photocatalysts is discussed in the literature. Recent results showed their ability to reduce aryl chlorides. In this example, the neutral donor-acceptor cyanoarene was reduced by ET with an amine sacrificial electron donor in a reductive quenching mechanism and irradiated with a second photon to form the radical anion's super-reducing excited state. However, the use of amines as sacrificial electron donors is not chemically innocent. One way to complement this study is by electrochemically reducing the cyanoarenes. In chapter III, the electrochemical generation of donor-acceptor cyanoarenes' radical anion is presented along with the study of both their photophysical properties and photochemical behavior in the presence of chlorobenzene.

Finally, chapter IV addresses the challenging cleavage of the fluorine-carbon bond in aryl fluorides. If these molecules are successfully provided an extra electron by ET, the carbon-fluorine bond is known to be able to dissociate to provide the fluoride anion as well as the corresponding aryl radical. This step requires strong reducing agents, and only few of them are reported in the literature. The visible light-mediated germanylation of aryl fluorides is reported with a particular focus on the super-reducing properties of the triphenylgermyl anion's excited state.

#### 4. References

- (1) Buzzetti, L. Photochemical Strategies for Carbon – Carbon Forming Processes. *Dr. Thesis* **2018**.
- (2) D’Orazio, J.; Jarrett, S.; Amaro-Ortiz, A.; Scott, T. UV Radiation and the Skin. *Int. J. Mol. Sci.* **2013**, *14* (6), 12222–12248. <https://doi.org/10.3390/ijms140612222>.
- (3) Papiorek, S.; Junker, R. R.; Alves-dos-Santos, I.; Melo, G. A. R.; Amaral-Neto, L. P.; Sazima, M.; Wolowski, M.; Freitas, L.; Lunau, K. Bees, Birds and Yellow Flowers: Pollinator-Dependent Convergent Evolution of UV Patterns. *Plant Biol.* **2016**, *18* (1), 46–55. <https://doi.org/10.1111/plb.12322>.
- (4) Gracheva, E. O.; Ingolia, N. T.; Kelly, Y. M.; Cordero-Morales, J. F.; Hollopeter, G.; Chesler, A. T.; Sánchez, E. E.; Perez, J. C.; Weissman, J. S.; Julius, D. Molecular Basis of Infrared Detection by Snakes. *Nature* **2010**, *464* (7291), 1006–1011. <https://doi.org/10.1038/nature08943>.
- (5) Concepcion, J. J.; House, R. L.; Papanikolas, J. M.; Meyer, T. J. Chemical Approaches to Artificial Photosynthesis. *Proc. Natl. Acad. Sci. U. S. A.* **2012**, *109* (39), 15560–15564. <https://doi.org/10.1073/pnas.1212254109>.
- (6) Armaroli, N.; Balzani, V. The Future of Energy Supply: Challenges and Opportunities. *Angew. Chemie - Int. Ed.* **2007**, *46* (1–2), 52–66. <https://doi.org/10.1002/anie.200602373>.
- (7) Erwin, S. What Is Matter ? *Sci. Am.* **1953**, *189* (3), 52–57.
- (8) Ciamician, G. The Photochemistry of the Future. *Science* **1912**, XXXVI (No), 926.
- (9) Jablonski, A. Efficiency of Anti-Stokes Fluorescence in Dyes. *Nature* **1933**, *131*, 839–840.
- (10) Behera, S. K.; Park, S. Y.; Gierschner, J. Dual Emission: Classes, Mechanisms, and Conditions. *Angew. Chemie - Int. Ed.* **2021**, *60* (42), 22624–22638. <https://doi.org/10.1002/anie.202009789>.
- (11) Hammond, G. S.; Saltiel, J.; Lamola, A. A.; Turro, N. J.; Bradshaw, J. S.; Cowan, D. O.; Counsell, R. C.; Vogt, V.; Dalton, C. Mechanisms of Photochemical Reactions in Solution. XXII.1 Photochemical Cis-Trans Isomerization. *J. Am. Chem. Soc.* **1964**, *86* (16), 3197–3217. <https://doi.org/10.1021/ja01070a002>.
- (12) Nicewicz, D. A.; MacMillan, D. W. C. Merging Photoredox Catalysis with

- Organocatalysis: The Direct Asymmetric Alkylation of Aldehydes. *Science* (80-. ). **2008**, 322, 73–79.
- (13) Ischay, M. A.; Anzovino, M. E.; Du, J.; Yoon, T. P. Efficient Visible Light Photocatalysis of [2+2] Enone Cycloadditions. *J. Am. Chem. Soc.* **2008**, 130 (39), 12886–12887. <https://doi.org/10.1021/ja805387f>.
- (14) Narayanam, J. M. R.; Tucker, J. W.; Stephenson, C. R. J. Electron-Transfer Photoredox Catalysis: Development of a Tin-Free Reductive Dehalogenation Reaction. *J. Am. Chem. Soc.* **2009**, 131 (25), 8756–8757. <https://doi.org/10.1021/ja9033582>.
- (15) Romero, N. A.; Nicewicz, D. A. Organic Photoredox Catalysis. *Chem. Rev.* **2016**, 116 (17), 10075–10166. <https://doi.org/10.1021/acs.chemrev.6b00057>.



# ***Chapter II:***

## ***EXPLORATION OF THE REACTIVITY OF FREE 1- MESITYLPHOSPHIRANE: VISIBLE-LIGHT MEDIATED QUATERNARIZATION AND RING OPENING***



## 1. Introduction

Phosphorus is a pnictogen that has three main allotropes including white, red, and black phosphorus. They all display different properties such as stability (thermal, chemical...), reactivity, density, melting, and boiling points. The thermal stability spans from 30 °C (for white phosphorus) to *ca.* 550 °C for black phosphorus.

The first allotrope to be isolated was white phosphorus (P<sub>4</sub>) in 1669 during experiments carried by the alchemist Hennig Brandt. The solid he obtained from the reduction of concentrated urine in the presence of sand and coal glowed in the dark. This property is now attributed to chemiluminescence resulting from the oxidation of P<sub>4</sub> by oxygen.<sup>1</sup> This uncommon naked-eye observable property gave it its name as we know it today: Φωσφόρος (in Greek, or Lucifer in Latin) that is now spelled phosphorus, which literally means Light-Bearer.<sup>a</sup>

It is naturally found under the phosphate form in phosphate rocks. Phosphates is a chemical function essential to life as it composes part of deoxyribonucleic acid (DNA, which contains genetic information), ribonucleic acid (RNA, related to genes expression), adenosine triphosphate (ATP, for energy production in all forms of life), and bones (made of calcium phosphate). In the modern world, it is also essential to the survival of humanity as a fertilizer that allows high agricultural yields thus preventing large-scale starvation. Phosphorus along with nitrogen, represent one of the nine planetary boundaries to keep a safe operating space for humanity in the Planetary Boundaries framework.<sup>2</sup> The phosphorus cycle moved from the safe zone in 2009 to the high risk one in 2015 because of the increase of its unbalanced flow from the solid phosphate rock form to the solubilized phosphate fertilizers in oceans where the excess amount of phosphorus induces eutrophication (half of the phosphate fertilizers end up unconsumed and act as pollutants).<sup>3,4</sup> A more careful use to prevent excess flow in oceans, implementing recycling and retention systems and improving the fertilizers geographical homogeneity use around the globe are factors that could help to delay or even avoid phosphorus shortages.<sup>3</sup> Most fundamentally, bringing consciousness on the long-term effects of our decisions seems more necessary than ever.<sup>b</sup> As of now, most organophosphorus compounds are obtained industrially by phosphate rock extraction, reduction to white phosphorus by the submerged-arc furnace process, chlorination to phosphorus trichloride (PCl<sub>3</sub>) followed by the appropriated chemical reaction to obtain the desired organophosphorus compound.<sup>1</sup>

---

<sup>a</sup> General information taken from <https://www.acs.org/molecule-of-the-week/archive/w/white-phosphorus.html> and <https://en.wikipedia.org/wiki/Phosphorus>

<sup>b</sup> <https://ourworldindata.org/about> aims for instance at making the knowledge on such problems accessible

Amongst the class of organophosphorus compounds (Figure II-1), phosphirane stands as one of the most uncommon phosphines with the highest known pyramidalization.<sup>5</sup>

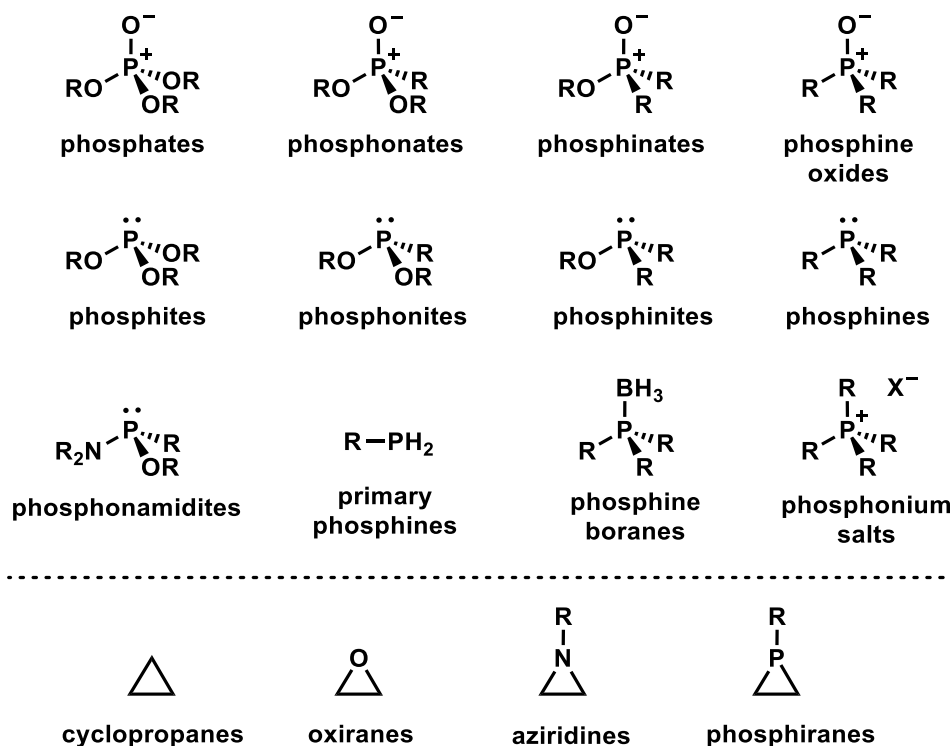


Figure II-1: Nomenclature of organophosphorus compounds and three membered rings

Little is known about it since its discovery in 1963 compared to its carbon, oxygen, and nitrogen counterparts: cyclopropane, oxirane and aziridine.<sup>6</sup> This is most likely due to its low thermal and air stability that combines with unpredictable and uncommon reactivities such as [2+1] cycloreversion, ring-chain rearrangement and polymerization.<sup>7</sup>

Free uncoordinated phosphiranes are usually unstable and tend to polymerize or decompose in different uncontrolled fashion. Therefore, most of the early work in the field was dedicated to their stabilization by tuning their steric and electronic properties. Because of the synthetic difficulty and unstable behavior, theoretical insights were of great value. Calculations assisted the rationalization of new species by providing a better understanding of phosphirane properties already from 1989 using the Hartree-Fock method,<sup>8</sup> and the interest carried out until now with a 2020 publication dedicated to a model for the prediction of the air-stability of a series phosphiranes, thus providing a guideline for the discovery of new stable phosphiranes.<sup>9</sup> Large  $\pi$ -conjugated system with bulky substituents around phosphorus along with aromatic substitution on one of the carbons of the small ring tend to be the most stabilizing patterns.

1-mesitylphosphirane already stood out as an ideal compromise between reactivity and stability in 1994,<sup>10</sup> the ortho-methyl groups from the mesityl moiety protecting the phosphorus through

steric hindrance (Figure II-2).<sup>9,11</sup> This phosphirane was selected as the phosphirane of choice for our work.

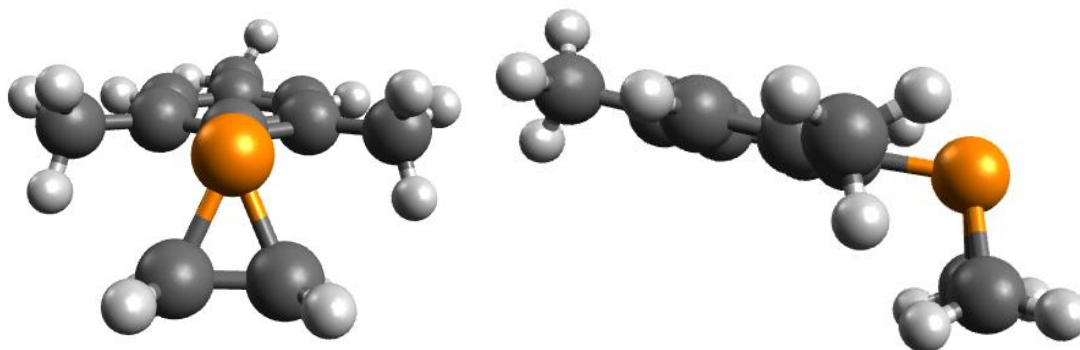


Figure II-2: DFT calculated 3D structure of 1-mesitylphosphirane. B3LYP and def2-TZVP parameters, more details on the calculation's methodology in part 2.6.

The HOMO of 1-mesitylphosphirane shows in Figure II-3 that, in addition to the phosphorus lone pair, the HOMO bears significant contributions from both the aromatic and the 3-membered ring, in line with the low nucleophilicity observed for phosphiranes.

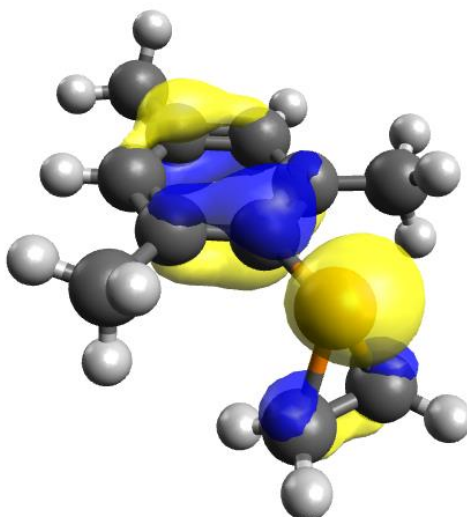


Figure II-3: DFT calculated HOMO of 1-mesitylphosphirane. B3LYP and def2-TZVP parameters, more details on the calculation's methodology in part 2.6.

Most notably, Mathey and Marinetti developed the tungsten coordinated phosphirane chemistry which encompasses the vast majority of the known reactivity of phosphiranes as it provides a stabilized version to work with.<sup>12</sup> We purposely won't discuss this chemistry in its totality as our work focuses on free phosphirane reactivity as a much less explored area. Selected examples will however be given along the course of this introduction.

The original synthesis of phosphirane was accidentally discovered by Wagner and coworkers when they attempted to synthesize 1,2-diphosphinoethane (Figure II-4). It consisted in the

reaction of the phosphinide ion  $\text{NaPH}_2$  with 1,2-dichloroethane in liquid ammonia and provided the room temperature unstable phosphirane up to 74% yield.<sup>6</sup>

**Original synthesis - 1963**

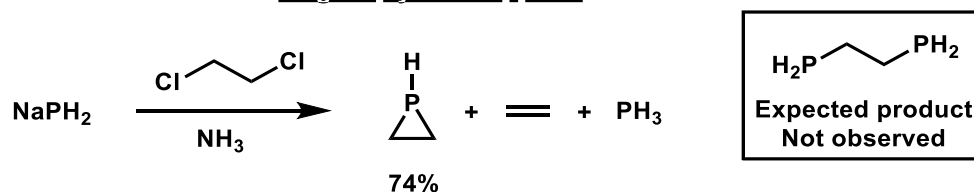


Figure II-4: Original phosphirane synthesis by Wagner and coworkers

Other approaches were then developed. We propose here to look at three different routes, which are the deprotonation of a primary phosphine and subsequent reaction on an ethyl moiety substituted by two leaving groups on each carbon (approach a), the attack of a phosphide anion on an oxirane (approach b), and the reaction of a phosphinidene with an alkene (approach c) (Figure II-5).

**Phosphiranes synthetic pathways**

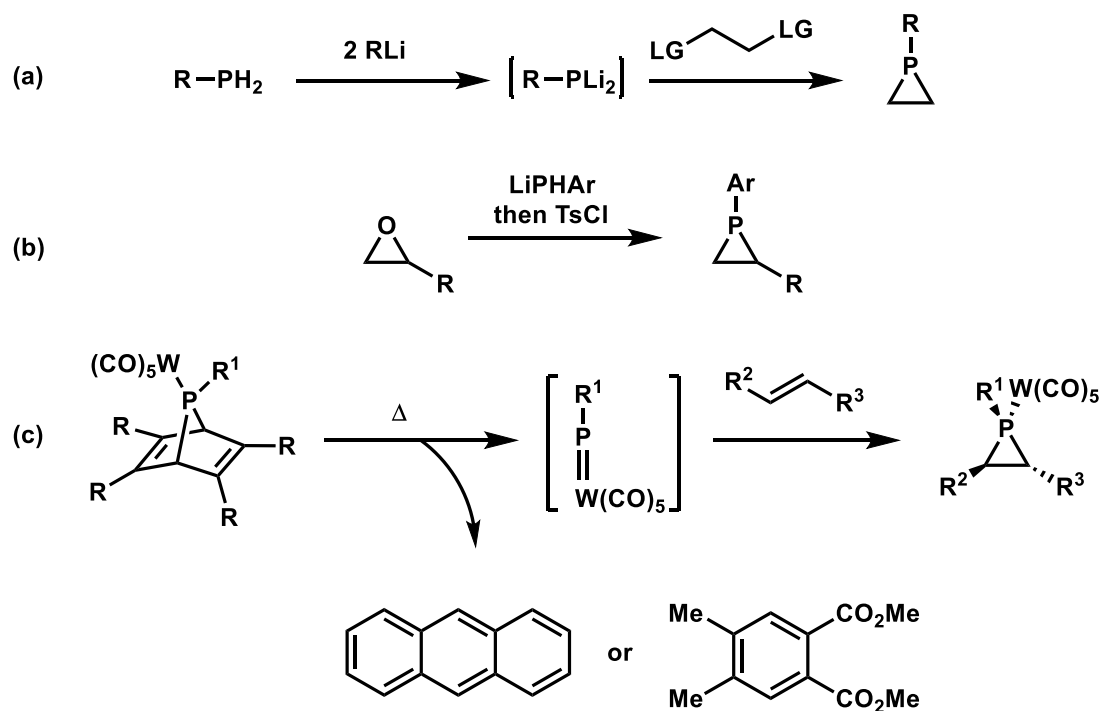


Figure II-5: Phosphiranes synthetic pathways : general overview

Primary phosphines are usually synthesized by the reduction of the corresponding dichlorophosphine with lithium aluminum hydride ( $\text{LiAlH}_4$ ). A manganese-mediated method developed by Montchamp and Berger allows for the C-H functionalization of aryl moieties with H-phosphinates and H-phosphonates. The resulting products can be reduced by  $\text{LiAlH}_4$  to the corresponding primary phosphine after acidification.<sup>13</sup> Primary phosphines can then be

deprotonated by methyl lithium to provide the corresponding lithiated phosphide that can subsequently react with 1,2-dichloroethane (or similar moieties where chlorines are replaced by good leaving groups such as triflates) to provide the corresponding phosphirane. Figure II-6 shows this method applied to the formation of 1-mesitylphosphirane as developed by Botella *et al* in 2021.<sup>14</sup>

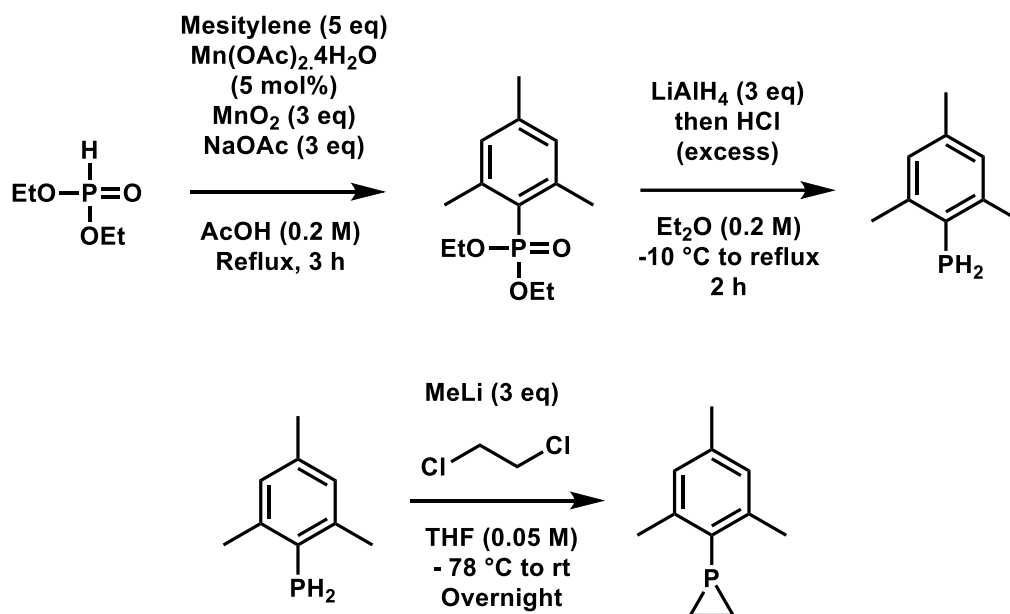


Figure II-6: 1-mesitylphosphirane synthesis according to Botella *et al*.

Ring opening of oxiranes with phosphides leads to the alcoholate. Addition of tosyl chloride turns the alcoholate into a tosylate, which is a good leaving group that favors the phosphirane ring formation (Figure II-7). Glueck and coworkers have recently dedicated significant efforts to understand the peculiar behavior of chiral phosphiranes and their phosphiranium salt counterparts during such synthesis.<sup>15–17</sup>

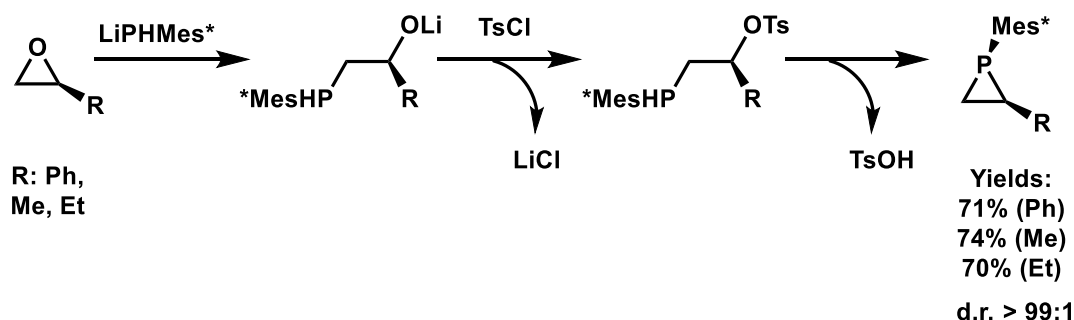


Figure II-7: Synthesis of phosphirane by attack on oxirane derivatives.  $\text{Mes}^*$ : supermesityl or 2,4,6-tri-*tert*-butylphenyl. Me: Methyl, Et: Ethyl, Ph: Phenyl, Ts: Tosyl or *p*-toluenesulfonyl

They studied the inversion of configuration at phosphorus in the diastereoselective and enantioselective synthesis of P-stereogenic syn-phosphiranes from chiral epoxides, as well as the P-epimerization of phosphiranium cation at  $60^\circ\text{C}$  in  $\text{CD}_2\text{Cl}_2$ . In both cases, the surprising

P-inversion, which usually has a high barrier to pyramidal inversion, was observed. Interestingly, the usually configurationally stable phosphorus center epimerized and the labile carbocation retained its configuration.

Finally, the synthesis using phosphinidene intermediates is made largely possible thanks to phosphanorbornadiene derivatives. Upon heating ( $\sim 100\text{ }^{\circ}\text{C}$ ), they release an aromatic structure that is usually either anthracene or 4,5-dimethylphthalic acid diethyl ester and the corresponding metal coordinated phosphinidene (Figure II-8).<sup>18</sup> Using these structures, heating can remain gentle and allows the success of the cycloaddition reaction, otherwise the low thermal stability of the phosphinidene leads to decomposition.<sup>19</sup>

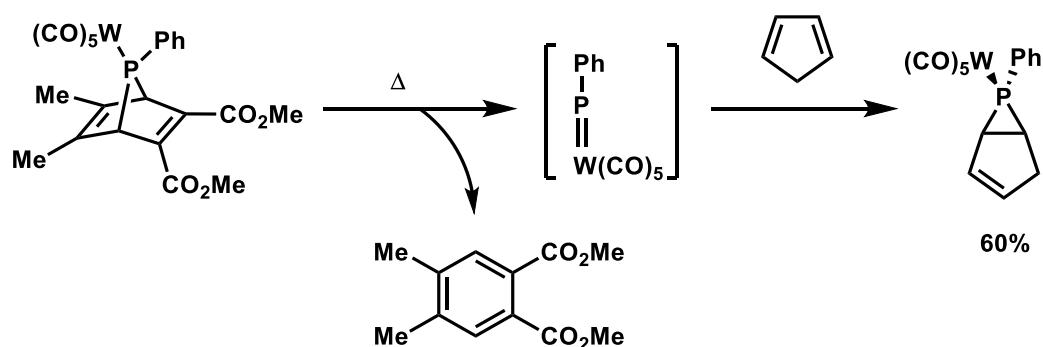


Figure II-8: Synthesis of tungsten coordinated phosphirane by 2+1 cycloaddition via phosphinidenes

A successful free phosphinidene version was published in 2017 by Cummins and coworkers using dibenzo-7-phosphanorbornadiene with dialkylamino substituents on phosphorus (Figure II-9). The aminophosphinidene reacted from its singlet state as shown by the stereospecificity of the cycloaddition on *cis*-4-octene. This was further supported by the absence of stereochemical deviation when the phosphinidene was reacted with *trans*-4-octene.<sup>20</sup> Furthermore, due to their high reactivity, singlet phosphinidenes are expected to react with alkenes in a barrierless fashion.<sup>21</sup>

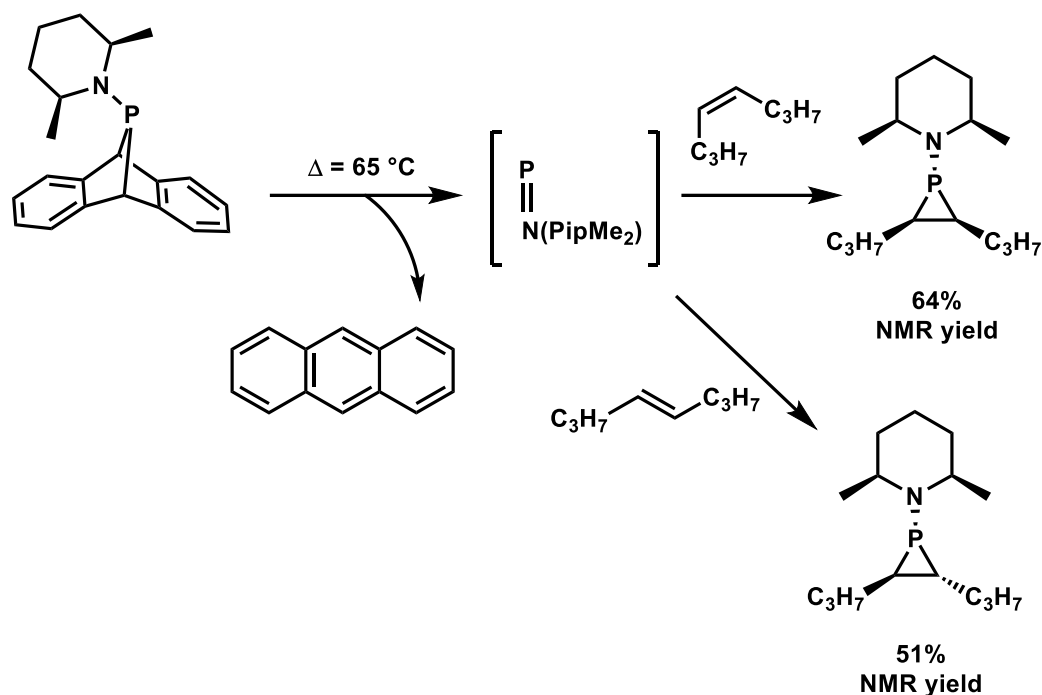


Figure II-9: Free phosphirane synthesis via the generation of singlet state stabilized aminophosphinidenes. PipMe<sub>2</sub> : *cis*-2,6-dimethylpiperidino

Phosphiranes reactivity is usually investigated from four perspectives: reactions with retention of the ring, reactions with cleavage of one P-C bond, reactions with cleavage of two P-C bonds, and reactions with ring extension. Amongst these reactivities, we will focus on four behaviors of phosphiranes: their coordination to metal centers, their reactivity with electrophiles to generate the corresponding phosphiranium salts, their uncommon ability to generate phosphinidenes, and their ring opening through ring strain release by attack on either the phosphorus or the carbon atom. Phosphiranes reactivity can be so diverse and unique depending on the substituents that it cannot be fully covered in this introduction. The selected examples however are meant to give an overall picture of their reactivity, except ring enlargement.

### Coordination to metal centers

We will distinguish two types of coordination: the coordination enabling the stabilization of phosphirane, and the one whose purpose is to modify metal-ligand complexes properties.

The most used metal complexes to stabilize phosphiranes are generally carbon monoxide complexes of tungsten ( $\text{W}(\text{CO})_5$ )<sup>21</sup> or molybdenum ( $\text{Mo}(\text{CO})_5$ ).<sup>7</sup> Chromium has also been used for such purpose.<sup>22</sup> Coordination modifies the properties of the free phosphirane. It usually makes it more prone to nucleophilic attacks while stabilizing it against oxygen and thermal decomposition. Decomplexation is possible under pressure of carbon monoxide of *ca.* 25 bars while heating at *ca.* 60 °C.<sup>7</sup>

Phosphiranes display specific properties that are required to fill the gaps of the stereoelectronic properties map of phosphine ligands.<sup>23</sup> There are only few examples where they have been used as exotic ligands.

An iridiumphosphirane complex was studied in 1997 in an attempt at showcasing the unusual properties of phosphirane compared to other phosphine ligands. The synthesis of the stable metal-free bulky phosphirane, 1-tert-butylphosphirane, was a key step towards this goal.<sup>24</sup>

A specific phosphirane ligand, BABAR-Phos (Figure II-10), was designed in 1999 by the group of Grützmacher.<sup>25</sup> The synthesis of this ligand occurs through the generation of an aminophosphinidene, which is formed from the corresponding phosphorus dichloride in a magnesium mediated reaction. An intramolecular [2+1] cycloaddition of the aminophosphinidene with the double bond takes place to yield the ligand in good yields. To prevent undesirable side reactions, the strained ring is stabilized by a polycyclic cage. BABAR-Phos ligands are not oxidized by oxygen or sulfur, do not undergo alkylation in the presence of strong alkylating agents, and do not degrade in the presence of aqueous acids and bases.<sup>26</sup> The phosphorus is strongly pyramidalized, which has important consequences when BABAR-Phos acts as a ligand, mainly for the improvement of its  $\pi$ -accepting properties.<sup>27</sup> This ligand was successfully used in platinum catalyzed hydrosilylation where other phosphine ligands displayed very poor reactivities,<sup>28</sup> and in rhodium catalyzed hydroboration reactions where the BABAR-Phos rhodium complex showed great O<sub>2</sub> and thermal stabilities over time compared to its triphenylphosphine equivalent.<sup>26</sup> This increased stability allowed its efficient recyclability.<sup>26,28</sup> Notably, an unprecedented reversible rhodium insertion into the three membered ring P-C bond was described.

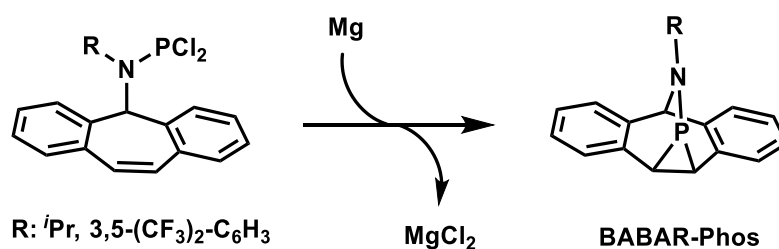


Figure II-10: Synthesis of BABAR-Phos ligand

1-trimethylsilylphosphirane was used as a ligand as well as a masked phosphirane (C<sub>2</sub>H<sub>4</sub>PH) in molybdenum (Figure II-11), chromium and iron organometallic complexes.



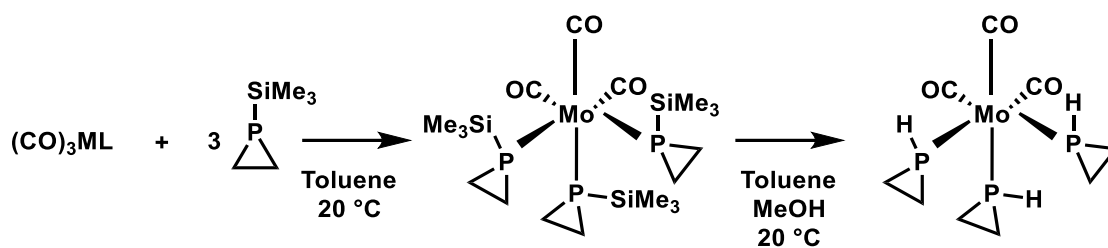


Figure II-11: 1-trimethylsilylphosphirane as a phosphine ligand and a masked phosphirane

Finally, several stereogenic metal-phosphirane complexes were reported in 2018 with gold, palladium, platinum, and rhodium. Both *syn* and *anti*-isomers of the same phosphirane were synthesized and studied (Figure II-12). The very bulky super-mesityl substituent was used on the phosphorus as a stabilizer to make manipulation under air easier, both for synthesis and further use. This work confirmed the poor  $\sigma$ -donor and good  $\pi$ -acceptor properties of phosphiranes.<sup>17</sup> It also opened the way for potential applications of metal-phosphirane complexes in asymmetric catalysis.

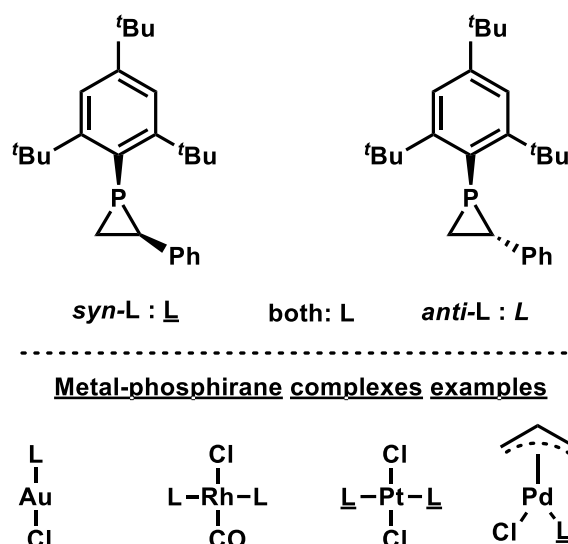


Figure II-12: Examples of metal-phosphirane complexes. L: ligands.

### Nucleophilic attack on electrophiles: Formation of phosphiranium salts

In 1990, phosphiranium salts were considered unstable and none had been isolated. The low nucleophilicity of phosphiranes was considered responsible for their decomposition in the presence of Bronsted acids or quaternizing agents.<sup>21</sup> Further development of the substituents on phosphorus and of reaction conditions allowed their stability to be improved and extended, starting in 1995 with a study by Wild and coworkers, who reported the first characterized phosphiranium salt as colorless crystals.<sup>29</sup> This was a huge leap as phosphiranium salts went from unstable to isolated and characterized with an assessed stability of several weeks under

argon. They used methyl trifluoromethanesulfonate ( $\text{CF}_3\text{SO}_3\text{Me}$ , or  $\text{MeOTf}$ ) as the alkylating agent, which resulted in 73% isolated yield of phosphiranium triflate (Figure II-13).

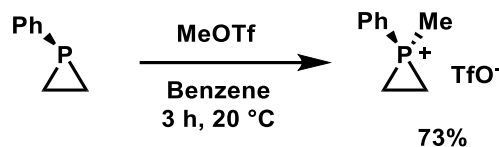


Figure II-13: Synthesis of methylphenylphosphiranium salt

Interestingly, phosphiranium salts in the presence of alkynes slowly exchange towards phosphirenium salts in high yields (Figure II-14).<sup>29,30</sup> Phosphirene and phosphirenium salts are another important part of phosphirane chemistry and is intentionally not discussed in this introduction. We note that many similarities exist between phosphirane and phosphirene and their derivatives as depicted by the opening paragraph of the most recent book chapter on phosphiranes and phosphirenes, which describes them both together as having CPC angles around  $50^\circ$  with very strained rings and important pyramidalization on the phosphorus center, which increases significantly their barrier of inversion as well as increasing the s character of the lone pair.<sup>31</sup> This high s character of the lone pair makes phosphiranes poor Lewis bases, in addition to their poor nucleophilicity, compared to other phosphines.

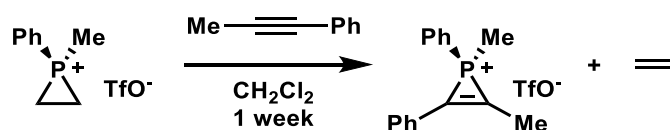


Figure II-14: Uncommon synthesis of phosphirenium salt

In 2011, the reaction of 1-([1,1'-binaphthalen]-2-yl)phosphirane with methyl trifluoromethanesulfonate presented by Higham and coworkers resulted in its quaternarization to the corresponding stable chiral phosphiranium salt (Figure II-15).<sup>19,32</sup> This achievement was possible thanks to works by the same group dedicated to find air-stable primary phosphines, a stability that usually transposes to phosphiranes and phosphiranium salts.<sup>33–35</sup> The same year, the group of Erker unlocked the access to phosphiranium borates zwitterions with the reaction between acetylene  $\text{Mes}_2\text{P-CC-Ar}$  and  $\text{B}(\text{C}_6\text{F}_5)_3$ .<sup>36</sup>

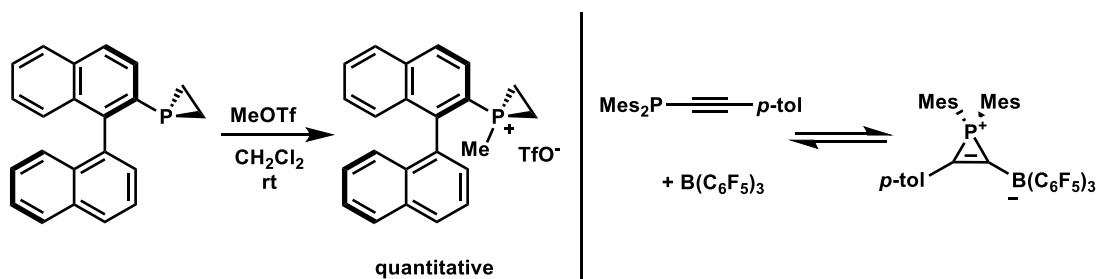


Figure II-15: Stable chiral phosphiranium salt synthesis (left) and phosphiranium borates zwitterion synthesis (right), *p-tol* : *para-tolyl*

A stable version of this phosphiranium borate zwitterion was obtained in 2018 by the same group by modifying  $B(C_6F_5)_3$  to  $ClB(C_6F_5)_2$ .<sup>37</sup>

Until 2020, all other quaternization reactions were done using MeOTf. The scope of this reaction was extended by the group of V. Dalla, using different alkyl triflates with arylphosphiranes (Figure II-16). In the same publication, the counteranion was changed from triflate to hexafluorophosphate for the first time using arylodonium salts as the quaternizing agents in a copper-catalyzed reaction.<sup>38</sup> Unfortunately, most of the phosphiranium salts were not stable and could not be purified. They were involved in the subsequent reactions without purifications.

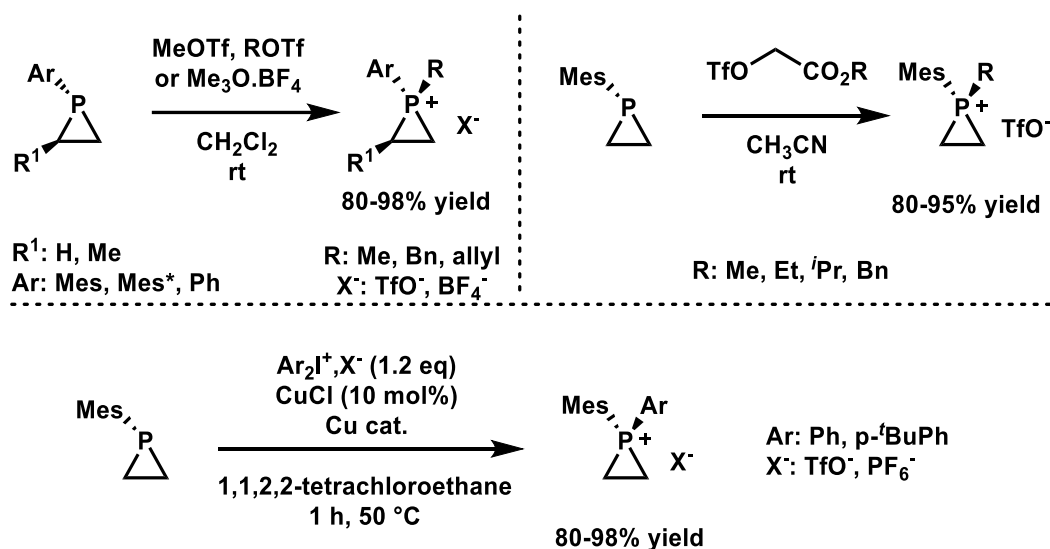


Figure II-16: Synthesis of multiple phosphiranium salts. Ar : Aryl, Mes : mesityl or 2,4,6-trimethylphenyl, Bn : Benzyl, <sup>i</sup>Pr : isopropyl Tf : triflyl

More recently, in 2023, Glueck and coworkers showed that protonation of 2-methyl-1-supermesitylphosphirane with triflic acid did not yield a stable product but led to ring opening and insertion of the phosphorus atom in a *tert*-butyl C-H bond (Figure II-17).<sup>39</sup>

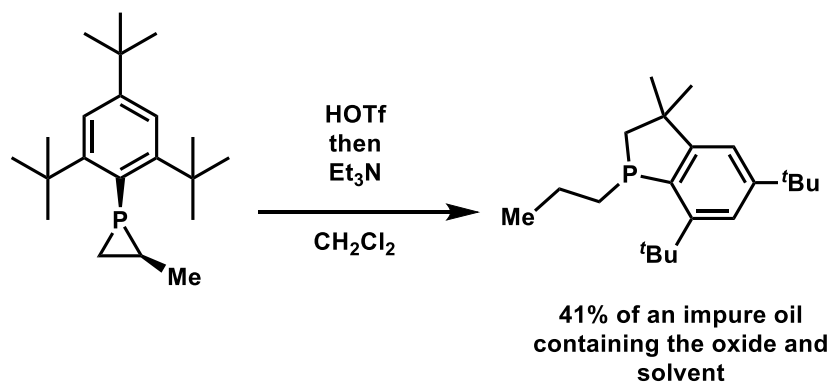


Figure II-17: Behavior of 2-methyl-1-supermesitylphosphirane in the presence of triflic acid

However, the scope of the synthetically useful quaternarization is limited by the intrinsic low nucleophilicity of phosphiranes and very little is still known about phosphiranium salts.<sup>15</sup>

### Phosphinidene generation

As briefly discussed before, phosphinidenes are key species for the synthesis of phosphorus-based molecules, including phosphiranes. They are the phosphorus equivalent of carbenes, nitrenes and silylenes. These phosphorus six-electron species were discovered in the 1980s and nicely reviewed in 2003 by Lammertsma.<sup>40</sup> Two classes exist that distinguish the singly-bonded free phosphinidenes (RP) from complexed phosphinidenes that are stabilized by an additional substituent (Figure II-18). A great deal of attention has been given by the scientific community to develop the access to phosphinidenes and the assessment of their properties and behavior, both in triplet and singlet state.<sup>40</sup> Phosphinidenes are in close relationship with phosphiranes for they can be used to access them or be generated from them. Knowledge about their behavior is important to recognize their potential implication as reaction intermediates.

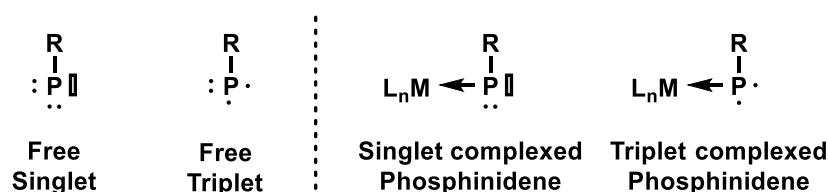


Figure II-18: Singlet and triplet phosphinidenes representation

Phosphinidene complexes can either be electrophilic or nucleophilic depending on the substituents of the coordinated metal center. The nature of the metal center itself proved to have little impact. However, with ligands such as cyclopentadienyl, a strong  $\sigma$ -donating ligand, the electron density on the phosphorus increases providing nucleophilic phosphinidenes. The energy of the  $\pi^*$  orbital of the complexed phosphinidenes increases along with their stability. On the other hand, electrophilic phosphinidenes are obtained when electron withdrawing ligands such as carbon monoxide are used on the metal, a substitution that comes with a decrease of the electron density on phosphorus. Electrophilic phosphinidenes are usually extremely reactive and unstable, and act as transient species only. Both types exist predominantly in their singlet state.

The opposite trend is observed for free phosphinidenes, which commonly display a triplet ground state. Nguyen and coworkers performed calculations that were of great support in the search for singlet state phosphinidenes. They used a calculated  $\Delta E_{ST}$ , the gap in energy between the triplet and singlet states, as a means of estimating which spin state of the phosphinidene

would be favored depending on the substitution pattern. The substitution pattern was proven to have a strong impact and that singlet states become favored in the case of aminophosphinidene and phosphinophosphinidene.<sup>41</sup>

Later on, Bertrand and coworkers isolated a room temperature stable singlet phosphinidene in 2016: a milestone for phosphinidene chemistry.<sup>42</sup> In a similar fashion, carbenes were only considered as curiosities before their isolation and characterization. It is only then that they became widely used as highly reactive carbon-based chemical tools. Phosphinidenes might be taking the same turn in the future. The important steric hindrance from an extremely bulky aromatic moiety (Figure II-19) was necessary to prevent the singlet phosphinidene from dimerizing towards the more stable diphosphene.

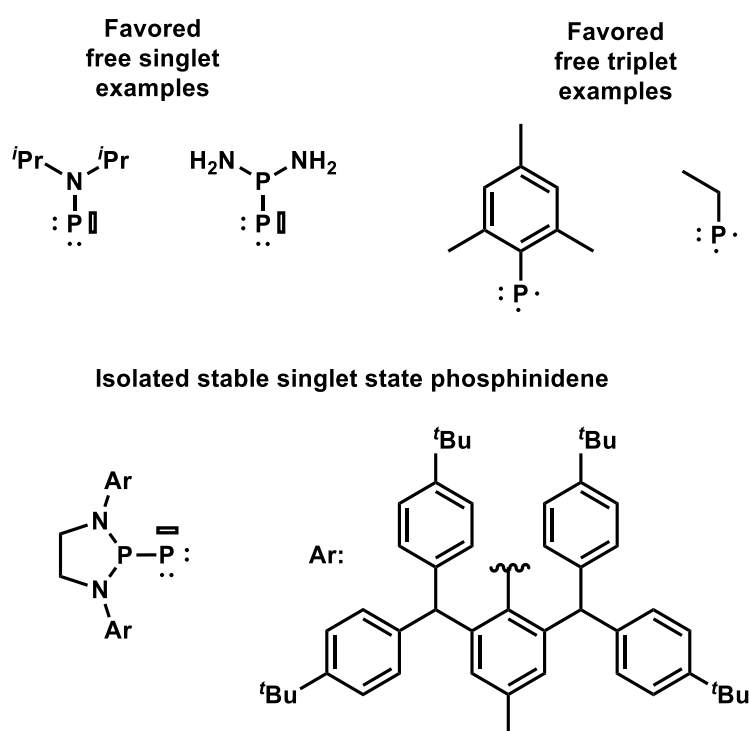


Figure II-19: Free singlet and triplet phosphinidenes examples

Most notably in the case of phosphirane, Gaspar and coworkers suggested to have generated free triplet state mesitylphosphinidene from 1-mesitylphosphirane either by UV light irradiation or by pyrolysis at 190 °C.<sup>43</sup> Their assumption was supported a few years later by the observation of an EPR signal of a UV light irradiated 2,3-dimethyl-1-mesitylphosphirane solution in glassy methylcyclohexane (MCH) at 77 K. They assigned this signal to triplet mesitylphosphinidene. Their observation could not be reproduced by the group of Lammertsma,<sup>44</sup> and what was assigned to triplet phosphinidene was shown in two subsequent papers to be the EPR signal of triplet oxygen in the frozen medium.<sup>45,46</sup> Gaspar himself later doubted that pyrolysis of phosphirane could lead to phosphinidenes, and acknowledged what

Mathey supported: free phosphinidenes were only supposed as intermediates based on reaction products that could always be obtained via an alternative pathway, and it was very likely that they were in fact not generated in the reaction disclosed.<sup>47</sup>

Further multiple works confirmed however the formation of triplet phosphinidene upon UV irradiation of 1-mesitylphosphirane. Reassignment of the EPR signal was done in strict oxygen-free conditions and the same EPR spectrum was obtained regardless of whether 1-mesitylphosphirane or 2,3-dimethyl-1-mesitylphosphirane was irradiated.<sup>46</sup> IR, UV-Vis and transient laser flash photolysis studies also unambiguously confirmed the formation of triplet mesitylphosphinidene, closing that debate.<sup>46</sup> Its lifetime was measured to be 13  $\mu$ s and two transient absorption bands were observed: a strong one at 285 nm and a weak one at 400-475 nm. EPR studies were extended to other phosphinidenes in 2020 as depicted in Figure II-20.<sup>48</sup>

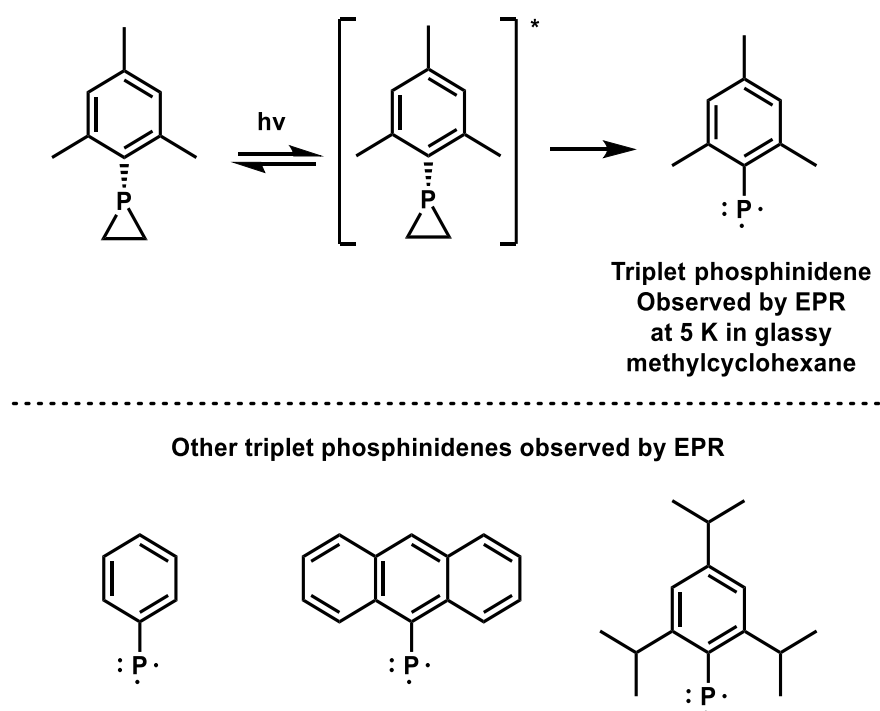


Figure II-20: Triplet phosphinidenes observed by EPR

1-mesitylphosphinidene is therefore generated by UV light induced fragmentation of 1-mesitylphosphirane but most likely not by its thermal fragmentation.

The evolution of 1-mesitylphosphinidene in the absence of coupling partners showed the presence of different by-products (Figure II-21). Cyclic trimers and tetramers of mesitylphosphinidene were the major products of the reaction. The unstable vinyl(mesityl)phosphine resulting from a stepwise ring opening and hydrogen atom transfer from carbon to phosphorus atom accounted for 8% of the products and the primary mesitylphosphine was identified as 1% of the products.

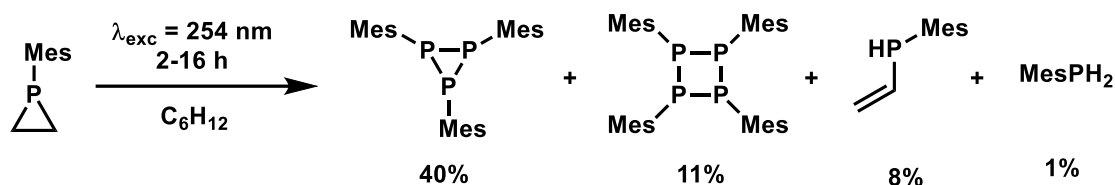


Figure II-21: Photolysis of mesitylphosphirane under UV light irradiation

The reactivity of triplet 1-mesitylphosphinidene was highlighted through the reaction with various partners such as alkynes, alkenes, and dienes. The ratio of products is shown in Figure II-22 where conversions between 16 and 55% were obtained.

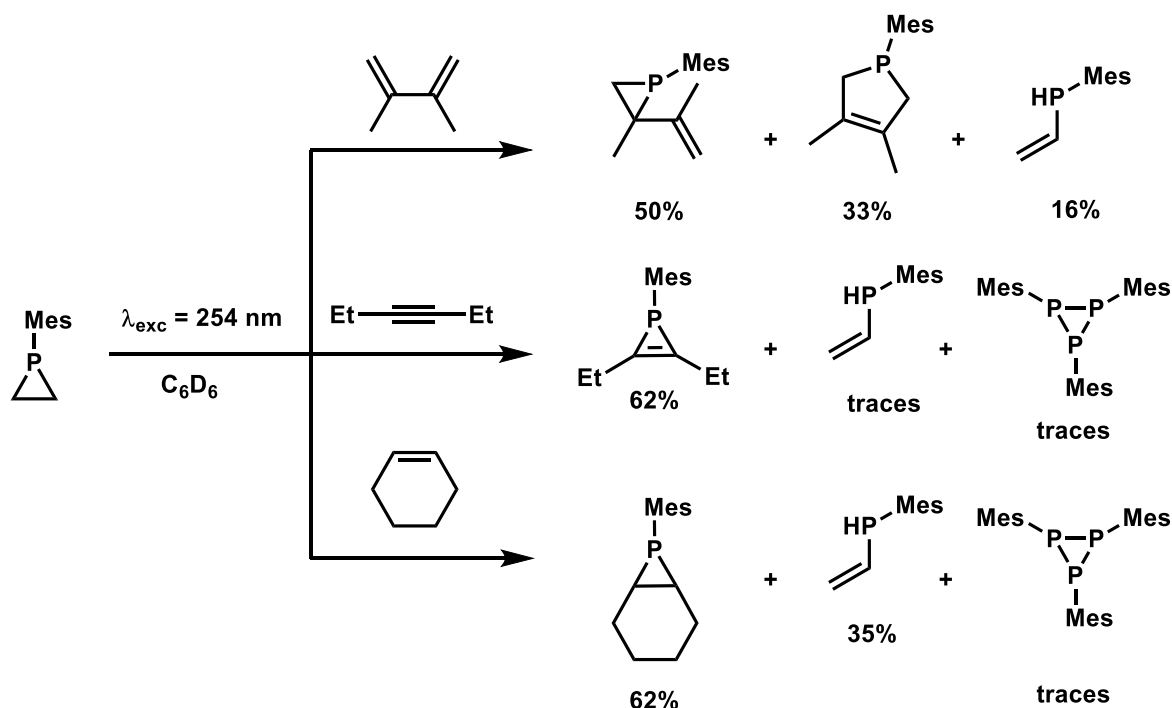


Figure II-22: Reactivity example of 1-mesitylphosphirane under UV light irradiation

Interestingly, modification of the substituent on phosphorus from mesityl to supermesityl (methyls replaced by *tert*-butyls) completely modified the reactivity and triplet phosphinidene could not be observed at all, even in further studies.<sup>48</sup> Instead, C-H insertion from the singlet state phosphinidene occurred prior to any ISC (Figure II-23).

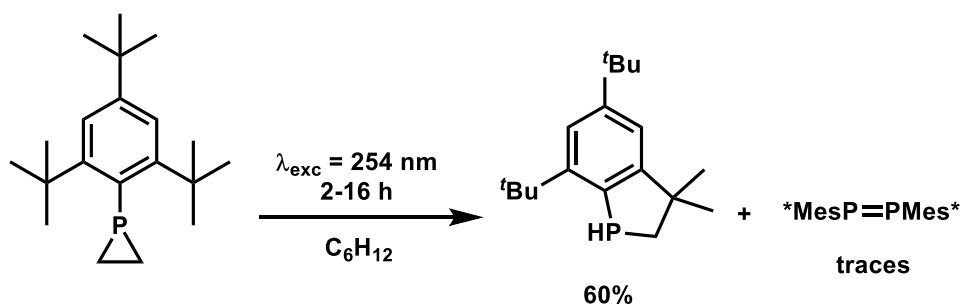


Figure II-23: Uncommon behavior of 1-supermesitylphosphirane under UV light irradiation

Phosphinidene chemistry is not straightforward and is to this day still not very well understood. Many different competitive reactions pathways come into play, and when irradiation is used, by-products can also absorb UV-light in a secondary activation. This field would clearly benefit from further clarifications and investigations.

### Ring opening

Phosphiranes are subject to ring opening. This is one of their most unique and interesting properties, that requires further development to find applications. In oxirane and aziridine, the electronegativity of the heteroelement is higher than the one of adjacent carbon atoms. The consequence is that the carbon atoms of the strained ring are more electrophilic and that nucleophilic attack on these systems will occur exclusively on the carbon followed by ring opening. Almost all the chemistry of oxiranes and aziridines stands on this ground. Activation of these rings to promote ring opening is sometimes necessary. For instance, aziridines can be quaternarized to aziridinium salts to increase the electrophilicity of the adjacent carbon atom and ease the ring opening.<sup>11</sup>

For phosphirane however, the polarity of the carbon-heteroatom bond is inverted: phosphorus is more electrophilic than the carbons. From this point, nucleophilic attacks can occur on both phosphorus or carbon sites and make the reactivity richer and the selectivity much more complex. Clean and efficient carbon centered ring opening is one of the current main challenges in phosphirane/phosphiranium chemistry. The following examples are an attempt to show the difficulty of such task.

An example from 1984 shows the ring opening of a vinylphosphirane derivative by the phosphonium ylide methylenetriethylphosphorane (Figure II-24). The attack occurs on the phosphorus atom and leads to the open product after hydrogen transfer in 85% overall yield.<sup>49</sup>

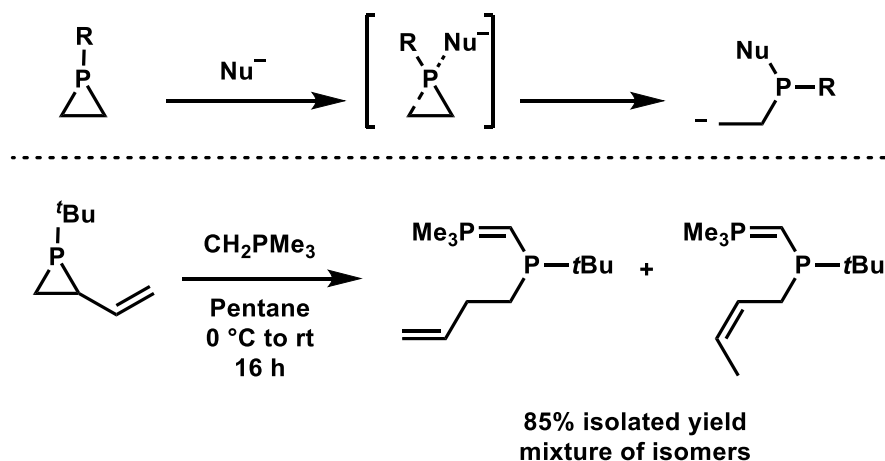


Figure II-24: Phosphirane ring opening by a nucleophile



Ring opening reactions were mainly studied with tungsten coordinated phosphiranes. Three possibilities exist, namely the C-attack, the P-attack and deprotonation of one of the carbons of the ring followed by a rearrangement (Figure II-25).

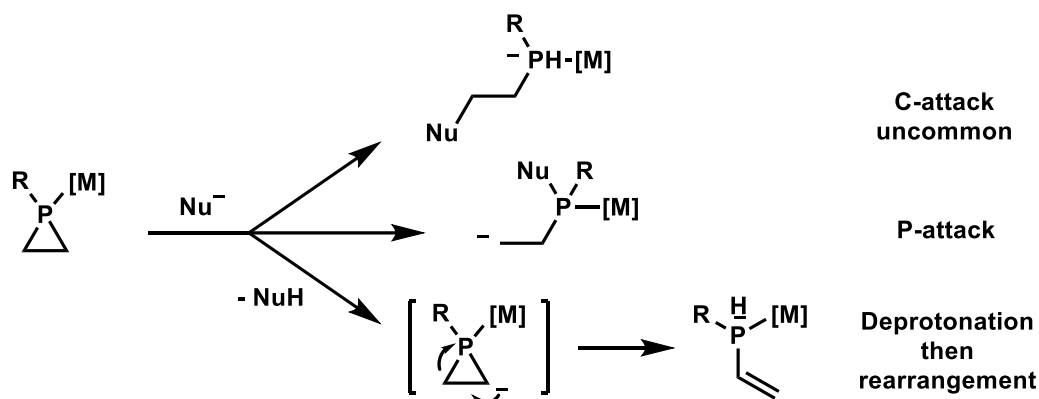


Figure II-25: Pathways for ring opening with metal coordinated phosphiranes

The first example of ring opening in this context with an attack on the carbon was published by Mathey and coworkers in 2016 (Figure II-26). An electron deficient group ( $\text{CO}_2\text{Me}$ ) was installed on the phosphorus that assisted the C-centered attack by diethylamine. The reaction proceeded at high temperatures and required long reaction times. The reaction was carried out on a 1 mmol scale (450 mg of starting phosphirane) and allowed the isolation of 58 mg of the product after purification over silica gel with an ethyl acetate 10:1 methanol mixture as the eluent. The fate of the ester is unknown and thus will not be discussed. Steric hindrance was invoked as the reason for this unorthodox reactivity without further development. This example clearly highlights the complexity of the C-centered ring opening reactivity.<sup>50</sup> On the other hand, two examples of P-attack are displayed in the same Figure (II-26), either by an oxygenated nucleophile (ethoxide anion) or by an amide anion (aniline anion), which provided the P-centered ring opening products in good yields. When the nucleophile is aprotic ( $\text{EtO}^-$ ), a protic medium ( $\text{EtOH}$ ) was necessary to protonate the carbanion obtained after ring opening. If the nucleophile is protic ( $\text{PhNH}^-$ ), then deprotonation from the carbanion occurs intramolecularly, and generates an amide that can be alkylated with methyl iodide to provide the methylated aminophosphine.<sup>12</sup> In the same paper, phosphorus nucleophiles had a very different behavior that led to the loss of styrene with two P-C bond breaking instead of ring opening with a single P-C bond breaking.

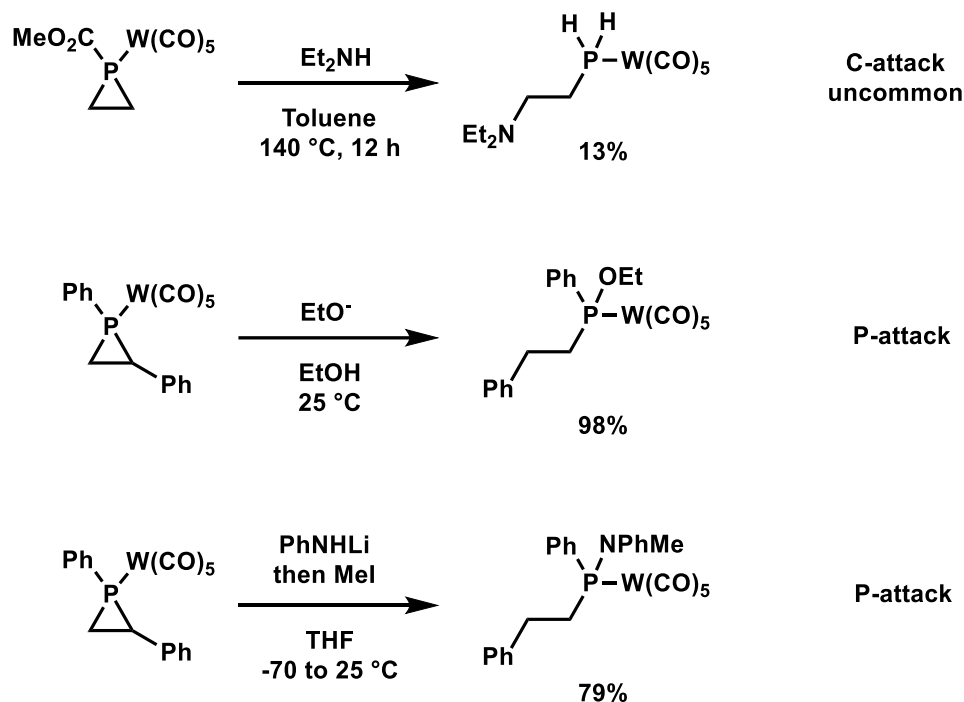
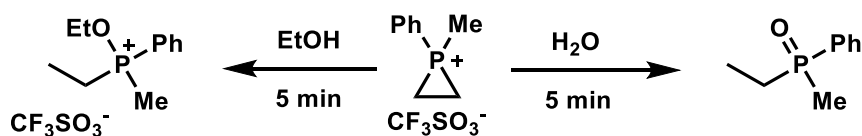


Figure II-26: Examples of ring opening of tungsten coordinated phosphiranes

The other known ring openings occur with phosphiranium salts. As mentioned before, they should be more prone to C-centered ring opening than phosphiranes. However, until 2020, only one C-centered ring opening was known: polymerization of supermesitylphosphirane with a cationic initiator.<sup>51</sup> P-centered ring openings occurred with oxygenated nucleophiles (water or alcohols) to provide either the phosphine oxide or the corresponding phosphonium salt (Figure II-27).<sup>29</sup>

### Phosphiranium P-centered ring opening



### Phosphiranium C-centered ring opening before 2020

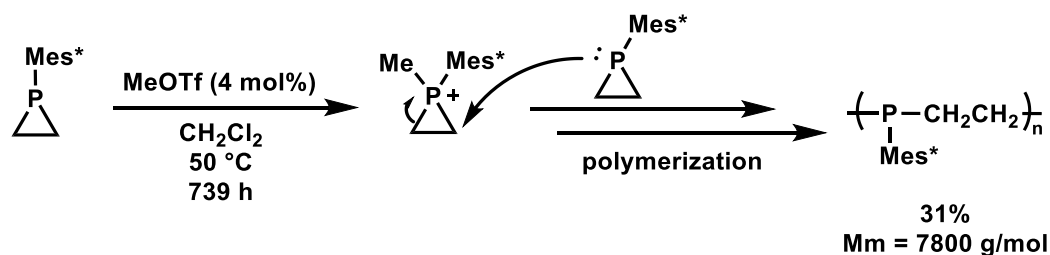


Figure II-27: Known examples of ring opening of phosphiranium salts prior to 2020

In 2020, an interesting development of the phosphiranium ring-opening chemistry was reported with the C-centered efficient nucleophilic ring opening of phosphiranium salts with aniline derivatives described by Dalla and coworkers.<sup>11</sup> A mixture of mono and di addition products was obtained with the mono addition product being highly favored, usually above 90% (Figure II-28).

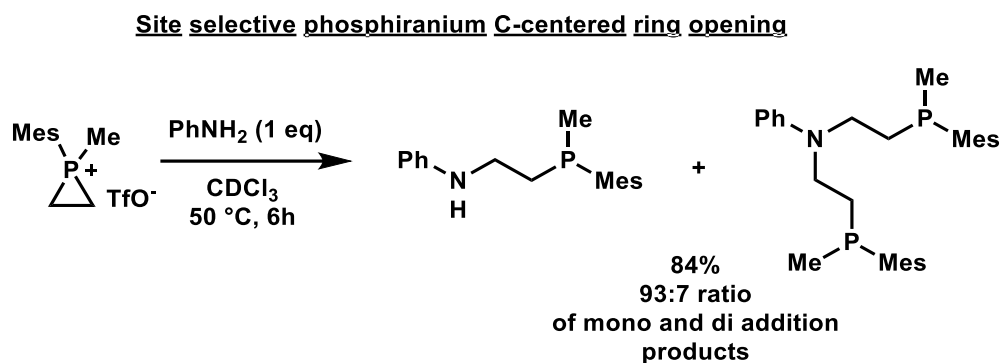


Figure II-28: First C-selective phosphiranium ring opening with aniline

A bulky substitution pattern on the phosphorus proved important for the reaction success, as both mesityl and supermesitylphosphiranes worked well under these conditions while phenylphosphirane failed to provide the expected product. Anilines with *para* electron donating groups (EDG) reacted faster than anilines with *para* electron withdrawing groups (4.5 hours against 5 days) but provided lower yields (59% against 80%). A higher reactivity might mean less selectivity and more by-products in that case, such as attack on phosphorus. The methyl substituent carried by the phosphorus atom of the phosphiranium salt was successfully modified to allyl, phenyl, or methylene ester. The authors hypothesized that the low yield obtained with methylene ester (27%) was due to side P-addition product and managed to increase the yield to 66% by making the nucleophile bulkier (mesitylamine). However, the reaction worked at room temperature in contrast to the 50 °C required in most cases, which in their protocol was a sign of excellent reactivity (Figure II-29).

**Scope selected examples**  
(Time, Temperature, Yield,  
Ratio of mono and di-substituted products)

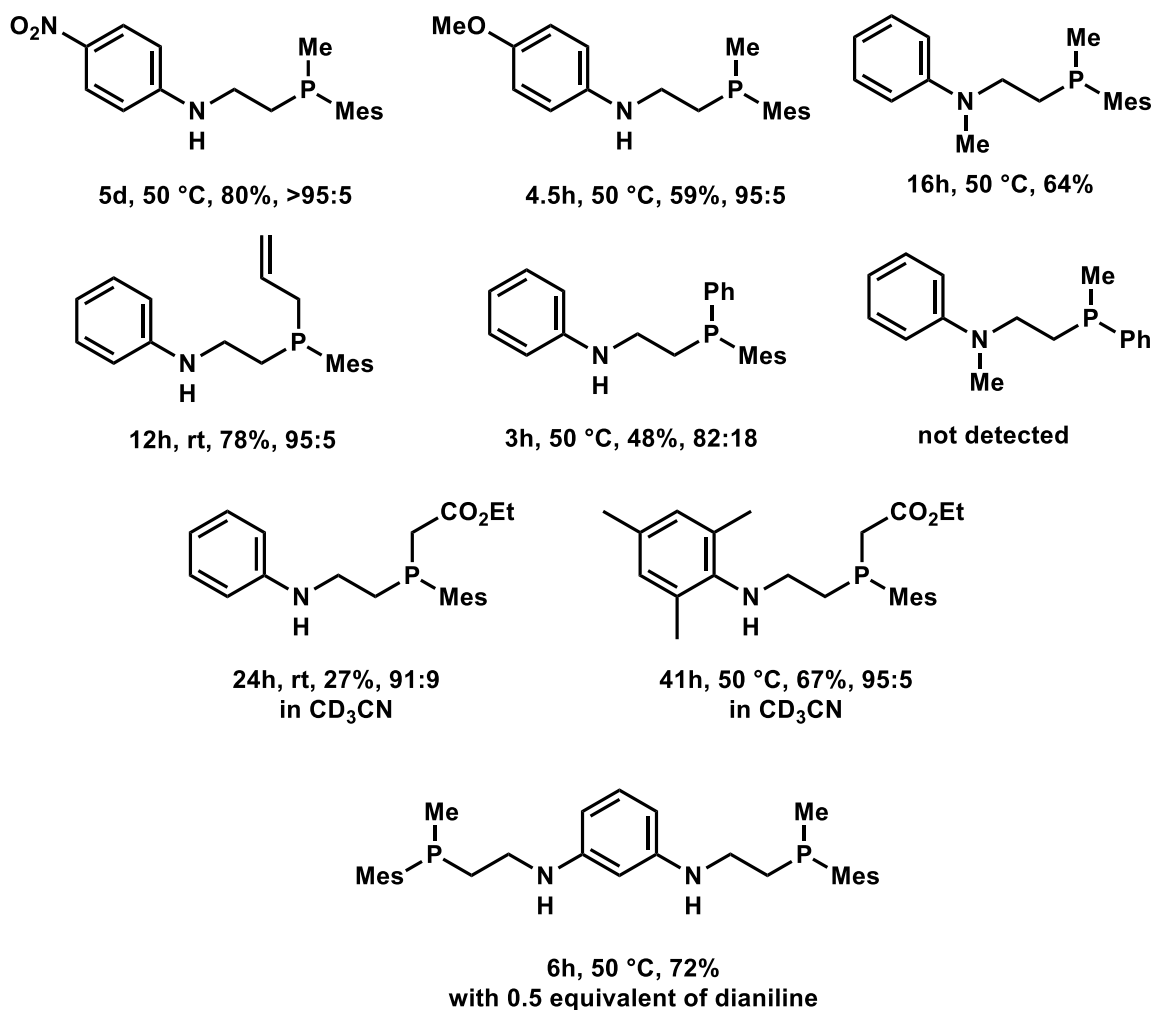


Figure II-29: Scope of the C-selective phosphiranium ring opening with aniline derivatives

This remarkable development of the selective ring opening of phosphiranium salts on the carbon atom was however limited to aromatic nitrogen nucleophiles. The reactivity with oxygen nucleophiles occurs preferentially on the phosphorus atom center, leading to the formation of phosphine oxides. It is in this context that, in a collaborative project with Dalla and coworkers, supported by the ANR, we were interested in developing an unprecedented methodology allowing the regioselective ring opening of phosphiranium salts with oxygen-based nucleophiles. This chapter details the rational design of a new type of phosphiranium salt and its reactivity with sulfur and oxygen nucleophiles.

## 2. Results and discussion

### 2.1. Phosphirane synthesis

To start our investigations, we performed the synthesis of phosphirane. We started with the synthesis previously reported by Botella *et al.*<sup>14</sup> We scaled-up the last step of the synthesis to obtain 1-mesitylphosphirane (**1**) on a gram scale and added a purification step to obtain a colorless oil (Figure II-30).

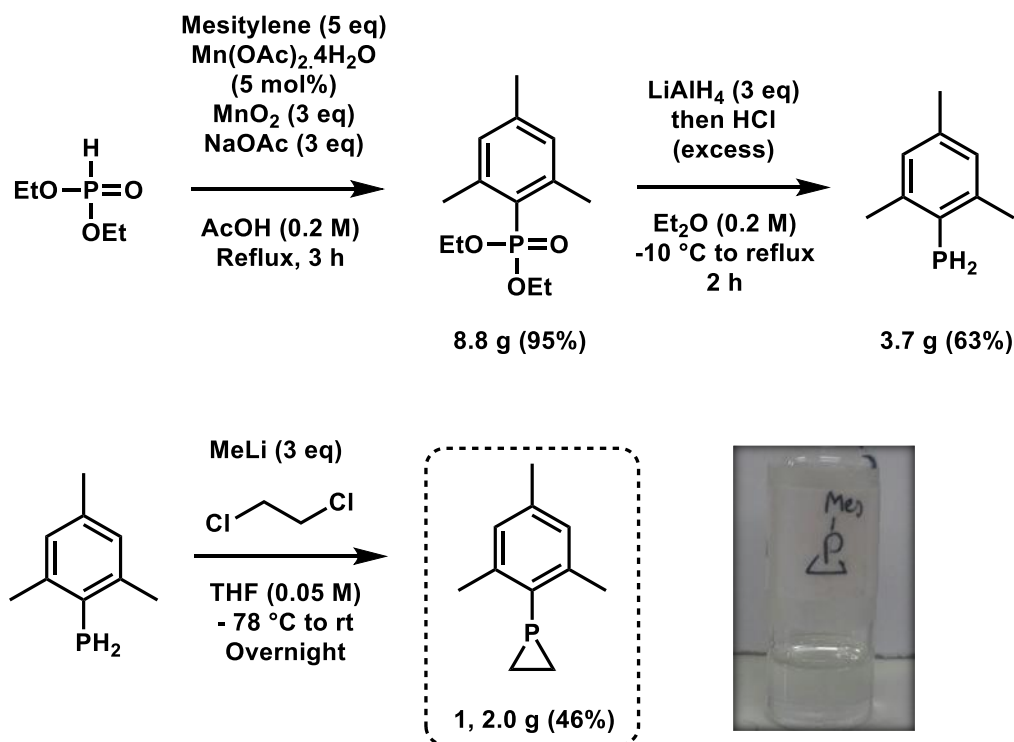


Figure II-30 : 1-mesitylphosphirane synthesis.  $\text{AcOH}$  : Acetic acid,  $\text{Et}_2\text{O}$  : diethyl ether,  $\text{THF}$  : tetrahydrofuran

The first step consists in the manganese-mediated C-H functionalization of mesitylene with diethyl phosphite. This reaction is easily run on a 20 mmol scale to obtain about 10 g of the phosphonate as a pure material. Reduction by lithium aluminum hydride followed by acidification with  $\text{HCl}$  allows the conversion of the phosphonate into the corresponding primary mesitylphosphine. This phosphine is remarkably robust towards oxidation for a primary phosphine. The last step consists in the deprotonation of the phosphine by methyllithium followed by addition of 1,2-dichloroethane. After column chromatography, 1-mesitylphosphirane **1** is obtained in a decent yield. The reproducibility of this last step using fresh commercial methyllithium is not optimal as yields ranged from 46% to 71%.

The  $^1\text{H}$  NMR spectrum shows two complex sets of signals between 1 and 1.5 ppm corresponding to the four protons of the phosphirane ring (Figure II-31) : One signal for the

two protons that are on the same side as the mesitylene moiety and one signal for the protons that are on the same side as the lone pair of phosphorus. The other signals are quite straightforward to assign with integrations of 3 for the *para*-methyl of the mesityl moiety, an integration of six for the ortho-methyl of the same moiety, and in the aromatic region a signal that accounts for the two aromatic protons of the mesityl.

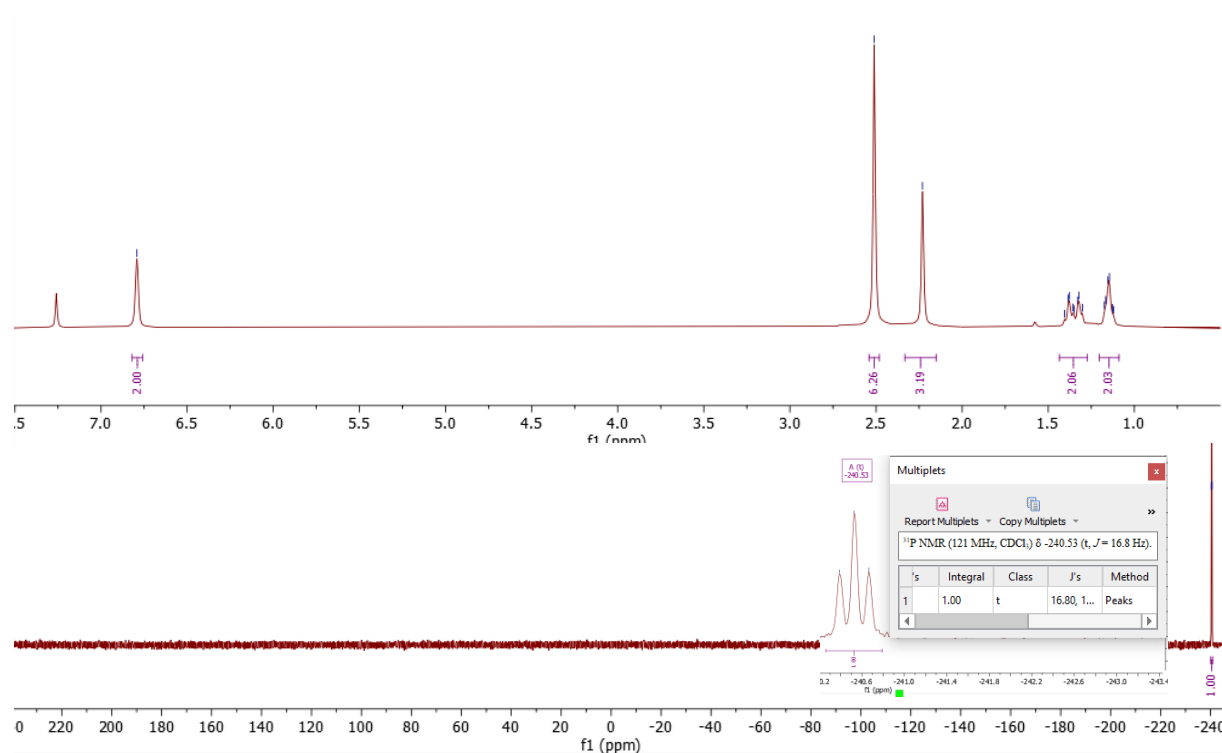


Figure II-31 :  $^1\text{H}$  (top) and  $^{31}\text{P}$  NMR (bottom) of 1-mesitylphosphirane. A zoom on the -241 ppm  $^{31}\text{P}$  NMR signal is shown to display the triplet shape

1-mesitylphosphirane **1** displays a triplet ( $^2J_{\text{P-H}} = 16.8$  Hz) at an astonishing -241 ppm chemical shift by  $^{31}\text{P}$  NMR. This value can be compared to the one of triphenylphosphine (-6 ppm), tributylphosphine (-31 ppm), tris(dimethylamino)phosphine (123 ppm) and phosphane  $\text{PH}_3$  (-241 ppm).

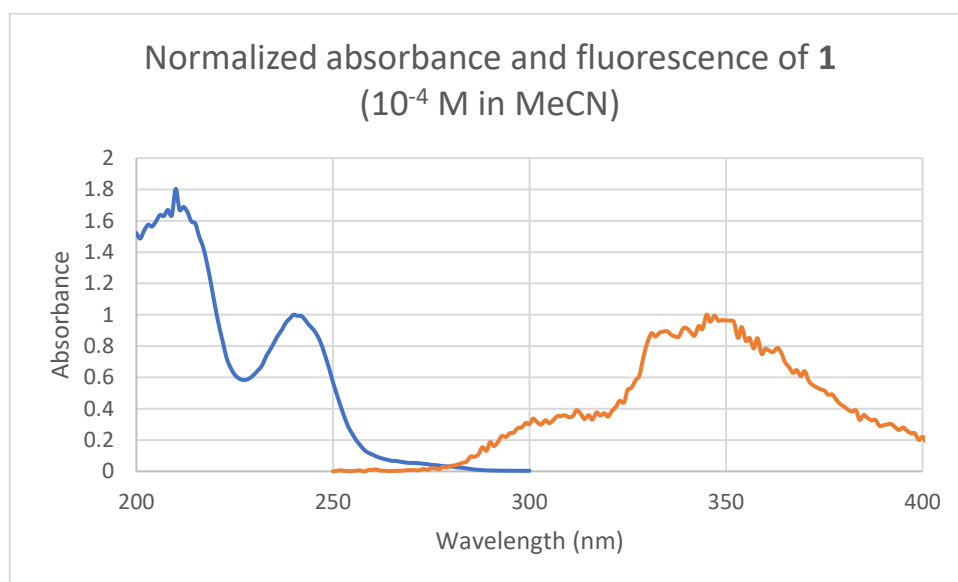


Figure II-32 : UV-Vis absorption and emission spectra of 1-mesitylphosphirane in MeCN

**1** absorbs UV light at  $\lambda_{\text{abs,max}} = 241$  nm and emits at  $\lambda_{\text{em,max}} = 345$  nm in MeCN at room temperature (Figure II-32). This allows to rule out any absorption of 1-mesitylphosphirane by visible-light light-emitting diode (LED) and provide an estimation of  $\Delta E_{0,0}$  of 4.4 eV.

With gram quantities of pure 1-mesitylphosphirane **1**, we then started our investigation.

## 2.2. Estimating phosphirane nucleophilicity and Lewis basicity

In 1994, Mayr and Patz developed a scale to estimate the feasibility of a reaction between a nucleophile and an electrophile. Prior to their work, several attempts were done to systematically quantify the nucleophilicity, the “strength”, of a nucleophile in  $S_N2$  reactions. No convincing conclusions could be reached, and in 1968 such quantification was thought to be impossible.<sup>52</sup> Mayr and Patz disproved this by introducing an equation and a method that allowed the quantification of nucleophilicity ( $N$ ) and electrophilicity ( $E$ ) parameters. This initial method required further optimization and was improved over time.<sup>53–55</sup> Equation (II.1) relates with the logarithm of the second-order rate constant ( $k$ ) with two parameters for the nucleophile ( $s_N$  and  $N$ ) and one parameter for the electrophile ( $E$ ).

$$\log k_{20^\circ\text{C}} = s_N(N + E) \quad (\text{equation II. 1})$$

Importantly, the parameters of nucleophilicity ( $N$ ) and electrophilicity ( $E$ ) can be measured separately and used considering no extra interaction parameter between one another. This makes the method useful for an everyday use. It is measured by reacting a nucleophile with different para-substituted diarylcarbenium cations (also known as benzhydryliums) (Figure II-33).

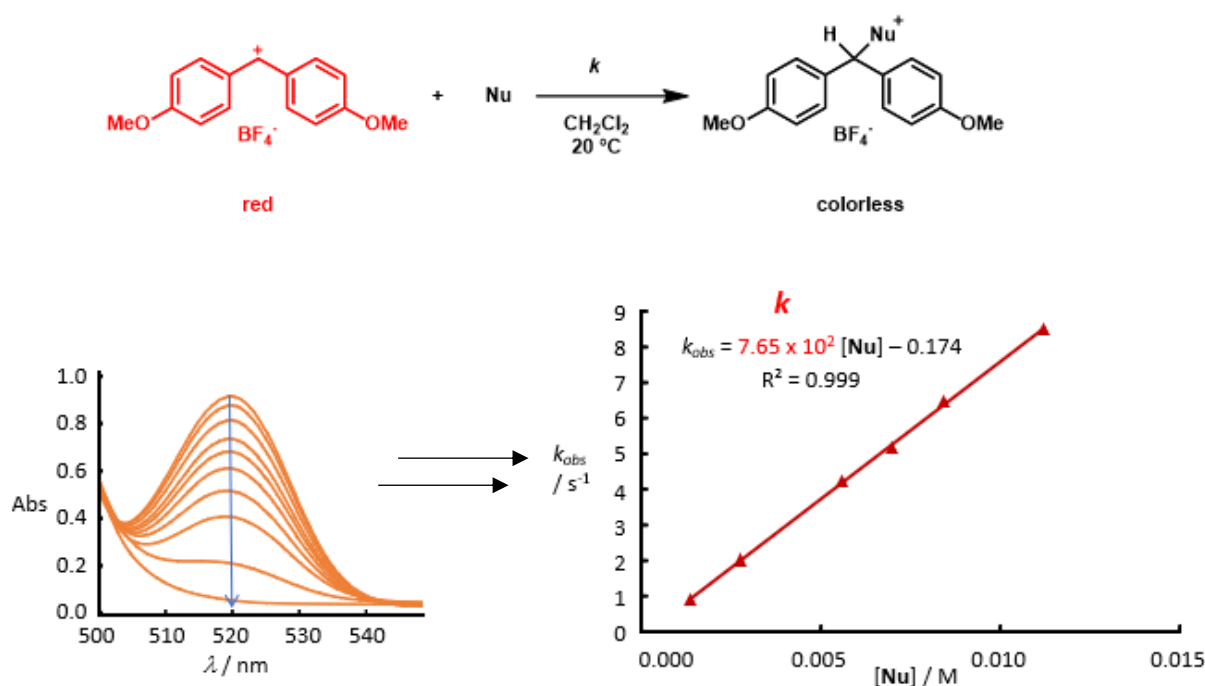


Figure II-33 : Reaction of a nucleophile with a benzhydrylium cation (top) Nu : Nucleophile.. Decrease of the absorption of the benzhydryliums cation overtime in the presence of a nucleophile (bottom left). Plot of the observed kinetic rate constant depending on the concentration of nucleophile (bottom right).

Diarylcarbeniums are colored molecules and the evolution of their absorbance at a given wavelength in the presence of different concentrations of quencher allows one to access the second-order rate constant  $k$ .

More than a thousand nucleophiles are listed in the current database and nucleophilicity values range over 38 orders of magnitude from -8.8 to 30.8.<sup>c</sup>

The rate constant could be estimated for 1-mesitylphosphirane **1** using di-(para-morpholino)phenylcarbenium  $(\text{mor})_2\text{CH}^+$  **2** as the diarylcarbenium partner ( $E = -5.53$ , Figure II-34).

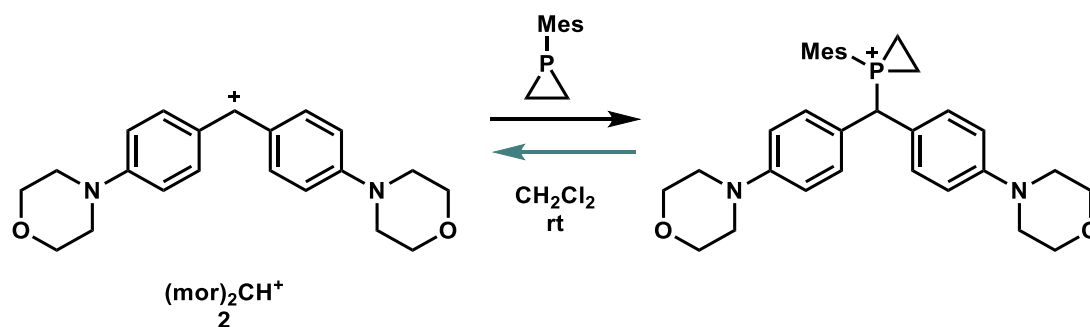


Figure II-34 : Reaction of 1-mesitylphosphirane with  $(\text{mor})_2\text{CH}^+$

<sup>c</sup> <https://www.cup.lmu.de/oc/mayr/reaktionsdatenbank/>



It is not the purpose of this investigation to determine accurately the  $N$  and  $LB$  values for the phosphirane, but to have a rough estimation of these values that is essential for the rationalization of the reactivity of phosphiranes. In this context, those parameters will be determined from the reaction of the 1-mesitylphosphirane with the benzhydrylium cation  $(\text{mor})_2\text{CH}^+$ . A concentration of  $10^{-5}$  M (in  $\text{CH}_2\text{Cl}_2$ ) of carbocation **2** was used to which were added in three different experiments 10, 20 and 30 equivalents of phosphirane **1**. The decay of the absorbance at 620 nm was followed by UV-Vis where an equilibrium was quickly reached. By fitting the decay before the equilibrium was reached, a value for  $k_{\text{obs}}$  was obtained, and by the absorbance at the equilibrium (compared to absorbance at the start) a value for the equilibrium constant  $K$  could be obtained. The determination of  $K$  and the related equations are disclosed after the determination of  $k$ .

Following equation (II.1), an estimation of the nucleophilicity of phosphirane could be obtained.

Where  $E$  is the electrophilicity of the carbocation **2** (-5.53),  $s_N$  is the nucleophilicity parameter of phosphirane **1**,  $N$  the nucleophilicity of phosphirane **1**, and  $k_{20^\circ\text{C}}$  the rate constant obtained from the slope of the linear correlation of the observed rate constants  $k_{\text{obs}}$  at each concentration depending on the concentration.

Table II-1 : experimental determination of  $k_{\text{obs}}$  for the reactions of 1-mesitylphosphirane (**1**) with  $(\text{mor})_2\text{CH}^+$  (**2**)

Phosphirane <b>1</b> equivalents	Phosphirane <b>1</b> concentration	$k_{\text{obs}}$
10	$1.10^{-4}$	0.0929
20	$2.10^{-4}$	0.122
30	$3.10^{-4}$	0.1667

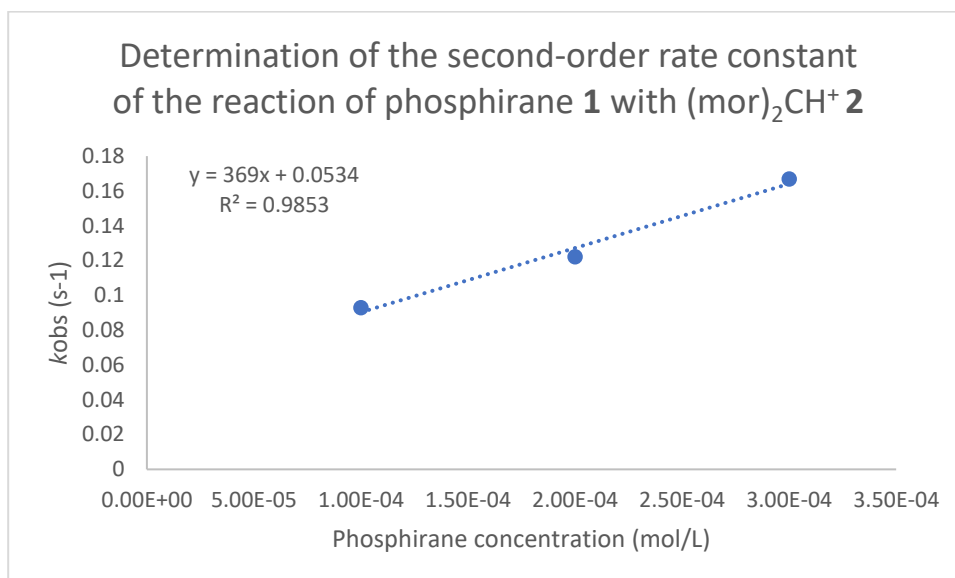


Figure II-35 : determination of  $k$  for the reaction of 1-mesitylphosphirane (**1**) with  $(mor)_2CH^+$  (**2**)

Linear fitting of the data provided  $k = 369 \text{ M}^{-1} \cdot \text{s}^{-1}$ .

To obtain the  $N$  and  $s_N$  parameters precisely, further experiments are required. An estimated range for the nucleophilicity of phosphirane **1** was obtained instead by picking the known minimum and maximum  $s_N$  values for phosphines as well as its average value (table II-2).<sup>56</sup>

Table II-2 : estimation of  $N$  for 1-mesitylphosphirane based on reported  $s_N$  values of phosphines

	Max $s_N = 0.88$	Min $s_N = 0.41$	Avg $s_N = 0.67$
$N$	8.45	11.79	9.39

One clearly sees that the value of nucleophilicity estimated spans over 3 orders of magnitude. We still obtained the useful insight that 1-mesitylphosphirane **1** has one of the lowest nucleophilicities for phosphines (Figure II-36). It has a comparable nucleophilicity to the least nucleophilic phosphine known (tris(*ortho*-methylphenyl)phosphine **3a**,  $N = 8.56$ ,  $s_N = 0.70$ ) and a lower nucleophilicity than the second least nucleophilic phosphine known di-*tert*-butylphenylphosphine **3b**,  $N = 12.40$ ,  $s_N = 0.55$ ). As a matter of comparison, the most nucleophilic phosphine known is tris(4-dimethylaminophenyl)phosphine **3c** ( $N = 18.39$ ,  $s_N = 0.64$ ), which means it is *ca.*  $10^{10}$  more nucleophilic than the least nucleophilic one. The reference molecule triphenylphosphine **3d** ( $N = 14.33$ ,  $s_N = 0.65$ ) is between 100 and 100,000 times more nucleophilic than **1**. Despite the roughness of the results, they match the idea that 1-mesitylphosphirane **1** has a very low nucleophilicity, which we quantify to be in the lowest range of all phosphines. In a similar fashion as phosphiranes fill the gaps in the phosphines

stereoelectronic ligand map, it seems they can also fill the gap in the nucleophilicity scale where very few phosphines were measured between 8 and 12 (Figure II-36).

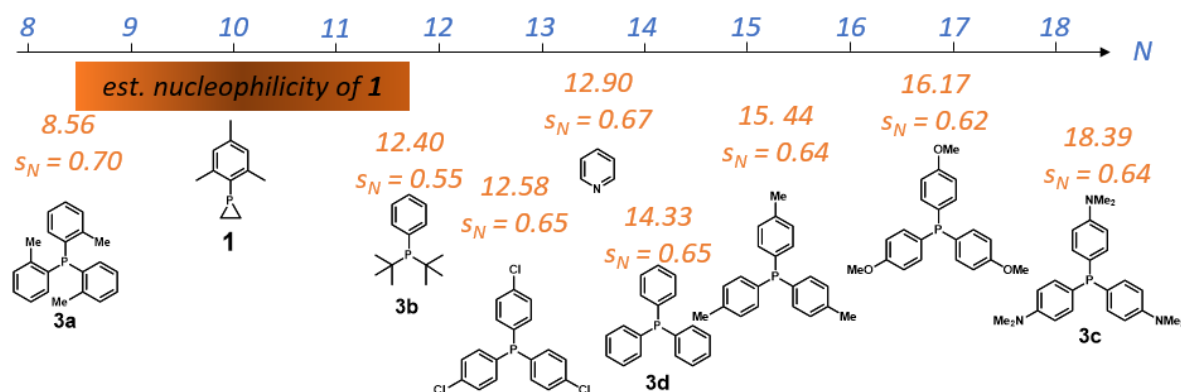


Figure II-36 : scale of nucleophilicity of phosphines and estimated value for 1-mesitylphosphirane **1**

Because the outcomes of a reaction between an electrophile and a nucleophile is not always governed by kinetic parameters, i.e. electrophilicity and nucleophilicity, Mayr introduced in 2015 a new tool to determine the Lewis basicity (*LB*) towards C-centered electrophiles, which provides an estimation for the reversibility of an addition by providing the equilibrium constant *K* for Lewis basicity versus the rate constant *k* for nucleophilicity.<sup>57</sup> Indeed, a nucleophile may add quickly on an electrophile (kinetics) but an equilibrium may prevent completion of the reaction if the thermodynamics do not favor the conversion.

Lewis basicity of phosphirane was determined according to Equations (II.2) and (II.3):

$$\log K = LA + LB \quad (\text{equation II.2})$$

$$\text{With } K = \frac{A_0 - A}{A * [Nu]} = \frac{A_0 - A}{A * ([Nu]_0 - \frac{A_0 - A}{\varepsilon \times l})} \text{ where } \varepsilon \times l = 1.455 \times 10^5 \times 1 = 1.455 \times 10^5 \text{ L/mol}^{57}$$

In our case, the (mor)<sub>2</sub>CH<sup>+</sup> carbocation **2** has a Lewis acidity of -6.82:

$$LB = \log K - LA = \log K + 6.82 \quad (\text{equation II.3})$$

Table II-3 : estimation of *LB* for 1-mesitylphosphirane (**1**) based on experimental data

[phosphirane] <sub>0</sub> mol/L	A <sub>0</sub>	A	A <sub>0</sub> - A	[phosphirane <b>1</b> ] mol/L	K	LB <sub>estimated</sub>
1.10 <sup>-4</sup>	1.209	0.9435	0.2655	9.63E-05	2.92E+03	10.29
2.10 <sup>-4</sup>	1.157	0.6743	0.4827	1.93E-04	3.70E+03	10.39
3.10 <sup>-4</sup>	1.133	0.4848	0.6482	2.91E-04	4.59E+03	10.48

The average Lewis basicity for each experiment provides an approximative value of 10.39 for 1-mesitylphosphirane (table II-3), which accounts for the lowest known value for phosphines

and is comparable to the Lewis basicity of pyridine. If compared to the reference triphenylphosphine **3d** ( $LB = 14.27$ ), the Lewis basicity of 1-mesitylphosphirane **1** is *ca.* 10,000 times smaller (Figure II-37).

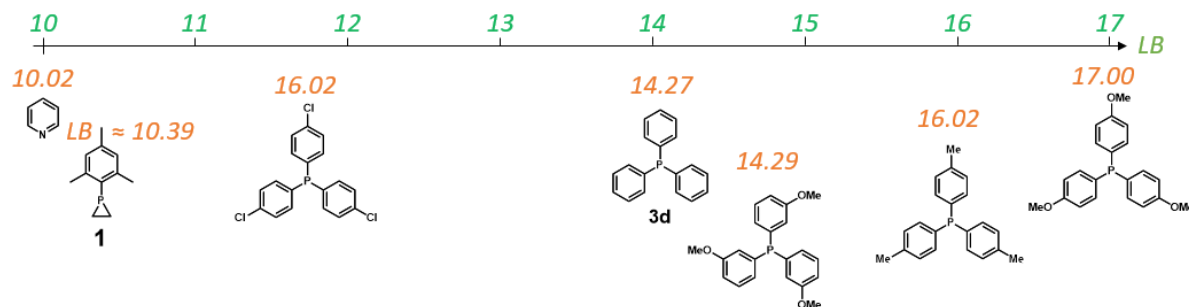


Figure II-37 : scale of Lewis basicity of phosphines and estimated value for 1-mesitylphosphirane

Although preliminary, these results were sufficient to rationalize some results from the literature concerning the low nucleophilicity and Lewis basicity of phosphiranes and to help us pick a suitable reaction partner for the quaternarization of 1-mesitylphosphirane **1**. Indeed, aiming at irreversible quaternarization, a strong Lewis acid is obviously compulsory.

### 2.3. Phosphiranium ylides and phosphiranium salts: exploration of a new phosphirane quaternarization method

In need of a strong Lewis acid to be reactive with the very weak Lewis base phosphirane **1** is, we thought about the light-generated electrophilic free carbenes from aryldiazoacetates **4** (Figure II-38). Their electrophilicity and Lewis acidity has not been measured, but their known highly reactive nature should make them ideal partners and, once carbenes **5** are trapped, the reaction wouldn't be able to go backwards.

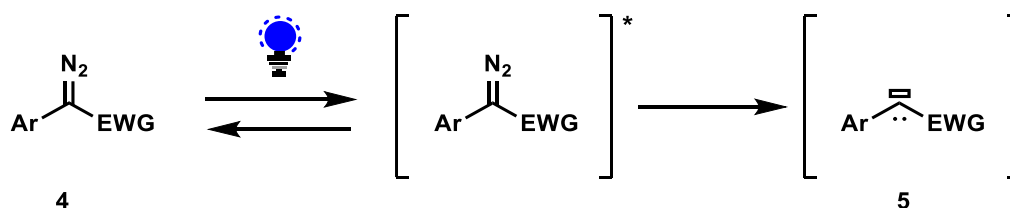


Figure II-38 : Light absorption of a diazo compound and following nitrogen loss to generate a free carbene. EWG : electron withdrawing group, Ar : aryl

We synthesized aryldiazoacetate compounds following literature procedures, starting from the phenylacetate derivative **6** deprotonation on the benzylic position by the non-nucleophilic base 1,8-Diazabicyclo(5.4.0)undec-7-ene (DBU) followed by addition on the nitrogen of 4-acetamidobenzenesulfonyl azide (ABSA) to obtain the desired methyl aryldiazoacetate products **4a-4e** without trouble (Figure II-39).<sup>58</sup>

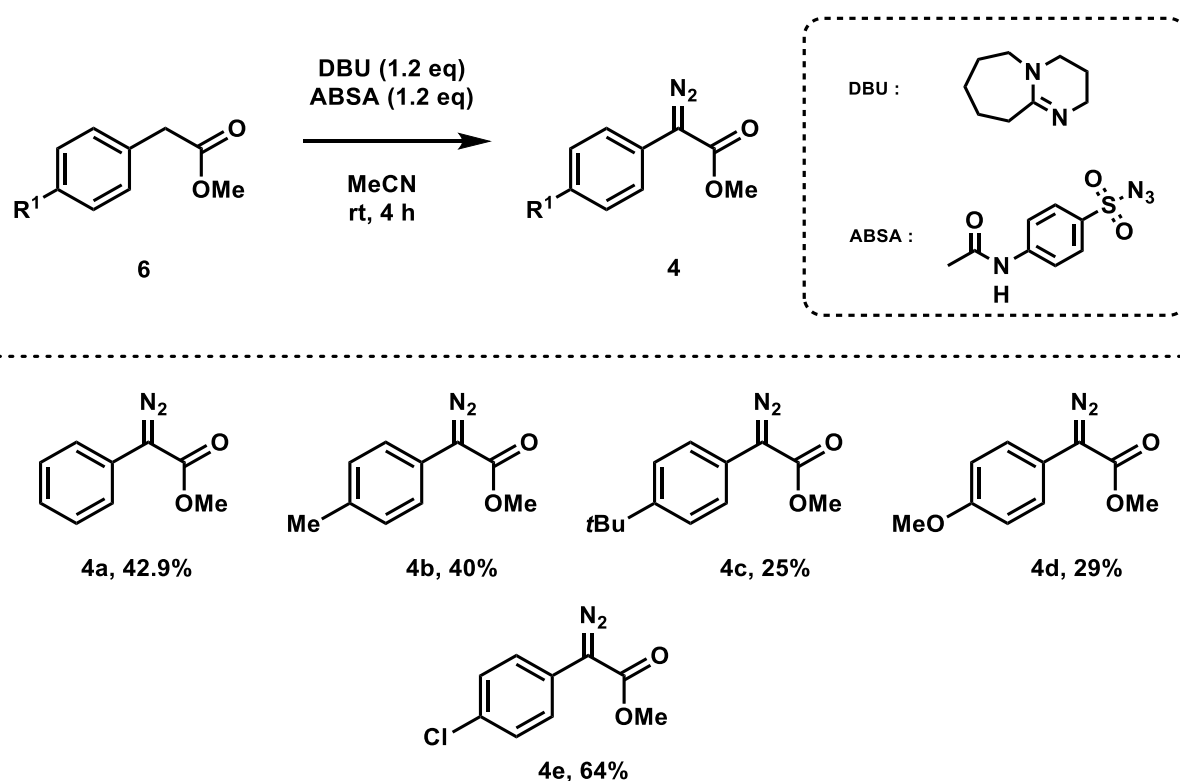


Figure II-39 : general synthesis scheme of aryldiazoacetates and isolated yields

Upon visible-light irradiation of these diazo compounds **4** in the presence of phosphirane **1**, addition of the lone pair of the phosphorus atom is expected to occur to the vacancy of the carbon atom of the carbene. The product of this reaction is expected to be a phosphiranium ylide **7** as seen in Figure II-40.

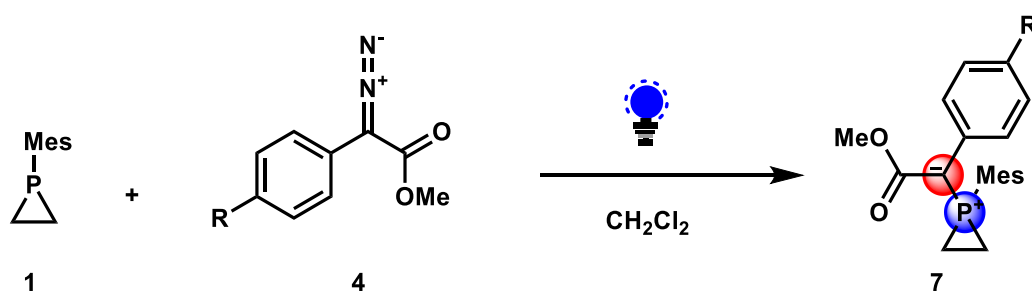


Figure II-40 : expected reactivity of phosphirane **1** with aryldiazoacetates **4** under blue light irradiation

Such molecules have never been synthesized before and their possible existence as well as their properties were completely unknown at the beginning of this project.

We first performed the reaction at room temperature with one equivalent of **1** and methyl *para*-chlorophenyldiazoacetate **4e** in dichloromethane with blue light irradiation overnight. We looked at the outcome of the reaction by  $^{31}\text{P}\{^1\text{H}\}$  NMR. During the exploration presented herein, proton decoupled phosphorus NMR along with crude proton NMR were used as qualitative estimation tools for the reaction outcome. The integrations from both types of

analysis correlated qualitatively in a good fashion. The result clearly shows that phosphirane **1** remained mostly intact and that the conversion led to an uncontrolled variety of degradation products (Figure II-41). Confident with the fact that phosphirane **1** and the light-generated carbene should react, we kept on investigating this reaction.

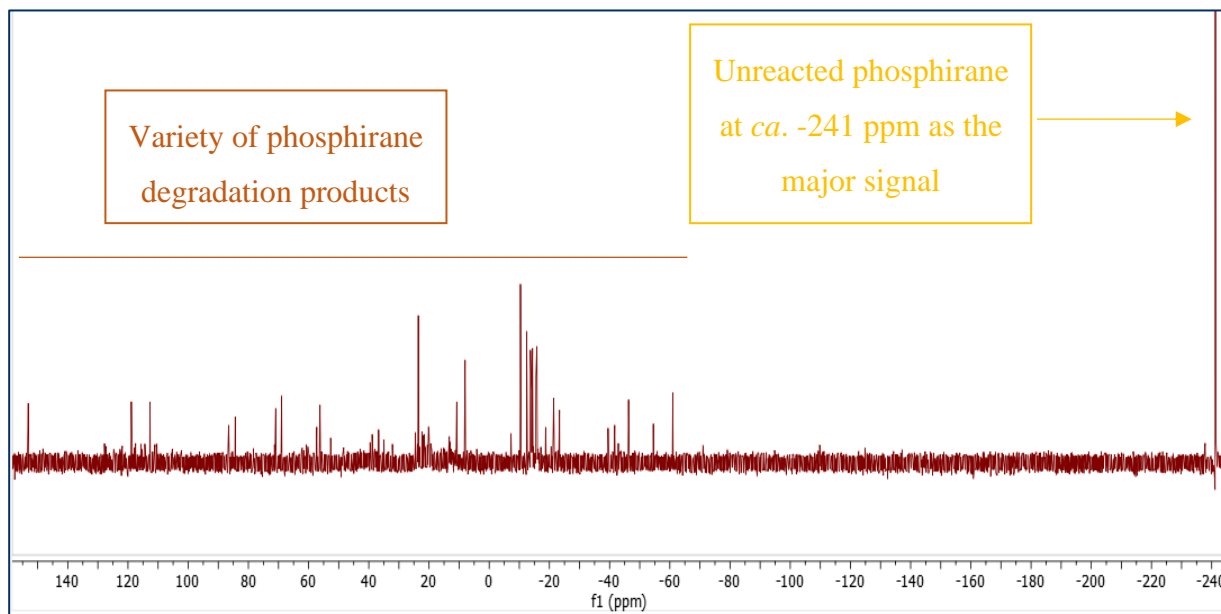


Figure II-41 :  $^{31}\text{P}\{^1\text{H}\}$  NMR of the reaction at room temperature of 1 equivalent of 1-mesitylphosphirane **1** with 1 equivalent of methyl para-chlorophenyldiazoacetate **4e** under blue light irradiation for 12 hours.

In the reaction conditions, it seemed that the reaction between 1-mesitylphosphirane **1** and the carbene **5e** was impaired by faster side-reactions. To favor the reaction between the two molecules, we increased the number of equivalents of aryldiazoacetate **4e** from one to five. After 12 h, most phosphirane **1** was consumed, fewer degradation product signals were observed, and a new broad signal appeared at -116 ppm (Figure II-42).

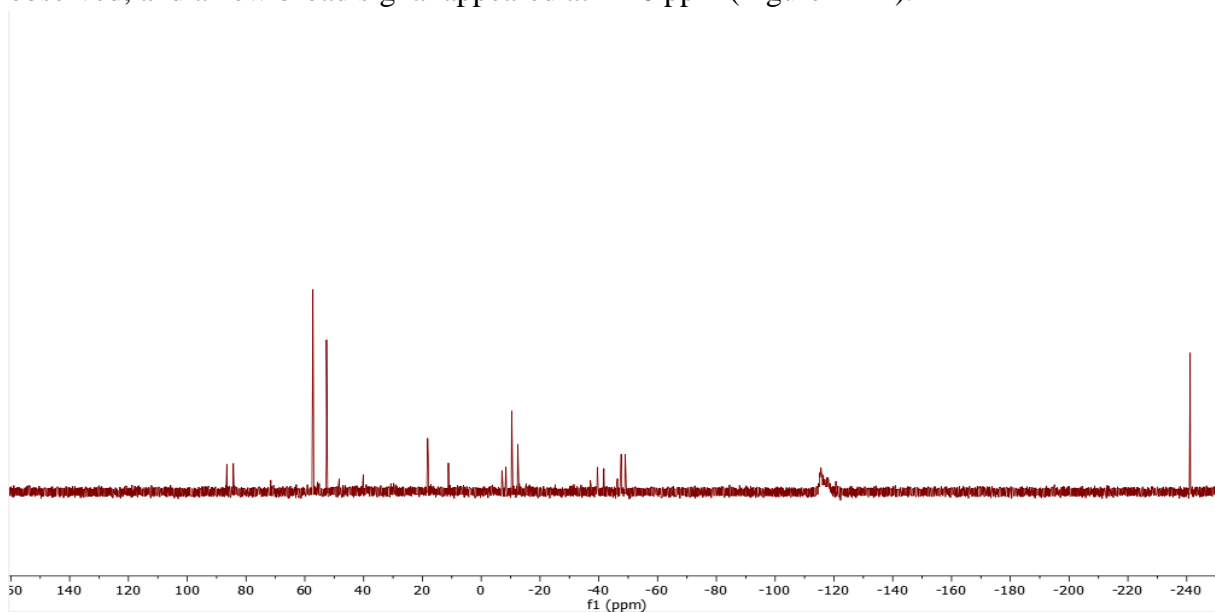


Figure II-42 :  $^{31}\text{P}\{^1\text{H}\}$  NMR of the reaction at room temperature of 1 equivalent of 1-mesitylphosphirane **1** with 5 equivalent of methyl para-chlorophenyldiazoacetate **4e** under blue light irradiation for 12 hours.

A broad NMR signal, with such a chemical shift, seemed to correlate well with an ylide for the shape and with a phosphiranium for the shift. Indeed, phosphonium ylides are more commonly found in the 20 ppm area, and the strained phosphirane ring is known to induce important upfield chemical shifts. A similar tendency as the one between triphenylphosphine **3d** (-6 ppm) and 1-mesitylphosphirane **1** (-241 ppm) is observed here (16.5 ppm for methyl(triphenylphosphoranylidene)acetate **8**<sup>59</sup> against -116 ppm for the new signal). This suggests the retention of the small strained 3-membered ring (Figure II-43).

**<sup>31</sup>P NMR chemical shifts of selected molecules**

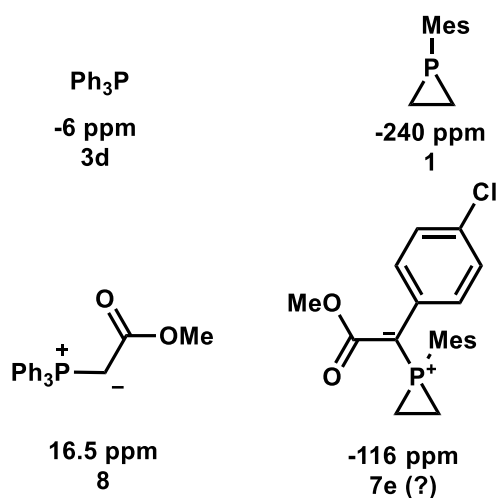


Figure II-43 : Phosphorus chemical shifts of phosphirane and phosphiranium ylide and closely resembling ring opened structures

It was difficult to know whether the by-products came from competing reactions or from the degradation of the phosphiranium ylide **7** at room temperature. In an attempt to prevent thermal degradation and ensure the reproducibility of the reaction, we decreased the temperature of the reaction from room temperature to -40 °C. To our delight, the conversion to the signal at -116 ppm became almost quantitative. <sup>1</sup>H NMR gave a relative 1:9.5 ratio between the aromatic protons from the mesityl of unreacted 1-mesitylphosphirane **1** and a new aromatic proton signal that we correlated to the <sup>31</sup>P NMR -116 ppm signal of the presumed phosphiranium ylide product **7e** (Figure II-44).

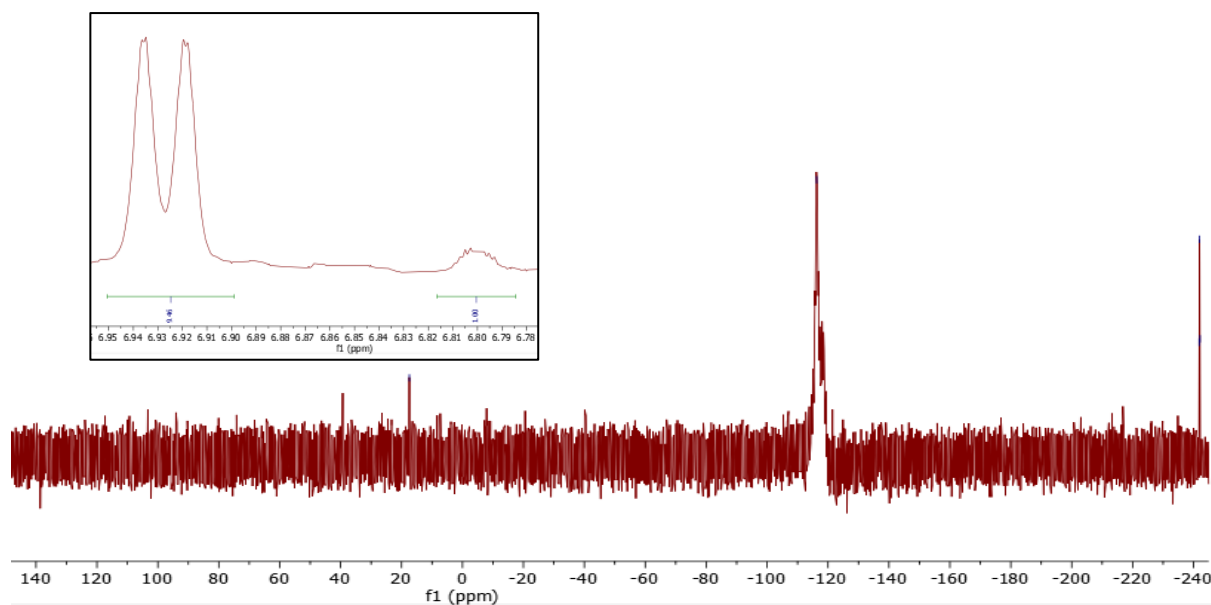


Figure II-44 :  $^{31}\text{P}\{^1\text{H}\}$  NMR of the reaction at  $-40\text{ }^{\circ}\text{C}$  of 1 equivalent of 1-mesitylphosphirane with 5 equivalents of methyl para-chlorophenyldiazoacetate **4e** under blue light irradiation for 12 hours. The zoomed spectrum on the top left shows the  $^1\text{H}$  NMR ratio of two aromatic signals typical from the mesityl moiety.

Variable temperature NMR was performed with the *para*-methoxyphenyldiazo acetate **4d** derived phosphiranium ylide **7d** and showed a splitting of the broad  $-116\text{ ppm}$   $^{31}\text{P}$  NMR signal in two sharp ones in a *ca.* 2:1 ratio from  $10\text{ }^{\circ}\text{C}$  and below. Total conversion towards the ylide **7d** was observed from this diazo compound (Figure II-45).

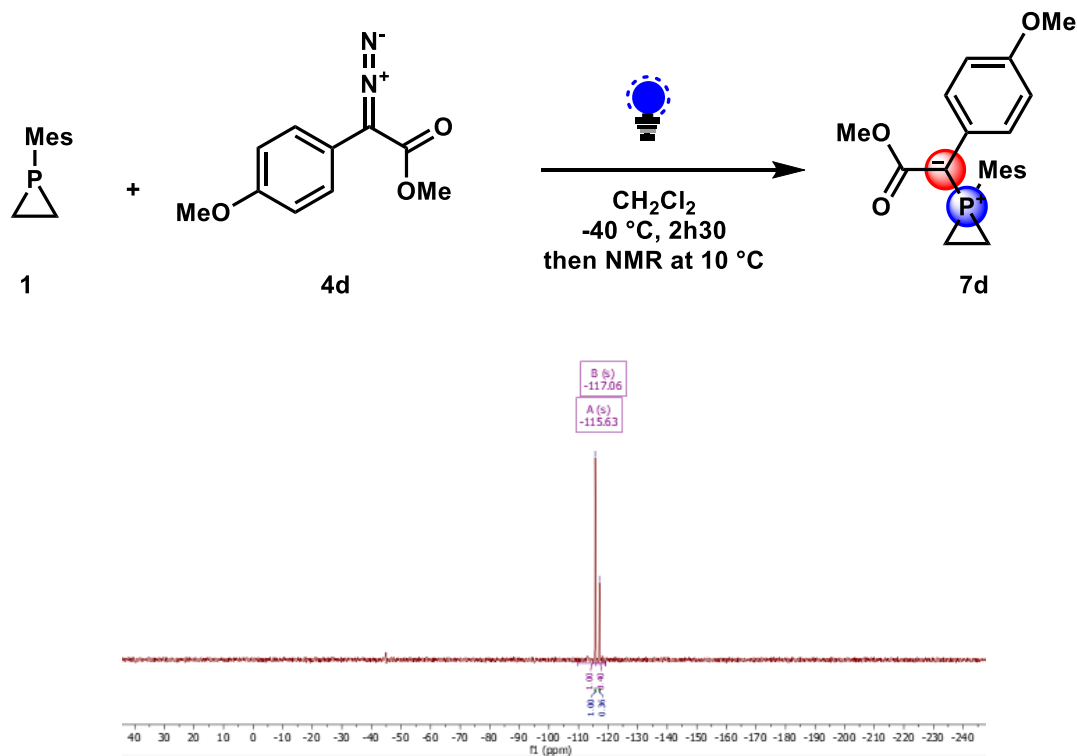


Figure II-45 : Reaction of 1-mesitylphosphirane **1** with methyl para-methoxyphenyldiazoacetate **4d** and the corresponding ylide product **7d**.  $^{31}\text{P}\{^1\text{H}\}$  NMR (variable temperature,  $+10\text{ }^{\circ}\text{C}$ ) of the reaction at  $-40\text{ }^{\circ}\text{C}$  of 1 equivalent of 1-mesitylphosphirane **1** with 2 equivalents of methyl para-methoxyphenyldiazoacetate **4d** under blue light irradiation for 2 hours 30.



We assigned the two signals to two P(V) isomers **7d<sub>a</sub>** and **7d<sub>b</sub>** (Figure II-46). The ratio indicates that a structure is more favored than the other one. This will be discussed later in this chapter assisted by DFT calculations. Lowering the temperature from 20 °C to 10 °C makes the free exchange between both forms unfavored and the phosphorus NMR signals go from broad to sharp.

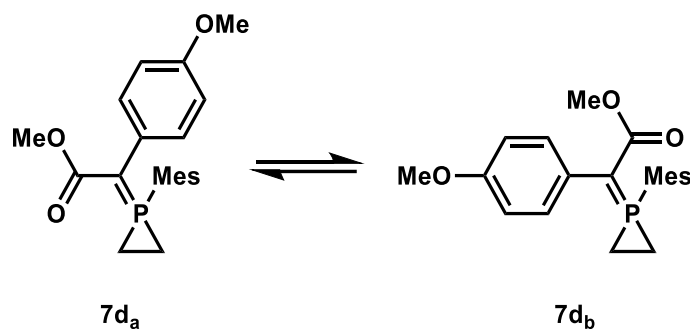


Figure II-46 : Two proposed isomers **7d<sub>a</sub>** and **7d<sub>b</sub>** of the phosphiranium ylide product **7d**

Running the reaction without irradiation resulted in no conversion at all, the reaction mixture being stable in the dark for 16 hours.

To gain more insights into the structure of the product, we thought that protonating the ylide **7e** with a Bronsted acid should lead to the phosphiranium product **9e**. As mentioned in the introduction, under acidic conditions, phosphiranes tend to decompose rather than protonate towards the phosphiranium salt.<sup>21</sup> However, phosphiranium salts are stable in acidic conditions because there is no basic site left on the molecule.<sup>29</sup> Here, protonation occurs on the carbon atom and provides the corresponding acidic-conditions-compatible phosphiranium salt **9e**. We used tetrafluoroboric acid  $\text{HBF}_4$  on the *para*-chloro derivative **7e** (Figure II-47). The broad signal at -116 ppm became a sharp one at -111 ppm.

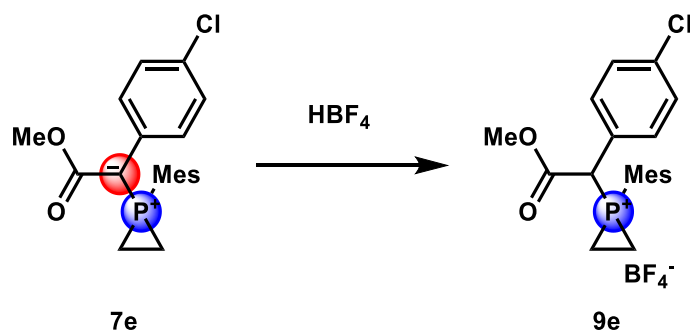


Figure II-47 : Protonation of phosphiranium ylide with  $\text{HBF}_4$

Crystals suitable for X-ray diffraction (Figure II-48) were obtained following entry 4 of table II-4 by liquid-liquid diffusion between heptane and ethyl acetate in a 1:1 ratio.

Table II-4 : Crystallization attempts of phosphiranium salt **9e**

Entry	Solvent	Method	Result	Comment
1	CDCl <sub>3</sub> :Pentane 1:1	Liquid-liquid diffusion	-	Oils were obtained
2	CH <sub>2</sub> Cl <sub>2</sub>	Slow evaporation	-	Small non monocrystalline solids obtained
3	Acetone	Slow evaporation	-	Sluggish residue
4	AcOEt:Heptane 1:1	Liquid-liquid diffusion	Crystals	After AcOEt addition, an AcOEt- insoluble residue was discarded before addition of heptane

The phosphiranium salt structure of **9e** could be confirmed (Figure II-48).

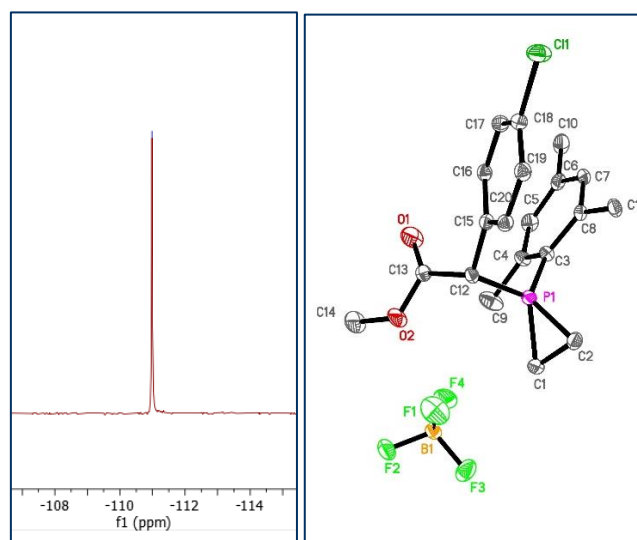


Figure II-48 :  $^{31}\text{P}\{^1\text{H}\}$  NMR of the protonated phosphiranium ylide (left) and the corresponding crystals obtained (right)

The proton NMR of the crystals redissolved in CDCl<sub>3</sub> gave broad proton signals (Figure II-49). The proton on C12 (from Figure II-48) could be identified at 5.29 ppm with a typical  $^2J_{\text{H-P}}$  coupling constant of 17.84 Hz. The molar mass of the molecule was confirmed by HRMS.

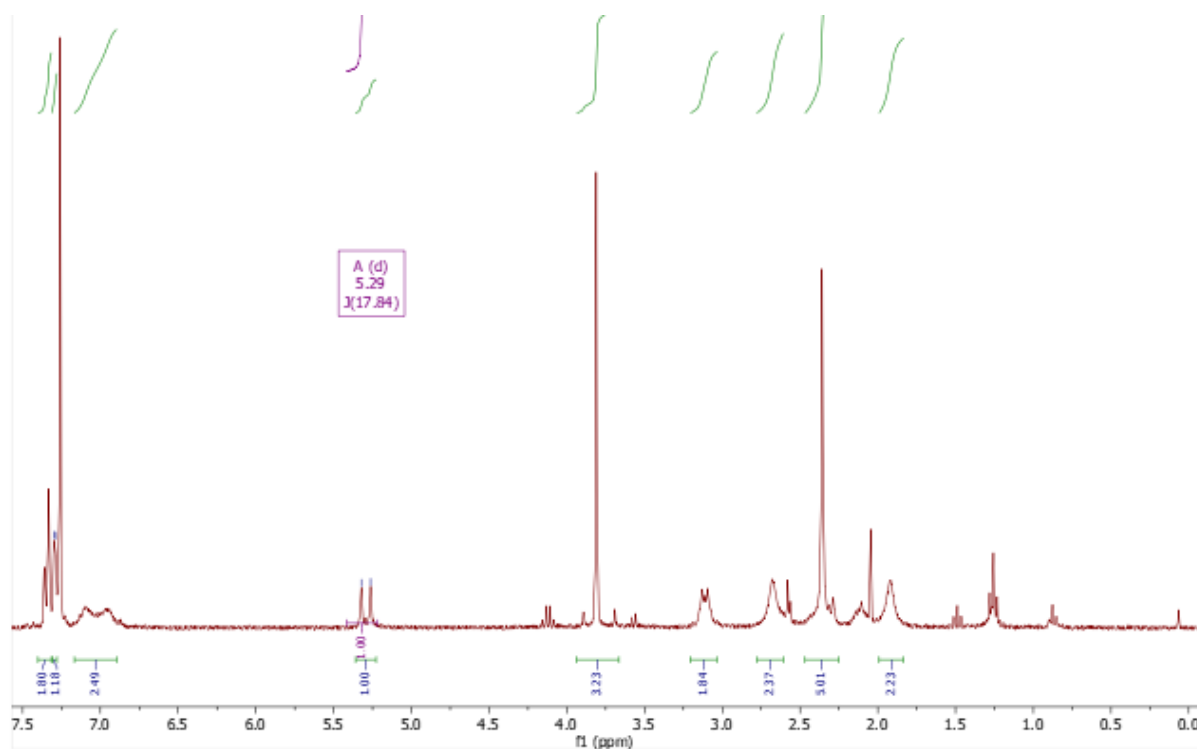


Figure II-49 :  $^1\text{H}$  NMR of the phosphiranium **9e** crystals with a typical signal at 5.29 ppm

The optimized method for phosphiranium salt **9** generation, where the number of equivalents of aryldiazoacetate could be decreased from 5 to 2 at  $-40^\circ\text{C}$ , was tested on three methyl aryldiazoacetate substrates with *para*-chloro **4e**, methoxy **4d** and methyl **4b** substituents (Figure II-50). The conversion towards the ylide was better for the *para*-methoxy **7d** and methyl **7b** substituents than for the chloro derivative **7e**. Quantitative conversions towards the phosphiranium salts **7d** and **7b** were assessed by phosphorus NMR without any degradation and total selectivity towards the desired products.

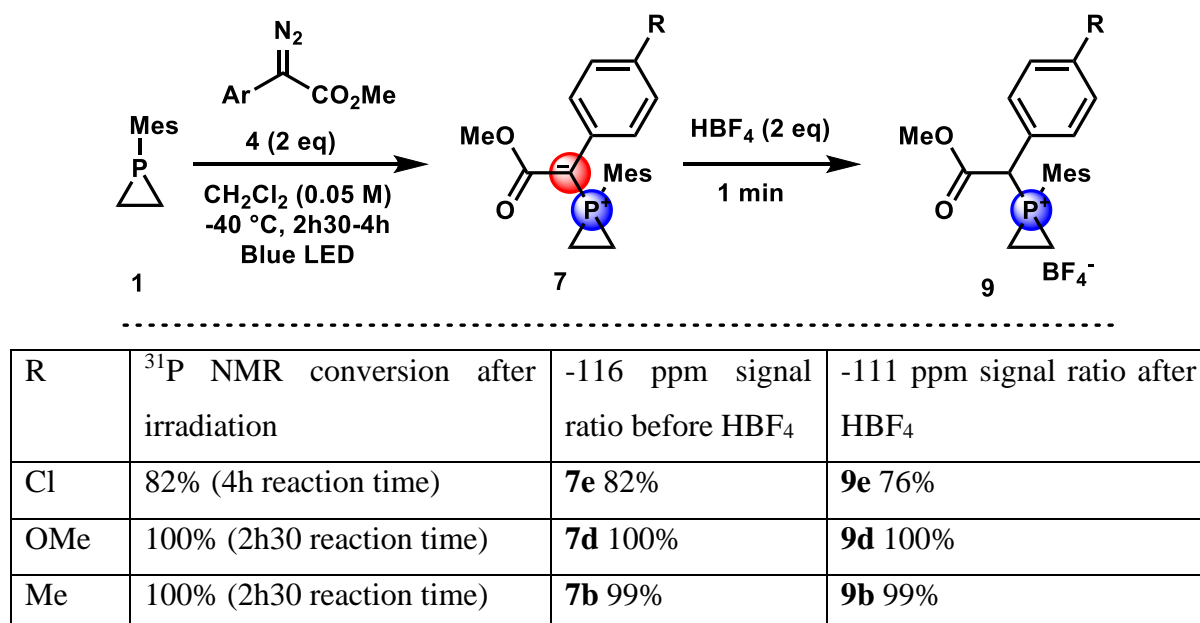


Figure II-50 : Formation of phosphiranium ylide and subsequent acidification with  $\text{HBF}_4$  on three different structures

All phosphiranium salts mentioned above were subjected to different recrystallization methodologies, but no crystals suitable for XRD could be obtained other than the one attempt that worked and that has been described above. The other unsuccessful recrystallization attempts included  $\text{CH}_2\text{Cl}_2$ - $\text{Et}_2\text{O}$  liquid-liquid diffusion at different temperatures (room temperature,  $-20\text{ }^\circ\text{C}$ ,  $-80\text{ }^\circ\text{C}$ ) and centrifugation of the same solutions.

A new method for the quaternarization of phosphiranes was then developed and allows modification of the substituents of the aryldiazoacetate moiety.

With an efficient method to generate novel the phosphiranium salts **9**, we first decided to get insights into their reactivity by investigating their known C-centered ring opening with aniline. In a second approach, we investigated the reactivity of the most interesting phosphiranium ylide **7**.

## 2.4. Reactivity of sterically hindered phosphiranium salts

Phosphiranium salts are known for being water sensitive and unstable under air. But, the same sample **9e** was subjected to different solvents and manipulations under air to obtain crystals, without any noticeable degradation. We thus hypothesized that the stability of the phosphiranium salts **9** we had generated was different than what was known in the literature. We first subjected the phosphiranium salt **9e** to hydrolysis (Figure II-51) by dissolving it in water. After adding water on **9e**, stirring for 5 minutes and subsequent extraction with  $\text{CH}_2\text{Cl}_2$ , the  $^{31}\text{P}$  NMR of the organic layer showed that **9e** remained mostly stable, with an additional signal at  $-44.8\text{ ppm}$  attributed in a first glance to the phosphirane oxide **10**. However, an attempt at purifying **9e** by flash chromatography led to its full decomposition towards the phosphine oxide **10** ( $-44.8\text{ ppm}$ ) (Figure II-52).

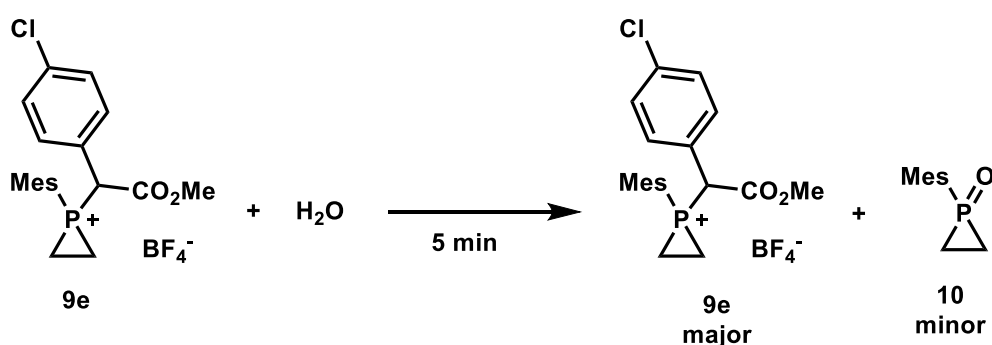


Figure II-51 : Hydrolysis attempt of phosphiranium salt **9e**

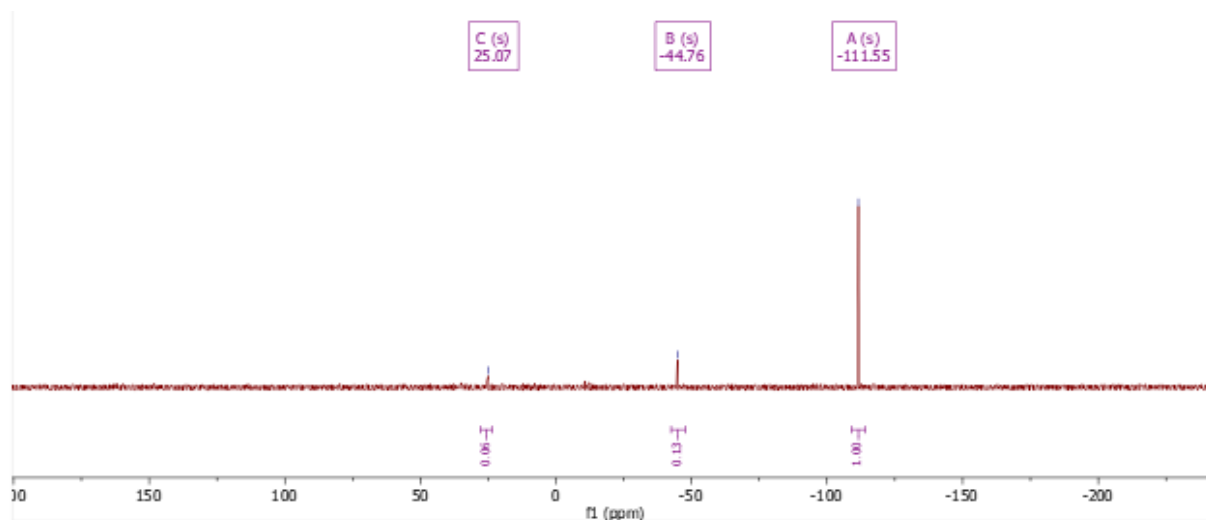


Figure II-52 :  $^{31}\text{P}\{^1\text{H}\}$  NMR after hydrolysis of the phosphiranium salt **9e** and before purification

To confirm the attribution of the -44.8 ppm signal to **10**, 1-mesitylphosphirane oxide  $^1\text{H}$  and  $^{31}\text{P}$  spectra were recorded after oxidation of a solution of phosphirane **1** with  $\text{H}_2\text{O}_2$ . The  $^{31}\text{P}$  NMR chemical shift was -44.4 ppm (Figure II-53), almost the same as the -44.8 ppm shift observed previously. We think it is safe to assume that both are the same product and that the small difference is due to the larger amount of water in  $\text{CDCl}_3$  after oxidation with  $\text{H}_2\text{O}_2$ .

The phosphiranium salts **9** we have generated, despite being unstable on silica as it is already known for other phosphiranium salts,<sup>14</sup> seem more robust towards hydrolysis.

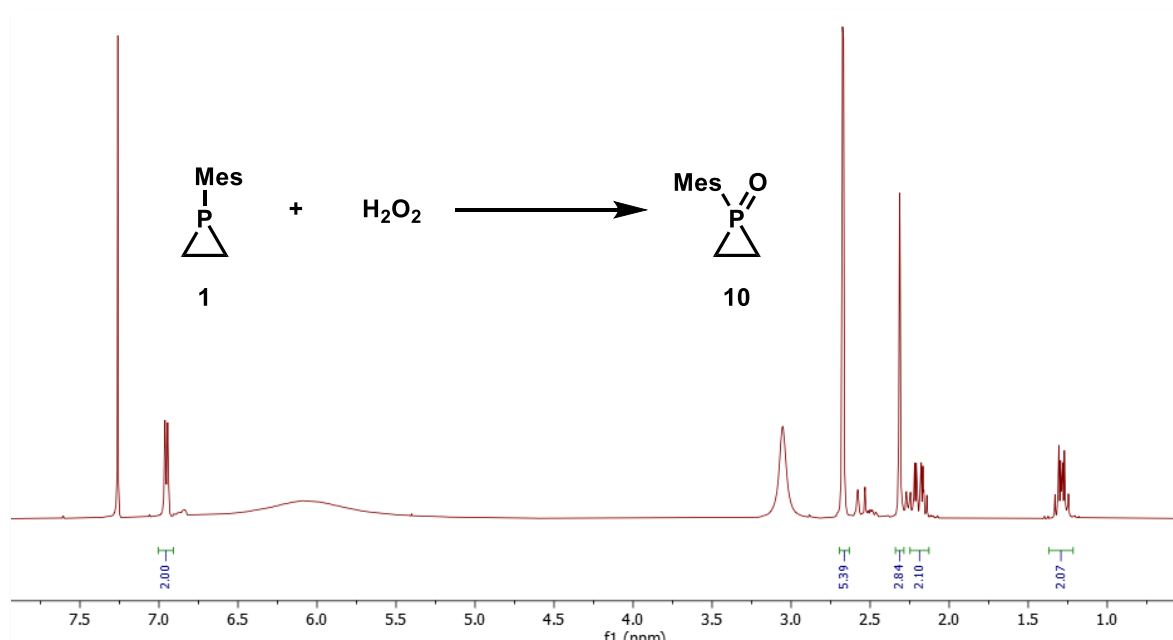


Figure II-53 :  $^1\text{H}$  NMR after oxidation of 1-mesitylphosphirane with  $\text{H}_2\text{O}_2$

Now knowing the relative robustness of our phosphiranium salts **9**, we added aniline to check if the reactivity was modified with the new substitution pattern. The  $^{31}\text{P}$  NMR spectrum obtained before purification for the ring opening of **9e** was not very encouraging. The ring

opening products **11e** and **12e** were isolated with difficulty as a mixture in a very poor yield (Figure II-54). We hypothesize that a combination of three factors could explain this result. The addition of excess  $\text{HBF}_4$ , initially intended to maximize the conversion towards the phosphiranium salt, makes the reaction conditions acidic. Aniline being a base, despite also being added in 2 equivalents, may have been partly quenched or seen its reactivity modified, which prevented clean and efficient ring opening. The intrinsically poor reactivity of the *para*-chloro phosphiranium salt **9e** towards ring opening could also explain the poor yields obtained. Finally, degradation on silica of the final phosphines **11e** and **12e** may have occurred and prevented efficient isolation.

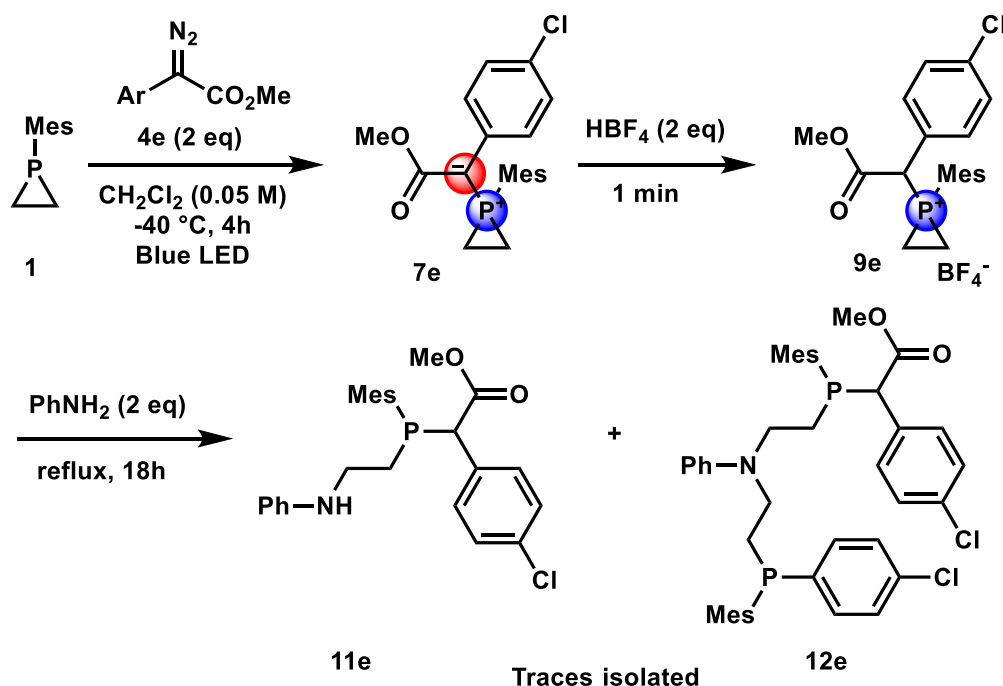


Figure II-54 : Ring opening attempt of phosphiranium salt **9e** with aniline. Ar : *para*-chlorophenyl

The reaction was repeated by using the *p*-methoxy derivative **4d** to complement the *p*-chloro data. The phosphiranium salt **9d** was obtained following the previous methodology and aniline was added. The reaction mixture was heated overnight at reflux and provided a full conversion. Treatment of the reaction medium with triethylamine to quench the excess acid provided an interesting  $^{31}\text{P}$  NMR profile (Figure II-55). Only signals that can be related to ring opening adducts were obtained in the -10 to -20 ppm region. The previously reported similar products had  $^{31}\text{P}$  NMR shifts between -30 and -50 ppm. Our results showed multiple signals that we assigned to uncontrolled mono and di-additions products **11d** and **12d** of aniline C-centered attack on the phosphiranium salt **9d**.

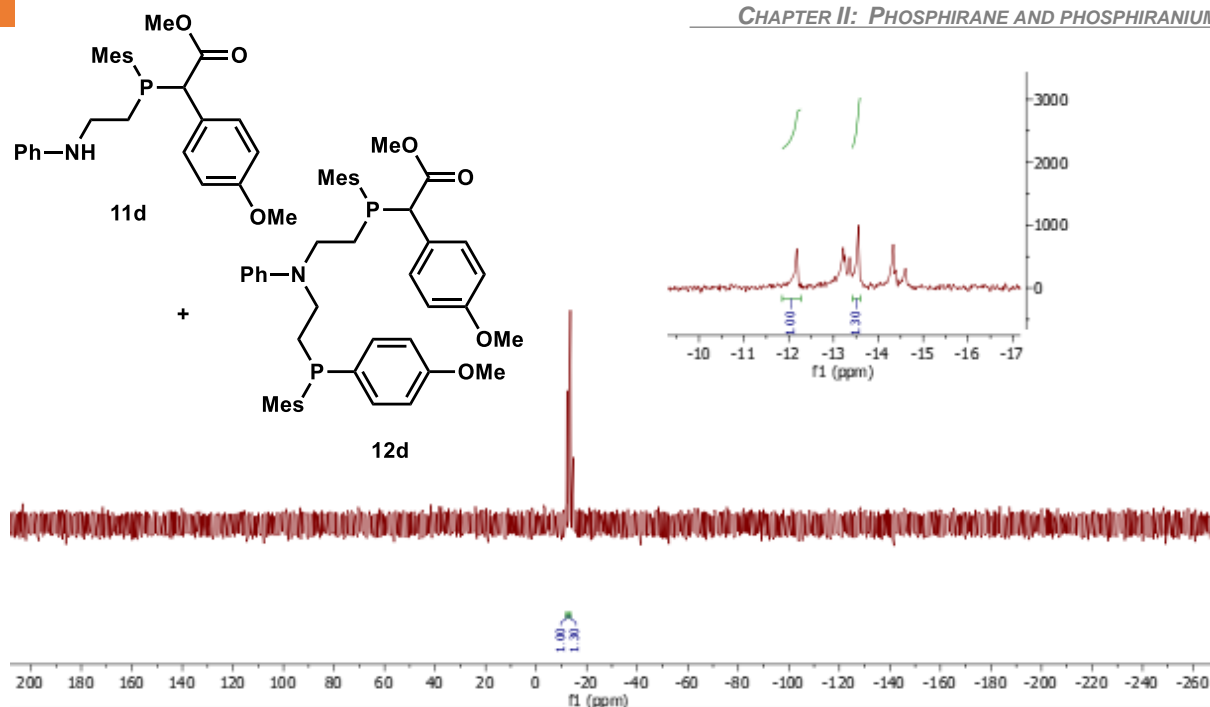


Figure II-55 : :  $^{31}\text{P}\{^1\text{H}\}$  NMR after addition of aniline (2 equivalents) on the phosphiranium salt **9d** and heating overnight. A mixture of mono and di-substitution products **11d** and **12d** is observed.

To test this hypothesis and prevent di-addition, we increased the number of equivalents of aniline from 2 to 10. The outcome was assigned to a total mono-addition selective ring opening towards **11d** (Figure II-56).

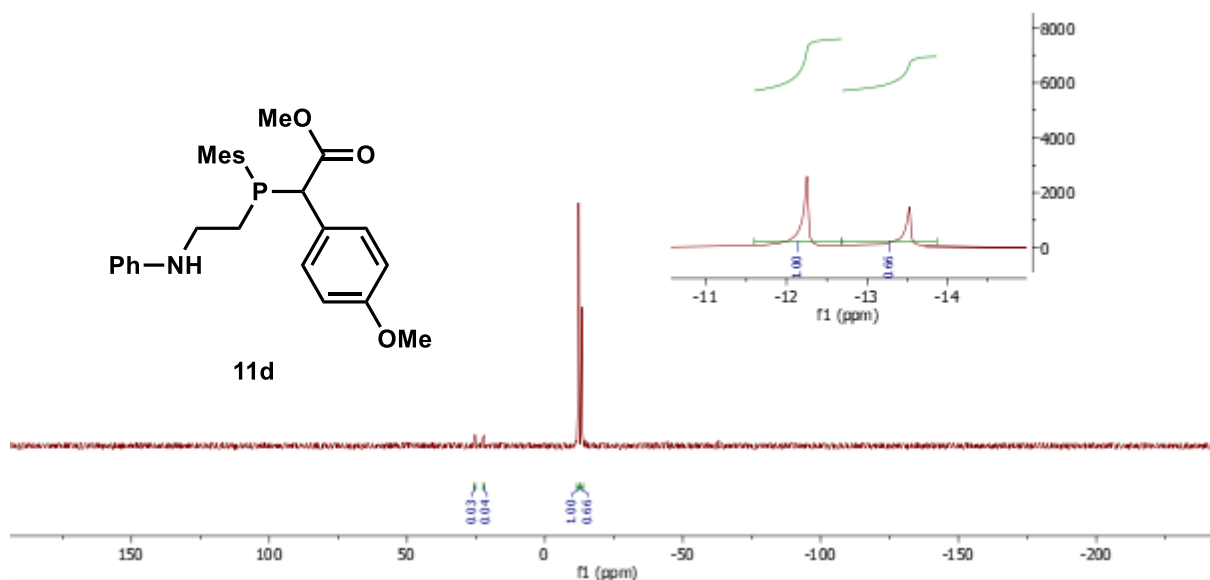


Figure II-56 : :  $^{31}\text{P}\{^1\text{H}\}$  NMR after addition of aniline (10 equivalents) on the phosphiranium salt and heating overnight. A mixture of mono and di-substitution products is observed.

Purification on this sample by flash chromatography provided 44% isolated yield of the mono-addition product **11d** as a mixture of two diastereoisomers **11d<sub>a</sub>** and **11d<sub>b</sub>** in a 2:1 ratio (Figure II-57).

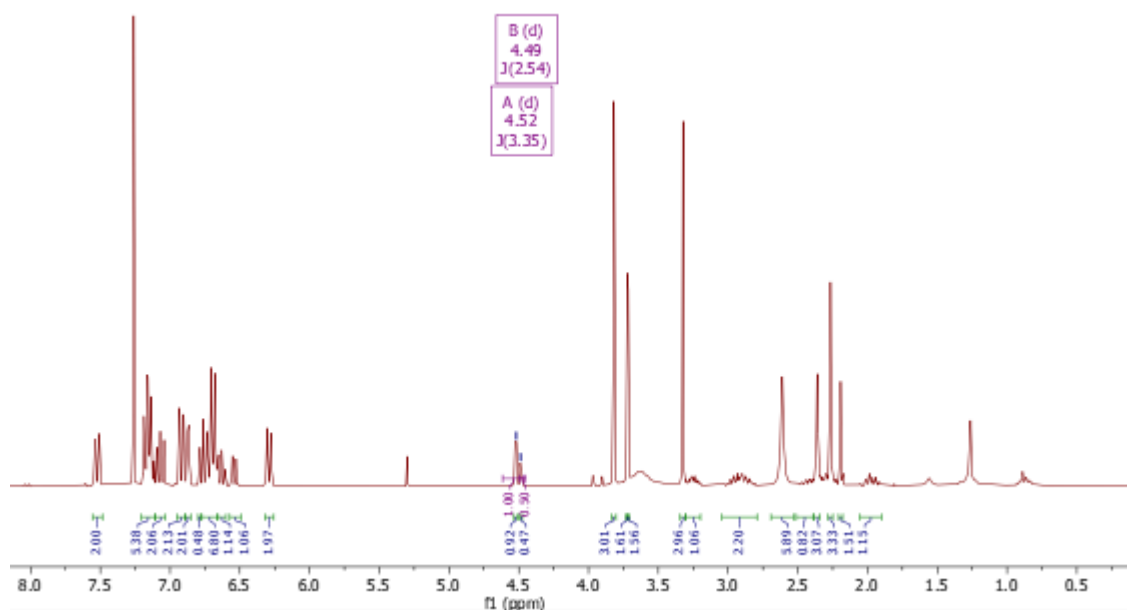


Figure II-57 :  $^1\text{H}$  of the isolated C-centered ring opening product **11d** with aniline

Some degradation may have occurred on silica gel as we could've expected a better isolated yield from the clean phosphorus NMR.

These results provide a good picture of the reactivity of the new phosphiranium salts generated with an unprecedented quaternarization method.

- ✓ No air sensitivity
- ✓ Ring opening is possible with aniline and was made selective towards the mono-addition using an excess amount of it in the given conditions

The reactivity of the phosphiranium salts **9** we have generated towards C-centered ring opening with aniline-type nucleophiles can then be undertaken to extend the observations made from this first exploration. We considered that despite having these first satisfying and encouraging results in hand, it would be better to focus our time and efforts towards the study of the completely unknown phosphiranium ylide **7**.

## 2.5. Reactivity of phosphiranium ylides: A regioselective C-centered ring opening

The reaction conditions for the generation of the ylide **7** were further investigated.

We have modified the concentration from 0.05 M to 0.1 and 0.2 M without any significant changes. Out of practicality regarding the ratio between the reactor size and the volume of solvent, the 0.05 M concentration was selected (Figure II-58).



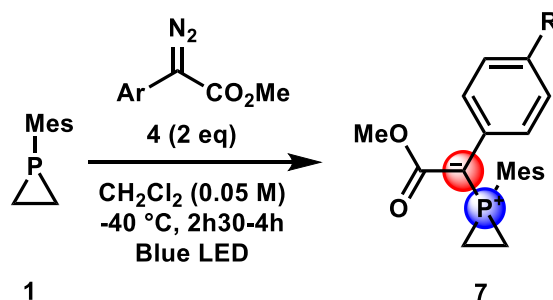


Figure II-58 : Optimized reaction conditions for the phosphiranium ylide generation

The robustness of the reaction was tested by changing the dry degassed solvent and the argon atmosphere. The *para*-chloro methylaryldiazoacetate **4e** was used for this exploration with 4 hours irradiation time. The reactions in entries 1 and 2 (Table II-5) were performed in commercial CD<sub>2</sub>Cl<sub>2</sub> that was further dried with molecular sieves and degassed by freeze-pump-thaw technique. Entry 1 was carried out under argon while entries 2-3-4 were carried out under air. The results were similar despite a small increase of the amount of phosphirane oxide **10**, indicating that the presence of oxygen in the atmosphere is a problem for the reaction. The same tendency was observed when commercial solvent was used straight as received with further increase of phosphirane oxide **10** and decrease of the ylide product **7e**. Finally, the reaction did not proceed at all when synthetic-grade solvent, that contains more water and is not degassed, was used. The amount of water seems to have been sufficient to quench the carbene before it could react with phosphirane **1**, and molecular oxygen oxidized some phosphirane over the course of the reaction.

Table II-5 : Exploration of the sensitivity of the standard reaction to oxygen

Entry	Solvent	Atmosphere	<sup>1</sup> H NMR ratio of the 3 products		
			Phosphirane oxide <b>10</b>	Ylide <b>7e</b>	Phosphirane <b>1</b>
1	Dry degassed CD <sub>2</sub> Cl <sub>2</sub>	Argon	0.3	7.3	1
2	Dry degassed CD <sub>2</sub> Cl <sub>2</sub>	Air	0.8	6.6	1
3	commercial CD <sub>2</sub> Cl <sub>2</sub> without further treatment	Air	1.4	5.9	1
4	commercial CH <sub>2</sub> Cl <sub>2</sub> without further treatment	Air	2.4	0	1

Overall, provided water and oxygen are excluded, one should be able to explore and take advantage of the potentially rich reactivity of the phosphiranium ylide **7**.

Phosphonium ylides are widely known as Wittig reaction's reagents. The first thing we have considered is therefore if a similar reactivity could be transposed to *phosphiranium ylides*. The usefulness of the phosphiranium ring for this type of transformation is unknown but could provide an important new addition to the current developments of the Wittig reaction, exactly 70 years after its original publication. A review from 2013 states that the current topics of interest for the Wittig reaction include new methodologies for the generation of the ylide, reactions with atypical stereoselectivity that can be induced by modification of the substituents on phosphorus, and one-pot reaction directly from the phosphine.<sup>60</sup> Both the phosphiranium ylides **7** and the method used to generate them enable us to foresee new interesting opportunities worth exploring.

The first major question is whether phosphiranium ylides **7** are stabilized or non-stabilized ylides. The presence of an EWG (CO<sub>2</sub>Me) and an aromatic substituent near the negative charge should act as stabilizing. This would of course depend on the nature of the R<sup>1</sup> substituents of the adjacent phenyl group (Figure II-59). However, the presence of the strained ring could make the ylide unstable. Maybe the ylide is electronically stabilized but unstable because of the ring strain? Furthermore, if the carbanion from the ylide adds on a ketone (R<sup>2</sup>C(O)R<sup>3</sup>), how will the alcoholate **13** behave? Will it add on phosphorus to generate a spiro-oxaphosphetane **14** that will evolve towards the alkene **15** and the phosphirane oxide **10**? Will it proceed to ring opening of the phosphirane ring of **13** and provide a highly substituted 1,4-oxaphosphorinane **16**, another class of exotic compounds? Or will something totally unexpected happen?

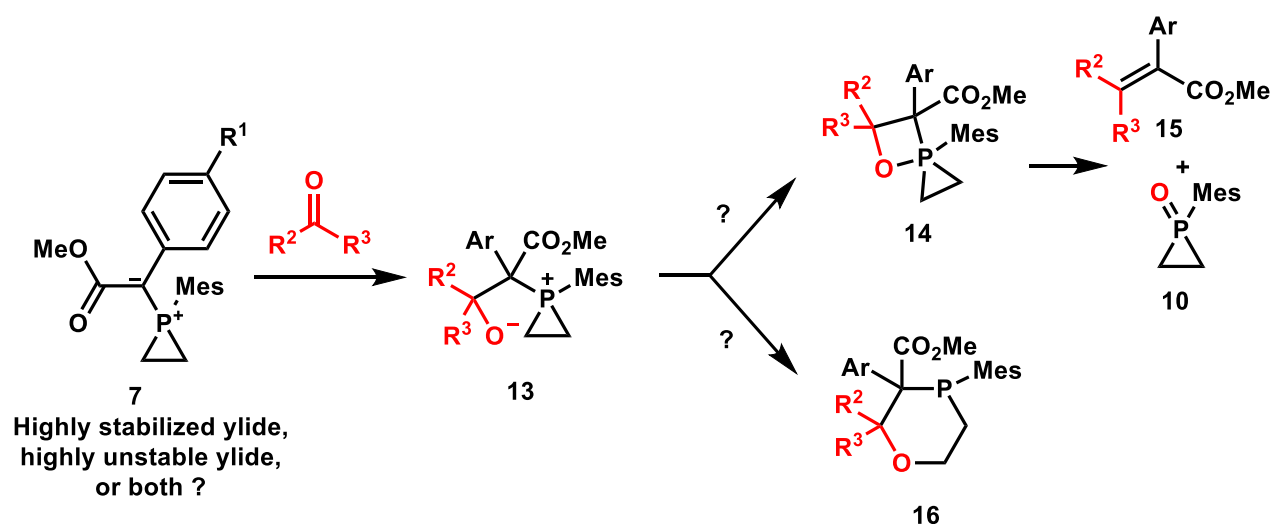


Figure II-59 : Envisioned possible mechanisms for the Wittig reaction with phosphiranium ylides

Another way to benefit from the peculiarity of phosphiranium ylides **7** could be for the challenging phosphiranium ring opening (Figure II-60). Indeed, in the presence of a nucleophile that could undergo deprotonation from the carbanion of the ylide, a highly reactive charged

nucleophile would be generated along with an electrophilic phosphiranium salt sterically hindered on the phosphorus. The competition between P-addition to provide **17** and C-addition to provide **18** may then be favored towards the carbon atom for steric reasons.

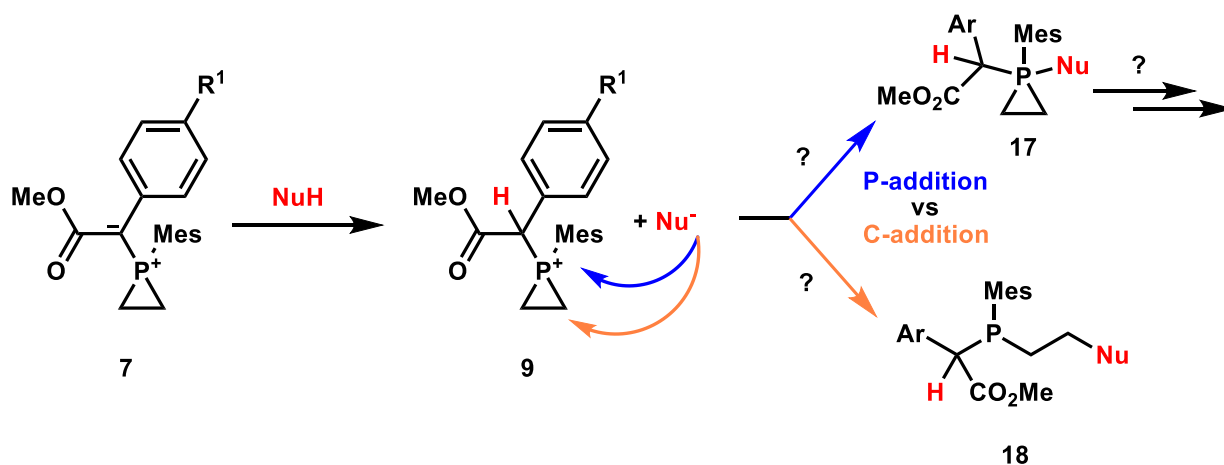


Figure II-60 : Envisioned possible mechanisms for the ring opening of phosphiranium ylides by protic nucleophiles

To help to identify which reaction to explore, we started by setting up two simple experiments. Both consisted in the generation of the phosphiranium ylide **7** following the previously described method, followed either by addition of an excess of benzaldehyde or by addition of an excess of phenol. The use of phenol was a risk because the nucleophile would be oxygenated, and therefore very likely to add on the phosphorus atom and not on the carbon atom. Nevertheless, it was worth trying that experiment to make one more step to clarify our vision of the topic.

The addition of benzaldehyde to the phosphiranium ylide **7e** did not result in full conversion after 72h (Figure II-61). The remaining phosphiranium ylide **7e** was transformed into phosphirane oxide **10** after evaporation of the solvent and addition of  $\text{CDCl}_3$  for NMR analysis (Figure II-62). However, the three main signals found by phosphorus NMR were the same as the ones observed before degradation of the ylide. They can be found at 24.9 ppm, 22.2 ppm and -44.7 ppm. The first two signals were unidentified and could not be recovered after column chromatography. The -44.7 ppm was phosphirane oxide **10**. Furthermore, column chromatography did not provide any Wittig reaction product.

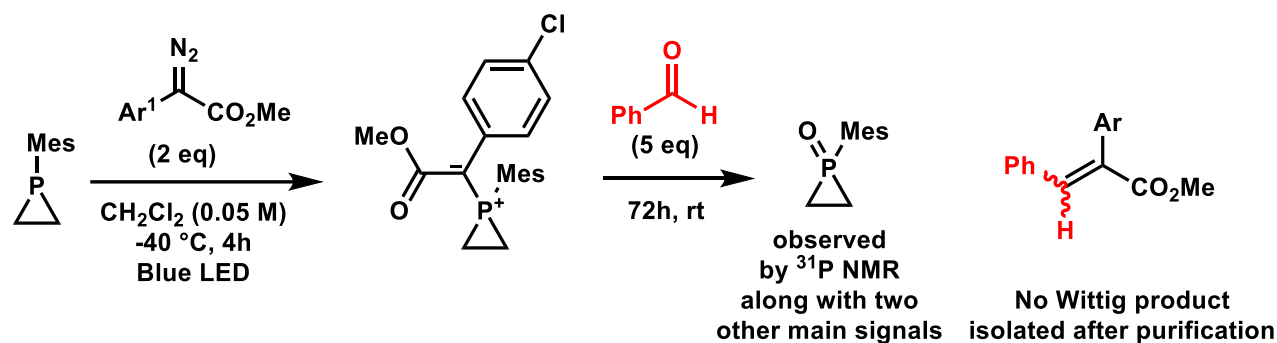


Figure II-61 : Wittig reaction attempt between phosphiranium ylide and benzaldehyde

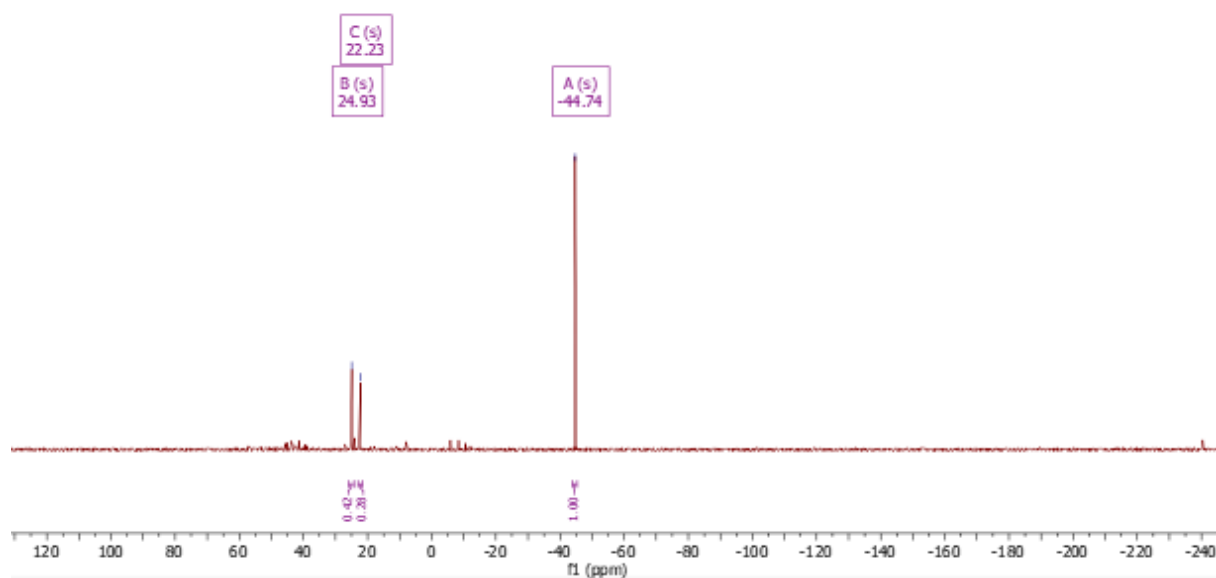


Figure II-62 :  $\{^1\text{H}\}^{31}\text{P}$  NMR of the air-exposed solution after Wittig reaction attempt between phosphiranium ylide and benzaldehyde

Conversely, the reaction of the phosphiranium ylide **7d** with phenol provided a very interesting result (Figure II-63). Several different phosphorus containing products were obtained, amongst which two products at with  $^{31}\text{P}\{^1\text{H}\}$  NMR shifts at -15.3 and -15.9 ppm, i.e. extremely similar to the C-centered ring opening products **11d** and **12d** obtained with aniline in this work (Figure II-64). Despite the presence of other products, these preliminary results are highly encouraging with respect to an unprecedented challenging C-centered ring opening of a phosphiranium ring **9d** with an oxygenated nucleophile towards phosphine **18**. Reaction occurred at room temperature, which was an indicator for an excellent reactivity in the previous phosphiranium C-centered ring opening publication.<sup>11</sup> This outstanding result led us to further explore this reactivity.

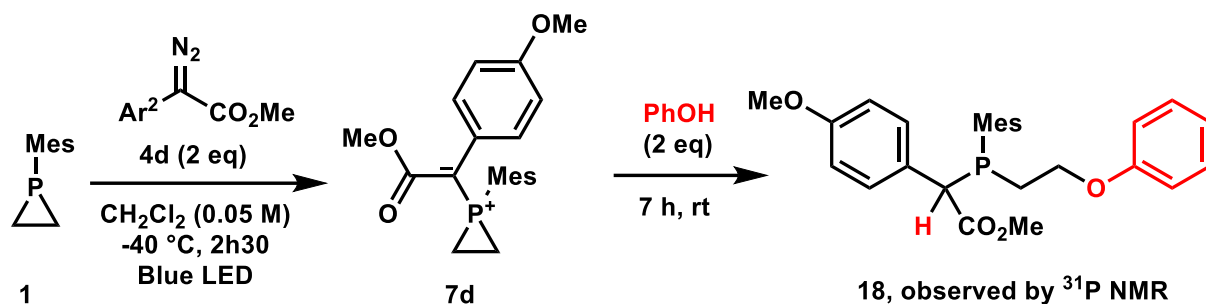


Figure II-63 : Ring opening attempt of phosphiranium ylide **7d** by phenol. Ar<sup>2</sup> : para-methoxyphenyl

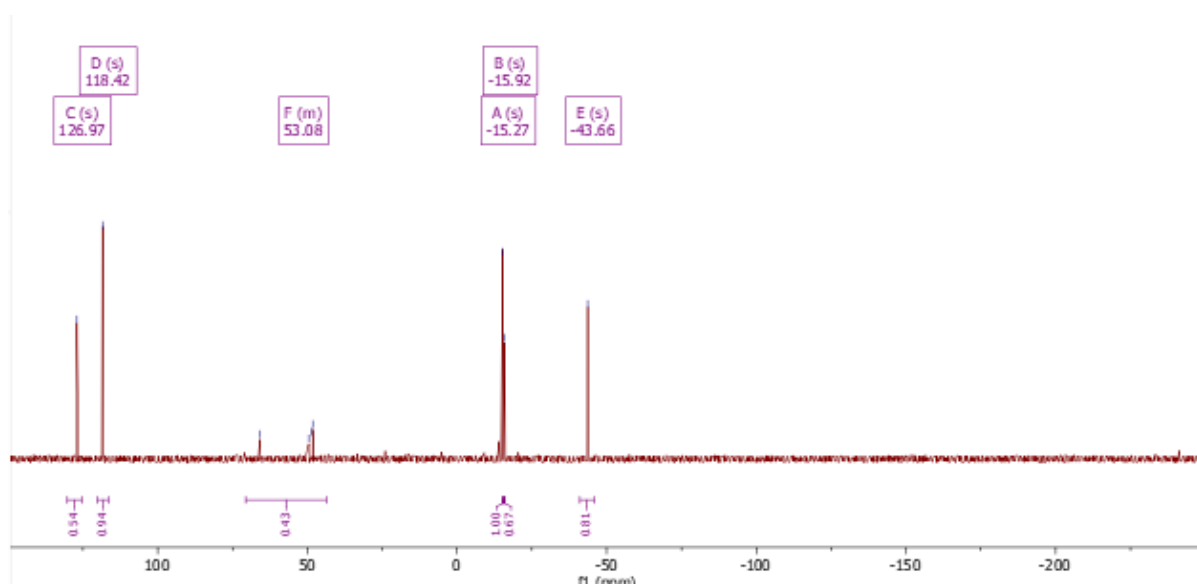


Figure II-64 : <sup>31</sup>P{<sup>1</sup>H} NMR of the ring opening of phosphiranium ylide **7d** by phenol

Using thiophenol instead of phenol, hoping to prevent any potential parasitic P-addition by replacing the oxygen atom from the nucleophile for a sulfur atom, we were thrilled to see that it worked extremely well to provide **19a** selectively (Figure II-65). What we assumed to be the two C-centered ring opening diastereoisomers **19a<sub>a</sub>** and **19a<sub>b</sub>** were almost the only signals in the <sup>31</sup>P{<sup>1</sup>H} NMR crude spectrum (Figure II-66). More surprisingly, the reaction was already complete at room temperature within 5 minutes (the time needed to reach the NMR spectrometer and the analysis to run).

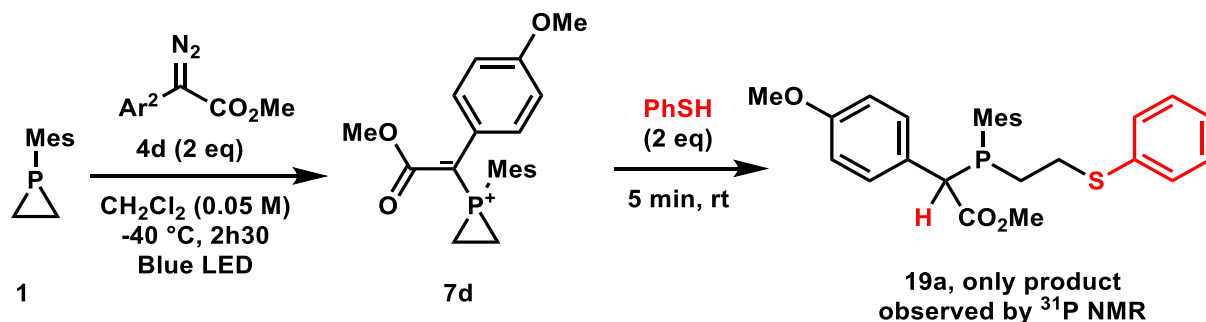


Figure II-65 : Ring opening attempt of phosphiranium ylide **7d** by thiophenol. Ar<sup>2</sup> : para-methoxyphenyl

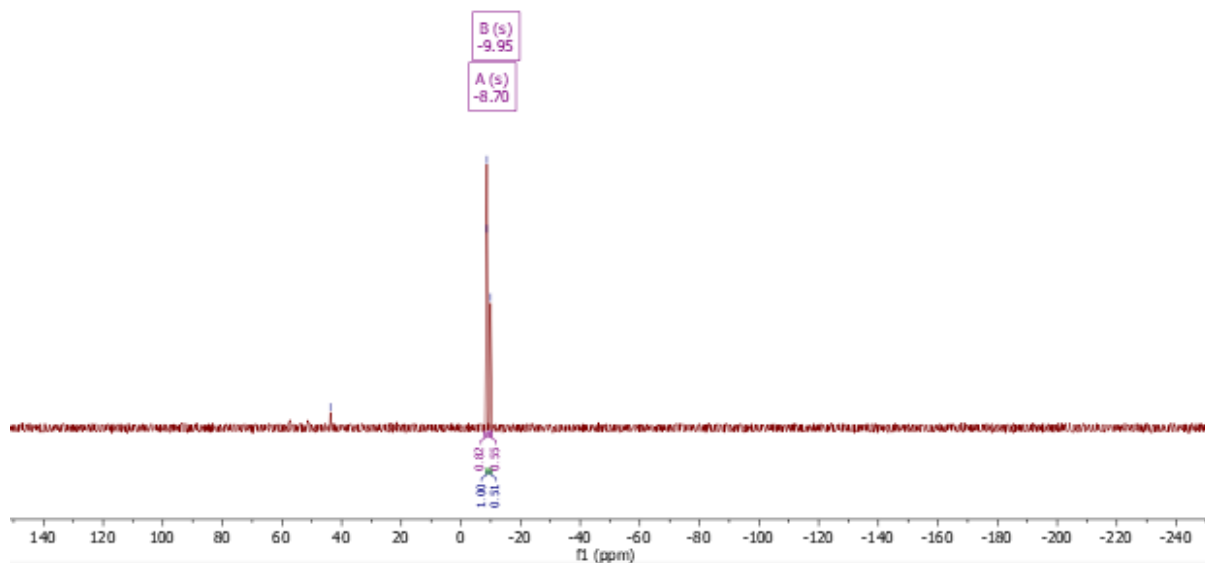


Figure II-66 :  $^{31}\text{P}\{^1\text{H}\}$  NMR of the ring opening of phosphiranium ylide **7d** by thiophenol to provide **19b<sub>a</sub>** and **19b<sub>b</sub>**

We then proceeded to check the applicability of the method by studying the scope of the reaction with different aryldiazoacetates **4** and different thiophenols. We monitored the reaction by  $^1\text{H}$  NMR, focusing on the aliphatic proton at the alpha position of the ester by comparing its integration against an internal standard (Figure II-67). The proton-phosphorus coupling constant for the alpha-ester of *ca.* 2-3 Hz is typical of the phosphine resulting from ring opening **19a**.

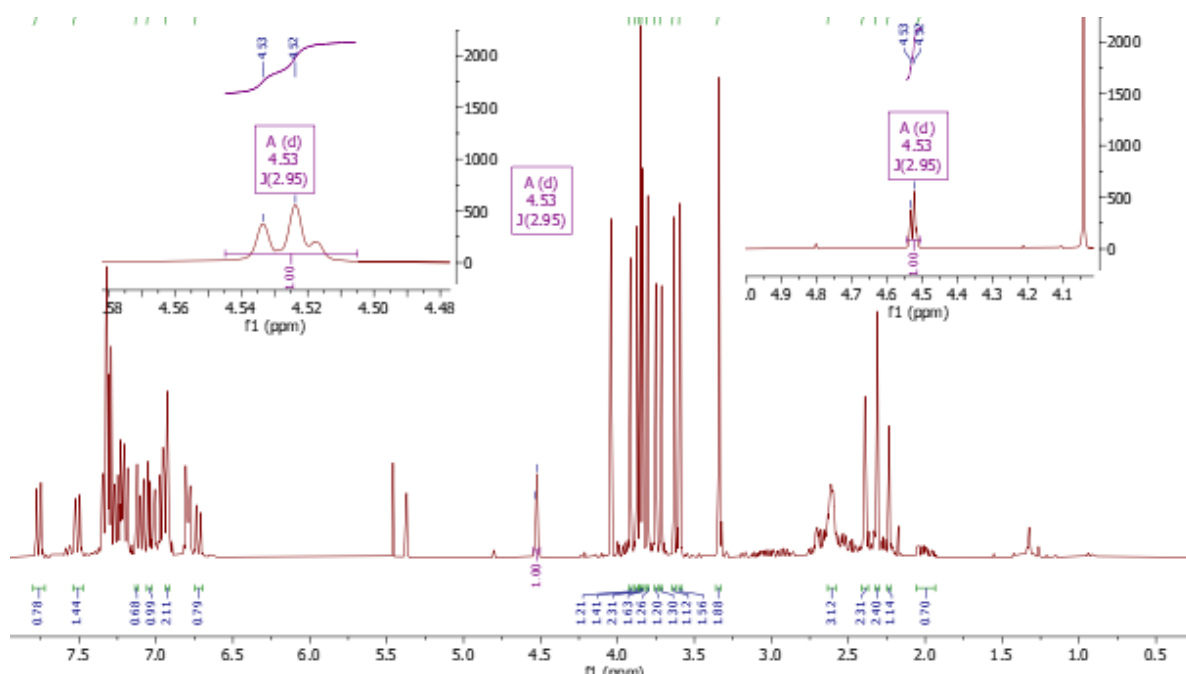


Figure II-67 :  $^1\text{H}$  NMR of the ring opening of phosphiranium ylide **7d** by thiophenol with several the same area zoomed twice to show that the signal has no parasitic signals next to it. The doublets of the two diastereoisomers are superimposed.

The aromatic protons from trimethoxybenzene (TMB), used as internal standard, also came out in a white region (6.05 ppm). We added 0.33 equivalents of TMB per NMR tube so that the integration of the signals of the proton from the ring opening product would give the NMR yield (76% in Figure II-68 with phosphine **19b** for which the diastereoisomers' proton signals are not superimposed).

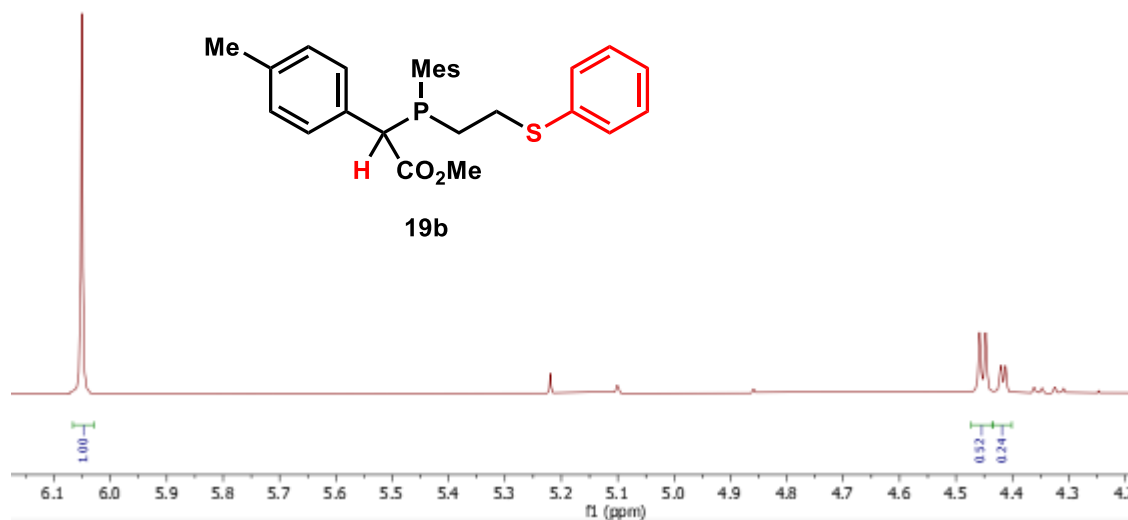


Figure II-68 :  $^1\text{H}$  NMR between 4.2 and 6.2 ppm after the ring opening of phosphiranium ylide **7b** by thiophenol with the signal of the internal standard (IS) at 6.05 ppm. Integration of the IS signal for 1 provides the NMR yield of the ring opening with the integration of both signals between 4.4 and 4.5 ppm which accounts for 0.76 in this example (0.52+0.24).

We then proceeded to investigate the scope of the reaction. We selected 15 thiophenols with different electronic and steric properties. 5 different *para*-substituted methyl aryldiazoacetates were also tested in this reaction. The reaction proceeded well and NMR yields ranged from 44 to 97%. For the methyl aryldiazoacetate scope, thiophenol was selected as the nucleophile for it comes without electronic or steric effects from substituents. The yields range from 59 to 97% and do not seem to be highly impacted whether the *para* substituent is a *para*-H, methyl, *tert*-butyl or chloro. The best (and excellent) result of 97% yield was obtained with methyl *para*-methoxyphenyldiazoacetate **4d**, which was selected as the reference diazo compound for the thiophenol scope. We assigned this observation to the fact that methyl *para*-methoxyphenyldiazoacetate provides the most stabilized carbene with a push-pull effect that leads to fewer side reactions in the ylide formation and an improved yield of ring opening by mitigating the electron density around phosphorus.

The thiophenol scope (Figure II-69) proved to be rather insensitive to electronic effects (*para*-methoxy **19f** 86%, *para*-nitro **19g** 84%), steric effects (xylenes **19q** 85% and **19r** 84%, mesitylene **19s** 76%) or heteroarene (2-pyridine **19p** 75%). The introduction of an aromatic amine (**19m**) did not change the course of the reaction while introduction of an aromatic alcohol

(19n) led to a decreased yield. Surprisingly, no side product resulting from an opening at the oxygen atom could be identified. We remind the reader that the reaction times with phenol were much higher (several hours required) than the ones with thiophenol (few minutes) in the first explorative experiments. .

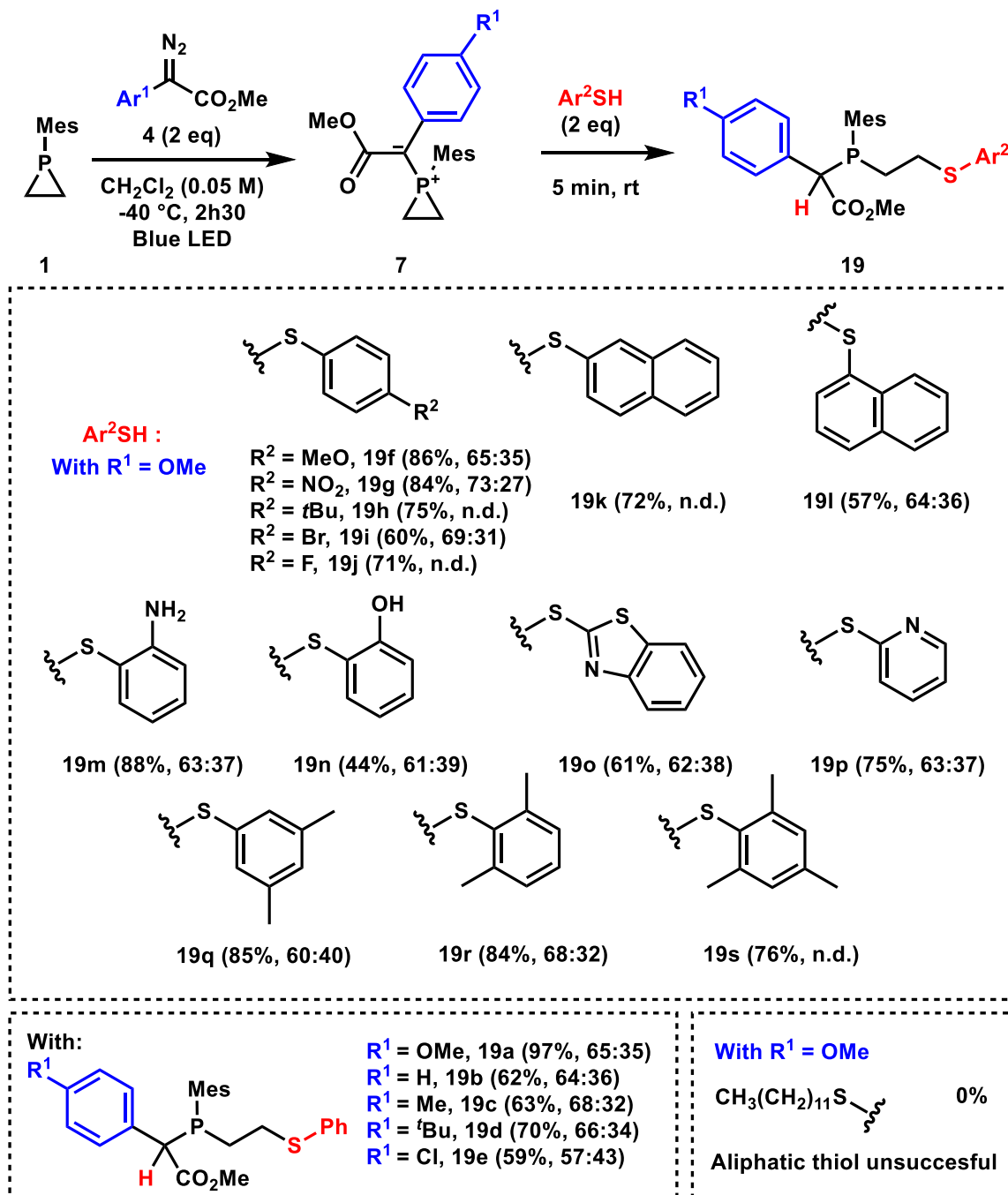


Figure II-69 : Conditions : 1-mesitylphosphirane (1 eq, 0.05 mmol), aryldiazoacetate (2 eq, 0.1 mmol) at  $-40^\circ\text{C}$  for 2h30 to 4h00 in  $\text{CH}_2\text{Cl}_2$  (0.05 M, 1 mL) then thiophenol (2 eq, 0.1 mmol) at rt for 5 min. NMR yields given against 1,3,5-trimethoxybenzene as internal standard. The diastereomeric ratios are given in parentheses and were obtained by comparison of the relative integration of the signal of each diastereoisomer either by proton or phosphorus NMR when possible. Phosphorus NMR integration was proved to be reliable in this case. n.d. : not determined



These results suggest that the driving force is most likely the ring strain release that makes the reaction quite insensitive to the nature of the substituents on the reactants.

Once the reactivity map was established from  $^1\text{H}$  NMR yields, we investigated ways to isolate the product. The purpose was to reach isolated yields and fully characterize the products, proving without ambiguity that phosphines were indeed formed. Four strategies were considered (Table II-6), including direct purification of the phosphine by flash chromatography, formation a phosphine-borane adduct followed by purification by flash chromatography, protonation to the phosphonium salt followed by ether wash or recrystallisation, and oxidation to the phosphine oxide followed by flash chromatography. The qualitative results are displayed in the table and discussed in more details in the following paragraphs.

Table II-6: Strategies tried and their result for isolation of the phosphines. mCPBA : meta-chloroperbenzoic acid, oxone : potassium peroxymonosulfate

Attempt n°	Isolation method	Reagent	Comment
1	Flash chromatography	Heptane-AcOEt	No desired product isolated, decomposition to the phosphirane oxide
2	Phosphine-borane formation then flash chromatography	$\text{BH}_3\cdot\text{SMe}_2$	Full conversion Clean reaction. Product was isolated but decomposes a little during purification and after towards the oxide. Yield not determined.
3	Phosphonium salt formation then ether wash or acetone/ether recrystallization	$\text{HBF}_4$ or TfOH	Full conversion Promising crude NMR No successful isolation
4	Oxidation then flash chromatography	Air bubbling	Full conversion Oxidation is not selective Discarded
5		mCPBA	Full conversion Oxidation is not selective (1, 1.2, or 4 equivalents) 56% isolated with 1.2 eq of mCPBA

6		Oxone	Solubility issues Discarded
7	Oxidation then flash chromatography	H <sub>2</sub> O <sub>2</sub>	1 eq: incomplete conversion 10 or 50 eq: full conversion, not selective 5 eq: full conversion, selective 83% isolated yield Robust and reproducible reaction/purification.

The main results obtained from the phosphine-borane (Figures 70-71), the phosphonium salt (Figures 72-73) and the phosphine oxide (Figures 74-75) are displayed thereafter in a combination of <sup>1</sup>H and <sup>31</sup>P NMR.

The phosphine-borane adduct **20** was formed quantitatively after addition of BH<sub>3</sub>.SMe<sub>2</sub> to a solution of **19a** in dichloromethane. The crude NMR spectra are displayed in Figure II-70 (bottom).

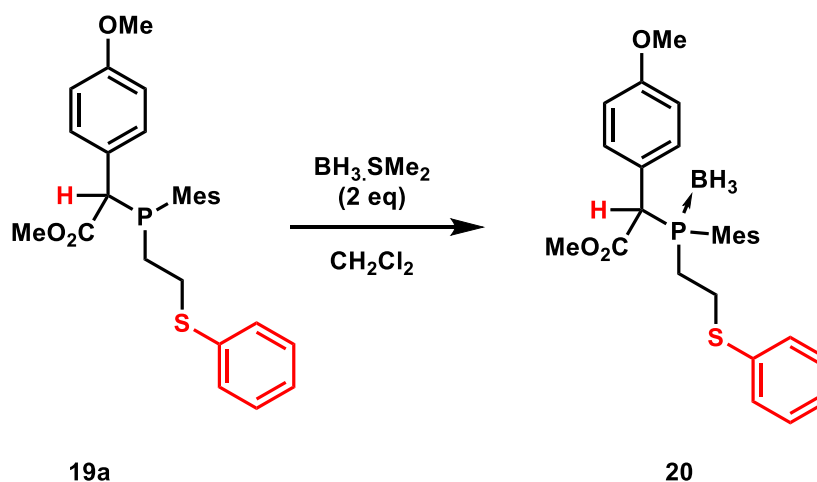


Figure II-70 (top) : Reaction scheme for the formation of phosphine-borane **20**

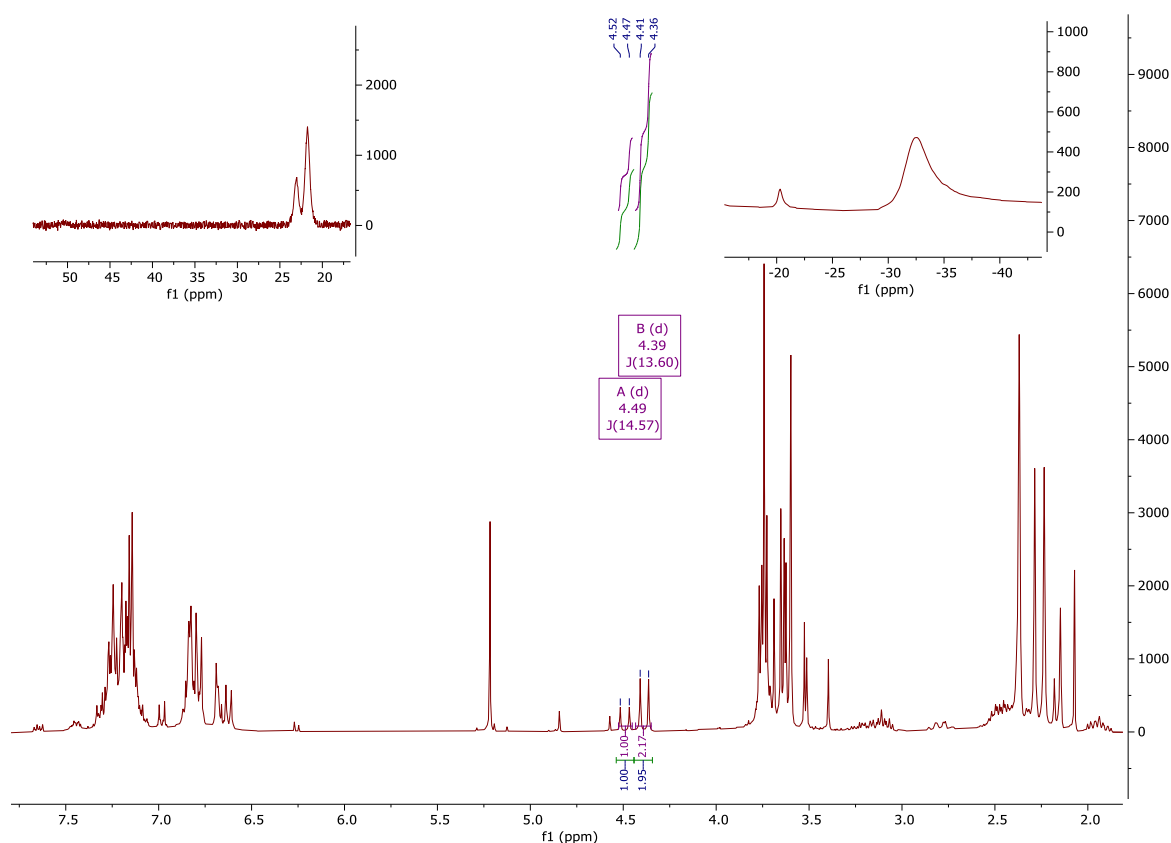


Figure II-70 (bottom) : Main spectrum:  $^1\text{H}$  NMR of the crude reaction. Top left:  $^{31}\text{P}$  NMR. Two broad signals are obtained at ca. 22 ppm, characteristic of phosphine-borane adducts. Top right:  $^{11}\text{B}$  NMR.  $\text{BH}_3\cdot\text{SMe}_2$  (-20.3 ppm) and the product signals (-32.2 ppm).  $^1\text{H}$  NMR: two doublets at 4.4 ppm and 4.5 ppm are characteristic of the phosphine-borane adduct.

After purification, NMR was recorded again (Figure II-71). The presence of two diastereoisomers is substantiated by the typical doublet signal for the proton shown in red in Figure II-70, now having a P-H coupling constant of 13.55 Hz ( $\delta = 4.43$  ppm), juxtaposed with a doublet with a P-H coupling constant of 14.54 Hz ( $\delta = 4.53$  ppm). The borane selective coordination on phosphorus was assessed by a single signal by  $^{11}\text{B}$  NMR at -32.2 ppm, getting rid of the excess  $\text{BH}_3\cdot\text{SMe}_2$  observed after reaction at -20.3 ppm. By phosphorus NMR, two broad signals were obtained at 21.8 and 23.1 ppm (Figure II-70, top left). After purification, new signals at ca. 41 ppm appeared, due to partial phosphine oxidation. The phosphine-borane adduct **20** is therefore relatively unstable (stable enough to be purified on silica but decomposes partially towards the phosphine oxide in the process).

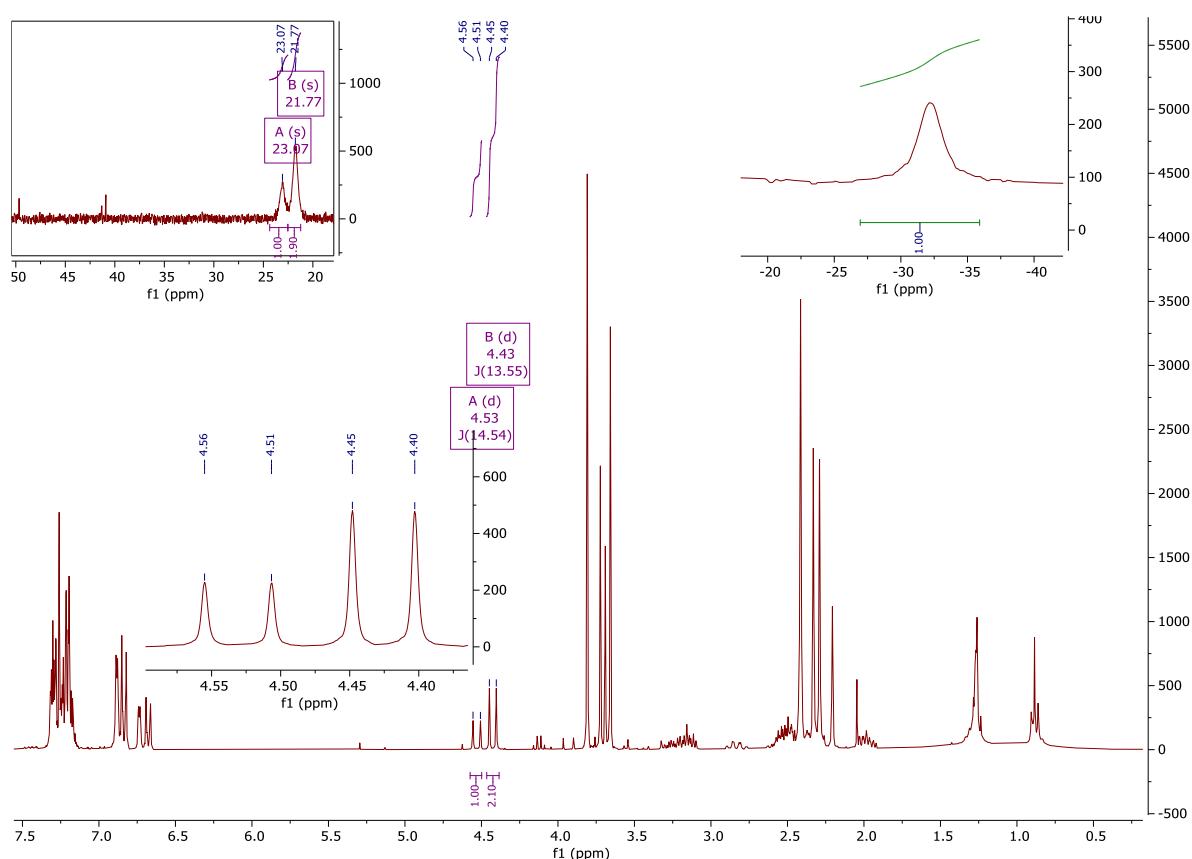


Figure II-71 : Main spectrum:  $^1\text{H}$  NMR of the phosphine-borane **20** after purification. Top left:  $^{31}\text{P}$  NMR. The presence of phosphine oxide is observed. Top right:  $^{11}\text{B}$  NMR. Only the product signal is obtained at -32.2 ppm.  $^1\text{H}$  NMR: two doublets at 4.4 ppm and 4.5 ppm are characteristic of the phosphine-borane adduct.

Another purification attempt was taken with the protonation of the phosphine with  $\text{HBF}_4$  which provided quantitative conversion to the phosphonium salt **21** (Figure II-72). The concentrated reaction mixture was washed with ether but the phosphonium was not isolated pure.

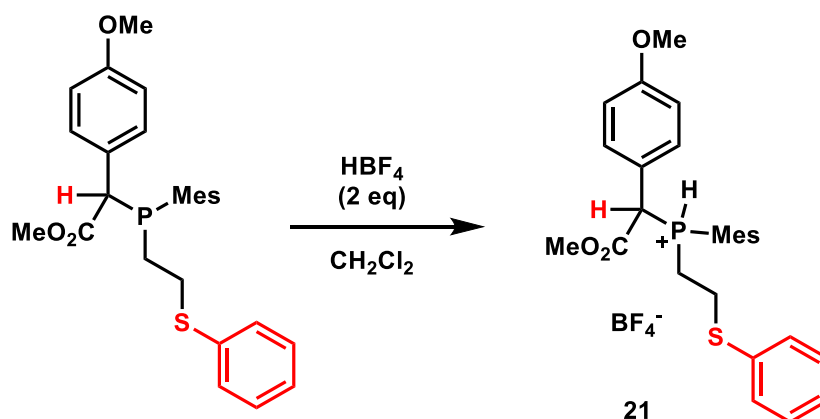


Figure II-72 : Reaction scheme of the protonation of the phosphine **19a** with  $\text{HBF}_4$

The typical diastereoisomers proton signals shifted from 4.53 ppm to 5.35 ppm as an apparent doublet of doublet with coupling constants of 9.7 and 12.8 Hz (top left box of Figure II-73) which after purification attempts was recorded at 5.36 ppm as a more complex superimposed signal apparent as a multiplet (top middle box of Figure II-73). This is consistent with the

presence of the coupling with one phosphorus atom in  $^2J$  and one hydrogen atom in  $^3J$ . The proton decoupled phosphorus signals shifted to 2.2 and 2.5 ppm (top right box of Figure II-73).

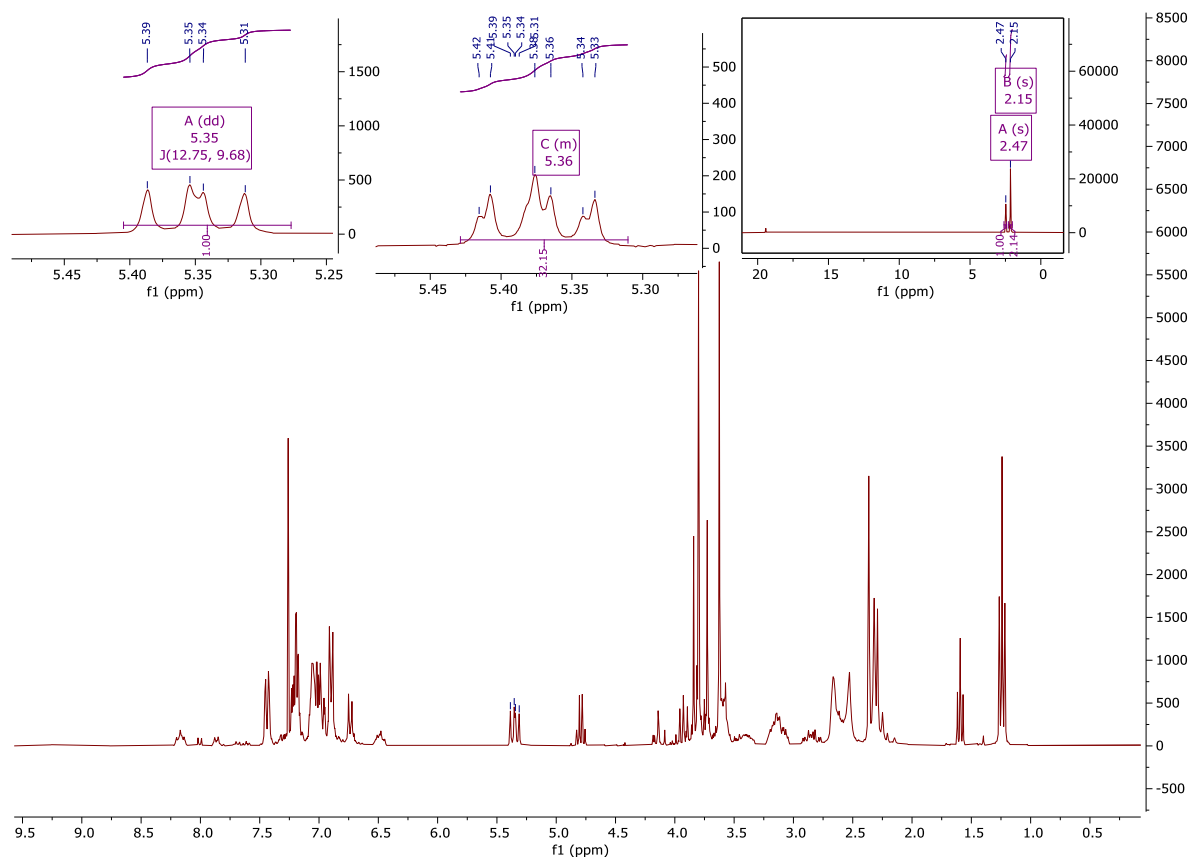


Figure II-73 : Main spectrum:  $^1\text{H}$  NMR of the phosphonium after diethyl ether wash. Top left:  $^1\text{H}$  NMR of the typical aliphatic signal before purification. Top middle:  $^1\text{H}$  NMR of the typical aliphatic signal after purification attempt. It now shows a multiplet. Top right:  $^{31}\text{P}$  NMR.

Finally, oxidation of the phosphine with hydrogen peroxide provided quantitative conversion towards the robust phosphine oxide **22a**, which could be handled easily without any further degradation (Figure II-74).

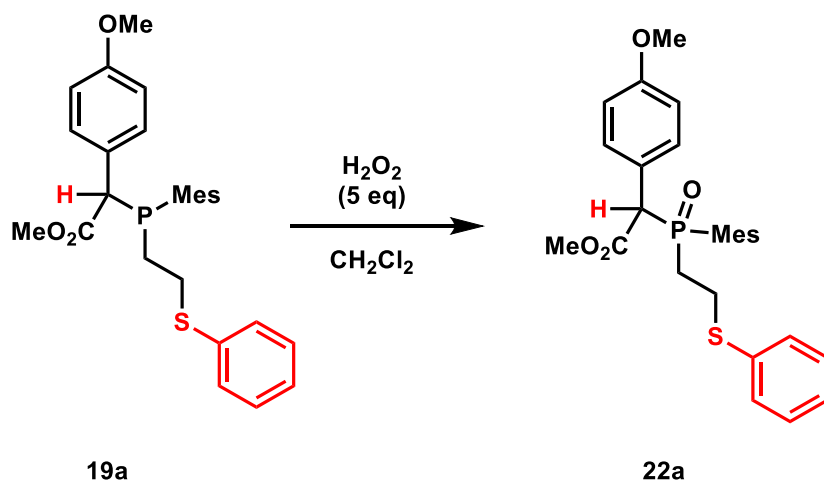


Figure II-74 : Reaction scheme of the oxide of the phosphine with  $\text{H}_2\text{O}_2$

The typical proton signals are found at 4.34 ppm ( $^2J_{\text{P-H}} = 11.3$  Hz) and 4.37 ppm ( $^2J_{\text{P-H}} = 11.1$  Hz). The phosphorus signals resonate at 40.9 and 41.4 ppm respectively (Figure II-75).

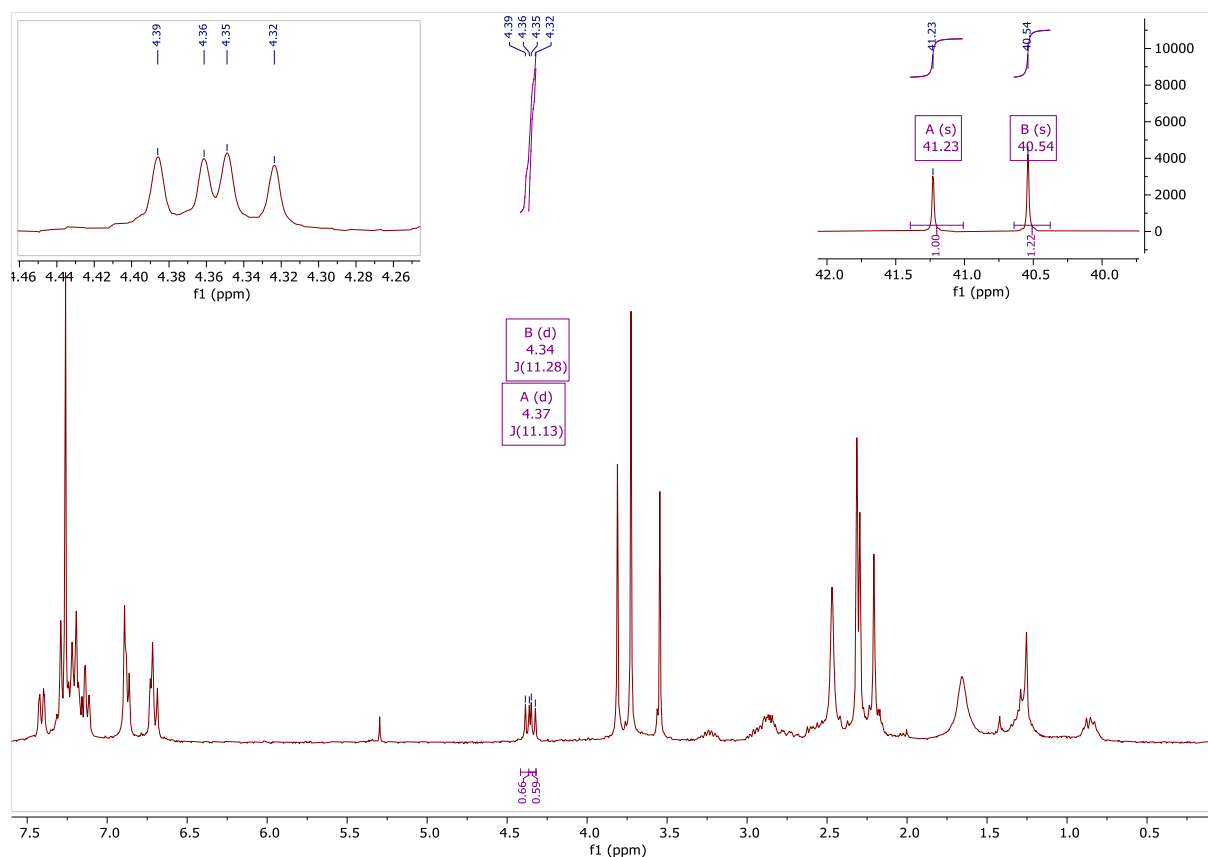


Figure II-75 : Main spectrum:  $^1\text{H}$  NMR of the phosphine oxide after purification. Top left:  $^1\text{H}$  NMR of the typical aliphatic signal before purification. Top right:  $^{31}\text{P}$  NMR with only two signals.

Table II-7 summarizes the chemical shifts and coupling constants of the most important signals obtained with each method.

Table II-7 : signal 1 and 2 for  $^1\text{H}$  NMR correspond to two characteristic proton of both diastereoisomers in their increasing ppm order, and signals a and b for  $^{31}\text{P}\{^1\text{H}\}$  NMR corresponding respectively to the major and minor signals.

Molecule	$^1\text{H}$ signal 1	$^1\text{H}$ signal 2	$^{31}\text{P}$ signal a	$^{31}\text{P}$ signal b
Phosphine <b>19a</b>	4.52 ppm $^2J_{\text{P-H}} = \text{n/a.}$	4.53 ppm $^2J_{\text{P-H}} = 3.0$ Hz	-8.7 ppm	-10.0 ppm
Phosphine-borane <b>20</b>	4.43 ppm $^2J_{\text{P-H}} = 13.6$ Hz	4.53 ppm $^2J_{\text{P-H}} = 14.5$ Hz	21.8 ppm	23.1 ppm
H-phosphonium <b>21</b>	5.36 ppm multiplet		2.2 ppm	2.5 ppm
Phosphine oxide <b>22a</b>	4.34 ppm $^2J_{\text{P-H}} = 11.3$ Hz	4.37 ppm $^2J_{\text{P-H}} = 11.1$ Hz	40.9 ppm	41.4 ppm

Oxidation of phosphine **19a** provided the most robust product **22a** in a selective fashion while phosphine-borane adduct **20** was also obtained selectively but proved less robust. Oxidation was thus selected as the method of choice for the scope of the reaction, taking advantage of isolated phosphine oxides **22** to avoid the unpredictable degradation of phosphine-borane adducts.

The phosphine oxide was isolated in 83% yield (Figure II-76).

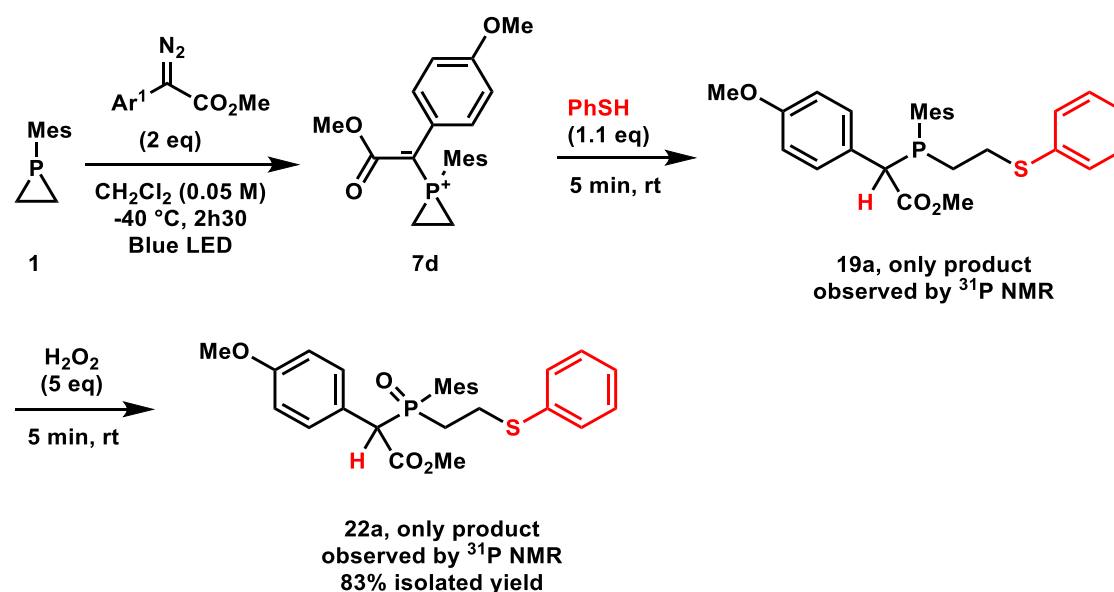


Figure II-76 : Complete reaction scheme for the formation of the phosphiranium ylide **7d** followed by ring opening with thiophenol and final oxidation of the phosphine with H<sub>2</sub>O<sub>2</sub> to provide **22a**. The final isolated yield is given. Ar<sup>1</sup>: *para*-methoxyphenyl

Unfortunately, NMR spectra of the isolated product showed the presence of a significant amounts of grease that we were not able to get rid of. Thus, the identification and the yields of this product was based on HRMS, <sup>1</sup>H and <sup>31</sup>P NMR. Aziz Arfa, a master's student who joined COP team for a short internship, worked on this project under my supervision to isolate some phosphine oxides **22**. The results of his work are not presented here as he was not able to get rid of the grease despite many attempts. On this basis and in the interest of time, we had to choose between the full characterization and scope of the reaction with thiophenols, or further exploration of their reactivity with other reaction partners. We decided to investigate the reaction with carboxylic acids, which were partners of higher interest. The reaction had chances to be successful since carboxylic acids bear an acidic proton and become nucleophilic after deprotonation. Furthermore, they are oxygenated nucleophiles, which are intrinsically more challenging, and therefore, more interesting reaction partners than thiophenols.

The test reaction with *para*-nitrobenzoic acid worked with great success, instantly at room temperature and the oxidation with H<sub>2</sub>O<sub>2</sub> was selective and total by <sup>31</sup>P NMR. Reaction

conditions were further optimized by lowering the number of equivalents of nucleophile from 2 to 1.1 while maintaining the same conversion (Figure II-77), as established by  $^{31}\text{P}$  NMR. The high 83% isolated yield for the single product **24a** encouraged us to further explore this novel reactivity.

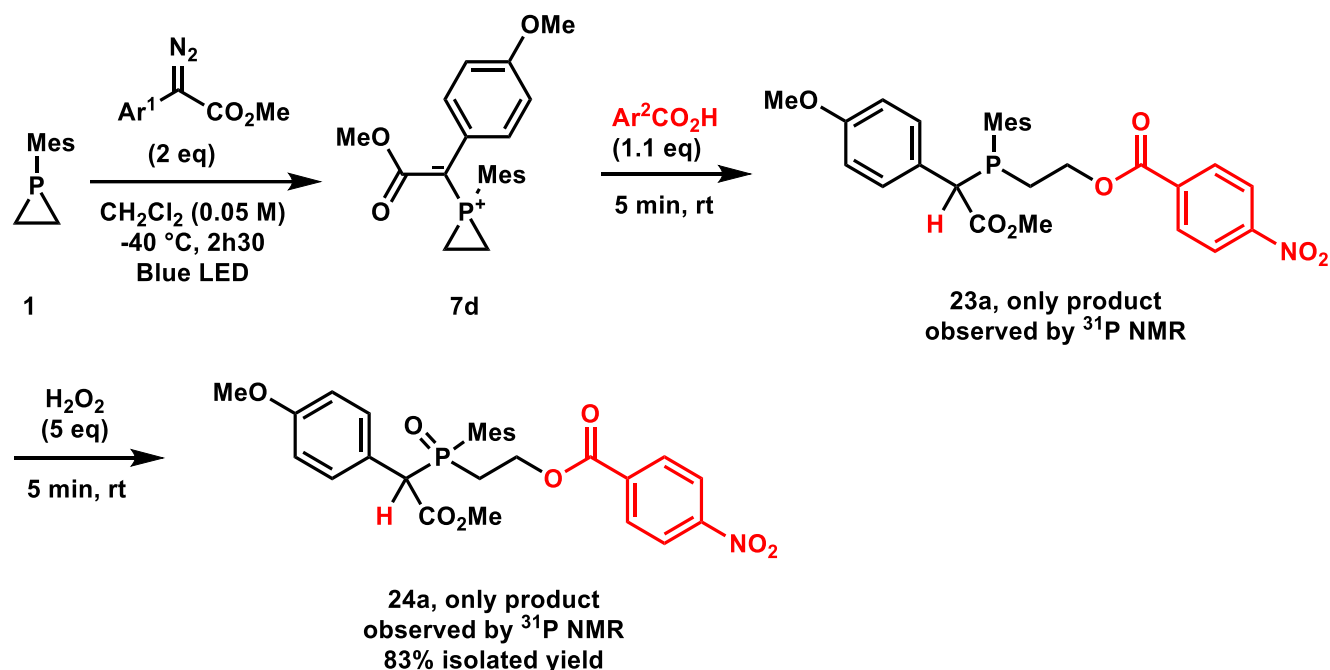
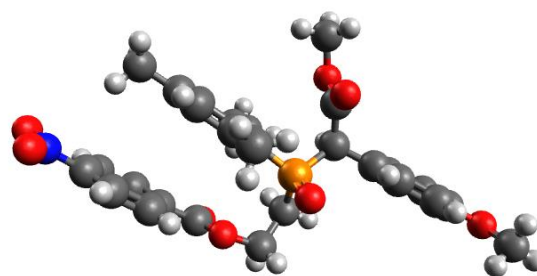


Figure II-77 : Complete reaction scheme for the formation of the phosphiranium ylide **7d** followed by ring opening with 4-nitrobenzoic acid and final oxidation of the phosphine with H<sub>2</sub>O<sub>2</sub> to provide **23a**. The isolated yield is given. Ar<sup>1</sup>: para-methoxyphenyl, Ar<sup>2</sup>: para-nitrophenyl

Crystals of **24a** suitable for X-ray diffraction were grown in a CH<sub>2</sub>Cl<sub>2</sub>-Heptane 1:1 mixture by liquid-liquid diffusion at 5 °C. The structure obtained confirmed the reaction displayed in Figure II-77 and is given in Figure II-78.

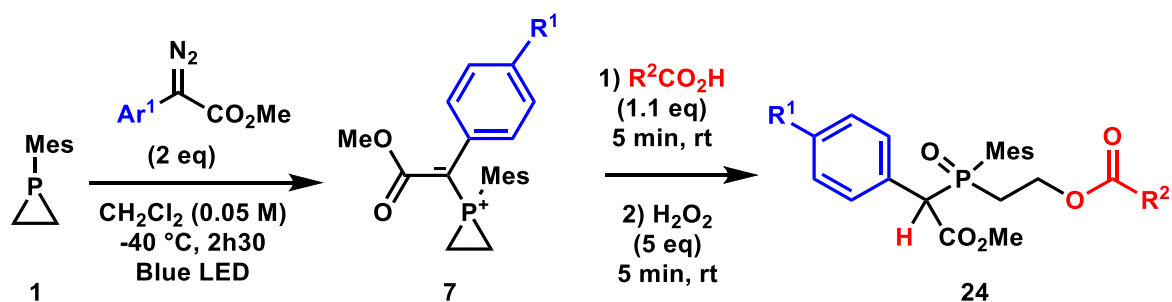
Figure II-78 (on the right) : XRD data of the phosphine oxide **24a** resulting from H<sub>2</sub>O<sub>2</sub> quenching of the phosphine after ring opening with 4-nitrobenzoic acid



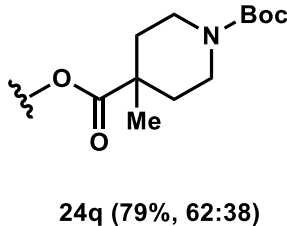
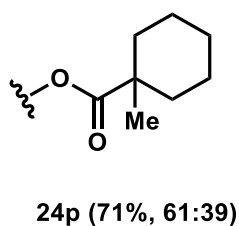
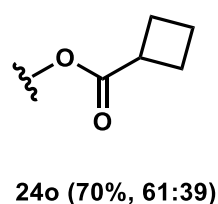
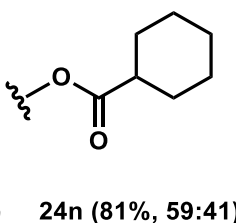
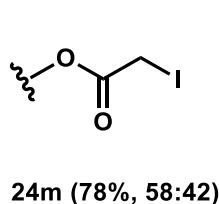
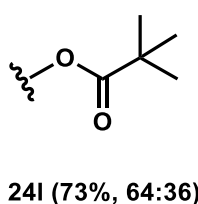
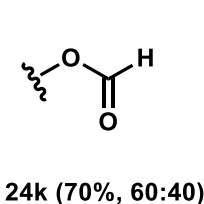
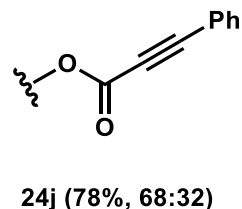
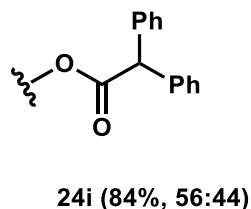
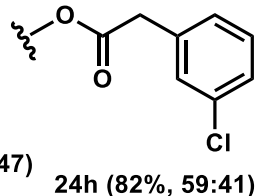
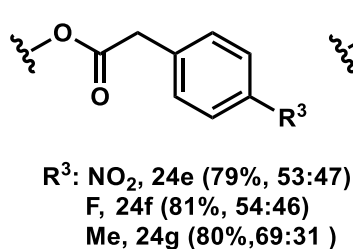
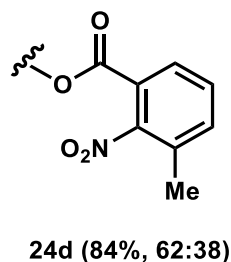
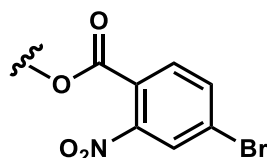
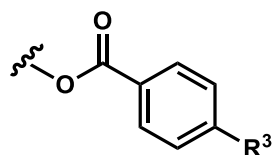
At this point, Avisek Ghosh, a PhD student from the COP team, joined the project to carry on with the synthetic and analytic work while my taste for the understanding of reaction mechanisms led me to learn and apply DFT calculations to this project.

Avisek Ghosh isolated and confirmed the structures of more than 20 compounds through a panel of analyses (HRMS,  $^1\text{H}$ ,  $^{13}\text{C}$ ,  $^{31}\text{P}$  NMR experiments) and performed 2D NMR investigations to assign all  $^1\text{H}$  and  $^{13}\text{C}$  signals. He performed the important scope that is displayed hereafter to provide an overview of the applicability of the reaction (Figure II-79).





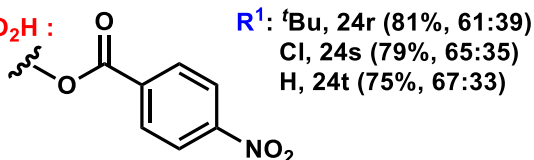
R<sup>2</sup>CO<sub>2</sub>H :  
With R<sup>1</sup> = OMe



This work  
was  
performed  
by Avishek  
Ghosh



With R<sup>2</sup>CO<sub>2</sub>H :



With R<sup>2</sup>CO<sub>2</sub>H :

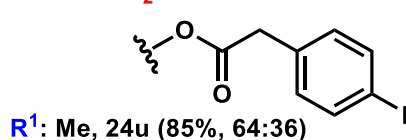


Figure II-79 : Conditions : 1-mesitylphosphirane (1 eq, 0.1 mmol), aryldiazoacetate (2 eq, 0.2 mmol) at - 40 °C for 2h30 to 4h00 in CH<sub>2</sub>Cl<sub>2</sub> (0.05 M, 2 mL) then carboxylic acid (1.1 eq, 0.11 mmol) at rt for at least 5 min, followed by addition of H<sub>2</sub>O<sub>2</sub> at rt and stirring for at least 5 min. Isolated yields are given and the diastereomeric ratios are given in parentheses. They were obtained by comparison of the relative integration of the signal of each diastereoisomer by phosphorus NMR. Phosphorus NMR integration was proved to be reliable in this case. Boc : tert-butyloxycarbonyl

The same observations as the ones of the thiophenol scope can be done here. All yields are high and little sensitive to the nature of the substituents. The scope could be extended in the case of carboxylic acids to benzylic and aliphatic substrates without major losses in the yield. The reactions conditions were tolerant towards functional groups such as protected amines NBoc, alkynes, aliphatic iodides and aromatic bromides, chlorides, and fluorides.

## 2.6. Computational studies

To get better insights into the mechanism of formation of the phosphiranium ylides **7** and their ring opening reaction in the presence of carboxylic acids, we have undertaken density-functional theory (DFT) calculations. This work was done under the supervision of Dr. Isabelle Dixon at the Laboratoire de Chimie et Physique Quantiques (LCPQ) in Toulouse.

### 2.6.1. Methodology

All DFT calculations were performed on the LPCQ cluster using the ORCA 5.0.3 quantum chemistry program package.<sup>61,62</sup>

To perform DFT calculations, a functional and a basis set are necessary. They cannot be chosen loosely and must suit the case studied in order for the results to be reliable. Besides, calculation times increase significantly with larger basis sets. Therefore, a compromise must be found between computational cost and accuracy. A best-practice DFT protocol was provided by Grimme and coworkers for such purpose, which has guided our decision-making.<sup>63</sup>

Ideally, experimental data is used as benchmark for the computational method. We had two XRD structures available for the reaction studied: the phosphine oxide **24a**, and the phosphiranium salt **9e** (Figure II-80), which may be an intermediate in the reaction.



Figure II-80 : Molecules for which XRD structures were used as a starting point for the calculations

The choice of functional was based on the comparison between DFT and XRD of the most important phosphiranium angles and distances and the P-C-C in the phosphine oxide. Previous calculations were reported on phosphirane and phosphiranium compounds including recent papers using B3LYP that also helped us in the decision making.<sup>9,15</sup>

Table II-8 shows the different parameters that have been tested and compared. Three common functionals have been tested: B3LYP, BHANDHLYP and PBE. B3LYP was selected as the functional of choice. We opted for the triple zeta basis set def2-TZVP after trying 5 of them including def2-TZVP(-f) and ones with extra polarization and diffusion functions (def2-TZVPP, def2-QZVPP, def2-TZVPPD). The latter only resulted in slightly improved numbers but highly increased calculation costs. We chose robustness and reasonable calculation costs over extra precision (i.e. third decimal in the interatomic distances) with high costs. As advised in Grimme and coworkers' guide, a dispersion correction was included with the latest version D4, mainly because there are several aromatic moieties in our molecules and that dispersion, which accounts for London forces, is suited for such case. Finally, we decided to work in the solvent we performed the reaction in, dichloromethane, using the standard implicit solvation model CPCM that comes with only a small extra calculation cost.

Table II-8: tested parameters during the optimization of the calculation method

Functional	B3LYP	BHANDHLYP	PBE
Basis set	TZVP(-f)	TZVP	TZVPP
	QSVPP	TZVPPD	
Dispersion	None	D3BJ	D4
Solvent (CPCM)	Gas phase	CH <sub>2</sub> Cl <sub>2</sub>	CH <sub>3</sub> CN

The RIJCOSX approximation with the auxiliary basis set def2/J was used to speed up the calculations (it is reported to bring important speed-ups without having an important impact on the accuracy).

Geometry optimizations were performed using tight convergence thresholds (keyword TightOpt) and were systematically followed by a frequency calculation to confirm that they had converged on minima (no imaginary frequency) or first order saddle points for transition states (one imaginary frequency).

Finally, the CREST program<sup>d,64</sup> was used to scan the various conformers of a given molecule. Systems with 1 to 3 conformers in a 3 kcal/mol window are considered rigid, the ones with

<sup>d</sup> CREST stands for Conformer–Rotamer Ensemble Sampling Tool

dozens of conformers are in the intermediate area while very flexible molecules have more than a hundred conformers/rotamers in this window.<sup>63</sup> Using the default CREST parameters (6 kcal/mol window) to identify such conformers, the phosphiranium salt **9e** provided more than 200 conformers while the phosphine oxide **24a** provided more than 700 conformers. CREST proved to be essential for our work. It also added a more dynamic view of the molecules compared to the static crystal reference, by allowing us to realize the wide variety of accessible conformers, which turned out to be of great help to minimize human bias in decision-making.

We developed the method shown in the flowchart of Figure II-81 and applied it to the structure optimization of all studied molecules.

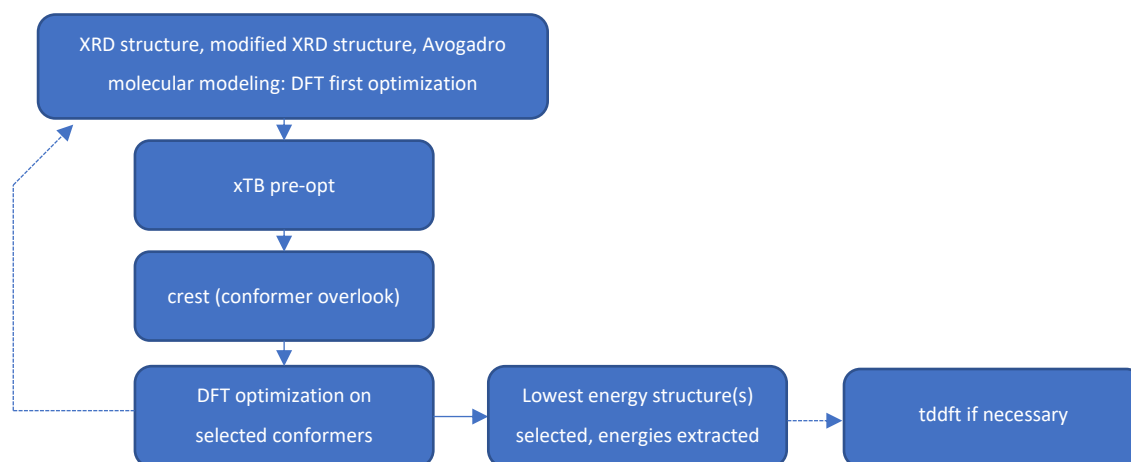


Figure II-81 : Flowchart for the final method selected as the standard calculation protocol.

It consists in building a molecular model either directly from the XRD structure (untouched), or by modifying an XRD structure with Avogadro, or from scratch for simple molecules. We then ran one structure optimization under our standard DFT protocol. This structure was then subjected to xTB<sup>65</sup> optimization<sup>e</sup> followed by CREST conformer search. Then, all significantly different conformers (rotamers excluded) were manually picked in CREST and re-optimized following the DFT protocol. Finally, the Gibbs free energy from the lowest lying conformer, as provided by the thermochemical analysis that follows from the frequency calculation, was extracted and used to build the Gibbs energy profile.

Below are the superimposed models phosphiranium **9e** (XRD) and phosphiranium **9d** (calculated, left) and phosphine oxide **24a** (XRD and calculated) (Figure II-82).

Phosphiranium **9d** was built by taking the XRD structure of its chloro equivalent and by replacing the chloro for a methoxy. Deletion of the counteranion from the XRD data had no important impact on the geometrical parameters of the phosphirane core. One can see that the

<sup>e</sup> xTB is a semi-empirical tight-binding method which is about ten times less costly than DFT and is the method of choice for handling large data sets such as a conformer search

computed structures have small (essentially angular) variations compared to the XRD structures but are overall very close for both charged and neutral molecules.

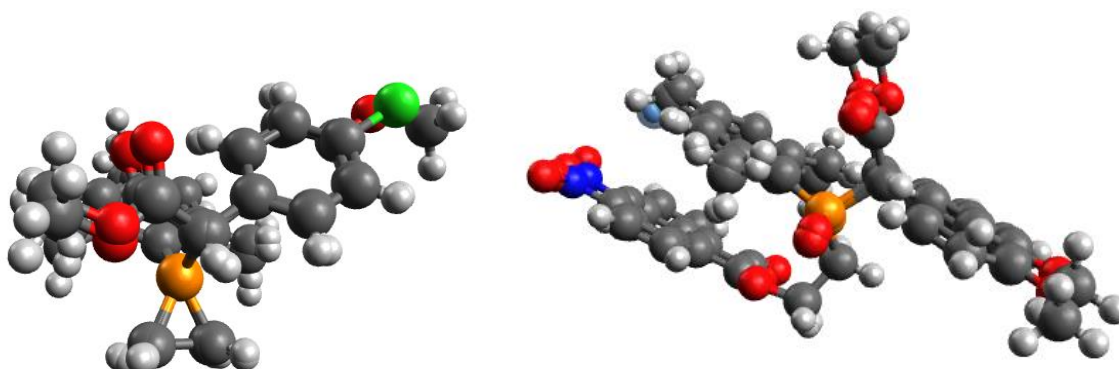


Figure II-82 : superimposed models phosphiranium **9e** (XRD) and phosphiranium **9d** (calculated, left) and phosphine oxide **24a** (XRD and calculated).

The transition states presented in the following parts were optimized using the NEB-TS command of Orca. It consists in providing the start and end points of a transformation and the algorithm optimizes a given number of (unphysical) images along the way between them (these images discretize the path). Once the NEB convergence criteria are fulfilled, i.e. when the Minimum Energy Path (MEP) is obtained, the highest image is taken as the guess for a transition state optimization. This proved crucial in our work.

### 2.6.2. Reaction energy profile for phosphiranium ylide formation

We first calculated the energy profile for the formation of the ylide **7d**. The reaction starts with the absorption of blue light by methyl *para*-methoxyphenyldiazoacetate **4d**, that gets promoted to its excited state. We have considered a photon with an energy of 62.1 kcal/mol | 2.70 eV | 460 nm | 21,720 cm<sup>-1</sup>, corresponding to the  $\lambda_{\text{max}}$  of the LED we have used for the reaction. Aryldiazoacetates are known to absorb in this area.<sup>58</sup> At the ground state geometry, the lowest excited singlet state of **4d** (i.e. S<sub>1</sub> Franck-Condon state) was computed by time-dependent DFT (TD-DFT) at 61.3 kcal/mol | 2.66 eV, perfectly matching the characteristics of the blue LED. We have optimized the structure of the S<sub>1</sub> excited state by TD-DFT : its energy went down to 38.9 kcal/mol | 1.69 eV, illustrating important structural changes occurring upon relaxation of S<sub>1</sub>.

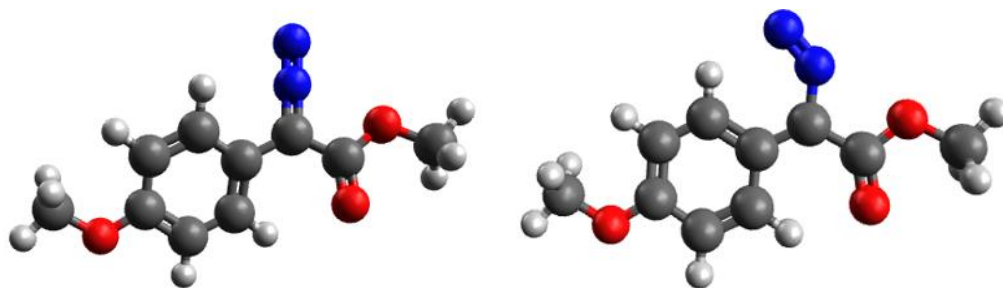


Figure II-83 : calculated structures of the diazo compound **4d** in its ground state (left) and optimized singlet excited state by TD-DFT (right)

The structural rearrangements occurring upon  $S_1$  optimization of **4d** consist in the decrease of the N-N-C angle which goes from quasilinear in  $S_0$  ( $178.9^\circ$ ) to bent ( $133.8^\circ$ ) in  $S_1^{\text{opt}}$ , and in the N-C bond distance increase from  $1.31 \text{ \AA}$  to  $1.42 \text{ \AA}$ , pointing to a diminished N-C bond order in  $S_1^{\text{opt}}$  (Figure II-83). These two major changes are in perfect agreement with the preparation for the loss of molecular nitrogen, which will form the carbene. Free electrophilic carbenes, in their ground state, may exist as both singlet and triplet states. Based on theoretical calculations, it was previously stated in the literature that methyl phenyldiazoacetate **5a** has a triplet ground state but reacts from its singlet state via a rapid singlet-triplet exchange.<sup>58,66</sup> The study was limited to a single carbene and the calculations were only reported in the gas phase. Their calculations showed that the  $\text{CO}_2\text{Me}$  moiety was orthogonal to the aromatic ring for the singlet state and in the same plane for the triplet state. We extended the calculations with our protocol to carbenes with the para substituents H, Me,  $t\text{Bu}$ , MeO Cl and  $\text{CF}_3$ , in implicit  $\text{CH}_2\text{Cl}_2$  and their singlet and triplet states showed the same structural differences. (Figure II-84).

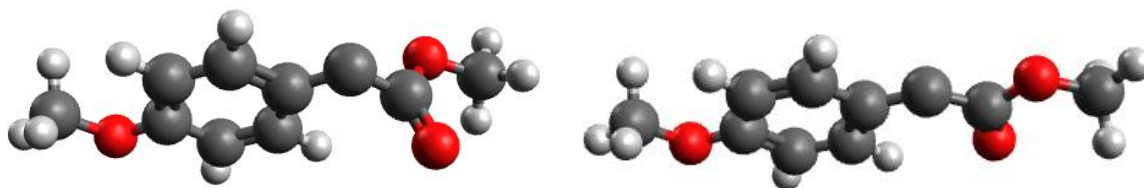


Figure II-84 : calculated structures for the carbene compound in its singlet state **5ds** (left) and triplet state **5dt** (right).

We provide in Table II-9 the Gibbs free energy difference between their singlet and triplet states  $\Delta E_{\text{ST}}$ . A positive value means that the triplet state is the lowest in energy while a negative value means that it is the singlet state instead.

Table II-9 Gibbs energy difference obtained between the singlet and triplet states of carbenes **5** with different *para* substituents on the aromatic ring.

<i>Para</i> -substituent	<b>5a</b> H	<b>5b</b> Me	<b>5c</b> <sup>t</sup> Bu	<b>5d</b> MeO	<b>5e</b> Cl	<b>5f</b> CF <sub>3</sub>
$\Delta E_{ST}$ (kcal/mol)	- 1.0	- 3.4	- 2.6	- 5.5	- 1.0	+ 1.6
$\Delta(\Delta E_{ST})$ (kcal/mol)	0	- 2.4	- 1.6	- 4.5	0	+ 2.6

Our results suggest a different trend than what was previously reported. For all substituents (**5a-5e**) except the trifluoromethyl group (**5f**), the singlet state is more stable than the triplet state. A trend is observed where more donating groups in the *para* position of the aryl moiety increase the stabilization of the singlet state. A methyl (+I effect, **5b**) substituent makes the  $\Delta E_{ST}$  2.4 kcal/mol lower (in the favor of the singlet state) compared to the naked methyl phenyldiazoacetate **5a**, and the methoxy substituent (+M effect, **5d**) 4.5 kcal/mol lower. The chloro substituent (**5e**) has no effect compared to the reference, most likely because its -I and +M effects compensate. Finally, the EWG CF<sub>3</sub> (**5f**) is the only example with an opposite behavior (+2.6 kcal/mol compared to **5a**), where the triplet state is more stable than the singlet state. These results suggest that *para*-substituents with good electron donating properties stabilize the singlet state while *para*-substituents with good electron withdrawing properties stabilize the triplet state. A more general conclusion is that the singlet and triplet states of free electrophilic carbenes **5** are almost degenerate and that they may be in equilibrium. Other parameters than the  $\Delta E_{ST}$  will decide which ones reacts with the substrate such as Wigner's rules. This rule states that the electron-spin angular momentum must be conserved in a collision.<sup>67</sup> In other words, singlet-singlet reactions are faster than singlet-triplet reactions, and if an equilibrium between the singlet and triplet states exist, consumption of the singlet state will drive the conversion. This statement is made possible by the fact that most organic molecules bear a singlet ground state. The proposed reaction profile (Figure II-89) displays the energy of the singlet state of the carbene **5d**, which is the one that most likely reacts with the singlet ground state 1-mesitylphosphirane **1**, according to Wigner's rules.

We then studied the ylide **7d**. We remind the reader that <sup>31</sup>P NMR spectra displayed two signals in a *ca.* 2:1 ratio at 10 °C. At room temperature, the two signals are broad and coalesce. We first qualitatively assigned both signals to two P(V) isomers **7da** and **7db** (Figure II-85). We were then interested in confronting this hypothesis to DFT calculations and, ideally, identifying which structure corresponds to the major signal.



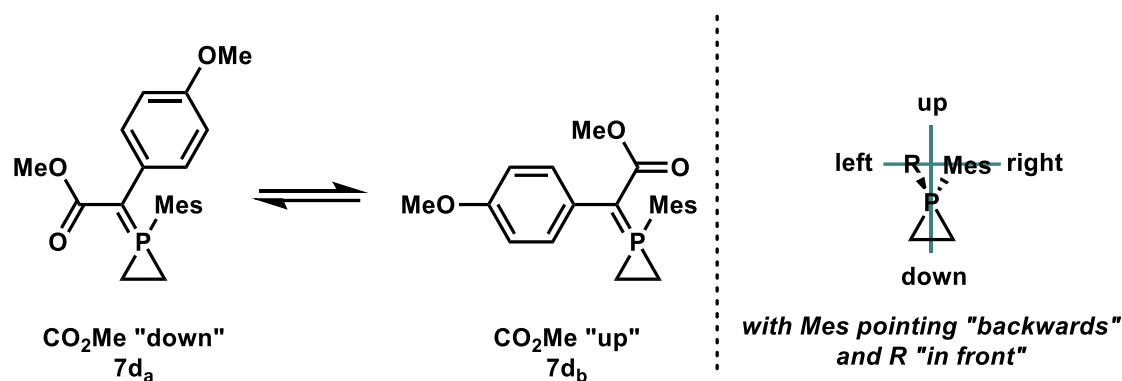


Figure II-85 : two conformers of the same phosphiranium ylide **7d** and nomenclature proposition for this manuscript to talk about the stereochemistry of phosphiranium ylides and phosphiranium salts.

We built the molecular model from the phosphiranium **9e** XRD structure by deleting the hydrogen on the carbon atom and modifying the chloro substituent for a methoxy. The overall charge of the molecule went from +1 for the phosphiranium salt **9e** to 0 for the ylide **7d**. By introducing these changes in the input command and applying our protocol we obtained a total of 7 conformers of **7d** in a range of 2.3 kcal/mol (the allowed energy window was 6 kcal/mol). It became clear that hydrogen bonds and C-H/ $\pi$  interactions were decisive in determining the energy minima. These conformers lied *ca.* 40 kcal/mol lower in energy than the reactants, which is a significant energy gain.

Two sets of structures could be identified with either the  $\text{CO}_2\text{Me}$  moiety "down" or "up" (Figure II-86). A clear trend in the energies favored the conformers with the  $\text{CO}_2\text{Me}$  "down" (< 1.2 kcal/mol compared to the lowest lying conformer from **7d<sub>1</sub>** to **7d<sub>4</sub>**) while the conformers with the  $\text{CO}_2\text{Me}$  "up" were unfavored (>1.2 kcal/mol, from **7d<sub>5</sub>** to **7d<sub>7</sub>**). Most importantly, the methyl groups from the mesityl substituent prevent an easy free rotation between the "up" and "down" forms, which is the main reason for the separation into two sets of structures.

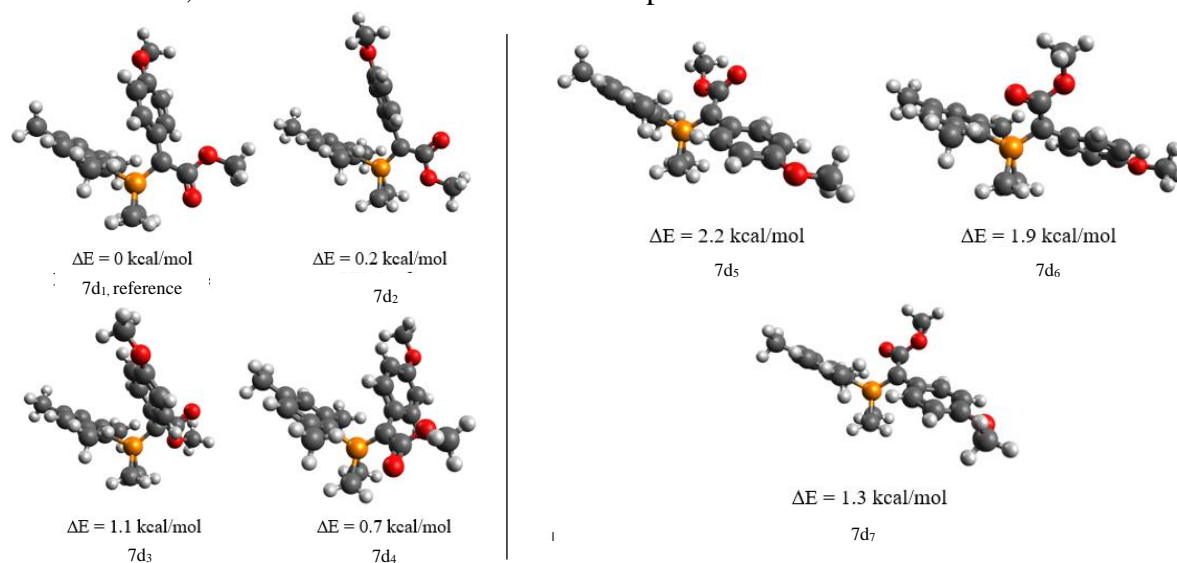


Figure II-86 : calculated structures of two sets of conformers of the same phosphiranium ylide **7d**



Based on these results, we propose to assign the main sharp signal observed by NMR at 10 °C to the "down" conformers and the minor signal to the "up" conformers. We did not assign the signals to one specific molecule (e.g. the lowest lying conformer of all) but to the sets of conformers co-existing following Boltzmann population (e.g., it is 6 times more probable to find **7d7** than finding **7d5** at -40 °C). It is important to note that with the computational method we have used, an error margin of 1-5 kcal/mol is expected. This error is in the lower range when comparing similar structures. With a 1 kcal/mol error (+/- 0.5 kcal/mol), we are still able to distinguish both sets from their lowest and highest lying conformers.

We have calculated the formation of the ylide **7d** by addition of 1-mesitylphosphirane **1** on carbene **5d** to be barrierless, as it was reported previously for the addition of methylamine on methyl phenyldiazoacetate.<sup>66</sup> We selected ylide **7d6** as the end point after several unsuccessful attempts with **7d1** because of parasitic local minima resulting from  $\pi$ - $\pi$  interactions between aromatic groups.

To ensure the physicality of our reaction model, we first inspected the orbitals of both reactants (Figure II-87). We then positioned the reactants so that the HOMO of 1-mesitylphosphirane **1** is facing the LUMO of the carbene **5d** (pz orbital) at *ca.* 4 Å distance. We ran the NEB-TS program to minimize the energy path connecting these reactants to the ylide **7d6**.

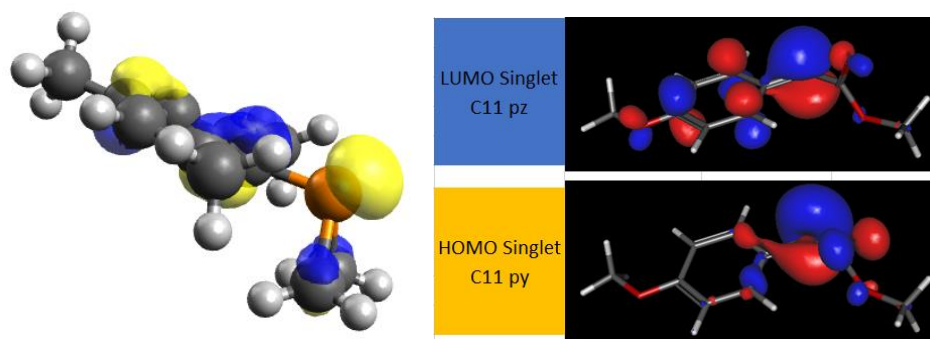


Figure II-87 : HOMO of 1-mesitylphosphirane; right, HOMO and LUMO of carbene. C11 corresponds to the carbon of the carbene

The electronic energy profile goes downhill all the way, meaning that this reaction is exothermic and barrierless (Figure II-88).

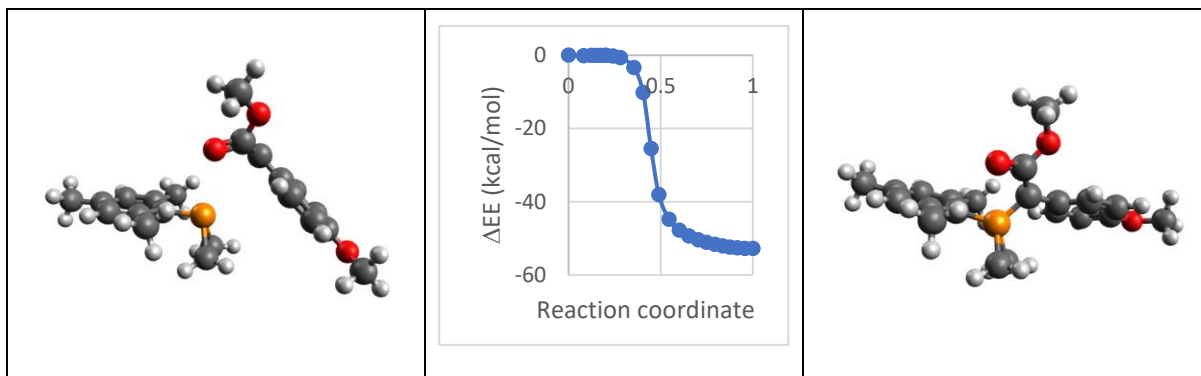


Figure II-88 : left: starting structure of the MEP (phosphirane **1** and carbene **5d**), right: arriving structure of the MEP (phosphiranium ylide **7d<sub>6</sub>**), middle: minimum energy path between the starting structure and the ending structure

A barrierless, downhill reaction profile consistent with the observed total reaction was obtained for ylide formation. Computational data allowed us to identify the most stable conformer for the ylide **7d**, as well as providing more insights into the electronic structure of phosphirane **1**, singlet and triplet carbenes **5**. The proposed profile is given in Figure II-89 and summarizes the different steps detailed before.

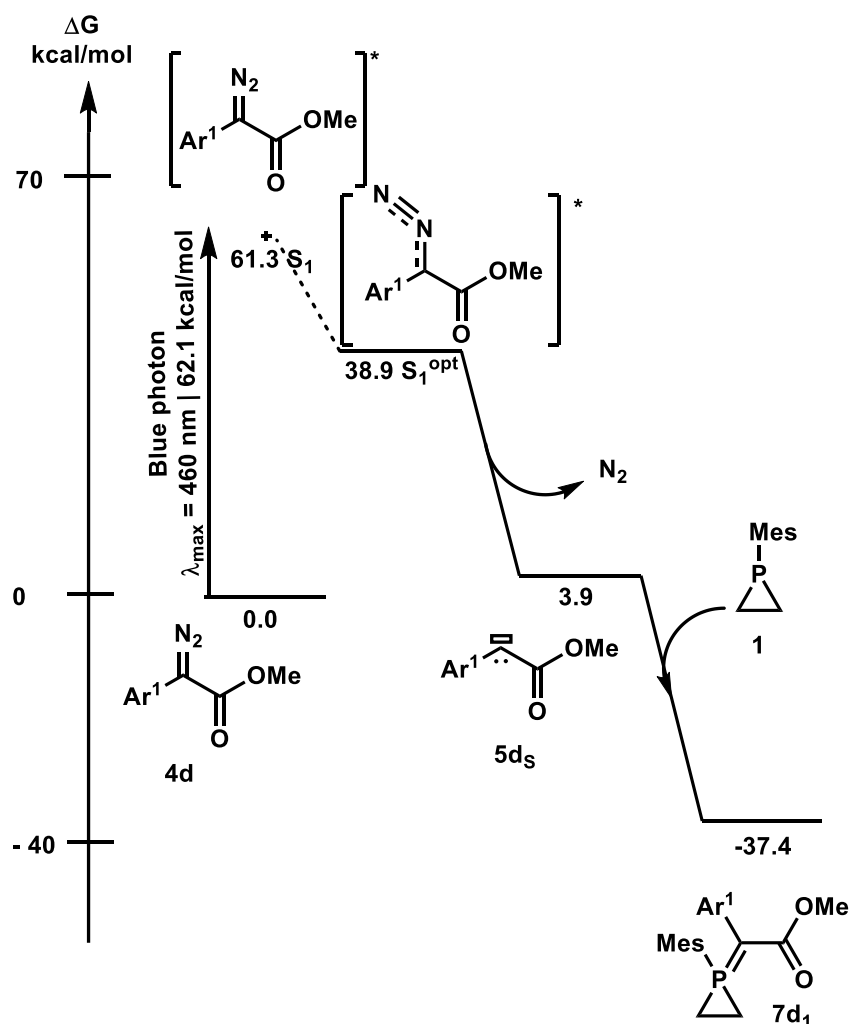


Figure II-89 : proposed Gibbs free energy profile for the formation of the phosphiranium ylide **7d**. The energy of the most stable singlet carbene **5ds** and the phosphiranium ylide **7d** was selected for the energy values. Ar<sup>1</sup> : para-methoxyphenyl

We then proceeded to calculate the more challenging reaction energy profile for the ring opening of the phosphiranium ylide with carboxylic acids.

### 2.6.3. C-centered ring opening productive mechanism

Experimentally we showed that addition of carboxylic acids on phosphiranium ylides leads to the C-centered ring opening phosphine product **24** with high yields (*ca.* 80%). Phosphine **23** oxidation to the phosphine oxide **24** was considered as a last step of small mechanistic interest. We therefore focused on the ring opening itself, and considered two main pathways that could lead to the phosphine **23a** : (i) concerted H-transfer and ring opening or (ii) stepwise H-transfer followed by ring opening (Figure II-90).

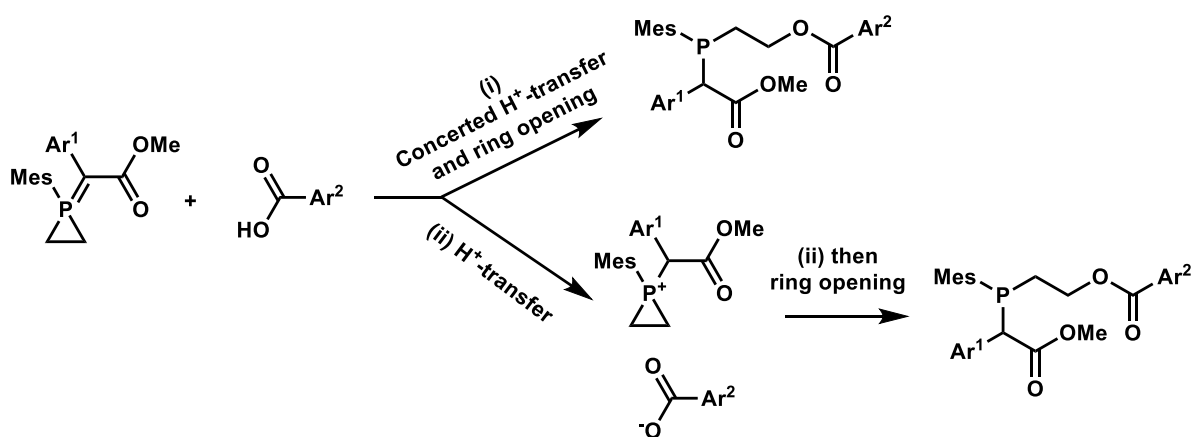


Figure II-90 : proposed two main pathways for the ring opening of phosphiranium ylide **7d** with para-nitrobenzoic acid

We started by applying our protocol to obtain the conformers of interest of both diastereoisomers of the phosphine **23a** and the phosphine oxide **24a** as well as the conformers of both enantiomers of the phosphiranium salt **9d**.

The phosphine **23a** molecular model (mm) was obtained by deleting the oxygen atom of the oxide from the XRD structure of the phosphine oxide **24a**. Our calculation protocol was then applied to obtain its conformers.

To obtain the molecular models of both the phosphine **23a** and the phosphine oxide **24a** diastereoisomers we manually exchanged the position of the CO<sub>2</sub>Me and the aromatic substituent of the methyl arylacetate moiety with Avogadro. We then subjected these molecular models to our protocol to obtain their conformers **23ad1/23ad2** and **24ad1/24ad2** (Figure II-91).

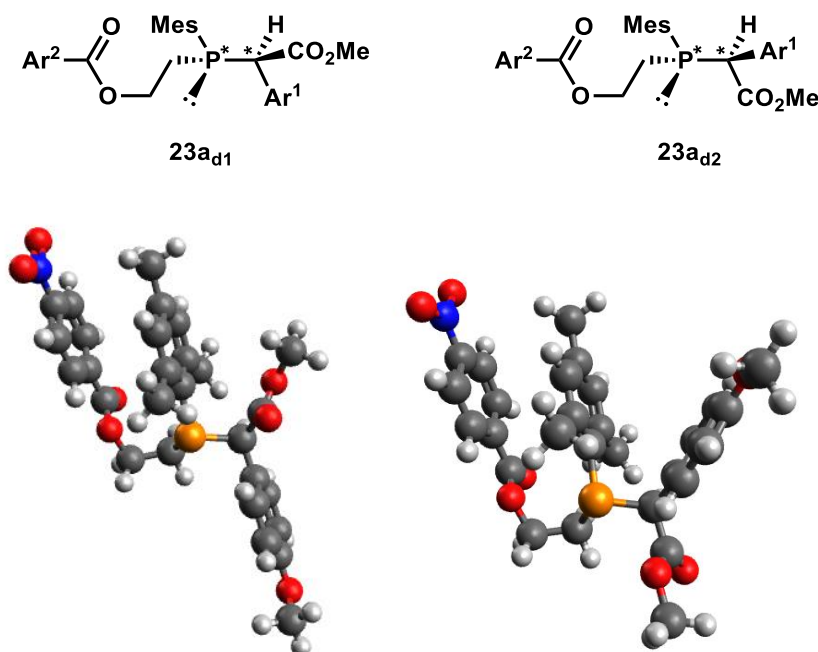


Figure II-91 : diastereoisomers structures selected for the calculations (left: **23a<sub>d1</sub>** ; right: **23a<sub>d2</sub>**) ( $\text{Ar}^2 = p\text{-NO}_2\text{Ph}$ ;  $\text{Ar}^1 = p\text{-MeOPh}$ )

The same method was used to obtain the enantiomers of phosphiranium salt **9d**. Having the structures of the enantiomers of **9d** was necessary because we looked at the possibilities with the attack on one specific carbon atom of the phosphiranium ring and varied the structure of the phosphiranium instead of fixing the structure of the phosphiranium and looking at the attack on both carbon atoms. We took this decision because we only had one XRD structure for the phosphine oxide **24a** and that the pattern of the open P-C-C bond suggested minimal rearrangement from the attack on one specific carbon atom. When looking at the structures with the mesityl moiety pointing backwards, the carbon atom on the left was the carbon center we studied (indicated by a black arrow on Figure II-92). This allowed us to focus on the calculation of structures in close agreement to the supporting experimental data.

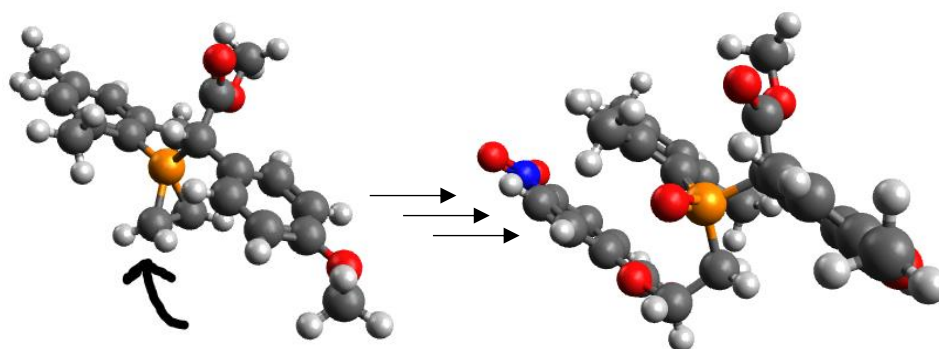


Figure II-92 : carbon atom considered for the ring opening indicated by a black arrow. Left: phosphiranium salt **9d** calculated structure, right: phosphine oxide **24a** XRD structure reoptimized by DFT

As a technical remark, the use of the "free ends" option of the NEB-TS program includes the preoptimization of the start and end points, which may or may not be needed depending on the situation. The end points were not always the most stable conformer but rather the ones structurally closest to what the product would look like right after ring opening. We then checked with a NEB calculation that the conformer obtained could easily relax to the most stable one.

The following table II-10 summarizes the number of conformers obtained for each data set, along with the Gibbs free energy differences between the lowest and highest lying conformer of a given set,  $\Delta G_{\text{low-high}}$  (the more degrees of freedom a molecule bears, the broader the energy range), and between the lowest lying conformers of two sets of enantiomers (phosphiranium **9d**) or diastereoisomers (phosphine **23a** and phosphine oxide **24a**),  $\Delta G_{\text{low}^1\text{-low}^2}$ . Importantly, both enantiomers of **9d** had almost exactly the same energy (0.05 kcal/mol), as expected, while the diastereoisomers of **23a** and **24a** had slightly more significant energy differences of 1.2 and 0.9 kcal/mol (all within the error bar of the method).

Table II-10: number of conformers obtained for each data set of the phosphiranium **9d** enantiomers and phosphine **23a** /phosphine oxide **24a** diastereoisomers, along with the Gibbs free energy differences between the lowest and highest lying conformers

Molecule	Number of conformers selected	$\Delta G_{\text{low-high}}$ (kcal/mol)	$\Delta G_{\text{low}^1\text{-low}^2}$ (kcal/mol)
Phosphiranium enantiomer <b>9d<sub>e1</sub></b>	8	1.2	0.05
Phosphiranium enantiomer <b>9d<sub>e2</sub></b>	2	1.0	
Phosphine diastereoisomer <b>23a<sub>d1</sub></b>	7	4.8	1.2
Phosphine diastereoisomer <b>23a<sub>d2</sub></b>	5	5.4	
Phosphine oxide diastereoisomer <b>24a<sub>d1</sub></b>	8	5.8	0.9
Phosphine oxide diastereoisomer <b>24a<sub>d2</sub></b>	5	6.9	

The Gibbs free energies of the lowest lying structures are reported in Figure II-93 where we can observe that each step leads to an energy gain except for the formation of the carboxylate phosphiranium salt **9d**. The formation of the phosphiranium salt **9d** leads to a 3.6 kcal/mol

energy loss while the ring opening leads to a 20.8 kcal/mol gain. To our knowledge, no phosphiranium salt ring strain energy has been reported before. As a matter of comparison, the energy gain value of 20.8 kcal/mol for the ring opening is in the range of the previously reported phosphirane ring strain energies that vary between 11.2 and 59 kcal/mol with the most reliable value of 38.0 kcal/mol.<sup>31,68</sup> We attribute most of the energy gain we observe in this step to the release of the ring strain of the phosphiranium ring **9d**. Final oxidation to the phosphine oxide **24a** leads to an important gain of *ca.* 100 kcal/mol, a common value for such step.<sup>69,70</sup>

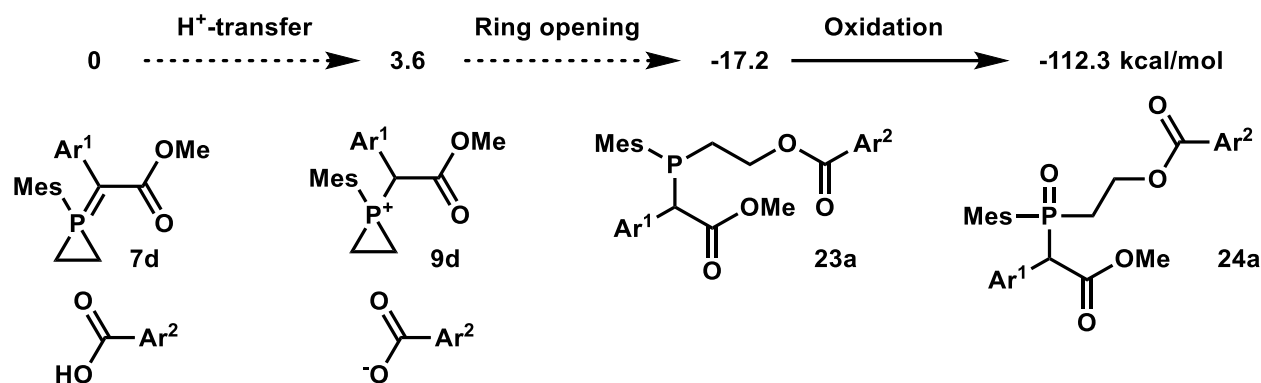


Figure II-93 : Gibbs free energy costs and gains for each step of the reaction mechanism

Now that we had all the minima along the reaction profile, we could then perform further investigations on the reaction mechanism by optimizing transition states.

We first investigated the concerted mechanism (i) using the most stable ylide conformer **7d<sub>1</sub>** as the reference structure. Two sub-mechanisms were considered where the same oxygen atom that is deprotonated attacks the carbon (ia) and where the two oxygen atoms take part in the mechanism (ib) (Figure II-94).

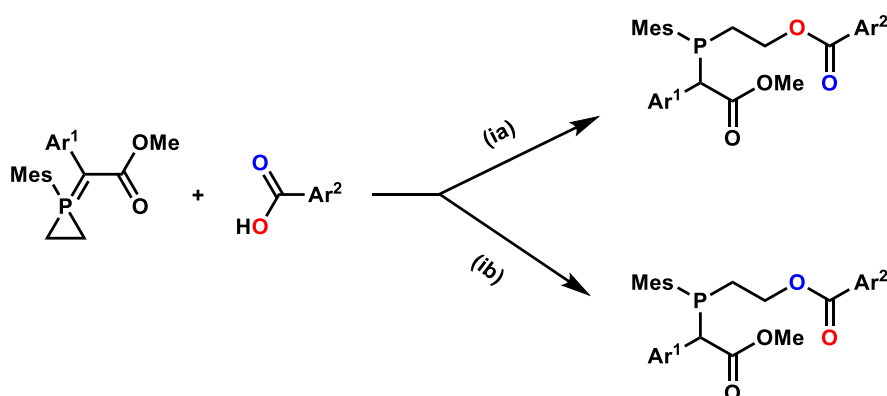


Figure II-94 : Two pathways (ia) and (ib) depending on which oxygen atom attacks the carbon atom for the ring opening reaction

Both pathways led to a consecutive  $H^+$ -transfer followed by ring opening as assessed by the “camel type” energy profile of the MEP of (ia) (Figure II-95, profile of (ib) not shown). These

results suggest that the concerted mechanism is not productive, and that proton transfer will take part prior to the nucleophilic attack that leads to ring opening.

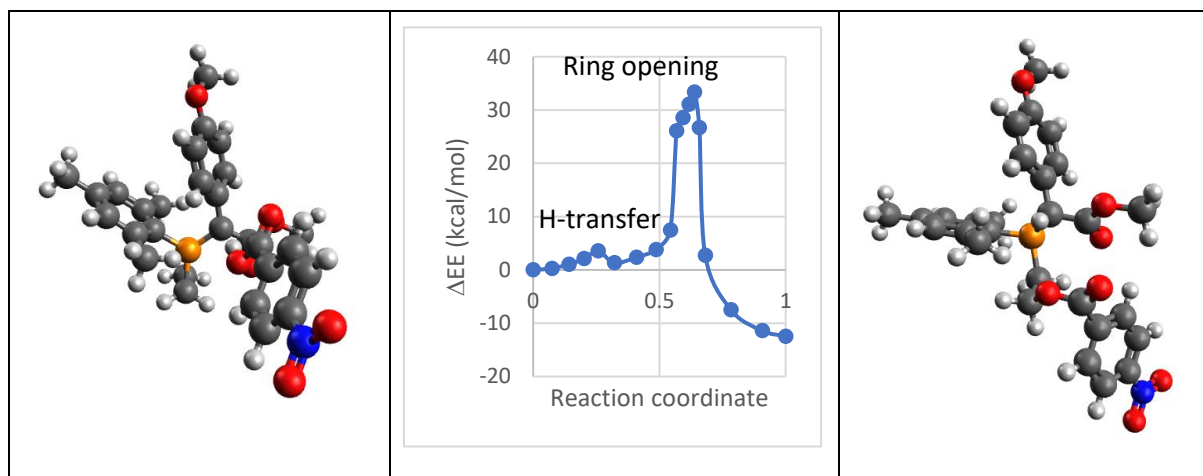


Figure II-95 : Minimum Energy Path (MEP) for the concerted attempt of proton transfer and ring opening

The minimum energy path for proton transfer is shown in Figure II-96. The very sharp shape of the curve around the highest image (x,y = 0.32, 4.3) suggests that this proton transfer step likely involves a tunneling effect,<sup>71</sup> i.e. requires significantly less than the computed 4.3 kcal/mol activation electronic energy.

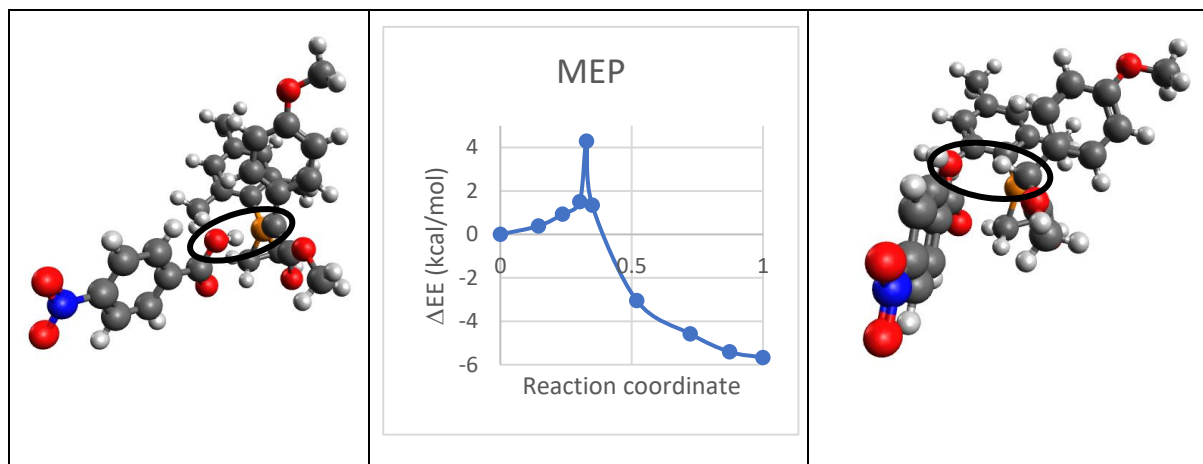


Figure II-96 : Minimum Energy Path for the concerted proton transfer that leads from 7d to 9d

The transition state obtained from this calculation has a single imaginary frequency at  $-1334\text{ cm}^{-1}$  (Figure II-). This frequency corresponds to the O-H bond breaking and H-transfer to the carbon of the ylide. Dispersion had a drastic effect on the optimization of the transition state by maximizing  $\pi$ - $\pi$  stabilization that led to the displacement of the carboxylic acid from the “side” of the ylide to “on top” of it (Figure II-97).

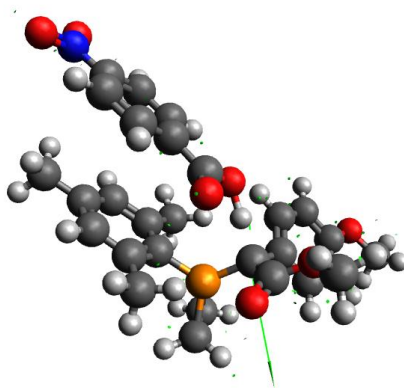


Figure II-97 : Atomic displacements associated with the  $-1134\text{ cm}^{-1}$  imaginary frequency at the transition state of the proton transfer between the carboxylic acid and the phosphiranium ylide **7d**. The atoms involved in the displacement are the hydrogen atom from the acid and the carbon atom from the ylide

The transition state corresponds to a Gibbs free energy activation barrier of 7 kcal/mol. It is the one included in the final productive reaction profile.

We were at first quite surprised that both the ylide **7d** (+ carboxylic acid) and the carboxylate + phosphiranium salt **9e** had almost degenerate energies, especially because the ylide **7d** is unstable at room temperature while its tetrafluoroborate phosphiranium salt equivalent **9e** could be manipulated under air at the same temperature. To ensure the consistency of the results, we proceeded to calculate the energies of  $\text{HBF}_4$  and  $\text{BF}_4^-$  to check if the difference between the ylide **7d** and the phosphiranium salt **9d** would get larger with tetrafluoroborate than with carboxylate (Table II-11).  $\text{HBF}_4$  proved to be a problematic structure to calculate, so we had to split it into HF and  $\text{BF}_3$ .

Table II-11: Gibbs free energy (Hartree) before and after proton transfer, and difference between the ylide **7d** and the phosphiranium salt **9d** (kcal/mol)

Protonation reactant	Ylide <b>7d</b> + acid	Phosphiranium <b>9d</b> + counterion	$\Delta G$ between the ylide <b>7d</b> and the phosphiranium salt <b>9d</b> (kcal/mol)
With 4- $\text{NO}_2\text{PhCO}_2\text{H}$	-2006.984671	-2006.978995	+3.6
With $\text{HBF}_4$	-1806.839568	-1806.888253	-30.5

This comparison confirms that the tetrafluoroborate counterion leads to a much more stable phosphiranium salt than the carboxylate counterion with a 34.1 kcal/mol difference. We show here that the counteranion has a drastic effect on the stability of the phosphiranium salt **9**. In the case of the carboxylate, the acid-base equilibrium is displaced towards the ylide **7d** +



carboxylic acid but the irreversible ring opening drives the reaction towards the phosphine **23a**. These results are in good agreement with variable temperature NMR experiments ran by Avishek Ghosh, who could not see an intermediate carboxylate phosphiranium salt **9d** formation at low temperature but only signals from the phosphiranium ylide **7d** and the phosphine **23a**. We wish to add some caution to this conclusion since comparing the energy of neutrals (phosphiranium ylide + carboxylic acid) and charged species (phosphiranium + carboxylate) is intrinsically difficult when they are obtained with the same computational protocol.

The next elementary step along the proposed reaction profile is the ring opening productive pathway. We have looked at different angles of attack for the carboxylate onto the carbon atom. One of them stood out by the smoothness of the transformation and provided a meaningful transition state with a single imaginary frequency of  $-400\text{ cm}^{-1}$  for both diastereoisomers. This frequency corresponded to the P-C bond breaking and O-C bond formation in both cases (Figure II-98).

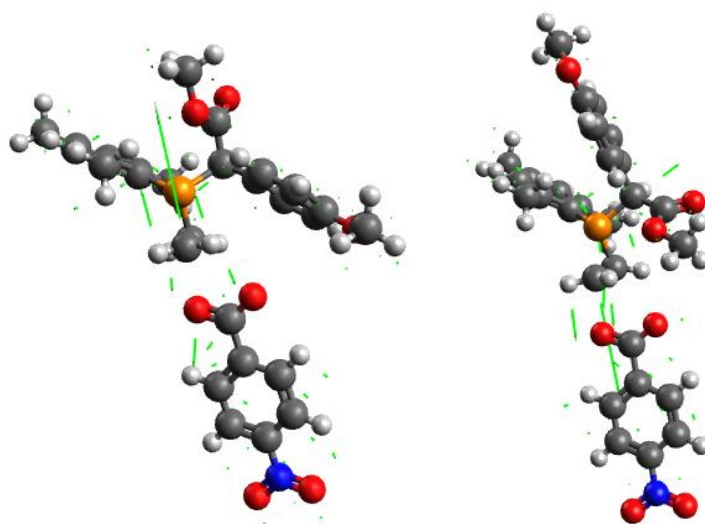
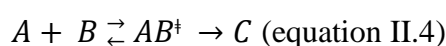


Figure II-98 : Atomic displacements of the transitions states found for the ring opening of the two enantiomers of the phosphiranium salt on the same carbon leading to two diastereoisomers.

A Gibbs free energy barrier  $\Delta G^\ddagger$  of 15.9 kcal/mol was found for the ring opening step, which is therefore the rate determining step of the reaction between the carboxylate phosphiranium salt **9d** and the ring opened phosphine **23a**.

For a chemical reaction following:



Eyring equation (equation II.5) allows to determine the reaction half-life  $t_{1/2}$  (equation II.6).

$$k = \kappa \frac{k_B T}{h} e^{-\frac{\Delta G^\ddagger}{RT}} \text{ (equation II.5)}$$

Where  $k$  is the rate constant,  $\kappa$  is the transmission coefficient that varies between 0 and 1 and accounts for the probability that the reaction proceeds to the product C after reaching the transition state (it is usually taken as 1),  $k_B$  is the Boltzmann's constant ( $1.381 \times 10^{-23}$  J/K),  $h$  the Planck's constant ( $6.626 \times 10^{-34}$  Js),  $\Delta G^\ddagger$  the calculated Gibbs activation free energy,  $R$  the gas constant ( $8,314$  J/(mol.K)) and  $T$  the temperature in Kelvin.

$$t_{1/2} = \frac{\ln(2)}{k} \text{ (equation II.6)}$$

Avisek Ghosh's variable temperature NMR monitoring of the reaction showed no product formation after 21 hours at  $-50^\circ\text{C}$  and within 3 hours at  $-40^\circ\text{C}$  only traces of the products could be observed. Bringing the sample at room temperature resulted in a quick reaction completion (on the scale of a minute). The barrier from the carboxylate phosphiranium salt is computed at  $15.9$  kcal/mol which means that the reaction would reach completion within 1 hour and 40 minutes at  $-50^\circ\text{C}$  (following Eyring equation and considering full completion at 10 half-lives. 5 half-lives correspond to a completion of 97%). This doesn't seem in agreement with experiments at first glance. We remind the reader that our computational method bears an intrinsic error margin of 1-5 kcal/mol. The phosphiranium **9d** with the carboxylate, especially, involving two charged molecules, is the least reliable calculations along the entire reaction profile and the maximum error should apply in this case. The activation energy from **9d** to **23a**, taking the 5 kcal/mol error margin into account, then covers the sensitive  $\Delta G^\ddagger$  area around 16 kcal/mol ( $13.5$ - $18.5$  kcal/mol) where reaction times ( $10 \cdot t_{1/2}$ ) go from ten milliseconds to one minute at room temperature (this transition state is the rate determining step in our mechanism). Following Eyring equation and taking the upper value of  $18.5$  kcal/mol, reaction half-lives are 4 seconds at  $25^\circ\text{C}$ , 12 seconds at  $15^\circ\text{C}$ , 10 hours at  $-40^\circ\text{C}$  and 2.3 days at  $-50^\circ\text{C}$ , which becomes consistent with VT-NMR experimental estimates. The energies of both diastereoisomeric transition states are within the error bar of the method. A difference of 1 kcal/mol on the transition states would translate into a 85:15 diastereomeric ratio. Experimentally, the diastereomeric ratio for this reaction was found at 58:42 (varies between *ca.* 50:50 and 70:30 for the scope). This corresponds to a  $\Delta\Delta G^\ddagger$  of 0.2 kcal/mol (between 0 and 0.5 kcal/mol for the scope) following equation II.7, while we found a 1.4 kcal/mol value which corresponds to a *ca.* 90:10 diastereomeric ratio.<sup>72</sup> The error bar of the method covers the very closely lying transitions states and supports the mechanistic pathway considered.

$$dr = \frac{k_R}{k_S} = \frac{\kappa_R}{\kappa_S} e^{\frac{-\Delta\Delta G^\ddagger}{RT}} \text{ (equation II.7)}$$

Overall, the robust calculation method we have selected covers a physically consistent range of energies for  $\Delta G^\ddagger$  and  $\Delta\Delta G^\ddagger$  within its error bar and supports the mechanism considered, going sequentially through (a) the formation of the phosphiranium ylide **7d** from the addition of phosphirane **1** on the carbene **5ds**, (b) proton transfer from the carboxylic acid to the ylide **7d**, (c) ring opening at one C atom of the phosphiranium ring **9d**, and (d) oxygen atom transfer from  $H_2O_2$  to the phosphorus atom of the phosphine **23a**.

Finally, no transition state for the oxidation of the phosphine **23a** to the phosphine oxide **24a** with  $H_2O_2$  was calculated. This step was of least interest because the phosphines have greater value than the phosphine oxides which were only synthesized for isolation and characterization. The spacefilling model of phosphine **23a** shows that the phosphorus atom is only accessible to small molecules because of the important hindrance around it (Figure II-99).

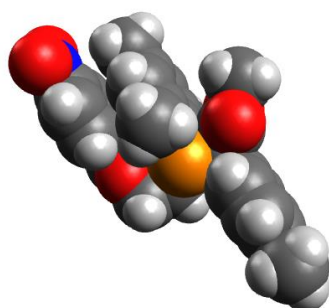


Figure II-99 : spacefilling model of phosphine **23a**

The final energy profile was then obtained as depicted in Figure II-100. The values in red represent the Gibbs free energies for the other diastereoisomer. They are close and within the error bar of the method. We were not able to draw decisive conclusions on the diastereoselectivity of the reaction and to attribute each major and minor specie to a structure without doubt. However, the trend is clearly in favor of molecule **23a<sub>d1</sub>** as the major isomer and **23a<sub>d2</sub>** as the minor one for the phosphine formation. For the phosphine oxide, the lowest lying isomer order is reversed only by a small margin which is not enough to conclude with confidence on their ratios.

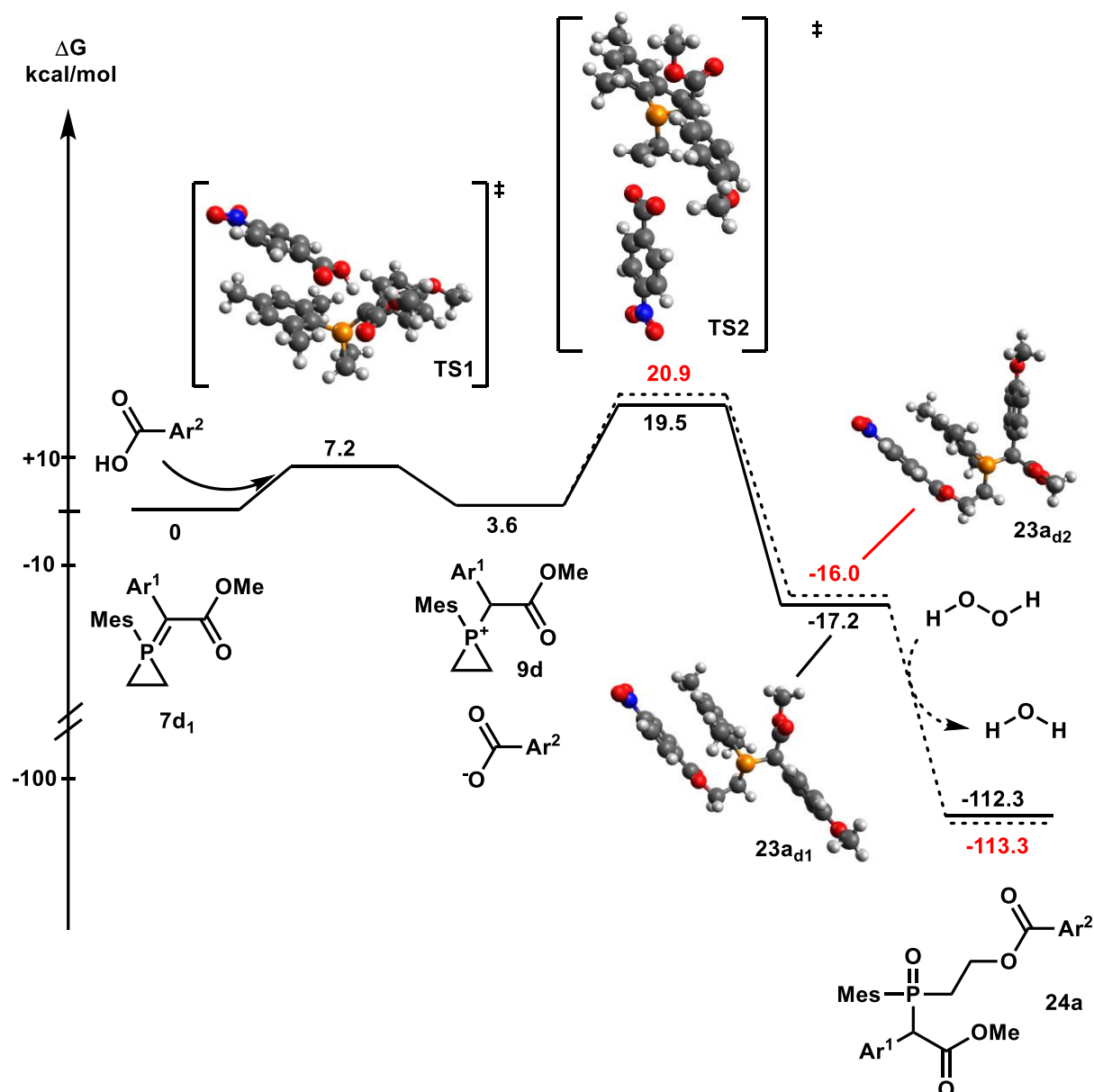


Figure II-100 : final Gibbs free energy profile for the formation of the phosphine oxide **24a** from the phosphiranium ylide **7d**. The energy of the most stable conformers for each diastereoisomer was selected for the energy values.

We can conclude that we are able to propose a productive reaction mechanism for the ring opening of phosphiranium ylides **7** at the carbon atom of the 3-membered ring by carboxylic acids, on the basis of DFT calculations, in good agreement with experimental observations.

#### 2.6.4. Alternative mechanism through a P(V) specie

The Mulliken atomic charges of phosphiranium **9d** show a +0.184 atomic charge on the phosphorus atom while the carbon atoms of the phosphirane core bear -0.222 and -0.264 atomic charges (Figure II-101).

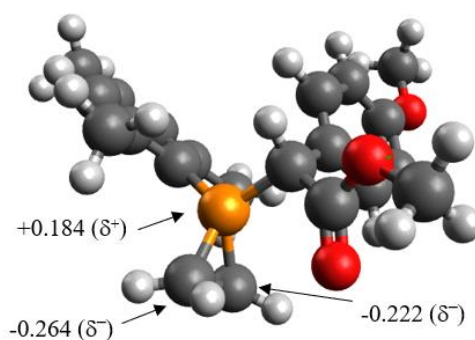


Figure II-101 : Mulliken atomic charges of phosphiranium **9d**

Intrigued by the possibility of another reaction mechanism involving an attack of the oxygen nucleophile on the electron deficient phosphorus (formation of a P(V) species **25**), we extended the DFT investigations. This addition to form a P(V) species would be followed by a reductive elimination-like process of the carboxylate and a carbon atom of the phosphiranium ring to yield the phosphine **23** (Figure II-102).

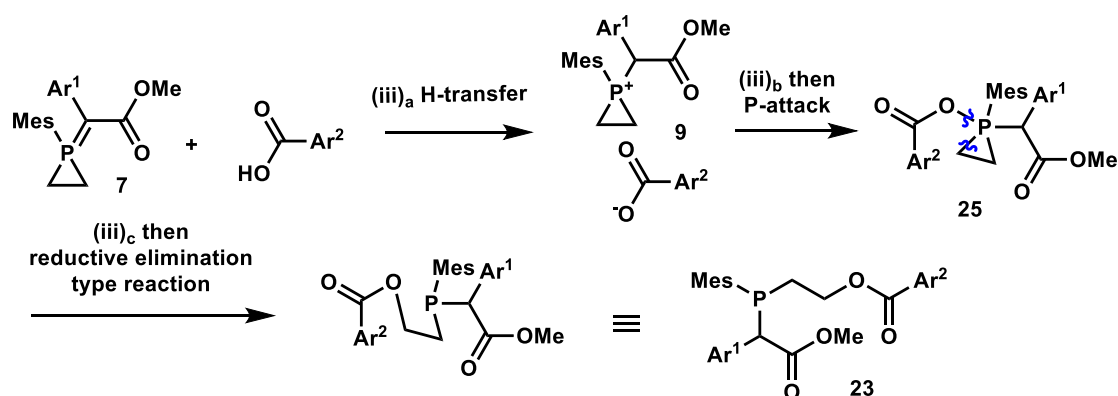


Figure II-102 : reaction mechanism involving an attack of the oxygen nucleophile on the electron deficient phosphorus followed by ring opening

We started by optimizing the structure of **25a**. Two structures were considered where each oxygen atom from the carboxylate moiety could be attached to the phosphorus (**25a1** and **25a2**, Figure II-103). No phosphorus-oxygen covalent bond could be formed as the distance between them varied from 2.16 to 2.18 Å upon optimization. We hypothesized that the steric hindrance around the phosphorus was too important to allow proper P-O bond formation. The most stable conformer **25a1**, which may be seen as a donor-acceptor adduct, lied 4.4 kcal/mol higher than the separated molecules, making the pathway through the P(V) species **25** unfavored.

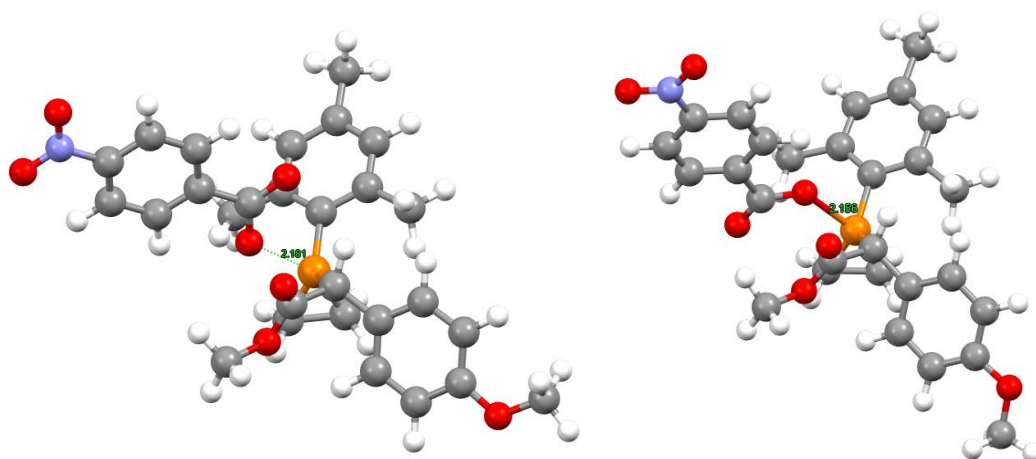


Figure II-103 : optimized structures of the P(V) adducts **25a<sub>1</sub>** (left) and **25a<sub>2</sub>** (right) with the carboxylate carbonyl's oxygen in two possible directions

We have nevertheless studied the two possibilities for P-C bond breaking and O-C bond formation displayed in Figure II-104.

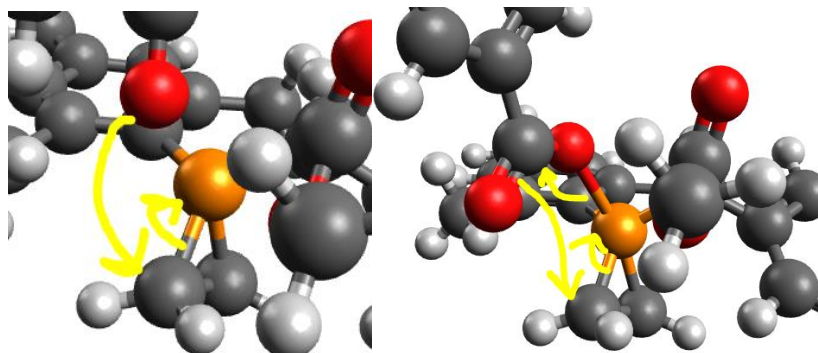


Figure II-104 : Lewis view of the two possible mechanisms : left, direct attack at the C atom (only one O atom involved); (ii) attachment by one O atom at the P atom, followed by attack of the other oxygen atom on the C atom.

Transition states were found at 29.7 kcal/mol and 31.7 kcal/mol higher than the reactants, with a single meaningful imaginary frequency of  $-194\text{ cm}^{-1}$  (an extra negative frequency of  $-15\text{ cm}^{-1}$  was found and attributed to a methyl rotation) and  $-209\text{ cm}^{-1}$  respectively. They required the carboxylate moiety to move away from the phosphiranium **9d** before attacking the carbon atom, thus breaking the unfavored P-O bond interaction and rendering its formation superfluous (Figure II-105).

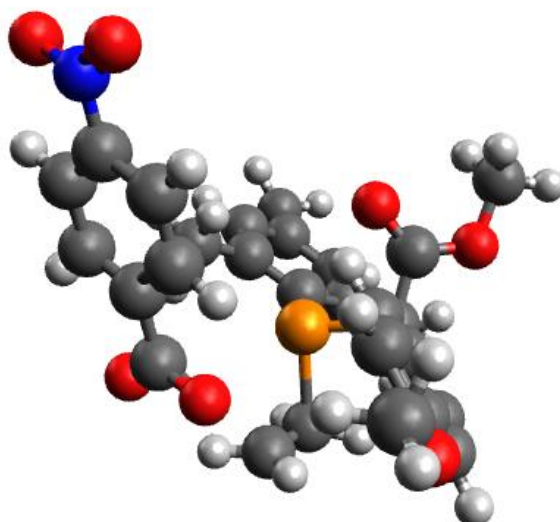


Figure II-105 : transition state found for the ring opening from the P(V) specie **25a<sub>1</sub>**

- there is no covalent P-O bond in the putative P(V) adduct **25a**
- the donor-acceptor adduct has a higher energy than the isolated carboxylate and phosphiranium (the same caution should be taken as previously, when comparing energies of neutral and charged species)
- the transition state along this pathway has a higher absolute energy than the one found for direct ring opening
- the carboxylate has to move away from the phosphorus before the ring opening can proceed, which renders the carboxylate/phosphiranium interaction superfluous

All these facts led us to discard the mechanistic hypothesis involving a P(V) specie.

### 3. Conclusion

This work showed how important was the steric hindrance from both the mesityl moiety and the aryl from the diazoacetate for the regioselectivity of the ring opening. This chemistry is not straightforward and a robust method was developed.

For the quaternarization of 1-mesitylphosphirane with aryl diazoacetate moieties under blue light irradiation, further development would include modification of the ester moiety (Figure II-106, red circle), of the substituent of the phosphorus of the starting phosphirane (blue circle), and of the substitution pattern of the carbon atoms of the phosphirane ring (green circle). All these parameters will induce modifications in the stability of the phosphirane and of the phosphiranium ylide. Introduction of substituents on the carbon atoms of the phosphirane ring will also introduce stereochemistry on the starting material and the challenges on selectivity that come with it. Besides, protonation of the phosphiranium ylide opens the way for investigating various counteranions (pink circle) by using acids other than tetrafluoroboric acid, a modification which was difficult to consider achieving until then. The modification of these different parameters will find the same interest for the ring opening reaction, which can be envisioned to work with other types of Bronsted acids (brown circle). The phosphirane-borane showed promising results, and it is important to show that the products are not limited to phosphine oxides (blue circle). Finally, trans-esterification of the aromatic ester could lead to the free alcohol which stability is unknown, and from which various modifications can be developed to further design the scaffold as a suitable phosphine ligand, for instance.

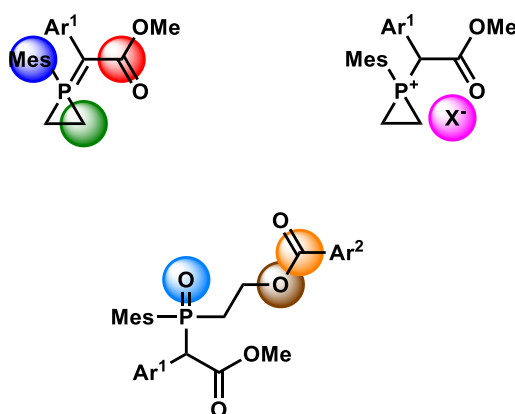


Figure II-106 : highlight of the perspectives of the project



#### 4. Experimental section

All the reactions were performed in flame-dried glassware under Nitrogen atmosphere using standard Glovebox techniques (glovebox maintained at  $< 0.1$  ppm  $\text{H}_2\text{O}$  and  $< 0.1$  ppm  $\text{O}_2$ ) or conventional Schlenk techniques. Solvents and solutions were transferred with syringes. All the solvents were dried using an MBRAUN Solvent Purification System (SPS) and sparged with argon. Used chemicals were purchased from *Sigma-Aldrich* and used without further purifications.

All the reaction mixture were irradiated with two blue 5W Vision-EL LEDs with maximum emission at 460 nm (Figure II-104).

Flash column chromatography was performed on silica gel 60 (0.040–0.063 mm) from *Merck*. Analytical thin-layer chromatography (TLC) was performed on *Merck* silica gel 60 F254 aluminum plates and the spots were visualized under UV light at 254 nm.

$^1\text{H}$  NMR (300 MHz);  $^{31}\text{P}$  (109 MHz)  $^{19}\text{F}$  (282 MHz) and  $^{13}\text{C}$  proton decoupling (75 MHz) spectra were recorded in  $\text{CDCl}_3$  on an Agilent Direct Drive spectrometer (Agilent Technologies, Santa Clara). Chemical shifts were reported in parts per million (ppm) and referred to the residual solvent resonance as internal standard ( $\text{CDCl}_3$ :  $\delta = 7.26$  ppm for  $^1\text{H}$  NMR and  $\delta = 77.16$  ppm for  $^{13}\text{C}$  NMR). All the data were reported as follows: Chemical shift, multiplicity (br = broad singlet, s = singlet, d = doublet, dd = doublet of doublet, m = multiplet), integration and coupling constant (Hz). All the High-resolution mass spectrometry (HRMS) analyses were performed on a Q Exactive Mass Spectrometer (ThermoFisher) using direct injection.

The aryldiazoacetate compounds were synthesized following literature procedures and analysis matched the literature data.

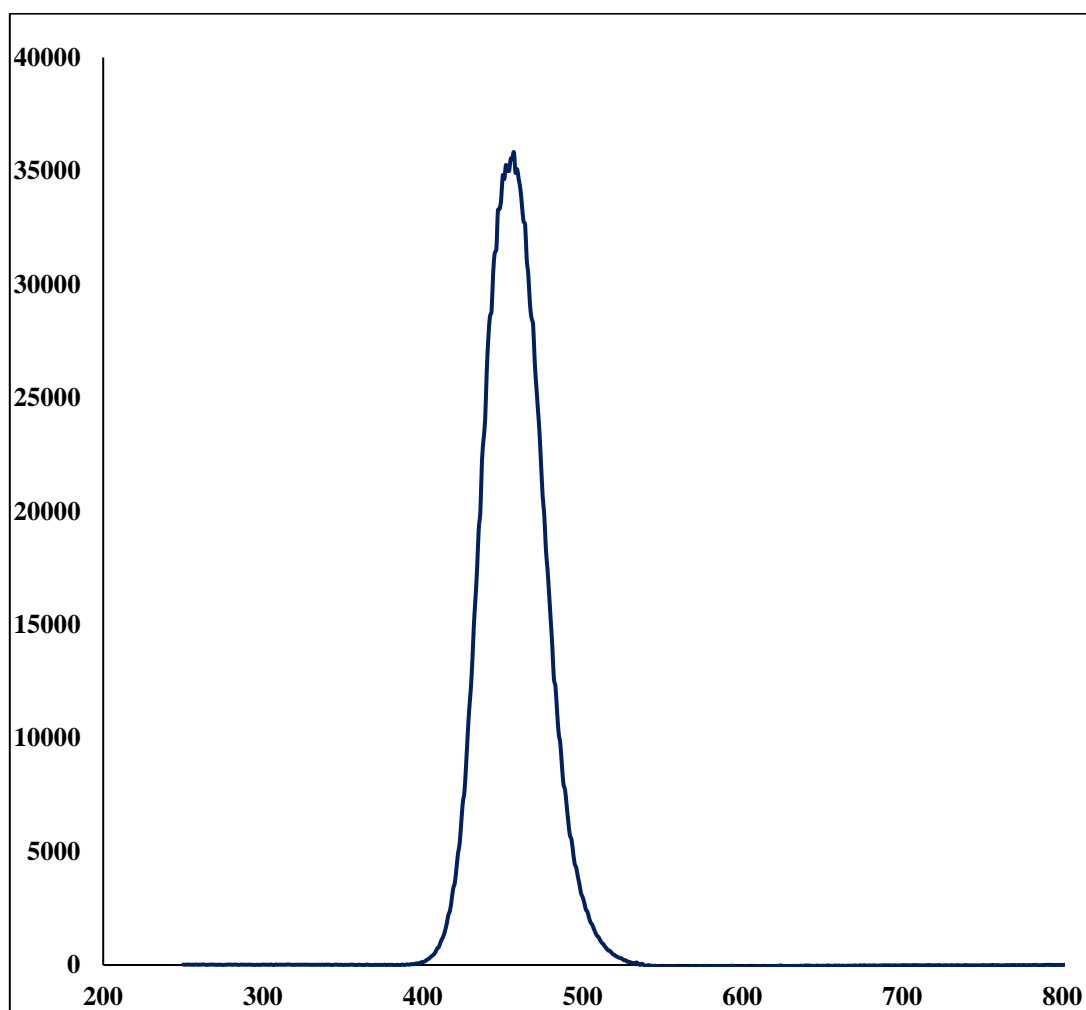
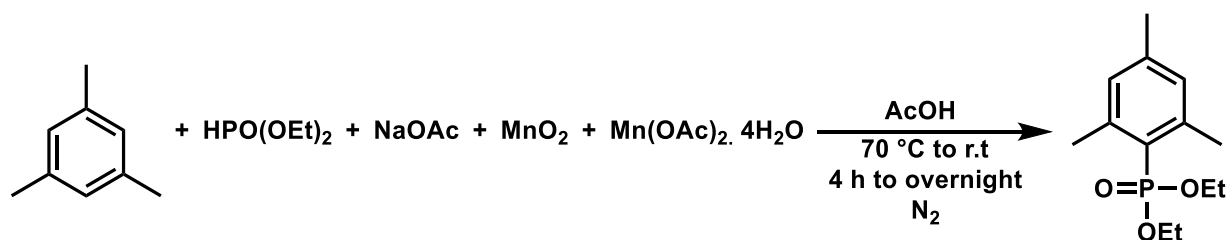


Figure II-107. Emission spectrum of the blue 5 W Vision-EL LED.

Synthesis of diethyl mesitylphosphonate:



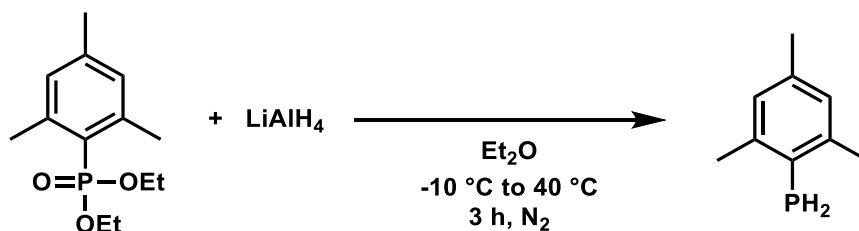
Synthesized according to literature procedure. An oven-dried three neck flask (500.0 ml) was charged with NaOAc (9.8 g, 120.0 mmol, 3.0 equiv), MnO<sub>2</sub> (10.1 g, 120.0 mmol, 3.0 equiv), Mn(OAc)<sub>2</sub>·4H<sub>2</sub>O (0.5 g, 2.0 mmol, 0.05 equiv) and followed by addition of acetic acid (120.0 ml) and mesitylene (27.8 ml, 200 mmol, 5.0 equiv) via a syringe under N<sub>2</sub> atmosphere. Then the reaction mixture was heated to 70 °C with condenser and the solution of HPO(OEt)<sub>2</sub> (5.7 ml, 40.0 mmol, 1.0 equiv) in acetic acid (80.0 ml) was added to the reaction mixture via a dropping funnel over 30 min. After that, the reaction mixture was stirred an additional 3h30 and then at room temperature overnight. Then the reaction mixture was transferred to 500 ml

round bottom flask and three-quarters of acetic acid were evaporated with a rotatory evaporator. The reaction mixture was then diluted with ethyl acetate (150 ml) and quenched with slow addition of the solution of 0.4 (M)  $\text{Na}_2\text{S}_2\text{O}_4$  with saturated solution of  $\text{NaHCO}_3$  (500.0 mml). Then it was filtered with celite and the filtrate was poured in a separating funnel. The organic layer was washed with the solution of 0.4 (M)  $\text{Na}_2\text{S}_2\text{O}_4$  with saturated solution of  $\text{NaHCO}_3$ ,  $\text{NaHCO}_{3\text{sat}}$  solution, and finally with a brine solution. The organic layer was dried over  $\text{Na}_2\text{SO}_4$  followed by concentration under reduced pressure. The resulting reaction mixture was purified with flash column chromatography on silica gel using (pentane/ethyl acetate 60/40) to obtain a pale yellow oil pure diethyl mesitylphosphonate with 98% yield.

$^1\text{H}$  NMR (300 MHz,  $\text{CDCl}_3$ ):  $\delta$  (ppm) 6.89 (d,  $J = 4.6$  Hz, 2H), 4.06 (m, 4H), 2.59 (d,  $J = 1.6$  Hz, 6H), 2.26 (s, 3H), 1.29 (t,  $J = 7.1$  Hz, 6H)

$^{31}\text{P}$  { $^1\text{H}$ } NMR (109 MHz,  $\text{CDCl}_3$ ):  $\delta$  20.47 ppm

Synthesis of the primary mesitylphosphine:



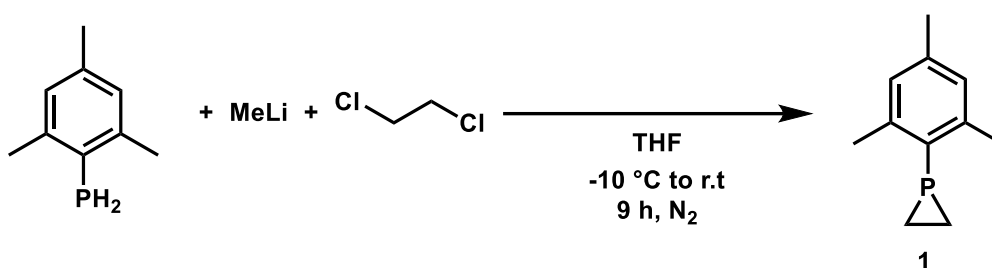
Synthesized according to literature procedure. To a suspension of  $\text{LiAlH}_4$  (3.9 g, 102.9 mmol, 3.0 equiv) in diethyl ether (150.0 ml) at  $-10^\circ\text{C}$  under  $\text{N}_2$  atmosphere, was added a solution of diethyl mesitylphosphonate (8.8 g, 34.3 mmol, 1.0 equiv) in 50 mL diethyl ether. Then the reaction mixture was refluxed for 3 h. The reaction was then allowed to cool to room temperature and 18.5%  $\text{HCl}$  (200.0 ml) was added at  $-10^\circ\text{C}$  (addition of  $\text{HCl}$  must be slow at first (gas evolution)). It was then filtered over celite in frit under  $\text{N}_2$  atmosphere. The Schlenk flask of the reaction mixture was washed well with diethyl ether (3 X 100.0 ml) and filtered over celite. Then the product was extracted with diethyl ether (3 X 150.0 ml) under  $\text{N}_2$  atmosphere with a cannula system and the organic layer was dried over  $\text{Na}_2\text{SO}_4$ . Afterwards, with the help of a filtering cannula the organic layer was transferred to a 2 L Schlenk flask and the mixture was concentrated under vacuum to obtained a pale-yellow colored oily compound, which was used for the next step without further purification.

$^{31}\text{P}$  NMR (109 MHz, diethyl ether):  $\delta$  -157.7 ppm (t,  $J = 201.3$  Hz)



Figure II-108: Extraction the crude product with diethyl ether

Synthesis of 1-mesitylphosphirane **1** :



Synthesized according to literature procedure. On the same day the primary mesitylphosphine (3.5 g, 23.0 mmol, 1.0 equiv) was dissolved in THF (500.0 ml) in the same 2 L round bottom flask under N<sub>2</sub> atmosphere. Then 1.6 (M) methyl lithium in diethyl ether (44 ml, 69.0 mmol, 3.0 equiv) was added dropwise at -10 °C. Afterwards, the reaction mixture was allowed to warm to room temperature and stirred for an additional 30 min. 1,2-dichloroethane (2 ml, 25.3 mmol, 1.1 equiv) was then added to the reaction mixture dropwise at -10 °C and allowed to stirred at room temperature for 9 h. The reaction was quenched with 100 ml distilled water sparged with argon. Then five of sixths part of the mixed organic and aqueous layer (THF/H<sub>2</sub>O) was evaporated under high vacuum and the extraction was performed with diethyl ether (5 X 150 ml). The organic layer was dried over Na<sub>2</sub>SO<sub>4</sub> and concentrated under vacuum. The resulting reaction mixture was purified by flash column chromatography using pentane under inert atmosphere. The eluent was collected under air and after quick check by TLC and evaporation under reduced pressure 1-mesitylphosphirane was obtained as colorless oil up to 70% yield and stored in a glove box fridge.

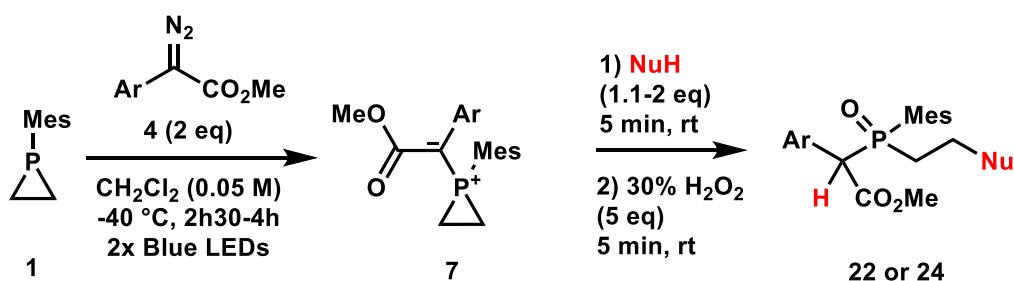
<sup>1</sup>H NMR (300 MHz, CDCl<sub>3</sub>): δ (ppm) 6.81-6.80 (m, 2H), 2.52 (s, 6H), 2.24 (s, 3H), 1.46-1.36 (m, 1H), 1.34-1.26 (m, 1H), 1.16 – 1.24 (m, 1H), 1.16- 1.08 (m, 1H)

<sup>31</sup>P NMR (109 MHz, CDCl<sub>3</sub>): δ – 240.7 ppm (*J* = 16.82 Hz)

General procedure 1 (GP1)

An oven dried NMR tube was charged with methyl aryldiazoacetate **4** (2.0 equiv), 1-mesitylphosphirane **1** (1.0 equiv) and dichloromethane (1 mL, 0.05 (M)) under N<sub>2</sub> atmosphere. Then the reaction mixture was irradiated with two blue LEDs for 2h30 to 4h at -40 °C. The reaction mixture was then taken out from the reactor and allowed to warm to room temperature. Thiophenol was then added (2 equiv). A solution of the internal standard trimethoxybenzene was added for NMR analysis.

The reactions were ran 4 at a time with solutions of the phosphirane **1**, the methyl aryldiazoacetate **4**, and of the internal standard to prevent important errors in the measurement of small quantities.

General procedure 2 (GP2)

A flame dried Schlenk tube was charged with methyl aryldiazoacetate **4** (2.0 equiv) and 1-mesitylphosphirane (1.0 equiv) in dichloromethane (2 mL, 0.05 (M)) under N<sub>2</sub> atmosphere. Then the reaction mixture was irradiated with two blue LEDs for 2h30 to 4h00 at -40 °C. After that the reaction mixture was taken out from the reactor and allowed to warm to room temperature. Then, the nucleophile (2 equiv. for the thiophenols and 1.1 equiv. for the carboxylic acids) was added (liquid as such and solids in solution in dichloromethane) and the solution was stirred for 20 min (the reaction proceeds within less than 5 minutes). Afterwards 30% H<sub>2</sub>O<sub>2</sub> aqueous solution (50 μL, 5.0 equiv) was added in order to oxidize the phosphine **19** or **23** to the phosphine oxide **22** or **24** and the mixture was stirred for 30 min (the reaction proceeds within less than 5 minutes). The resulting mixture was dried on Na<sub>2</sub>SO<sub>4</sub> and purified by flash column chromatography with silica using ethyl acetate to yield the desired compounds.

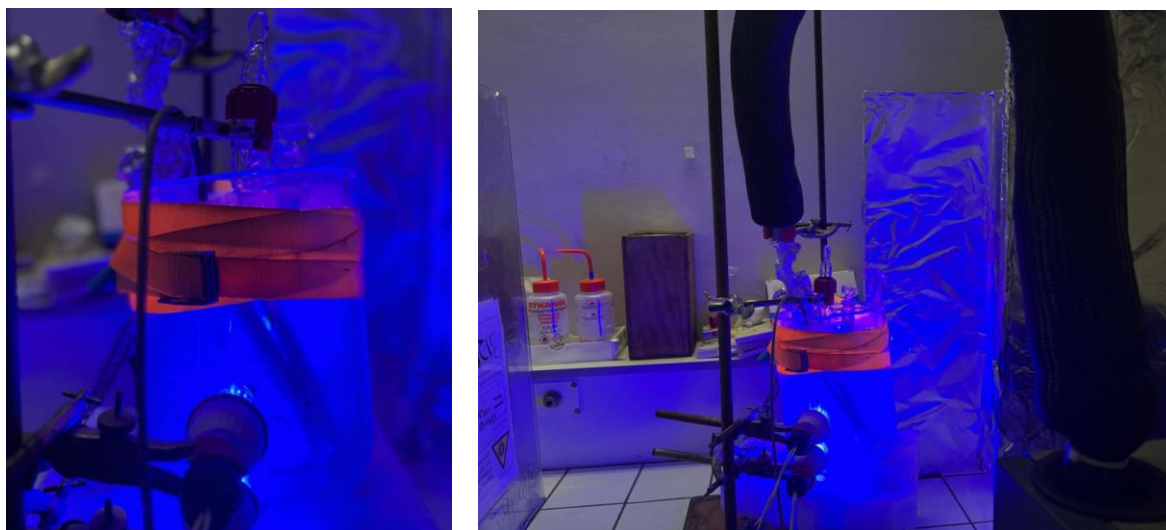
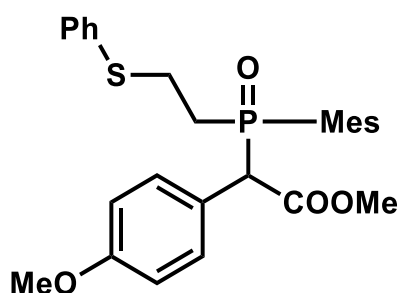


Figure II-109 : Irradiation of the solution in GP2

Experimental details for the compounds obtained from (GP2):

Phosphine oxide **22a** : ring opening of phosphiranium ylide **7d** with thiophenol



**Chemical Formula:** C<sub>27</sub>H<sub>31</sub>O<sub>4</sub>PS  
**Molecular Weight:** 482.57

Prepared according to **GP2**, using 1-mesitylphosphirane (17.8 mg, 1.0 equiv) and methyl 4-methoxyphenyldiazoacetate (41.2 mg, 2.0 equiv) in 0.05 M dichloromethane, followed by addition of thiophenol (21  $\mu$ L, 2 equiv), and then 30 % H<sub>2</sub>O<sub>2</sub> aqueous solution (50  $\mu$ L, 5.0 equiv). Purification was done by column chromatography on silica gel using ethyl acetate as eluent afforded the desired product **22a** (40.1 mg, 0.083 mmol 83% yield) as a pale-yellow oil.

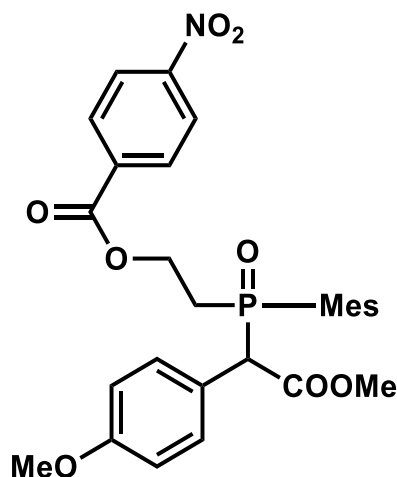
**<sup>1</sup>H NMR** (300 MHz, CDCl<sub>3</sub>) (*dr* = 60:40)  $\delta$  7.41 (m, 2H), 7.33-7.10 (m, 17H including CDCl<sub>3</sub>), 6.90 (m, 4H), 6.71 (m, 4H), 4.37 (d, *J*=11.13 Hz, 1H), 4.34 (d, *J*=11.28 Hz, 1H), 3.81 (s, 3H), 3.73 (s, 6H), 3.54 (s, 3H), 3.24 (m, 1H), 3.02-2.70 (m, 3H), 2.65-2.00 (m, 22H).

The <sup>1</sup>H NMR sets of signals in the aliphatic region were all superimposed and too complex to be identified individually. The integration could not be properly verified because of the presence of an important solvent peak in the aromatic region. Important amounts of grease were present as well.

$^{31}\text{P}\{^1\text{H}\}$  NMR (121.5 MHz,  $\text{CDCl}_3$ ):  $\delta$  (ppm) 40.52, 39.96.

HRMS (ESI+) for  $\text{C}_{14}\text{H}_{12}$   $[\text{M}+\text{H}]^+$ : calc. 483.1759; found : 483.1759.

Phosphine oxide **24a** : ring opening of phosphiranium ylide **7d** with 4-nitrobenzoic acid



Chemical Formula:  $\text{C}_{28}\text{H}_{30}\text{NO}_8\text{P}$   
Molecular Weight: 539.52

Prepared according to **GP2**, using 1-mesitylphosphirane (17.8 mg, 1.0 equiv, 0.1 mmol) and methyl 4-methoxyphenyldiazoacetate (41.2 mg, 2.0 equiv) in 0.05 M dichloromethane, followed by addition of 4-nitrobenzoic acid (18.0 mg, 1.1 equiv), and then 30 %  $\text{H}_2\text{O}_2$  aqueous solution (50  $\mu\text{L}$ , 5.0 equiv). Purification was done by column chromatography on silica gel using ethylacetate as eluent afforded the desired product **24a** (45.0 mg, 0.083 mmol, 83% yield) as a pale-yellow solid.

$^1\text{H}$  NMR (300 MHz,  $\text{CDCl}_3$ ) ( $dr = 58:42$ ):  $\delta$  (ppm) 8.16-8.11 (m, 4H), 7.90-7.80 (m, 4H), 7.50-7.47 (m, 2H), 7.25-7.22 (m, 2H), 6.96-6.89 (m, 2H), 6.84 (d,  $J = 3.8$  Hz, 2H), 6.73-6.68 (m, 2H), 6.65 (d,  $J = 3.8$  Hz, 2H), 4.77-4.73 (m, 1H), 4.72-4.68 (m, 1H), 4.66-4.53 (m, 1H), 4.51-4.39 (m, 1H), 4.46 (d,  $J = 10.82$  Hz, 1H), 4.42 (d,  $J = 11.07$  Hz, 1H), 3.81 (s, 6H), 3.72 (s, 3H), 3.53 (s, 3H), 3.01-2.95 (m, 1H), 2.93-2.85 (m, 1H), 2.68-2.52 (m, 1H), 2.57 (br s, 6H), 2.40 (s, 6H), 2.33-2.19 (m, 1H), 2.23 (s, 3H), 2.12 (s, 3H).

$^{31}\text{P}\{^1\text{H}\}$  NMR (121.5 MHz,  $\text{CDCl}_3$ ):  $\delta$  (ppm) 39.4, 39.0.

HRMS (ESI+) for  $\text{C}_{14}\text{H}_{12}$   $[\text{M}+\text{H}]^+$ : calc. 540.1787; found :540.1769.

Analytical data related to compounds synthesized by Avisek Ghosh are not reported here.

## 5. References

- (1) Montchamp, J. Phosphinate Chemistry in the 21st Century : A Viable Alternative to the Use of Phosphorus Trichloride in Organophosphorus Synthesis. *Acc. Chem. Res.* **2014**, 47 (1), 77–87.
- (2) Rockström, J.; Steffen, W.; K. Noone; Å. Persson; Chapin, F. S.; E. F. Lambin; T. M. Lenton; M. Scheffer; C. Folke; H. J. Schellnhuber; B. Nykvist; C. A. de Wit; T. Hughes; S. van der Leeuw; H. Rodhe; S. Sörlin; P. K. Snyder; R. Costanza; U. Svedin; M. Falkenmark; L. Karlberg; R. W. Corell; V. J. Fabry; J. Hansen; B. Walker; D. Liverman; K. Richardson; P. Crutzen; J. A. Foley. A Safe Operation Space for Humanity. *Nature* **2009**, 461 (September), 472–475.
- (3) Carpenter, S. R.; Bennett, E. M. Reconsideration of the Planetary Boundary for Phosphorus. *Environ. Res. Lett.* **2011**, 6 (1). <https://doi.org/10.1088/1748-9326/6/1/014009>.
- (4) Steffen, W.; Richardson, K.; Rockström, J.; Cornell, S. E.; Fetzer, I.; Bennett, E. M.; Biggs, R.; Carpenter, S. R.; De Vries, W.; De Wit, C. A.; Folke, C.; Gerten, D.; Heinke, J.; Mace, G. M.; Persson, L. M.; Ramanathan, V.; Reyers, B.; Sörlin, S. Planetary Boundaries: Guiding Human Development on a Changing Planet. *Science* (80-. ). **2015**, 347 (6223). <https://doi.org/10.1126/science.1259855>.
- (5) Kendall, A. J.; Tyler, D. R. The Synthesis of Heteroleptic Phosphines. *Dalt. Trans.* **2015**, 44 (28), 12473–12483. <https://doi.org/10.1039/c5dt01617g>.
- (6) Freeman, L. D.; Wagner, I.; Goldwhite, H.; Roswell, D. G. Phosphiran. *J. Am. Chem. Soc.* **1967**, 89 (5), 1102–1104.
- (7) Van Assema, S. G. A.; De Kanter, F. J. J.; Schakel, M.; Lammertsma, K. Decomplexation of Phosphirane and Phosphirene Complexes. *Organometallics* **2006**, 25 (22), 5286–5291. <https://doi.org/10.1021/om060570t>.
- (8) Bachrach, S. M. Theoretical Studies of Phosphirane and Phosphetane. *J. Phys. Chem.* **1989**, 93 (23), 7780–7784. <https://doi.org/10.1021/j100360a011>.
- (9) Gaston, J. J.; McCosker, P. M.; Yu, H.; Keller, P. A. Predicting Phosphirane Air Stability Using Density Functional Theory. *J. Phys. Org. Chem.* **2020**, 33 (10), 1–10. <https://doi.org/10.1002/poc.4110>.
- (10) Li, X.; Weissman, S. I.; Lin, T.; Gaspar, P. P.; Smirnov, A. I. Observation of a Triplet



- Phosphinidene by ESR Spectroscopy. *J. Am. Chem. Soc.* **1994**, *116*, 7899–7900.
- (11) Gasnot, J.; Botella, C.; Comesse, S.; Lakhdar, S.; Alayrac, C.; Gaumont, A. C.; Dalla, V.; Taillier, C. Taming the Reactivity of Phosphiranium Salts: Site-Selective C-Centered Ring Opening for Direct Synthesis of Phosphinoethylamines. *Angew. Chemie - Int. Ed.* **2020**, *59* (29), 11769–11773. <https://doi.org/10.1002/anie.201916449>.
  - (12) Marinetti, A.; Mathey, F. OPENING OF PHOSPHIRANE-TUNGSTEN-COMPLEXES BY NUCLEOPHILES. *Tetrahedron* **1989**, *45* (10), 3061–3070.
  - (13) Berger, O.; Montchamp, J. L. Manganese-Mediated Intermolecular Arylation of H-Phosphinates and Related Compounds. *Chem. - A Eur. J.* **2014**, *20* (39), 12385–12388. <https://doi.org/10.1002/chem.201404507>.
  - (14) Botella, C. Etude Des Ions Phosphiranium : Synthèse et Réactivité. *Normandie Univ. HAL Id tel-03543976* **2021**.
  - (15) Tipker, R. M.; Muldoon, J. A.; Pham, D. H.; Varga, B. R.; Hughes, R. P.; Glueck, D. S.; Balaich, G. J.; Rheingold, A. L. Configurational Lability at Tetrahedral Phosphorus: Syn/Anti-Isomerization of a P-Stereogenic Phosphiranium Cation by Intramolecular Epimerization at Phosphorus. *Angew. Chemie - Int. Ed.* **2022**, *61* (1). <https://doi.org/10.1002/anie.202110753>.
  - (16) Muldoon, J. A.; Varga, B. R.; Deegan, M. M.; Chapp, T. W.; Eördögh, Á. M.; Hughes, R. P.; Glueck, D. S.; Moore, C. E.; Rheingold, A. L. Inversion of Configuration at the Phosphorus Nucleophile in the Diastereoselective and Enantioselective Synthesis of P-Stereogenic Syn-Phosphiranes from Chiral Epoxides. *Angew. Chemie - Int. Ed.* **2018**, *57* (18), 5047–5051. <https://doi.org/10.1002/anie.201801427>.
  - (17) Deegan, M. M.; Muldoon, J. A.; Hughes, R. P.; Glueck, D. S.; Rheingold, A. L. Synthesis and Structure of Metal Complexes of P-Stereogenic Chiral Phosphiranes: An EDA-NOCV Analysis of the Donor-Acceptor Properties of Phosphirane Ligands. *Organometallics* **2018**, *37* (9), 1473–1482. <https://doi.org/10.1021/acs.organomet.8b00123>.
  - (18) Mathey, F. The Development of a Carbene-like Chemistry with Terminal Phosphinidene Complexes. *Angew. Chemie Int. Ed. English* **1987**, *26* (4), 275–370.
  - (19) Heydt, H. Phosphiranes, Phosphirenes, and Heavier Analogues. *Compr. Heterocycl. Chem.* **2008**, *III*, 457–481.

- (20) Transue, W. J.; Velian, A.; Nava, M.; García-Iriepa, C.; Temprado, M.; Cummins, C. C. Mechanism and Scope of Phosphinidene Transfer from Dibenzo-7-Phosphanorbornadiene Compounds. *J. Am. Chem. Soc.* **2017**, *139* (31), 10822–10831. <https://doi.org/10.1021/jacs.7b05464>.
- (21) Mathey, F. Chemistry of 3-Membered Carbon-Phosphorus Heterocycles. *Chem. Rev.* **1990**, *90*, 997–1025.
- (22) Tallis, H. A.; Newman, P. D.; Edwards, P. G.; Ooi, L.; Stasch, A. 1-Trimethylsilylphosphirane as a Ligand and as a Stable Masked Reagent for Phosphirane. *J. Chem. Soc. Dalt. Trans.* **2007**, No. 1, 47–53. <https://doi.org/10.1039/b715327a>.
- (23) Cooney, K. D.; Cundari, T. R.; Hoffman, N. W.; Pittard, K. A.; Temple, M. D.; Zhao, Y. A Priori Assessment of the Stereoelectronic Profile of Phosphines and Phosphites. *J. Am. Chem. Soc.* **2003**, *125* (14), 4318–4324. <https://doi.org/10.1021/ja021254i>.
- (24) Mézailles, N.; Fanwick, P. E.; Kubiak, C. P. Synthesis and Reactivity of Phosphirane Ligands and the Structural Characterization of Cp\*IrCl<sub>2</sub>(Tert-Butylphosphirane). *Organometallics* **1997**, *16* (8), 1526–1530. <https://doi.org/10.1021/om960400o>.
- (25) Liedtke, J.; Loss, S.; Alcaraz, G.; Gramlich, V.; Grützmacher, H. Very Stable Phosphiranes. *Angew. Chemie - Int. Ed.* **1999**, *38* (11), 1623–1626. [https://doi.org/10.1002/\(SICI\)1521-3773\(19990601\)38:11<1623::AID-ANIE1623>3.0.CO;2-K](https://doi.org/10.1002/(SICI)1521-3773(19990601)38:11<1623::AID-ANIE1623>3.0.CO;2-K).
- (26) Liedtke, J.; Rüegger, H.; Loss, S.; Grützmacher, H. BABAR-PHOS-Rhodium Complexes: Reversible Metal Insertion into a Three-Membered Ring and Catalytic Hydroborations. *Angew. Chemie - Int. Ed.* **2000**, *39* (14), 2478–2481. [https://doi.org/10.1002/1521-3773\(20000717\)39:14<2478::AID-ANIE2478>3.0.CO;2-G](https://doi.org/10.1002/1521-3773(20000717)39:14<2478::AID-ANIE2478>3.0.CO;2-G).
- (27) Laporte, C.; Frison, G.; Grützmacher, H.; Hillier, A. C.; Sommer, W.; Nolan, S. P. Binding of Specialty Phosphines to Metals: Synthesis, Structure, and Solution Calorimetry of the Phosphirane Complex [PtMe<sub>2</sub>(IPrBABAR-Phos)<sub>2</sub>]. *Organometallics* **2003**, *22* (11), 2202–2208. <https://doi.org/10.1021/om020642q>.
- (28) Grützmacher, H. ; Liedtke, J. ; Loss, S. ; Widauer, C. Phosphiranes as Ligands for Platinum Catalysed Hydrosilylations. *Tetrahedron* **2000**, *56*, 143–156.
- (29) Hockless, D. C. R.; McDonald, M. A.; Pabel, M.; Wild, S. B. 1-Methyl-1-Phenylphosphiranium Triflate: Synthesis, Structure and Reactivity. *Chem. Commun.*

- 1995, 257–258.
- (30) Brasch, N. E.; Hamilton, I. G.; Krenske, E. H.; Wild, S. B.  $\pi$ -Ligand Exchange on Phosphenium Ions: Reversible Exchange between Free and Coordinated Alkynes in Phosphirenium Salts. *Organometallics* **2004**, 23 (2), 299–302. <https://doi.org/10.1021/om030607z>.
- (31) Glueck, D. S. Comprehensive Heterocyclic Chemistry. *Compr. Heterocycl. Chem.* **2021**. <https://doi.org/10.1016/C2009-0-15932-9>.
- (32) Ficks, A.; Martinez-Botella, I.; Stewart, B.; Harrington, R. W.; Clegg, W.; Higham, L. J. Taming Functionality: Easy-to-Handle Chiral Phosphiranes. *Chem. Commun.* **2011**, 47 (29), 8274–8276. <https://doi.org/10.1039/c1cc12440d>.
- (33) Hiney, R. M.; Ficks, A.; Müller-Bunz, H.; Gilheany, D. G.; Higham, L. J. Air-Stable Chiral Primary Phosphines Part (i) Synthesis, Stability and Applications. *Organomet. Chem.* **2011**, 37 (i), 27–45. <https://doi.org/10.1039/9781849732802-00027>.
- (34) Stewart, B.; Harriman, A.; Higham, L. J. Predicting the Air Stability of Phosphines. *Organometallics* **2011**, 30 (20), 5338–5343. <https://doi.org/10.1021/om200070a>.
- (35) Ficks, A.; Sibbald, C.; Ojo, S.; Harrington, R. W.; Clegg, W.; Higham, L. J. Efficient Multigram Syntheses of Air-Stable, Chiral Primary Phosphine Ligand Precursors via Palladium-Catalyzed Phosphylation of Aryltriflates. *Synth.* **2013**, 45 (2), 265–271. <https://doi.org/10.1055/s-0032-1316825>.
- (36) Ekkert, O.; Kehr, G.; Fröhlich, R.; Erker, G. Phosphirenium-Borate Zwitterion: Formation in the 1,1-Carboboration Reaction of Phosphinylalkyne. *Chem. Commun.* **2011**, 47, 10482–10484.
- (37) Ueno, A.; Möricke, J.; Daniuluc, C. G.; Kehr, G.; Erker, G. Phosphirenium Borate Betaines from Alkynylphosphanes and the Halogeno-B(C<sub>6</sub>F<sub>5</sub>)<sub>2</sub> Reagents. *Chem. Commun.* **2018**, 54, 13746–13749.
- (38) Gasnot, J.; Botella, C.; Comesse, S.; Lakhdar, S.; Alayrac, C.; Gaumont, A. C.; Dalla, V.; Taillier, C. Access to Stable Quaternary Phosphiranium Salts by P-Alkylation and P-Arylation of Phosphiranes. *Synlett* **2020**, 31 (9), 883–888. <https://doi.org/10.1055/s-0040-1708000>.
- (39) Tipker, R. M.; Muldoon, J. A.; Jo, J.; Connors, C. S.; Varga, B. R.; Hughes, R. P.; Glueck, D. S. Protonation of P-Stereogenic Phosphiranes: Phospholane Formation via

- Ring Opening and C-H Activation. *ACS Omega* **2023**, *4* (Scheme 3), 4–11. <https://doi.org/10.1021/acsomega.3c00885>.
- (40) Lammertsma, K. Phosphinidenes. *Top. Curr. Chem.* **2003**, *229*, 95–119. <https://doi.org/10.1007/b11152>.
- (41) Nguyen, M. T.; Van Keer, A.; Vanquickenborne, L. G. In Search of Singlet Phosphinidenes. *J. Org. Chem.* **1996**, *61* (20), 7077–7084. <https://doi.org/10.1021/jo9604393>.
- (42) Liu, L.; Ruiz, D. A.; Munz, D.; Bertrand, G. A Singlet Phosphinidene Stable at Room Temperature. *Chem* **2016**, *1* (1), 147–153. <https://doi.org/10.1016/j.chempr.2016.04.001>.
- (43) Li, X.; Lei, D.; Chiang, M. Y.; Gaspar, P. P. General Approaches to Phosphinidenes via Retroadditions. *J. Am. Chem. Soc.* **1992**, *114* (22), 8526–8531. <https://doi.org/10.1021/ja00048a026>.
- (44) Bucher, G.; Borst, M. L. G.; Ehlers, A. W.; Lammertsma, K.; Ceola, S.; Huber, M.; Grote, D.; Sander, W. Infrared, UV/Vis, and W-Band EPR Spectroscopic Characterization and Photochemistry of Triplet Mesitylphosphinidene. *Angew. Chemie - Int. Ed.* **2005**, *44* (21), 3289–3293. <https://doi.org/10.1002/anie.200462862>.
- (45) Tsuji, K.; Sasaki, S.; Yoshifuji, M. Synthesis and Photolysis of Phosphiranes and Diphosphiranes Carrying Sterically Protecting Groups on the Phosphorus Atoms. *Heteroat. Chem.* **1998**, *9* (7), 607–613. [https://doi.org/10.1002/\(SICI\)1098-1071\(1998\)9:7<607::AID-HC3>3.0.CO;2-5](https://doi.org/10.1002/(SICI)1098-1071(1998)9:7<607::AID-HC3>3.0.CO;2-5).
- (46) Akimov, A. V.; Ganushevich, Y. S.; Korchagin, D. V.; Miluykov, V. A.; Misochko, E. Y. The EPR Spectrum of Triplet Mesitylphosphinidene: Reassignment and New Assignment. *Angew. Chemie - Int. Ed.* **2017**, *56* (27), 7944–7947. <https://doi.org/10.1002/anie.201703629>.
- (47) Lam, W. H.; Gaspar, P. P.; Hrovat, D. A.; Trieber, D. A.; Davidson, E. R.; Borden, W. T. Computational Studies of the Thermal Fragmentation of P-Arylphosphiranes: Have Arylphosphinidenes Been Generated by This Method? *J. Am. Chem. Soc.* **2005**, *127* (27), 9886–9894. <https://doi.org/10.1021/ja050891g>.
- (48) Misochko, E. Y.; Akimov, A. V.; Korchagin, D. V.; Ganushevich, Y. S.; Melnikov, E. A.; Miluykov, V. A. Generation and Direct EPR Spectroscopic Observation of Triplet Arylphosphinidenes: Stabilisation: Versus Internal Rearrangements. *Phys. Chem. Chem.*

- Phys.* **2020**, 22 (47), 27626–27631. <https://doi.org/10.1039/d0cp05254j>.
- (49) Benn, R.; Mynott, R.; Richter, W. J.; Schroth, G. Reactions of Vinylphosphirane with Methylenetrimethylphosphorane. *Tetrahedron* **1984**, 40 (17), 3273–3276.
- (50) Hao, Y.; Zhang, C.; Mei, Y.; Tian, R.; Duan, Z.; Mathey, F. The Chemistry of Parent Phosphiranide in the Coordination Sphere of Tungsten. *Dalt. Trans.* **2016**, 45 (19), 8284–8290. <https://doi.org/10.1039/c6dt00964f>.
- (51) Kadokawa, J. I.; Kobayashi, S. New Ring-Opening Polymerization of Phosphorus-Containing Cyclic Monomers. *Phosphorus, Sulfur Silicon Relat. Elem.* **2002**, 177 (6–7), 1387–1390. <https://doi.org/10.1080/10426500212283>.
- (52) Mayr, H.; Patz, M. Scales of Nucleophilicity and Electrophilicity: A System for Ordering Polar Organic and Organometallic Reactions. *Angew. Chem. Int. Ed. Engl.* **1994**, 33, 938–957.
- (53) Mayr, H.; Bug, T.; Gotta, M. F.; Hering, N.; Irrgang, B.; Janker, B.; Kempf, B.; Loos, R.; Ofial, A. R.; Remennikov, G.; Schimmel, H. Reference Scales for the Characterization of Cationic Electrophiles and Neutral Nucleophiles. *J. Am. Chem. Soc.* **2001**, 123 (39), 9500–9512. <https://doi.org/10.1021/ja010890y>.
- (54) Mayr, H.; Kempf, B.; Ofial, A. R.  $\pi$ -Nucleophilicity in Carbon-Carbon Bond Forming Reactions. *Acc. Chem. Res.* **2003**, 36 (1), 66–77.
- (55) Jüstel, P. M.; Pignot, C. D.; Ofial, A. R. Nucleophilic Reactivities of Thiophenolates. *J. Org. Chem.* **2021**, 86 (8), 5965–5972. <https://doi.org/10.1021/acs.joc.1c00025>.
- (56) Kempf, B.; Mayr, H. Rates and Equilibria of the Reactions of Tertiary Phosphanes and Phosphites with Benzhydrylium Ions. *Chem. - A Eur. J.* **2005**, 11 (3), 917–927. <https://doi.org/10.1002/chem.200400696>.
- (57) Mayr, H.; Ammer, J.; Baidya, M.; Maji, B.; Nigst, T. A.; Ofial, A. R.; Singer, T. Scales of Lewis Basicities toward C-Centered Lewis Acids (Carbocations). *J. Am. Chem. Soc.* **2015**, 137 (7), 2580–2599. <https://doi.org/10.1021/ja511639b>.
- (58) Yang, Z.; Stivanin, M. L.; Jurberg, I. D.; Koenigs, R. M. Visible Light-Promoted Reactions with Diazo Compounds: A Mild and Practical Strategy towards Free Carbene Intermediates. *Chem. Soc. Rev.* **2020**, 49 (19), 6833–6847. <https://doi.org/10.1039/d0cs00224k>.
- (59) Edition, I. Cascade Reactions of Nitrogen and Phosphorus Containing Ylides with

- Methyl Diazoacetate and in Situ Generated Diazocyclopropane. **2006**, 55 (1), 112–117.
- (60) Byrne, P. A.; Gilheany, D. G. The Modern Interpretation of the Wittig Reaction Mechanism. *Chem. Soc. Rev.* **2013**, 42 (16), 6670–6696. <https://doi.org/10.1039/c3cs60105f>.
- (61) Neese, F. The ORCA Program System. *Wiley Interdiscip. Rev. Comput. Mol. Sci.* **2012**, 2 (1), 73–78. <https://doi.org/10.1002/wcms.81>.
- (62) Neese, F.; Wennmohs, F.; Becker, U.; Riplinger, C. The ORCA Quantum Chemistry Program Package. *J. Chem. Phys.* **2020**, 152 (22). <https://doi.org/10.1063/5.0004608>.
- (63) Bursch, M.; Mewes, J. M.; Hansen, A.; Grimme, S. Best-Practice DFT Protocols for Basic Molecular Computational Chemistry\*\*. *Angew. Chemie - Int. Ed.* **2022**, 61 (42). <https://doi.org/10.1002/anie.202205735>.
- (64) Grimme, S. Exploration of Chemical Compound, Conformer, and Reaction Space with Meta-Dynamics Simulations Based on Tight-Binding Quantum Chemical Calculations. **2019**. <https://doi.org/10.1021/acs.jctc.9b00143>.
- (65) Bannwarth, C.; Ehlert, S.; Grimme, S. GFN2-XTB □ An Accurate and Broadly Parametrized Self-Consistent Tight-Binding Quantum Chemical Method with Multipole Electrostatics and Density-Dependent Dispersion Contributions. **2019**. <https://doi.org/10.1021/acs.jctc.8b01176>.
- (66) Hansen, S. R.; Spangler, J. E.; Hansen, J. H.; Davies, H. M. L. Metal-Free N - H Insertions of Donor / Acceptor Carbenes. *Org. Lett.* **2012**, 14 (17), 2998–2999.
- (67) Moore, J. H. Investigation of the Wigner Spin Rule in Collisions of N<sup>+</sup> with He, Ne, Ar, N<sub>2</sub>, and O<sub>2</sub>. *Phys. Rev. A* **1973**, 8 (5), 2359–2362. <https://doi.org/10.1103/PhysRevA.8.2359>.
- (68) Rey Planells, A.; Espinosa Ferao, A. Accurate Ring Strain Energies of Unsaturated Three-Membered Heterocycles with One Group 13–16 Element. *Inorg. Chem.* **2022**, 61 (17), 6459–6468. <https://doi.org/10.1021/acs.inorgchem.2c00067>.
- (69) Van Kalker, H. A.; Van Delft, F. L.; Rutjes, F. P. J. T. Organophosphorus Catalysis to Bypass Phosphine Oxide Waste. *ChemSusChem* **2013**, 6 (9), 1615–1624. <https://doi.org/10.1002/cssc.201300368>.
- (70) Manabe, S.; Wong, C. M.; Sevov, C. S. Direct and Scalable Electroreduction of Triphenylphosphine Oxide to Triphenylphosphine. *J. Am. Chem. Soc.* **2020**, 142 (6),

- 3024–3031. <https://doi.org/10.1021/jacs.9b12112>.
- (71) Schreiner, P. R. Tunneling Control of Chemical Reactions: The Third Reactivity Paradigm. *J. Am. Chem. Soc.* **2017**, *139* (43), 15276–15283. <https://doi.org/https://doi.org/10.1021/jacs.7b06035>.
- (72) Peng, Q.; Duarte, F.; Robert S., P. Computing Organic Stereoselectivity – from Concepts to Quantitative Calculations and Predictions. *Chem. Soc. Rev.* **2016**, *45* (22), 6093–6107. <https://doi.org/10.1039/x0xx00000x>.

# ***Chapter III:***

## ***DONOR-ACCEPTOR CYANOARENES AS POWERFUL ORGANIC PHOTOCATALYSTS***



## 1. Donor-Acceptor Cyanoarenes: General introduction

*“The more views we get, that we can integrate, make coherent, the deeper our understanding of the reality is. When I say the reality, the essence would be called “the true being”. That, really, we never get hold on, apparently. It’s unlimited. Everything, every view is limited. It’s like a mirror looking this way, and another, many many mirrors, each one gives a view, a limited view. Theories don’t give final true knowledge. They give a way of looking at it. The very word “theoria” in Greek means theater, it’s sort of a theater of the mind that gives insight into the thing. Right?”* -Theoretical physicist David Bohm, interviewed in 1990 by Bill Angelos

The current chapter will focus on donor-acceptor cyanoarenes (examples given in Figure III-1) and more specifically on the photophysical and photochemical behavior of their radical anions.

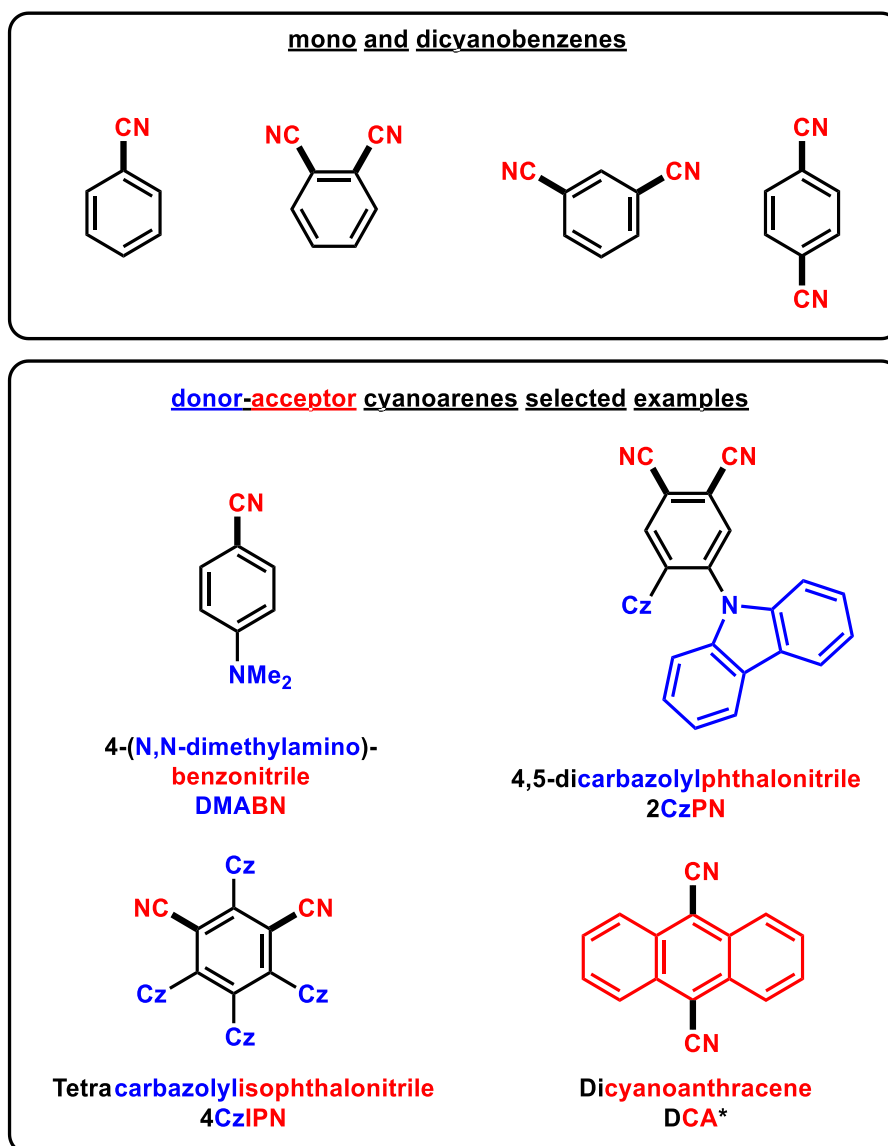


Figure III-1: Donor-Acceptor Cyanoarenes examples. \*Dicyanoanthracene (DCA) is included despite not having a donor-acceptor core because it is an extensively studied acceptor cyanoarene that can serve as a reference. Cz: Carbazole linked from its nitrogen, one is displayed on 2CzPN structure as an example.

Donor-acceptor (D-A) cyanoarenes have known a spiking interest in the past 10 years. Several reasons are involved: easily synthesized, non-toxic, metal-free, tunable structure and properties, subject to the interesting thermally activated delayed fluorescence (TADF) in most cases and overall redox and photophysical properties that compete with efficient heavy metals complexes such as iridium and ruthenium.<sup>1</sup>

Compared to Ancient Greek philosophy, donor-acceptor studies fall into the newborn category. However, in less than a century, their development has been astonishing. A short historical review is then given thereafter.

Donor-acceptor cyanoarenes studies -as we know them today, such as 2,4,5,6-Tetrakis(9H-carbazol-9-yl) isophthalonitrile (4CzIPN), started with a rather simple molecule: 4-N,N-dimethylamino-benzonitrile (DMABN)<sup>a</sup>, a phenyl aromatic ring with a benzonitrile electron deficient core and a dimethylamino electron donating substituent in *para* position (Figure III-2).

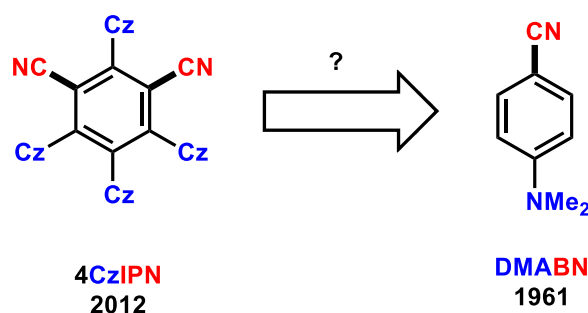


Figure III-2: 51 years' time gap between 4CzIPN and DMABN photophysical studies

DMABN exhibits uncommon luminescence properties. Instead of the common single emission band usually observed, a second “anomalous” red-shifted signal was reported by Lipert *et al.* (Figure III-3) in 1961.<sup>2,3</sup> The ratio between the two was modified by temperature and solvent polarity.<sup>4</sup>

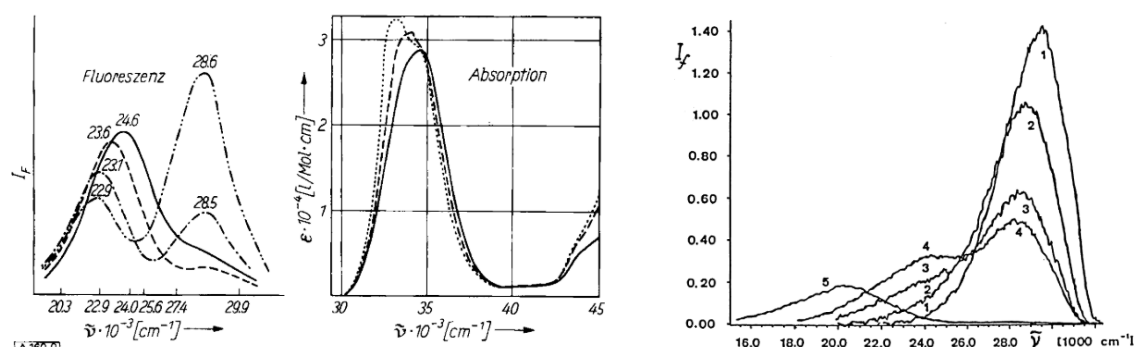


Figure III-3: Dual emission (DE) from DMABN in Lipert *et al.* and Rotkiewicz *et al.* publications. Reproduced with permission from references 3 (Copyright 1961 Wiley-VCH publishers) and 4 (Copyright 1992 The Indian Academy of Science).

<sup>a</sup> *p*-cyanodimethylaniline (CDMA) denomination was also used for some time

In apolar solvents -such as *n*-hexane, a single fluorescence band<sup>b</sup> is observed at [ 344 nm | 29,100 cm<sup>-1</sup> | 3.61 eV ].<sup>4</sup> When the polarity of the medium increases, a second band appears. This band redshifts from 24,000 to 20,000 cm<sup>-1</sup> when the solvent diethyl ether is changed to acetonitrile [ $\Delta\bar{\nu} = 4,000$  cm<sup>-1</sup> |  $\Delta\lambda = 86$  nm |  $\Delta E = 0.5$  eV] while the “normal” fluorescence at 29,100 cm<sup>-1</sup> almost completely disappears.

Each fluorescence band was attributed to two distinct emissive excited states with different polarities:  $L_a$  and  $L_b$  (Figure III-4).<sup>5</sup>

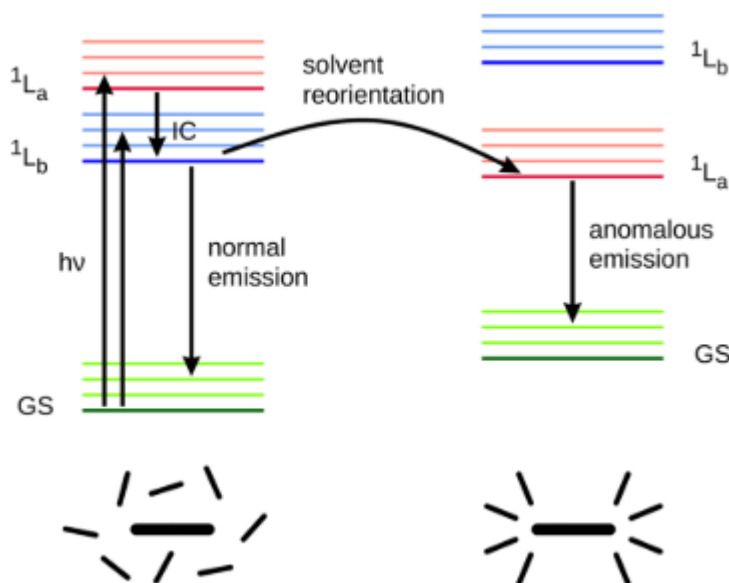


Figure III-4: Old nomenclature with  $L_a$  and  $L_b$  states (now CT and LE) with solvent reorganization.  
Reproduced with permission from reference 5 (Copyright 2020 American Chemical Society).

The  $L_b$  state was later called locally excited state (LE, slightly polar state favored in apolar solvents) and  $L_a$  was called charge transfer state (CT, highly polar state favored in polar solvents).<sup>c</sup> In solvents of mixed polarity, LE and CT states are degenerated for DMABN, and two emission bands are observed: dual emission (DE) occurs.

Recommended review on Dual Emission:

✓ *Angew. Chem. Int. Ed.* **2021**, 60, 22624-22638

This property is linked to the presence of the donor (amine) and acceptor (nitrile) moieties that allow for the charge transfer to be accessible. It is named Intramolecular Charge Transfer (ICT).<sup>d</sup>

<sup>b</sup> concentration, temperature and excitation wavelength were not clearly reported in the paper.<sup>4</sup>

<sup>c</sup> in 1992, the term charge separation or charge separated state (CSS) was also used.<sup>4</sup>

<sup>d</sup> Intermolecular Charge Transfer is abbreviated iMCT

The mechanism that takes place behind this observation is not straightforward and started to find a consensus in 2003.<sup>3,5–12,13,14</sup>

The several theories regarding the nature of the ICT involved behind the DE of DMABN were PICT (planar ICT), TICT (twisted ICT), RICT or WICT (rehybridized or wagging ICT), as well as other theories including exciplexes and proton transfer. The detailed review of Grabowski from 2003 extensively explains each proposition and its limits regarding available data at that time.<sup>10</sup> The most accepted theory to this day is the Twisted Intramolecular Charge Transfer (TICT) proposed by Grabowski in 1973, where the excited state undergoes twisting in polar solvents to bring the amino group perpendicular to the aromatic ring, thus spatially separating the HOMO and LUMO to the donor and acceptor respectively (Figure III-5).

This has drastic consequences, which we will detail thereafter.

Recommended reviews on TICT:

- ✓ *Chem. Soc. Rev.*, **2021**, 50, 12656-12678
- ✓ *Chemosensors*, **2023**, 11, 87

To our surprise, even the latest reviews on TICT do not mention multi-carbazoles derived donor-acceptor cyanoarenes, and multi-carbazoles derived donor-acceptor cyanoarenes do not mention TICT studies.

Subsequent work was done to further elaborate on the link between the donor-acceptor singly bonded moieties and their excited states tridimensional structure, electronic distribution, solvent polarity and temperature, expanding the structures studied beyond DMABN.<sup>6,15–17</sup> It was shown that the fluorescence evolved overtime from the LE emission to the CT emission, highlighting the structural rearrangement that occurs (Figure III-5).<sup>14,18</sup>

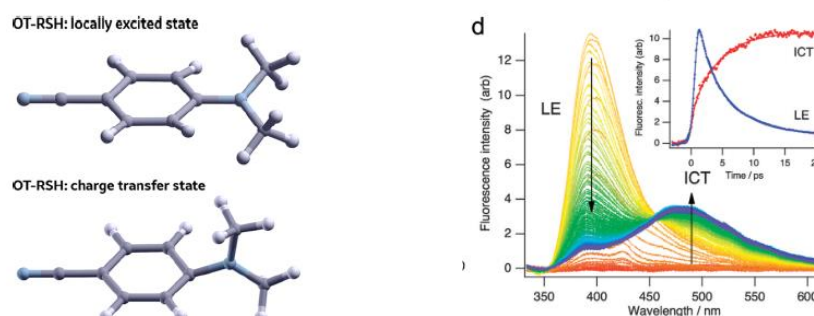


Figure III-5: DMABN LE and CT states spatial configuration (left) and evolution of luminescence overtime (right). Reproduced with permission from references 18 (left, Copyright 2020 American Chemical Society) and 14 (right, Licensee MDPI CC BY).

This debate highlights the important interest in understanding the nature of the states involved in luminescent electronic transition of donor-acceptor cyanoarenes to understand their photophysical properties and photochemical behavior.

The mechanism involved was shown to depend on the ground state molecular structure, in direct correlation with the molecule's properties (such as lifetime, emission wavelength, redox potentials,  $\Delta E_{ST}$ , luminescence yields, non-radiative decays...).<sup>14</sup> TICT state-like transitions were then favored from an already twisted ground state as shown in Figure III-6 with 4-dimethylamino-3,5-dimethylbenzonitrile and 4-(9H-carbazol-9-yl)benzonitrile.

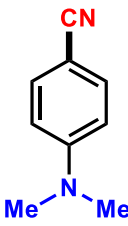
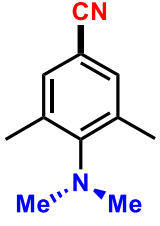
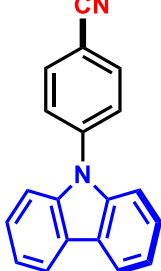
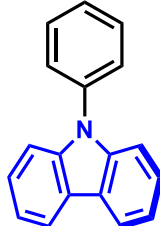
<u>Structure-emissive state relationship</u>				
				
Hexane	LE	CT	LE	LE
CH <sub>2</sub> Cl <sub>2</sub>	DE	CT	CT	LE
MeCN	CT	CT	CT	LE

Figure III-6 : Selected examples to highlight LE and CT emissions in cyanoarenes.<sup>8</sup> DE: Dual Emission. DMABN is planar while the three other moieties have a ground state twisted amino group.

Interestingly, carbazolyl benzene didn't show dual fluorescence at all; in solvents with medium polarity such as CH<sub>2</sub>Cl<sub>2</sub>, a <sup>1</sup>LE character was observed for 4-carbazol-9-yl-benzene (attributed to the poor electron affinity (EA) of benzene of -1.2 eV which prevents charge transfer) while a <sup>1</sup>CT was observed for moieties with electron deficient character on the central aromatic ring such as a nitrile substituent (Figure III-6).<sup>7</sup> As said before, the orientation of the substituents in the ground state assists the availability of the CT state. From Figure III-7, one can clearly see that the TICT state which brings donor and acceptor moieties perpendicular to each other reduces the gap between singlet and triplet states: the basis factor that favors thermally activated delayed fluorescence (TADF), a property at the root of the interest in D-A cyanoarenes. The known moduable ability of carbazol-9-yl-dicyanobenzenes (CDCB) to promote charge transfer and TADF then dates from the 90's.

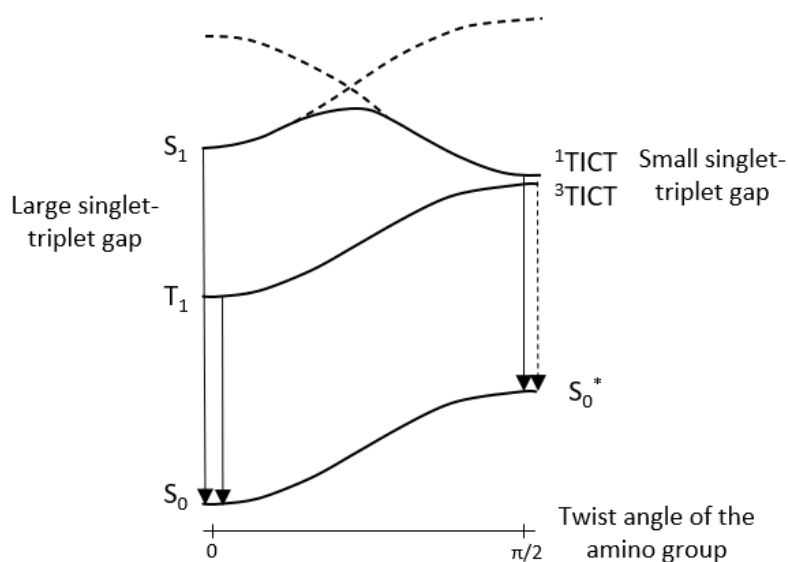


Figure III-7: Evolution of singlet and triplet states energies with and without twist of the dimethylamino group in regards of the aromatic ring.

Carbazole substituted donor-acceptor cyanoarenes found a renewed interest in 2012 when Adachi and coworkers showed their high efficiency as organic light-emitting diodes (OLEDs). Six molecules were studied (namely 2CzPN, 4CzIPN, 4CzPN, 4CzTPN, 4CzTPN-Me and 4CzTPN-Ph, see 2.1 for nomenclature). They modified the core by changing the benzonitrile ring to dicyanobenzene derivatives and by increasing the number of carbazole substituent to two or four, thus reducing non-radiative decays by important steric effects. 4CzIPN stood out as the best standard. In fact, regarding what has been discussed before, 4CzIPN excited state can be considered as a “forced TICT” from its ground state structure because of the important steric hindrance resulting from the four carbazoles moieties (Figure III-8).

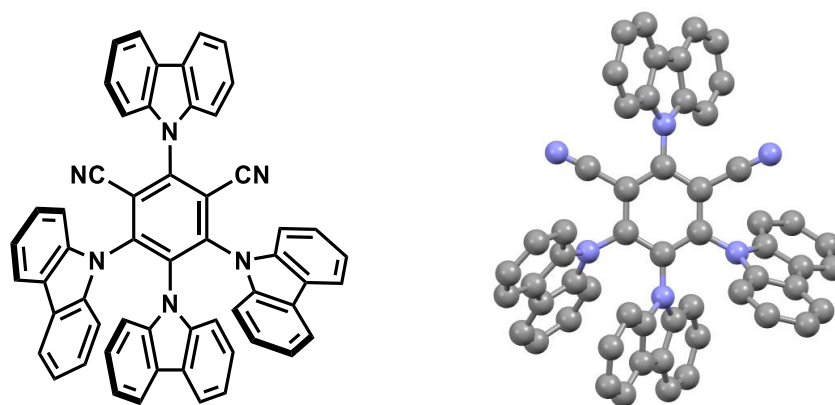


Figure III-8 : 4CzIPN 3D structure

The main achievement of this work was the use of TADF (already observed in the 1920's by Perrin and Boudin for Eosin, better understood in 1961 and coined E-type fluorescence)<sup>19,20</sup> to take advantage of the normally non-emissive organic molecule triplet state in luminescent devices.<sup>21</sup>

This molecule displays an unconventional singlet-triplet gap ( $\Delta E_{ST} < 0.1$  eV) for an organic molecule (usually 0.5-1 eV). This small gap between the lowest singlet and triplet states makes intersystemcrossing (ISC) and reverse intersystem crossing (RISC) more likely to occur. The long-lived triplet state becomes a resting state for electrons by ISC that become emissive after RISC to the singlet state. Furthermore, the quantum yield increases as non-radiative pathways decrease.<sup>22</sup>

4CzIPN and its derivatives were introduced four years later in synthetic organic chemistry by Zhang and Luo.<sup>23</sup> They showed the applicability of D-A cyanoarenes in photoredox catalysis through photoredox/Ni dual catalysis cross coupling reactions. These were according to the author the first examples of photoredox/Ni dual catalytic C(sp<sup>3</sup>)-C(sp<sup>2</sup>) cross coupling reactions using a fully organic photocatalyst. The avenue for photocatalysis applications was opened.

This short introduction reminds that the complexity occurring at the electronic level (structures, energies, radiative and non-radiative processes), which dictates the reactivity, can be easily grasped by simple analysis such as absorbance and fluorescence. A proper understanding of these mechanisms can lead to a fine control of the reactivity.

This chapter being written from a mixed synthetic and physical organic chemistry point of view, an overview of donor-acceptor cyanoarenes will first cover two other fields of study and application to widen the view of the “big picture”: materials science and biomedicine.

Then, donor-acceptor cyanoarenes properties will be discussed along with several photochemistry selected examples.

The focus will be on donor-acceptor cyanoarenes deriving from (and including) 4CzIPN in the past 10 years.

Finally, the results obtained in this work through electrochemical and photophysical studies of D-A cyanoarenes radical anions will be presented and discussed.

### 1.1. Cyanoarenes in materials science

Advised review on the history of OLEDs:

✓ Adv. Mater. **2021**, 33, 2005630

In the field of materials science, the research on organic light-emitting diodes (OLEDs) is very active in both academia and industry. They find two main applications in lighting and display devices as they outperform previous and current technologies, such a liquid crystal display (LCDs). OLEDs display allow lighter and thinner devices, as well as improved resolution,

viewing angle, contrast colors, response time, and the possibility to be transparent and bent.<sup>24</sup> Obviously, since such devices are not commonly found in our daily life yet, obstacles are faced and prevent widespread applications. This is where research comes in play, and we will look at it through the prism of donor-acceptor cyanoarenes.

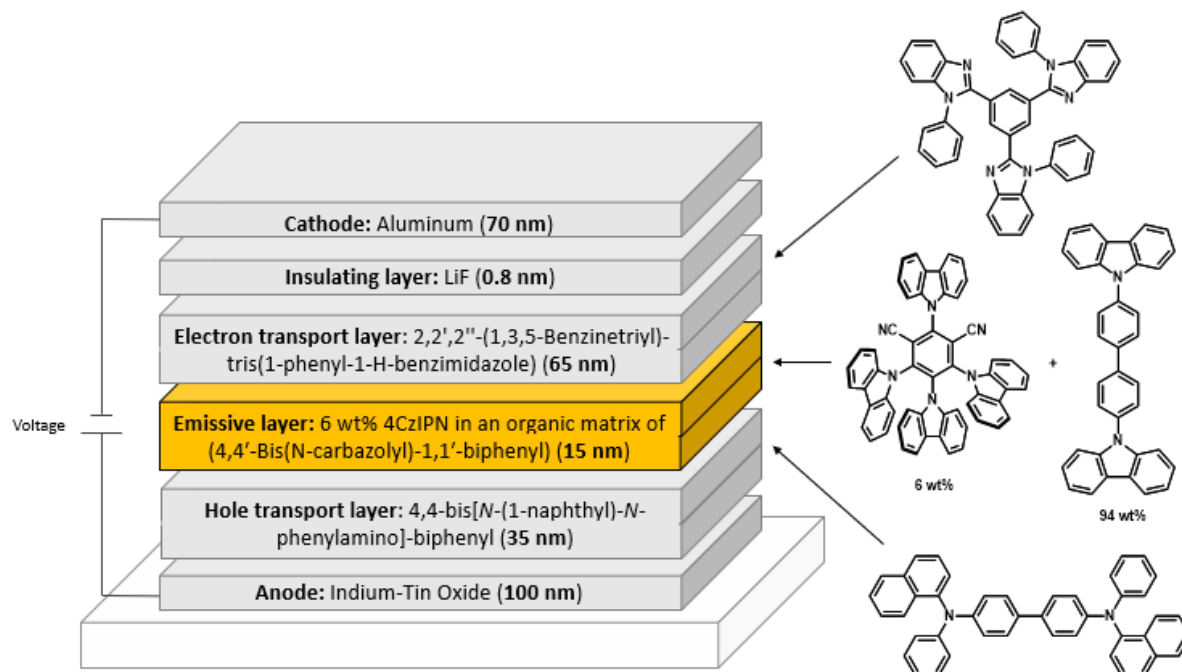


Figure III-9 : Layers structure of an OLED (example taken from ref<sup>21</sup>)

An OLED allows the emission of light thanks to an emissive layer sandwiched between a cathode and an anode, along with electron and hole transport layers. Holes are generated at the anode by draining electrons to the cathode where they are injected. Then, appropriate layers transport both holes and electrons at the center of the device where positive and negative charges recombine in the emissive layer. Hole transport layers include electron rich molecules while electron transport layers include electron deficient molecules. The emissive layer is made of a host matrix doped with the emissive molecule (examples given in Figure III-9).

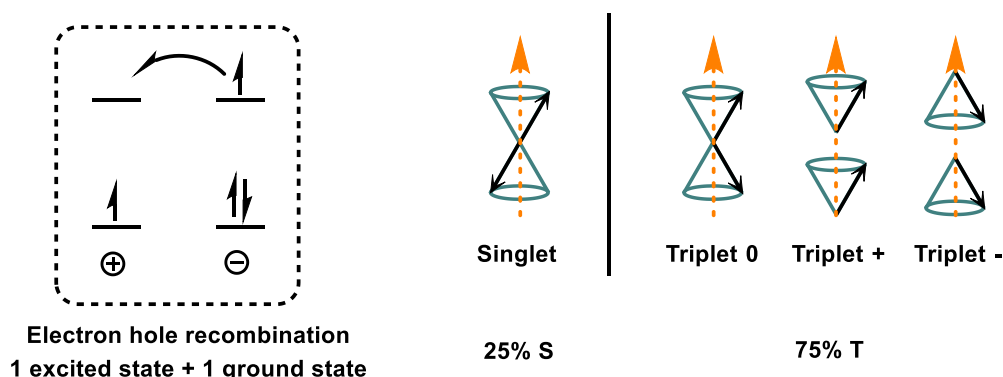


Figure III-10: Spin statistics and singlet triplet distribution



The recombination of doublet radical cation and doublet radical anion generates emissive excitons in 1:3 singlet to triplet ratio.<sup>25</sup> This ratio is explained by spin statistics (Figure III-10).<sup>26</sup>

This ratio differs in photocatalysis where the singlet state only is formed in the first step by photon absorption, which then may evolve to the triplet state by ISC.

Achieving high quantum efficiency is a main concern for OLED devices because of it takes part in dictating its viability. Other priorities regard color purity and device lifetime. Two quantum efficiency parameters exist: the internal quantum efficiency (IQE) and the external quantum efficiency (EQE).

IQE corresponds to the fraction of injected charge carriers (electron-hole pairs) converted into photons. Depending on the emissive mechanism, the IQE has two different theoretical upper limits: 25 if singlet states only are emissive, or 100% if both singlet and triplet states are emissive.

An experimental IQE of 100% cannot be directly related to the final efficiency of the device, because only about 20% of the photons generated inside the cell reach its outside in current devices, while 80% are trapped by internal reflection.<sup>19</sup>

In publications, most researchers give the EQE which corresponds to the fraction of injected charge carriers (electron-hole pairs) converted into photons reaching the outside of the cell.

The light extraction efficiency from the device is the ratio of the two (IQE/EQE), which is equal to the number of the photons emitted outside the cell divided by the total number of photons generated inside the cell. Intensive research is ongoing to improve this extraction efficiency.

The history of OLEDs, nicely overviewed by Bräse, can be divided into three devices generations, each one divided in three sub-categories following primary colors: red, green and blue emissions.<sup>24</sup>

Figure III-11 provides selected examples of OLEDs emitters, including an example for each generation and each color. For simplicity, the selected examples provide one example per color per generation, and examples evolve chronologically from first generation to fourth generation (in orange).

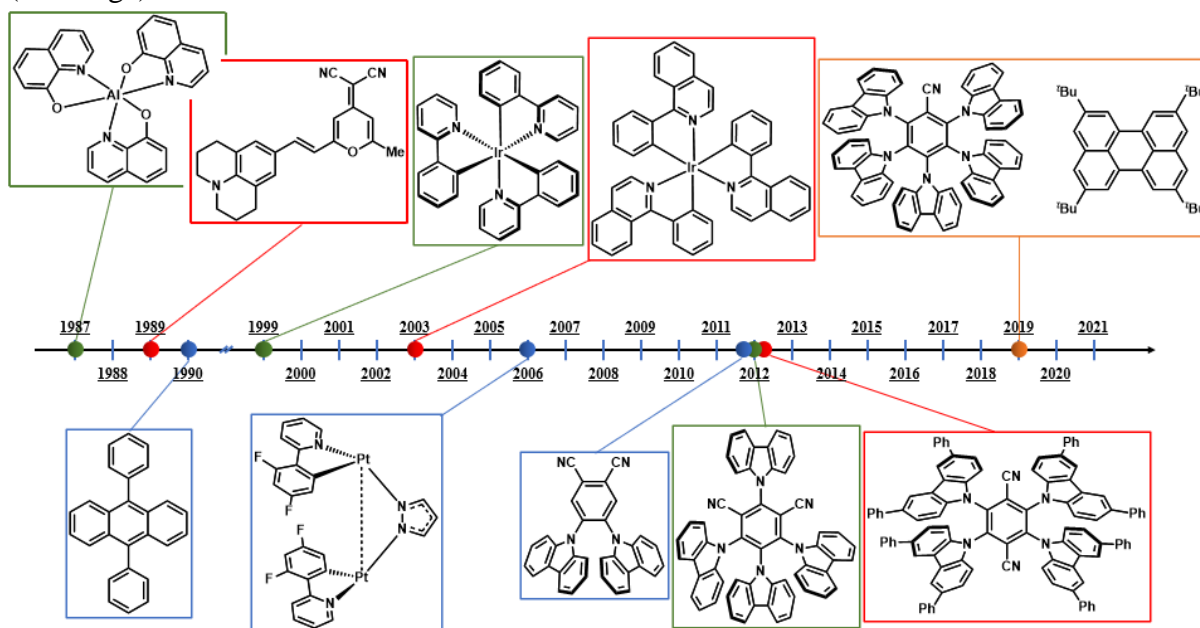


Figure III-11: Four generations of OLEDs and introduction of D-A cyanoarenes as OLED TADF emitters in 2012

The first generation concerns fluorescent OLEDs. Organic dyes were mostly used. The IQE of these systems was intrinsically limited to 25% (*ca.* 5% EQE) because of the emissive mechanism involved behind fluorescence. As mentioned before, upon electron-hole recombination and following spin statistics, the excited states are generated in a 1:3 singlet to triplet ratio. Since fluorescence occurs when there is a transition between singlets states, the maximum internal quantum efficiency was the one of singlet population. Three emitting molecules examples for green, red, and blue first-generation OLEDs are given in Figure III-11 from 1987, 1989 and 1990 respectively.

The IQE 25% upper limit issue was overcome in the second generation of OLEDs by harvesting the remaining 75% excitons through phosphorescence. The use of organometallic complexes containing heavy-metals such as platinum or iridium accelerated inter-system crossing and radiative emission from triplet states through enhanced spin-orbit coupling (SOC). Experimental IQE of 100% were reached, a crucial step to achieve high EQE's! However, the large-scale development of second-generation OLEDs was impaired by the scarcity and toxicity of heavy metals. The development of emitters that had a lower environmental and economic cost attracted attention. In 2010, a collaboration between industry and academia published their work using a specific copper complex as the emitter in an OLED device, a gigantic leap in the

field, for two main reasons. The first one is the use of copper instead of iridium or platinum. It is a much more available metal, improving by several folds the previously mentioned issues. The second reason is that it didn't use phosphorescence as the emissive mechanism, but instead found the very first application of "E(osin)-type fluorescence" (also known as TADF) to make the triplet excitons emissive via RISC followed by fluorescence.<sup>27</sup>

A year later, in 2011, an avenue was opened by Adachi and coworkers with the use of the same mechanism, which allows a theoretical 100% IQE, using purely organic emitters.<sup>27</sup>

The third generation of OLEDs was born.<sup>28</sup> The most resonating paper from Adachi and coworkers, published in 2012, used D-A cyanoarenes in the emitting layer and allowed a wide variety of emissive colors with structural modifications of the same family of molecules.<sup>21</sup>

This third generation has several drawbacks, including color purity. The small  $\Delta E_{ST}$  in DA-TADF molecules is directly related to the CT nature of the emissive state. This charge transfer, which implies the movement of an electron through the system on the scale of several bonds in two spatially separated parts of the molecule, is considered to broaden of the fluorescence signal.<sup>29</sup> The color purity of 3<sup>rd</sup> generation OLEDs is therefore not optimal.

In 2019, "the ultimate solution for OLEDs display" was claimed to have been found according to their developers. They coined it "hyperfluorescence<sup>TM</sup>" and the mechanism involved is different enough from the 3<sup>rd</sup> generation to start a 4<sup>th</sup> generation of OLEDs.

"Hyperfluorescence" (Figure III-12), also named "TADF-assisted fluorescence" (TAF), makes use of the long-lived triplet state of TADF molecules as a transient reservoir from which electrons, after RISC to  $S_1$ , are transferred to another emissive molecule by Förster resonance energy transfer (FRET). That other molecule possesses a LE emissive state which drastically improves color purity. This is made possible by the fact that kinetics of energy transfer are higher than that of fluorescence from the dopant. In this generation D-A cyanoarenes also display their high efficiency as assistant dopant.

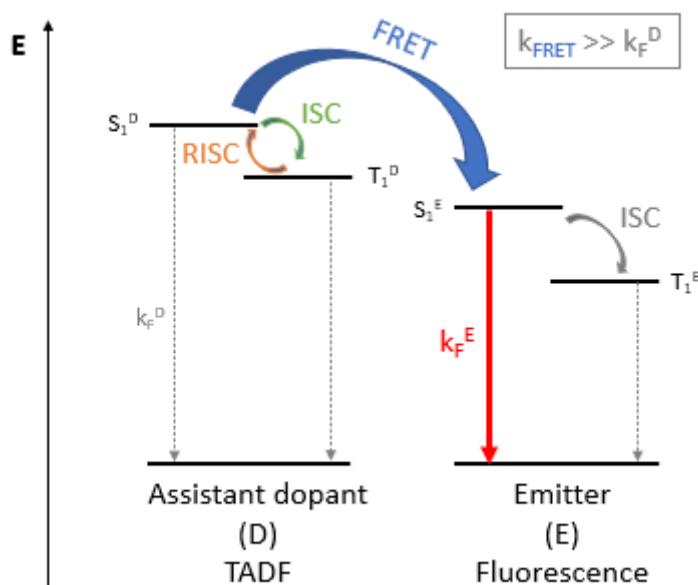


Figure III-12 : OLED emission mechanism by FRET from a TADF dopant to a fluorescent molecule

A new mechanism has also been discovered in 2016, coined MR-TADF (multi resonance). It replaces the long-range donor-acceptor charge transfer state by a short-range multi-resonance charge transfer state, improving  $\Delta E_{ST}$  and color purity (FWHM), while remaining a purely organic based TADF mechanism. In a way, it has all the advantages of a LE and (T)ICT combined. This field remains to be explored and does not concern donor-acceptor cyanoarenes.

Table III-1 summarizes the different pros and cons of each generation of OLED.

Table III-1: Pros and cons of different OLED generations

Generation	Emissive mechanism	Cost	Efficiency	Color purity
1 <sup>st</sup>	Fluorescence	Low	Low	High
2 <sup>nd</sup>	Phosphorescence	High	High	Low
3 <sup>rd</sup>	TADF	Low	High	Low
4 <sup>th</sup>	“Hyperfluorescence <sup>TM</sup> ” Fluorescence from TADF EnT	Low	High	High
5 <sup>th</sup> (?)	MR-TADF	Low	High	High

Donor-acceptor cyanoarenes also find applications in solar cells as luminescent solar concentrators, an avenue to include them in photovoltaic cells and harvest solar energy.<sup>30</sup>

Finally, we wish to mention the importance of the device lifetime to achieve commercialization. Many studies have been carried out on the degradation mechanisms. Despite the TADF molecule chemical degradation seemingly not being the main obstacle, we wish to highlight that the overall need to better understand radical cations and anions behavior also applies in the case of OLEDs.<sup>31,32</sup>

## 1.2. Biomedical applications

Advised review on the medical applications of TADF materials:

✓ Adv. Sci. **2021**, 8, 2102970

We have shown that TADF molecules can be considered as widely studied and applied in OLEDs. However, their use is only emerging in the medical research field, as expressed by Lee and coworkers in 2019 where they envisioned photodynamic therapy is a target of choice for these systems.<sup>33–36</sup> They can find applicability in tumor local treatment through non-invasive techniques. Visible to near-IR irradiation can activate TADF molecules who then eventually engage in triplet-triplet energy transfer with molecular oxygen to lead to the cytotoxic singlet oxygen (Figure III-13).

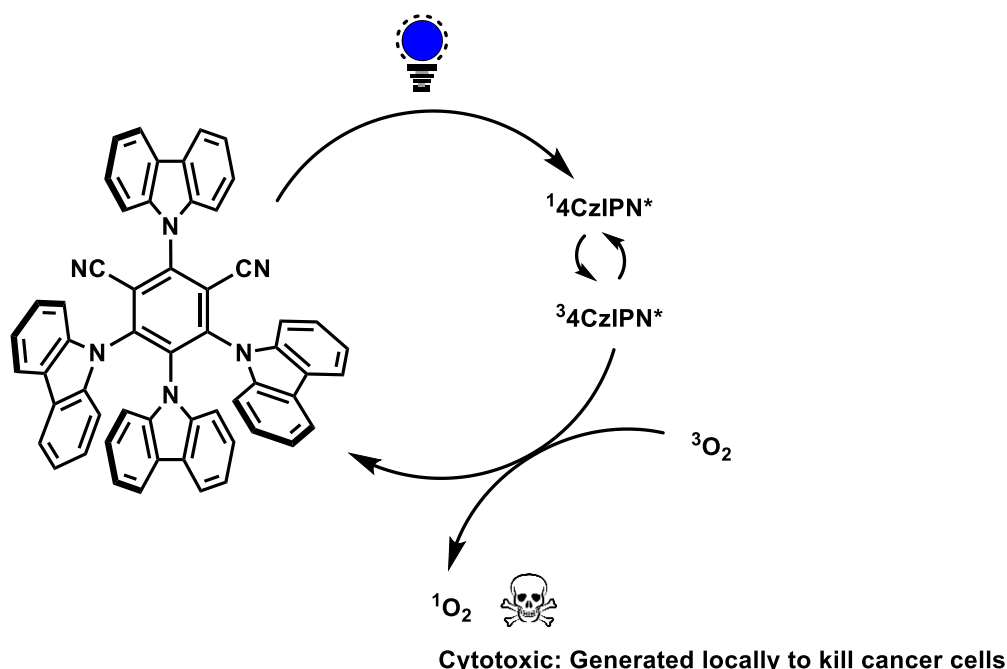


Figure III-13 : Production of cytotoxic singlet oxygen by energy transfer

Amongst the challenges faced is the poor water solubility of the commonly hydrophobic TADF molecules resulting in low bioavailability. Nanoparticles (NPs) were successfully synthesized

and proved to overcome this limitation. It can also be used as a surface treatment for skin cancer.

Visible light has a low cell penetration power, which is not the case for IR radiation. Therefore, it is common for PDT to use a “two-photons process” using two near-IR photons to induce double excitation to  $S_1$  with suitable molecules.

Bio-imaging with such species thanks to time-resolved luminescence imaging (TRLI) is also an emerging field and finds promising application.<sup>35,37,38</sup>

## 2. Donor-Acceptor Cyanoarenes General Properties: A First Approach

### 2.1. Structure, Geometry and Orbitals

The family of D-A cyanoarenes studied in this manuscript has a specific nomenclature which requires explanations. The naming method for these donor-acceptor cyanoarenes is as follows.

The suffix regards the aromatic core and is abbreviated at the end (Figure III-14) : BN for benzonitrile, PN for phthalonitrile (1,2-dicyanobenzene), INP for isophthalonitrile (1,3-dicyanobenzene), TPN for terephthalonitrile (1,4-dicyanobenzene).

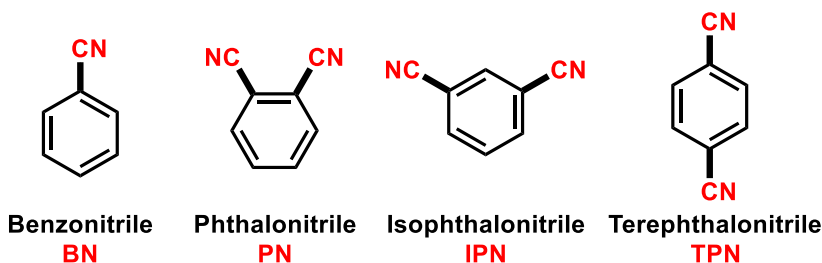


Figure III-14: Cyanoarenes cores names

The prefix indicates the substituents on the aromatic ring. A number is used to tell how many sites are substituted by the corresponding substituent, for instance 4Cz means four carbazoles substitute the aromatic core (Figure III-15). 3DPA2F means that 3 diphenylamino substituents and 2 fluoro substituents are present on the aromatic core. Note that in this last example 5 of the 6 benzenic ring positions are occupied, leaving only one position for the cyano: benzonitrile (BN) will be the accepting core providing 3DPA2FBN. The position of the substituents is not indicated, and one should look at the structure to have this information. 3CzEPAIPN stands for 3 carbazoles and one ethylphenylamine substituting an isophthalonitrile core.

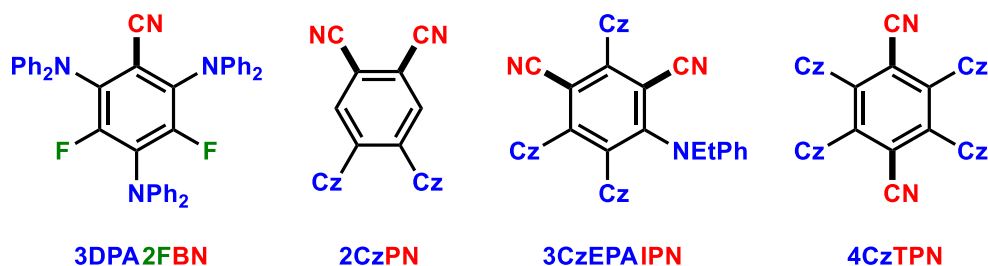


Figure III-15: Donor-acceptor cyanoarenes nomenclature examples

When the substituents themselves are substituted, this information may be added in two fashions. These substituents, on carbazoles, are usually on the symmetric 3,6 positions, providing for instance 3MeOCzEPAIPN, a variation of 3CzEPAIPN according to the first fashion (Figure III-16). The other fashion would be 3CzEPAIPN-MeO and is less common.

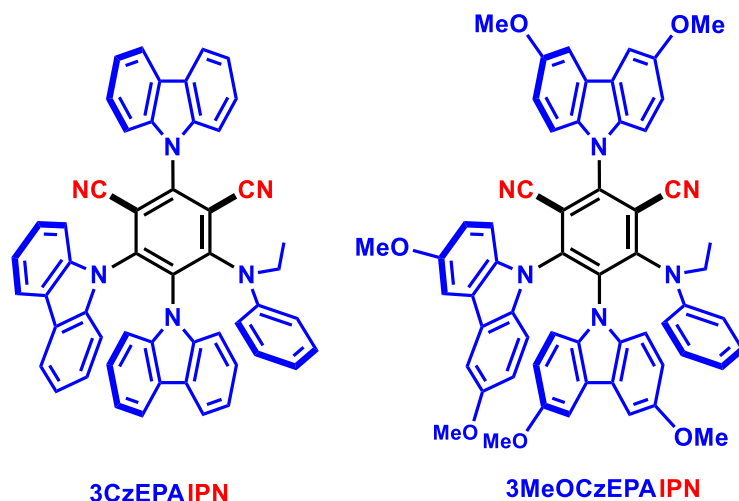


Figure III-16: 3CzEPAIPN and its methoxy substituted equivalent

Donor-acceptor cyanoarenes have specific ground state “twisted” geometries. The substituents are not co-planar with the core (di)cyanobenzene aromatic ring. They display a twisted dihedral angle of about  $60^\circ$ . This value shifts from *ca.*  $45^\circ$  up to  $70^\circ$ . It may be observed in 3CzEPAIPN DFT calculated geometry (Figure III-17).

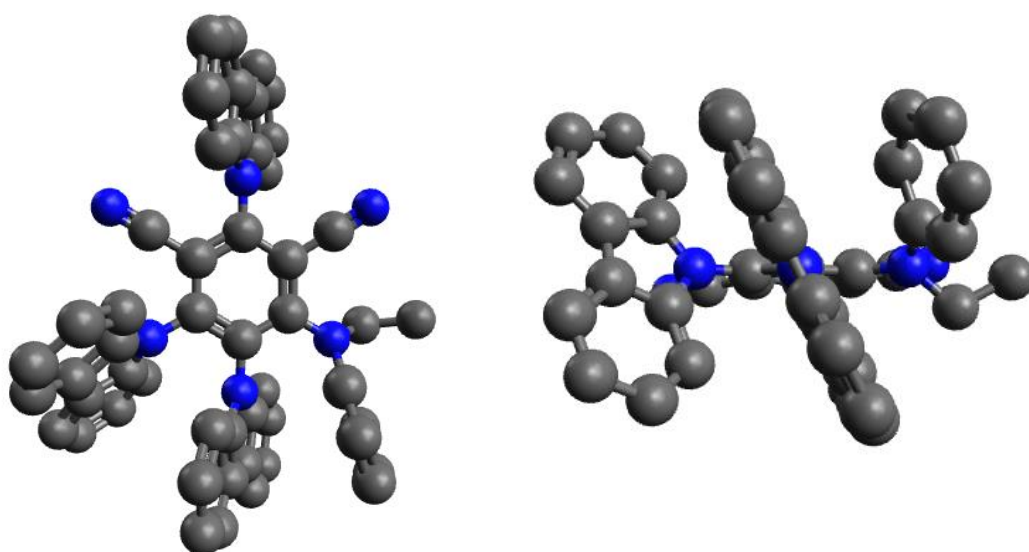


Figure III-17: 3CzEPAIPN 3D calculated structure with two different view angles, showing the ground state twist of amino substituents to the isophthalonitrile core

A similarly twisted dihedral angle ( $50.4^\circ$ ) is observed in 4-carbazolyl-benzonitrile (Figure III-18).

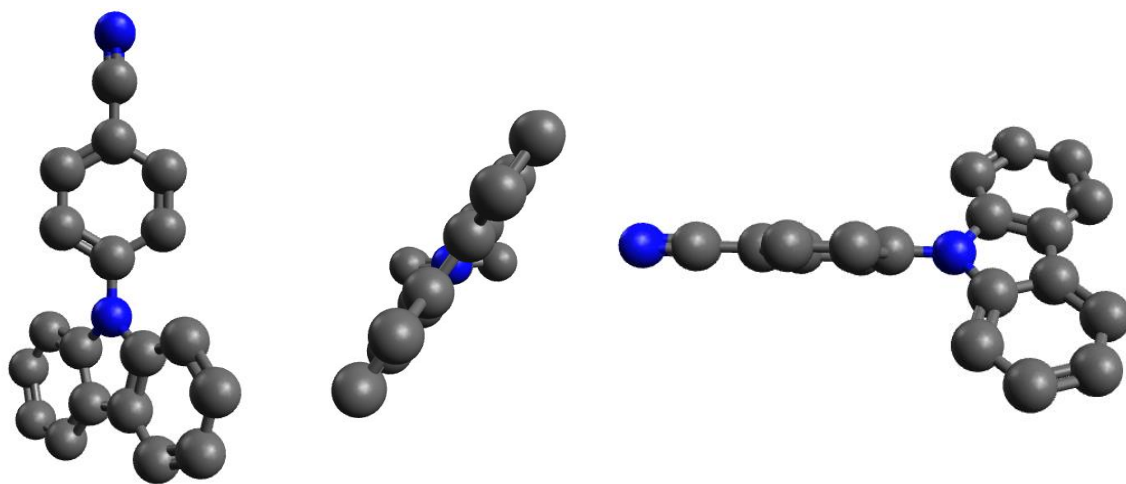


Figure III-18: 4-carbazolylbenzonitrile 3D structure with three different view angles, showing the ground state twist



This enhanced orthogonality is the reason behind the HOMO and LUMO good spatial separation (Figure III-19).

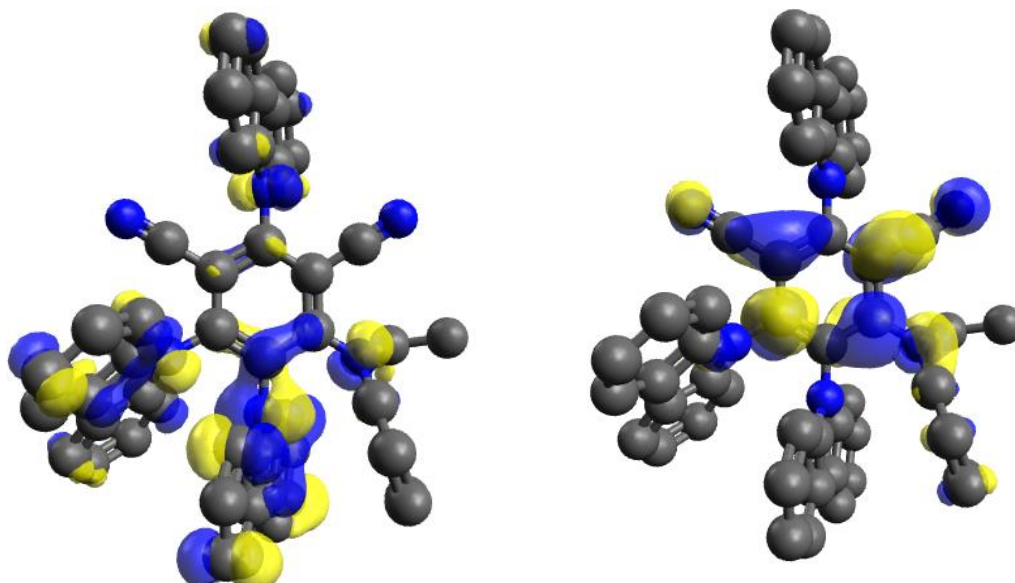


Figure III-19: Spatially separated HOMO (left) and LUMO (right) of 3CzEPAIPN

Because of that separation and the inability for heavy structural reorganization, both lowest singlet and triplet states (which are of charge transfer nature) are extremely close in energy.

The great advantage that comes along with the frontier molecular orbitals (FMOs) separation is that the substituents can be modified to tune the properties. Fine tuning of the HOMO on one side without impacting the LUMO can be done easily through a “toolbox approach” by changing the acceptor moieties alone. The LUMO can be modified by changing the accepting core, usually benzonitrile or dicyanobenzene with various substitution patterns, without touching the HOMO. This approach is extremely similar to organometallic complexes modifications through ligand and metal modifications and is applied to fully organic molecules.

Zeitler and coworkers did a wonderful work by displaying this “toolbox approach” following the work by Adachi and coworkers.<sup>21,39</sup> Two main modification patterns were highlighted on isophthalonitriles and cyanobenzenes, namely the halogen and the donor effect (Figure III-20). Switching a given donor moiety (*e.g.* a carbazole) for a more donating one (*e.g.* a diphenylamine) lowers the value of  $E(PC^{\bullet+}/PC)$ . Indeed, it is easier to take an electron to the ground state specie if the subsequent radical cation is more stabilized by groups with good electron donating ability. Tuning  $E(PC/PC^{\bullet-})$  however proved more difficult. The halogen effect is more difficult to rationalize since important variations are observed depending on the nature of the halogen. Fluorine displayed a peculiar effect allowing to reach  $E(PC/PC^{\bullet-})$  as low as -1.92 V vs SCE in MeCN for 3DPA2FBN.

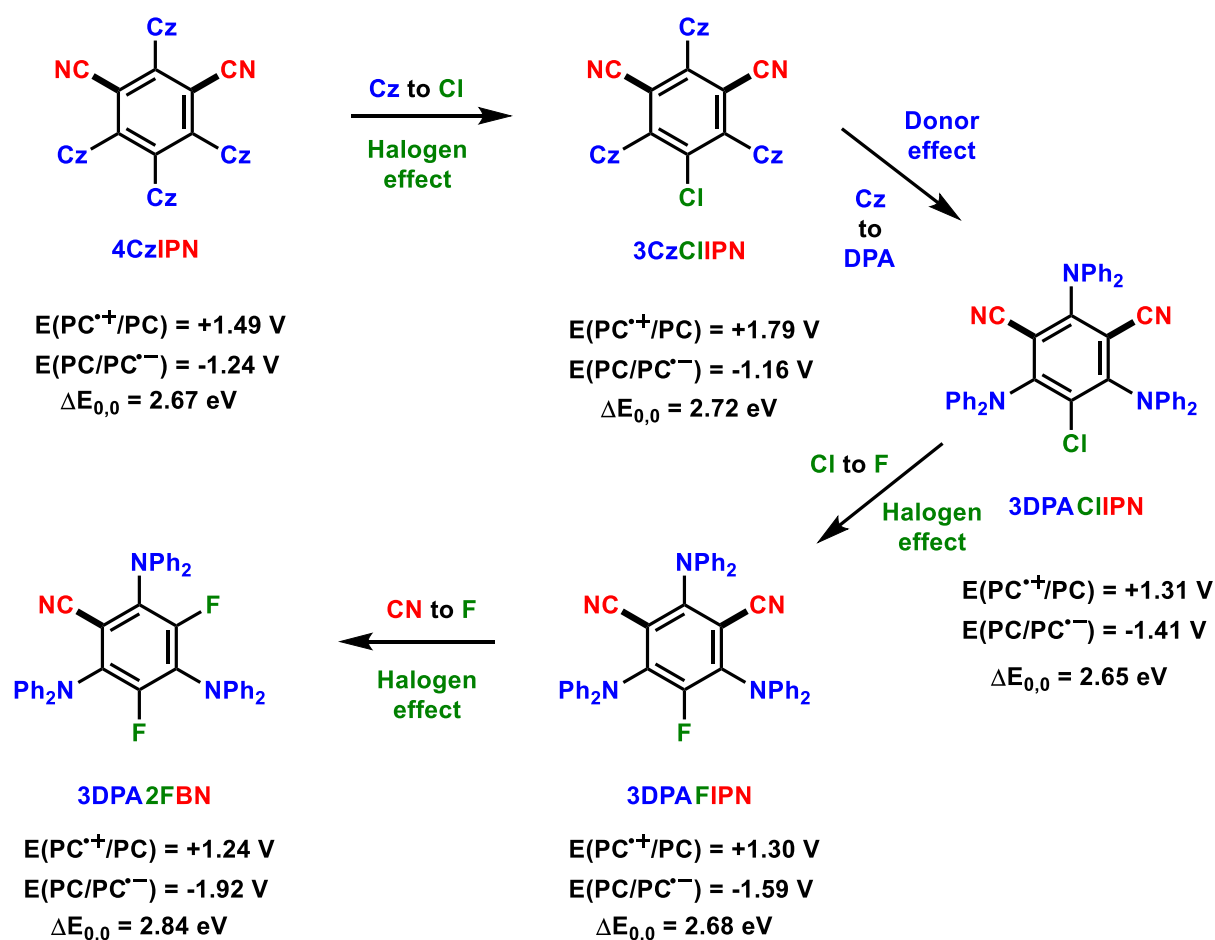


Figure III-20: Halogen and donor effect on the redox potentials of D-A cyanoarenes. 3DPA2FBN properties were measured in  $CH_2Cl_2$

The modifications impact of the structure on the properties is made visually obvious thanks to the following picture which displays luminescence according to structure variations (Figure III-21).<sup>21</sup>

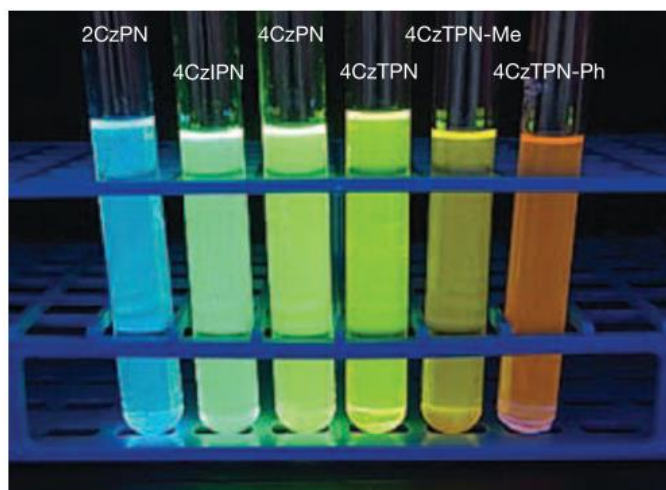


Figure III-21: Luminescence of different versions of D-A cyanoarenes from blue to red, covering the full visible light spectrum. Reproduced with permission from reference 21 (Copyright 2020 MacMillan Publishers Limited).

## 2.2. Excited states multiplicity and lifetimes

The link between TADF and the success of D-A cyanoarenes as photocatalysts is not quite straightforward. In electron or energy transfer mechanisms, the delayed fluorescence is not a productive pathway since the molecule releases its energy through emission. If fluorescence, delayed or not, or phosphorescence occurs, then the full photophysical process happened without interaction and the photochemical reaction was missed.

Still, TADF comes along with a set of properties that match the needs for photochemical reactions success. The spatially well-separated HOMO and LUMO allow for a small  $\Delta E_{ST}$ . Both singlet and triplet states are of charge transfer nature. It was shown that by having multiple bulky amino substituents on the aromatic core the nature of the lowest triplet state shifted from LE to CT.<sup>40</sup> The gap between  $^3LE$  and  $^3CT$  is of great importance because a small gap between the two allows for faster reversed intersystem crossing.<sup>41</sup> Depending on the chemistry that is meant to follow, it might be desirable or not, but always worth to consider as a tunable parameter with important impact on properties.<sup>42</sup>

Compared to fluorescence where only the singlet state can be active, and phosphorescence where only the triplet state can be active, both singlet and triplet states can be chemically active in TADF D-A cyanoarenes. This obviously opens the way for a diversity of reactivities. Furthermore, a small  $\Delta E_{ST}$  also means a small energy loss in the ISC process, and a highly energetic triplet state.

The reactivity between these excited states and substrates requires them to meet “physically”, with a minimum distance that varies with the mechanism involved. Pre-association of the photocatalyst and the substrate allows the reactivity with short-lived excited states. For the rest

of the reactions, they are at least limited by diffusion control. An excited state lifetime in the order of few nanoseconds to tens of nanoseconds is necessary for the encounter to be considered reasonable (with a 0.1 M substrate concentration).

TADF D-A cyanoarenes exhibit prompt fluorescence in this range of 1-50 ns, but most notably the delayed thermally activated effect allows for delayed fluorescence lifetimes  $> 1 \mu\text{s}$ .

The ISC kinetic rate and the ratio of  $k_{\text{ISC}}/k_{\text{RISC}}$  is highly solvent dependent for 4CzIPN. In MeCN,  $k_{\text{ISC}}$  is equal to  $2.2 \times 10^6 \text{ s}^{-1}$ . This value is in accordance with the ones for such compounds which are generally  $< 10^7 \text{ s}^{-1}$ . However, in MeCN, the ISC quantum yield is 0.04 against 0.73 in toluene. The difference is enormous and means that in MeCN, 4CzIPN reacts almost uniquely from its singlet state while in toluene it may react from both singlet and triplet states.<sup>43</sup>

Both singlet and triplet states engaged in SET and energy transfer events display different behaviors. Notably, back electron transfer is less likely to occur in triplet state electron transfer because of the forbidden necessary spin flip (Figure III-22), making the cage escape more favorable than from the singlet contact radical ion pair (SCRIP).

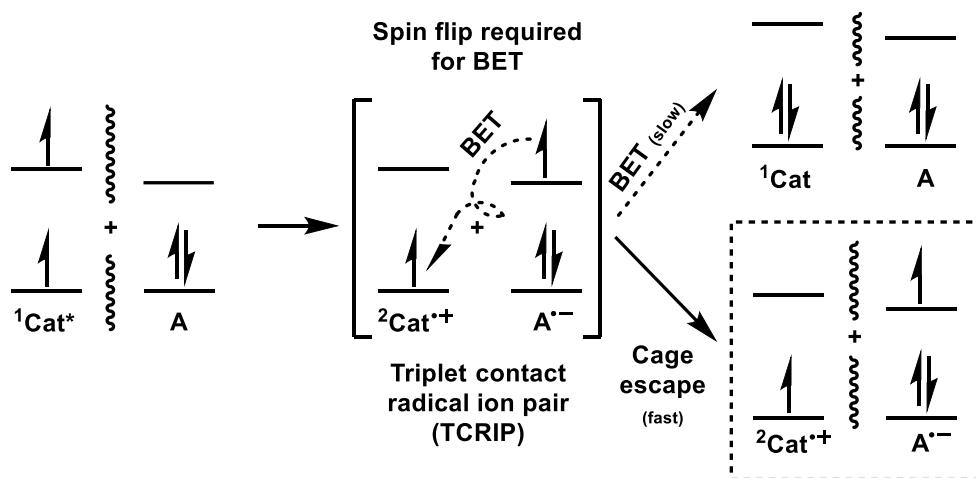


Figure III-22: Electron transfer mechanism from a triplet state to an electron acceptor A

Other parameters whose combination is extremely difficult to apprehend also have an impact on the photophysical behavior, properties, and on the reaction mechanism itself. These parameters include concentration, dimer formation and exciplexes. Several studies address these topics.<sup>44-46</sup>

Solvation important role on the photocatalyst geometry also impacts the stability of the excited states. Solvatochromism was investigated and showed that more polar solvents improve the stability of the  $S_1$  state, decrease the singlet-triplet energy gap -RISC and TADF are then

*avored*, and increase non-radiative deactivation processes -*which leads to a reduction of the quantum yield*.

Finally, one mustn't forget that important non-radiative decays are intrinsically limited in D-A acceptor cyanoarenes because of the steric hindrance which grows with the number of bulky amino substituents.

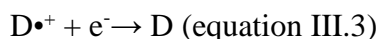
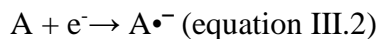
### 2.3. Redox Potentials

The most discussed properties in photoredox catalysis are redox potentials. They have shown great utility in estimating whether an electron transfer between two molecules is thermodynamically favorable or not. If they match, the reaction is likely to proceed. If not, the occurrence of a reaction can most likely be ruled out. Such "red or green light" tool is appreciable for a daily use.

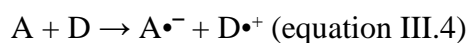
Potentials are said to match when the potential of the donor is inferior to the potential of the acceptor, resulting in a positive driving force. The larger the difference the bigger the electron transfer driving force.

$$E(A/A^{\bullet-}) - E(D^{\bullet+}/D) > 0 \text{ (equation III.1)}$$

The donor (D) refers to the molecule that can provide an electron and the acceptor (A) refers to the molecule that can receive that electron. Each potential relates to its half reaction:



Their combination provides the electron transfer reaction:



The group of donor-acceptor cyanoarenes studied by Zeitler and coworkers in 2018 displays a wide range of ground state redox potentials: from -1.16 to -1.92 V vs SCE for  $E(A/A^{\bullet-})$  and from +1.02 to +1.79 V vs SCE for  $E(D^{\bullet+}/D)$  (Figure III-23).<sup>39</sup>

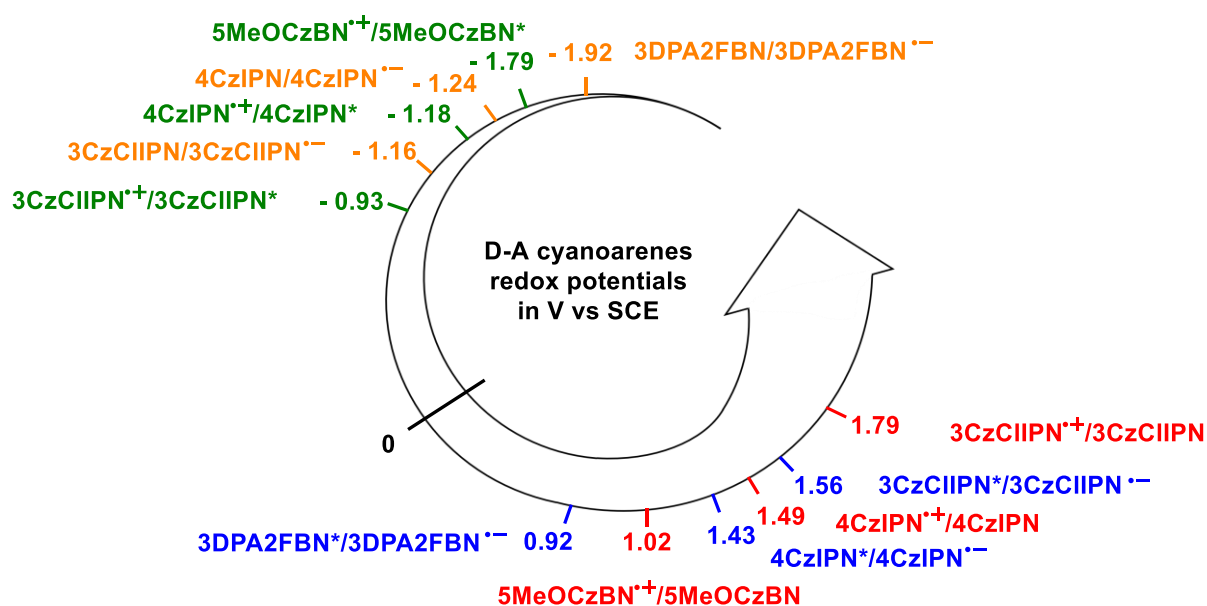


Figure III-23: Range of redox potentials of selected examples of D-A cyanoarenes

Most notably, their excited state potentials reach high values for organic molecules. In the same study,  $E(A^*/A^{\bullet-})$  goes from +0.92 to +1.56 V vs SCE and  $E(D^{\bullet+}/D^*)$  from -0.93 to -1.79 V vs SCE.

Table III-2 compares the redox potentials of the benchmark iridium photocatalyst  $\text{Ir(ppy)}_3$  and the “leading donor-acceptor cyanoarene photocatalyst” 4CzIPN from which the versatility is clearly highlighted. This versatility is directly linked with the rigid donor-acceptor structure.

For a more complete table, see 2.4.

Table III-2: Redox properties comparison between  $\text{Ir(ppy)}_3$  and 4CzIPN

Name	$\lambda_{\text{max}}$	$E_{0,0}$ (eV)	$E_{\text{red}}$ $E_{A^*/A^{\bullet-}}$ (V vs SCE)	$E_{\text{ox}}$ $E_{D^{\bullet+}/D}$ (V vs SCE)	$E_{\text{red}}^*$ $E_{A^*/A^{\bullet-}}$ (V vs SCE)	$E_{\text{ox}}^*$ $E_{D^{\bullet+}/D^*}$ (V vs SCE)
$\text{Ir(ppy)}_3$	375	2.75	-2.19	0.77	0.31	-1.73
4CzIPN	435	2.67	-1.21	+1.52	+1.46	-1.15

All values given in MeCN at room temperature

Redox potentials are key parameters to estimate the feasibility of an electron transfer. They can be measured experimentally by performing cyclic voltammetry with a potentiostat. A potential

is given in volts (V) against a reference. The reference may vary, but two potentials must only be compared when expressed against the same reference electrode. Converting a given potential to another reference electrode is done by adding or subtracting the potential difference between the two references. Table III-3 gives the correspondence between common electrodes and saturated calomel electrode (SCE) or normal hydrogen electrode (NHE).<sup>47,48</sup> The standard reduction potential of the ferrocenium/ferrocene couple is also given in the last column.

Table III-3: Conversion values between different reference electrodes

All values in MeCN	Conversion to SCE	Conversion to NHE	Conversion to 10 mM Ag/AgNO <sub>3</sub>	Approximate potential of Fc <sup>+</sup> /Fc for the given electrode (in V, +/-0.100 V)
SCE	0	+0.244	-0.300	+0.400
NHE	-0.244	0	drift	+0.644
Ag/AgCl Satd KCl	-0.045	+0.199	-0.345	+0.445
Ag/AgCl 3 M KCl	-0.022	+0.222	-0.322	+0.422
Ag/AgCl 0.1 M KCl	+0.044	+0.288	-0.256	+0.356
0.1 M Ag/AgNO <sub>3</sub>	+0.352	drift	+0.052	+0.048
10 mM Ag/AgNO <sub>3</sub>	+0.300	drift	0	+0.100

To illustrate this table, let's take the oxidation potential of triethylamine  $E(\text{Et}_3\text{N}^{\bullet+}/\text{Et}_3\text{N}) = 0.83$  V vs SCE. Versus NHE, the potential is  $0.83 + 0.244 = 1.074$  V. Versus 10 mM Ag/AgNO<sub>3</sub>, the potential is  $0.83 - 0.300 = 0.53$  V.

The Ag/AgNO<sub>3</sub> is a non-aqueous reference electrode and proves handy when it comes to dry and inert atmospheres such as in gloveboxes.

Ferrocene is commonly added after a measurement as an internal reference. Its potential (Fc<sup>+</sup>/Fc) against SCE can be approximated to 0.400 V +/-0.100 V in MeCN. It is a convenient

system because of the excellent reversibility of ferrocene oxidation ( $\Delta E_p = 59$  mV). Care must be taken with the trust given to operated conversions, since even (Fc<sup>+</sup>/Fc) potential varies depending on the measurement conditions.<sup>49</sup> This value of 0.400 V in MeCN is only given as an approximation and not as a fixed universal value (varies between 0.307 and 0.480 in ref<sup>49</sup>, approximated to 0.400 +/- 0.100 V here). Any measured potential including another measurement with a ferrocene reference may then be directly estimated against SCE as:

$$E_{vsSCE} = E_{measured} - E_{(Fc+/Fc)measured} + 0.400 \text{ (equation III.5)}$$

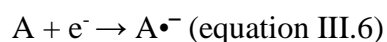
Temperature directly impacts the potential value. As a rule of thumb, one can consider that the potential measured evolves between -1 and + 1 mV/ °C. Potentials values are given at 25 °C. If a measurement is done at 15 °C, one should expect a maximum 10 mV drift using the same reference electrode and up to 20 mV drift when converting between two reference electrodes. This small value is usually neglected for good reasons but remains worth having in mind.

There is an important ground of confusion in the handling of redox potentials.  $E_{red}$  and  $E_{ox}$ , representing the electrode potentials of a molecule redox couple that is effectively reduced or oxidized in the electron transfer event, respectively, are highly misleading and might be to blame. This use is most likely an implicit convention for organic chemists convention.

One frequently asked question is: What is  $E_{red}$ ? Is  $E_{red}$  the potential giving information about the molecule's ability to reduce another molecule or the ability to be reduced?

From this question arises a clear misunderstanding of the meaning and usage of potentials.

$E_{red}$  refers to the electrode reduction potential of the half reaction (not to be confused with chemical potential, electrochemical potential, or electrical potential), where A is considered an electron acceptor:



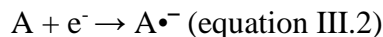
The potential should be noted  $E(A/A^{\bullet-})$  to avoid any confusion.  $E^0(A/A^{\bullet-})$  refers to standard conditions, including standard temperature (298,15 K | 25 °C), pressure (1 bar), and concentration (1 M, considered in ideal systems). These conditions are usually not respected. Out of rigor, we decided to refer to the vague  $E(A/A^{\bullet-})$ . Precisions are given when known and interesting, such as  $E^{1/2}(A/A^{\bullet-})$  when the potential is obtained by the average of the anodic and cathodic potential maxima for reversible waves ( $E^{1/2} = \frac{E_{pa} + E_{pc}}{2}$ ), or as  $E^{p/2}(A/A^{\bullet-})$  when the potential is obtained from an irreversible wave at half the current intensity maxima value.

Its common appellation, "reduction potential of A", is not advised by IUPAC.

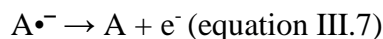


On one hand, the electrode potential is defined by half reactions and concerns only one redox couple.

As stated before, the reduction potential of a given couple (*e.g.* A/A<sup>•-</sup>) provides a value for the half reaction:



The appellation “oxidation potential” of the same couple, E<sub>ox</sub>(A/A<sup>•-</sup>), refers to the half reaction:



This half reaction potential has an opposite sign compared to E<sub>red</sub>(A/A<sup>•-</sup>). This means that regarding the correct terminology:

$$E_{\text{ox}}(A^{\bullet-}/A) = -E_{\text{red}}(A/A^{\bullet-}) \text{ (equation III.8)}$$

The scientific formalism settled on using the reduction potential for potential measurements. All potentials referred to in photoredox catalysis are therefore reduction potentials.

The usual scale on CVs, going roughly from -3 V to +3 V, is then based on reduction potentials as defined in the previous discussion.

On the other hand, there is the chemical reaction.

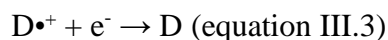
In the reaction considered (*e.g.* single electron transfer between two molecules), a molecule is reduced and another one is oxidized following the reaction equation:



It is tempting to say, from the fact that A is actually reduced and D is actually oxidized, that we should be able to attribute a reduction potential to A and an oxidation potential to D. However, reduction and oxidation potential appellations already exist and depict the reduction or oxidation half reactions of redox couples, not isolated molecules, as stated before. Furthermore, because of the accepted formalism, the values measured and reported in the literature are all reduction potentials, regardless of whether the molecule is reduced or oxidized in the actual reaction conditions. The reasoning presented at the beginning of this paragraph is highly misleading, at best, and can be considered as the source of confusion.

The idea “E<sub>red</sub> refers to the ability of A to reduce a molecule” should simply be ruled out of the thinking process. We advise it should be replaced by “E(A/A<sup>•-</sup>) refers to the reduction potential of the half reaction from A to A<sup>•-</sup>”.

Similarly,  $E_{ox}$  should be replaced by “ $E(D^{\bullet+}/D)$  refers to the reduction potential of the half reaction from  $D^{\bullet+}$  to  $D$ ”.



Half reaction equations can be mathematically swapped by a minus sign. When combining  $E(D^{\bullet+}/D)$  and  $E(A/A^{\bullet-})$  in the same mathematical equation according to:

$$\Delta E_{A-D} = E(A/A^{\bullet-}) - E(D^{\bullet+}/D) \text{ (equation III.11)}$$

then the reaction equation becomes, as stated before:



We propose  $\Delta E_{A-D}$  to be formally called the cell voltage and written  $E_{cell}$ , which will be used in this manuscript.

The electron transfer is thermodynamically favorable if the Gibbs free energy  $\Delta G_{ET}$  is negative.

The general equation relating the standard Gibbs free energy for an electron transfer  $\Delta G_{ET}$  to the redox couple standard potential difference  $E_{cell}$  is:

$$\Delta G_{ET} = -n.F.E_{cell} \text{ (equation III.12)}$$

Where:

The components  $w$  and  $\Delta E_{0,0}$  from the full equation  $\Delta G_{PET} = -n.F.E_{cell} - w - \Delta E_{0,0}$  are omitted in the above expression.  $w$  is the electrostatic work term which depends on solvent-related energy difference. This difference comes from the electrostatic changes of charge separation. Its variation is highly system dependent and cannot be predicted accurately. It is only known to tend to have a high value in apolar solvents and a small value in polar solvents. Since its contribution is usually  $< 0.1$  eV, it is omitted as an acceptable approximation.  $\Delta E_{0,0}$  is also omitted for now, because it implies photoactivation, and for the moment we are only looking at ground state molecules for the sake of clarity.  $\Delta E_{0,0}$  will be added in the equation and discussed further in the discussion. Note that we are looking at  $\Delta G_{ET}$  which accounts for the electron transfer and not  $\Delta G_{PET}$  that accounts for the photoinduced electron transfer.

$n$  is the quantity of matter expressed in moles.

$F$  is Faraday's constant ( $96\,485 \text{ C.mol}^{-1} \mid 23.061 \text{ kcal.mol}^{-1}.\text{V}^{-1} \mid 1 \text{ eV}.\text{V}^{-1}$ ). It represents the amount of electricity that is carried by one mole of electron. In other words, it is equal to the charge of an electron multiplied by Avogadro's constant:  $F = e.N_A$ .

$\Delta G_{ET}$  is the standard Gibbs free energy difference of the electron transfer process expressed in eV.

$E_{cell}$  is the standard electrode potential difference between the acceptor and the donor redox couples, in this specific order. It is expressed in V:  $E_{cell} = E(A/A\bullet^-) - E(D\bullet^+/D)$ .

In a single electron transfer reaction, since only one electron is considered:  $n = \frac{1}{N_A}$ . Therefore, the term  $n.F$  becomes  $n.F = \frac{1}{N_A} . e . N_A = e$ , the charge carried by a single electron ( $\sim 1.602 \times 10^{-19}$  C). The Gibbs free energy can then be written:

$$\Delta G_{ET} = -e.E_{cell} \text{ (equation III.13)}$$

We stated before that the reaction is thermodynamically favorable if:

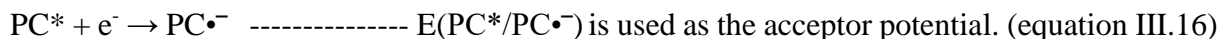
$$\Delta G_{ET} < 0 \text{ (equation III.14)}$$

$$E_{cell} = E(A/A\bullet^-) - E(D\bullet^+/D) > 0 \text{ (equation III.15)}$$

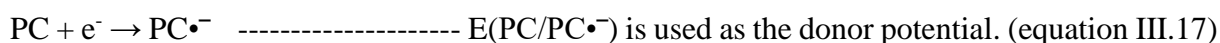
In other words, the reaction  $D + A \rightarrow D\bullet^+ + A\bullet^-$  is thermodynamically favorable if the potential of the redox couple of the electron acceptor is greater than the potential of the redox couple of the electron donor.

For the sake of clarity in the examples given previously, electron acceptor couples were written  $A/A\bullet^-$  and electron donor couples  $D\bullet^+/D$ . Any combination may in fact exist, and A and D should be replaced by the appropriate molecule in the appropriate state at the stage of the reaction. The oxidized version of the couple is always on the left side of the slash and the reduced version on the right side.

For instance, in a reductive quenching, after light absorption, the excited state of the photocatalyst acts as an electron acceptor:



In the subsequent step, the photocatalyst radical anion  $PC\bullet^-$  goes back to its ground state by acting as an electron donor to the substrate according to the reduction half reaction:



The values of  $E_{A/A\bullet^-}$  are generally negative because the reduction of a ground state neutral molecule is energetically unfavorable while the values of  $E_{D\bullet^+/D}$  are generally positive because the reduction of a radical cation is energetically favorable.

However, for a photoinduced electron transfer, the Gibbs free energy formula is modified to:

$$\Delta G_{\text{PET}} = -e \cdot E_{\text{cell}} - \Delta E_{0,0} \text{ (equation III.18)}$$

Where  $\Delta E_{0,0}$  corresponds to the energy gap in eV between the zero vibrational states of the ground and the first excited state.

$\Delta E_{0,0}$  can be specified as  $\Delta E_{0,0}^{S1}$  for the singlet state and  $\Delta E_{0,0}^{T1}$  for the triplet state. We insist on the fact that  $\Delta E_{0,0}$  is not a standard electrode potential and is not expressed in volts.

The elementary charge can be distributed to the terms in the parentheses:

$$\Delta G_{\text{PET}} = -(eE(A/A^{\bullet-}) - eE(D^{\bullet+}/D)) - \Delta E_{0,0} \text{ (equation III.19)}$$

In the specific case of electron transfer, the electrode potentials expressed in volts can then be mathematically converted to electron volts, providing:

$$\Delta G_{\text{PET}} = -(E(A/A^{\bullet-})_{\text{eV}} - E(D^{\bullet+}/D)_{\text{eV}}) - \Delta E_{0,0} \text{ (equation III.20)}$$

From this point,  $\Delta E_{0,0}$  and  $E_{\text{eV}}$  have the same units and can be merged for the estimation of an excited state electrode potential.

In the case where the PC excited state acts as a donor, the formula may be written:

$$\Delta G_{\text{PET}} = -(E(A/A^{\bullet-})_{\text{eV}} - E(PC^{\bullet+}/PC^*)_{\text{eV}}) \text{ (equation III.21)}$$

where

$$E(PC^{\bullet+}/PC^*)_{\text{eV}} = E(PC^{\bullet+}/PC)_{\text{eV}} - \Delta E_{0,0} \text{ (equation III.22)}$$

Figure III-24 exemplifies these calculations with commonly encountered electron transfer partners.

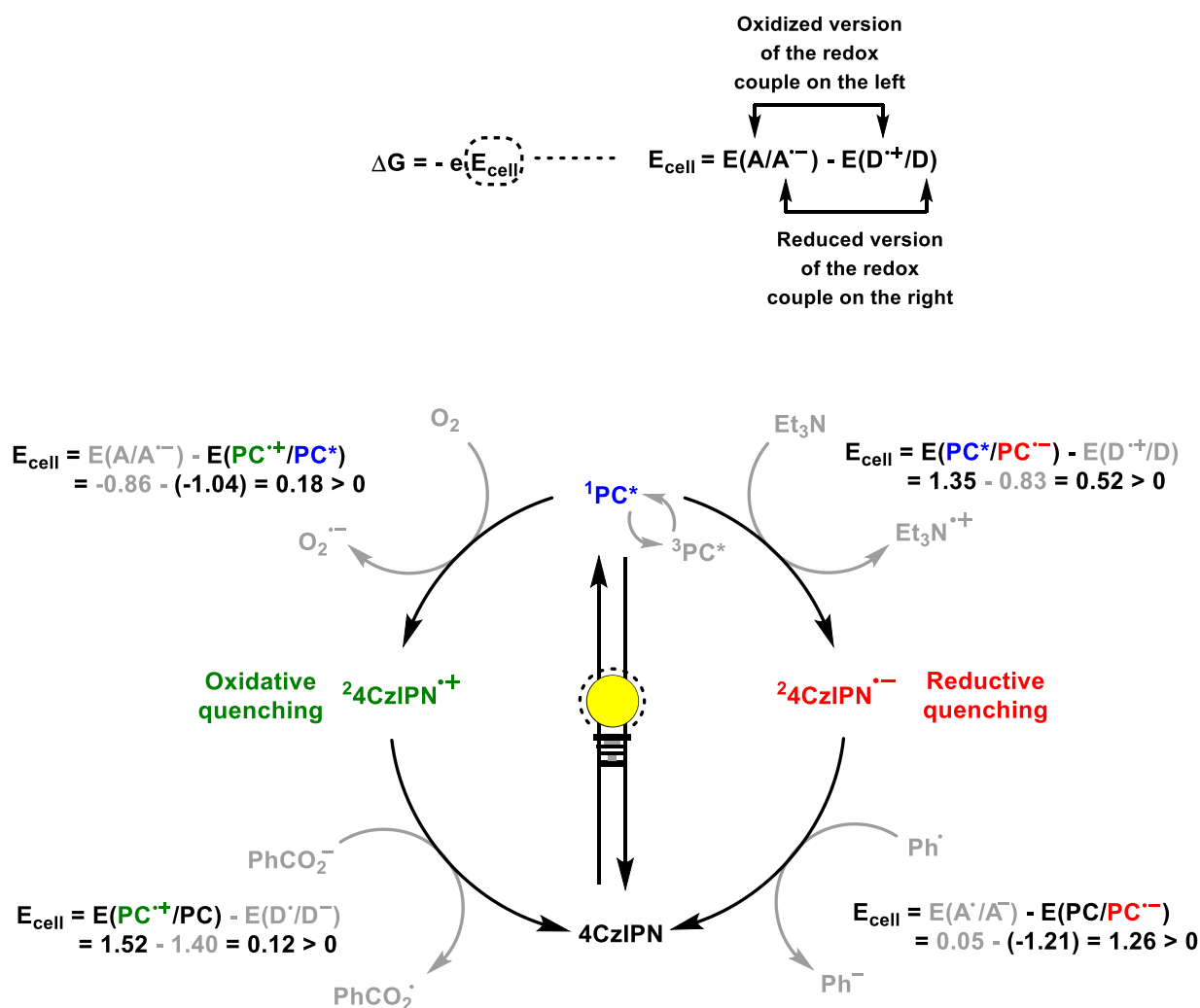


Figure III-24: Examples of thermodynamically favorable electron transfer calculations

Consecutive photoinduced electron transfer (ConPET) and electrophotocatalysis (e-PC) are methods used to generate strongly reducing agents. One can easily understand why. After either reduction of  $PC^*$  by a sacrificial electron donor or electrochemical reduction of PC by electrolysis,  $PC^{\cdot-}$  is obtained. In some cases, including some donor-acceptor cyanoarenes, this radical anion can absorb another photon, reaching its excited state  $PC^{\cdot-*}$ . The normal evolution of the radical anion excited state is to give its electron to a partner to go back to the more stable ground neutral state PC.  $PC^{\cdot-*}$  is then an electron donor, and the estimate electrode potential of the PC/ $PC^{\cdot-*}$  redox couple is:

$$E(PC/PC^{\cdot-*})_{\text{eV}} = E(PC/PC^{\cdot-})_{\text{eV}} - \Delta E_{0,0} \text{ (equation III.23)}$$

The electrode potential  $E(PC/PC^{\cdot-})_{\text{eV}}$  is usually negative, and to this negative value is subtracted the positive  $\Delta E_{0,0}$  resulting in a highly negative  $E(PC/PC^{\cdot-*})_{\text{eV}}$ . The higher  $\Delta E_{0,0}$ , the more reducing is  $PC^{\cdot-*}$ . In the case of D-A acceptor cyanoarenes, because of the steric hindrance of the bulky amino substituents, little structural change is expected between the

ground and excited state structures. This leads to minimal vibrational and reorganization energy dissipation and allows high  $E_{0,0}$  ( $E_{0,0}^{S1} = 2.64$  eV for 4CzIPN). This means that for a photon absorbed at 4CzIPN  $\lambda_{\text{max}}$  of 430 nm | 2.88 eV, only 8% of the initial photon energy is lost upon relaxation. It is astonishing! Radical anion excited state electrode potential values below -3 V are then achievable, providing the so called “super reducing agents”.

When looking at a single electron transfer, 1 eV = 1 V can be assumed as a correct conversion. The previous -3 V is considered equivalent to -3 eV out of handiness since electrode potentials are expressed in Volts. One should keep in mind the specific conditions that allow such simplification. Direct measurement of these potentials is extremely difficult and most of the time impossible because their values exceed the solvent wall, the potential at which no measurement can be done because the solvent starts to be either reduced or oxidized. The supporting electrolyte may also limit the available range of measurement.

In the case of the PC excited state acting as an acceptor, the formula may be written:

$$\Delta G_{\text{PET}} = -(E(\text{PC}^*/\text{PC}^{\bullet-})_{\text{eV}} - E(\text{D}^+/\text{D})_{\text{eV}}) \text{ (equation III.24)}$$

where

$$E(\text{PC}^*/\text{PC}^{\bullet-})_{\text{eV}} = E(\text{PC}/\text{PC}^{\bullet-})_{\text{eV}} + \Delta E_{0,0} \text{ (equation III.25)}$$

When generating radical ions electrochemically in e-PC, other factors including mass transport, back electron transfer to the electrode and local heating become important. This in-depth study requires expertise, and can be apprehended in a first approach with the paper “Electrophotocatalysis: CV as an analytical tool” from Costentin *et al.*<sup>50</sup>

The difficulty to estimate redox potentials for most organic molecules comes from the irreversible character of the process.<sup>51</sup> In such case,  $E_{1/2}$  cannot be obtained and  $E_{p/2}$  is used as shown in Figure III-25.  $E_{p/2}$ , the potential at half-maximum, is considered a better approximation than  $E_{\text{pa}}$ , the anodic peak maximum, for the estimation of  $E_{1/2}$ . This rule also applies for system with partial reversibility.<sup>52</sup>

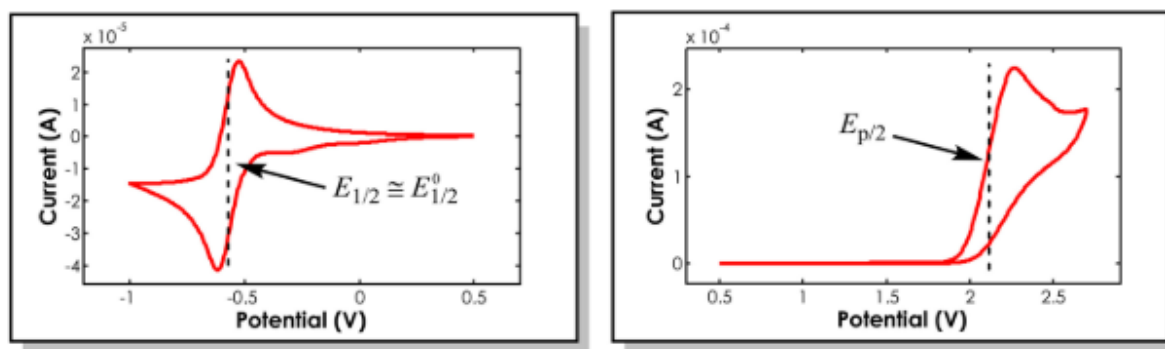


Figure III-25: Determination of a redox potential whether the wave is reversible (left) or irreversible (right). Reproduced with permission from reference 51 (Copyright 2016 Georg Thieme Verlag Stuttgart · New York).

Finally, various methods exist to determine the excited state redox potential  $\Delta E_{0,0}$ . Depending on the method applied, with the example of 3CzEPAIPN, a reasonable uncertainty of  $\pm 0.1$  eV is obtained.

Considering everything that has been discussed herein, it is reasonable to consider an uncertainty of *ca.*  $\pm 0.2$  V on excited state potentials and  $\pm 0.1$  V for ground state potentials, when compared together.

We note that a harmonization towards the most precise method could make the excited state potentials values more accurate and reliable. Similarly, a harmonization towards clearly defined and detailed working conditions could make ground state potentials more reliable, since the imprecision doesn't come from an intrinsic unreliability of electrochemical measurement. The current fact is that it isn't the case, and that one should always have in mind an uncertainty of about  $\pm 0.2$  V between reported values in similar conditions. During the writing of this report, ACS incorporated electrochemical reports guidelines to its general guidelines to address this issue.<sup>53</sup>

## 2.4. Table of selected D-A cyanoarenes properties

Table III-4: Selected D-A cyanoarenes photophysical and redox properties

Name <sup>ref</sup>	$\lambda_{max}^{abs}$ (nm   eV)	$\tau_p$ (ns)	$E_{0,0}^S$ (eV)	$E_{red}$ $E_{PC^{\bullet-}/PC^-}$ (eV or V)	$E_{ox}$ $E_{PC^{\bullet+}/PC^+}$ (eV or V)	$E_{red}^*$ $E_{PC^{\bullet-}/PC^{\bullet-}}$ (eV or V)	$E_{ox}^*$ $E_{PC^{\bullet+}/PC^{\bullet+}}$ (eV or V)
DCA <sup>54-56</sup>	422   2.90	14.9	2.90	-0.91	n/a	+1.99	n/a
4CzIPN <sup>57</sup>	430   2.88	12.7 <sup>a</sup> (main text) 19.6 (SI)	2.66	-1.24	+1.50	+1.42	-1.16
4CzIPN <sup>43</sup>	435   2.85	18.7	2.67	-1.21	+1.52	+1.35 <sup>b</sup>	-1.04 <sup>b</sup>

		1390 ( $\tau_d$ )				+1.46 <sup>c</sup>	-1.15 <sup>c</sup>
4CzIPN <sup>58</sup>	n/a	n/a	2.64	-1.32	+1.22	+1.21	-1.31
4tBuCzIPN <sup>58</sup>	<b>468</b>   2.65	n/a	2.53	-1.32	+1.22	+1.21	-1.31
4tBuCzIPN <sup>43</sup>	<b>380</b>   3.26	10 1640 ( $\tau_d$ )	2.53	-1.32	+1.22	+1.21	-1.31
4DPAIPN <sup>58</sup>	n/a	n/a	2.55	-1.65	+1.03	+0.9	-1.52
4DPAIPN <sup>43</sup>	<b>425</b>   2.92	n/a	2.62	-1.52	+1.34	+1.1	-1.28
3CzEPAIPN <sup>57</sup>	<b>427</b>   2.90	0.5	2.67	-1.42	+1.33	+1.25	-1.34
2CzPN <sup>59,60</sup>	<b>370</b>   3.35	8.5	2.86	-1.44	+1.49	+1.42	-1.37
3CzCIIPN <sup>39</sup>	<b>390<sup>d</sup></b>   3.18 <sup>d</sup>	6.9	2.72	-1.16	+1.79	+1.56	-0.93
3DPACIIPN <sup>39</sup>	<b>430<sup>d</sup></b>   2.88 <sup>d</sup>	11.5	2.65	-1.41	+1.31	+1.24	-1.34
3DPAFIPN <sup>39</sup>	<b>440<sup>d</sup></b>   2.82 <sup>d</sup>	4.2	2.68	-1.59	+1.30	+1.09	-1.38
3DPA2FBN <sup>39</sup>	<b>410<sup>d</sup></b>   3.02 <sup>d</sup>	4.2	2.84	-1.92 <sup>e</sup>	+1.24 <sup>e</sup>	+0.92 <sup>e</sup>	-1.60 <sup>e</sup>
5CzBN <sup>39</sup>	<b>400<sup>d</sup></b>   3.10 <sup>d</sup>	16.3	2.83	-1.52	+1.41	+1.31	-1.42

<sup>a</sup>the exact working conditions for these results were not found

<sup>b</sup>the excited state potential values given do not match the one obtained from the calculation with the  $\Delta E_{0,0}$  given

<sup>c</sup>value obtained from our calculations with the given values

<sup>d</sup>estimated visually from the provided absorbance spectra provided in SI

<sup>e</sup>from measurements done in CH<sub>2</sub>Cl<sub>2</sub>

### 3. Donor-Acceptor Cyanoarenes as Efficient Organic Photocatalysts: A Broad Applicability

The use of cyanoarenes in photocatalysis was already a topic before D-A cyanoarenes emerged. They were first studied as photochemical reagents and later as photocatalysts. Three photocatalysts were mainly used: dicyanobenzene (DCB), dicyanonaphthalene (DCN) and dicyanoanthracene (DCA).<sup>61,62–64</sup>

Advised review on cyanoarenes as photocatalysts before 2016:

✓ Chem. Rev. 2016, 116, 10075–1016



The absence of donor on these substrates limited their photocatalytic application to electron transfer by reductive quenching. They are however good electron acceptors bearing two cyano acceptor groups as well as extended aromatic rings for DCN and DCA with good electron affinity. They also display weak absorption bands in the visible region which allows the use of visible light to activate them preferentially over colorless reagents.

The combination of DCA and biphenyl allowed for example the generation of  $\alpha$ -alkoxy radicals from  $\alpha$ -silyl ethers and their subsequent addition to electron-poor alkenes.<sup>65</sup> The reaction conditions included water and organophotocatalysts loading below 10 mol%. A selected example is given in Figure III-26.

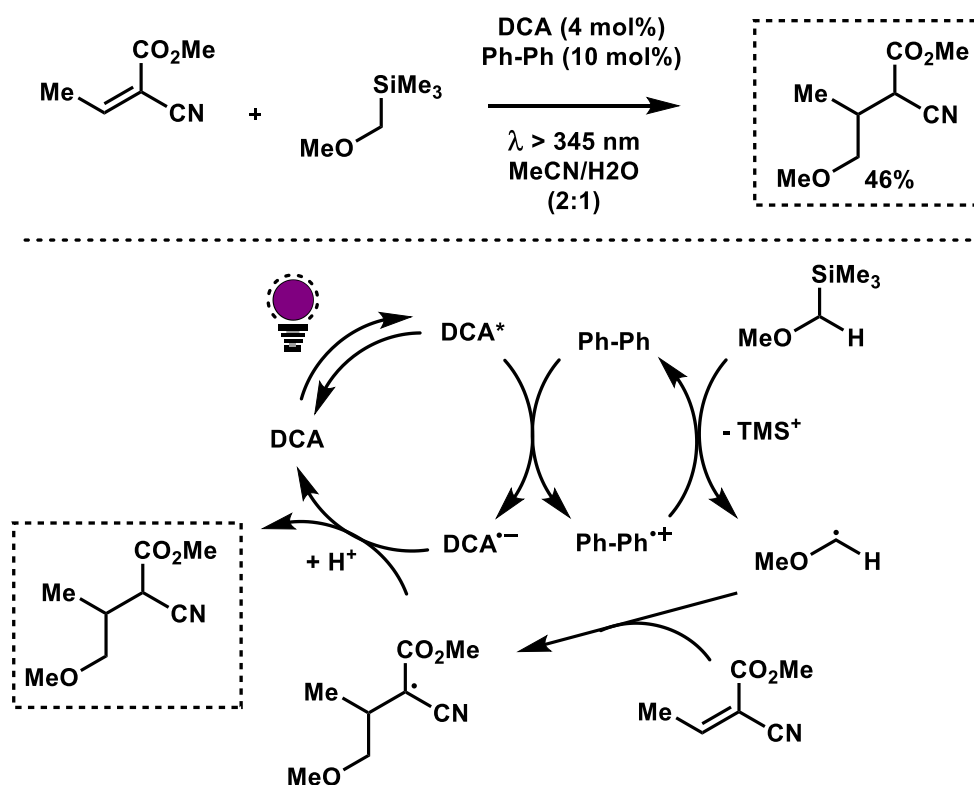


Figure III-26: Example and proposed mechanism for the photocatalytic activity of dicyanoanthracene in photoinduced hydroxymethyl radical addition on electron deficient alkene. TMS: trimethylsilyl.

Another interesting example arises from the use of DCN as a pseudo-catalytic electron acceptor for the intramolecular cyclisation of electron-rich arenes with a silyl enol ether backbone (Figure III-27). The authors proposed the PET to occur between the reactant's excited state and DCN ground state. Indeed, after comparison of the UV-Vis absorption spectra in the irradiation region, it appeared that 99% of the incident light was in fact absorbed by the reactant and not by DCN. The spectra are however not provided in the publication. We note that in the advised review by Nicewicz and Romero another mechanism is proposed.

The reaction proceeds in the presence of water and oxygen. Molecular oxygen proved crucial for the regeneration of DCN by accepting the extra electron of DCN radical anion. If ran under inert atmosphere, quick degradation of DCN was observed along with a complex mixture of products.<sup>66</sup>

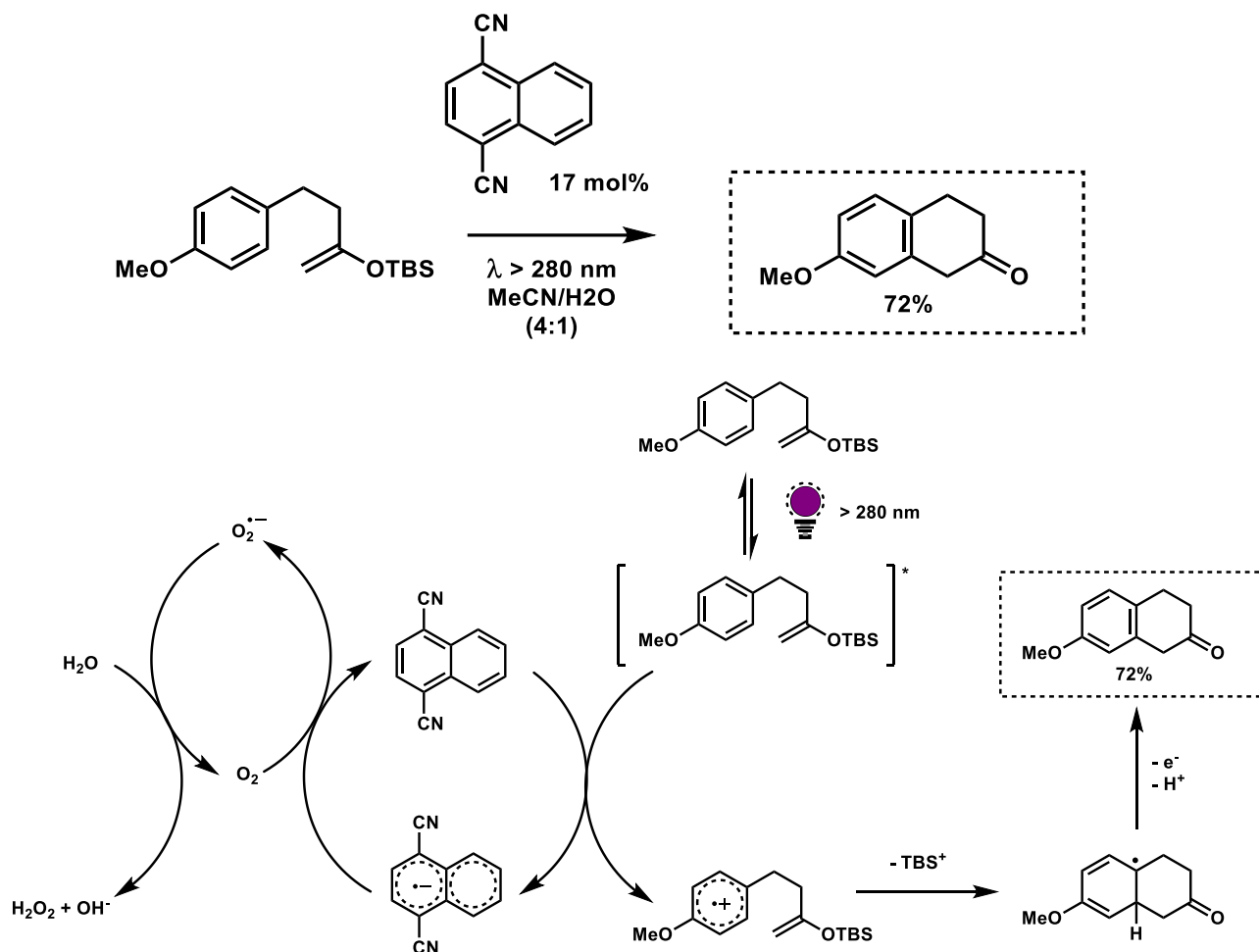


Figure III-27: Example and proposed mechanism for the activity of dicyanoanthracene as an electron transfer reagent in the photochemical intramolecular cyclization reaction of silyl enol ethers. TBS: *tert*-butyldimethylsilyl

The main limitation to the extension of cyanoarenes use prior to 2016, besides their intrinsic photophysical properties, was their poor stability. Most examples highlighted in the advised review required high catalyst loading (20 mol%), which the authors attributed to cyanoarene degradation pathways in the presence of radical and radical anions including decyanation and dearomatization.<sup>61</sup>

The decyanation of electron deficient cyanoarenes in the presence of benzyl-dihydropyridine (Bn-DHP) under 405 nm light excitation in the absence of photocatalyst was shown in 2017 (Figure III-28).<sup>67</sup> Electron transfer from the excited state of Bn-DHP to the ground state of the cyanoarenes generated the radical cation of Bn-DHP and the radical anion of cyanoarene. The radical cation of Bn-DHP evolved to provide pyridine, benzyl radical and a proton. The radical

anion of cyanoarene reacted with the benzyl radical to generate the correspond anion quickly followed by decyanation.

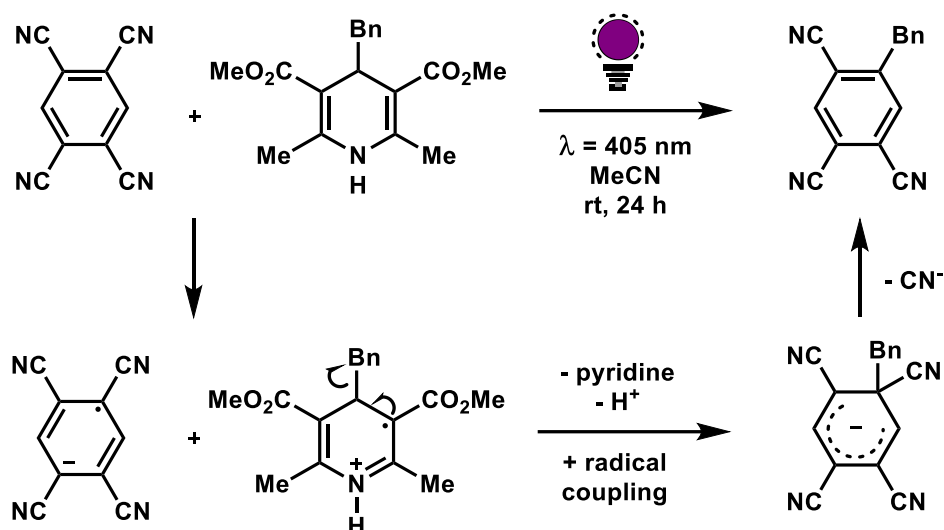


Figure III-28: Example and proposed mechanism for the photochemically benzyl-dihydropyridine triggered decyanation of tetracyanobenzene

Another example following a different strategy but a similar underlying idea uses an iridium photocatalyst to induce the electron transfer to 1,4-dicyanobenzene (DCB) followed by radical coupling and decyanation, further highlighting the ease of chemical modification of the cyanoarene core in the presence of radicals and compatible electron transfer reagents (Figure III-29).<sup>68</sup>

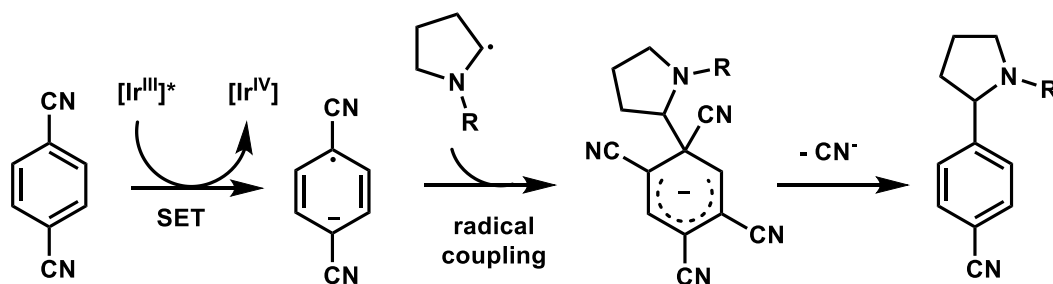


Figure III-29: Iridium photocatalyzed decyanation of dicyanobenzene by  $\alpha$ -aminyl radical

Donor-acceptor cyanoarenes were mentioned at the end of the review as promising catalysts with high activity. This guess proved right as we will show in the following part, which isn't aimed to be exhaustive.

For further details, we advise the following reviews:

- ✓ *Chem. Soc. Rev.*, **2021**, 50, 7587-7680
- ✓ *Angew. Chem. Int. Ed.*, **2021**, 60, 19526-19549

### 3.1. Electron Transfer

D-A cyanoarenes are now “standard” photocatalysts for photoinduced electron transfer (PET) reactions. Their versatile properties allows their use in both oxidative and reductive quenching.<sup>69–71</sup> Figure III-30 shows the most common electron donors and acceptors in both quenching types compatible with donor-acceptor cyanoarenes.

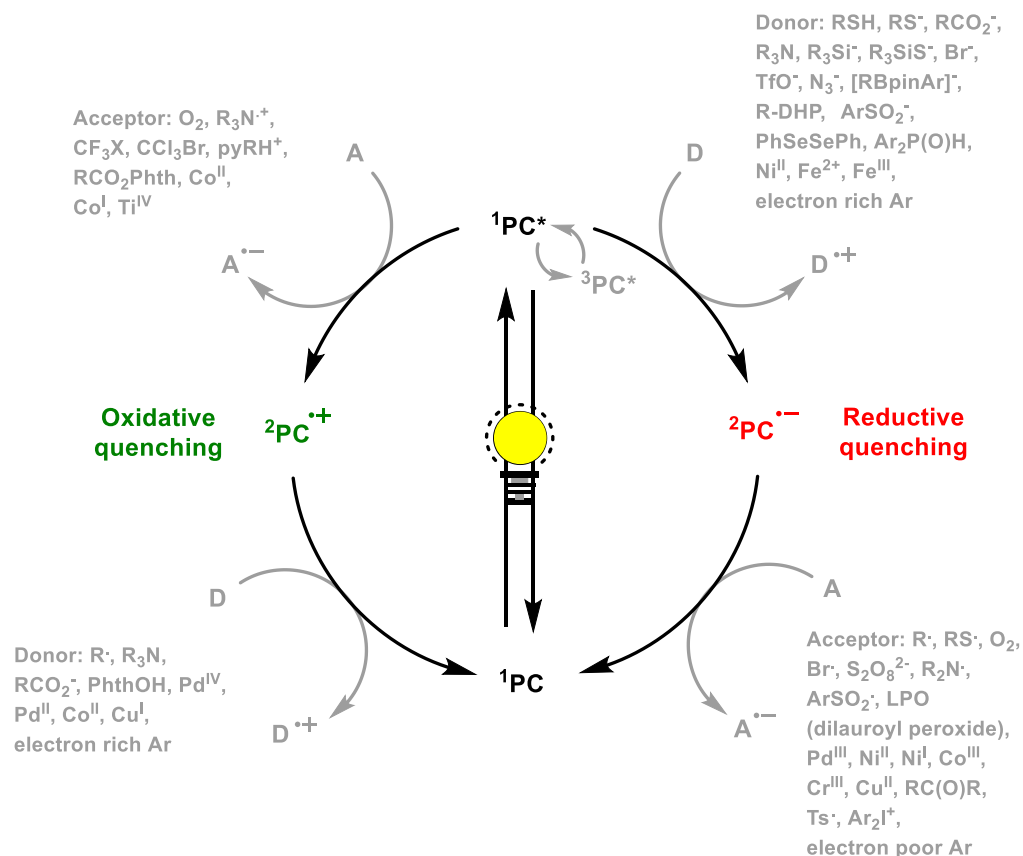


Figure III-30: Donor and acceptor examples that can engage in electron transfer in both oxidative and reductive quenching with D-A cyanoarenes under irradiation

Obviously, most electron donors from the reductive quenching include anions and electron rich partners while most electron acceptors include cations and electron poor partners. Exceptions are always to be expected. We propose here a quick overview of the radical generation through electron transfer process with various donor and acceptor functionalities. A few synthetic examples will also be given to highlight the high functional group tolerance and mild reaction conditions.

The PC is 4CzIPN for the following examples unless stated otherwise. It means that for any displayed reaction, 4CzIPN has suitable redox potentials, lifetime, and stability for each SET to occur within the given conditions. This shows how applicable one molecule can be.

### Carboxylic acids and derivatives (reductive and oxidative quenching)

Carboxylic acids are interesting in the way that after a SET event, decarboxylation can occur to provide the corresponding radical (Figure III-31).

In the reductive quenching cycle, carboxylic acids can be used without modification. A base is usually required to initiate their deprotonation to the corresponding carboxylate, the active form that engages in SET processes with either the photoexcited photocatalyst (reductive quenching cycle) or the oxidized photocatalyst  $PC^{\bullet+}$  (oxidative quenching cycle).

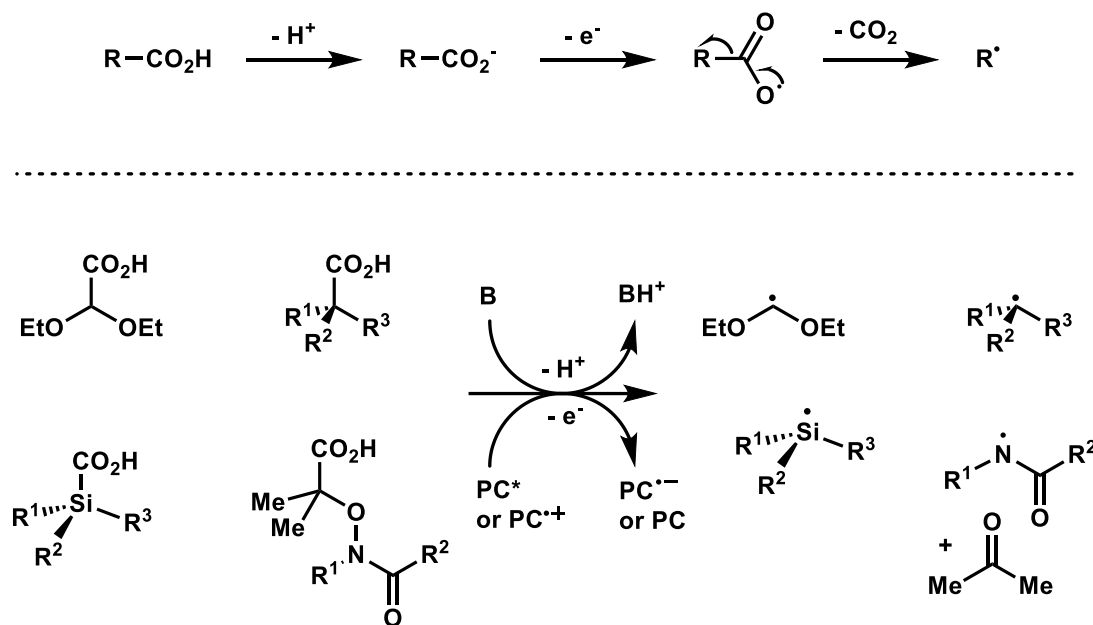


Figure III-31: Photocatalytic decarboxylative generation of radicals' examples

Once generated, these radicals can engage in a variety of reactions, including addition on alkenes bearing electron withdrawing substituents, intramolecular hydrogen atom transfer, cyclization on aromatic rings... the list goes on and is substrate dependent. The example given in Figure III-32 shows the generation of a radical from a carboxylic acid that adds on an alkene. The alpha-aromatic stabilized radical then undergoes radical recombination to afford the product after acidification with HCl.<sup>72</sup>

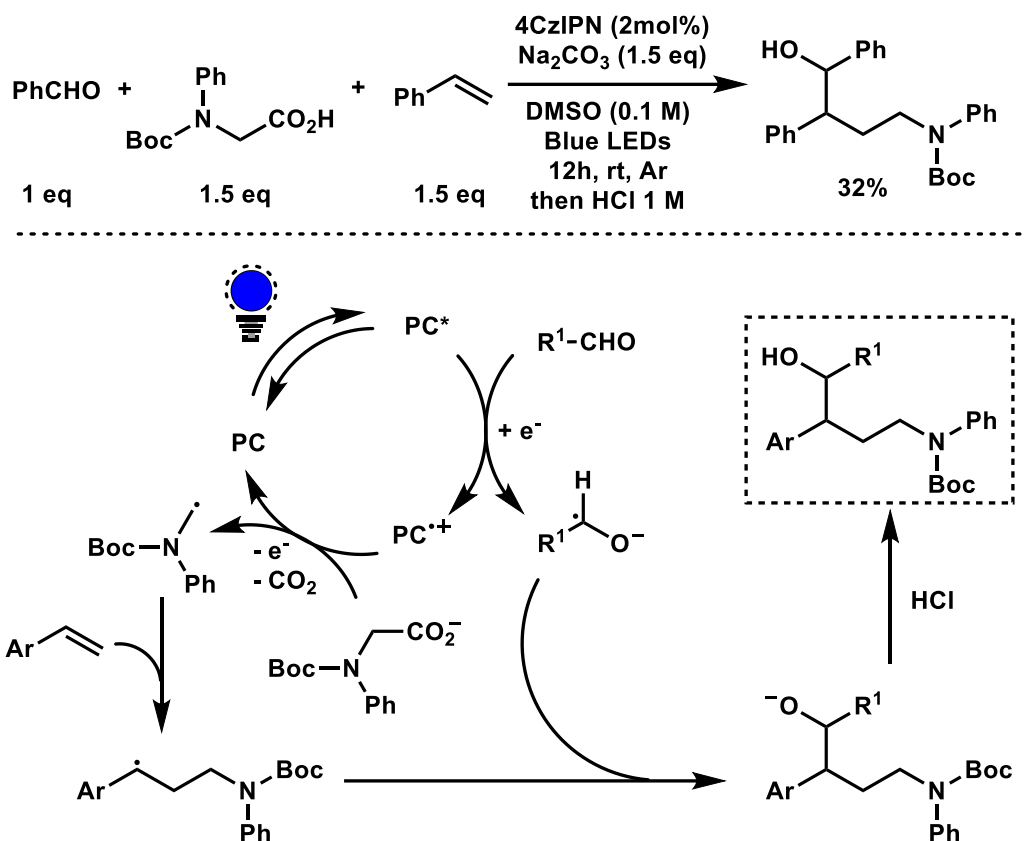


Figure III-32: Example and proposed mechanism for the visible-light-mediated decarboxylative radical addition bifunctionalization cascade

To be effectively used in oxidative quenching mechanism as electron acceptors, modifications are required. An effective method is to transform the carboxylic acid in a N-acyloxyphthalimide able to accept an extra electron leading to the O-N bond cleavage thus forming the phthalimide anion and a radical base on the acid moiety (Figure III-33). This moiety, as expressed in the previous paragraph, undergoes decarboxylation to provide the correspond R radical.

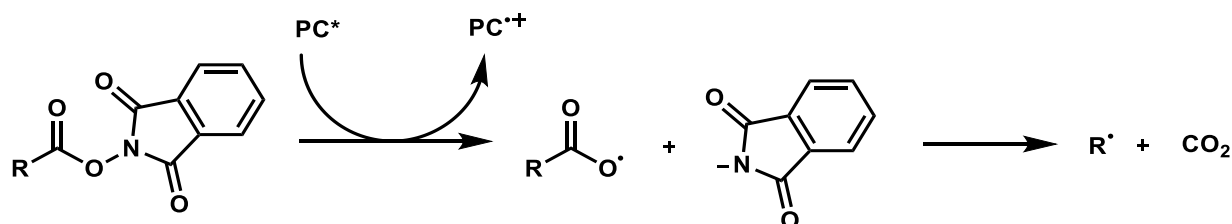


Figure III-33: Schematic radical generation from N-acyloxyphthalimide by electron transfer

Since these radicals are generated following an oxidative quenching cycle, the substituents around the radical are more commonly electron donating group to assist the stabilization of the cation that is likely to be formed in the second photocatalytic SET event where the oxidized photocatalyst is reduced. Decarboxylative fluorination of electron-rich naphthalene derivatives was thus achieved (Figure III-34).<sup>73</sup>

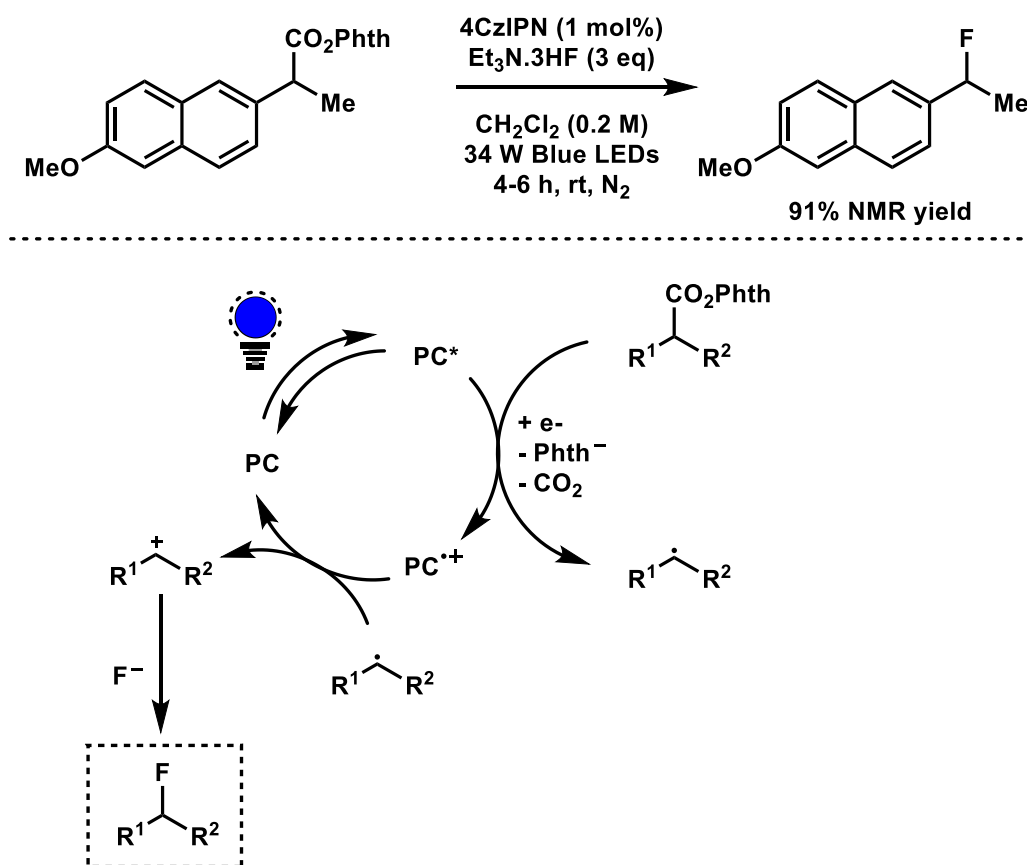


Figure III-34: Example and proposed mechanism for the decarboxylative fluorination of the benzylic position of electron-rich naphthalene derivative

### Pyridinium salts

Pyridinium salts are excellent radical precursors when subjected to photoredox catalysis with an electron donating photocatalyst. Alkoxy, aminyl and alkyl radicals can easily be generated by this method to engage in various chemical reactions. In Figure III-35, a Minisci type reaction on the pyridinium itself using Eosin Y as the PC is highlighted.<sup>74</sup> The (N,N-methyltosyl)aminyl radical addition on an electron-rich alkene reverses the philicity of the radical. It switches from an electrophilic aminyl radical to a nucleophilic  $\alpha$ -alkoxy-alkyl radical after the addition, which is much more compatible for the reaction on the electron deficient pyridinium salt. Two reviews were dedicated to this type of chemistry in 2019.<sup>75,76</sup> With a quantum yield greater than 30, this reaction definitely also follows a radical chain mechanism. To our surprise, D-A cyanoarenes are almost absent from this field. Iridium and ruthenium catalysts are however widely employed. We do not clearly understand the reasons behind this, for there is no apparent incompatibility between the systems.

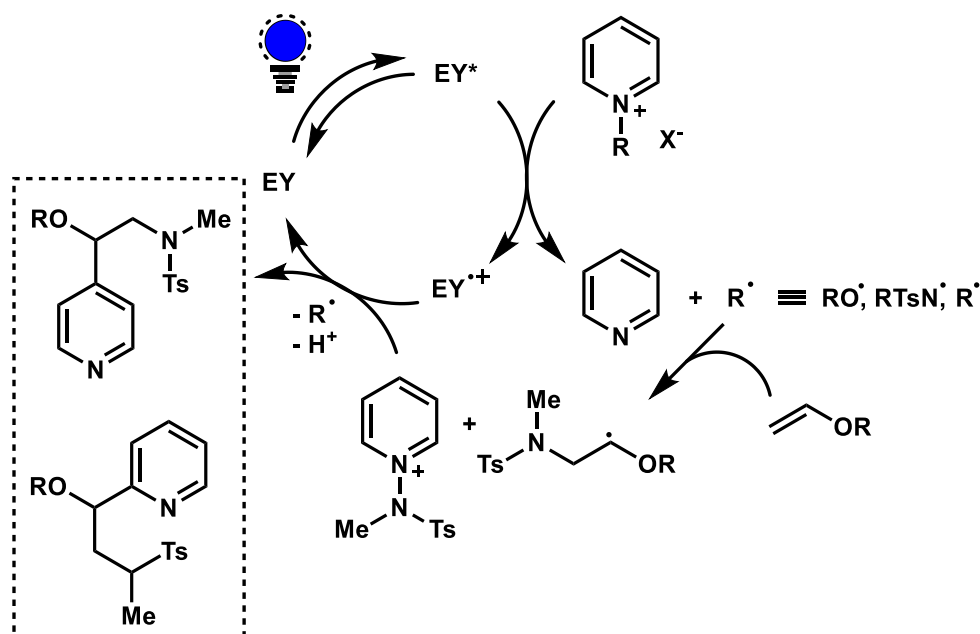


Figure III-35: Proposed mechanism for the Eosin-Y photocatalyzed Minisci-type reaction from pyridinium salts

4CzIPN was used in 2021 as a PC to promote a SET with N-alkoxy-4-cyanopyridinium salts to generate alkoxy radicals that readily engage in HAT with methylformate (Figure III-36). The formate radical then adds on alkenes and the product is oxidized by 4CzIPN to generate the carbocation that can be quenched in different fashion.<sup>77</sup>





## Hantzsch ester and derivatives -dihydropyridines

162

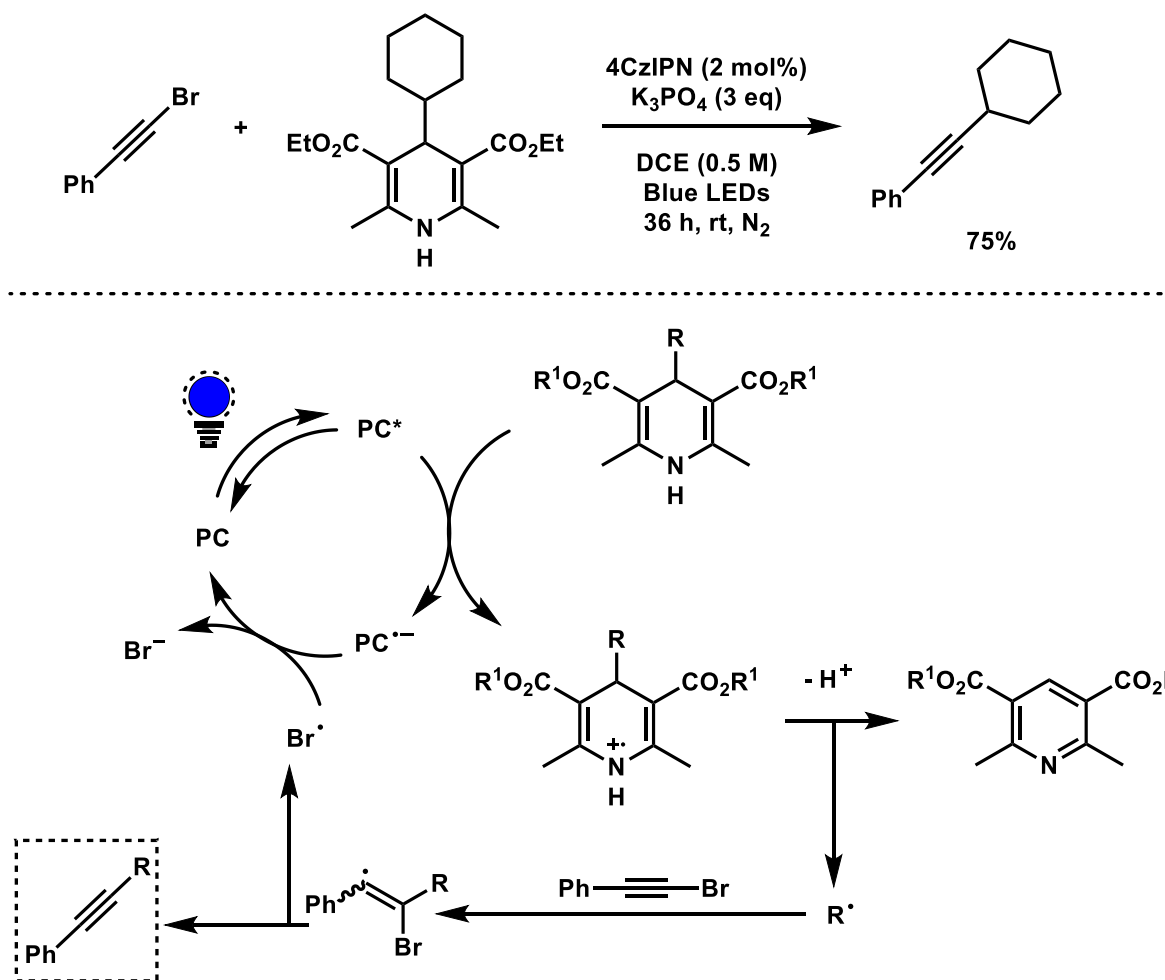


Figure III-37: Example and proposed mechanism for the visible light promoted coupling of alkynyl bromides and Hantzsch esters for the synthesis of internal alkynes

### Silanes

Photoredox with donor-acceptor cyanoarenes is also compatible with silanes to generate silyl radicals. It has been presented before that silyl radicals can be generated from their carboxylic acid substituted version. However, the main method consists in hydrogen atom transfer from another radical, most commonly with a bromyl radical. An interplay between HAT/XAT (halogen atom transfer) is often used to generate radicals from alkyl bromides.<sup>79</sup> A visible-light induced alkyl radical addition on a pyridine used this interplay to effectively add aliphatic 6-membered rings on a pyridine core (Figure III-38).

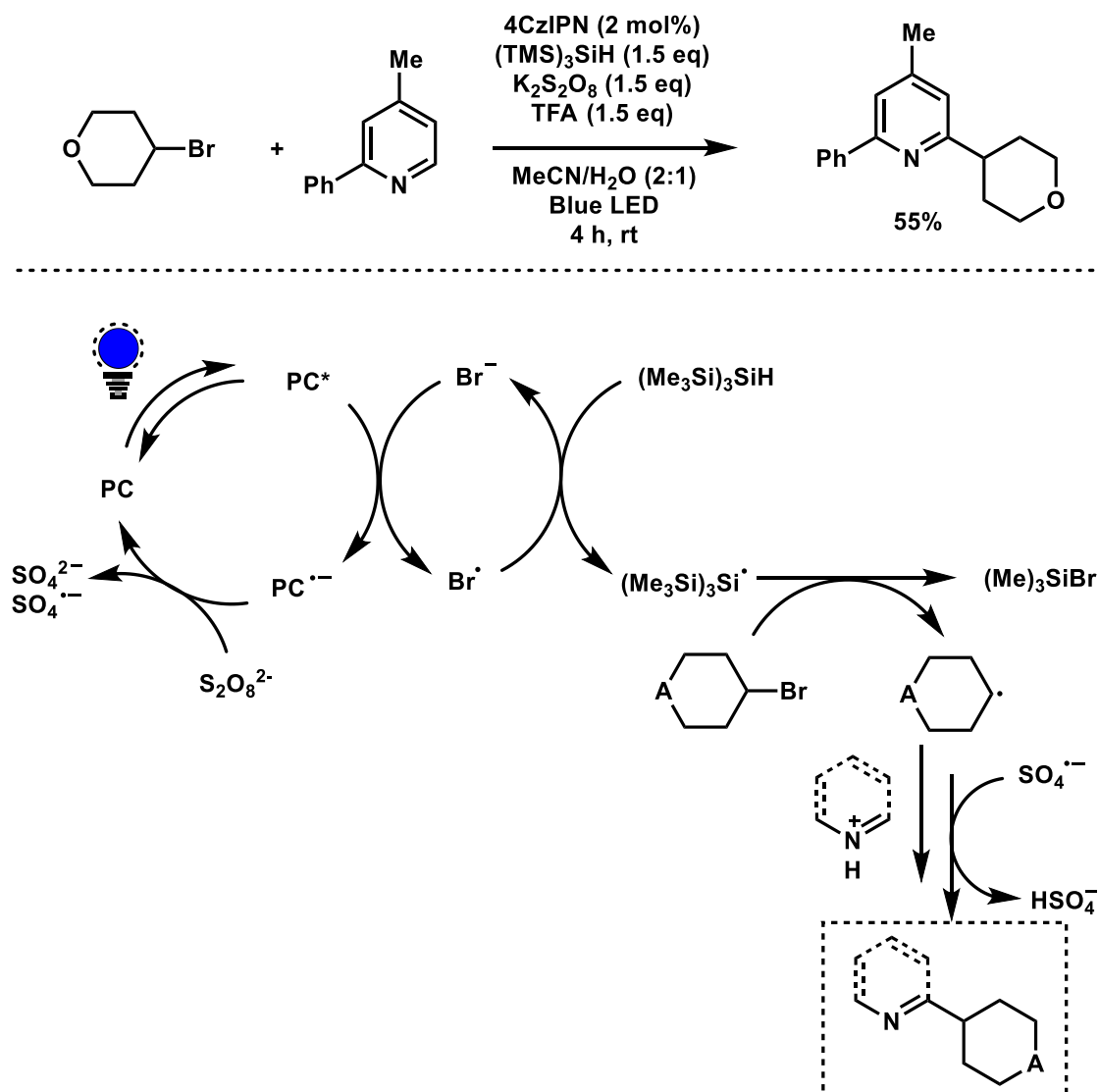


Figure III-38: Example and proposed mechanism for the visible-light induced alkyl radical addition on a pyridine derivative through halogen atom transfer. A: O or NBz with Bz:benzoyl.

In the reaction depicted in Figure III-39, a silanol is deprotonated by an inorganic base to provide, after Brook rearrangement, a silyl anion. The PC then abstracts an electron from the negative charge, yielding a silyl radical that acts as an excellent halogen abstractor. After bromide abstraction, an aryl radical is obtained and reacts on the electrophilic carbon of TsCN. Quick elimination of the good Ts radical leaving group provides the desired benzonitrile. The remaining tosyl radical is transformed into an anion after single electron transfer with the reduced photocatalyst, thus closing the photocatalytic cycle.<sup>80</sup>

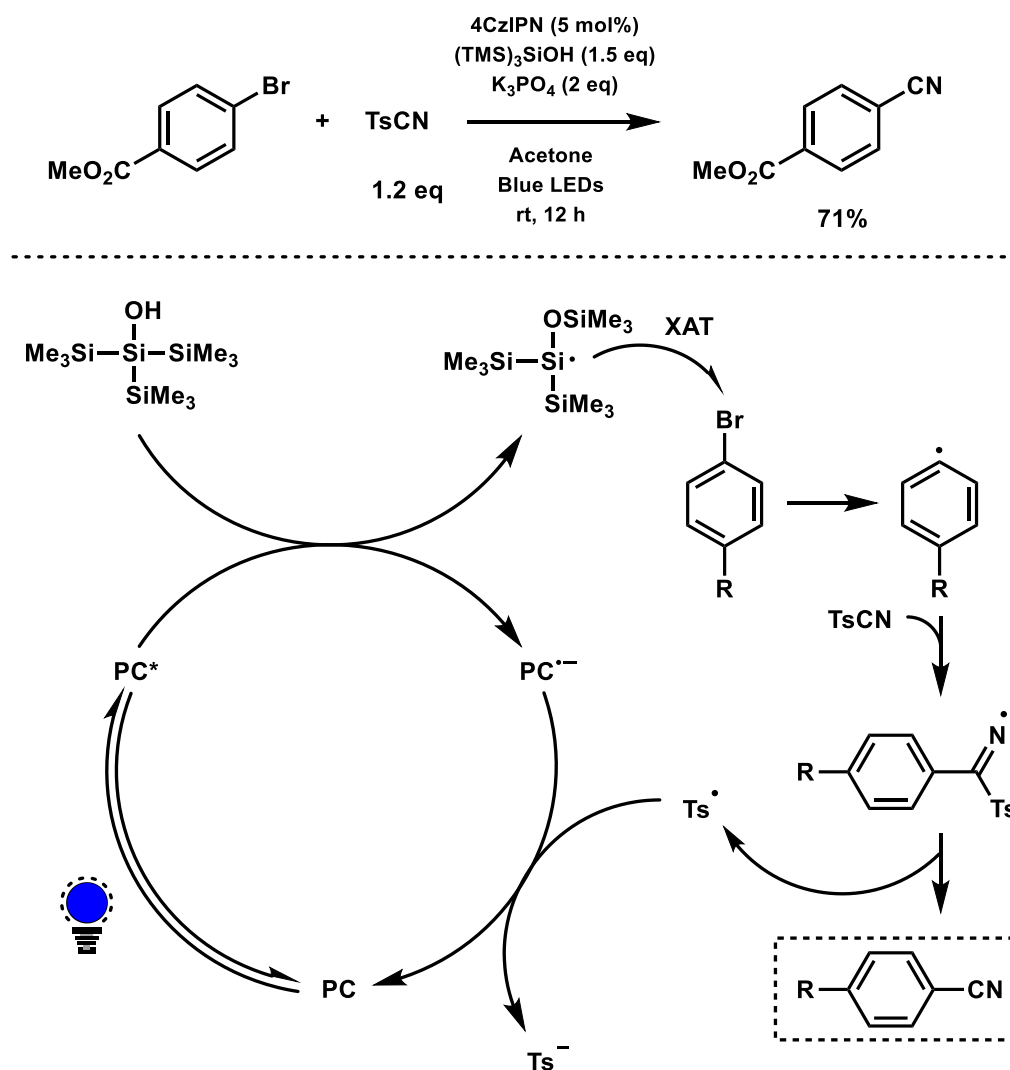


Figure III-39: Example and proposed mechanism for the visible-light induced dehalogenative cyanation of electron poor aromatic ring

### Halogens and halogenoalkanes

Halogenoalkanes and halogenoarenes are difficult to reduce, as assessed by their highly negative reduction potentials. Therefore, common direct SET methods from D-A cyanoarenes cannot be used and intermediate radicals must be involved. This difficulty can be bypassed by using silyl radicals which are good halogen atom abstractors, thus generating the corresponding alkyl or aryl radical. Another method implies dual catalysis with metals to cleave the carbon-halogen bond by oxidative addition on the metal center. Such example will be highlighted shortly after, in the dual catalysis part.

The potential of bromide anion/bromyl radical ( $\text{Br}^-/\text{Br}^\bullet$ ) however matches the one of 4CzIPN excited state. They can act either as acceptor (bromyl radical) or donor (bromide anion).

## Thiols and thiolates

HAT is a major mechanism in synthetic chemistry. It allows for the generation of highly reactive species from non-activated substrates. Thiols and thiolates are important coupling partners with D-A cyanoarenes that become excellent HAT agents after SET: thiyl radicals. A base is required for the deprotonation of the thiol. The methodology in Figure III-40 applied thiyl radicals as HAT agents for the hydrosilylation of electron rich alkenes under photocatalytic conditions using 4CzIPN as the photocatalyst.<sup>81</sup> Triisopropylsilanethiol is the most common HAT agent. Thiols display the ability to be used catalytically.

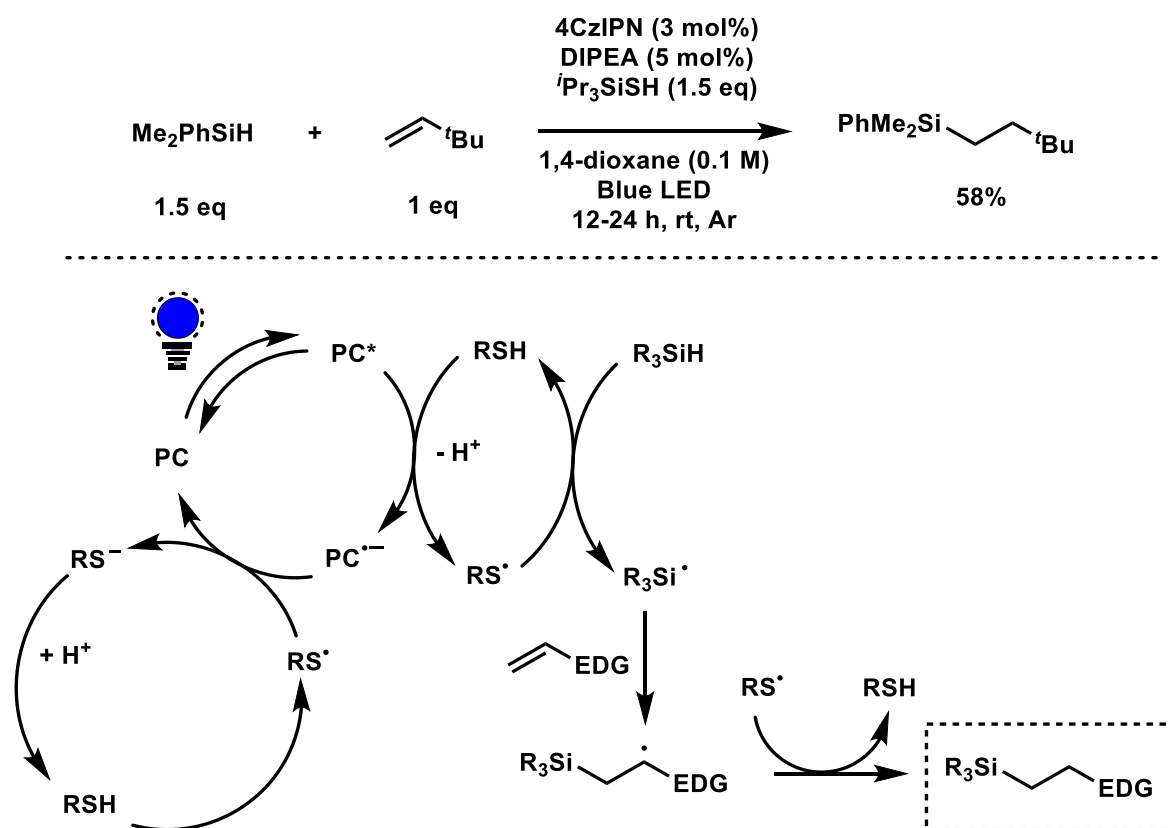


Figure III-40: Example and proposed mechanism for the photocatalytic silyl radical generation and addition on electron rich alkenes. EDG: Electron donating group.

## Amines

Amines are an important class of SET partners. They can be used as HAT, just like thiols, in a reductive quenching cycle. Quinuclidine is the amine of choice for this process. It was used in the same paper previously described for thiols (with electron rich alkenes) but for the hydrosilylation of electron deficient alkenes instead (Figure III-41).

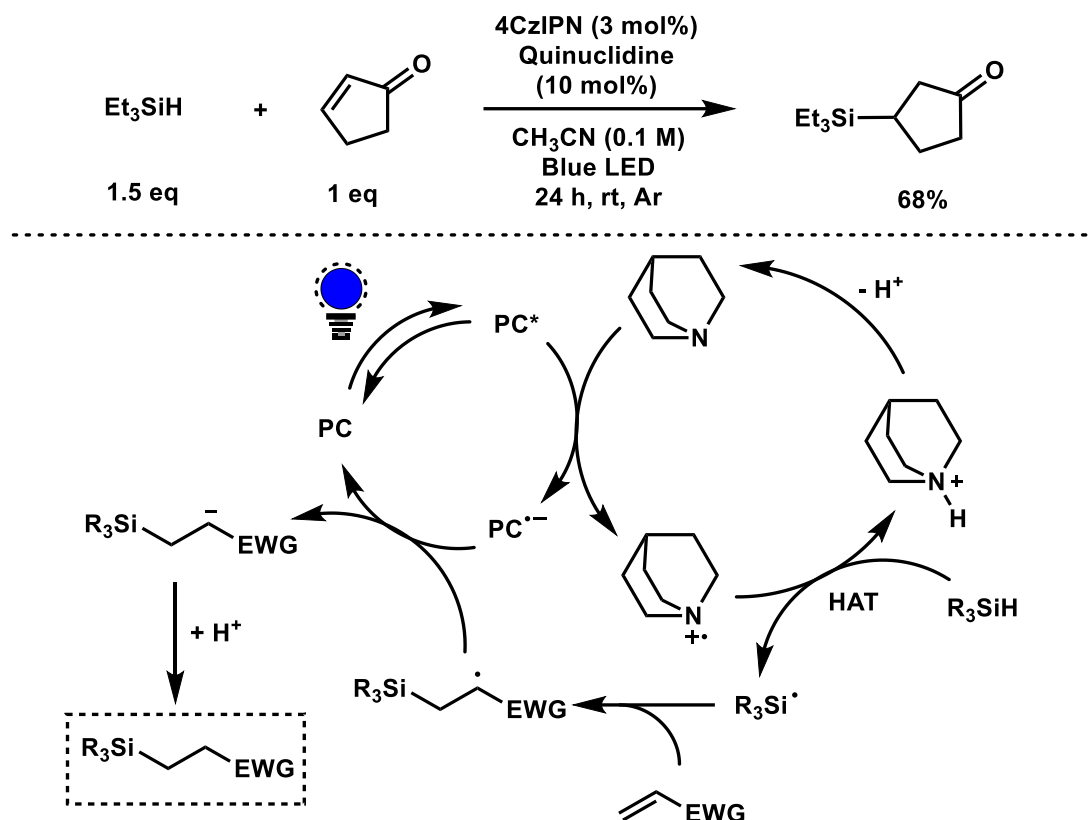


Figure III-41: Example and proposed mechanism for the photocatalytic silyl radical generation and addition on electron poor alkenes. EWG: Electron withdrawing group.

Their most widespread use is as sacrificial electron donor. They allow the generation of the reduced form of most photocatalysts that can then be engaged in the desired chemical reaction. The evolution of the aminyl radical cation depends on the reaction conditions and may either undergo deprotonation to provide an  $\alpha$ -aminyl radical or undergo HAT to provide the corresponding iminium (Figure III-42). The question of the innocence of these by-products in chemical processes is a matter of discussion and have been proved to interfere in some of them.<sup>82</sup>

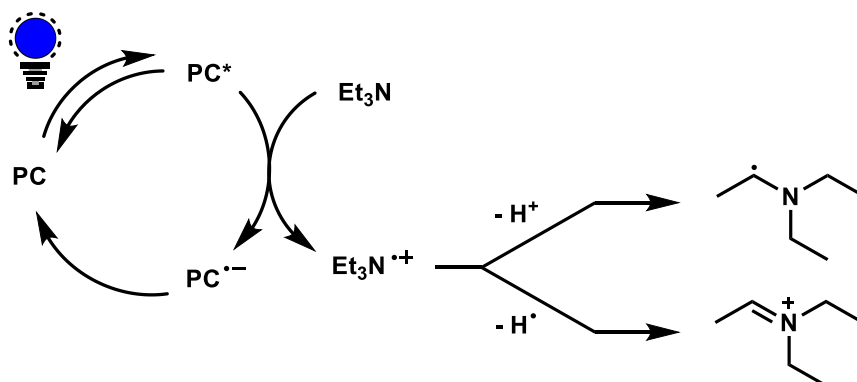


Figure III-42: Two proposed evolution pathways of photocatalytically generated amine radical cation (deprotonation and hydrogen atom transfer)

### Metallaphotoredox<sup>23,83</sup>

Metallaphotoredox consists in assisting metal catalysis with a photocatalyst that can either abstract or provide an electron to the metal complex during its catalytic cycle. This allows new reactivities that wouldn't be possible otherwise. This dual catalysis between metals and D-A cyanoarenes started with Nickel/4CzIPN dual catalysis in 2016 (Figure III-43). Since then, many metals were successfully combined with D-A cyanoarenes, including cobalt, palladium, platinum, copper, chromium, titanium, and iron.

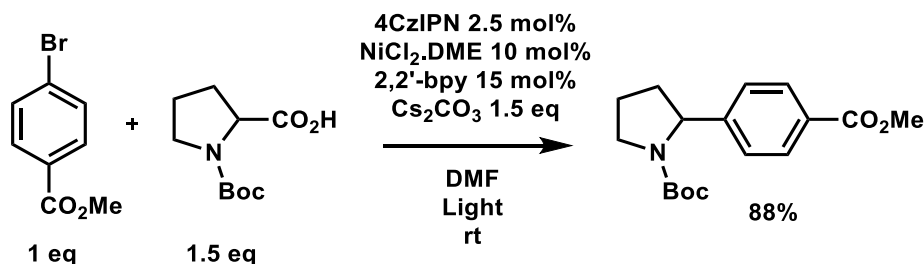


Figure III-43: Example for the first D-A cyanoarene/Nickel dual catalysis

This dual catalysis enabled cross-coupling reactions by photocatalytic radical formation on one side and oxidative addition of an aryl halide on the metal center followed by radical addition and reductive elimination to provide the product of interest. The photocatalytic cycle is closed with the regeneration of the active  $\text{Ni}^0$  catalyst by electron transfer from  $\text{PC}^{\bullet-}$  (Figure III-44). A whole set of arylation, vinylation and alkylation from the corresponding aryl bromide, terminal alkyne or alkyne bromide, and alkyl bromide could be achieved.

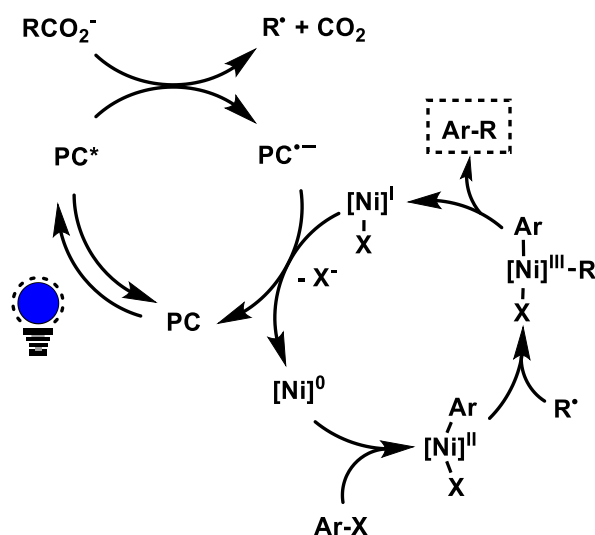


Figure III-44: Proposed mechanism for the 4CzIPN/Nickel dual catalysis example presented in Figure III-.

One interesting example arises in the dual catalytic radical cascade coupling with dienes, sulfates and aryl halides. In this paper,  $\text{Ir}(\text{dtbbpy})(\text{ppy})_2\text{PF}_6$  was selected as the photocatalyst

for the study because it gave a 91% yield during the optimization against 89% for 4CzIPN (Figure III-45). Nevertheless, 4CzIPN proved largely capable of performing the reaction.<sup>84</sup>

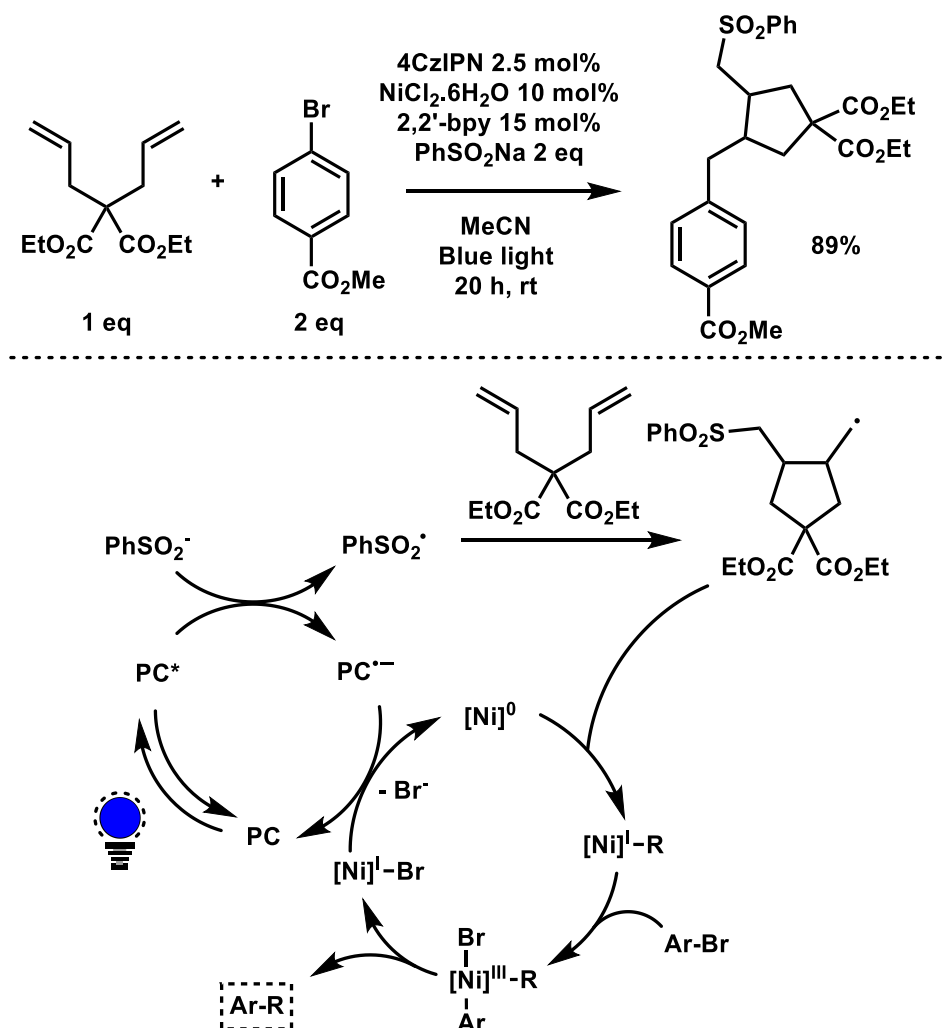


Figure III-45: Example and proposed mechanism for the dual catalytic radical cascade coupling with dienes.

### Beyond SETs: Consecutive photoinduced electron transfer (ConPET)<sup>57,82,85</sup>

More details on this topic are given in chapter III.4.

The use of a single blue light photon limits the range of redox potentials. A blue photon with a  $\lambda = 410$  nm may provide a maximum energy of 3 eV to the molecule that absorbs it. This amount of energy dissipates in various extent through relaxation, commonly around 50%. Thus, with a redox potential (PC\*/PC•<sup>+</sup>) of -1.73 V vs SCE in acetonitrile, fac-Ir(ppy)<sub>3</sub> is amongst the best excited state reducing agents. 4CzIPN displays a (PC\*/PC•<sup>+</sup>) redox potential of -1.04 V vs SCE. However, many organic molecules display high reduction potentials, such as benzyl chloride with a  $E(\text{PhCl}/\text{PhCl}^{\bullet-}) = -2.8$  V vs SCE. One can see that neither 4CzIPN nor fac-Ir(ppy)<sub>3</sub> can reduce chlorobenzene in their excited state.



In 2014, König and coworkers demonstrated the concept of consecutive photoinduced electron transfer (ConPET) using perylene diimide (PDI, Figure III-46).<sup>86</sup>

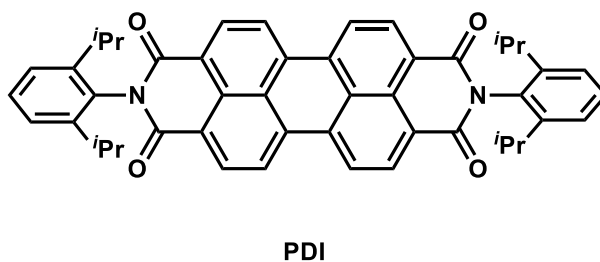


Figure III-46 : Structure of the perylene diimide PDI

This method first follows a normal photocatalytic cycle: Light absorption by the PC to reach its excited state from which it exchanges an electron with a sacrificial electron donor (usually an amine, such as diisopropylethylamine DIPEA) to provide  $PC^{\bullet-}$ . In the ConPET mechanism, the resulting photocatalyst radical anion absorbs a second photon to generate the radical anion excited state  $PC^{\bullet-*}$ . This specie can reach extremely high reduction potentials, neighboring -3 V vs SCE in the case of some D-A cyanoarenes and -1.87 V vs SCE for  $PDI^{\bullet-*}$ .<sup>87</sup>

The subsequent electron transfer between  $PC^{\bullet-*}$  and the aryl halide generates the aryl halide radical anion which is known to undergo carbon-halogen bond cleavage to provide the aryl radical and the halogen anion (Figure III-47).

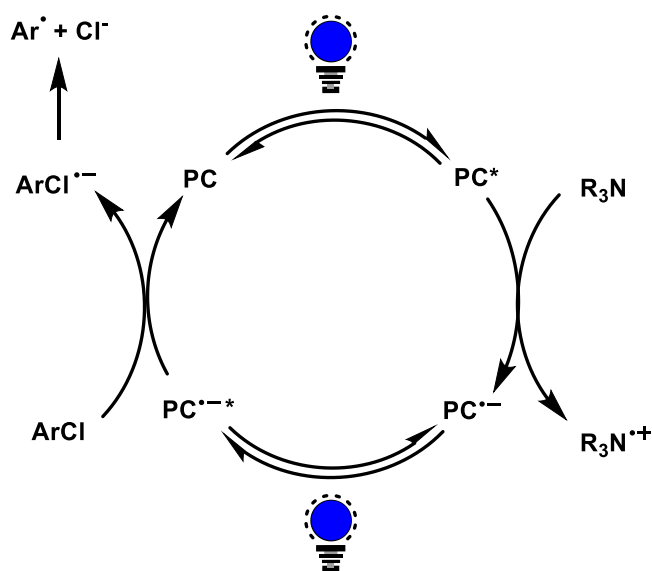


Figure III-47: Proposed mechanism for the aryl chloride reduction in the ConPET mechanism

This aryl radical was successfully added to pyrrole derivatives on the aromatic ring  $\alpha$ -position of the nitrogen (Figure III-48).

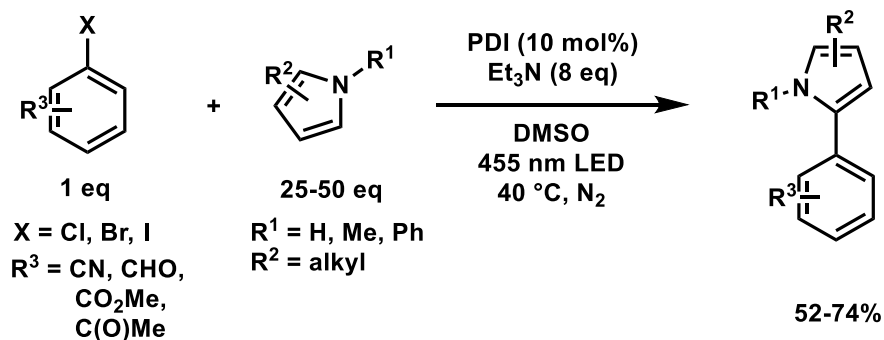


Figure III-48: C–H aromatic substitution reactions of aryl halides with substituted pyrroles.

In 2021, Wu and coworkers demonstrated the ability of 3CzEPAIPN (Figure III-49) to engage in ConPET and effectively induce the reduction of aryl chlorides with potentials as high as -2.9 V vs SCE. The sacrificial electron donor was either sodium ascorbate or DIPEA.

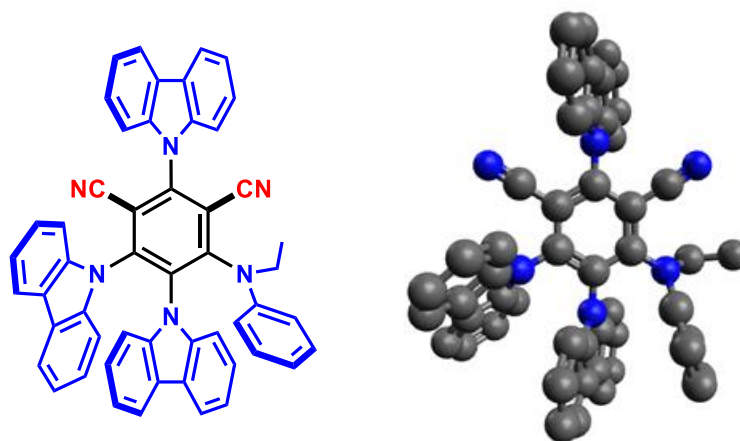


Figure III-49: 3D structure of 3CzEPAIPN

Mechanistic studies were undertaken to gather information supporting the ConPET mechanism. The radical anion was supposed to be generated upon 5 minutes irradiation of a solution of the photocatalyst in the presence of DIPEA. Absorbance and luminescence studies showed a surprising blueshift of both absorbance and luminescence upon irradiation, where a redshift is usually expected between a neutral molecule and its radical anion counterpart. EPR confirmed the presence of a radical specie in the solution, going in the direction of a radical anion generation. Most notably, NMR analysis of an sample showed a broadening of all aromatic signals after irradiation. The results remained unchanged for 3 hours under argon and exposure to air gave back a similar spectrum to the one before irradiation. This indicates that there is little to no photodegradation upon irradiation and that the electron transfer in presence of an excess of amine is close to 100%. The evolution of the signals in the aliphatic region is however not provided. Time-correlated single-photon counting experiment on the irradiated solution provided two lifetimes of 2.24 ns (20.94%) and 13.43 ns (79.06%). The authors give the average value of 12.95 ns as the lifetime of the radical anion. This lifetime is exceptionally high for a

radical anion, especially considering that 3CzEPAIPN\* has a much lower lifetime of 0.5 ns. This average lifetime value of 12.95 ns was quenched in the presence of different concentration of chlorobenzene in the solution. A closer look at the lifetime values show that the long lifetime component of 13.43 ns corresponds to the active quenching entity. A quenching kinetic rate constant of  $1.5 \times 10^7 \text{ M}^{-1} \cdot \text{s}^{-1}$  was obtained. It relates to a low quenching rate value. With such value, a recent study provides an estimation of needed quencher concentration of 100 M to quench 90% of the excited state (lifetime of *ca.* 10 ns) with an incoming continuous photons flux of  $1.63 \times 10^{-5} \text{ photons/s}$ .<sup>88</sup> The message here is that the electron transfer is amongst the most inefficient, but remains thermodynamically feasible.

The aryl radical was captured by different partners including phosphines, phosphites, diboron esters (Figure III-50), and tailored scaffolds that underwent intramolecular cyclization.

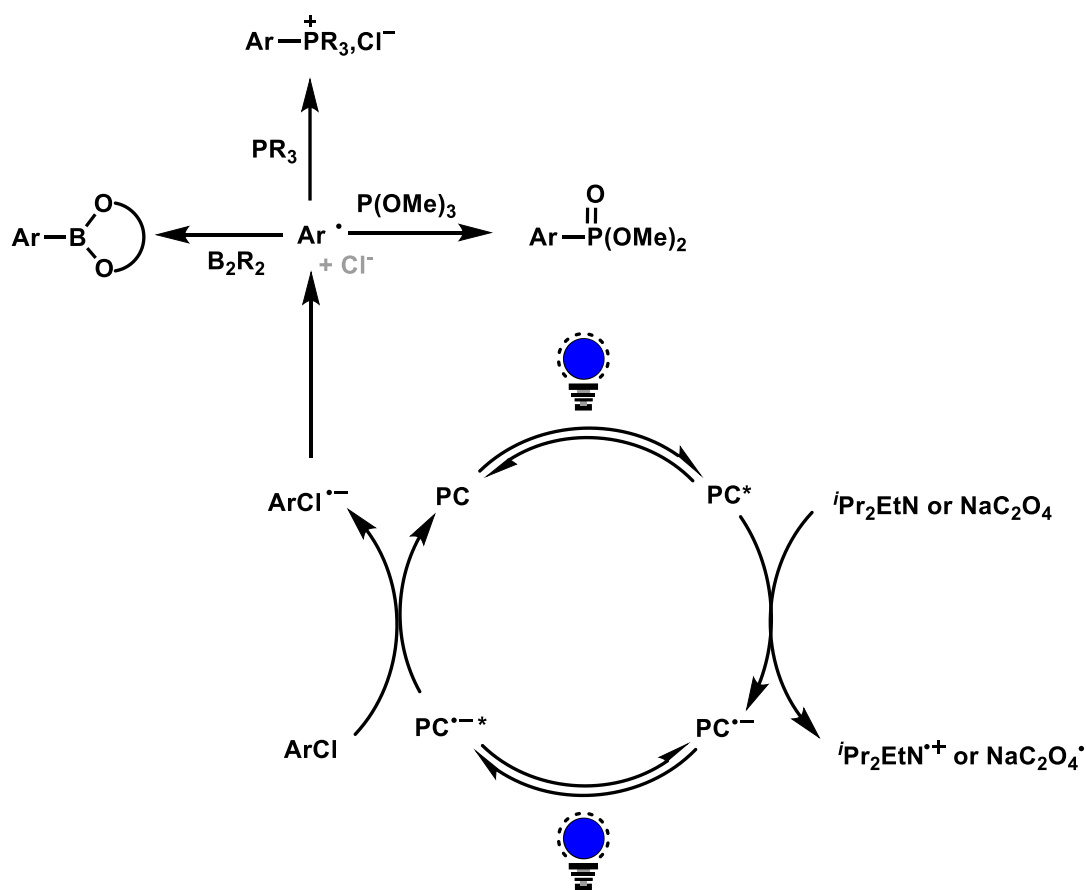


Figure III-50: Coupling examples and proposed mechanism of the aryl radical generated by ConPET.

This topic of radical anion excited states as super-reducing agents currently knows a debate about the link between the lifetime of radical anions and their credibility as active reducing agents. It will be detailed further in this chapter and is the starting point of this work, through the study of D-A cyanoarenes radical anion solutions under irradiation.

**Beyond SETs: Electrophotocatalysis (e-PC)**<sup>89,90,91,92</sup>

More details on this topic are given in chapters III.4 and 5.

In the ConPET process, reduction of the PC occurs through SET with a sacrificial electron donor. The use of several equivalents of sacrificial electron donor is not without consequences, and alternative pathways for the generation of the photocatalyst radical anion are necessary. Electrochemistry comes as the method of choice to do it. The radical anion can be generated by electrolysis if the potential applied to the solution is lower than the redox potential of PC/PC $\cdot^-$ . It allows to get rid of sacrificial electron donor at the cost of a usually unreactive supporting electrolyte such as tetrabutylammonium hexafluorophosphate TBAPF<sub>6</sub> (0.1 M). Combined with light irradiation in the surroundings of the electrolysis electrode, it becomes electrophotocatalysis (e-PC).

It was demonstrated to work in several examples using for instance a PDI derivative – NpMI, as the electrophotocatalyst (Figure III-51).<sup>92</sup>

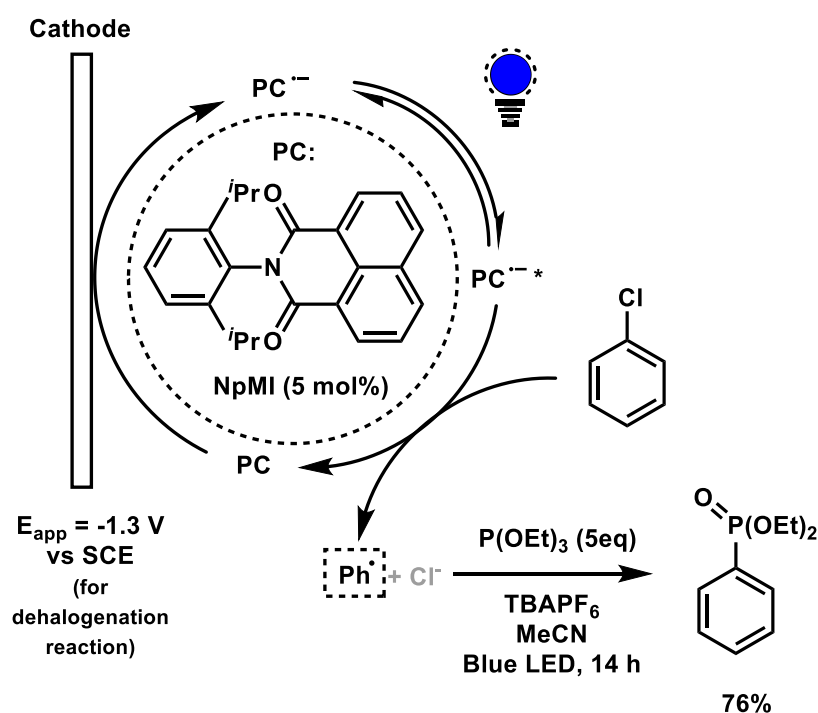


Figure III-51: Example and proposed mechanism for the aryl chloride reduction by e-PC using NpMI followed by phosphorylation.

This method was also applied successfully to D-A cyanoarenes using 4DPAIPN to induce cleavage of C(sp<sup>2</sup>)-N or C(sp<sup>2</sup>)-O bonds in aromatic ammoniums or phosphate esters (Figure III-52).<sup>89</sup> The same study also showed that NpMI, previously described, displayed an atypical kinetic profile that indicates decomposition towards a more active specie. 4DPAIPN however remained stable and could reduce a substrate with a redox potential as low as -3.54 V vs SCE.

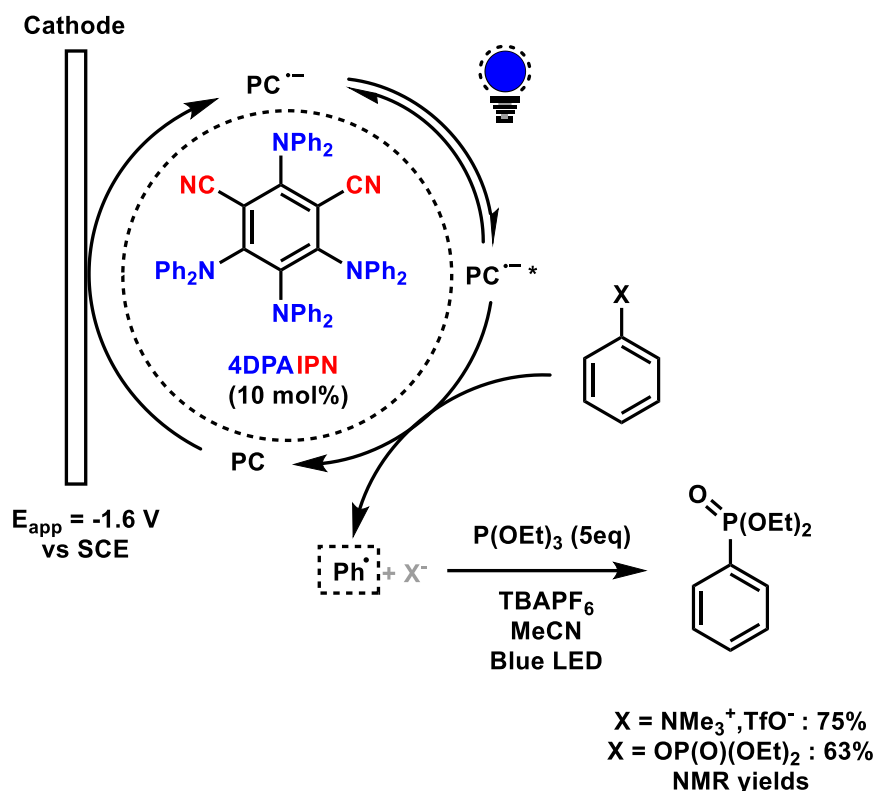


Figure III-52: Example and proposed mechanism for the Ar-X reduction by e-PC using 4DPAIPN followed by phosphorylation.

### 3.2. Energy Transfer

Before jumping into more details on the methods, mentioning energy transfer examples seem necessary as this process also involves a key reactivity of excited state photocatalysts.<sup>93,94</sup>

D-A cyanoarenes as energy transfer mediated photocatalysts was elegantly studied and applied by Zhang and coworkers in *E* to *Z* stilbene isomerization and in Ni/photoredox dual catalysis for the cross-coupling of carboxylic acids and aryl bromides.<sup>95</sup> They showed that the properties of the photocatalyst can be finely tuned through structural changes to improve triplet-triplet energy transfer efficiency. The results for the isomerization of stilbenes of over 10 D-A cyanoarenes were compared to their triplet state energies. The best results were obtained with 4CzTPN which triplet state energy lies below the one of *Z*-stilbene and above the one of *E*-stilbene. Photocatalysts with higher triplet energy than *Z*-stilbene resulted in much lower selectivity. Regarding the cross-coupling reaction, they showed that two pathways were available, providing two different products. Namely the ET product resulting from electron transfer and the EnT product resulting from energy transfer. Depending on the oxidation potential of the photocatalyst, one or the other could be favored. 4CzIPN yielded only the ET product, owing to its high excited state oxidation potential, while 4DPAPN yielded mostly the EnT adduct.

In a similar line of work, Lakhdar and coworkers merged olefin metathesis with energy transfer mediated photocatalysis to afford the selective synthesis of Z-stilbene derivatives using the normally *E*-selective Grubbs catalyst and 4CzIPN.<sup>96</sup>

The example depicted in Figure III-53 shows the alkylation of lepidine (4-methylquinoline) with an alkyl radical generated from a non-activated alkane: cyclohexane.<sup>97</sup> The two key steps are on one hand the generation of the  $\text{SO}_4^{\bullet-}$  radical anion that engages in HAT with cyclohexane and on the other hand the energy transfer between 4CzIPN excited state and lepidine ground state. The combination of the alkyl radical with the excited state lepidine allows the formation of the alkylated lepidine after a final HAT from  $\text{SO}_4^{\bullet-}$ .

Regarding the formation mechanism of  $\text{SO}_4^{\bullet-}$ , two productive energy transfer pathways were considered. Energy transfer from 4CzIPN\* to lepidine and to peroxodisulfate ion. Stern-Volmer experiments indeed showed that both lepidine and peroxodisulfate quench 4CzIPN excited state, despite lepidine display quenching kinetics 7 times the ones of peroxodisulfate. Direct light absorption of light from peroxodisulfate was also proposed as a productive pathway.

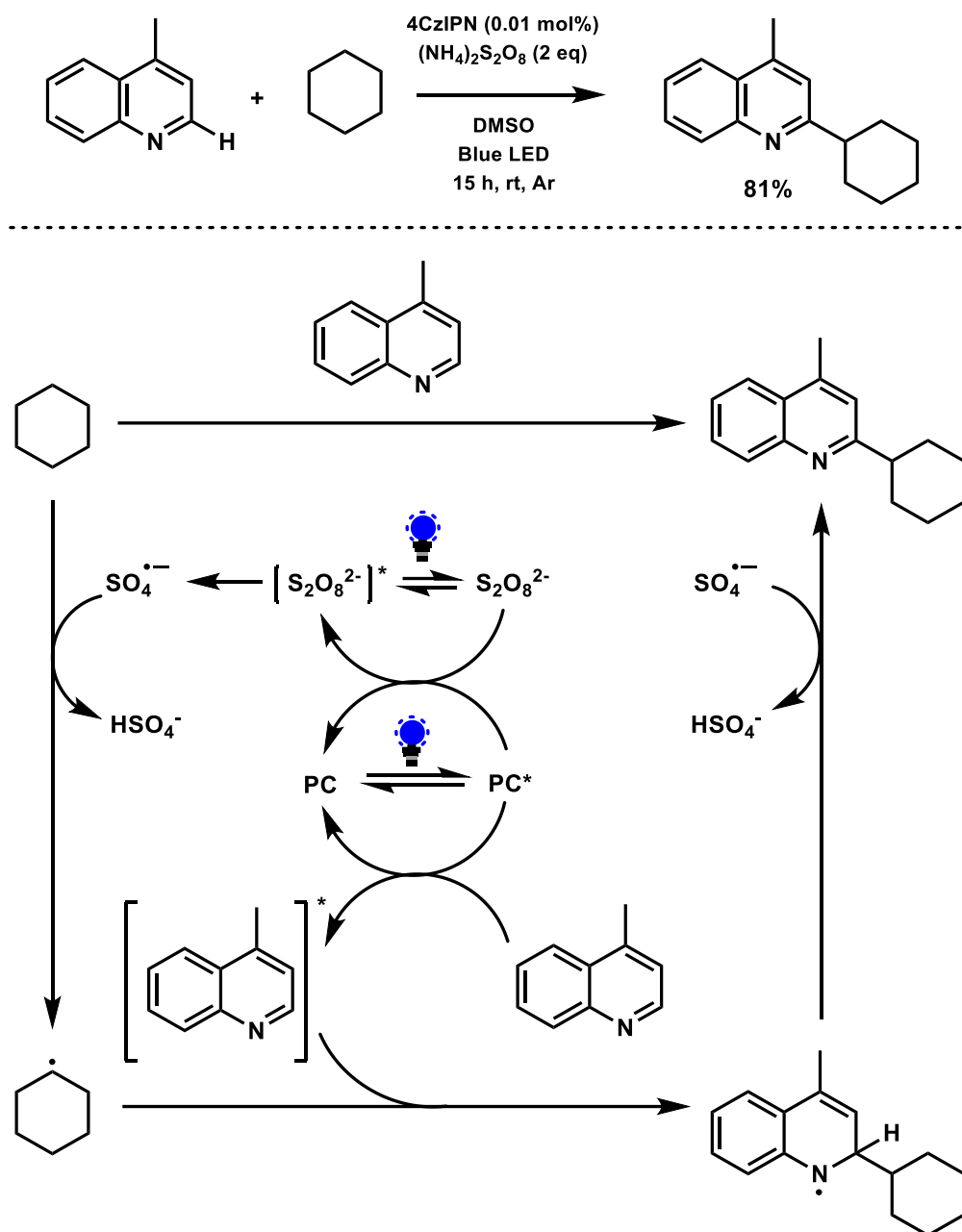


Figure III-53: Example and proposed mechanism for the energy transfer mediated radical alkylation of lepidine

### 3.3. Combined Electron and Energy Transfers

Obviously, electron and energy transfers are not two completely independent separated processes. Both may occur in the same reaction, in various extents. They may occur in the same catalytic cycle as well, provided the conditions match this criterion.

Similarly to the previous energy transfer induced isomerization, energy transfer to the E-alkene product of a copper/photoredox dual catalysis cross-coupling resulting in its isomerization to the Z isomer in a good 80:20 ratio.<sup>98</sup>

The example in Figure III-54 shows a combination of electron transfer and energy transfer. Electron transfer follows a classical photoredox cycle between the photocatalyst excited state and a dihydropyridine derivative to generate an alkyl radical. The alkyl radical then reacts with a thiosulfonate to yield a thioether. Triplet-triplet energy transfer from the photocatalyst to triplet oxygen for the generation of singlet oxygen allows the oxidation of the thioether previously formed to a sulfoxide.<sup>99</sup>

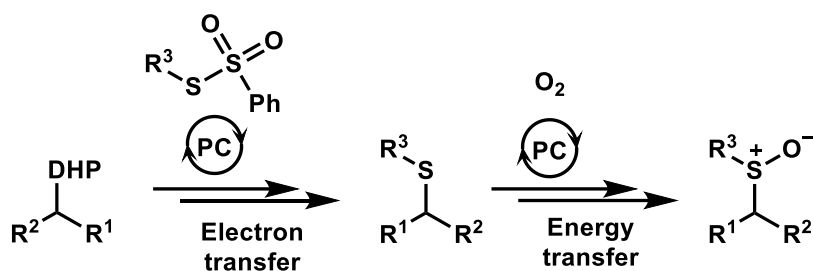


Figure III-54: Consecutive electron and energy transfer example

#### 4. Donor-Acceptor Cyanoarenes Radical Anions

##### 4.1. Excited states multiplicity and lifetimes: The lifetime debate

We have discussed singlet and triplet states. Much less is known about the photophysical and photochemical behaviors of the corresponding doublet states  $A\bullet^-$  and  $D\bullet^+$ . The quartets may be worth considering in that case, but it is beyond the limits of this work. They will be considered inaccessible as an acceptable general consideration.

The fate of excited doublet states and their activity in photochemical transformations is currently debated.

To discuss this, we must expand the view from donor-acceptor cyanoarenes to other photocatalysts, namely perylene diimide PDI and dicyanoanthracene DCA. Other photocatalysts were also developed and won't be discussed here (Figure III-55).



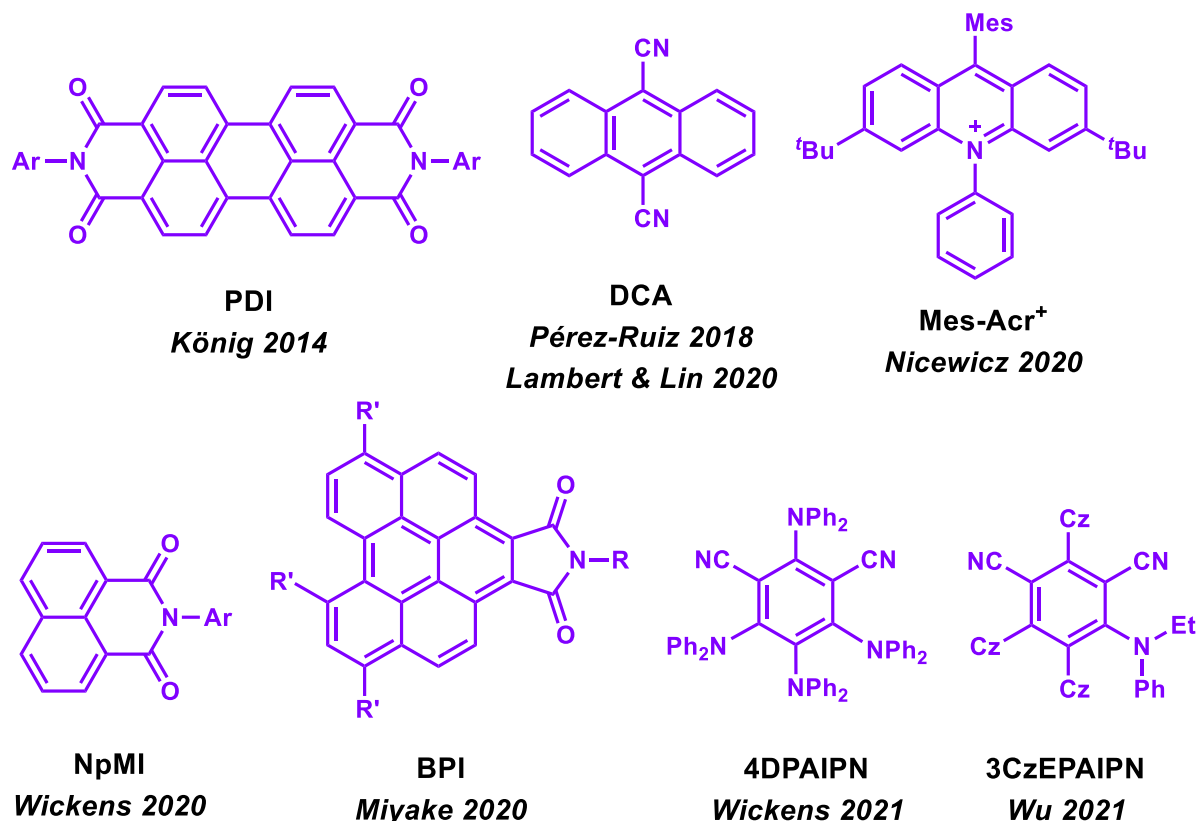


Figure III-55: Electron primed photocatalysts examples (ConPET or e-PC) since 2014

A photocatalyst radical anion is generated through single electron transfer in photoredox reductive quenching cycles or by electrochemical methods. Methodologies to enhance the reducing power of photocatalysts has been to irradiate the radical anion to generate the PC doublet excited state (conPET, e-PC), which is believed to be highly reducing for several species.<sup>100</sup> Analysis seem to correlate quite well with the theory since nanosecond lifetimes are observed and required to reach molecules encounter and interaction timescales.

Several authors have claimed the effective use of PDI<sup>•-</sup>\* (E(PDI/PDI<sup>•-</sup>\*) ~ -1.87 V vs SCE) and DCA<sup>•-</sup>\* (E(DCA/DCA<sup>•-</sup>\*) ~ -3.2 V vs SCE) as “super reducing agents” for chemical transformations.

However, as stated by Nocera, doublet excited states lifetime is commonly extremely short, on the picosecond timescale (Figure III-56), because nonradiative decay to the doublet ground state is almost barrierless.<sup>101</sup> Therefore, the observed lifetime, obtained through indirect measurements, may not be the radical anion's but the ones of by-products. Results claiming DCA radical anion excited state to be the active super-reducing specie were proven wrong; impurities from the degradation of the radical anion excited state were instead involved. The same observations were made for perylenediimide (PDI).<sup>102,103</sup> Another study confirmed the activity of PDI<sup>•-</sup>\* on some electron deficient aryl substrates with redox potentials > -1.7 V vs

SCE but does not observe quenching for the ones with redox potentials  $< -1.7$  V vs SCE.<sup>87</sup> A supposition is given that the reduction for those substrates still occurs but with very limited efficiency which explains the low conversion and slow reaction kinetics. So far, the unambiguous measurement provided a radical anion excited state lifetime similar to PDI was 0.53 ns.<sup>104</sup> PDI $\bullet^-$  is said to have a lifetime of 145 ps, while DCA $\bullet^-$  is said to have 5-10 ns lifetime in some papers,<sup>102</sup> or to be much smaller than 5 ns,<sup>105</sup> a statement which is supported by a recent publication which provides a 3-5 ps lifetime instead.<sup>106</sup>

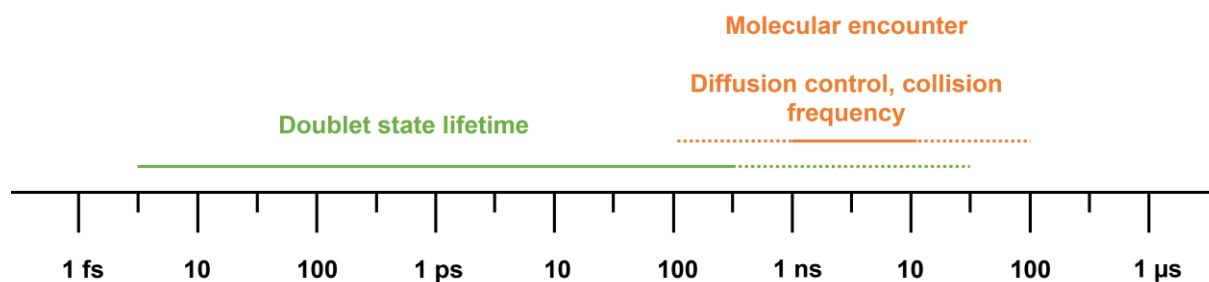


Figure III-56 : Time scale showing the difficulty for doublet states excited states to engage in bimolecular electron transfer.

The applicability of D-A cyanoarenes was recently widened with the work of Wu and coworkers who showed a consecutive photoinduced electron transfer (ConPET) occurring supposedly from 3CzEPAIPN $\bullet^-$ . The authors suggest a long-lived radical anion excited state (12.95 ns), which is either astonishing or wrong according to the previous discussion. A similar work was also carried on 4DPAIPN. E(4DPAIPN/4DPAIPN $\bullet^-$ ) according to the publication is estimated at about -3.38 V vs SCE. If all these information are in fact true, we could talk about a mini revolution in the scientific area!

However, these results stand on the ground of the debate regarding the active species in photoinduced reduction mechanisms.

It then becomes important to further investigate 3CzEPAIPN behavior, which could be a useful milestone to feed the current debate.

Notably, in Wu's method, diisopropylethylamine was used as a sacrificial electron donor.

Amines are commonly used in photoredox chemistry for such purpose. However, it is known that the generated by-products, including transient radicals, are far from innocent, and could even act as active dehalogenation agents through XAT as proposed by Leonori *et al.*

What we believe to be contradictory information in the supporting information of Wu's paper also sparked the curiosity to find another approach to the generation of the radical anion's excited state and study it. In the main text, the radical anion solution is described as "light yellow", which can be seen in the supporting information (Figure III-57, top). However, in the

same supporting information, the radical anion solution obtention in NMR tube provides a deep orange solution (Figure III-57, bottom).

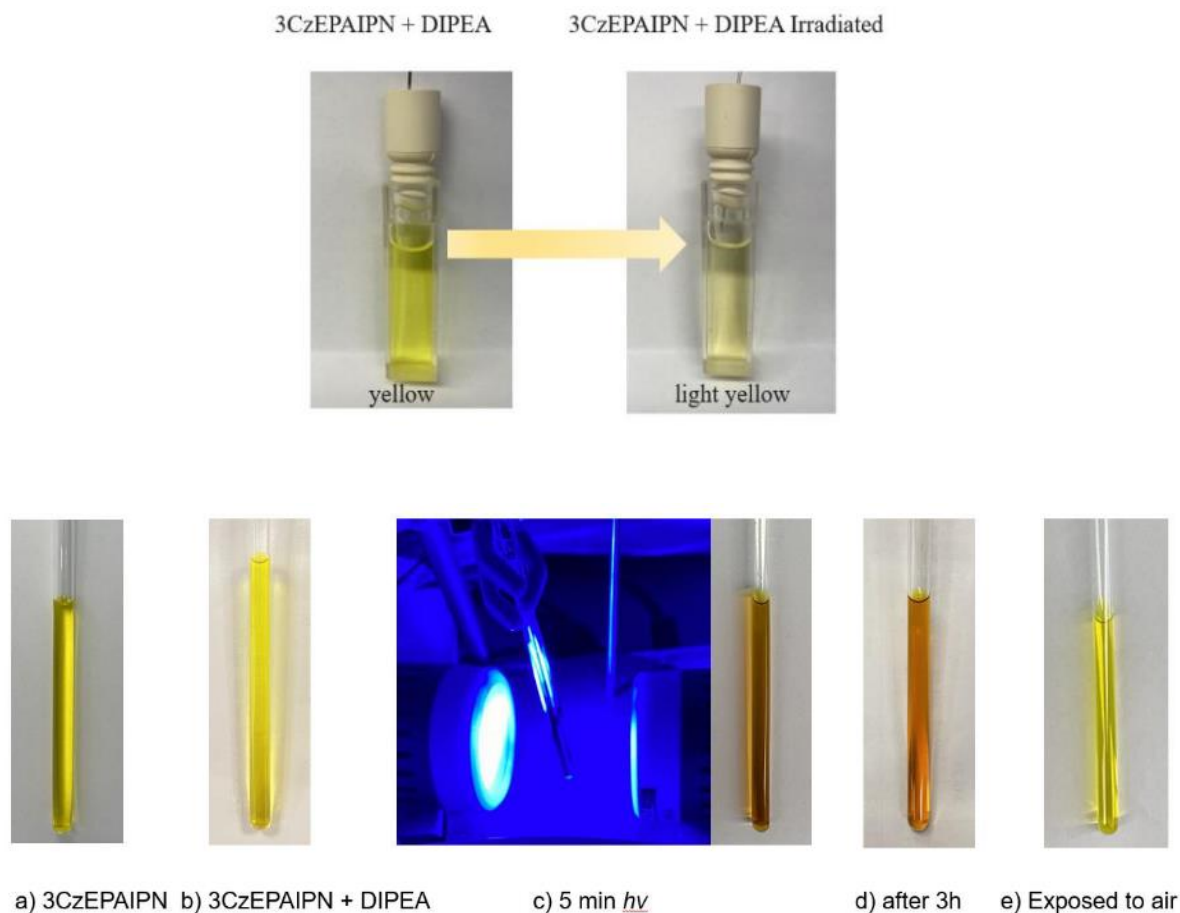


Figure III-57: Inconsistency in the irradiation of a 3CzEPAIPN+DIPEA solution, top picture provides a light yellow solution while the bottom one provides an orange solution. The concentration of both examples differs. Reproduced with permission from the supporting information of reference 57 (Copyright 2021 American Chemical Society).

This work addresses the radical anion generation by electrochemical methods to discard the possibility of an amine interference.

#### 4.2. Photocatalyst stability: Degradation pathways and incognito active species

As mentioned before, photocatalysts are prone to chemical modification, commonly called decomposition.

Donor-acceptor cyanoarenes are prone to decarbazolylolation.<sup>82,32</sup> Carbazole was indeed observed by HR-MS in reaction mixtures, and is most likely the degradation pathway of PC<sup>-</sup> which displays an irreversible redox wave in CV. This mechanism is most likely non-productive, thus considered as a “degradation pathway”.

In donor-acceptor cyanoarenes, nitriles may act as good leaving groups. We have presented decyanation of 1,4-dicyanobenzene and 1,2,4,5-tetracyanobenzene by alkyl radicals at the beginning of part 3.1.<sup>67,68</sup>

The photostability issue of donor-acceptor cyanoarenes was mentioned as a limiting factor at the end of part 1.<sup>23</sup>

Correlation between photostability and decyanation was indeed demonstrated recently in the presence of alkyl radical.<sup>60</sup> The alkyl radical, generated by SET from the PC to the corresponding carboxylate, was proposed to add on PC<sup>•-</sup> in ipso position of a nitrile. Subsequent elimination of CN<sup>-</sup> led to the photosubstituted adduct. Decent (~40%) to excellent yields (~90%) were obtained. The substitution product displays competing properties compared to the starting cyanoarene photocatalyst. This mechanism cannot be considered as inactive in other photocatalytic cycles, reminding once again the difficulty to easily rationalize reaction mechanisms.

Another study on this topic was published in 2023, addressing the formation and degradation of donor-acceptor cyanoarenes radical anions engaged in the ConPET process.<sup>82</sup> Sacrificial amine electron donor is used and was assessed to impact the reaction in halogenoarenes reductive elimination. Extremely low catalyst loadings were attainable (0.005 mol%) where Ir(ppy)<sub>3</sub> efficiency dropped from 100 to 26% at 0.05 mol%; another example where organic photocatalyst proved superior to heavy-metal organometallic complexes.

Because carboxylates and amines are used as the most common sacrificial electron donors to generate photocatalyst radical anion, and that radical anions are potent photoreductants able to reduce the recalcitrant aryl chlorides, both carboxylates and amines have been studied in aryl chlorides reduction reactions.<sup>107,108</sup>

Knowing their potent “parasite” activity, we thus decided to explore 3CzEPAIPN<sup>•-</sup> properties by electrochemical means and its potent compatibility with e-PC.

## 5. Results and discussion

The aim of this work, done in a collaboration with Cyrille Costentin and coworkers, is to get insights into the photophysical and photochemical properties of D-A acceptor cyanoarene radical anions to clarify current literature results and clear the way for future investigations. All experiments were performed in Département de Chimie Moléculaire (DCM) in Grenoble.

The methodology involves 7 steps:

- Assessment of the potential and reversibility of the PC/PC $\bullet^-$  redox wave by CV in a glovebox.
- Measurement of the UV-Vis absorption spectrum of the PC.
- Bulk electrolysis by applying a potential below  $E_{1/2}(\text{PC}/\text{PC}\bullet^-)$  and *in-situ* measurement of the evolution of the UV-Vis spectrum. When electrolysis is complete, the UV-Vis spectrum of PC $\bullet^-$  is obtained.
- EPR of the electrolyzed solution to assess the presence of a radical specie.
- Luminescence analysis of the electrolyzed (PC $\bullet^-$ ) and non-electrolyzed (PC) solutions at the wavelength of the pulse of the time-resolved fluorescence apparatus ( $\lambda_{\text{exc}} = 409$  nm).
- Nanosecond excited states lifetime measurement of the electrolyzed (PC $\bullet^-$ ) and non-electrolyzed (PC) solutions by time-resolved fluorescence measurement ( $\lambda_{\text{exc}} = 409$  nm).
- Quenching studies of the excited states lifetime of the radical anion solutions using various concentrations of chlorobenzene.

For practical reasons, all analysis couldn't be carried out on each of the 5 molecules available. The method could be fully applied to 3CzEPAIPN and 4CzIPN.

## 5.1. 3CzEPAIPN and 3CzEPAIPN $\bullet^-$

3CzEPAIPN was the molecule of choice for this study, since direct comparison with the literature is possible.<sup>57</sup> This D-A cyanoarene surprisingly doesn't display TADF. Such observation is only explained with the vague involvement of "flexibility" introduced with the "flexible" ethyl and phenyl moiety which seems incompatible with the long radical anion excited state lifetime measured. This explanation is quite incomplete and unsatisfactory. What is sure is that a singular behaviour is induced by the modification of one carbazole for an ethylphenylamine moiety.

### 5.1.1. Characterization

#### Cyclic voltammetry

The first characterization was done by electrochemistry to reproduce literature results and verify that everything was in good agreement with previous reports.

The cyclic voltammetry of a 0.5 mM 3CzEPAIPN solution in MeCN with 0.1 M TBAPF<sub>6</sub> as the supporting electrolyte provided the following potentials (Figure III-58):

$E_{\text{pc}} = -1.738$  V vs 10 mM Ag/AgNO<sub>3</sub>,  $E_{\text{pa}} = -1.668$  V, and  $\Delta E_{\text{p}} = 70$  mV.

$E_{1/2}(3\text{CzEPAIPN}/3\text{CzEPAIPN}^{\bullet-}) = -1.703 \text{ V vs } 10 \text{ mM Ag/AgNO}_3 \text{ or } -1.403 \text{ vs SCE}$  which correlates nicely with the literature value of  $-1.42 \text{ V vs SCE}$ .

From this point, all potentials values will be given as measured vs  $10 \text{ mM Ag/AgNO}_3$  reference electrode in MeCN with  $0.1 \text{ M TBAPF}_6$  supporting electrolyte using IUPAC plotting convention, platinum wire counter electrode and glassy carbon working electrode.

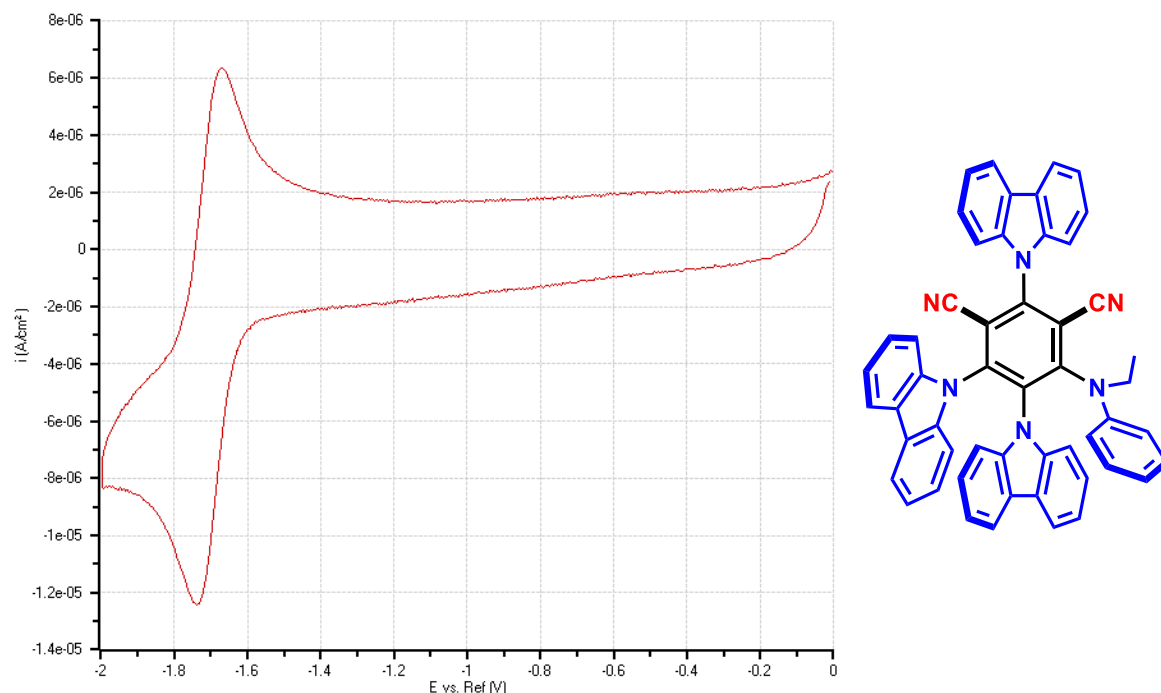


Figure III-58: Voltammogram of a  $0.5 \text{ mM } 3\text{CzEPAIPN}$  solution in MeCN with  $0.1 \text{ M TBAPF}_6$  from 0 to  $-2 \text{ V}$ . Sweeping direction from right to left at  $100 \text{ mV/s}$  scan rate. On the right, a reminder of  $3\text{CzEPAIPN}$  structure.

When necessary, measured values are expressed vs SCE by applying a  $+0.300 \text{ V}$  conversion factor to measured values. Ferrocene was not used as the internal standard for these preliminary results (and we showed that up to  $0.2 \text{ V}$  shift can also be expected with this method anyway depending on the value chosen for the correlation between ferrocenium/ferrocene and SCE).

Figure III-59 shows the cyclic voltammetry when the potential is pushed up to  $-3 \text{ V}$  and a second irreversible wave that we can attribute to the anion of  $3\text{CzEPAIPN}$  is obtained. The decomposition most likely leads to a loss of carbazole as it was shown in the literature for  $4\text{CzIPN}$ .<sup>32</sup>

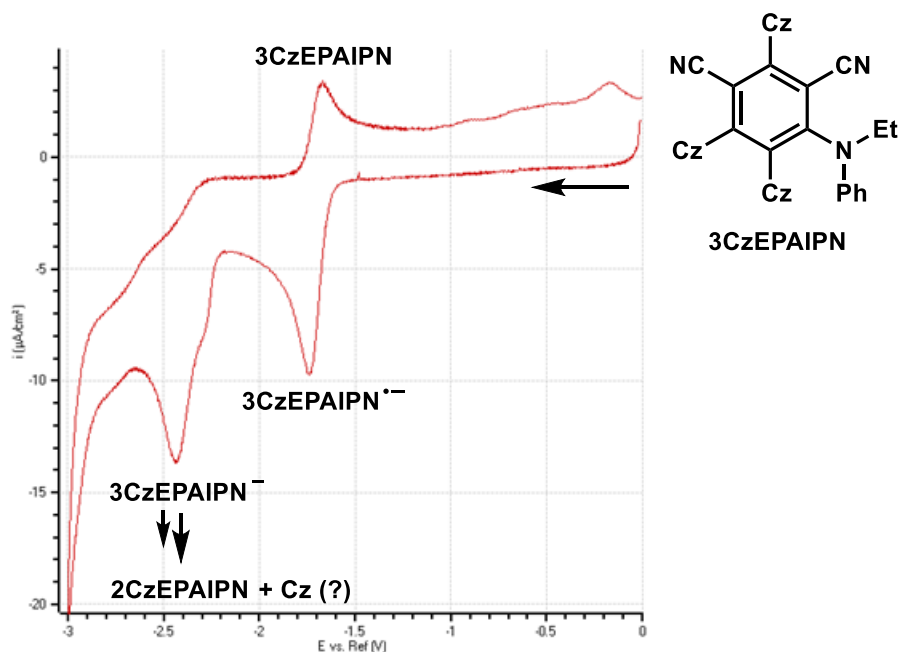


Figure III-59: Voltammogram of a 0.5 mM 3CzEPAIPN solution in MeCN from 0 to -3 V. Sweeping direction from right to left at 100 mV/s scan rate

With a  $\Delta E_p = 70$  mV, the reversibility of the electron transfer can be considered good (the ideal theoretical value is 57 mV at 25 °C).<sup>48</sup>

The bulk electrolysis applied potential ( $E_{app}$ ) was picked at -1.9 V. Indeed, one can see on the scan that goes down to -3 V that -1.9 V stands way before the second redox wave representative of the redox couple  $3CzEPAIPN^{\bullet-}/3CzEPAIPN^-$  which is irreversible (Figure III-59).

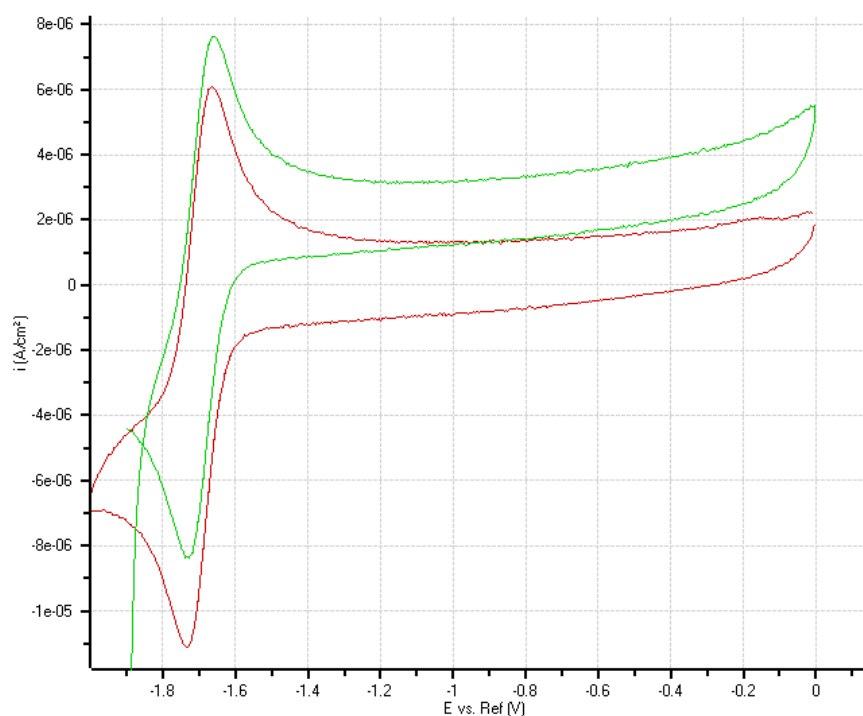


Figure III-60: Voltammogram of a 0.5 mM 3CzEPAIPN solution before (red, from 0 to -2 V. Sweeping direction from right to left at 100 mV/s scan rate) and after electrolysis (green, from -1.9 V to 0 V. Sweeping direction from right to left at 100 mV/s scan rate)

The reversibility of the one electron reduction of 3CzEPAIPN was also assessed by performing CV from -1.9 V to 0 V after bulk electrolysis which gave a similar profile as before electrolysis (Figure III-60).

The working conditions were assessed to reproduce correctly previous literature observations.

### UV-Vis absorption spectra

Reduction by bulk electrolysis ( $E_{app} = -1.9$  V vs 10 mM Ag/AgNO<sub>3</sub>) of 3CzEPAIPN occurred smoothly, providing the UV-Vis spectra overtime as seen in Figure III-61. The duration of electrolysis ranged between 30 and 60 minutes whether a carbon felt or a glassy carbon plate was used. To prevent reproducibility issues and the experimental difficulties that arose when the carbon felt fell in the solution, the glassy carbon plate was selected as the bulk electrolysis electrode of choice.

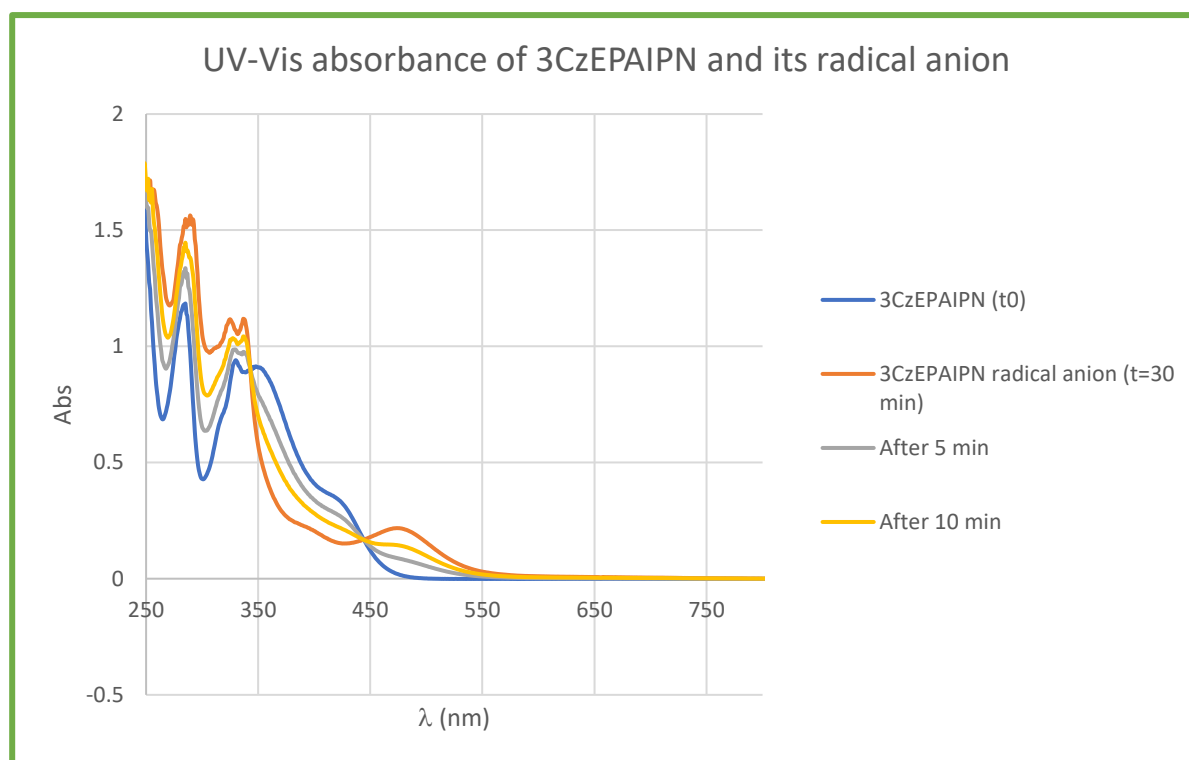


Figure III-61: Absorbance profile of 3CzEPAIPN solution overtime during electrolysis ( $E_{app} = -1.9$  V).  $E_{app}$ : applied potential.

Two isosbestic points are clearly observed at 344 and 446 nm. These points, where the absorbance of the solution doesn't change, show that the electron transfer is clean and that a single reduction product is obtained from a single reactant.

When the absorbance profile does not evolve anymore, it is considered as the one of the radical anion. However, the reduction may be incomplete for several reasons. The spectrum is attributed to the radical anion as a very close guess to the expected pure 3CzEPAIPN<sup>•-</sup> solution



spectrum. A clear modification of the spectrum is observed. Furthermore, *ca.* one electron per molecule was provided as *ca.* 0.6 C passed through the solution. Following Faraday's law which provides the expected electric charge to pass through the solution depending on the number of moles of electrons injected:

$$Q = nF \text{ (equation III.26)}$$

with  $n = 0.5 \text{ (mM)} \times 12 \text{ (mL)} = 0.6 \text{ nmol}$  (1 electron per molecule),  $Q = 0.6 \times 10^{-6} \times 96,485 = 0.58 \text{ C}$ .

The current of the solution also stabilized after some time and neighbored 0 which indicates that the reduction is almost quantitative and cannot go any further. On Figure III-62 which shows the evolution of the current overtime during bulk electrolysis, the current depletes by 85% over 60 minutes and then stabilizes.

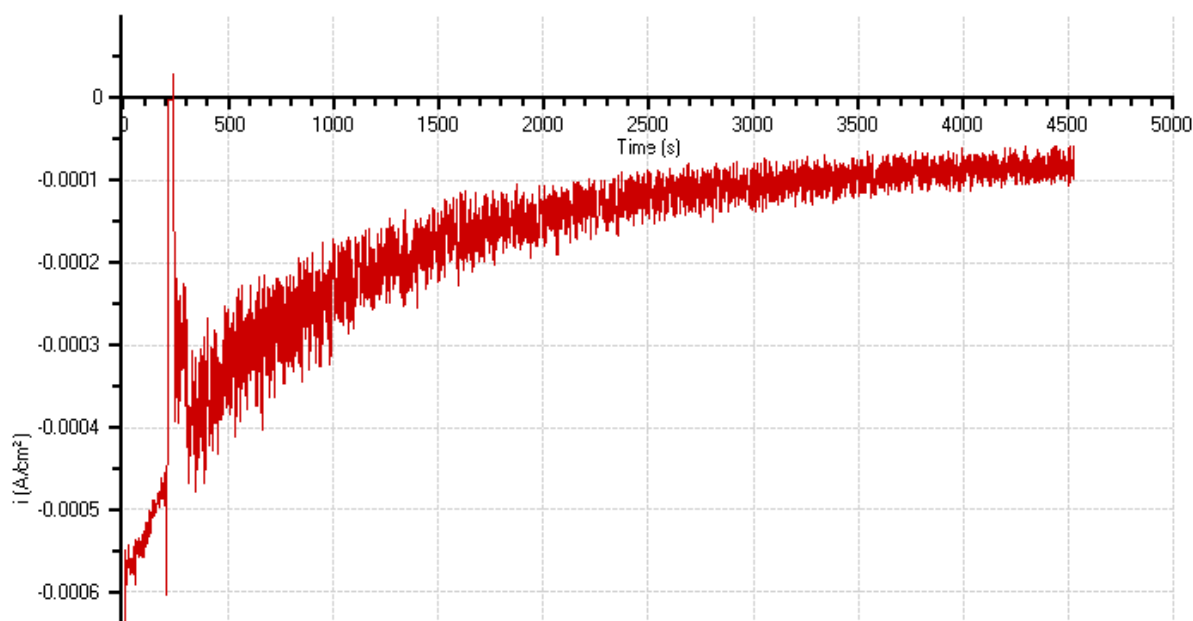


Figure III-62: Current overtime during the bulk electrolysis of a 0.5 mM 3CzEPAIPN solution. An artifact is observed around 200 s as the working electrode disconnected until it was properly reconnected.

An increase of absorption between 450 and 600 nm matches the naked-eye orange solution observed.

The spectrum obtained for the radical anion differs from the one given by Wu and coworkers in their publication ( $3.2 \times 10^{-5} \text{ M}$  3CzEPAIPN+DIPEA solution in MeCN). It seems however more coherent in all regards and fits the colour they obtained by 456 nm irradiation of a  $1.42 \times 10^{-2} \text{ M}$  3CzEPAIPN+DIPEA solution in MeCN in NMR tubes (shown in their supplementary information).

Calculations done by Isabelle Dixon in a collaboration are presented hereafter and go in the way of our experimental results (Figure III-63).

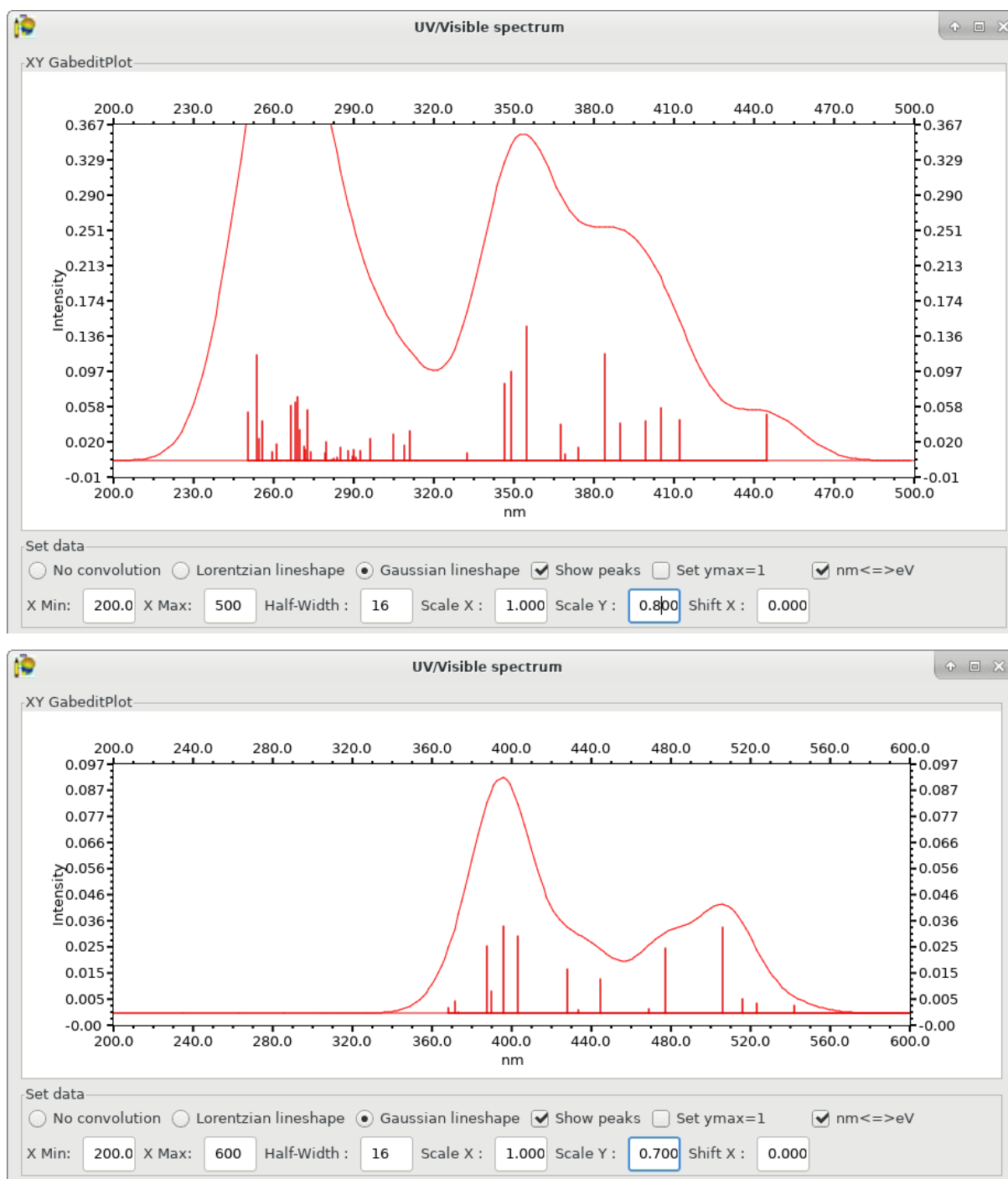


Figure III-63: Plotted UV-Vis calculation results for 3CzEPAIPN (top) and 3CzEPAIPN•<sup>-</sup> (bottom)

Comparable theoretical and experimental discrepancy for 3CzEPAIPN and 3CzEPAIPN•<sup>-</sup> was obtained showing the relevance of the comparison between computed absorptions. Good theoretical and experimental agreement for the absolute values was also obtained with a  $\Delta_{\text{exp-theo}}$  of 0.17 eV for 3CzEPAIPN and 0.13 eV for 3CzEPAIPN•<sup>-</sup> (NB: discrepancies up to 0.3 eV are usual in the literature).

Theoretical calculations agree that the radical anion will have a red-shifted absorption with respect to neutral.

The radical anion first strong absorption involves the amine moiety and the next strong absorption involves the state D<sub>9</sub> at 478nm | 2.596 eV and relates to a HOMO-LUMO+8 transition which is purely (PhCN)•<sup>-</sup> to Ph<sub>NEtPh</sub>. These results have the same trend as the calculations done in 2023 by Kwong and coworkers in the case of 4DPAIPN<sup>82</sup> and support the importance of the phenylethylamine moiety in the photophysical behaviour of 3CzEPAIPN.

An explanation for the mismatch between the two experiments was proposed by Kwong and coworkers during the peer review of their publication (Figure III-64).<sup>82</sup> They have shown that a similar UV-Vis absorption shift to the one given by Wu and coworkers (that displays a blueshift instead of a redshift of the absorption) was obtained when one 4DPAIPN nitrile was substituted by a methyl (4DPA-Me-BN).

For 3CzEPAIPN in the presence of DIPEA, one nitrile can be substituted by an ethyl to provide 3CzEPA-Et-BN since one DIPEA radical cation major evolution pathway was shown to be ethyl radical generation through 1,2-methyl shift. The substitution could also be done by a methyl radical.

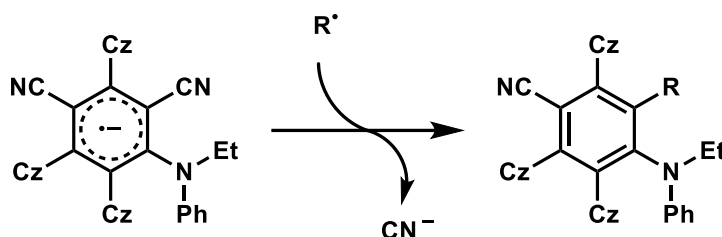


Figure III-64: Radical substitution of a nitrile from 3CzEPAIPN radical anion

The stability of 3CzEPAIPN•<sup>-</sup> was quantified by following the evolution of the UV-Vis spectrum of the 3CzEPAIPN•<sup>-</sup> solution overtime after electrolysis. By following the evolution of the absorbance value at 500 nm where the absorption of 3CzEPAIPN is null, we could estimate a 23% conversion back to the neutral 3CzEPAIPN over 2 hours and 15 minutes. It means that the radical anion remains stable long enough to measure its properties by photophysical analysis under inert atmosphere. Putting the solution in contact with air resulted in a change of coloration from orange to yellow within a few seconds.

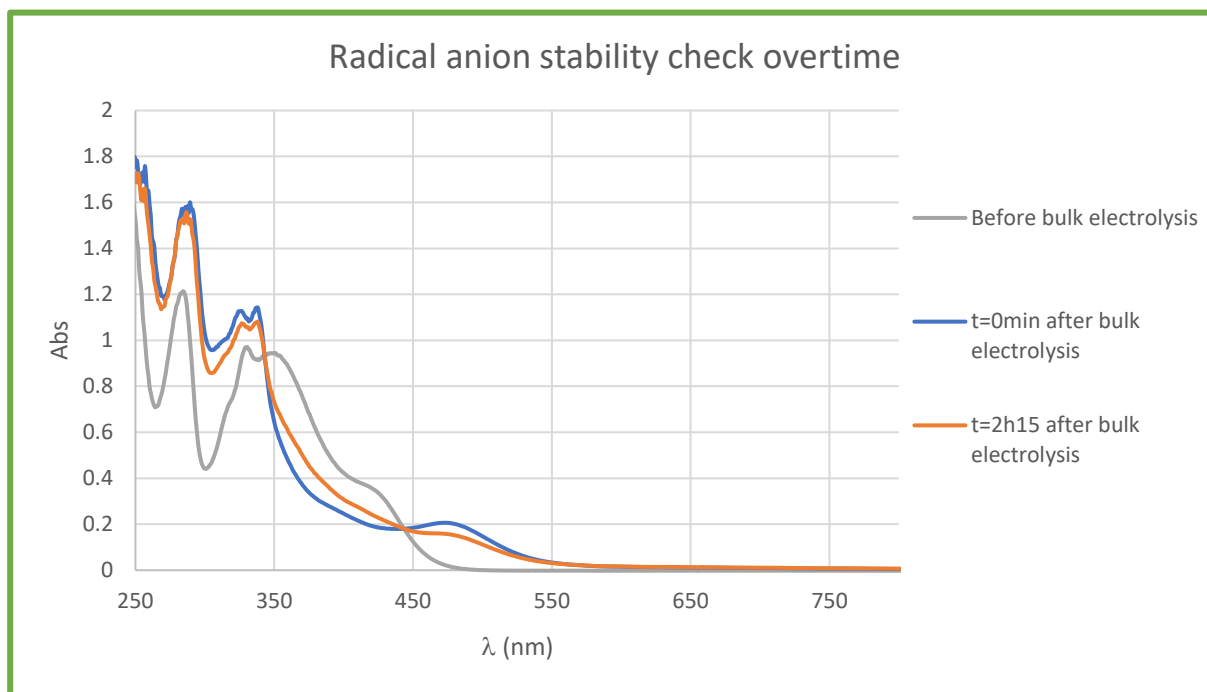


Figure III-65: Radical anion of 3CzEPAIPN stability check overtime 2h15.

We can conclude that electrochemistry is a clean and efficient method for cyanoarene radical anion generation.

### Electron paramagnetic resonance (EPR)

An EPR sample of the previous solution was prepared inside the glovebox and analysed. This experimental analysis allows the observation unpaired electrons. This experiment provided the same signal as the literature (Figure III-66).<sup>57</sup> This confirms the presence of the radical anion and supports the viability of the electrochemical generation of 3CzEPAIPN<sup>•-</sup>.

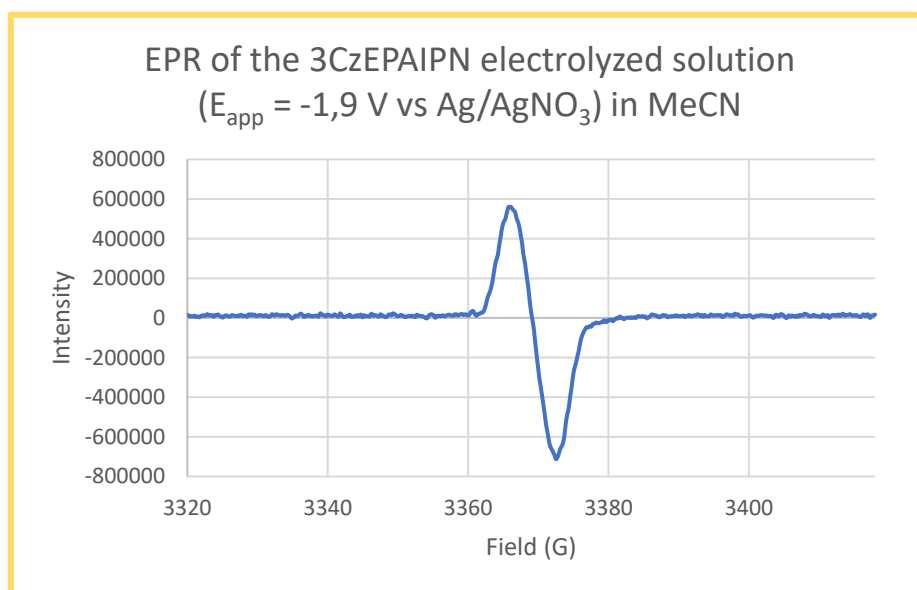


Figure III-66: EPR of the 3CzEPAIPN radical anion solution after bulk electrolysis.

## Luminescence

The luminescence of solutions of 3CzEPAIPN and its radical anion were measured.

Two very different results were obtained. The luminescence of the 3CzEPAIPN solution fits the literature with a  $\lambda_{\text{em}} = 594 \text{ nm} \mid 2.09 \text{ eV}$  and a FWHM = 127 nm | 0.44 eV. The shape of the emission of the solution of 3CzEPAIPN $\bullet^-$  is however very surprising. First, the shape of the emission does not correlate to a single gaussian function. Instead, three emission maxima are observed at 446 nm, along with two lesser ones at 477 nm and 518 nm. Starting from 630 nm, both spectra (3CzEPAIPN $\bullet^-$  and 3CzEPAIPN) superimpose, indicating the possible presence of 3CzEPAIPN in the radical anion solution. Then, the intensity of the emission increases by a substantial margin compared to 3CzEPAIPN.

The excitation wavelength (375 nm in the literature) used here was 409 nm for experimental reasons to match the time-resolved fluorescence apparatus used that has a fixed pulse wavelength of 409 nm.

These results were unexpected and peculiar (Figure III-67).

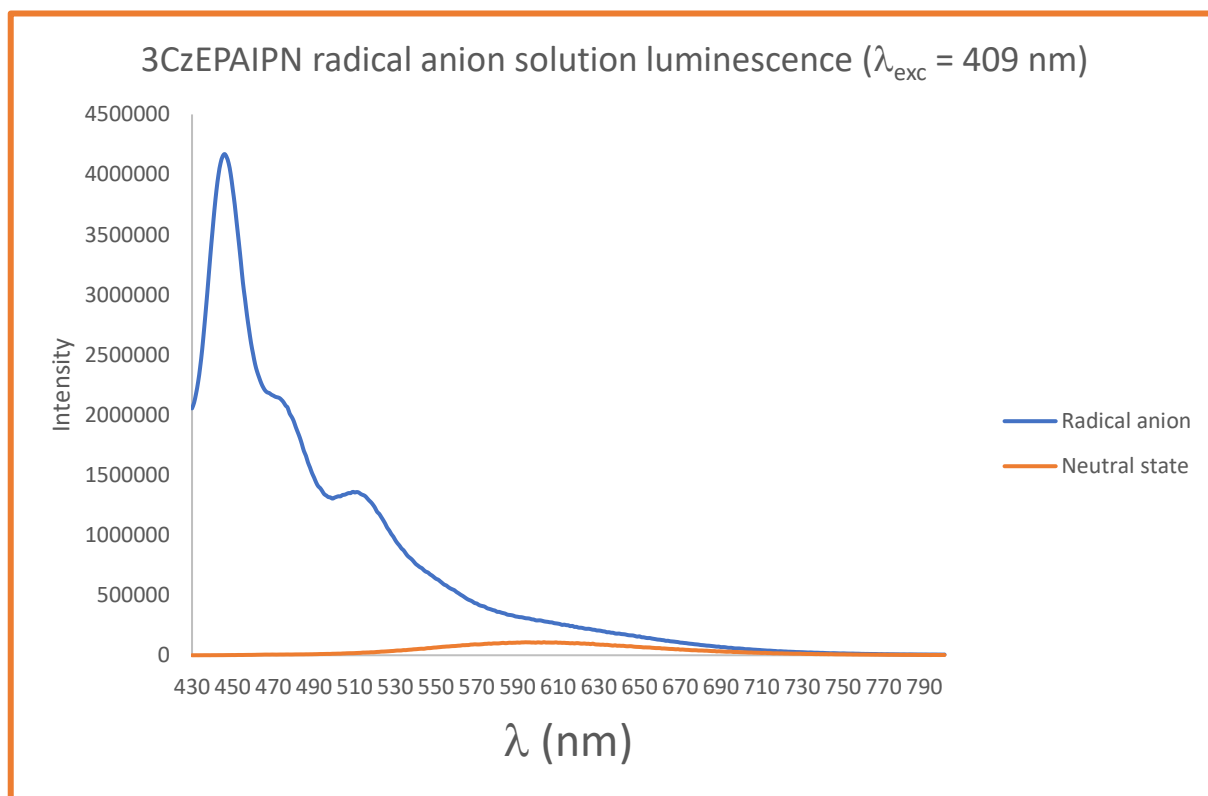


Figure III-67: Luminescence of solutions of 3CzEPAIPN radical anion and 3CzEPAIPN, excitation at 409 nm.

It looks like dual emission with an extra third emission, with a LE emission at a higher energy (lower wavelength, 446 nm) than the CT emission at a lower energy (higher wavelength, 518 nm) with a bigger FWHM. But even then, the third emission at 477 nm isn't explained. These emissions could also be related to different molecules in solution resulting from degradation (protonation of the ethylphenylamine moiety for instance, disproportionation to neutral and anionic species which then degrades), to the presence of excimers (between the neutral and reduced version of the photocatalyst), exciplexes (with the solvent, the supporting electrolyte), ISC to the quartet state, or vibronic structures (Figure III-68).

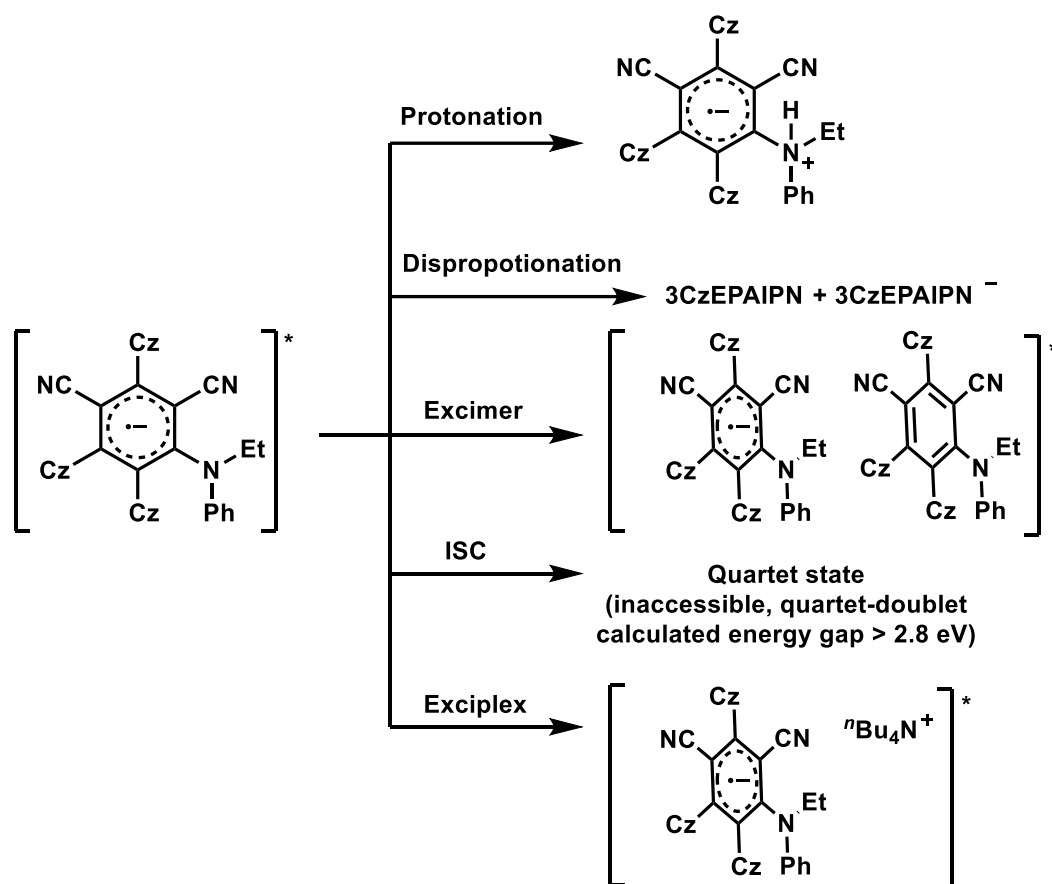


Figure III-68: Radical anion excited state proposed evolution pathways.

Anti-Kasha emission is an emerging topic of interest in material, computational and life science, photophysics and optical spectroscopy.<sup>109–111</sup> In none of them the question of DE in doublet states is mentioned, and photochemical applications of DE from doublet states is to our

knowledge nonexistent. At this point, we wish to state that the determination of the exact origin of this observation requires further in-depth investigation.

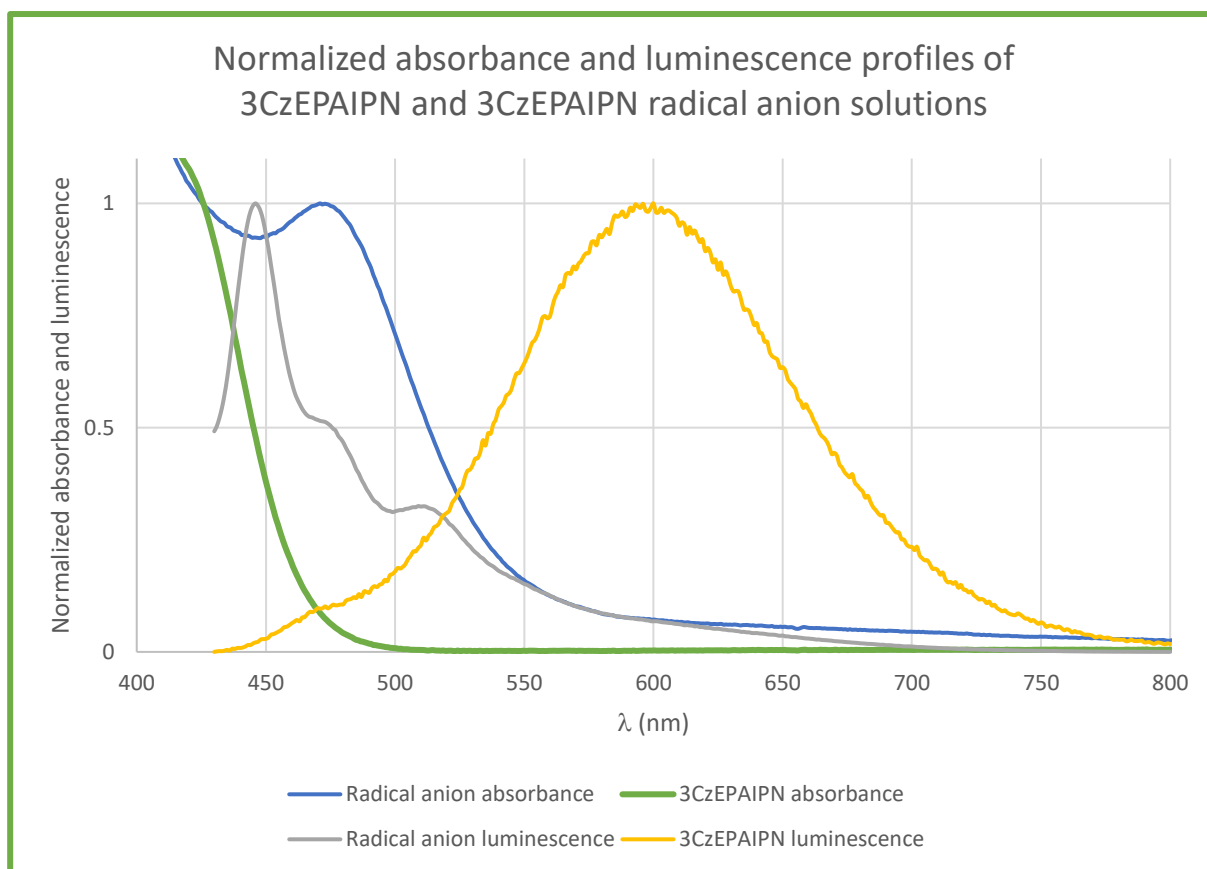


Figure III-69 : EPR of the 3CzEPAIPN radical anion solution after bulk electrolysis.

From Figure III-69, we can see that the radical anion solutions absorbance and luminescence are superimposed. This may mean that the lifetime of the excited state can be virtually extended through self-excitation.

### 5.1.2. Excited-state lifetime measurement by time-correlated single photon counting

In this part, time-correlated single photon counting (TCSPC) experiments were ran on solutions of 3CzEPAIPN and 3CzEPAIPN<sup>•-</sup>. This allows for the determination of the excited state lifetimes present in solution. We have shown previously that the emission profile is composed of multiple maxima.

Four wavelengths were then considered, each one of them correlating to a region on the luminescence profile: 450 nm, 477 nm, 520 nm, 600 nm.

Each lifetime decay requires a proper fitting equation of the form:

$$y = \sum_{i=1}^n A_i e^{-x/t_i} \text{ (equation III.27)}$$

To reach an acceptable tolerance on the error of the fitting values, between one and three parameters usually must be used. The error between the experimental and the fitting curves is measured with  $\chi^2$ .  $\chi^2$  must be between 1 and 1.2 to consider the fitting model acceptable. Each parameter implies a value of A and a value of  $\tau$ . "A" corresponds to the "weight" of the parameter and  $\tau$  to a lifetime.

Let's take as an example the fitting of a curve with the fitting equation that would give the result:

$$y = 80e^{-x/5} + 20 e^{-x/30} \text{ (equation III.28)}$$

This would mean that a 5 ns lifetime weighs for 80% of the intensity decay and a 30 ns lifetime that accounts for 20% of the intensity decay. We then correlate these mathematical values with the lifetimes of physical states.

Fitting worked best in our case with three parameters for 3CzEPAIPN $\bullet^-$  solutions and two parameters for 3CzEPAIPN solutions.

In Wu's paper,<sup>57</sup> 3CzEPAIPN $\bullet^-$  lifetime is obtained as the average value of all lifetimes. Following the previous example, that would mean (30 ns \* 20% + 5 ns \* 80%) that would equal to an average lifetime of 10 ns.

An average lifetime of 19.21 ns (followed at 450 nm) or 9.21 ns (followed at 477 nm) was obtained in our case following this method, longer and shorter lifetimes than the 12.95 ns (followed at 480 nm) given in literature. Several hypotheses must be accepted to say that the lifetime of the radical anion is the one of the average lifetime value, hypotheses with which we disagree.

To obtain the average lifetime following literature procedure, we stated before the equation:

$$\tau_{\text{avg}} = \sum_{i=1 \rightarrow n} [\tau_i \times \%(\tau_i)] \text{ (equation III.29)}$$

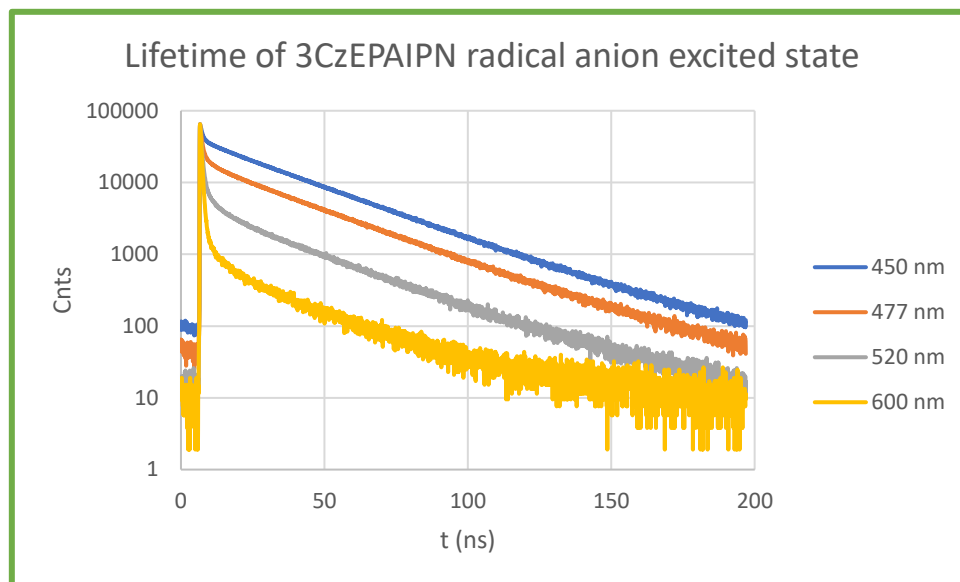
Then, one must agree that this mathematically averaged value physically corresponds to the lifetime of 3CzEPAIPN $\bullet^-$ .

We believe it is more accurate, on the contrary, to consider each lifetime to correspond to an individual physical reality.

We will still display this mathematical average to compare our results to the literature.



In our case, we clearly see that the results depend on the wavelength considered which forbid the simplification to express the results without considering the corresponding emission wavelength. Figure III-70 shows the results of TCSPC analysis of the 3CzEPAIPN $\bullet^-$  solution obtained at four different wavelengths.



$\lambda_{exc}$	3CzEPAIPN $\bullet^-$ *				3CzEPAIPN*			
409 nm								
$\lambda_{em}$	$\tau_1$ (ns) (weight %)	$\tau_2$ (ns) (weight %)	$\tau_3$ (ns) (weight %)	$\tau_m$ (ns)	$\tau_1$ (ns) (weight %)	$\tau_2$ (ns) (weight %)	$\tau_3$ (ns) (weight %)	$\tau_m$ (ns)
450 nm	30.335 (60.95%)	0.746 (32.27%)	7.13 (6.78%)	19.213	n/a	n/a	n/a	n/a
477 nm	30.030 (27.55%)	0.712 (63.22%)	5.32 (9.23%)	9.215	n/a	n/a	n/a	n/a
520 nm	29.47 (6.64%)	0.661 (85.74%)	4.92 (7.62%)	2.90	0.516 (97.84%)	15.94 (2.16%)	n/a	0.85
600 nm	28.71 (1.03%)	0.548 (96.92%)	5.28 (2.04%)	0.93	0.504 (99.78%)	17.6 (0.22%)	n/a	0.5

Figure III-70 : Visual decay of the TCSPC results of 3CzEPAIPN radical anion solution at four different wavelengths (top) and the table providing the lifetimes and their weight for each fitting. Results obtained with 3CzEPAIPN from the same solution before bulk electrolysis are displayed at 520 and 600 nm as a comparison.

At all wavelengths, three similar lifetimes are obtained for 3CzEPAIPN $\bullet^-$ \*: ca. 29.5  $\pm$  1.0 ns, 0.6  $\pm$  0.1 ns, and 6.0  $\pm$  1.2 ns. They will be respectively referred to as long, short, and medium

lifetimes to simplify the discussion. Despite their similarity they can't be considered to represent the same decays without a further look into the results.

The long lifetime represents an important part at 450 nm and its contribution only decreases when the wavelength studied increases, from 61 to 1%. Its contribution significantly drops from 61% to 28% between 450 and 477 nm. It seems coherent with the small FWHM of the 450 nm signal which implies a quick decay of intensity when the wavelength increases. On the other hand, the contribution from the short lifetime goes from 32% to 63% between 450 and 477 nm, and from 63 to 86% between 477 and 520 nm with a diminished value (0.71 to 0.66 ns). The short lifetime values shift from 0.75 ns to 0.55 ns between 450 and 600 nm. We know that at 600 nm the contribution from the neutral 3CzEPAIPN\* should be 0.5 ns. It seems like the lifetime's values are extended at 450 nm because of self-re-excitation. However, because 3CzEPAIPN emission is very low at 450 nm, its 0.5 ns component cannot be responsible for the 0.75 ns observed at 450 nm for 3CzEPAIPN<sup>•-</sup> which suggests another emitting entity with a similar lifetime.

Because of the superposition of the emissions, each value may be impacted by the one of another state and virtually modified. What seems to come out of these results is one long 30 ns lifetime related to the 450 nm emission, one short 0.5 ns related to 600 nm, one medium lifetime that is more difficult to attribute but seems coherent with 477 nm (maximum contribution at this wavelength). These assumptions are to take with care because of the high related uncertainty. They are an attempt at clarifying the complex results obtained with reasonable propositions.

Experiments were repeated twice at 450 nm to ensure reproducibility. Only small variations were observed between experiments.

*Table III-5 : Reproducibility verification of the electrochemical reduction followed by TCSPC experimental procedure.*

$\lambda_{\text{exc}}$ 409 nm	3CzEPAIPN <sup>•-</sup> * run n°1				3CzEPAIPN <sup>•-</sup> * run n°2			
$\lambda_{\text{em}}$	$\tau_1$ (ns) (weight %)	$\tau_2$ (ns) (weight %)	$\tau_3$ (ns) (weight %)	$\tau_m$ (ns)	$\tau_1$ (ns) (weight %)	$\tau_2$ (ns) (weight %)	$\tau_3$ (ns) (weight %)	$\tau_m$ (ns)
450 nm	30.335 (60.95%)	0.746 (32.27%)	7.13 (6.78%)	19.213	30.283 (58.01%)	0.827 (34.47%)	6.73 (7.52%)	18.358

The proposition at this point is that the wavelength of interest is 450 nm with the longest lifetime. An emission at this wavelength from a radical anion excited state would be surprising

because they are known to quickly decay non radiatively and should display long wavelength emission ( $> 550$  nm).

### 5.1.3. Chlorobenzene quenching experiments

Once the lifetimes of the 3CzEPAIPN radical anion solution excited states are determined, we ran quenching studies by adding different concentrations of PhCl (in excess).

In Figure III-71, the 450 nm emission signal is the one that drops drastically with increased concentrations of chlorobenzene (PhCl). The 0.5 M PhCl solution measurement is considered as a measurement artifact for the present study.

Our focus was then on the 446 nm signal, followed at 450 nm as a compromise to compare it with different D-A cyanoarenes that have emission in the same area.

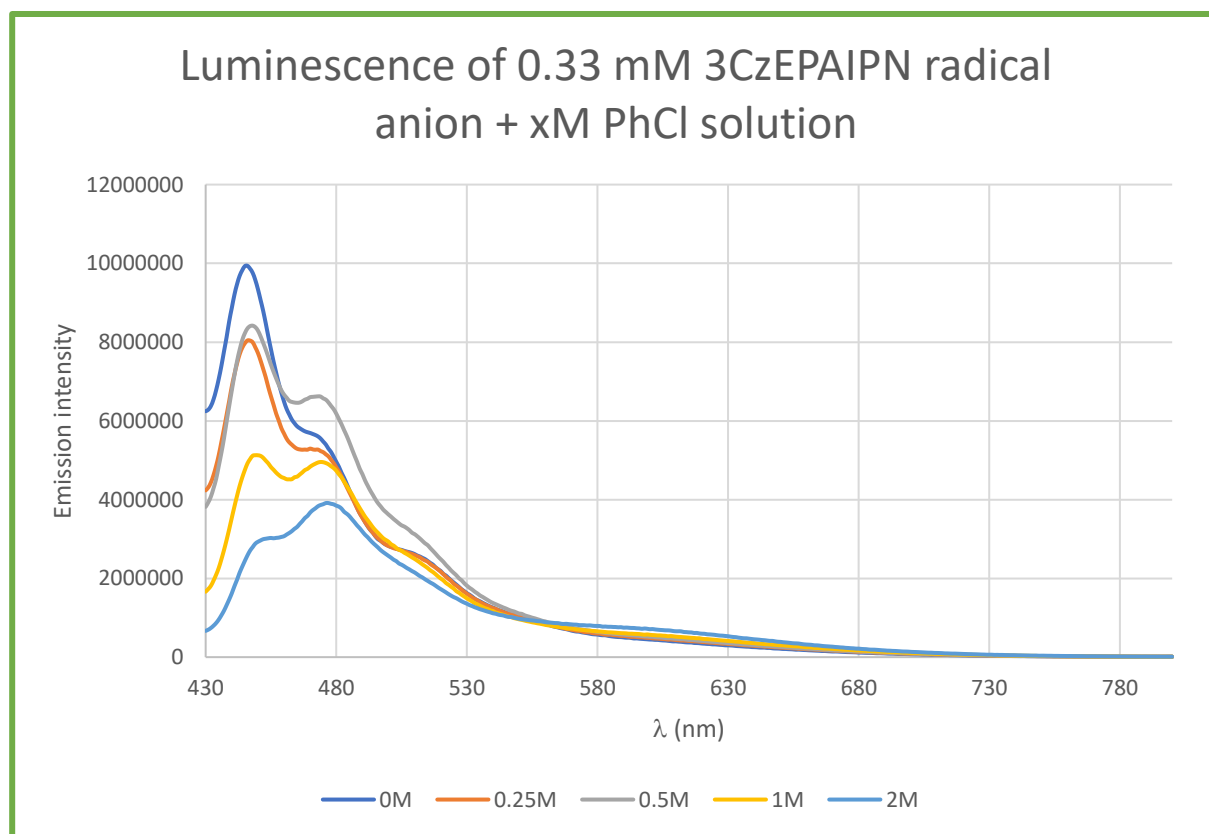


Figure III-71: Emission profiles of 3CzEPAIPN radical anion solutions with different concentrations of PhCl

The radical anion itself is unable to reduce PhCl effectively because of the redox potential difference. However, its excited state can do so. The study shows a lifetime decaying accordingly with an increased PhCl concentration (Figure III-72 and table III-6).

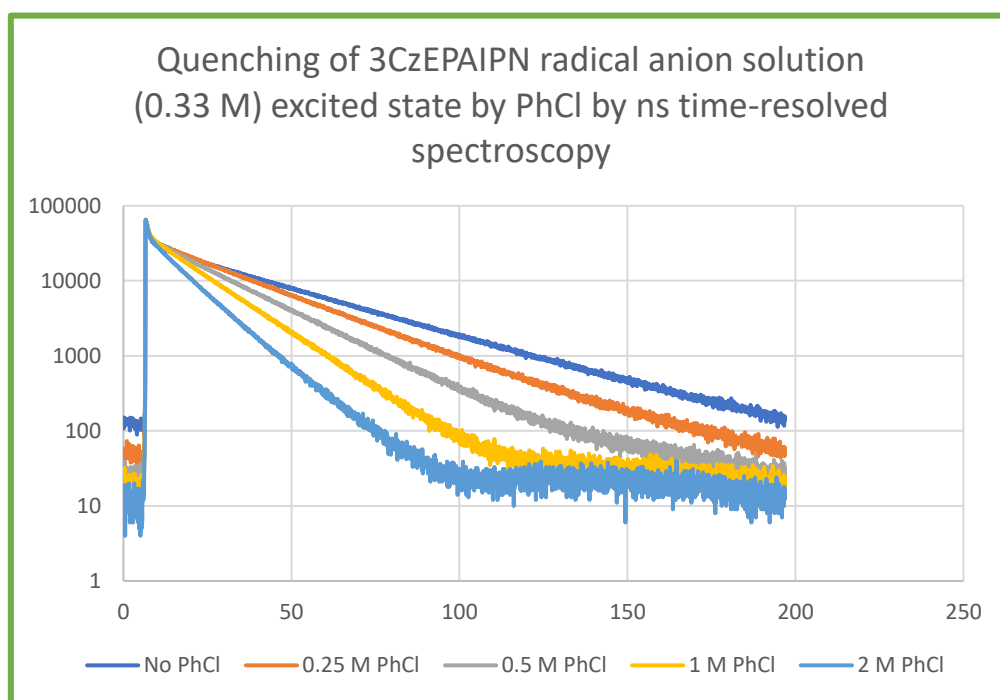


Figure III-72: Time-correlated single-photon counting experiment of 3CzEPAIPN radical anion solutions in presence of different concentrations of PhCl.

Table III-6: Fitting results for the exponential decays of 3CzEPAIPN solutions in presence of different concentration of PhCl.

PhCl concentration	Lifetimes $\tau_n$ (ns)	Weight (%)	Average $\tau$ (ns)
0 M	33.822	50.27	17.857
	0.757	41.69	
	6.69	8.04	
0.25 M	26.324	57.47	16.163
	0.720	35.36	
	10.88	7.17	
0.5 M	20.124	60.2	12.937
	0.667	32.25	
	8.04	7.55	
1 M	14.596	67.64	10.199
	0.598	26.95	
	3.05	5.42	
2 M	12.073	42.62	7.387
	0.607	29.16	
	7.316	28.23	

The electrolyzed solution was diluted by 33% (2 mL with 1-x mL MeCN/x mL PhCl) resulting in the study of a 0.33 mM solution instead of 0.5 mM. The long lifetime of the radical anion solution is impacted, as it increases from 30 ns to 33 ns and its contribution to the total lifetimes goes down from 61 to 50%. It suggests that the concentration has an important impact on the photophysical properties. It is in good correlation with the surprising differences between NMR and UV-Vis studies of solutions with different concentrations in Wu's publication.

Nonetheless, the long lifetime component obviously decreased in presence of PhCl and could be quantified.

The Stern-Volmer equation states:

$$\frac{\tau_0}{\tau} = 1 + K[Q] \text{ (equation III.30)}$$

where

$$K = k_q \times \tau_0 \text{ (equation III.31)}$$

One can build the graph representing  $\frac{\tau_0}{\tau}$  as a function of the quencher concentration [Q] (Figure III-73). The slope of the linear regression divided by  $\tau_0$  then provides the quenching constant  $k_q$ . Supposing that the quenching occurs only through electron transfer to chlorobenzene, one may estimate  $k_{ET}$  as it is done in Wu's publication. We stick here to the expression of  $k_q$ .

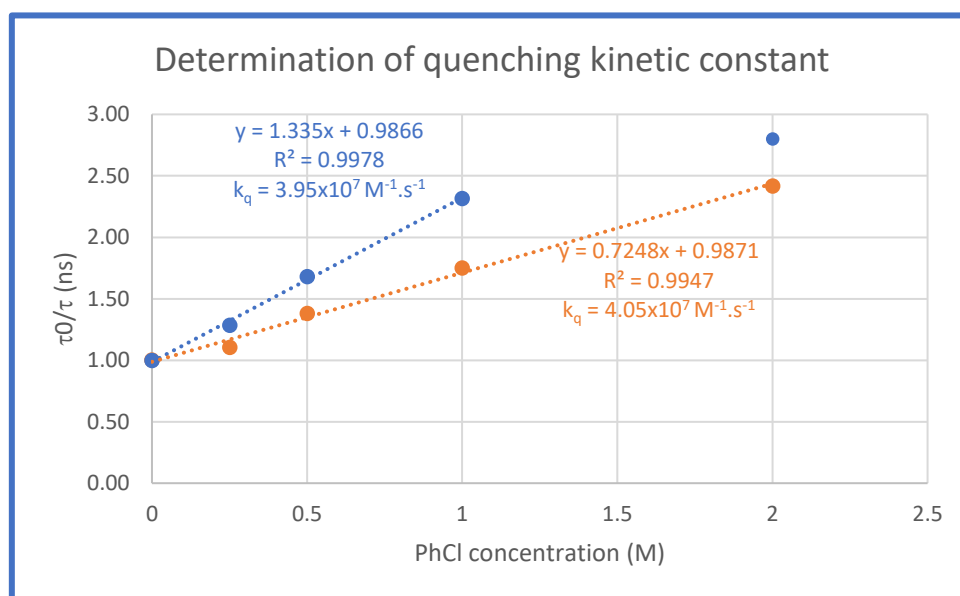


Figure III-73: Graph allowing the determination of 3CzEPAIPN radical anion excited state by PhCl at 450 nm

We drew two different lines. One where the long lifetime value was taken as  $\tau$  (blue) and one where the average mathematical lifetime value is used (orange, to compare to Wu's result).

The point 2 M on the blue line was not included. If it is included,  $R^2$  drops from 0.99 to 0.94 and the slope from 1.335 to 0.9074 which results in  $k_q = 2.98 \times 10^7 \text{ M}^{-1} \cdot \text{s}^{-1}$ . We note here an uncertainty on the result. We believe another mechanism takes place in that case, which may include a contra-thermodynamic electron transfer when the quencher concentration neighbors 2 M against the 0.33 mM maximum concentration of the reducing agent.

The kinetics obtained by e-PC show a kinetic constant between 2 and 2.5 times higher than the one from the ConPET mechanism ( $1.5 \times 10^7 \text{ M}^{-1} \cdot \text{s}^{-1}$ ).

A chlorobenzene dependent quenching is observed for the emission at 450 nm. It suggests there is a molecule or association of molecules in the solution which excited state can transfer an electron to chlorobenzene.

The question remains whether it is the radical anion or another molecule, and follow-up studies are needed.

Nonetheless, an active quenching specie could be confirmed by the electrochemical generation of the radical anion. A clear difference with results from the literature indicates that the problem is more complex than initially expressed and that our understanding of the mechanism is currently a “dark area” of knowledge worth of investigation.

#### 5.1.4. 3CzEPAIPN radical anion isolation

X-Ray diffraction and NMR analysis of the pure isolated radical anion can bring important information about its properties and behaviour. We tried to isolate it from an electrochemically generated 3CzEPAIPN $\cdot^-$  solution according to the following protocol.

Tetramethylammonium tetrafluoroborate (TMABF<sub>4</sub>, 0.06 M) was used as supporting electrolyte in MeCN for the electrolysis of 3CzEPAIPN (1 mmol in 20 mL). After electrolysis, MeCN was evaporated from inside the glovebox. Then, CH<sub>2</sub>Cl<sub>2</sub> (3x3 mL) was used to solubilize the radical anion (the supporting electrolyte being non soluble in CH<sub>2</sub>Cl<sub>2</sub>) and transferred in another flask. Evaporation of CH<sub>2</sub>Cl<sub>2</sub> was then carried out to obtain a brown/red/orange solid along with some yellow solid traces (Figure III-74).



Figure III-74: Photograph of the isolation attempt of 3CzEPAIPN radical anion (orange, in the flask) next to the starting 3CzEPAIPN (yellow, in the vial).

Transfer of this orange solid into a UV-Vis cuvette for analysis most likely resulted in a yellow-coloured solution. Re-oxidation to the neutral 3CzEPAIPN is believed to have occurred during the second  $\text{CH}_2\text{Cl}_2$  transfer.

Stricter oxygen free conditions are probably needed for this procedure to be successful, and more attempts could lead to a successful isolation as suggested by the orange powder observed.

#### 5.1.5. Impact of the D-A cyanoarenes coordination to the $\text{B}(\text{C}_6\text{F}_5)_3$ Lewis acid

We then explored a two-fold strategy: the complexation of Lewis acid(s) (LA) to the nitrile group(s) of D-A cyanoarenes. The first effect is direct modification of the photocatalyst properties by steric and electronic effects. The second one is the envisioned stabilization of the radical anion.

In the organic semi-conductors' field,  $\text{B}(\text{C}_6\text{F}_5)_3$  (BCF) has drawn considerable interest in the past years, either as a molecular dopant,<sup>112</sup> as an additive to prevent excimer formation in the solid state,<sup>113</sup> or as a way to allow important modulation of the photophysical properties of another molecule.<sup>114,115</sup> It displays the ability to coordinate to Lewis basic sites and has been

coordinated to dicyanoanthracene (DCA) in 2021 which coordinated adduct displayed a very different behavior in both absorbance and fluorescence.<sup>113</sup> However, it has never been studied with D-A cyanoarenes to our knowledge.

We started with the synthesis, isolation, and characterization of the BCF coordinated D-A cyanoarenes. The synthetic was undertaken by Romaric Lenk which results are presented hereafter.

The synthesis occurs by mixing the D-A cyanoarene with 1.05 equivalents of BCF per nitrile in toluene. The reaction mixture is taken to reflux to ensure solubilization of all material and the success of the coordination is assessed by a strong deep colored solution. After workup, the pure coordinated products could be obtained in 58-91% yield as deep colored solids (Figure III-75). In the solid state, they are better kept in air and moisture free conditions because of their tendency to decoordinate.

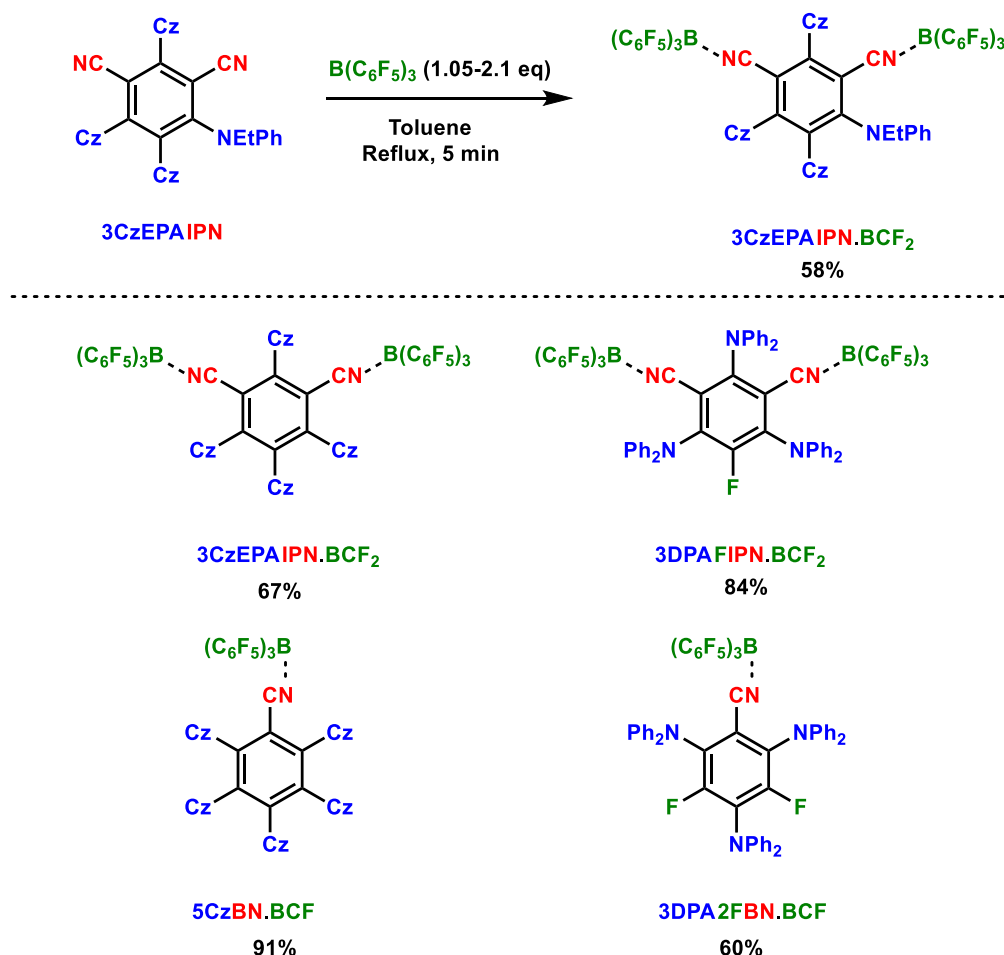


Figure III-75: Isolated yields of BCF coordinated D-A cyanoarenes.



Crystals structures could be obtained for each one of them. For 4CzIPN, the change is impressive as the dihedral angle of the carbazole between the two nitriles goes from 57 to 81° (Figure III-76).

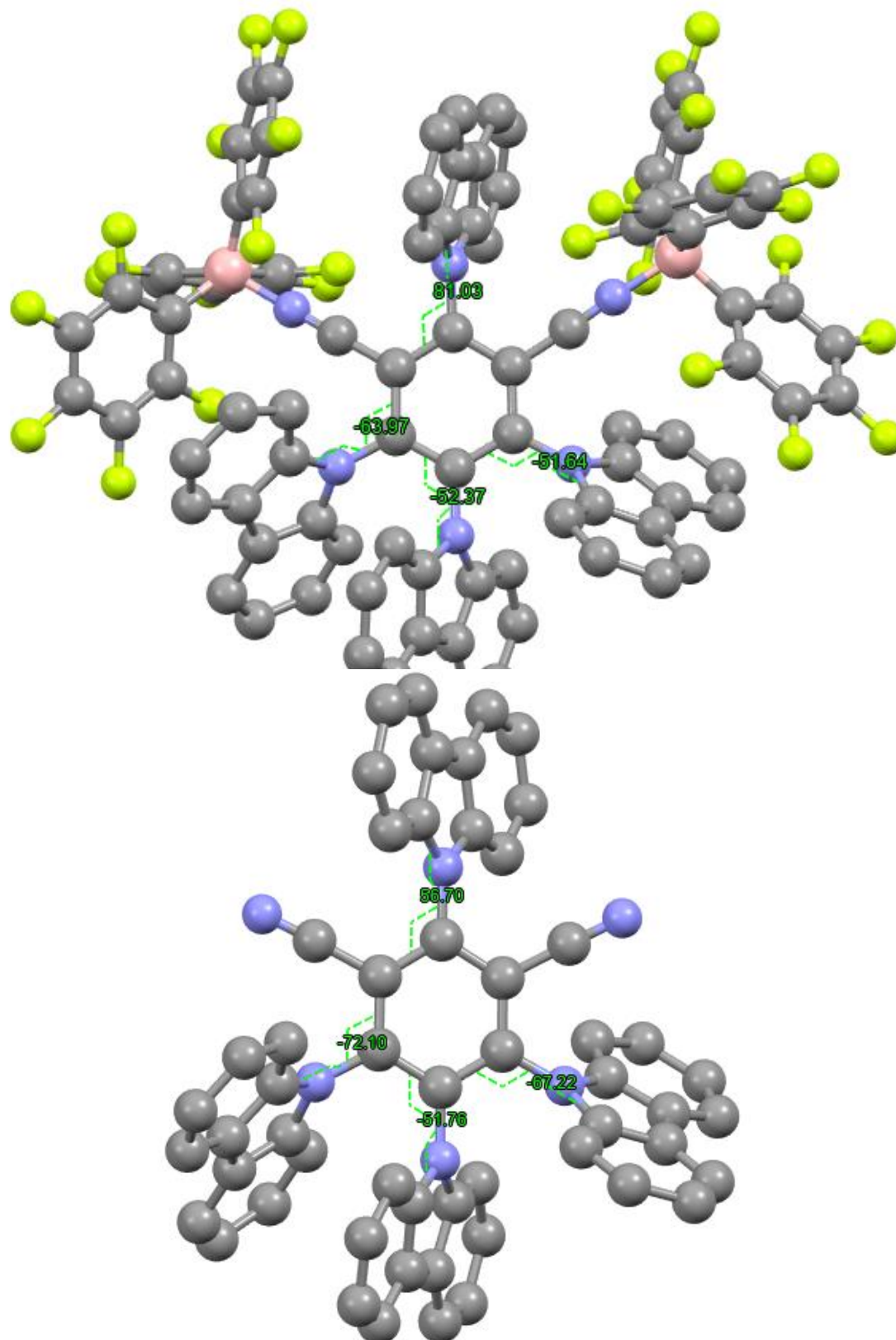


Figure III-76: XRD structures of 4CzIPN.BCF<sub>2</sub> (top) and 4CzIPN (bottom) along with dihedral angles between the core aromatic ring and the amino substituents.

For 3CzEPAIPN, the change in geometry is not as marked but more than a  $10^\circ$  dihedral angle change is observed for one of the aromatics from  $-59$  to  $-70^\circ$  (Figure III-77). The other X-Ray structures are presented in the experimental of this chapter.

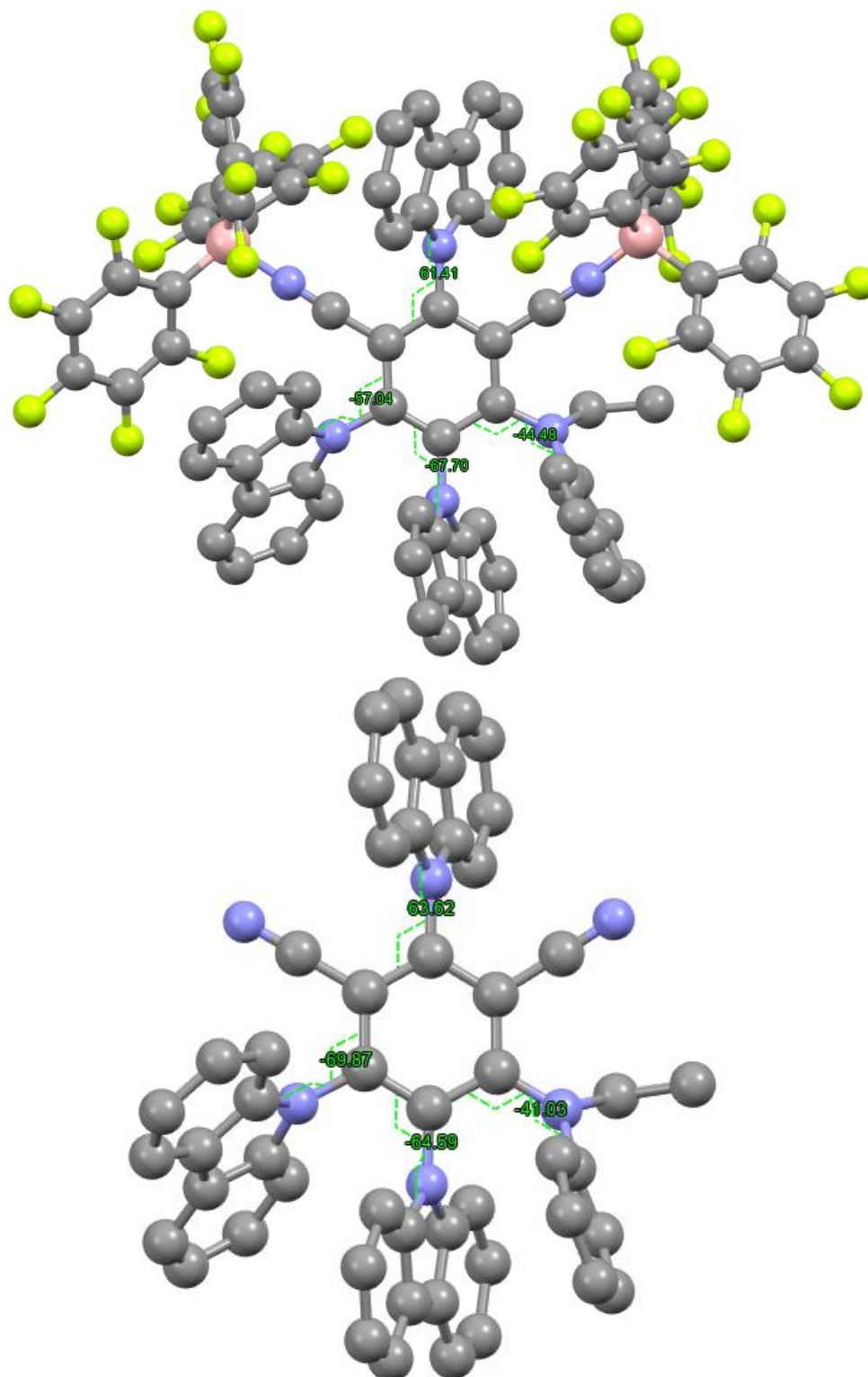


Figure III-77: XRD structures of 3CzEPAIPN.BCF<sub>2</sub> (top) and 3CzEPAIPN (bottom) along with dihedral angles between the core aromatic ring and the amino substituents.

An important redshift of the tail of the absorbance (*ca.* 100 nm) was observed by UV-Vis and the slight to important modification of the orthogonality of the amino substituents are key parameters that show the importance of the BCF. The results for changes in absorption and emission for 4CzIPN coordination to BCF are presented in Figure III-78). The behavior of these molecules in solutions was not trivial, as complete decooordination occurred when the concentration was lowered to  $10^{-5}$  M. The fluorescence of a solution of 4CzIPN.BCF<sub>2</sub> displayed a redshifted emission of 74 nm | 0.27 eV when irradiated at 530 nm. However, this emission was modified when irradiation was done at 409 nm and the apparatus saturated, showing the presence of several species in solution. The results for 3CzEPAIPN.BCF<sub>2</sub> follow the same trend. To further investigate, these observations were followed by electrochemical reduction of the BCF coordinated adducts and the wish to study the photophysical properties of the corresponding radical anions.

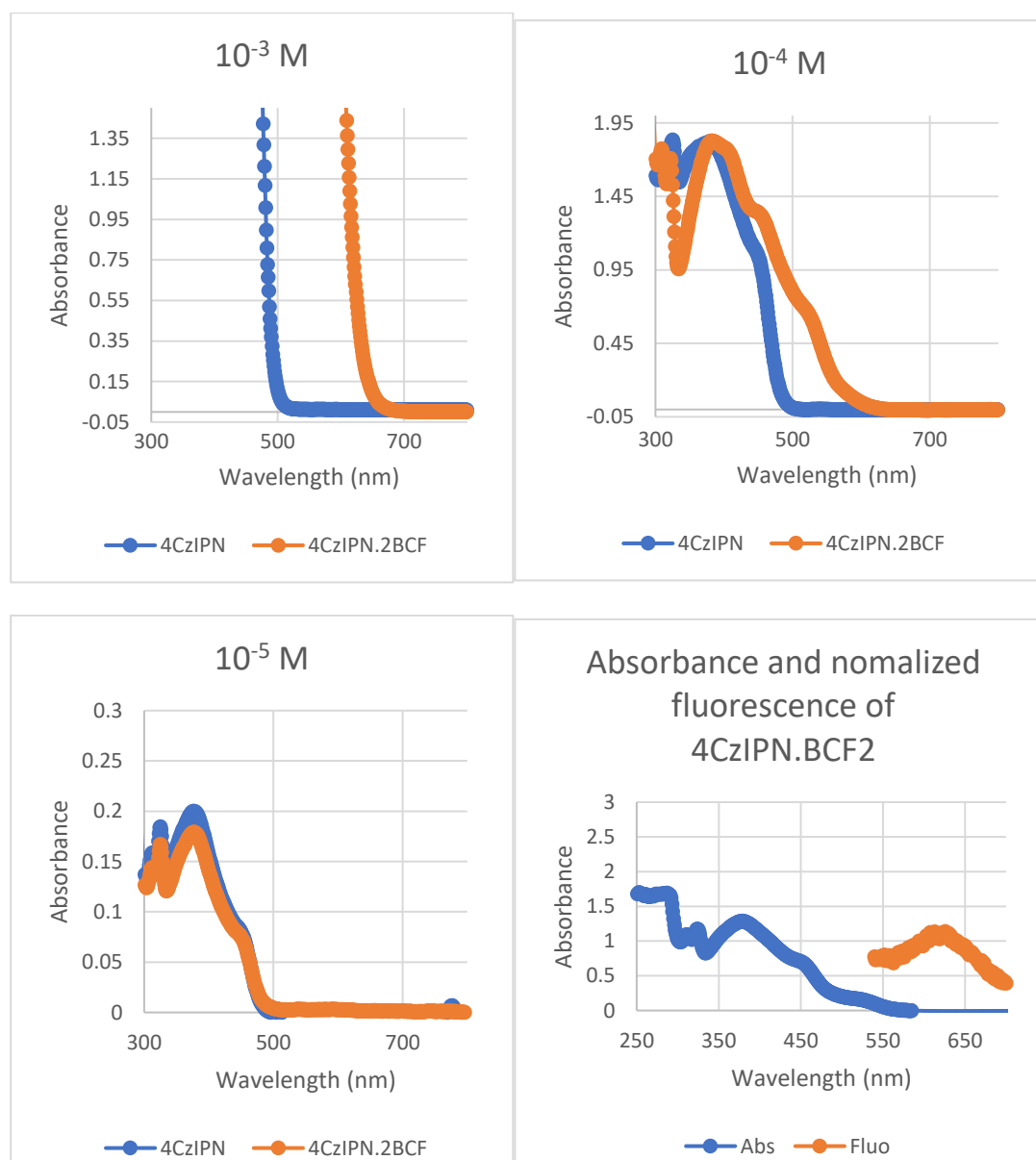


Figure III-78: Absorption spectra of solutions of 4CzIPN and 4CzIPN.BCF<sub>2</sub> in CH<sub>2</sub>Cl<sub>2</sub> at different concentrations (top and bottom left) and superimposed absorbance and normalized fluorescence of a  $10^{-4}$  M solution of 4CzIPN.BCF<sub>2</sub>

We were particularly curious about the BCF coordination impact on the stability of the isolated solid state radical anions and on the lifetime of the excited states.

Coordination in solution is quite weak and reversible in the presence of traces of coordinating solvent. In extremely dry conditions with a non-coordinating solvent (such as ortho-difluorobenzene), and the dry low-coordinating supporting electrolyte tetra-*n*-butylammonium tetrakis[3,5-bis(trifluoromethyl)phenyl]borate (TBABArF), it was possible to study 3CzEPAIPN.BCF<sub>2</sub> behavior in solution.

We were not able however to prevent decooordination in the given electrochemical glovebox working conditions, most likely because of water traces in the solvent. We were still able to extract crucial information about the electrochemical behavior of 3CzEPAIPN radical anion in presence of BCF. The other molecules were not included in this study.

We propose the reduction/coordination pattern in Figure III-79.

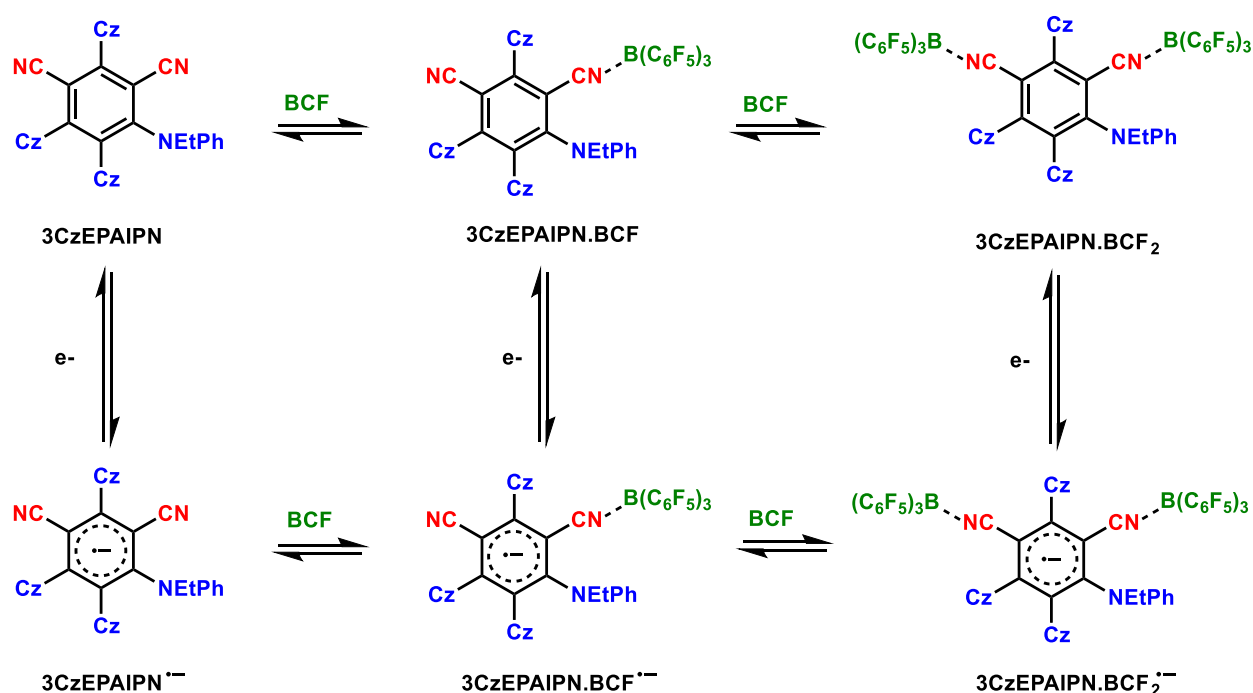


Figure III-79: Proposed BCF coordination pattern to 3CzEPAIPN during cyclic voltammetry.

We recognize on the cyclic voltammetry profile the reduction wave that is characteristic of 3CzEPAIPN at -1,7 V vs 10 mM Ag/AgNO<sub>3</sub> (Figure III-80, 3CzEPAIPN (red) and 3CzEPAIPN.BCF<sub>2</sub> (green) are superimposed). This wave becomes irreversible in the presence of 2 equivalents of BCF. It indicates that the radical anion is formed but reacts too quickly to be observed by CV at a scanning rate of 100 mV/s. Two new waves are observed during the oxidation scan.

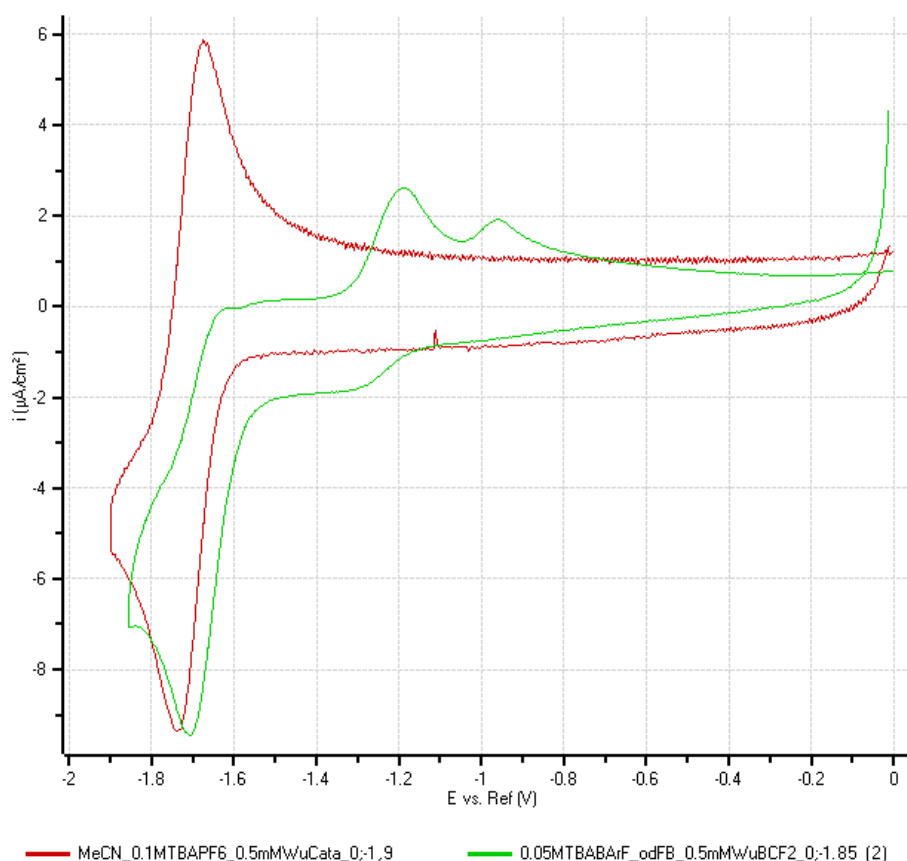


Figure III-80: CV profile of 3CzEPAIPN.BCF<sub>2</sub> (green, in orthodifluorobenzene with 0.05 M TBABArF supporting electrolyte) from 0 to -1.85 V at 100 mV/s) superimposed with 3CzEPAIPN profile (red, in MeCN with 0.1 M TBAPF<sub>6</sub> from 0 to -1.9 V at 100 mV/s).

This indicates that once 3CzEPAIPN gets reduced to its radical anion form, it becomes reactive towards Lewis acids and coordinates quickly to the BCF present in solution.

We then varied the number of equivalents of BCF from 2 to 50. Thanks to these results, we were able to identify and attribute each wave to the corresponding molecules proposed in Figure III-81.

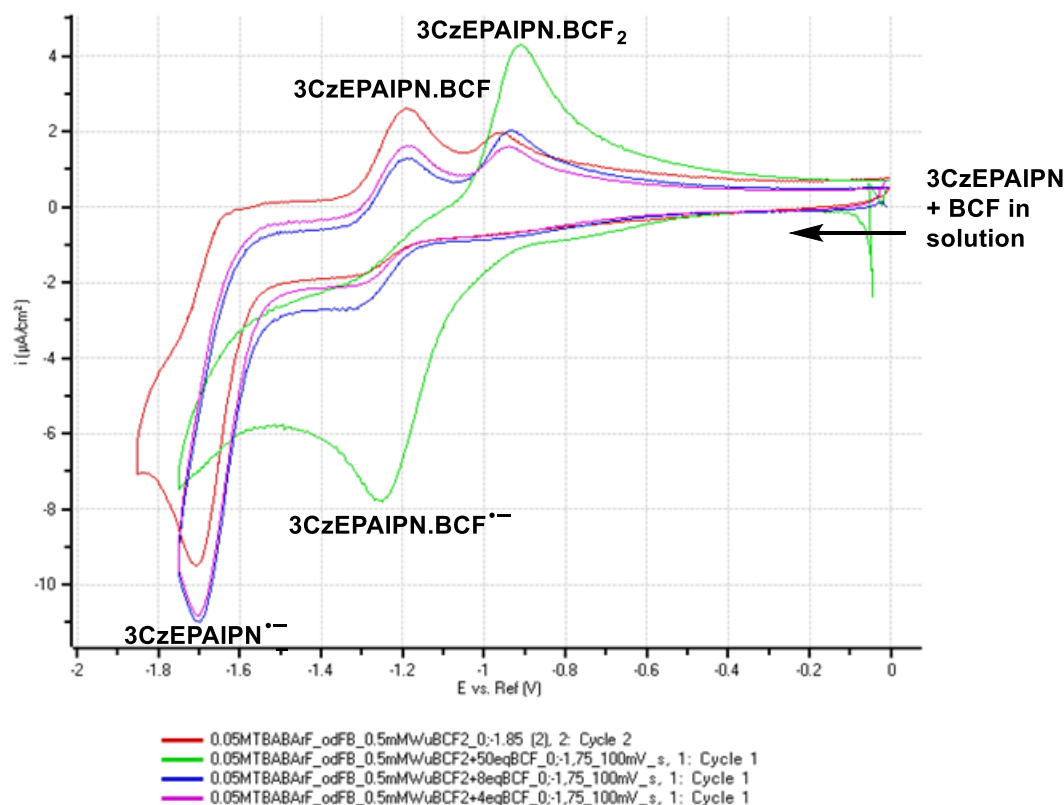


Figure III-81: CV profile of 3CzEPAIPN.BCF<sub>2</sub> (red, in orthodifluorobenzene with 0.05 M TBABArF supporting electrolyte) from 0 to -1.85 V at 100 mV/s in presence of different equivalents of BCF (pink: with 4 extra equivalents of BCF, blue: with 8 extra equivalents of BCF, green: with 50 extra equivalents of BCF ).

The more the coordination the lower the redox potential. It goes in the sense of stabilizing effect from the coordination of BCF. Indeed, a lower PC/PC<sup>•-</sup> redox potential means that is easier to provide an electron to the molecule thanks to a less reactive radical anion product.

With 50 equivalents of BCF, the solution became orange, and we were able to gather a UV-Vis spectra which shows a clear red-shift (Figure III-82). This indicates that coordination in the ground state is favored by an increase of BCF equivalents in solution. The electrochemical profile in the presence of 50 equivalents indicates that the mono coordinated molecule is the main form present in solution.

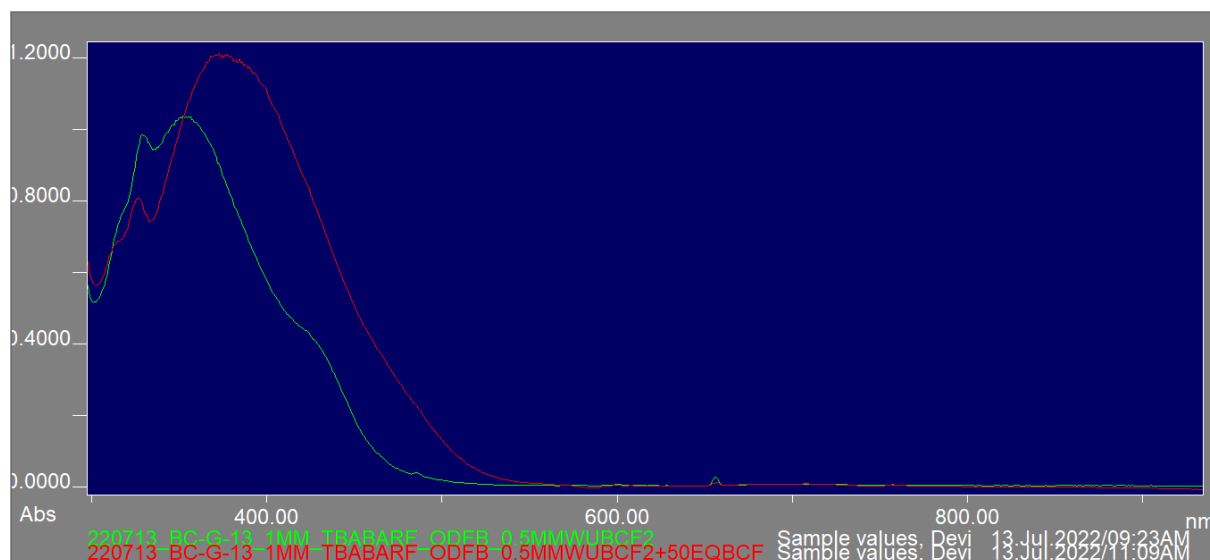


Figure III-82 : UV-Vis of  $3\text{CzEPAIPN.BCF}_2$  (green) and  $3\text{CzEPAIPN.BCF}_2 + 50 \text{ eq BCF}$  (red) in orthodifluorobenzene

Finally, the scanning speed was varied between 50 and 500 mV/s in the presence of 4 equivalents of BCF. At 50 mV/s (Figure III-83, red line), the redox wave of  $3\text{CzEPAIPN}$  is irreversible and  $3\text{CzEPAIPN.BCF}_2$  (obtained from the oxidation of  $3\text{CzEPAIPN.BCF}_2^{\bullet-}$ ) is the most intense signal. On the contrary, at 500 mV/s, the redox wave of  $3\text{CzEPAIPN}$  becomes slightly reversible as  $3\text{CzEPAIPN}^{\bullet-}$  is observed. At the same speed, the mono coordinated  $3\text{CzEPAIPN.BCF}^{\bullet-}$  is the major product in solution as the wave corresponding to its oxidation is the most intense.

We observe a variation of the CV profile with the scanning speed which means that the molecules distribution evolves on the scale of seconds.

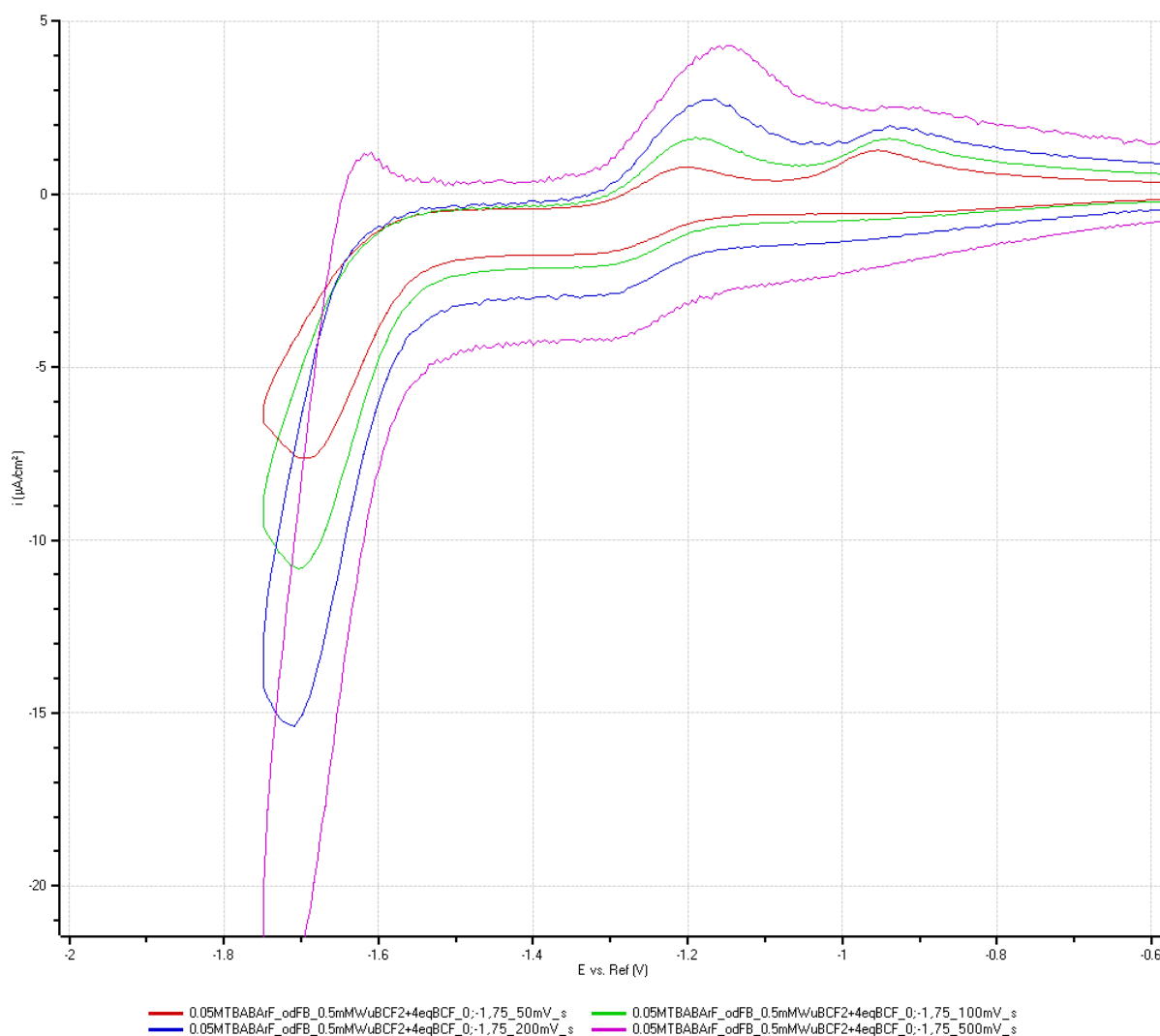


Figure III-83: CV profile of 3CzEPAIPN.BCF<sub>2</sub> + 4 equivalents of BCF at different scanning rates (red: 50 mV/s, green: 100 mV/s, blue: 200 mV/s, pink: 500 mV/s).

With 50 eq of BCF in the solution, the favored form is the neutral mono-BCF-coordinated 3CzEPAIPN which is easier to reduce than 3CzEPAIPN. We attempted an electrolysis at -1.25 V to accumulate BCF-coordinated radical anion. CV after electrolysis showed the 3CzEPAIPN/3CzEPAIPN<sup>•-</sup> reversible wave only. We suppose that BCF decoordinated from 3CzEPAIPN by leaving with the electron and polymerized afterwards.<sup>116</sup> A study showed that in THF BCF<sup>•-</sup> has a lifetime of 10 minutes.<sup>117</sup> Since we conducted the electrolysis over 120 minutes, we believe it decomposed and became invisible by CV in the range of potentials studied.



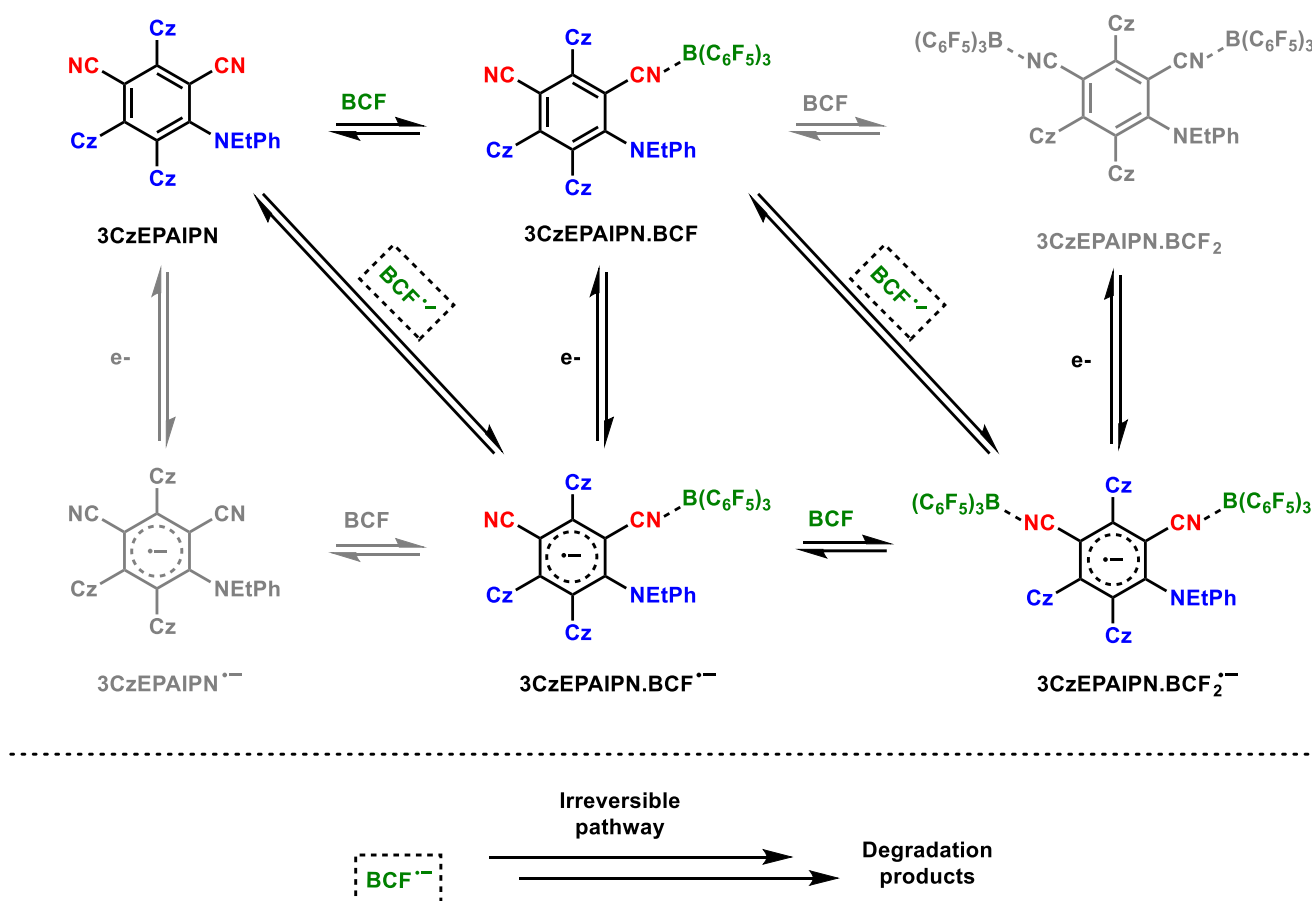


Figure III-84: Proposed 3CzEPAIPN+BCF solution behavior during electrolysis at -1.25 V vs 10 mM Ag/AgNO<sub>3</sub>

These results prevented further photophysical properties investigation. However, this doesn't mean that the BCF coordinated radical anion cannot have a photocatalytic activity in solution. Everything depends on the BCF radical anion decooordination kinetic against the electron transfer kinetic for the chemical reaction considered. Additionally, given the stability of the cyanoarenes/BCF complexes in the solid state, it should be important to investigate the use of those complexes as catalysts in heterogenous catalysis or even more in material sciences. This project is under investigation in the COP team.

## 5.2. Other D-A cyanoarenes

We extended the initial method to four other D-A cyanoarenes: 4CzIPN, 5CzBN, 3DPAFIPN and 3DPA2FBN (Figure III-85). The method was fully applied to 4CzIPN which results are discussed hereafter. For other cyanoarenes, the results are discussed at the end of this chapter and can be found in the experimental part.

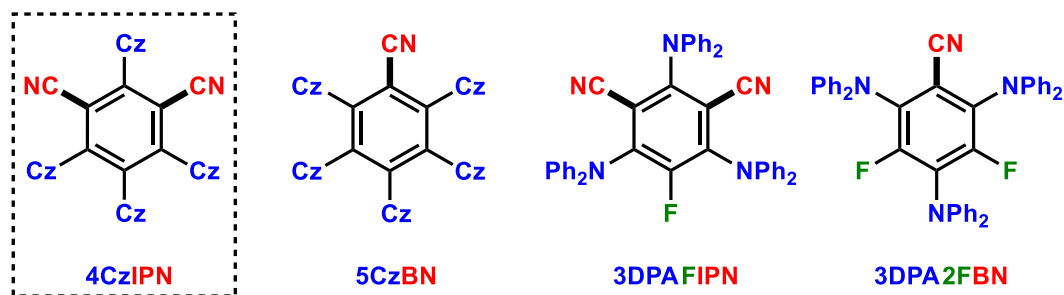


Figure III-85: Structures of 4CzIPN, 5CzBN, 3DPAFIPN and 3DPA2FBN

The results obtained for 4CzIPN are summarized in the following Figures III-86 and 87. The absorbance of the 4CzIPN solution during bulk electrolysis displays a similar evolution as for 3CzEPAIPN. Two isosbestic points are obtained and the reduction is therefore clean and provides a single product, the radical anion of 4CzIPN. EPR analysis confirmed the presence of a radical and matched literature data. The profile of 4CzIPN radical anion is the same as the one obtained by the same method by Kwong and coworkers. In their case with 4DPAIPN<sup>•-</sup>, no luminescence was observed by an irradiation at 540 nm. In our case with an excitation at 409 nm, we observe a new emission signal at 450 nm which is the same one as observed by Wu and coworkers.

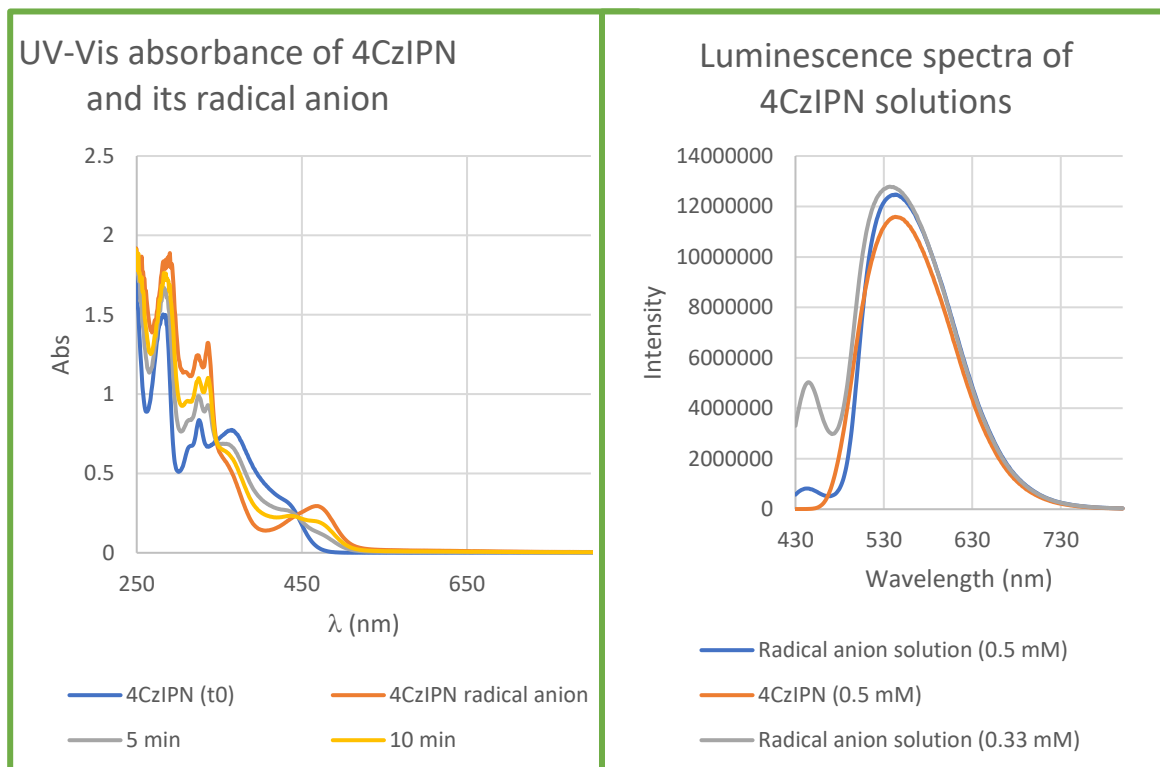


Figure III-86: Absorbance of 4CzIPN solution overtime during electrolysis ( $E_{app} = -1.8$  V). The radical anion solution is obtained after XX mn (left). The luminescence analysis of solutions of 4CzIPN and 4CzIPN radical anion is shown on the right. The radical anion was obtained by electrochemical reduction following the same methodology and in the same conditions as the ones reported earlier in this chapter for 3CzEPAIPN. The fluorescence of two concentrations of the radical anion solutions were measured and displayed different emission intensities (at 0.33 and 0.5 mM).

Lowering the concentration of the radical anion from 0.5 mM to 0.33 mM increased the emission intensity at 450 nm. A 5 nm | 0.02 eV blueshift of the 545 nm band was also observed with the decrease of concentration. This suggests that the ground state and the radical anion interact in their excited state, provided that the two emission bands relate to those molecules.

The decrease of the concentration has an important impact on the lifetime distribution. A new component of 29.5 ns appears at 450 nm with a 0.33 M concentration. This surprising result should be confirmed by repeating the analysis because at 0.033 M this isn't what was observed by Wu and coworkers. This 29.5 ns component is referred as the long lifetime component.

A very complex set of signals was obtained during the quenching experiments of the radical anion solution with PhCl. A counter-intuitive increase of the 450 nm band was observed with increased concentrations of PhCl. A splitting of the 540 nm signal in two signals that further split the more PhCl is added is also observed.

$\lambda_{\text{exc}}$	4CzIPN $\bullet^-$ *				4CzIPN*			
409 nm								
$\lambda_{\text{em}}$	$\tau_1$ (ns) (weight %)	$\tau_2$ (ns) (weight %)	$\tau_3$ (ns) (weight %)	$\tau_m$ (ns)	$\tau_1$ (ns) (weight %)	$\tau_2$ (ns) (weight %)	$\tau_3$ (ns) (weight %)	$\tau_m$ (ns)
450 nm (0.5 mM)	6.813 (83.51%)	2.374 (14.88%)	24.29 (1.61%)	6.433	n/a	n/a	n/a	n/a
450 nm (0.33 mM)	6.277 (70.25%)	29.501 (29.75%)	n/a	13.186				
600 nm (0.5 mM)	17.941 (90.86%)	4.55 (9.14%)	n/a	16.716	19.534 (96.75%)	7.39 (3.25%)	n/a	19.139

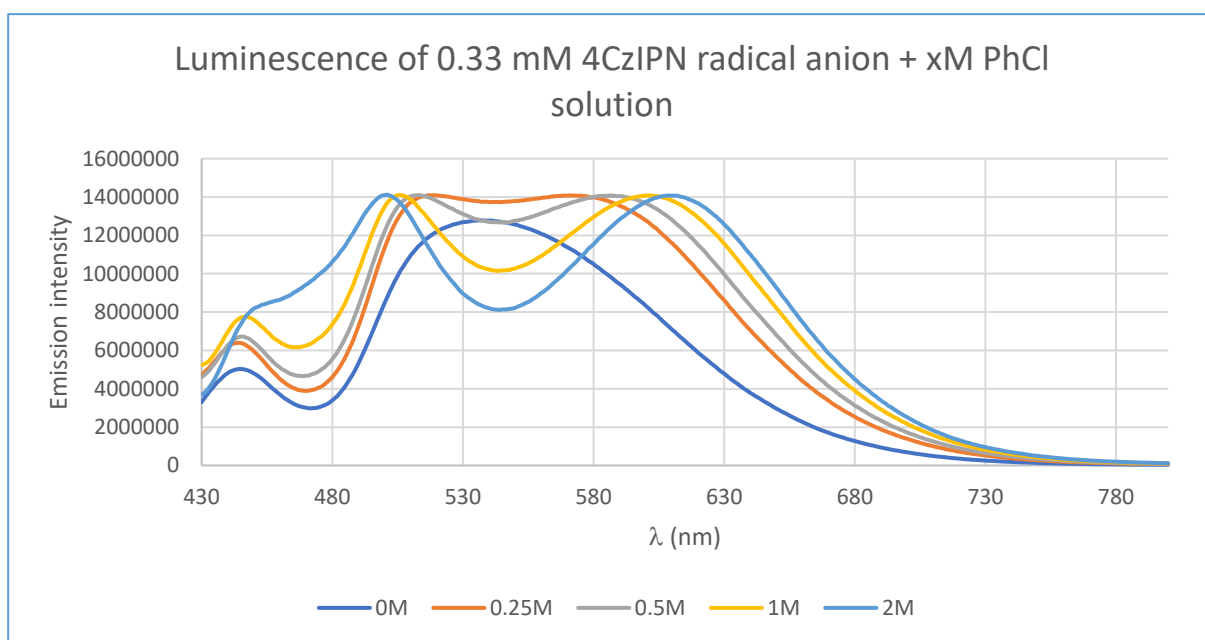


Figure III-87: Table providing the results of TCSPC of 4CzIPN and 4CzIPN electrolyzed solutions at two different concentrations (top) and the luminescence of the 4CzIPN electrolyzed solution in presence of different concentrations of PhCl (bottom).

We have selected two wavelengths to follow the lifetime of the excited states, respectively at 450 and 600 nm. With the 0.5 mM solution, similar results as the literature were obtained (table III-7).

Table III-7: comparison of the lifetime results for 4CzIPN and its radical anion between our experimental data. The radical anion was obtained by electrochemical reduction in our case and in the literature it was obtained by ConPET.

	$\lambda_{\text{exc}}$ (nm)	$\lambda_{\text{em}}$ (nm)	Concentration (mM)	$\tau_1$ (ns) Weight (%)	$\tau_2$ (ns) Weight (%)	$\tau_3$ (ns) Weight (%)
4CzIPN <sub>exp</sub>	409	545	~ 0.5	19.534 86.75%	7.39 3.25%	n/a
4CzIPN <sub>lit</sub>	375	550	~ 0.033	19.56 100%	n/a	n/a
4CzIPN $\bullet^-$ <sub>exp</sub>	409	450	~ 0.5	6.813 83.51%	2.374 14.88%	24.29 1.61%
4CzIPN $\bullet^-$ <sub>lit</sub>	375	450	~ 0.033	6.47 88.19%	1.32 11.81%	n/a

Either the formation of excimers/exciplexes or the presence of an impurity seem the outcome of these analysis.

A good correlation for the long lifetime component of 4CzIPN 0.33 M radical anion solution excited state quenching by chlorobenzene is obtained (Figure III-88). A quenching rate constant of  $2.84 \times 10^7 \text{ M}^{-1} \cdot \text{s}^{-1}$  is obtained, very similar to the one obtained with 3CzEPAIPN $\bullet^-$ . However, it is difficult to rely on these results to draw conclusions because of the discrepancy observed between the 0.5 and 0.33 mM radical anion solutions.

PhCl concentration	Lifetimes $\tau_n$ (ns)	Weight (%)	Mean
0 M	6.277	70.25	13.186
	29.501	29.75	
0.25 M	6.351	70.26	11.237
	22.779	29.74	
0.5 M	6.429	72.59	9.655
	18.198	27.41	
1 M	6.289	63.64	9.229
	14.374	36.36	
2 M	6.388	65.62	7.940
	10.903	34.38	

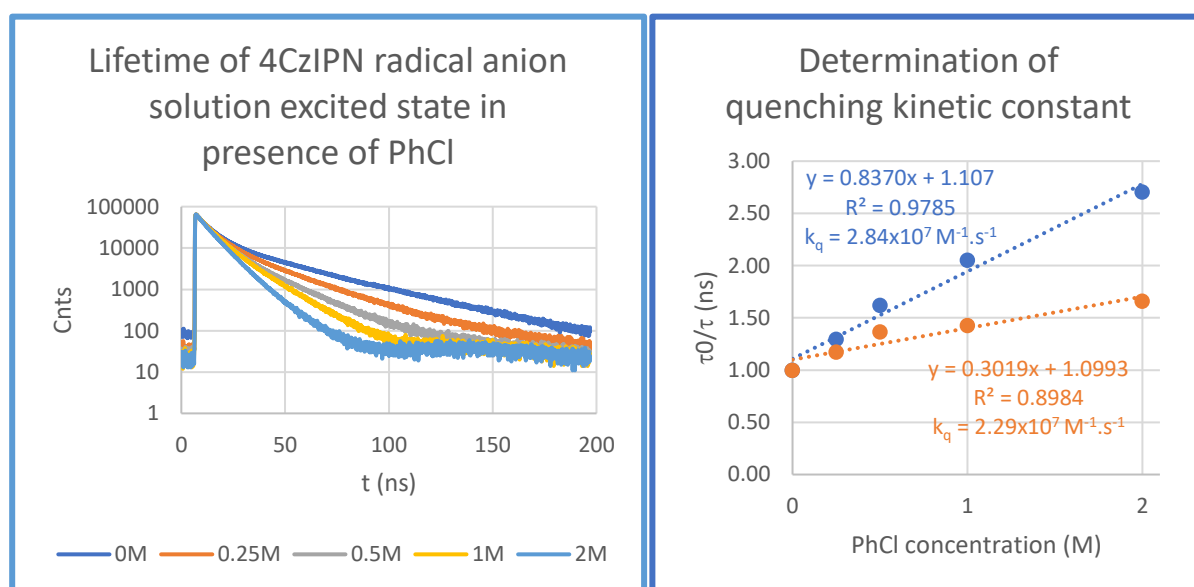


Figure III-88: Table of the lifetimes obtained by TCSPC of 4CzIPN radical anion solution (0.33 mM) with different concentrations of chlorobenzene (top). On the bottom left exponential decay variation during the quenching experiments with PhCl and on the bottom right quenching kinetic constant determination for the long lifetime component (blue) and average lifetime (orange)

Concerning other D-A cyanoarenes, only electrolysis with UV-Vis follow was done. The reduction occurred smoothly for all substrates except 3DPA2FBN which decomposed during electrolysis. We suspect that defluorination occurred in that case. For 3DPAFIPN, the same absorbance profile as Kwong and coworkers was obtained, assisting the reproducibility of the method. For 5CzBN, a redshifted absorbance profile was obtained, suggesting that 5CzBN $\cdot^-$  was also smoothly formed.

## 6. Conclusion

The electrochemical generation of D-A cyanoarene radical anions with *in-situ* UV-Vis spectroscopic analysis overtime allowed for the clean and unambiguous one electron reduction of the parent D-A cyanoarene. The absorbance profile of 3CzEPAIPN $\bullet^-$  was proved to be very different from what was previously reported in the literature.<sup>57</sup> The radical anion redshift compared to the neutral molecule observed matches the more recent results from the literature with 4DPAIPN and other D-A cyanoarenes (3CzEPAIPN was not included).<sup>82</sup> Both publications generated the radical anions by consecutive photoinduced electron transfer (ConPET) while we produced them with the cleanest constant potential electrolysis method.

An excellent stability of several hours in inert atmosphere conditions was measured for 3CzEPAIPN $\bullet^-$ . The luminescence analysis however showed an anti-Kasha behavior with three distinct emission bands instead of the single gaussian one report in the literature prior to our work. The time-correlated single-photon counting experiments ran resulted in the measurement of a long-excited state lifetime of *ca.* 30 ns which was quenched by chlorobenzene. It seems unlikely that this corresponds to the 3CzEPAIPN radical anion's excited state lifetime. Further investigations are required to assess the nature of the three emissive states observed. We suspect exciplexes formation to be highly probable.

These investigations should incorporate a study of the impact of the concentration of D-A cyanoarene (*e.g.*  $10^{-6}$  to  $10^{-2}$  M) in at least three different solvents (MeCN, toluene and  $\text{CH}_2\text{Cl}_2$ ) on the radical anion absorbance and luminescence profiles. The wavelength of excitation should be scanned at 375 nm (same as Wu's publication), 409 nm (to compare to the current results) and at a wavelength where the radical anion solution absorbs but not the neutral state one (around 550 nm, no luminescence may be expected in MeCN). The corresponding excited state lifetimes should be measured.

A practical application of 3CzEPAIPN $\bullet^-$  to e-PC with different chloroarene substrates would be highly valuable, aside from the mechanistic considerations.

The behavior of the BCF Lewis acid coordination was studied and showed that the coordination became highly favored upon one electron reduction of 3CzEPAIPN. However, BCF $\bullet^-$  acted as leaving group and underwent subsequent degradation.

As discussed in the introduction part of this chapter, the ability of cyanoarene photocatalysts to undergo consecutive photoinduced electron transfer (ConPET) to achieve very high reduction potentials is controversial. The present results show that, in contrast to the common beliefs, the

cyanoarene radical anions are stable in their ground states and we were able to univocally characterize them by different means (spectrophotometry and EPR). We showed also that spectroscopic signature of the radical anion derived from the Wu photocatalyst is in contrast to that reported by Wu and colleagues, and we explained the reasons of these discrepancies.

The interaction of blue light with the different cyanoarenes radical anions turned out to be more complex to rationalize by means of fluorescence, as different species seemed to be formed upon excitation. While our fluorescence quenching experiments of the different radical anions with chlorobenzene showed fast and efficient reactions, it was very difficult to assign which species is responsible of the observed reactivity. Based on these observations, we proposed reasonable pathways that may account for our observations. These suggestions warrant further studies notably by laser flash photolysis and TD-DFT calculations.

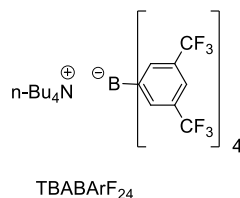


## 7. Experimental section

### Synthesis

This synthesis section was performed by Romaric Lenk whose compiled results have been included here. We wish to express our immense gratitude for his help.

Tetra-*n*-butyl ammonium tetrakis[3,5-bis(trifluoromethyl)phenyl]borate



Prerequisite:

For safety consideration, NaBArF<sub>24</sub> was prepared according to Brown et Al. procedure.<sup>e</sup> After treating the ether solution with activated charcoal and Na<sub>2</sub>SO<sub>4</sub>, then solvent was removed under vacuum leaving waxy brown solid further dried for minimum one hour under vacuum. Then NaBArF<sub>24</sub> was purified according to Weller et Al. procedure,<sup>f</sup> 20 gr of crude NaBArF<sub>24</sub> were dissolved in 1:1 mixture of CH<sub>2</sub>Cl<sub>2</sub> and THF and slowly cooled to -23 °C allowing first crystallization. The resulting solid was filtered, washed with pentane and dried under vacuum for one hour. The process was repeated a second time leading to beige microcrystalline solid. This solid was further dried heating at 80°C with vigorous stirring (compound was shown to be extremely pulverulent therefor vacuum hose should be protected with cotton plug to avoid excessive losses).

The resulting beige white solid was stored on bench in a tight vial.

Tetra-*n*-butylammonium chloride was dried by melting the commercial solid under vacuum at 125 °C with P<sub>2</sub>O<sub>5</sub> trap overnight.

<sup>e</sup> *Inorganic Syntheses, Volume 34, 5 - 8, ISBN 0-471-64750-0*

<sup>f</sup> *Dalton Trans.*, 2019, 48, 3551–3554, DOI: 10.1039/c9dt00235a

Optimised synthesis:

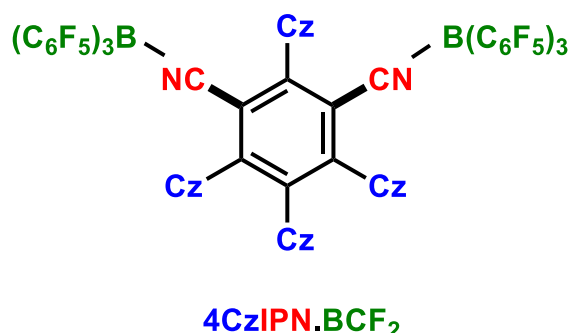
A solution of tetrabutylammonium chloride (1.88 gr, 6.7 mmol, 1 eq) in 2 -3 mL of acetone was added to a solution of NaBArF<sub>24</sub> (6 g, 6.7 mmol, 1 eq) dissolved in acetone (10 mL), leading to brown light precipitate. The mixture was stirred for 15 min, paper filtered, and solvent evaporated under vacuum. The resulting solid was dried for 1h under vacuum then purified by silica filtration in DCM (silica bed dimensions: diam. 3 cm, 15 cm height).

After solvent evaporation, solvent and water traces were removed by melting gently the solid with heat gun under vacuum, until no more gas evolution was visible. After cooling, TBABArF<sub>24</sub> was obtained as a clear yellow pale solid and stored in a glovebox.

General procedures for the synthesis of cyanoarenes BCF complexes:

Purity of cyanoarenes was found to be crucial to obtain pure compounds, especially the absence of lewis base, therefor additional purification steps were added in some case.

4CzIPN.[B(C<sub>6</sub>F<sub>5</sub>)<sub>3</sub>]<sub>2</sub>:



4CzIPN was prepared according to Kelly et al procedure,<sup>8</sup> triturated in pentane and dried under vacuum for 4 hours at 70 °C with vigorous stirring.

4CzIPN (293 mg, 0.37 mmol, and B(C<sub>6</sub>F<sub>5</sub>)<sub>3</sub> (400 mg, 0.78 mmol, 2.1 eq) were weighed in a schlenk tube. Anhydrous toluene (5mL) was added and heated to reflux until all material dissolve (5 min), leading to deep purple solution. After cooling, solvent was removed under vacuum and residue was triturated in pentane (10 mL). After decantation, supernatant was syringed out and powder was washed by the same process with pentane (2 x 5 mL). Powder was dried under vacuum at 60°C for two hours.

<sup>8</sup> *Org. Synth.* 2019, 96, 455-473, DOI: 10.15227/orgsyn.096.0455

4CzIPN.BCF<sub>2</sub> was obtained as a deep purple powder (456 mg, 67 % yield).

X-ray quality single crystals could be grown by concentration of a solution of the compound in CDCl<sub>3</sub>.

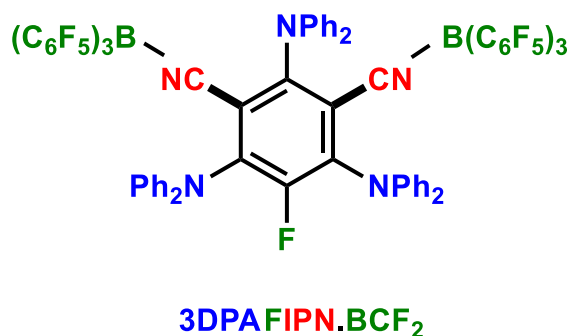
NMR:

<sup>1</sup>H NMR (CDCl<sub>3</sub>, 500 MHz,  $\delta$  in ppm): 8.03 (d, 2H,  $J_{HH}$  = 7.7 Hz), 7.81 (d, 2H,  $J_{HH}$  = 8.2 Hz), 7.74 (dd, 1H,  $J_{HH}$  = 7.4 Hz,  $J_{HH}$  = 1.0 Hz), 7.72 (dd, 1H,  $J_{HH}$  = 7.3 Hz,  $J_{HH}$  = 1.0 Hz), 7.61 (d, 4H,  $J_{HH}$  = 7.5 Hz), 7.42 (dd, 1H,  $J_{HH}$  = 7.4 Hz,  $J_{HH}$  = 0.7 Hz), 7.41 (dd, 1H,  $J_{HH}$  = 7.4 Hz,  $J_{HH}$  = 0.7 Hz), 7.32 (d, 2H,  $J_{HH}$  = 7.6 Hz), 7.07 (dd, 2H,  $J_{HH}$  = 7.4 Hz,  $J_{HH}$  = 0.7 Hz), 7.06 (dd, 2H,  $J_{HH}$  = 7.6 Hz,  $J_{HH}$  = 0.8 Hz), 7.01 (dd, 2H,  $J_{HH}$  = 7.7 Hz,  $J_{HH}$  = 1.0 Hz), 6.99 (dd, 2H,  $J_{HH}$  = 7.7 Hz,  $J_{HH}$  = 1.2 Hz), 6.85 (dd, 1H,  $J_{HH}$  = 7.3 Hz,  $J_{HH}$  = 0.8 Hz), 6.84 (dd, 1H,  $J_{HH}$  = 7.5 Hz,  $J_{HH}$  = 0.8 Hz), 6.63 (d, 2H,  $J_{HH}$  = 8.0 Hz), 6.56 (dd, 1H,  $J_{HH}$  = 7.7 Hz,  $J_{HH}$  = 1.1 Hz), 6.54 (dd, 1H,  $J_{HH}$  = 7.7 Hz,  $J_{HH}$  = 1.1 Hz).

<sup>13</sup>C NMR (CDCl<sub>3</sub>, 100 MHz,  $\delta$  in ppm): 150.6 (C<sub>quat.</sub>), 150.2 (C<sub>quat.</sub>), 147.7 (C<sub>quat.</sub>), 147.3 (C-F,  $J_{CF}$  = 240 Hz,  $J_{CF}$  = 10 Hz), 140.2 (C-F,  $J_{CF}$  = 247 Hz), 139.2 (C<sub>quat. carbazole</sub>), 136.7 (C-F,  $J_{CF}$  = 250.0 Hz,  $J_{CF}$  = 15.5 Hz), 135.9 (C<sub>quat. carbazole</sub>), 133.5, (C<sub>quat.</sub>), 128.4 (CH<sub>carbazole</sub>), 127.7 (CH<sub>carbazole</sub>), 126.5 (CH<sub>carbazole</sub>), 125.3 (CH<sub>carbazole</sub>), 124.2 (C<sub>quat. carbazole</sub>), 123.9 (CH<sub>carbazole</sub>), 123.6 (CH<sub>carbazole</sub>), 122.1 (CH<sub>carbazole</sub>), 122.0 (CH<sub>carbazole</sub>), 121.4 (CH<sub>carbazole</sub>), 120.7 (CH<sub>carbazole</sub>), 120.1 (CH<sub>carbazole</sub>), 112.7 (C-B), 109.5 (CH<sub>carbazole</sub>), 108.7 (CH<sub>carbazole</sub>), 108.2 (CH<sub>carbazole</sub>), 107.9 (CN cyano)

<sup>19</sup>F NMR (CDCl<sub>3</sub>, 376 MHz,  $\delta$  in ppm): -134.0 (m, 6F, B(C<sub>6</sub>F<sub>5</sub>)<sub>3</sub>), -155.3 (m, 3F, B(C<sub>6</sub>F<sub>5</sub>)<sub>3</sub>), -162.8 (m, 6F, B(C<sub>6</sub>F<sub>5</sub>)<sub>3</sub>).

3DPAFIPN.[B(C<sub>6</sub>F<sub>5</sub>)<sub>3</sub>]<sub>2</sub>:

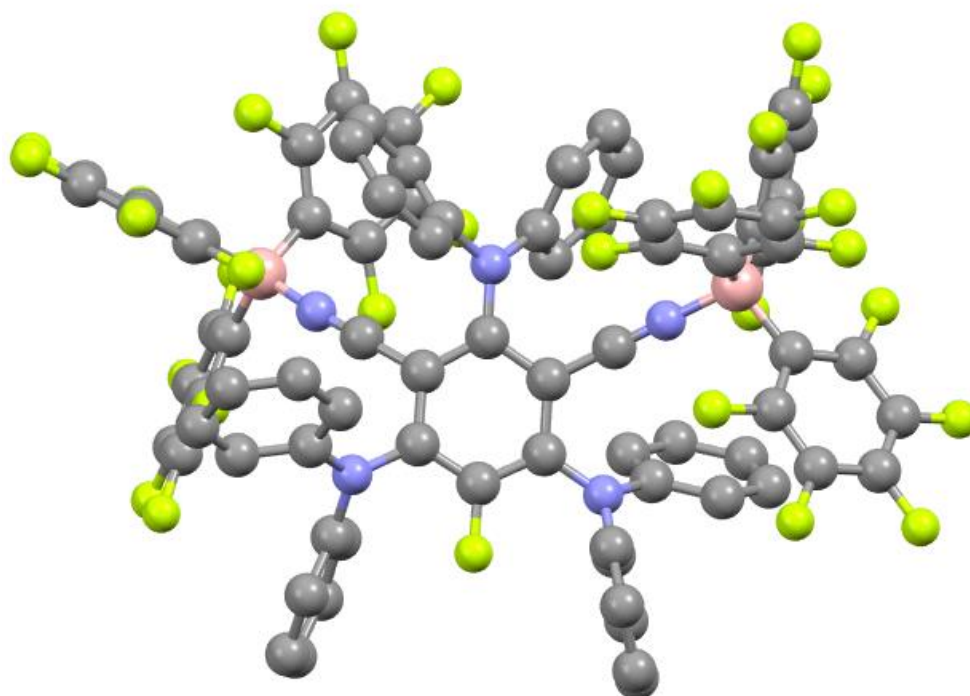


3DPAFIPN was prepared according to Zeitler et Al procedure with slight modifications:<sup>h</sup> instead of flash chromatography, typical batch of 4 gr of 3DPAFIPN, was sonicated and washed with MeOH (2x20 mL), then Et<sub>2</sub>O (3x10 mL) and pentane (2x10 mL) and finally dried under vacuum at 70°C for 3 hours under vigorous stirring.

3DPAFIPN.BCF<sub>2</sub> was prepared with the same procedure than 4CzIPN.BCF<sub>2</sub>:

Reaction of 3DPAFIPN (150 mg, 1 eq, 0.23 mmol) with B(C<sub>6</sub>F<sub>5</sub>)<sub>3</sub> (261 mg, 2.2 eq, 0.5 mmol) in PhMe (5mL) lead after workup to 3DPAFIPN.BCF<sub>2</sub>, as bright red powder (326 mg, yield = 84 %).

X-Ray quality single crystals could be grown by recrystallizing compound by dissolution in boiling toluene, followed by slow cooling to -20 °C.



<sup>1</sup>H NMR (CDCl<sub>3</sub>, 500 MHz, δ in ppm): 7.19 -7.11 (m, 8H, HNPh<sub>2</sub>), 7.12-7.06 (m, 4H, H NPh<sub>2</sub>), 7.05 -6.95 (m, 6H, H NPh<sub>2</sub>), 6.85 (m, 8H, H NPh<sub>2</sub>), 6.68 (m, 4H, H NPh<sub>2</sub>).

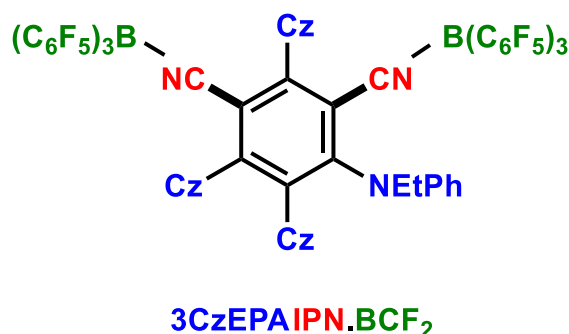
<sup>13</sup>C NMR (CDCl<sub>3</sub>, 100 MHz, δ in ppm): 157.2 (C<sub>quat.</sub>), 150.4 (d overlapped, C-F<sub>Ar</sub> core, J<sub>CF</sub> = 262 Hz), 147.9 (m, C-F B(C<sub>6</sub>F<sub>5</sub>)<sub>3</sub>, J<sub>CF</sub> = 242 Hz), 147.1 (d, J<sub>CF</sub> = 9.1 Hz), 144.5 (C NPh<sub>2</sub> quat.), 144.0 (C NPh<sub>2</sub> quat.), 140.9 (m, C-F B(C<sub>6</sub>F<sub>5</sub>)<sub>3</sub>, J<sub>CF</sub> = 252 Hz), 137.03 (m, C-F B(C<sub>6</sub>F<sub>5</sub>)<sub>3</sub>, J<sub>CF</sub> = 240 Hz), 129.7 (C-H NPh<sub>2</sub>), 129.6 (C-H NPh<sub>2</sub>), 126.7 (C-H NPh<sub>2</sub>), 126.0 (C-H NPh<sub>2</sub>), 123.1 (C-H

<sup>h</sup> Zeitler et Al - *J. Am. Chem. Soc.* 2018, 140, 45, 15353–15365 ; DOI : 10.1021/jacs.8b08933

NPh<sub>2</sub>), 121.9 (C-H NPh<sub>2</sub>), 114.6 (br m, C-B B(C<sub>6</sub>F<sub>5</sub>)<sub>3</sub>), 111.4 (d, CN<sub>cyano</sub>, J<sub>CF</sub> = 2.7 Hz), 97.7 (d, C<sub>quat</sub>, J<sub>CF</sub> = 2.7 Hz).

<sup>19</sup>F NMR (CDCl<sub>3</sub>, 376 MHz, δ in ppm): -118.5 (s, 1F, F<sub>Ar core</sub>), -133.0 (dd, 12F, B(C<sub>6</sub>F<sub>5</sub>)<sub>3</sub>, J<sub>FF</sub> = 22.8 Hz, J<sub>FF</sub> = 6.8 Hz), -156.4 (m, 6F, B(C<sub>6</sub>F<sub>5</sub>)<sub>3</sub>), -163.4 (m, 12F, B(C<sub>6</sub>F<sub>5</sub>)<sub>3</sub>).

3CzEPAIPN. [B(C<sub>6</sub>F<sub>5</sub>)<sub>3</sub>]<sub>2</sub>:



3CzEPAIPN was prepared according to Wu et al. procedure with some modifications in the purification steps:<sup>i</sup> MeCN/water recrystallization was replaced by recrystallization in a boiling mixture of PhMe/CHCl<sub>3</sub>. Typical amounts for 3 gr (20 mL of CHCl<sub>3</sub>, 20 mL of PhMe). After recrystallization, powder was triturated and washed with pentane (3x15 mL) and dried 3 hours at 70°C under vacuum with vigorous stirring.

3CzEPAIPN. [B(C<sub>6</sub>F<sub>5</sub>)<sub>3</sub>]<sub>2</sub> was prepared with the same procedure than 4CzIPN.BCF<sub>2</sub>:

Reaction of 3CzEPAIPN (200 mg, 1 eq, 0.26 mmol) with B(C<sub>6</sub>F<sub>5</sub>)<sub>3</sub> (303 mg, 2.1 eq, 0.6 mmol) in PhMe (5 mL) lead after workup to 3CzEPAIPN.BCF<sub>2</sub>, as brown-orange powder (280 mg, yield = 58 %).

<sup>1</sup>H NMR (CDCl<sub>3</sub>, 500 MHz, δ in ppm): 7.98 (d, 2H, J<sub>HH</sub> = 7.7 Hz), 7.64 (d, 2H, J<sub>HH</sub> = 8.2 Hz), 7.57 -7.45 (m, 6H), 7.33 (dd, 1H, J<sub>HH</sub> = 7.0 Hz, J<sub>HH</sub> = 0.8 Hz), 7.31 (dd, 1H, J<sub>HH</sub> = 7.1 Hz, J<sub>HH</sub> = 0.8 Hz), 7.15 -7.10 (m, 2H), 7.06 -6.93 (m, 7H), 6.84 (d, 2H, J<sub>HH</sub> = 7.8 Hz), 6.71 (m, 2H), 6.59 (m, 2H), 3.82 (quad, 2H, CH<sub>2</sub> NEt J<sub>HH</sub> = 7.1 Hz), 0.95 (t, 3H, CH<sub>3</sub> NEt, J<sub>HH</sub> = 7.1 Hz)

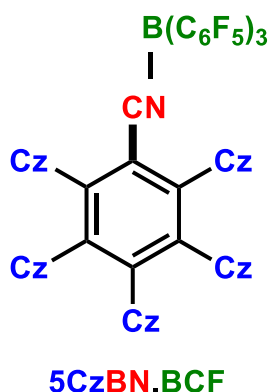
<sup>13</sup>C NMR (CDCl<sub>3</sub>, 100 MHz, δ in ppm): 160.4 (C<sub>quat</sub>. PhN), 150.7 (C<sub>quat</sub>.), 149.5 (C<sub>quat</sub>.), 147.6 (br d, C-F B(C<sub>6</sub>F<sub>5</sub>)<sub>3</sub>, J<sub>CF</sub> = 193.6 Hz), 147.2 (br d, C-F B(C<sub>6</sub>F<sub>5</sub>)<sub>3</sub>, J<sub>CF</sub> = 194.6 Hz), 142.5 (C<sub>quat</sub>.NPh), 140.4 (br d, C-F B(C<sub>6</sub>F<sub>5</sub>)<sub>3</sub>, J<sub>CF</sub> = 201.5 Hz), 140.0 (br d, C-F B(C<sub>6</sub>F<sub>5</sub>)<sub>3</sub>, J<sub>CF</sub> = 201.0), 138.1 (C<sub>quat</sub>.), 137.2 (C<sub>quat</sub>.), 136.9 (br d, C-F B(C<sub>6</sub>F<sub>5</sub>)<sub>3</sub>, J<sub>CF</sub> = 199.6 Hz), 136.6 (br d, C-F B(C<sub>6</sub>F<sub>5</sub>)<sub>3</sub>, J<sub>CF</sub> = 200.5 Hz), 131.1 (C<sub>quat</sub>.), 129.2 (C-H<sub>Ar</sub>), 127.4 (C-H<sub>Ar</sub>), 126.6 (C-H<sub>Ar</sub>), 125.9

<sup>i</sup> Wu et Al - J. Am. Chem. Soc. 2021, 143, 33, 13266–13273 ; DOI : [10.1021/jacs.1c05994](https://doi.org/10.1021/jacs.1c05994)

(C-H<sub>Ar</sub>), 125.4 (C<sub>quat.</sub>), 125.3 (C-H<sub>Ar</sub>), 124.5 (C-H<sub>Ar</sub>), 124.0 (C<sub>quat.</sub>), 123.8 (C-H<sub>Ar</sub>), 122.5 (C-H<sub>Ar</sub>), 121.7 (C-H<sub>Ar</sub>), 121.6 (C-H<sub>Ar</sub>), 121.3 (C-H<sub>Ar</sub>), 120.4 (C-H<sub>Ar</sub>), 120.2 (C-H<sub>Ar</sub>), 113.3 (br s, C-B B(C<sub>6</sub>F<sub>5</sub>)<sub>3</sub>), 110.4 (C<sub>quat.</sub>, CN), 109.6 (C-H<sub>Ar</sub>), 109.3 (C-H<sub>Ar</sub>), 108.8 (C-H<sub>Ar</sub>), 108.7 (C<sub>quat.</sub>), 102.8 (?), 102.1 (C-H<sub>Ar</sub>), 50.8 (CH<sub>2</sub> NEt), 12.7 (CH<sub>3</sub> NEt).

<sup>19</sup>F NMR (CDCl<sub>3</sub>, 376 MHz, δ in ppm): -133.7 (3F, B(C<sub>6</sub>F<sub>5</sub>)<sub>3</sub>, J<sub>FF</sub> = 19.0 Hz), -134.2 (3F, B(C<sub>6</sub>F<sub>5</sub>)<sub>3</sub>, J<sub>FF</sub> = 19.8 Hz), -155.5 (br dd, 3F B(C<sub>6</sub>F<sub>5</sub>)<sub>3</sub>, J<sub>FF</sub> = 16.5 Hz), -156.5 (dd, 3F B(C<sub>6</sub>F<sub>5</sub>)<sub>3</sub>, J<sub>FF</sub> = 19.7 Hz), -162.7 (br dd, 3F B(C<sub>6</sub>F<sub>5</sub>)<sub>3</sub>, J<sub>FF</sub> = 17.5 Hz), -163.2 (dd, 3F B(C<sub>6</sub>F<sub>5</sub>)<sub>3</sub>, J<sub>FF</sub> = 18.9 Hz).

5CzBN. [B(C<sub>6</sub>F<sub>5</sub>)<sub>3</sub>]:

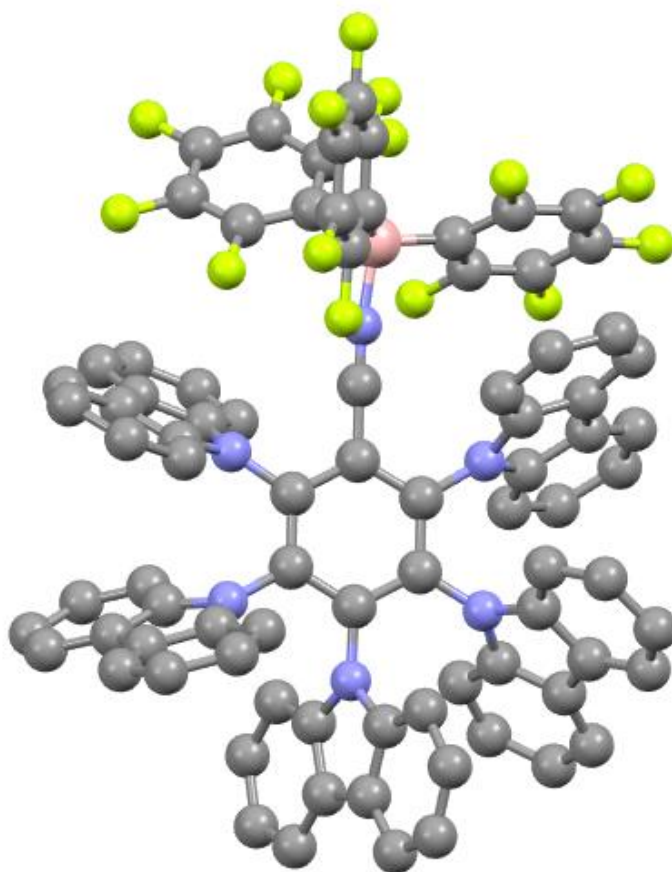


5CzBN was prepared according to Zeitler et Al procedure, solid was washed with MeOH, Et<sub>2</sub>O and pentane, and dried under vacuum at 60 °C for 2 hours.

5CzBN.[B(C<sub>6</sub>F<sub>5</sub>)<sub>3</sub>] was prepared with the same procedure than 4CzIPN.BCF<sub>2</sub> :

Reaction of 5CzBN (150 mg, 1 eq, 0.16 mmol) with B(C<sub>6</sub>F<sub>5</sub>)<sub>3</sub> (131 mg, 1.2 eq, 0.19 mmol) in PhMe (5 mL) lead after workup to 5CzBN.B(C<sub>6</sub>F<sub>5</sub>)<sub>3</sub>, as a bright orange powder (213 mg, yield = 91%).

X-Ray quality single crystals could be grown by recrystallizing compound by dissolution in boiling toluene, followed by slow cooling to -20 °C.

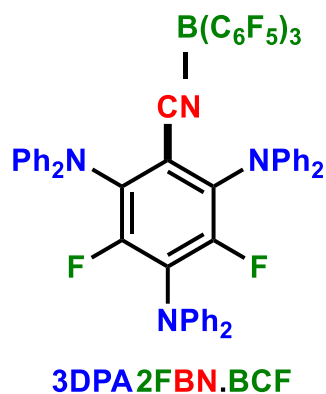


$^1\text{H}$  NMR ( $\text{C}_6\text{D}_6$ , 500 MHz,  $\delta$  in ppm): 7.49 (m, 4H), 7.09 (m, 2H), 7.02 (m, 4H), 6.95 (m, 2H), 6.86 (m, 8H).

$^{13}\text{C}$  NMR ( $\text{C}_6\text{D}_6$ , 100 MHz,  $\delta$  in ppm): 147.6 (br d, C-F B( $\text{C}_6\text{F}_5$ )<sub>3</sub>,  $J_{\text{CF}}$  = 245 Hz), 146.4 (?), 142.3 ( $\text{C}_{\text{quat.}}$ ), 140.4 (br d, C-F B( $\text{C}_6\text{F}_5$ )<sub>3</sub>,  $J_{\text{CF}}$  = 249 Hz), 138.6 ( $\text{C}_{\text{quat.}}$ ), 137.6 ( $\text{C}_{\text{quat.}}$ ), 137.5 ( $\text{C}_{\text{quat.}}$ ), 137.3 ( $\text{C}_{\text{quat.}}$ ), 137.0 (br d, C-F B( $\text{C}_6\text{F}_5$ )<sub>3</sub>,  $J_{\text{CF}}$  = 250 Hz), 125.9 (C- $\text{H}_{\text{Ar}}$ ), 124.8 (C- $\text{H}_{\text{Ar}}$ ), 124.7 (C- $\text{H}_{\text{Ar}}$ ), 124.4 ( $\text{C}_{\text{quat.}}$ ), 124.1 ( $\text{C}_{\text{quat.}}$ ), 122.4 (C- $\text{H}_{\text{Ar}}$ ), 121.9 (C- $\text{H}_{\text{Ar}}$ ), 120.6 (C- $\text{H}_{\text{Ar}}$ ), 120.2 (C- $\text{H}_{\text{Ar}}$ ), 120.1 (C- $\text{H}_{\text{Ar}}$ ), 111.0 (C- $\text{H}_{\text{Ar}}$ ), 110.3 (C- $\text{H}_{\text{Ar}}$ ), 109.8 (C- $\text{H}_{\text{Ar}}$ ).

$^{19}\text{F}$  NMR ( $\text{C}_6\text{D}_6$ , 376 MHz,  $\delta$  in ppm): -133.73 (m, 6F, F B( $\text{C}_6\text{F}_5$ )<sub>3</sub>), -155.62 (m, 3F, F B( $\text{C}_6\text{F}_5$ )<sub>3</sub>), -163.14 (m, 6F, F B( $\text{C}_6\text{F}_5$ )<sub>3</sub>).

3DPA2FBN.  $[B(C_6F_5)_3]$ :



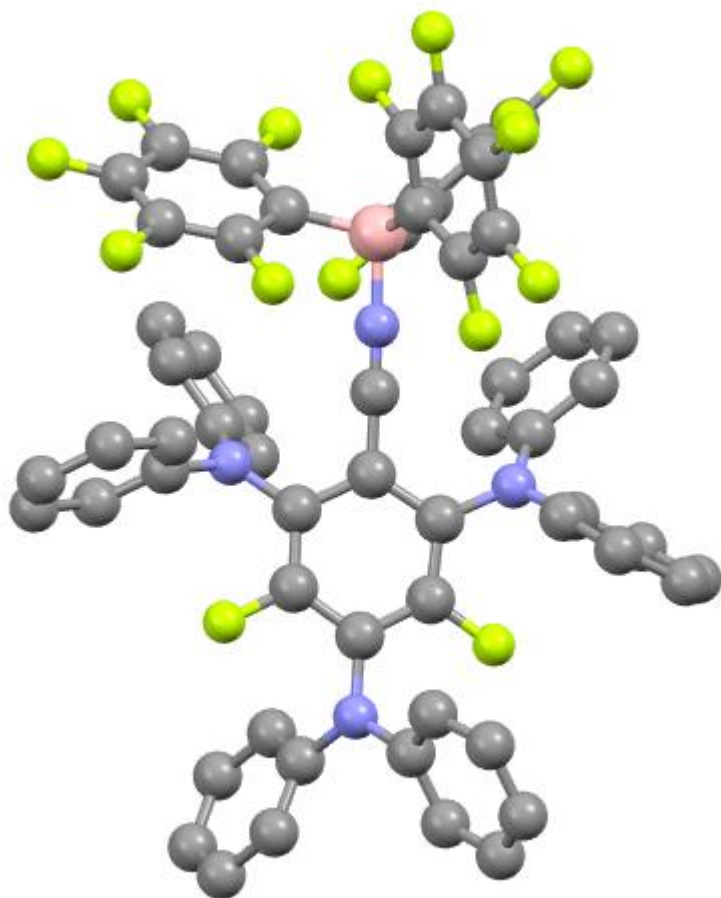
3DPA2FBN was prepared according to Zeitler et Al procedure, solid was washed with MeOH, Et<sub>2</sub>O and Pentane, and dried under vacuum at 60 °C for 2 hours.

3DPA2FBN. $[B(C_6F_5)_3]$  was prepared with the same procedure than 4CzIPN.BCF<sub>2</sub> :

Reaction of 3DPA2FBN (300 mg, 1 eq, 0.46 mmol) with  $B(C_6F_5)_3$  (287 mg, 1.2 eq, 0.56 mmol) in PhMe (5 mL) lead after workup to 3DPA2FBN. $B(C_6F_5)_3$ , as a bright orange powder (318 mg, yield = 60 %).



X-Ray quality single crystals could be grown by recrystallizing compound by dissolution in boiling toluene, followed by slow cooling to  $-20^{\circ}\text{C}$ .



$^1\text{H}$  NMR ( $\text{CDCl}_3$ , 500 MHz,  $\delta$  in ppm): 7.22 (m, 4H,  $\text{NPh}_2$ ), 7.14 (m, 8H,  $\text{NPh}_2$ ), 7.07 (m, 2H,  $\text{HNPh}_2$ ), 6.99 (m, 4H,  $\text{HNPh}_2$ ), 6.93 (m, 4H,  $\text{HNPh}_2$ ), 6.80 (m, 8H,  $\text{HNPh}_2$ ).

$^{13}\text{C}$  NMR ( $\text{CDCl}_3$ , 100 MHz,  $\delta$  in ppm): 153.6 (dd, C-F,  $J_{\text{CF}} = 261.7$  Hz,  $J_{\text{CF}} = 5.6$  Hz), 147.8 (br d, C-F,  $J_{\text{CF}} = 242.6$  Hz), 145.2 ( $\text{C}_{\text{quat.}}$ ), 145.1 ( $\text{C}_{\text{quat.}}$ ), 144.2 (br d, C-F,  $J_{\text{CF}} = 251.6$  Hz), 137.4 (dd, C-F,  $J_{\text{CF}} = 11.6$  Hz,  $J_{\text{CF}} = 4.5$  Hz), 136.9 (br d, C-F,  $J_{\text{CF}} = 250.3$  Hz), 135.2 (dd, C-F,  $J_{\text{CF}} = 10.7$  Hz,  $J_{\text{CF}} = 10.7$  Hz).

$^{19}\text{F}$  NMR ( $\text{CDCl}_3$ , 376 MHz,  $\delta$  in ppm): -118.3 (s, 2F,  $\text{F}_{\text{Ar core}}$ ), -133.3 (dd, F  $\text{B}(\text{C}_6\text{F}_5)_3$ ,  $J_{\text{FF}} = 23.0$  Hz,  $J_{\text{FF}} = 7.1$  Hz), -157.1 (dd, F  $\text{B}(\text{C}_6\text{F}_5)_3$ ,  $J_{\text{FF}} = 20.2$  Hz,  $J_{\text{FF}} = 20.2$  Hz), -163.8 (ddd, F  $\text{B}(\text{C}_6\text{F}_5)_3$ ,  $J_{\text{FF}} = 22.7$  Hz,  $J_{\text{FF}} = 22.7$  Hz,  $J_{\text{FF}} = 7.2$  Hz).

### Electrochemistry - Cyclic voltammetry

Solartron Analytical Instrument potentiostat (Modulab XM MTS) with XM-studio as software was used to performed electrochemical measurements (CV and bulk electrolysis) at RT in a glovebox. Tetrabutylammonium hexafluorophosphate ( $n\text{-Bu}_4\text{NPF}_6$ , TBAPF<sub>6</sub>) were used as supporting electrolyte. Ag/Ag<sup>+</sup> (AgNO<sub>3</sub> 10 mM in acetonitrile + 0.1 M  $n\text{-Bu}_4\text{NPF}_6$ ) was the reference electrode and Pt wire immersed in electrolyte solution (acetonitrile + 0.1 M  $n\text{-Bu}_4\text{NPF}_6$ ) separated from the electrolytic solution by glass frit was used as the counter electrode. 3 mm-diameter glassy carbon (GC) disk was employed as working electrode.

Unless otherwise stated, all potentials are reported vs. Ag<sup>+</sup>/Ag and can be translated vs. SCE according to:

$$E (\text{vs. SCE}) = E (\text{vs. Ag}^+ / \text{Ag}) + 0.30 \text{ V.}$$

Experiments carried out in MeCN unless otherwise noted (for BCF experiment, orthodifluorobenzene was used).

Tetrabutylammonium hexafluorophosphate  $n\text{-Bu}_4\text{NPF}_6$  or TBAPF<sub>6</sub> (0.1 M) was used unless otherwise noted. Tetrabutylammonium tetrakis[(3,5-trifluoromethyl)phenyl]borate (TBABArF<sub>24</sub>) (0.05 M, for BCF study) was used as supporting electrolyte for BCF study.

### Electrolysis and UV-vis spectroelectrochemistry (SEC)

Same instrument and electrodes (reference, working electrode and counter electrode) were used as describe above. Experiments were performed in a glovebox. Zeiss MCS501 spectrophotometer equipped with an optic fiber was used to make UV-vis measurement following in situ the progress of electrolysis.

### Controlled potential electrolysis (CPE)

To performed electrolysis, Solartron Analytical Instrument potentiostat (Modulab XM MTS) with XM-studio as software was used. The CPE were carried out in a conventional hermetic three-electrode cell (50 mL) with a glassy carbon plate (1x3 cm, *ca.* 1x1.5 cm immersed) as working electrode, Ag/Ag<sup>+</sup> (AgNO<sub>3</sub> 10 mM in acetonitrile + 0.1 M  $n\text{-Bu}_4\text{NPF}_6$ ) as reference electrode and the counter electrode was Pt wire immersed in electrolyte solution (acetonitrile + 0.1 M  $n\text{-Bu}_4\text{NPF}_6$ ) which was separated from the electrolytic solution by a glass frit.

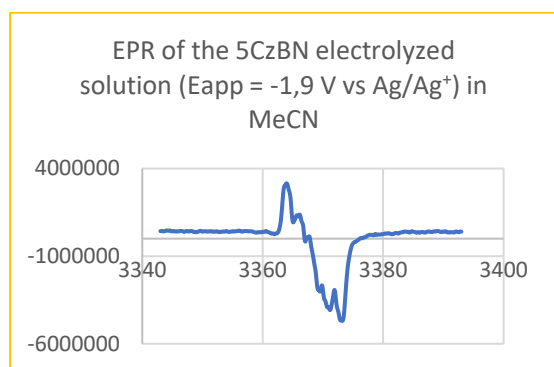
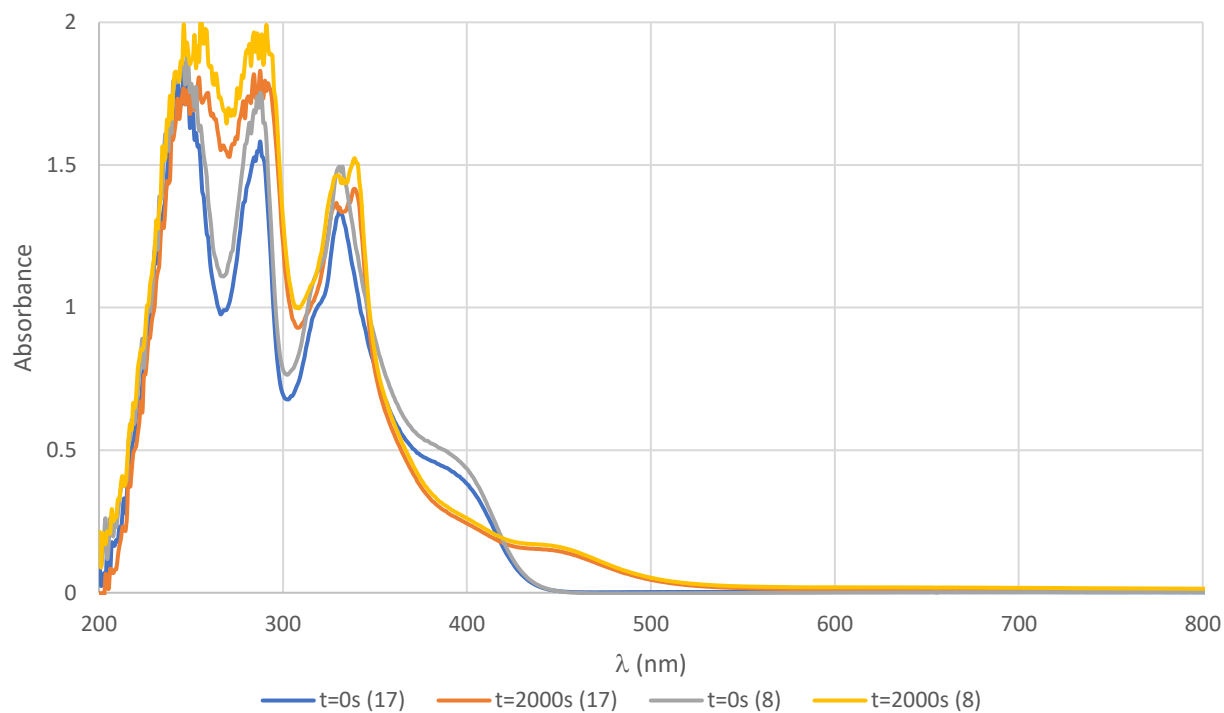
### Additional Data:

#### 5CzBN

$$E_{\text{pc}} = -1.849 \text{ V} \quad E_{\text{pa}} = -1.779 \text{ V} \quad \Delta E_{\text{p}} = 70 \text{ mV}$$

$$E_{1/2}(5\text{CzBN}/5\text{CzBN}^{\bullet-}) = -1.814 \text{ V vs } 10 \text{ mM Ag/AgNO}_3$$

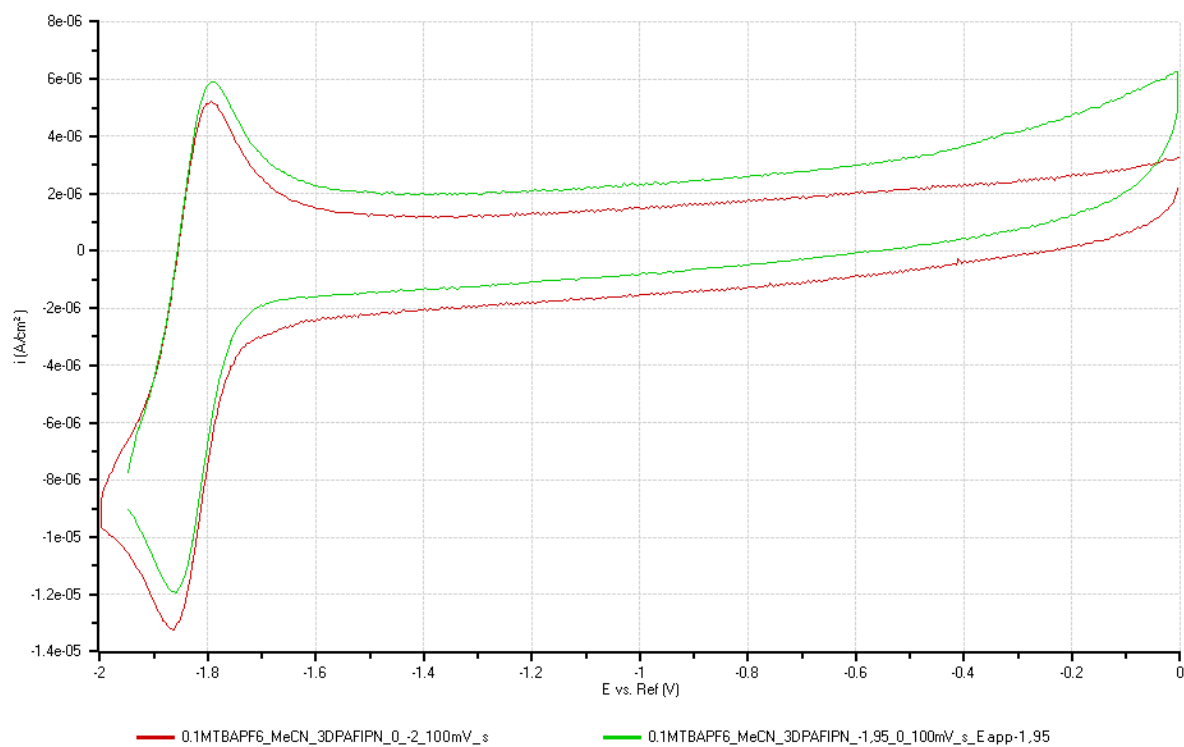
### UV-Vis absorption of a 0.5 mM 5CzBN solution overtime during electrolysis (2 tests)



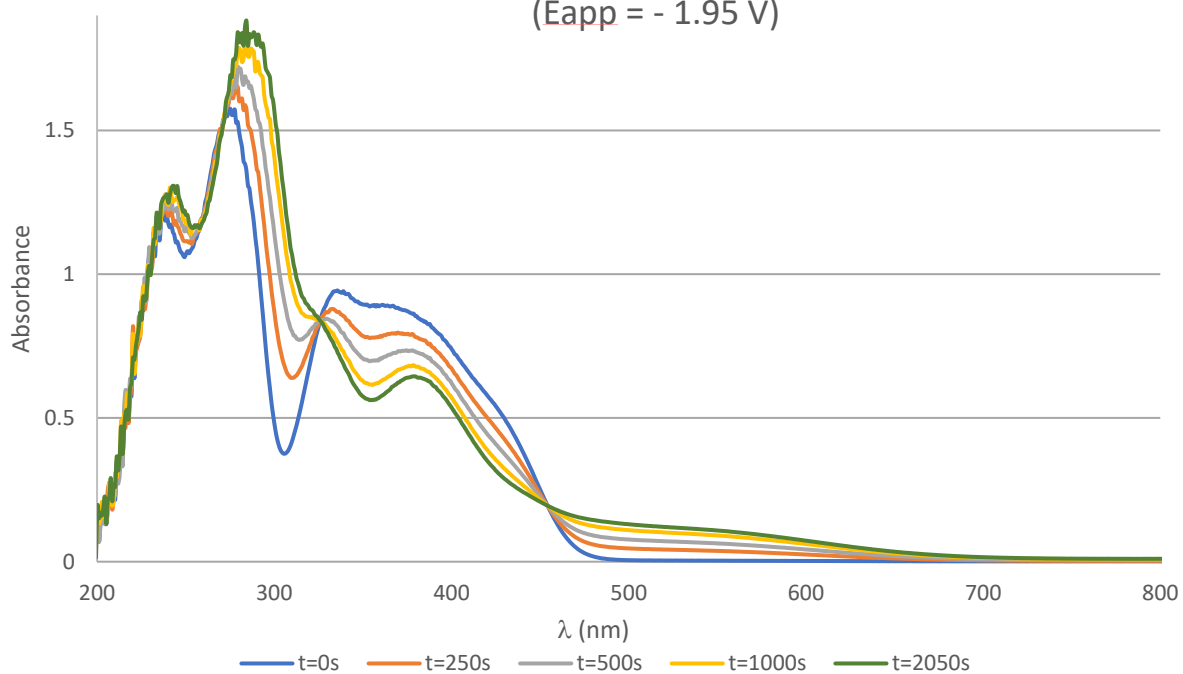
### 3DPAFIPN

$$E_{\text{pc}} = -1.868 \text{ V} \quad E_{\text{pa}} = -1.799 \text{ V} \quad \Delta E_{\text{p}} = 69 \text{ mV}$$

$$E_{1/2}(3\text{DPAFIPN}/3\text{DPAFIPN}^{\bullet-}) = -1.834 \text{ V vs } 10 \text{ mM Ag/AgNO}_3$$



UV-Vis absorption of a 0.5 mM 3DPAFIPN solution overtime during electrolysis ( $E_{app} = -1.95$  V)



### 3DPA2FBN

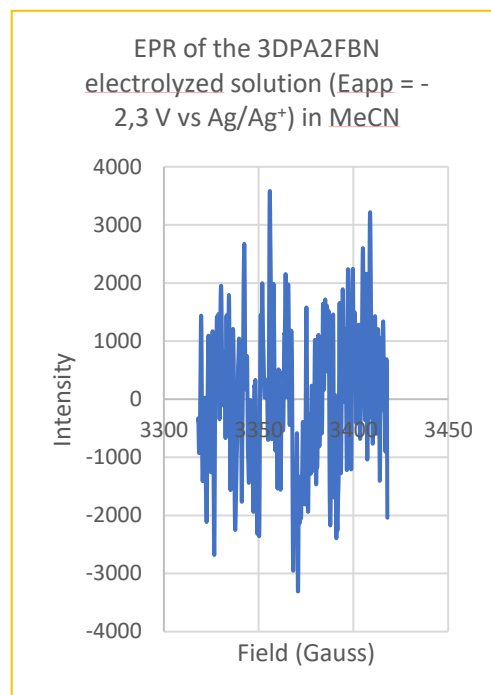
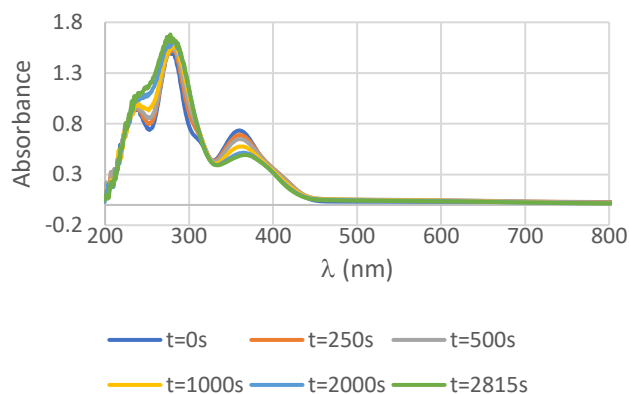
$E_{pc} = -2.143$  V

$E_{pa} = -2.068$  V

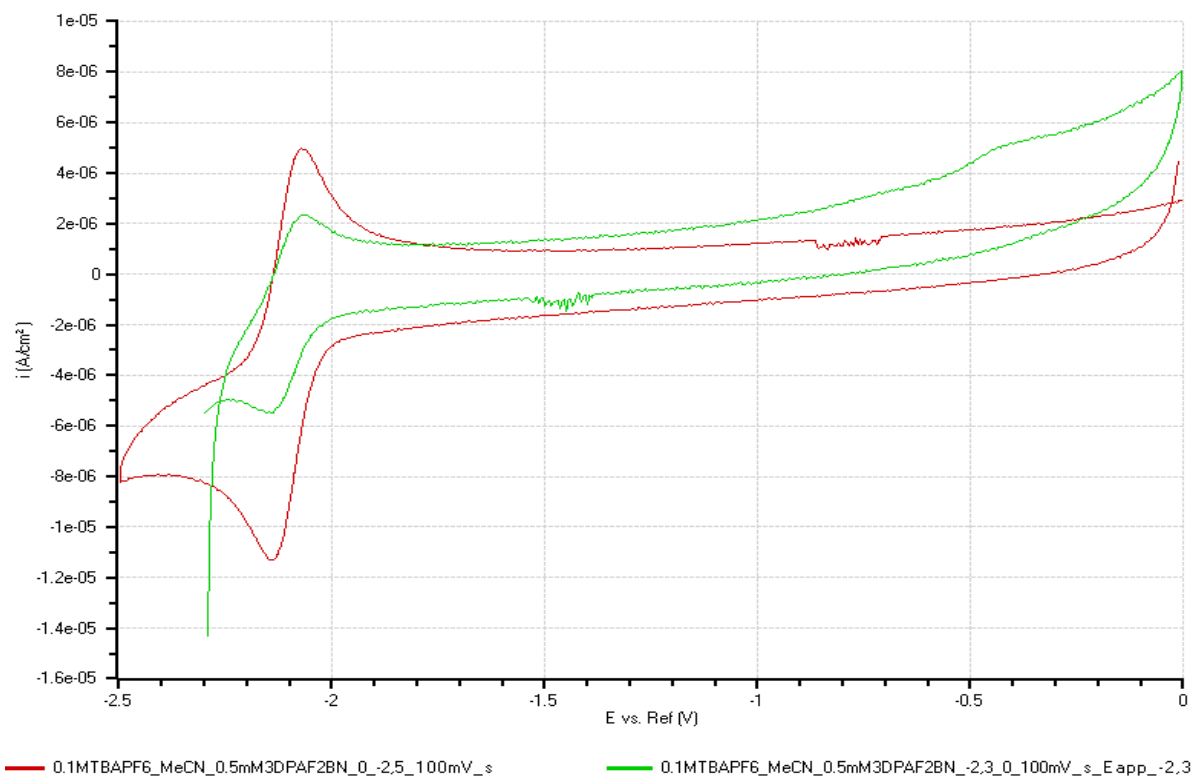
$\Delta E_p = 75$  mV

$$E_{1/2}(3\text{DPA2FBN}/3\text{DPA2FBN}^{\bullet-}) = -2.106 \text{ V vs } 10 \text{ mM Ag}/\text{AgNO}_3$$

UV-Vis absorption of a 0.5 mM 3DPA2FBN solution overtime during electrolysis ( $E_{\text{app}} = -2.3 \text{ V}$ )



Degradation of 3DPA2FBN occurred upon electrolysis.



## 8. References

- (1) Shang, T. Y.; Lu, L. H.; Cao, Z.; Liu, Y.; He, W. M.; Yu, B. Recent Advances of 1,2,3,5-Tetrakis(Carbazol-9-Yl)-4,6-Dicyanobenzene (4CzIPN) in Photocatalytic Transformations. *Chem. Commun.* **2019**, 55 (38), 5408–5419. <https://doi.org/10.1039/c9cc01047e>.
- (2) Lippert, E.; Lüder, W.; Boos, H. Fluoreszenzspektrum Und Franck-Condon Prinzip in Lösungen Aromatischer Verbindungen. *Adv. Mol. Spectrosc. Eur. Conf. Mol. Spectrosc.* **1959**, ed. by A.
- (3) Lippert, E.; Lüder, W.; Moll, F.; Nägele, W.; Boos, H.; Prigge, H.; Seibold-Blankenstein, I. Umwandlung von Elektronenanregungsenergie. *Angew. Chemie* **1961**, 73 (21), 695–706. <https://doi.org/10.1002/ange.19610732103>.
- (4) Köhler, G.; Wolschann, P.; Rotkiewicz, K. Solvent Effects on Intramolecular Charge Separation. *Proc. Indian Acad. Sci. - Chem. Sci.* **1992**, 104 (2), 197–207. <https://doi.org/10.1007/BF02863364>.
- (5) Kochman, M. A.; Durbeej, B. Simulating the Nonadiabatic Relaxation Dynamics of 4-(N,N-Dimethylamino)Benzonitrile (DMABN) in Polar Solution. *J. Phys. Chem. A* **2020**, 124 (11), 2193–2206. <https://doi.org/10.1021/acs.jpca.9b10588>.
- (6) Rotkiewicz, K.; Grellmann, K. H.; Grabowski, Z. R. Reinterpretation of the Anomalous Fluorescence of P-n,n-Dimethylamino-Benzonitrile. *Chem. Phys. Lett.* **1973**, 19 (3), 315–318. [https://doi.org/10.1016/0009-2614\(73\)80367-7](https://doi.org/10.1016/0009-2614(73)80367-7).
- (7) Rettig, W.; Zander, M. On Twisted Intramolecular Charge Transfer (TICT) States in N-Aryl Carbazoles. *Chem. Phys. Lett.* **1982**, 87 (3), 229–234. [https://doi.org/10.1016/0009-2614\(82\)83131-X](https://doi.org/10.1016/0009-2614(82)83131-X).
- (8) Zander, M.; Rettig, W. Über Die Löschung von „Twisted Intramolecular Charge Transfer“ (TICT) -Fluoreszenzen Durch Äu SSere Schweratom -Störer. *Naturforsch* **1984**, 39a, 41–48.
- (9) Payne, R.; Dalton, G.; Garrett, A.; Matthews, I. The PICT Model for Dual Fluorescence of Aminobenzonitriles. *J. Inst. Br. Telecommun. Eng.* **2002**, 3 (1), 24–28. [https://doi.org/10.1007/978-3-030-58292-0\\_160525](https://doi.org/10.1007/978-3-030-58292-0_160525).

- (10) Grabowski, Z. R.; Rotkiewicz, K.; Rettig, W. Structural Changes Accompanying Intramolecular Electron Transfer: Focus on Twisted Intramolecular Charge-Transfer States and Structures. *Chem. Rev.* **2003**, *103* (10), 3899–4031. <https://doi.org/10.1021/cr940745l>.
- (11) Gómez, I.; Reguero, M.; Boggio-Pasqua, M.; Robb, M. A. Intramolecular Charge Transfer in 4-Aminobenzonitriles Does Not Necessarily Need the Twist. *J. Am. Chem. Soc.* **2005**, *127* (19), 7119–7129. <https://doi.org/10.1021/ja042413w>.
- (12) Sasaki, S.; Drummen, G. P. C.; Konishi, G. I. Recent Advances in Twisted Intramolecular Charge Transfer (TICT) Fluorescence and Related Phenomena in Materials Chemistry. *J. Mater. Chem. C* **2016**, *4* (14), 2731–2743. <https://doi.org/10.1039/c5tc03933a>.
- (13) Wang, C.; Chi, W.; Qiao, Q.; Tan, D.; Xu, Z.; Liu, X. Twisted Intramolecular Charge Transfer (TICT) and Twists beyond TICT: From Mechanisms to Rational Designs of Bright and Sensitive Fluorophores. *Chem. Soc. Rev.* **2021**, *50* (22), 12656–12678. <https://doi.org/10.1039/d1cs00239b>.
- (14) Chen, C.; Fang, C. Fluorescence Modulation by Amines: Mechanistic Insights into Twisted Intramolecular Charge Transfer (TICT) and Beyond. *Chemosensors* **2023**, *11* (2), 87. <https://doi.org/10.3390/chemosensors11020087>.
- (15) Herbich, J.; Kapturkiewicz, A.; Nowacki, J. Phosphorescent Intramolecular Charge Transfer Triplet States. *Chem. Phys. Lett.* **1996**, *262* (5), 633–642. [https://doi.org/10.1016/S0009-2614\(96\)01122-0](https://doi.org/10.1016/S0009-2614(96)01122-0).
- (16) Kapturkiewicz, A.; Herbich, J.; Karpiuk, J.; Nowacki, J. Intramolecular Radiative and Radiationless Charge Recombination Processes in Donor - Acceptor Carbazole Derivatives. *J. Phys. Chem. A* **1997**, *101* (12), 2332–2344. <https://doi.org/10.1021/jp9634565>.
- (17) Borowicz, P.; Herbich, J.; Kapturkiewicz, A.; Nowacki, J. Excited Charge Transfer States in Donor-Acceptor Indole Derivatives. *Chem. Phys.* **1999**, *244* (2–3), 251–261. [https://doi.org/10.1016/S0301-0104\(99\)00142-1](https://doi.org/10.1016/S0301-0104(99)00142-1).
- (18) Kretz, B.; Egger, D. A. Accurate Molecular Geometries in Complex Excited-State Potential Energy Surfaces from Time-Dependent Density Functional Theory. *J. Chem. Theory Comput.* **2021**, *17* (1), 357–366. <https://doi.org/10.1021/acs.jctc.0c00858>.

- (19) Nakanotani, H.; Tsuchiya, Y.; Adachi, C. Thermally-Activated Delayed Fluorescence for Light-Emitting Devices. *Chem. Lett.* **2021**, 50 (5), 938–948. <https://doi.org/10.1246/cl.200915>.
- (20) Boudin, S. PHOSPHORESCENCE DES SOLUTIONS GLYCÉRIQUES D'ÉOSINE. *J. Chim. Phys.* **1930**, No. 4, 1894.
- (21) Uoyama, H.; Goushi, K.; Shizu, K.; Nomura, H.; Adachi, C. Highly Efficient Organic Light-Emitting Diodes from Delayed Fluorescence. *Nature* **2012**, 492 (7428), 234–238. <https://doi.org/10.1038/nature11687>.
- (22) Dias, F. B.; Santos, J.; Graves, D. R.; Data, P.; Nobuyasu, R. S.; Fox, M. A.; Batsanov, A. S.; Palmeira, T.; Berberan-Santos, M. N.; Bryce, M. R.; Monkman, A. P. The Role of Local Triplet Excited States and D-A Relative Orientation in Thermally Activated Delayed Fluorescence: Photophysics and Devices. *Adv. Sci.* **2016**, 3 (12), 1–10. <https://doi.org/10.1002/advs.201600080>.
- (23) Luo, J.; Zhang, J. Donor-Acceptor Fluorophores for Visible-Light-Promoted Organic Synthesis: Photoredox/Ni Dual Catalytic C(Sp<sup>3</sup>)-C(Sp<sup>2</sup>) Cross-Coupling. *ACS Catal.* **2016**, 6 (2), 873–877. <https://doi.org/10.1021/acscatal.5b02204>.
- (24) Hong, G.; Gan, X.; Leonhardt, C.; Zhang, Z.; Seibert, J.; Busch, J. M.; Bräse, S. A Brief History of OLEDs—Emitter Development and Industry Milestones. *Adv. Mater.* **2021**, 33 (9). <https://doi.org/10.1002/adma.202005630>.
- (25) Baldo, M. A.; You, D. F. O.; Shoustikov, A.; Sibley, S.; Thompson, M. E.; Forrest, S. R. Highly Efficient Phosphorescent Emission from Organic Electroluminescent Devices. *Nature* **1998**, 395 (September), 151.
- (26) Adachi, C.; Sandanayaka, A. S. D. The Leap from Organic Light-Emitting Diodes to Organic Semiconductor Laser Diodes. *CCS Chem.* **2020**, 2 (4), 1203–1216. <https://doi.org/10.31635/ccschem.020.202000327>.
- (27) Endo, A.; Sato, K.; Yoshimura, K.; Kai, T.; Kawada, A.; Miyazaki, H.; Adachi, C. Efficient Up-Conversion of Triplet Excitons into a Singlet State and Its Application for Organic Light Emitting Diodes. *Appl. Phys. Lett.* **2011**, 98 (8), 10–13. <https://doi.org/10.1063/1.3558906>.
- (28) Adachi, C. Third-Generation Organic Electroluminescence Materials. *Jpn. J. Appl. Phys.*



- 2014**, 53 (6). <https://doi.org/10.7567/JJAP.53.060101>.
- (29) Huang, J. W.; Hsu, Y. C.; Wu, X.; Wang, S.; Gan, X. Q.; Zheng, W. Q.; Zhang, H.; Gong, Y. Z.; Hung, W. Y.; Chou, P. T.; Zhu, W. Influence of Charge Transfer Strength on Emission Bandwidth for Multiple-Resonance Emitters via Systematically Tuning the Acceptor-Donor Assembly. *J. Mater. Chem. C* **2022**, 10 (20), 7866–7874. <https://doi.org/10.1039/d1tc06165h>.
- (30) Mateen, F.; Lee, S. Y.; Hong, S. K. Luminescent Solar Concentrators Based on Thermally Activated Delayed Fluorescence Dyes. *J. Mater. Chem. A* **2020**, 8 (7), 3708–3716. <https://doi.org/10.1039/c9ta13312g>.
- (31) Schmidbauer, S.; Hohenleutner, A.; König, B. Chemical Degradation in Organic Light-Emitting Devices: Mechanisms and Implications for the Design of New Materials. *Adv. Mater.* **2013**, 25 (15), 2114–2129. <https://doi.org/10.1002/adma.201205022>.
- (32) Sandanayaka, A. S. D.; Matsushima, T.; Adachi, C. Degradation Mechanisms of Organic Light-Emitting Diodes Based on Thermally Activated Delayed Fluorescence Molecules. *J. Phys. Chem. C* **2015**, 119 (42), 23845–23851. <https://doi.org/10.1021/acs.jpcc.5b07084>.
- (33) Fang, F.; Yuan, Y.; Wan, Y.; Li, J.; Song, Y.; Chen, W. C.; Zhao, D.; Chi, Y.; Li, M.; Lee, C. S.; Zhang, J. Near-Infrared Thermally Activated Delayed Fluorescence Nanoparticle: A Metal-Free Photosensitizer for Two-Photon-Activated Photodynamic Therapy at the Cell and Small Animal Levels. *Small* **2022**, 18 (6). <https://doi.org/10.1002/sml.202106215>.
- (34) Hu, S.; Huang, B.; Pu, Y.; Xia, C.; Zhang, Q.; Guo, S.; Wang, Y.; Huang, X. A Thermally Activated Delayed Fluorescence Photosensitizer for Photodynamic Therapy of Oral Squamous Cell Carcinoma under Low Laser Intensity. *J. Mater. Chem. B* **2021**, 9 (28), 5645–5655. <https://doi.org/10.1039/d1tb00719j>.
- (35) Fang, F.; Zhu, L.; Li, M.; Song, Y.; Sun, M.; Zhao, D.; Zhang, J. Thermally Activated Delayed Fluorescence Material: An Emerging Class of Metal-Free Luminophores for Biomedical Applications. *Adv. Sci.* **2021**, 8 (24), 1–19. <https://doi.org/10.1002/adv.202102970>.
- (36) Zhang, J.; Fang, F.; Liu, B.; Tan, J. H.; Chen, W. C.; Zhu, Z.; Yuan, Y.; Wan, Y.; Cui, X.; Li,

- S.; Tong, Q. X.; Zhao, J.; Meng, X. M.; Lee, C. S. Intrinsically Cancer-Mitochondria-Targeted Thermally Activated Delayed Fluorescence Nanoparticles for Two-Photon-Activated Fluorescence Imaging and Photodynamic Therapy. *ACS Appl. Mater. Interfaces* **2019**, *11* (44), 41051–41061. <https://doi.org/10.1021/acsami.9b14552>.
- (37) Ni, F.; Zhu, Z.; Tong, X.; Zeng, W.; An, K.; Wei, D.; Gong, S.; Zhao, Q.; Zhou, X.; Yang, C. Hydrophilic, Red-Emitting, and Thermally Activated Delayed Fluorescence Emitter for Time-Resolved Luminescence Imaging by Mitochondrion-Induced Aggregation in Living Cells. *Adv. Sci.* **2019**, *6* (5), 1–10. <https://doi.org/10.1002/advs.201801729>.
- (38) Zhu, Z.; Tian, D.; Gao, P.; Wang, K.; Li, Y.; Shu, X.; Zhu, J.; Zhao, Q. Cell-Penetrating Peptides Transport Noncovalently Linked Thermally Activated Delayed Fluorescence Nanoparticles for Time-Resolved Luminescence Imaging. *J. Am. Chem. Soc.* **2018**, *140* (50), 17484–17491. <https://doi.org/10.1021/jacs.8b08438>.
- (39) Speckmeier, E.; Fischer, T. G.; Zeitler, K. A Toolbox Approach to Construct Broadly Applicable Metal-Free Catalysts for Photoredox Chemistry: Deliberate Tuning of Redox Potentials and Importance of Halogens in Donor-Acceptor Cyanoarenes. *J. Am. Chem. Soc.* **2018**, *140* (45), 15353–15365. <https://doi.org/10.1021/jacs.8b08933>.
- (40) Lee, K.; Kim, D. Local-Excitation versus Charge-Transfer Characters in the Triplet State: Theoretical Insight into the Singlet-Triplet Energy Differences of Carbazolyl-Phthalonitrile-Based Thermally Activated Delayed Fluorescence Materials. *J. Phys. Chem. C* **2016**, *120* (49), 28330–28336. <https://doi.org/10.1021/acs.jpcc.6b10161>.
- (41) Serdiuk, I. E.; Jung, S.; Mońka, M.; Ryoo, C. H.; Park, S. Y. Contradictory Role of Locally-Excited Triplet States in Blue Thermally Activated Delayed Fluorescence of s-Triazine-Based Emitters. *J. Phys. Chem. C* **2022**. <https://doi.org/10.1021/acs.jpcc.2c06445>.
- (42) Chen, J. X.; Xiao, Y. F.; Wang, K.; Sun, D.; Fan, X. C.; Zhang, X.; Zhang, M.; Shi, Y. Z.; Yu, J.; Geng, F. X.; Lee, C. S.; Zhang, X. H. Managing Locally Excited and Charge-Transfer Triplet States to Facilitate Up-Conversion in Red TADF Emitters That Are Available for Both Vacuum- and Solution-Processes. *Angew. Chemie - Int. Ed.* **2021**, *60* (5), 2478–2484. <https://doi.org/10.1002/anie.202012070>.
- (43) Bryden, M. A.; Zysman-Colman, E. Organic Thermally Activated Delayed Fluorescence (TADF) Compounds Used in Photocatalysis. *Chem. Soc. Rev.* **2021**, *50* (13), 7587–7680.

<https://doi.org/10.1039/d1cs00198a>.

- (44) Wu, T. L.; Liao, S. Y.; Huang, P. Y.; Hong, Z. S.; Huang, M. P.; Lin, C. C.; Cheng, M. J.; Cheng, C. H. Exciplex Organic Light-Emitting Diodes with Nearly 20% External Quantum Efficiency: Effect of Intermolecular Steric Hindrance between the Donor and Acceptor Pair. *ACS Appl. Mater. Interfaces* **2019**. <https://doi.org/10.1021/acsami.9b04365>.
- (45) Etherington, M. K.; Kukhta, N. A.; Higginbotham, H. F.; Danos, A.; Bismillah, A. N.; Graves, D. R.; McGonigal, P. R.; Haase, N.; Morherr, A.; Batsanov, A. S.; Pflumm, C.; Bhalla, V.; Bryce, M. R.; Monkman, A. P. Persistent Dimer Emission in Thermally Activated Delayed Fluorescence Materials. *J. Phys. Chem. C* **2019**, *123* (17), 11109–11117. <https://doi.org/10.1021/acs.jpcc.9b01458>.
- (46) Imato, T.; Nakano, K.; Adachi, C.; Shizu, K.; Matsunami, S.; Ishimatsu, R. Solvent Effect on Thermally Activated Delayed Fluorescence by 1,2,3,5-Tetrakis(Carbazol-9-Yl)-4,6-Dicyanobenzene. *J. Phys. Chem. A* **2013**, *117*, 5607–5612.
- (47) Le Vaillant, F.; Garreau, M.; Nicolai, S.; Gryn'Ova, G.; Corminboeuf, C.; Waser, J. Fine-Tuned Organic Photoredox Catalysts for Fragmentation-Alkynylation Cascades of Cyclic Oxime Ethers. *Chem. Sci.* **2018**, *9* (27), 5883–5889. <https://doi.org/10.1039/c8sc01818a>.
- (48) Elgrishi, N.; Rountree, K. J.; McCarthy, B. D.; Rountree, E. S.; Eisenhart, T. T.; Dempsey, J. L. A Practical Beginner's Guide to Cyclic Voltammetry. *J. Chem. Educ.* **2018**, *95* (2), 197–206. <https://doi.org/10.1021/acs.jchemed.7b00361>.
- (49) Pavlishchuk, V. V.; Addison, A. W. Conversion Constants for Redox Potentials Measured versus Different Reference Electrodes in Acetonitrile Solutions at 25°C. *Inorganica Chim. Acta* **2000**, *298* (1), 97–102. [https://doi.org/10.1016/S0020-1693\(99\)00407-7](https://doi.org/10.1016/S0020-1693(99)00407-7).
- (50) Costentin, C.; Fortage, J.; Collomb, M. N. Electrophotocatalysis: Cyclic Voltammetry as an Analytical Tool. *J. Phys. Chem. Lett.* **2020**, *11* (15), 6097–6104. <https://doi.org/10.1021/acs.jpcllett.0c01662>.
- (51) Roth, H. G.; Romero, N. A.; Nicewicz, D. A. Experimental and Calculated Electrochemical Potentials of Common Organic Molecules for Applications to Single-Electron Redox Chemistry. *Synlett* **2016**, *27* (5), 714–723. <https://doi.org/10.1055/s-0035-1561297>.
- (52) Espinoza, E. M.; Clark, J. A.; Soliman, J.; Derr, J. B.; Morales, M.; Vullev, V. I. Practical

- Aspects of Cyclic Voltammetry: How to Estimate Reduction Potentials When Irreversibility Prevails. *J. Electrochem. Soc.* **2019**, *166* (5), H3175–H3187. <https://doi.org/10.1149/2.0241905jes>.
- (53) Minter, S.; Chen, J.; Lin, S.; Crudden, C.; Dehnen, S.; Kamat, P. V.; Kozlowski, M.; Masson, G.; Miller, S. J. New Guidelines for Presenting Electrochemical Data in All ACS Journals. *ACS Energy Lett.* **2023**, 1793–1794. <https://doi.org/10.1021/acsenergylett.3c00470>.
- (54) Gould, I. R.; Ege, D.; Moser, J. E.; Farid, S. Efficiencies of Photoinduced Electron-Transfer Reactions: Role of the Marcus Inverted Region in Return Electron Transfer within Geminate Radical-Ion Pairs. *J. Am. Chem. Soc.* **1990**, *112* (11), 4290–4301. <https://doi.org/10.1021/ja00167a027>.
- (55) Wang, Y.; Haze, O.; Dinnocenzo, J. P.; Farid, S.; Farid, R. S.; Gould, I. R. Bonded Exciplexes. A New Concept in Photochemical Reactions. *J. Org. Chem.* **2007**, *72* (18), 6970–6981. <https://doi.org/10.1021/jo071157d>.
- (56) Wu, Y.; Kim, D.; Teets, T. S. Photophysical Properties and Redox Potentials of Photosensitizers for Organic Photoredox Transformations. *Synlett* **2022**, *33* (12), 1154–1179. <https://doi.org/10.1055/a-1390-9065>.
- (57) Xu, J.; Cao, J.; Wu, X.; Wang, H.; Yang, X.; Tang, X.; Toh, R. W.; Zhou, R.; Yeow, E. K. L.; Wu, J. Unveiling Extreme Photoreduction Potentials of Donor-Acceptor Cyanoarenes to Access Aryl Radicals from Aryl Chlorides. *J. Am. Chem. Soc.* **2021**, *143* (33), 13266–13273. <https://doi.org/10.1021/jacs.1c05994>.
- (58) Garreau, M.; Le Vaillant, F.; Waser, J. C-Terminal Bioconjugation of Peptides through Photoredox Catalyzed Decarboxylative Alkynylation. *Angew. Chemie - Int. Ed.* **2019**, *58* (24), 8182–8186. <https://doi.org/10.1002/anie.201901922>.
- (59) Ishimatsu, R.; Matsunami, S.; Kasahara, T.; Mizuno, J.; Edura, T.; Adachi, C.; Nakano, K.; Imato, T. Electrogenated Chemiluminescence of Donor-Acceptor Molecules with Thermally Activated Delayed Fluorescence. *Angew. Chemie* **2014**, *126* (27), 7113–7116. <https://doi.org/10.1002/ange.201402615>.
- (60) Grotjahn, S.; König, B. Photosubstitution in Dicyanobenzene-Based Photocatalysts. *Org. Lett.* **2021**, *23* (8), 3146–3150. <https://doi.org/10.1021/acs.orglett.1c00836>.

- (61) Romero, N. A.; Nicewicz, D. A. Organic Photoredox Catalysis. *Chem. Rev.* **2016**, *116* (17), 10075–10166. <https://doi.org/10.1021/acs.chemrev.6b00057>.
- (62) Yoshio, O.; Ichinose, N.; Mizuno, K. Photochemistry of 9,10-Dicyanoanthracene-1,2-Diarylcyclopropane Systems. Photocycloaddition and Photoisomerization. *J. Org. Chem.* **1992**, *57*, 1855–1860.
- (63) Borg, M.; Arnold, R.; Stanley, A. N. D. T.; Stanley, T. Dicyanobenzenes and Alkyl Olefins. *Can. J. Chem.* **1984**, *62* (7), 1785–1802.
- (64) Ohashi, M.; Miyake, K.; Tsujimoto, K. Photochemical Reactions of Dicyanobenzenes with Aliphatic Amines. *Bulletin of the Chemical Society of Japan*. 1980, pp 1683–1688. <https://doi.org/10.1246/bcsj.53.1683>.
- (65) Gutenberger, G.; Steckhan, E.; Blechert, S.  $\alpha$ -Silyl Ethers As Hydroxymethyl Anion Equivalents in Photoinduced Radical Electron Transfer Additions. *Angew. Chemie - Int. Ed.* **1998**, *37* (5), 660–662. [https://doi.org/10.1002/\(SICI\)1521-3773\(19980316\)37:5<660::AID-ANIE660>3.0.CO;2-8](https://doi.org/10.1002/(SICI)1521-3773(19980316)37:5<660::AID-ANIE660>3.0.CO;2-8).
- (66) Pandey, G.; Karthikeyan, M.; Murugan, A. New Intramolecular  $\alpha$ -Arylation Strategy of Ketones by the Reaction of Silyl Enol Ethers to Photosensitized Electron Transfer Generated Arene Radical Cations: Construction of Benzannulated and Benzospiroannulated Compounds. *J. Org. Chem.* **1998**, *63* (9), 2867–2872. <https://doi.org/10.1021/jo9718612>.
- (67) Buzzetti, L.; Prieto, A.; Roy, S. R.; Melchiorre, P. Radical-Based C–C Bond-Forming Processes Enabled by the Photoexcitation of 4-Alkyl-1,4-Dihydropyridines. *Angew. Chemie* **2017**, *129* (47), 15235–15239. <https://doi.org/10.1002/ange.201709571>.
- (68) Tong, S.; Li, K.; Ouyang, X.; Song, R.; Li, J. Recent Advances in the Radical-Mediated Decyanative Alkylation of Cyano(Hetero)Arene. *Green Synth. Catal.* **2021**, *2* (2), 145–155. <https://doi.org/10.1016/j.gresc.2021.04.003>.
- (69) Yu, Z. J.; Lou, W. Y.; Junge, H.; Pöpcke, A.; Chen, H.; Xia, L. M.; Xu, B.; Wang, M. M.; Wang, X. J.; Wu, Q. A.; Lou, B. Y.; Lochbrunner, S.; Beller, M.; Luo, S. P. Thermally Activated Delayed Fluorescence (TADF) Dyes as Efficient Organic Photosensitizers for Photocatalytic Water Reduction. *Catal. Commun.* **2019**, *119* (September 2018), 11–15. <https://doi.org/10.1016/j.catcom.2018.09.018>.

- (70) Berger, A. L.; Donabauer, K.; König, B. Photocatalytic Carbanion Generation from C-H Bonds-Reductant Free Barbier/Grignard-Type Reactions. *Chem. Sci.* **2019**, *10* (48), 10991–10996. <https://doi.org/10.1039/c9sc04987h>.
- (71) Tlili, A.; Lakhdar, S. Acridinium Salts and Cyanoarenes as Powerful Photocatalysts: Opportunities in Organic Synthesis. *Angew. Chemie - Int. Ed.* **2021**, *60* (36), 19526–19549. <https://doi.org/10.1002/anie.202102262>.
- (72) Bao, Q. F.; Li, M.; Xia, Y.; Wang, Y. Z.; Zhou, Z. Z.; Liang, Y. M. Visible-Light-Mediated Decarboxylative Radical Addition Bifunctionalization Cascade for the Production of 1,4-Amino Alcohols. *Org. Lett.* **2021**, *23* (3), 1107–1112. <https://doi.org/10.1021/acs.orglett.1c00034>.
- (73) Webb, E. W.; Park, J. B.; Cole, E. L.; Donnelly, D. J.; Bonacorsi, S. J.; Ewing, W. R.; Doyle, A. G. Nucleophilic (Radio)Fluorination of Redox-Active Esters via Radical-Polar Crossover Enabled by Photoredox Catalysis. *J. Am. Chem. Soc.* **2020**, *142* (20), 9493–9500. <https://doi.org/10.1021/jacs.0c03125>.
- (74) Moon, Y.; Park, B.; Kim, I.; Kang, G.; Shin, S.; Kang, D.; Baik, M. H.; Hong, S. Visible Light Induced Alkene Aminopyridylation Using N-Aminopyridinium Salts as Bifunctional Reagents. *Nat. Commun.* **2019**, *10* (1), 1–9. <https://doi.org/10.1038/s41467-019-12216-3>.
- (75) Rössler, S. L.; Jelier, B. J.; Magnier, E.; Dagousset, G.; Carreira, E. M.; Togni, A. Pyridinium Salts as Redox-Active Functional Group Transfer Reagents. *Angew. Chemie - Int. Ed.* **2020**, *59* (24), 9264–9280. <https://doi.org/10.1002/anie.201911660>.
- (76) He, F. S.; Ye, S.; Wu, J. Recent Advances in Pyridinium Salts as Radical Reservoirs in Organic Synthesis. *ACS Catal.* **2019**, *9* (10), 8943–8960. <https://doi.org/10.1021/acscatal.9b03084>.
- (77) Zheng, M.; Hou, J.; Zhan, L. W.; Huang, Y.; Chen, L.; Hua, L. L.; Li, Y.; Tang, W. Y.; Li, B. D. Visible-Light-Driven, Metal-Free Divergent Difunctionalization of Alkenes Using Alkyl Formates. *ACS Catal.* **2021**, *11* (2), 542–553. <https://doi.org/10.1021/acscatal.0c04332>.
- (78) Song, Z. Y.; Zhang, C. L.; Ye, S. Visible Light Promoted Coupling of Alkynyl Bromides and Hantzsch Esters for the Synthesis of Internal Alkynes. *Org. Biomol. Chem.* **2019**, *17* (1), 181–185. <https://doi.org/10.1039/c8ob02912a>.

- (79) Perkins, J. J.; Schubert, J. W.; Streckfuss, E. C.; Balsells, J.; ElMarrouni, A. Photoredox Catalysis for Silyl-Mediated C–H Alkylation of Heterocycles with Non-Activated Alkyl Bromides. *European J. Org. Chem.* **2020**, 2020 (10), 1515–1522. <https://doi.org/10.1002/ejoc.201900611>.
- (80) Shee, M.; Shah, S. S.; Singh, N. D. P. Organophotoredox Assisted Cyanation of Bromoarenes: Via Silyl-Radical-Mediated Bromine Abstraction. *Chem. Commun.* **2020**, 56 (30), 4240–4243. <https://doi.org/10.1039/d0cc00163e>.
- (81) Zhou, R.; Goh, Y. Y.; Liu, H.; Tao, H.; Li, L.; Wu, J. Visible-Light-Mediated Metal-Free Hydrosilylation of Alkenes through Selective Hydrogen Atom Transfer for Si–H Activation. *Angew. Chemie - Int. Ed.* **2017**, 56 (52), 16621–16625. <https://doi.org/10.1002/anie.201711250>.
- (82) Kwon, Y.; Lee, J.; Noh, Y.; Kim, D.; Lee, Y.; Yu, C.; Roldao, J. C.; Feng, S.; Gierschner, J.; Wannemacher, R.; Kwon, M. S. Formation and Degradation of Strongly Reducing Cyanoarene-Based Radical Anions towards Efficient Radical Anion-Mediated Photoredox Catalysis. *Nat. Commun.* **2023**, 14 (92), 1–15. <https://doi.org/10.1038/s41467-022-35774-5>.
- (83) Gandini, T.; Dolcini, L.; Di Leo, L.; Fornara, M.; Bossi, A.; Penconi, M.; Dal Corso, A.; Gennari, C.; Pignataro, L. Metallaphotoredox C–O and C–N Cross-Coupling Using Donor-Acceptor Cyanoarene Photocatalysts. *ChemCatChem* **2022**. <https://doi.org/10.1002/cctc.202200990>.
- (84) Huang, L.; Zhu, C.; Yi, L.; Yue, H.; Kancharla, R.; Rueping, M. Cascade Cross-Coupling of Dienes: Photoredox and Nickel Dual Catalysis. *Angew. Chemie - Int. Ed.* **2020**, 59 (1), 457–464. <https://doi.org/10.1002/anie.201911109>.
- (85) Fang, Y.; Liu, T.; Chen, L.; Chao, D. Exploiting Consecutive Photoinduced Electron Transfer (ConPET) in CO<sub>2</sub> Photoreduction. *Chem. Commun.* **2022**, 58 (57), 7972–7975. <https://doi.org/10.1039/d2cc02356c>.
- (86) Ghosh, I.; Ghosh, T.; Bardagi, J. I.; König, B. Reduction of Aryl Halides by Consecutive Visible Light-Induced Electron Transfer Processes. *Science*. **2014**, 346 (6210), 725–728.
- (87) Zeman, C. J.; Kim, S.; Zhang, F.; Schanze, K. S. Direct Observation of the Reduction of Aryl Halides by a Photoexcited Perylene Diimide Radical Anion. *J. Am. Chem. Soc.* **2020**,



- 142 (5), 2204–2207. <https://doi.org/10.1021/jacs.9b13027>.
- (88) Soto, X. L.; Swierk, J. R. Using Lifetime and Quenching Rate Constant to Determine Optimal Quencher Concentration. *ACS Omega* **2022**, *7* (29), 25532–25536. <https://doi.org/10.1021/acsomega.2c02638>.
- (89) Chernowsky, C. P.; Chmiel, A. F.; Wickens, Z. K. Electrochemical Activation of Diverse Conventional Photoredox Catalysts Induces Potent Photoreductant Activity\*\*. *Angew. Chemie - Int. Ed.* **2021**, *60* (39), 21418–21425. <https://doi.org/10.1002/anie.202107169>.
- (90) Wu, S.; Kaur, J.; Karl, T. A.; Tian, X.; Barham, J. P. Synthetic Molecular Photoelectrochemistry: New Frontiers in Synthetic Applications, Mechanistic Insights and Scalability. *Angew. Chemie - Int. Ed.* **2022**, *61* (12). <https://doi.org/10.1002/anie.202107811>.
- (91) Liu, J.; Lu, L.; Wood, D.; Lin, S. New Redox Strategies in Organic Synthesis by Means of Electrochemistry and Photochemistry. *ACS Cent. Sci.* **2020**, *6* (8), 1317–1340. <https://doi.org/10.1021/acscentsci.0c00549>.
- (92) Cowper, N. G. W.; Chernowsky, C. P.; Williams, O. P.; Wickens, Z. K. Potent Reductants via Electron-Primed Photoredox Catalysis: Unlocking Aryl Chlorides for Radical Coupling. *J. Am. Chem. Soc.* **2020**, *142* (5), 2093–2099. <https://doi.org/10.1021/jacs.9b12328>.
- (93) Strieth-Kalthoff, F.; James, M. J.; Teders, M.; Pitzer, L.; Glorius, F. Energy Transfer Catalysis Mediated by Visible Light: Principles, Applications, Directions. *Chem. Soc. Rev.* **2018**, *47* (19), 7190–7202. <https://doi.org/10.1039/c8cs00054a>.
- (94) Chen, D. F.; Chrisman, C. H.; Miyake, G. M. Bromine Radical Catalysis by Energy Transfer Photosensitization. *ACS Catal.* **2020**, *10* (4), 2609–2614. <https://doi.org/10.1021/acscatal.0c00281>.
- (95) Lu, J.; Pattengale, B.; Liu, Q.; Yang, S.; Li, S.; Huang, J.; Zhang, J. Donor-Acceptor Fluorophores for Energy-Transfer-Mediated Photocatalysis. *J. Am. Chem. Soc.* **2018**, *140* (42), 13719–13725. <https://doi.org/10.1021/jacs.8b07271>.
- (96) Chérif, S. E.; Ghosh, A.; Chelli, S.; Dixon, I. M.; Kraiem, J.; Lakhdar, S. Merging Grubbs Second-Generation Catalyst with Photocatalysis Enables Z-Selective Metathesis of



- Olefins: Scope, Limitations, and Mechanism. *Chem. Sci.* **2022**, 12065–12070. <https://doi.org/10.1039/d2sc03961c>.
- (97) Tian, H.; Yang, H.; Tian, C.; An, G.; Li, G. Cross-Dehydrogenative Coupling of Strong C(Sp<sup>3</sup>)-H with N-Heteroarenes through Visible-Light-Induced Energy Transfer. *Org. Lett.* **2020**, 22 (19), 7709–7715. <https://doi.org/10.1021/acs.orglett.0c02912>.
- (98) Mastandrea, M. M.; Cañellas, S.; Caldentey, X.; Pericàs, M. A. Decarboxylative Hydroalkylation of Alkynes via Dual Copper-Photoredox Catalysis. *ACS Catal.* **2020**, 10 (11), 6402–6408. <https://doi.org/10.1021/acscatal.0c01742>.
- (99) Dai, C.; Zhan, Y.; Liu, P.; Sun, P. Organic Photoredox Catalyzed C-H Silylation of Quinoxalinones or Electron-Deficient Heteroarenes under Ambient Air Conditions. *Green Chem.* **2021**, 23 (1), 314–319. <https://doi.org/10.1039/d0gc03697h>.
- (100) Lee, Y.; Kwon, M. S. Emerging Organic Photoredox Catalysts for Organic Transformations. *European J. Org. Chem.* **2020**, 2020 (38), 6028–6043. <https://doi.org/10.1002/ejoc.202000720>.
- (101) Rieth, A. J.; Gonzalez, M. I.; Kudisch, B.; Nava, M.; Nocera, D. G. How Radical Are “Radical” Photocatalysts? A Closed-Shell Meisenheimer Complex Is Identified as a Super-Reducing Photoreagent. *J. Am. Chem. Soc.* **2021**, 143 (35), 14352–14359. <https://doi.org/10.1021/jacs.1c06844>.
- (102) Glaser, F.; Kerzig, C.; Wenger, O. S. Multi-Photon Excitation in Photoredox Catalysis: Concepts, Applications, Methods. *Angew. Chemie - Int. Ed.* **2020**, 59 (26), 10266–10284. <https://doi.org/10.1002/anie.201915762>.
- (103) Marchini, M.; Gualandi, A.; Mengozzi, L.; Franchi, P.; Lucarini, M.; Cozzi, P. G.; Balzani, V.; Ceroni, P. Mechanistic Insights into Two-Photon-Driven Photocatalysis in Organic Synthesis. *Phys. Chem. Chem. Phys.* **2018**, 20 (12), 8071–8076. <https://doi.org/10.1039/c7cp08011e>.
- (104) Gosztola, D.; Niemczyk, M. P.; Svec, W.; Lukas, A. S.; Wasielewski, M. R. Excited Doublet States of Electrochemically Generated Aromatic Imide and Diimide Radical Anions. *J. Phys. Chem. A* **2000**, 104 (28), 6545–6551. <https://doi.org/10.1021/jp000706f>.
- (105) Gummy, J. C.; Vauthey, E. Investigation of the Excited-State Dynamics of Radical Ions in the Condensed Phase Using the Picosecond Transient Grating Technique. *J. Phys. Chem.*

- A **1997**, *101* (46), 0–5.
- (106) Beckwith, J. S.; Aster, A.; Vauthey, E. The Excited-State Dynamics of the Radical Anions of Cyanoanthracenes. *Phys. Chem. Chem. Phys.* **2022**, *24* (1), 568–577. <https://doi.org/10.1039/d1cp04014f>.
- (107) Constantin, T.; Zanini, M.; Regni, A.; Sheikh, N. S.; Juliá, F.; Leonori, D. Aminoalkyl Radicals as Halogen-Atom Transfer Agents for Activation of Alkyl and Aryl Halides. *Science* (80-. ). **2020**, *367* (6481), 1021–1026. <https://doi.org/10.1126/science.aba2419>.
- (108) Chmiel, A. F.; Williams, O. P.; Chernowsky, C. P.; Yeung, C. S.; Wickens, Z. K. Non-Innocent Radical Ion Intermediates in Photoredox Catalysis: Parallel Reduction Modes Enable Coupling of Diverse Aryl Chlorides. *J. Am. Chem. Soc.* **2021**, *143* (29), 10882–10889. <https://doi.org/10.1021/jacs.1c05988>.
- (109) Behera, S. K.; Park, S. Y.; Gierschner, J. Dual Emission: Classes, Mechanisms, and Conditions. *Angew. Chemie - Int. Ed.* **2021**, *60* (42), 22624–22638. <https://doi.org/10.1002/anie.202009789>.
- (110) Wang, H.; Wang, J.; Zhang, T.; Xie, Z.; Zhang, X.; Sun, H.; Xiao, Y.; Yu, T.; Huang, W. Breaching Kasha's Rule for Dual Emission: Mechanisms, Materials and Applications. *J. Mater. Chem. C* **2021**, *9* (32), 10154–10172. <https://doi.org/10.1039/d1tc01970h>.
- (111) Veys, K.; Escudero, D. Anti-Kasha Fluorescence in Molecular Entities: Central Role of Electron-Vibrational Coupling. *Acc. Chem. Res.* **2022**, *55* (18), 2698–2707. <https://doi.org/10.1021/acs.accounts.2c00453>.
- (112) Marqués, P. S.; Londi, G.; Yurash, B.; Nguyen, T. Q.; Barlow, S.; Marder, S. R.; Beljonne, D. Understanding How Lewis Acids Dope Organic Semiconductors: A “Complex” Story. *Chem. Sci.* **2021**, *12* (20), 7012–7022. <https://doi.org/10.1039/d1sc01268a>.
- (113) Imagawa, T.; Nakamoto, M.; Shang, R.; Adachi, Y.; Ohshita, J.; Tsunoji, N.; Yamamoto, Y. Complexation of B(C<sub>6</sub>F<sub>5</sub>)<sub>3</sub> and 9,10-Dicyanoanthracene: Dual Role of Borane as Spatial and Electronic Tuner. *Chem. Lett.* **2020**, *49* (9), 1022–1025. <https://doi.org/10.1246/CL.200339>.
- (114) Welch, G. C.; Bazan, G. C. Lewis Acid Adducts of Narrow Band Gap Conjugated Polymers. *J. Am. Chem. Soc.* **2011**, *133* (12), 4632–4644. <https://doi.org/10.1021/ja110968m>.

- (115) Mori, T.; Yoshigoe, Y.; Kuninobu, Y. Control of Multicolor and White Emission by Adjusting the Equilibrium between Fluorophores, Lewis Acids, and Their Complexes in Polymers. *Angew. Chemie - Int. Ed.* **2019**, *58* (41), 14457–14461. <https://doi.org/10.1002/anie.201903408>.
- (116) Lawrence, E. J.; Oganessian, V. S.; Wildgoose, G. G.; Ashley, A. E. Exploring the Fate of the Tris(Pentafluorophenyl)Borane Radical Anion in Weakly Coordinating Solvents. *Dalt. Trans.* **2013**, *42* (3), 782–789. <https://doi.org/10.1039/c2dt31622f>.
- (117) Kwaan, R. J.; Harlan, C. J.; Norton, J. R. Generation and Characterization of the Tris(Pentafluorophenyl)Borane Radical Anion. *Organometallics* **2001**, *20* (17), 3818–3820. <https://doi.org/10.1021/om010272q>.

# ***Chapter IV:***

## ***VISIBLE-LIGHT-MEDIATED GERMANYLATION OF ARYL FLUORIDES: SYNTHETIC AND MECHANISTIC INSIGHTS***

The work presented in this chapter was published in the journal *Synthesis* (2023) by Valentin Magné, Corentin Bellanger, Aqeel A. Hussein, Nathalie Saffon-Merceron and Sami Lakhdar (DOI: 10.1055/a-2012-5078). Reproduction of the content was obtained from the publisher (Georg Thieme Verlag).

## 1. Introduction

Due to their low toxicity, hydrophobicity, and remarkable robustness, organogermanes ( $\text{ArGeR}_3$ ) have interesting applications in various fields ranging from medicinal chemistry to material science.<sup>1</sup>

As depicted in Figure IV-1, existing methods enabling the synthesis of these molecules can mainly be divided into three major approaches: (i) the reaction of electrophilic germane species with in situ generated organometallic nucleophiles at low temperatures,<sup>2</sup> (ii) the use of palladium catalysis to couple halogenated precursors with germanes or digermanes,<sup>3,4</sup> and (iii) the selective functionalization of C–H arenes bonds through palladium catalysis<sup>5–8</sup> or more elegantly under metal-free conditions by employing dibenzothiophenium salts and the bench stable and readily available  $\text{R}_3\text{Ge-SiR}_3$ .<sup>9,10</sup>

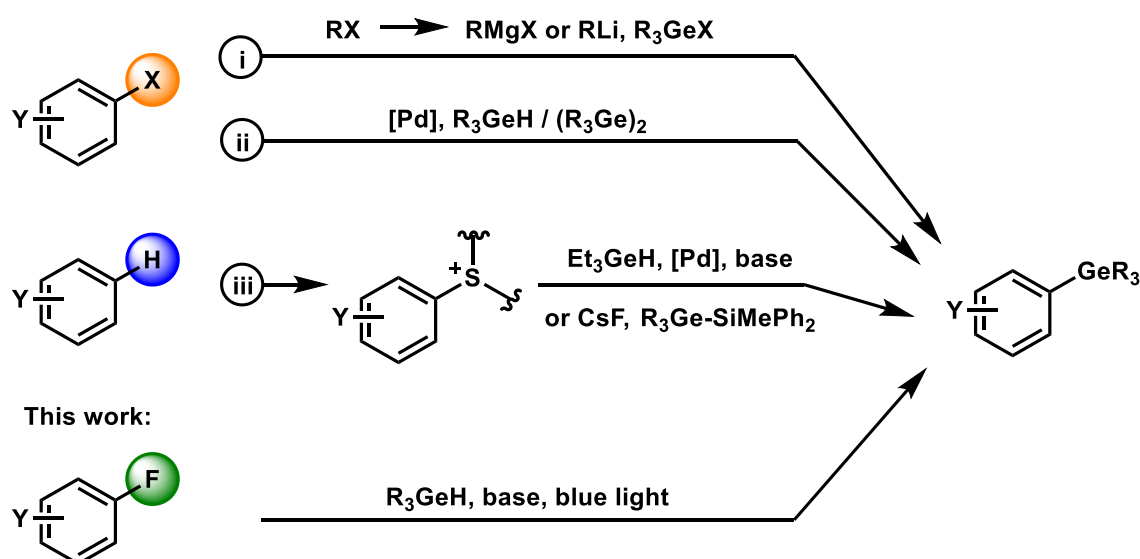


Figure IV-1: Selected methods enabling access to arylgermanes (i–iii) and this work. Y: substituent.

Both synthetic methods using sulfonium intermediates are given in Figure IV-2. They tolerate many functional groups that include nitrile, nitro, aldehyde, amino, fluoro, chloro, bromo, iodo, methoxy and alkyls moieties with excellent yields (46–93%).

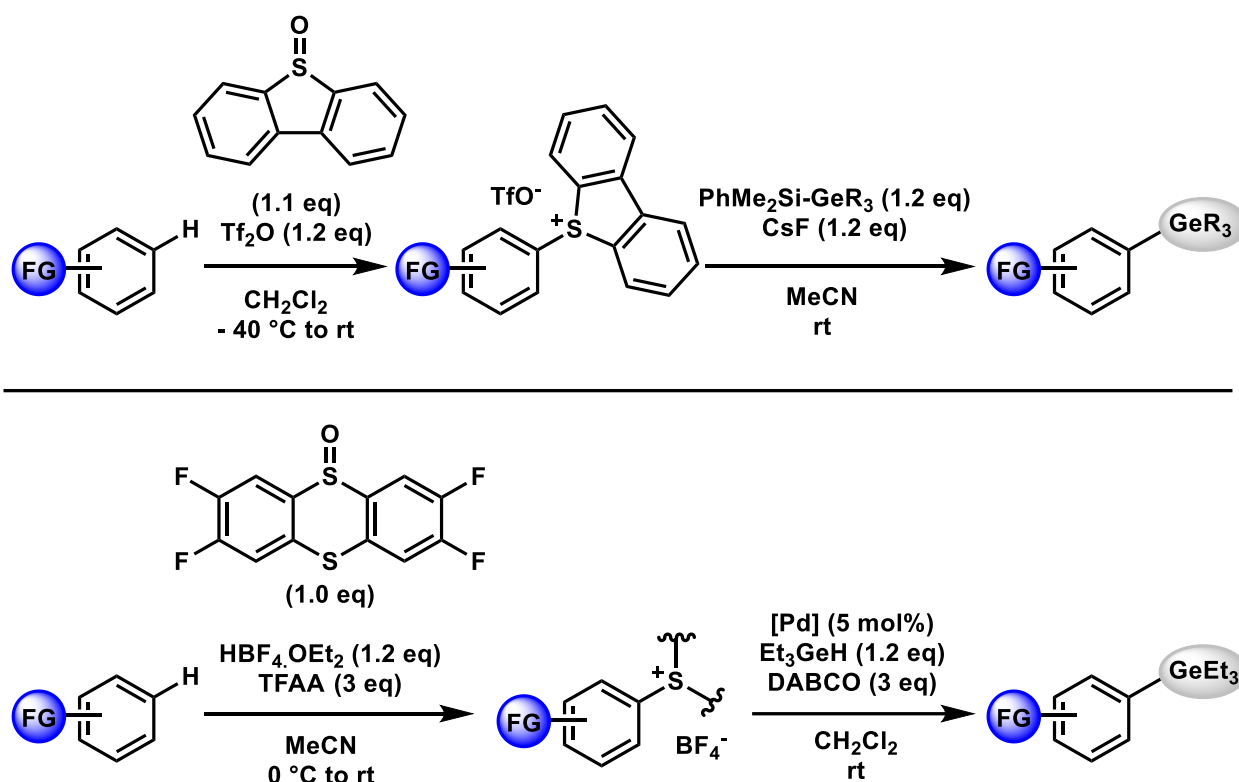


Figure IV-2: Detailed synthesis of arylgermanes via sulfonium intermediates. FG: functional group.  $\text{Trf}_2\text{O}$ : Triflic Anhydride. TFAA: Trifluoroacetic anhydride. DABCO: 1,4-Diazabicyclo[2.2.2]octane.

An elegant report from 1982 describes the reactivity of diverse aryl halides with the triethylgermyl anion.<sup>11</sup> This anion engaged in aromatic substitution of fluorine in decent yields (Figure IV-3). With chlorine, it deprotonated the aromatic ring instead to provide benzyne, as indicated by the meta-para 50:50 mixture when reacted with para-chlorotoluene. The reactivity is extremely cation dependent. Potassium and lithium provided the ortho, meta or para fluorine-substitution products in variable yields. However, the sodium equivalent  $\text{Et}_3\text{GeNa}$  didn't provide yields above 5%. These results highlight the excellent reactivity of the germanyl anion and the possibilities it carries for aromatic substitutions.

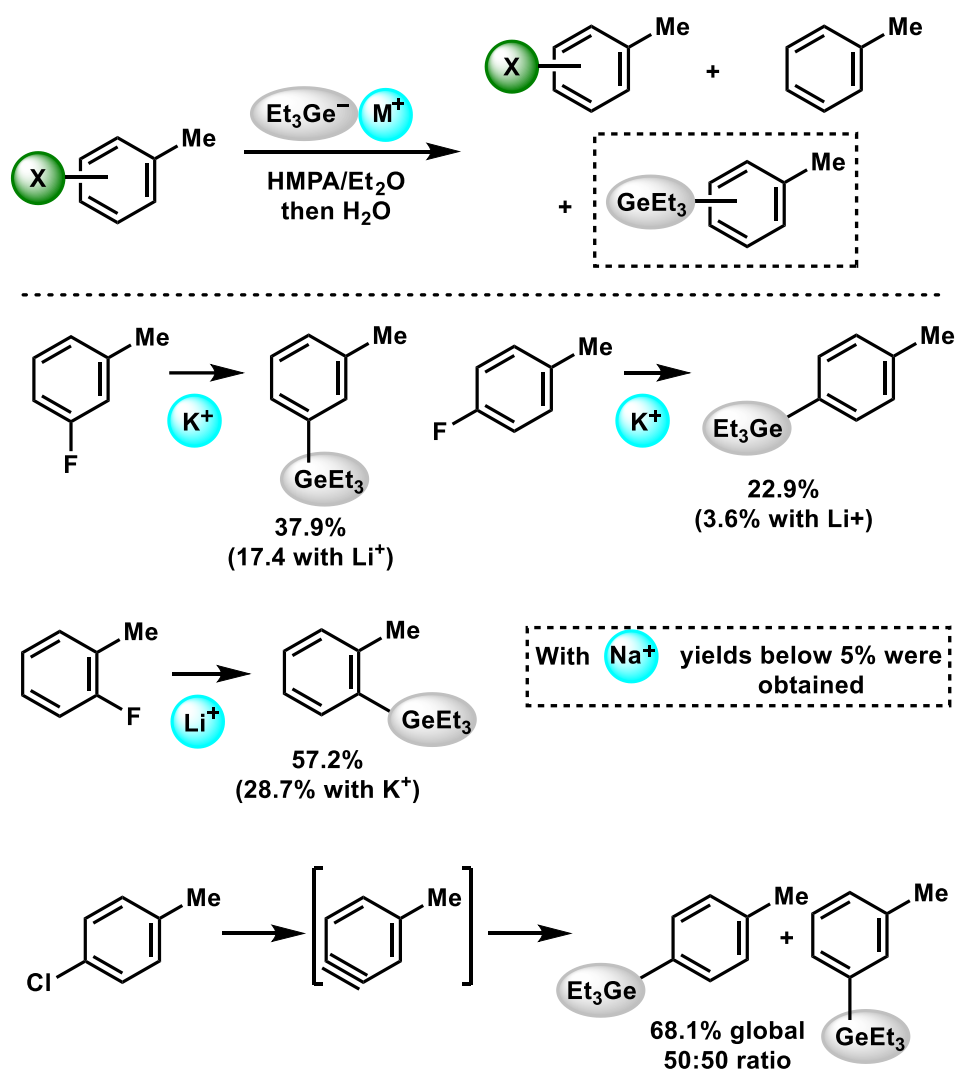


Figure IV-3: Reactivity of diverse aryl halides with the triethylgermyl anion. HMPA: hexamethylphosphoramide ( $\text{Me}_2\text{N}$ )<sub>3</sub>PO

Importantly, between 2019 and 2022, the Schoenebeck group has demonstrated the synthetic utility of these scaffolds as cross coupling partners in transition metal-catalyzed reactions.<sup>1,12-14</sup>

Palladium is usually used as a cross-coupling reactions catalyst, but organogermanes are not good partners for homogeneous palladium catalysis. However, the first gold-catalyzed C–H functionalization of aromatics using organogermanes by Schoenebeck group disclosed their suitability in gold catalysis.<sup>13</sup> The methodology uses bench stable reactants that can be manipulated and reacted under air conditions. The reaction is air and moisture insensitive, and the reagents are non-toxic. The only downside to safety is the carcinogenic solvent 1,4-dioxane. The gold catalyst chloro(triphenylphosphine)gold(I) used in a 5 mol% loading (against aryltriethylgermane) requires 1.5 equivalents of the stoichiometric oxidant  $\text{PhI}(\text{OCSA})_2$  (Figure IV-4). The  $^- \text{OCSA}$  (camphorsulfonate) moiety ends up acting as the gold(I) counter-anion in

the catalytic process and revealed crucial. Using  $\text{AcO}^-$  or  $\text{Br}^-$  instead resulted in no conversion of the organogermane. This milestone showed the ability of germane to act as a robust coupling partner for cross-coupling reactions, thus adding one more tool to the cross-coupling methodology to increase the flexibility and functional group tolerance compared to the boronic acid, tin, silane, organozinc, or Grignard reagents equivalents.

All four halogens (fluorine, chlorine, bromine, and iodine) as well as a trifluoromethyl moiety were tolerated in the reaction displayed in Figure IV-4. The other coupling partners are electron rich aromatics (the C-H substitution occurs in para position of the most electron donating group)

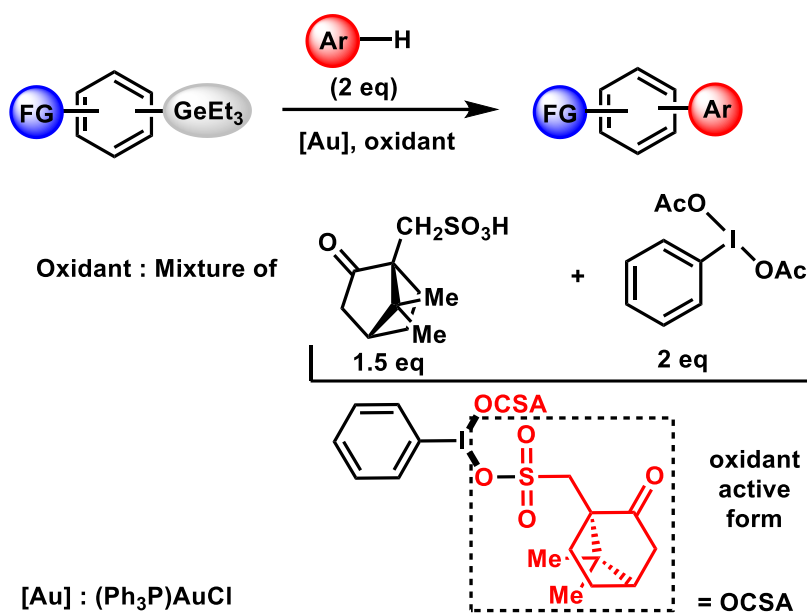


Figure IV-4: Gold-catalyzed C-H functionalization of aromatics using organogermanes. FG: functional group. Ar: aromatic. OAc: acetate.

and allow halogens (bromine, chlorine, iodine), methyl, ester and methoxy substituents.

It was followed one month after with a publication from the same group on the successful heterogeneous palladium catalytic activity with organogermanes (Figure IV-5).<sup>12</sup> Interestingly, homogeneous palladium catalysis allowed cross-coupling of iodoarenes or diaryliodonium salts with organogermane without touching the germane moiety while heterogeneous palladium catalysis using palladium nanoparticles instead afforded cross-coupling with the germane moiety without affecting the other functional groups. These functional groups include fluorine, bromine, triflate, silane, methoxy and boranes. Heteroarenes bearing the germane moiety were also successful in this reaction, while the iodoarenes coupling partners reacted selectively on from the iodine leaving the bromine, chlorine, fluorine, trifluoromethyl, ester, and methoxy moieties untouched.



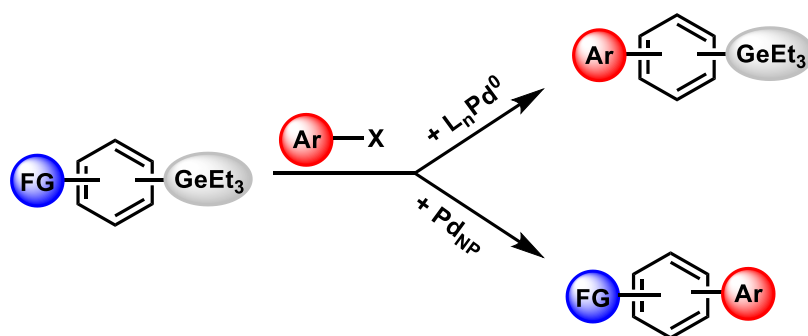
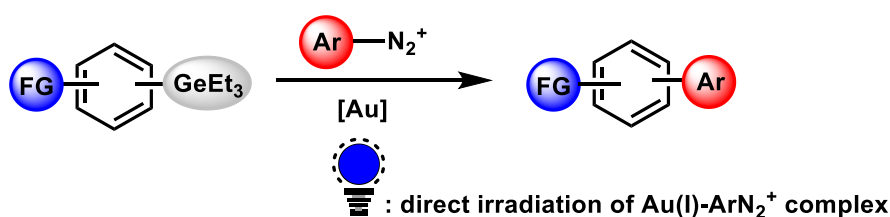


Figure IV-5: Homogenous palladium and palladium nanoparticle catalysis with organogermanes. FG: functional group. Ar: aromatic. NP: nanoparticles.

Less than a year later, the Schoenebeck group expended the selective arylation of arylgermanes over the borane, silane, and halogens moieties by light-activated gold catalysis (Figure IV-6).<sup>14</sup> This methodology uses diazonium salts as the coupling partners and different gold catalyst depending on the electron rich or poor nature of the diazoniums salts. Chloro(triphenylphosphine)gold(I) (10 mol% loading) was used for electron poor  $\text{ArN}_2^+$  while Chloro(dimethylsulfide)gold(I) with 1,2-bis(diphenylphosphino)ethane added ligand in combination with  $\text{Ru}(\text{bpy})_3(\text{PF}_6)_2$  as the photocatalyst was used for electron rich  $\text{ArN}_2^+$ . Two different mechanisms were proposed regardless the diazoniums salts  $\text{ArN}_2^+$  were electron rich or electron poor. Direct light activation of the diazonium-gold complex occurs when electron poor diazonium salts are employed and allows the  $\text{C}_{\text{Ar}}\text{-N}$  bond cleavage followed by addition of the aromatic on gold.

#### Electron poor diazonium salts



#### Electron rich diazonium salts

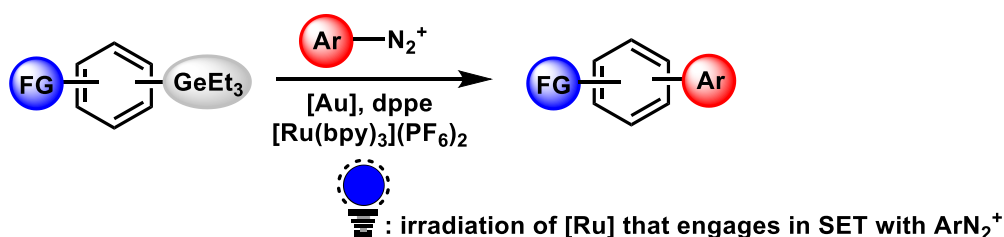


Figure IV-6: Selective arylation of arylgermanes over the borane, silane, and halogens moieties by light-activated gold catalysis. FG: functional group. Ar: aromatic.

However, dissociation of the diazonium salts proceeds via a prior electron transfer from a ruthenium photocatalyst excited state to the diazonium in the case of electron rich diazonium salts (Figure IV-7).

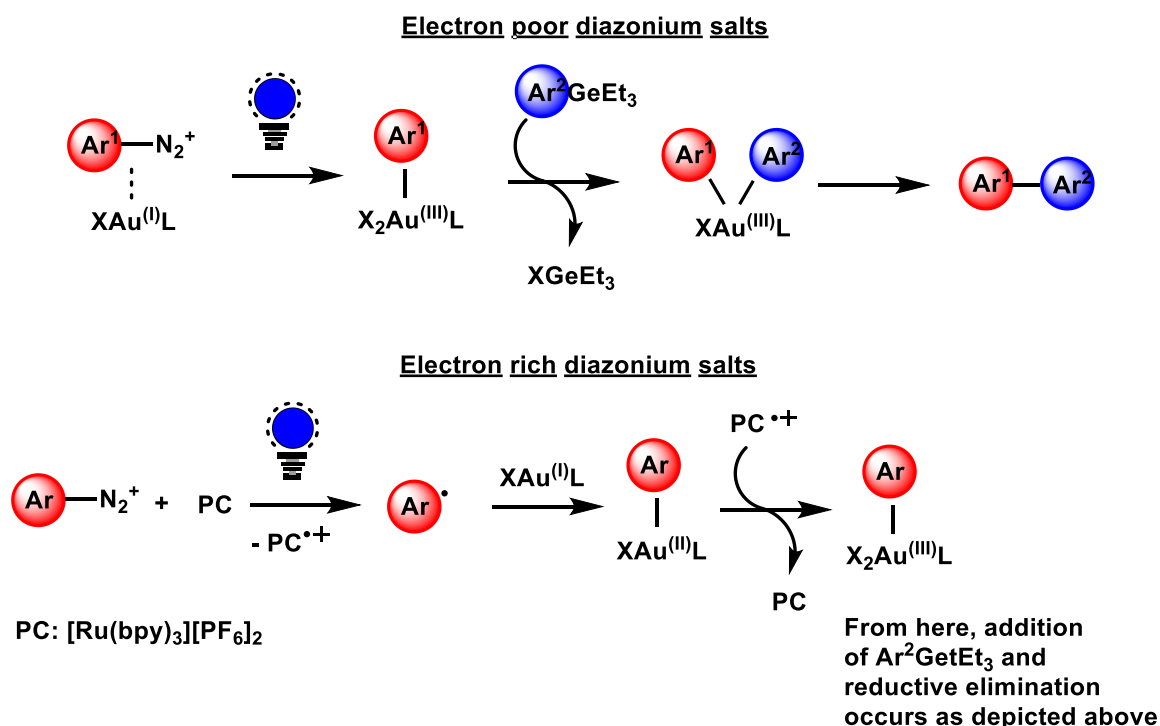


Figure IV-7: Selective arylation of arylgermanes over the borane, silane, and halogens moieties by light-activated gold catalysis. FG: functional group. Ar: aromatic.

These advances have significantly increased interest in the synthesis of arylgermanes.

A recent contribution by Uchiyama and co-workers<sup>15</sup> shows the highly reducing ability of the excited state of stannyl anions through C–Sn bonds formation with alkynes (Figure IV-8).

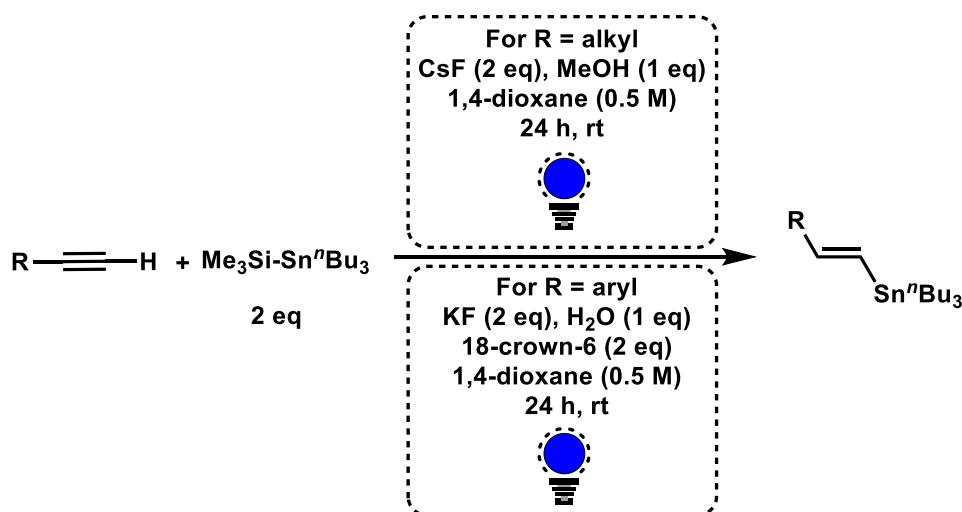


Figure IV-8: Visible-light induced stannylation of various alkynes

The mechanism proceeds through cleavage of the Si-Sn bond by a fluoride anion to generate the stannyl anion (Figure IV-9). The stannyl anion can absorb visible light to reach its singlet excited state which may convert to the triplet state by a heavy-atom effect favored intersystem crossing. The authors report a calculated 4 kcal/mol difference between the singlet and triplet states. It is stated that the anion reacts with alkynes through SET from its more stable triplet state. The outcome of the SET is an alkyne radical anion and a stannyl radical which may combine to provide the corresponding alkene anion. After deprotonation of methanol or water, the hydrostannylation of the starting alkyne is complete.

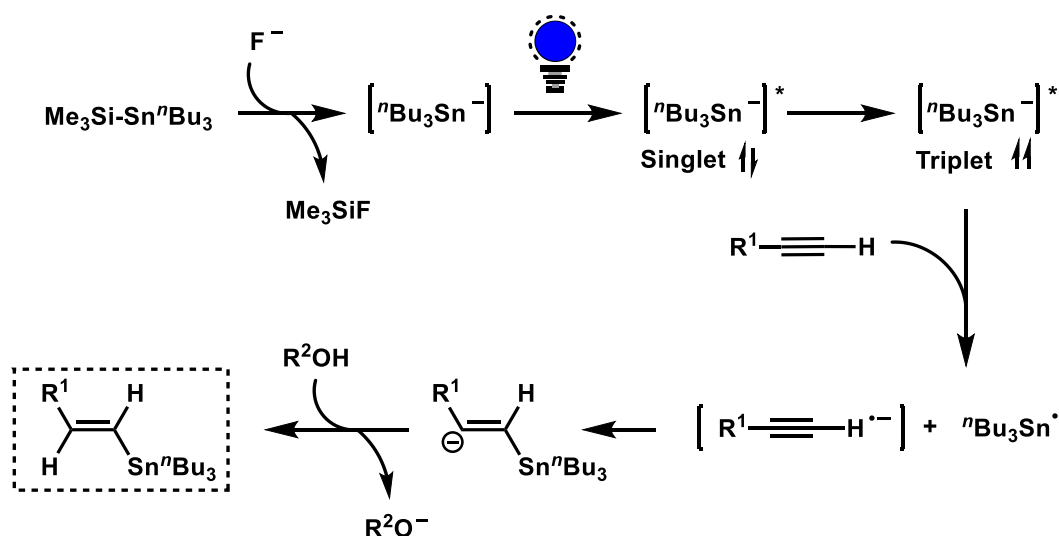


Figure IV-9: Proposed mechanism for the visible-light induced stannylation of various alkynes

Tin and germane have similar properties as they share the same column in the periodic table of elements. We reasoned that accessing the excited state of the germyl anion could lead to a straightforward reaction manifold to access a variety of organogermanes from accessible starting materials. More precisely, the photoexcitation of the germyl anion, formed from the deprotonation of the starting germane with a base, could display strong reducing properties capable of inducing C(sp<sup>2</sup>)-F bond cleavage, followed by C-Ge bond formation through a classical SR<sub>1</sub>N mechanism.<sup>16-18</sup>

Strong C(sp<sup>2</sup>)-F bonds can be found in numerous biologically relevant molecules and functional materials,<sup>19</sup> and the activation of such bonds is an important field of research.

Recent developments for the activation of these bonds, other than the multi-photon processes<sup>20</sup> or electrophotocatalytic settings<sup>21</sup> mentioned before, include the use of a stoichiometric amount of a commercial reagent: tetrakis(dimethylamino)ethylene (TDAE, Figure IV-10).<sup>22</sup> The photoexcited state of this molecule displays a gigantic redox potential of *ca.* -3.4 V vs SCE and

a long 17.3 ns lifetime in cyclohexane. It was applied to the dehalogenation of aromatic rings, as TDAE\* is capable of easily reducing both fluoro and chloroarenes.

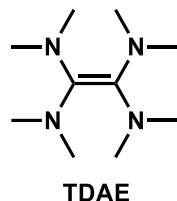


Figure IV-10: Structure of tetrakis(dimethylamino)ethylene (TDAE)

## 2. Results and discussions

### 2.1. Optimization of the visible-light induced germylation of fluoro-arenes reaction conditions

This project was carried out in collaboration with Dr. Valentin Magné. The synthetic and analytical work was shared. The DFT calculations were performed by Aqeel A. Hussein from Komar University of Science and Technology in Iraq.

To test our working hypothesis, we reacted either triethyl or triphenylgermane (**1**) with sodium *tert*-butoxide in DMSO to first generate the germyl anion stabilized in a polar solvent. 4-fluorotoluene (**2a**) was then chosen as the fluorinated coupling partner of choice since its methyl group allowed for an aliphatic signal NMR probe. Under blue irradiation ( $\lambda_{\text{max}} = 460 \text{ nm}$ ) the aryltriphenylgermane desired adduct (**3a**) was obtained within 15 min in 75% NMR yield and was isolated in 72% yield (Table IV-1, entry 1). However, no product was obtained with the aliphatic triethylgermane (entry 2).

To exclude a possible nucleophilic aromatic substitution  $\text{S}_{\text{N}}\text{Ar}$  between the germyl anion and **2a** as shown by Matsushige and Mochida in 1982 with  $\text{Et}_3\text{Ge}^-$ ,<sup>11</sup> the reaction was tested in the dark for 15 h at room temperature (entry 3). Since LEDs are known to provide heat and may cause reaction temperature to increase, another experiment was run in the dark at 50 °C (entry 4). Importantly, no trace of the desired adduct **3a** was observed in both cases, thus showing that the reaction does not proceed in the absence of light. This result was further confirmed by DFT calculations, where an activation energy of 33.3 kcal/mol was obtained. The effect of the concentration of germane **1** was examined and the same yield of **3a** was obtained when the concentration of **1** was either divided by two or multiplied by five (entries 5 and 6). The concentration in the 0.05 – 0.5 M range therefore has no impact on the reaction. Thus a concentration of 0.1 M was selected out of practical handiness. The nature of the counterion

played an important role on the reactivity as changing  $t\text{BuONa}$  to  $t\text{BuOLi}$  resulted in a significant decrease in the yield of **3a** from 75% to 22% (entry 7). This observation goes in the opposite direction as the one observed for the nucleophilic aromatic substitution described in 1982. Indeed, we remind that  $\text{Et}_3\text{GeNa}$  provided less than 5% fluorine substitution while  $\text{Et}_3\text{GeLi}$  gave the substitution product with yields up to 57.2%. Interestingly, the addition of a radical trap, such as nitrobenzene or TEMPO, to the reaction mixture resulted in no reaction (entries 8 and 9). These results indicate that the reaction proceeds presumably via a radical pathway, further supporting the electron transfer mechanism considered in our initial hypothesis.

Finally, the effect of the solvent proved to be important as the defluorohydrogenation product was obtained when using THF (entry 10). DMSO high polarity also undoubtedly plays a role in the stabilization of the anion through polar effects and most likely also in its excited state stability. The defluorohydrogenation product observed in THF probably arises from hydrogen atom transfer (HAT) from the solvent by the aryl radical (see DFT).

Table IV-1: Optimization study and standard reaction. nd: not detected <sup>a</sup>isolated yield <sup>b</sup>PhMe was obtained

Entry	Deviation from standard conditions	NMR yield (%)
1	none	75 (72) <sup>a</sup>
2	$\text{Et}_3\text{GeH}$ instead of $\text{Ph}_3\text{GeH}$	n.d.
3	Dark (15h)	n.d.
4	Dark (50 °C)	n.d.
5	[ <b>1</b> ] = 0.05 M	71
6	[ <b>1</b> ] = 0.5 M	71
7	Base = $t\text{BuOLi}$	22
8	+ 1 eq $\text{PhNO}_2$	n.d.
9	+1 eq TEMPO	n.d.
10	Solvent = THF	n.d. <sup>b</sup>

With the optimization reaction conditions in hand, we then examined the scope of the reaction by testing the reactivity of various fluoro(hetero)arenes towards triphenylgermane.

## 2.2. Application of the methodology to a scope of fluoro-arenes

As shown in Figure IV-11, the reaction proceeds smoothly with the three isomers of fluorotoluene (*ortho*, *meta*, *para*) giving **3a–c** in 63–84% yields. The lowest yield was obtained with the *ortho* isomer most likely due to steric hindrance. It also works with fluoroarenes bearing either electron-withdrawing (**3d**) and donating groups (**3e**). A better yield was obtained with an electron rich aromatic (*p*-MeO, 82%) than electron deficient one (*p*-CN, 44%). The conjugated system fluorobiphenyl (**3f**) provided the desired product in 54% yield. Importantly, the reaction is chemoselective with difluoro (**3g**, **3h**, and **3i**) and hexafluoroarenes (**3j**) as the germylation occurs only at one C–F bond. Finally, it is noteworthy that photoinduced germylation also proceeds with heteroarenes such as fluoropyridine (**3k**) and fluorindole (**3l**).

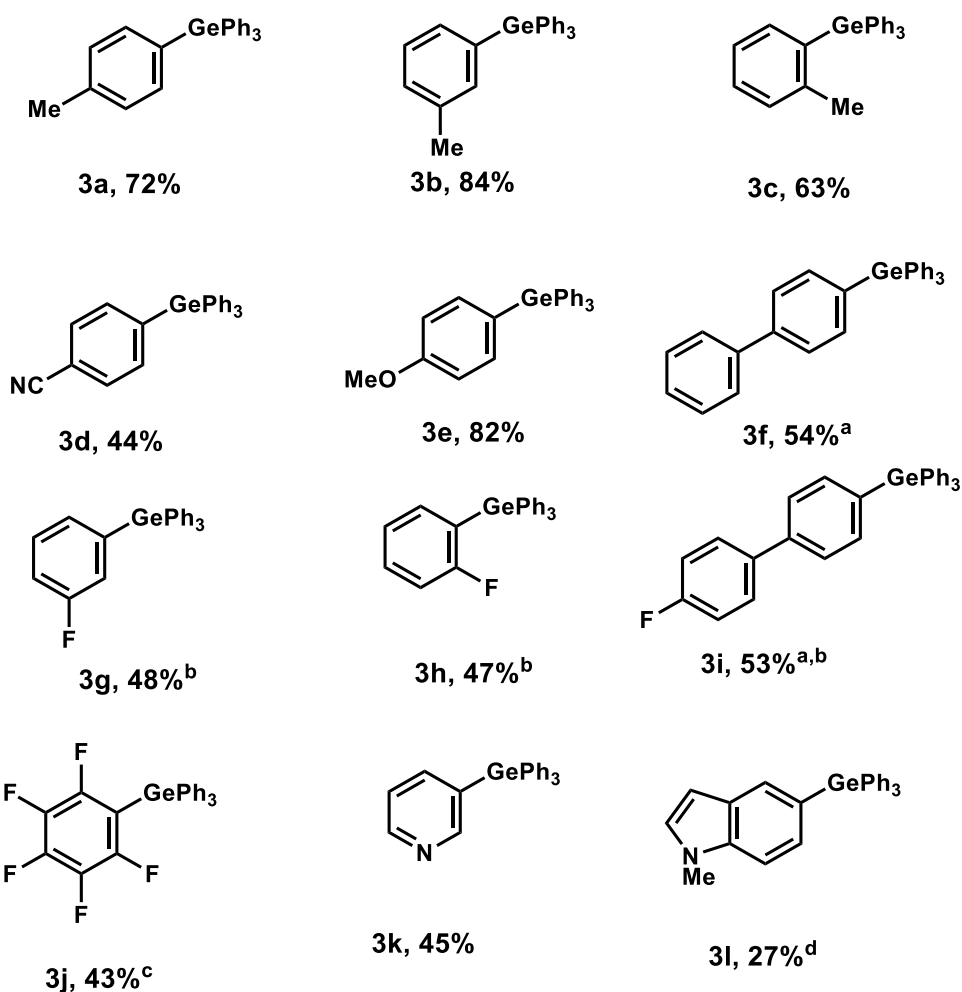


Figure IV-11 : Scope of the photoinduced germylation of fluoro(hetero)arenes. Reagents and conditions: Fluoro(hetero)arene (1.2 eq),  $\text{Ph}_3\text{GeH}$  (1 eq),  $t\text{BuONa}$  (2.0 eq), 15 min. <sup>a</sup>Reaction time 15 h. <sup>b</sup>Fluoro(hetero)arene (2.4 eq) was used. <sup>c</sup>Fluoro(hetero)arene (5 equiv) was used. <sup>d</sup>Fluoro(hetero)arene (1.0 eq),  $\text{Ph}_3\text{GeH}$  (2.0 equiv),  $t\text{BuONa}$  (4.0 equiv) were used.

Crystals suitable for X-Ray diffraction were obtained for compound **3i** and the structure is shown in Figure IV-12. One can see that only one of the two fluorides of the reactant engaged in the reaction.

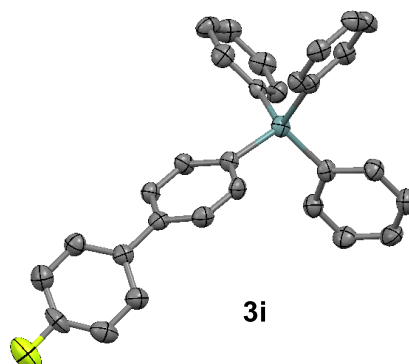


Figure IV-12 : XRD structure of compound **3i**

Surprisingly, the photoinduced germanylation with 1-fluoro-4-(trifluoromethyl)benzene did not provide the  $Csp^2$ -F substitution product but instead yielded the adduct **4a** (Figure IV-13). This reactivity might be attributed to single electron transfer (SET) that leads to the generation of a radical anion followed by exclusion of the fluorine atom at the  $C(sp^3)$  center. The methylene linker itself probably arises from a hydrogen atom transfer (HAT) process after consecutive SET.

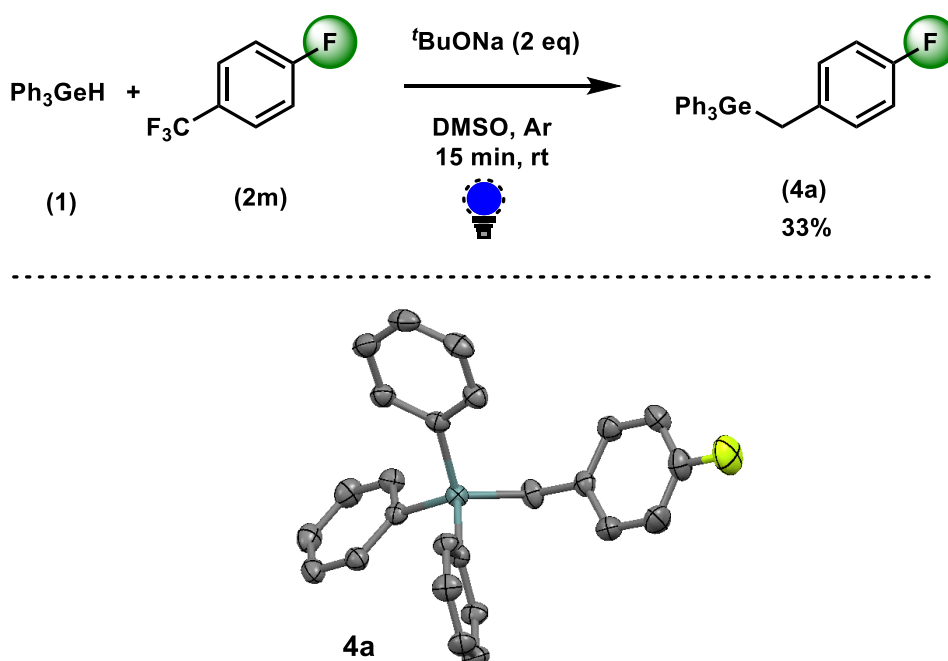


Figure IV-13 : Photoinduced germanylation of 1-fluoro-4-(trifluoromethyl)benzene, yield and XRD structure

The germanylation of 4-fluorostyrene gave (4-fluorophenethyl)triphenylgermane (**4b**) in 92% yield (Figure IV-14). However, this reaction worked in the dark, highlighting the strong electron donating ability of the germanyl anion in its ground state.

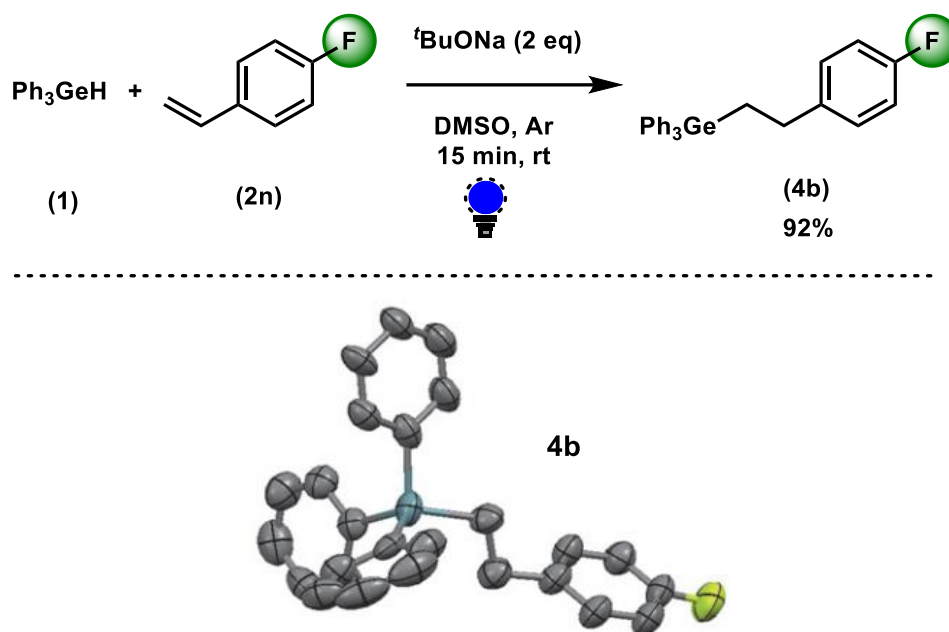


Figure IV-14 : Germanylation of 4-fluorostyrene, yield and XRD structure

Additionally, because of the high nucleophilicity, Brønsted basicity, and strong reducing properties of the germanyl anions, many moieties are not supported by these reaction conditions. Notably, fluoroarenes bearing carbonyls, alcohols, or boronic acid groups are not compatible with our reaction conditions (Figure IV-15).



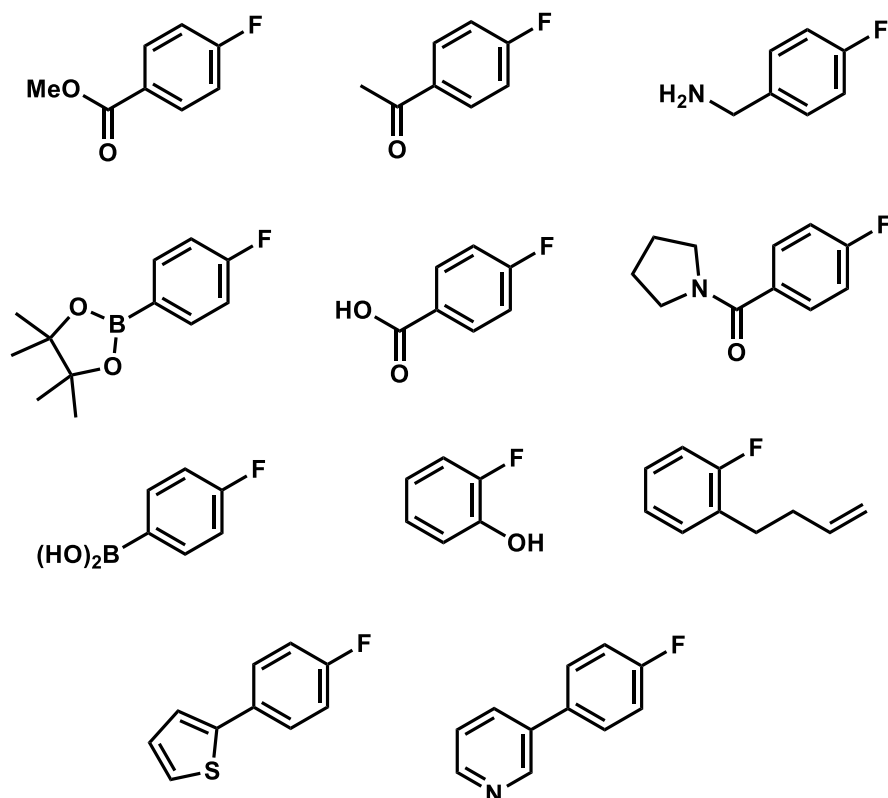


Figure IV-15: non-working substrates, limitations of the scope.

Alcohols, carboxylic acids and boronic acids are incompatible because of their acidic character ( $pK_a < 32$  in DMSO). Deprotonation occurs in basic conditions and impairs electron transfer on the electron enriched anion. Indeed, while reactions with aryl fluorides bearing esters, amides, and ketones gave the corresponding reduced products, no reactions were observed with substrates bearing acids and boronic esters.

To gain insights into the mechanism of the reaction, we isolated the germanyl anion **5** through the deprotonation of triphenylgermane with one equivalent of  $n\text{BuLi}$  in THF (Figure IV-16). The colorless crystalline solid obtained was fully characterized both in solution and in the solid state. The X-ray structure shows the germanium atom linked to the lithium ion ( $d_{\text{Ge-Li}} = 2.667(5)$  Å), which is coordinated with three molecules of THF.

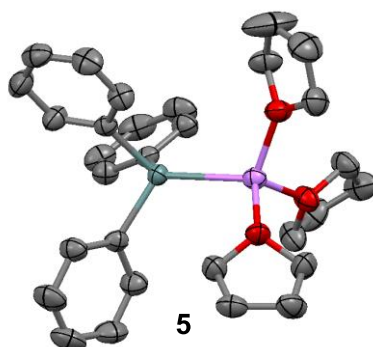
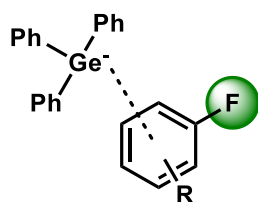


Figure IV-16 : Isolation of the lithiated germyl anion and its THF-coordinated XRD structure

Interestingly, the UV-visible spectrum of this anion in DMSO shows an absorbance in the visible region (Figure IV-18), which might be responsible for the observed photoreactivity as suggested in our working hypothesis. To exclude the formation of an electron donor-acceptor complex (Figure IV-17), we combined the germyl anion with different concentrations of fluorobenzene.



**Electron donor-acceptor  
complex : not observed**

Figure IV-17: Proposed EDA complex formation which was denied by experiment

However, we did not observe the appearance of a new band that might be attributed to the formation of such complex when we compared the absorption of solutions of  $\text{Ph}_3\text{GeNa}$  with and without 4-fluorotoluene. The two absorption spectra were identical in the given reaction conditions. Perhaps an increase in 4-fluorotoluene concentration is necessary to confirm that no charge transfer occurs.

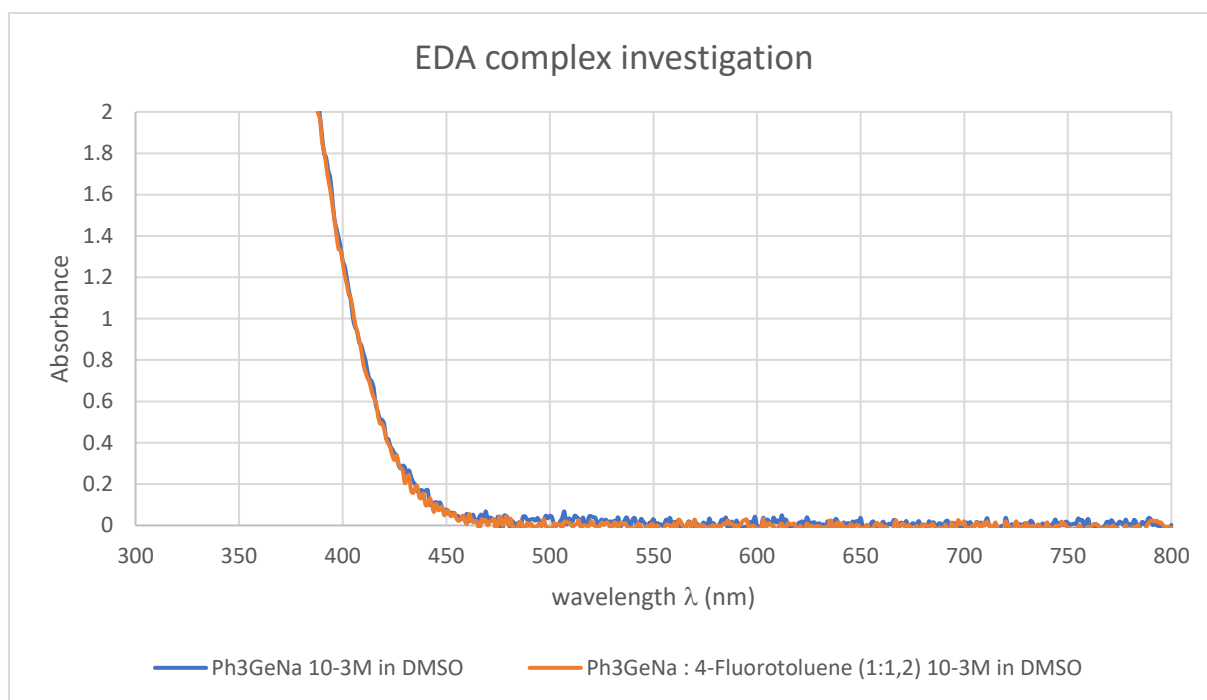


Figure IV-18: UV-Vis absorption spectra of the triphenylgermyl anion in DMSO and proof that no EDA complex is formed in the reaction conditions

### 2.3. Mechanism of the reaction: DFT investigations

To gain further information about the photoreactivity of the germanyl anion, we performed preliminarily density functional theory (DFT) simulations. The excitation energy for the anion  $\text{Ph}_3\text{Ge}^-$  was calculated using time-dependent DFT (TD-DFT) calculations (Figure IV-19). Our calculation predicted an excitation to a singlet excited state  $^1[\text{Ph}_3\text{Ge}]^-*$  at 390.1 nm (73.2 kcal/mol) as a very strong peak with strong oscillator strength ( $f = 0.180$ ) which is in an excellent agreement with the range of the blue LED used in the reaction. According to the frontier molecular orbital (FMO) results, highest occupied molecular orbitals (HOMOs) and lowest unoccupied molecular orbitals (LUMOs), this absorption band is clearly assigned to the HOMO  $\rightarrow$  LUMO transition for the ground and excited states of the anion (Figure IV-20). The HOMOs ( $-6.298$  eV) are mainly located on the Ge atom and the LUMOs ( $-1.374$  eV) are distributed nearly equally over the phenyl rings. To validate the nature of transition, natural transition orbital (NTO) calculation has been performed for the transition at 390.1 nm and exhibited that the singlet excited state is a 98.9% HOMO-LUMO transition. Next, following an excitation, a rapid intersystem crossing (ISC) is observed from the singlet excited state  $^1[\text{Ph}_3\text{Ge}]^-*$  to the triplet excited state  $^3[\text{Ph}_3\text{Ge}]^-*$  at 450.3 nm (63.5 kcal/mol).

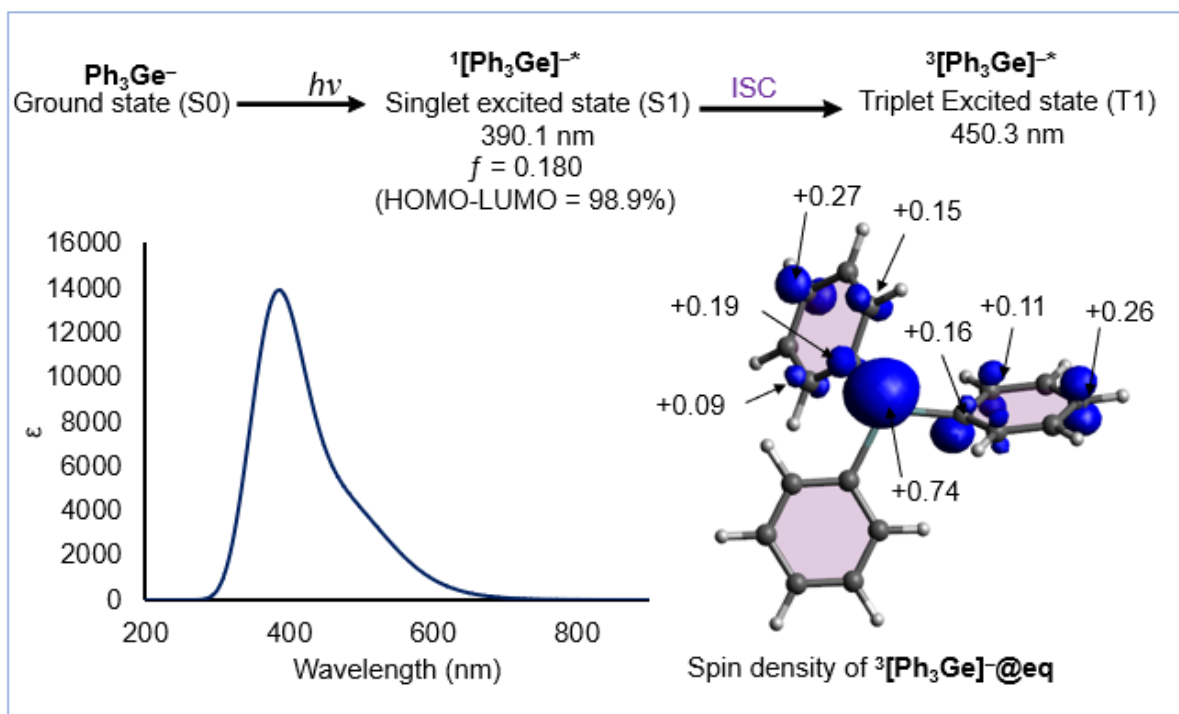


Figure IV-19: Calculated absorption spectrum of the triphenylgermanyl anion and excitation energy for the anion  $\text{Ph}_3\text{Ge}^-$  along with its singlet and triplet states

The resultant triplet anion  $^3[\text{Ph}_3\text{Ge}]^*$  has two types of singly occupied MOs (SOMOs) with the following characteristics (Figure IV-20). First, the high energy SOMO ( $-2.884$  eV) of  $^3[\text{Ph}_3\text{Ge}]^*\text{eq}$  is located on the  $\pi^*$  orbital of the ring and on the  $\sigma^*\text{Ge-C}$ . Reasonably, this orbital is not able to participate in a new bond formation, instead it potentially has a single-electron transfer (SET) ability.

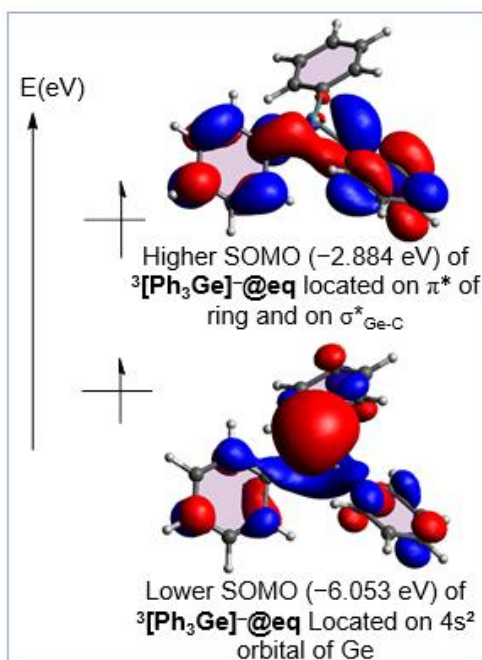


Figure IV-20: Singly occupied molecular orbitals of triplet state of the germanyl anion

Second, the low energy SOMO ( $-6.053$  eV) of  $^3[\text{Ph}_3\text{Ge}]^{-*\text{eq}}$  is located on  $4s^2$  orbital of Ge which is capable of participating in a new bond formation through nucleophilic radical addition. Spin density calculations appear to show a major lobe belonging to a single electron located on Ge whereas the other electron lobes are located on the two phenyl rings. Following our understanding for the electronic characteristic of  $\text{Ph}_3\text{Ge}^-$  before and after excitation, we calculated the reaction mechanism shown in Figure IV-21. The *in-situ* generated triphenylgermanyl anion  $\text{Ph}_3\text{Ge}^-$  is initially photoexcited to the singlet excited state ( $^1[\text{Ph}_3\text{Ge}]^{-*}$ ) by irradiation with blue LED, followed by an ISC process to the triplet intermediate ( $^3[\text{Ph}_3\text{Ge}]^{-*}$ ). Then, two SET pathways may occur to generate the  $\text{Ph}_3\text{Ge}\cdot$  and the paratolyl ( $\text{T}\cdot$ ) radicals prior to radical combination that will release the final product. On one hand, the first pathway is a stepwise process; an exergonic complexation ( $\Delta G = -5.5$  kcal/mol) between the triplet diradical and the aryl fluoride PFT, namely p-fluorotoluene, to give  $^3[\text{Ph}_3\text{Ge\_PFT}]^-$  that is followed by a favorable SET through a charge-transfer (CT) complex ( $\Delta G_{\text{SET}} = 12.9$  kcal/mol) to form the triphenylgermanyl radical ( $\text{Ph}_3\text{Ge}\cdot$ ) and toluene radical ( $\text{T}\cdot$ ) and expels a fluoride ion. In regard to the proposed complex  $^3[\text{Ph}_3\text{Ge\_PFT}]^-$ , the intermolecular reaction has been calculated to be disfavored ( $\Delta G^\ddagger = 11.7$  kcal/mol) compared to the SET via CT complex process. On the other hand, the triplet diradical  $^3[\text{Ph}_3\text{Ge}]^{-*\text{eq}}$  undergoes an outer sphere SET ( $\Delta G_{\text{SET}} = -7.9$  kcal/mol) with PFT rather than complexation as an energetically more favorable process, giving the  $\text{Ph}_3\text{Ge}\cdot$  and radical anion  $\text{PFT}\cdot^-$ . The latter subsequently ejects  $\text{F}^-$  as an exergonic step ( $\Delta G = -10.5$  kcal/mol) to give  $\text{T}\cdot$ .

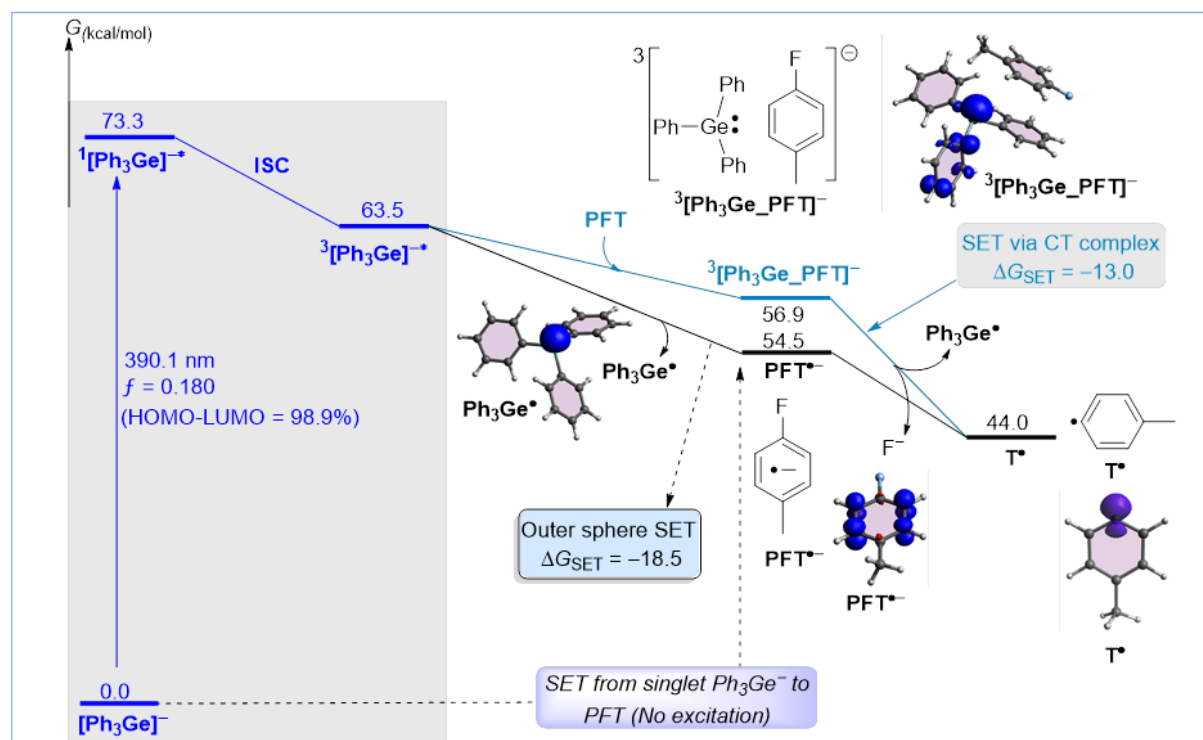


Figure IV-21: Calculated reaction mechanism for the reduction of aryl fluorides by the germanyl anion

Finally, radical-radical recombination was calculated to be barrierless and to have an important stabilizing effect as shown in Figure IV-22.

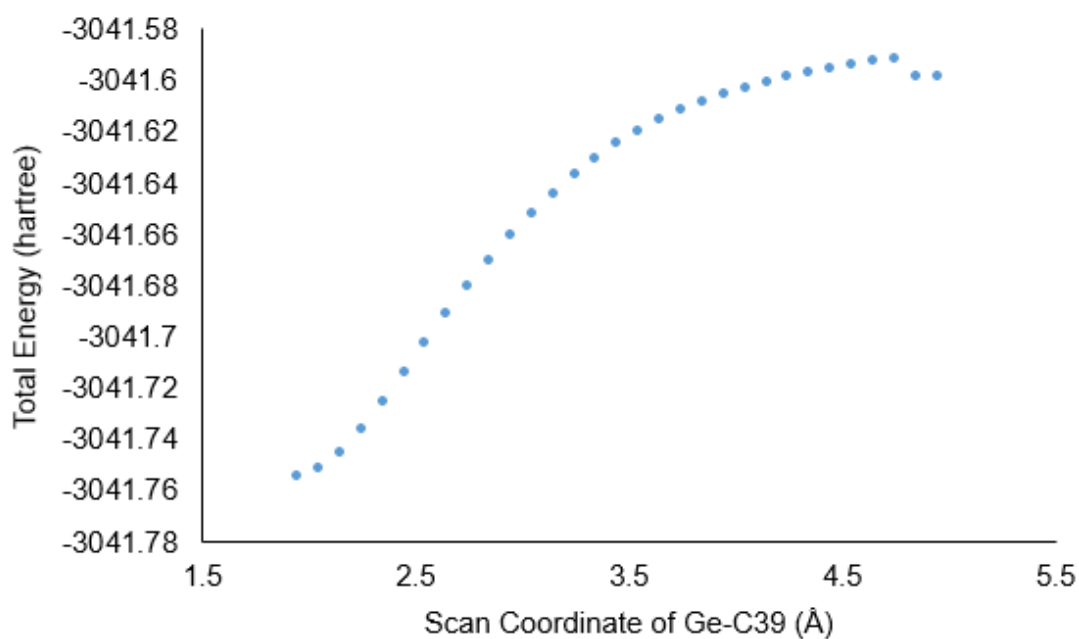


Figure IV-22: Evolution of the energy for the radical-radical recombination of the tolyl and germanyl radicals

### 3. Conclusion

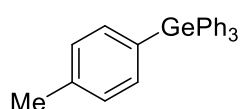
In conclusion, we developed a visible-light-photoinduced germanylation of fluoro(het)arenes with triphenylgermane in the presence of  $t\text{BuONa}$  under blue light irradiation. The reaction proceeds smoothly with various fluoroarenes and tolerates a few functionalities. Experimental and computational studies suggest that the excitation of the germanyl anion generates a highly reducing state that is capable of cleaving the strong  $\text{C}(\text{sp}^2)\text{--F}$  bond. One should highlight the limitations of this approach notably in terms of functional group compatibility presumably due to the high nucleophilicity and Lewis basicity of the germanyl anion. This photocatalyst-free transformation will likely open new avenues in the emerging field of germane and main group chemistry.

#### 4. Experimental section

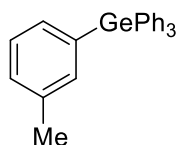
All required fine chemicals were used directly without purification. All air and moisture sensitive reactions were carried out under argon atmosphere using standard Schlenk manifold technique. All column solvents were bought indistinctively from VWR, Carlo Erba or Sigma-Aldrich. Extra-dry DMSO was bought from Sigma-Aldrich (>99.9%), stored over activated molecular sieves, and thoroughly degassed by sparging with argon.  $^1\text{H}$  and  $^{13}\text{C}$  Nuclear Magnetic Resonance (NMR) spectra were acquired at various field strengths as indicated and were referenced to  $\text{CHCl}_3$  (7.26 and 77.16 ppm for  $^1\text{H}$  and  $^{13}\text{C}$  respectively).  $^1\text{H}$  NMR coupling constants are reported in Hertz and refer to apparent multiplicities and not true coupling constants. Data are reported as follows: chemical shift, multiplicity (s = singlet, br s = broad singlet, d = doublet, t = triplet, q = quartet, qi = quintet, sx = sextet, sp = septet, m = multiplet, dd = doublet of doublets, etc.), integration. Infra-red spectra were recorded using a Nicolet 6700 Thermoscientific diamond ATR spectrometer. High-resolution mass spectra were obtained using a Waters GCT Premier spectrometer. Spectra were obtained using chemical ionization (DCI- $\text{CH}_4$ ) technique. Analytical TLC: aluminum backed plates pre-coated (0.25 mm) with Merck Silica Gel 60 F254. Compounds were visualized by exposure to UV-light or by dipping the plates in permanganate ( $\text{KMnO}_4$ ) stain followed by heating. Flash column chromatography was performed using Merck Silica Gel 60 (40–63  $\mu\text{m}$ ). All mixed solvent eluents are reported as v/v solutions. Absorption spectra were obtained using an Agilent Cary 60 UV-Vis. 1 or 10 mm High Precision Cell made of quartz from Hellma Analytics were used. The LEDs used are high-power Vision-EL (5W,  $\lambda = 460 \pm 10$  nm, 410 lm). All the reactions were conducted in standard glass Schlenk tubes.

**General procedure:** triphenylgermanium hydride (30.5 mg, 0.1 mmol, 1 equiv.) and sodium *tert*-butanolate (19.2 mg, 0.2 mmol, 2.0 equiv.) were weighted in a Schlenk. If solid, the fluoroarene (0.12 mmol, 1.2 equiv.) was added. The Schlenk was sealed with a septum, then evacuated and backfilled with argon three time. If liquid, the fluoroarene was added by the means of a micro-syringe, and dried and degassed DMSO was added (1 mL). The bright yellow solution was then stirred and irradiated using a Blue LED for 15 minutes leading to a colourless solution, before adding aqueous saturated  $\text{NH}_4\text{Cl}$  solution (5 mL). In a separatory funnel the crude mixture was then extracted thrice using  $\text{Et}_2\text{O}$  (3\*10 mL). The combined organic layers were washed with water (3\*10 mL), dried over  $\text{Na}_2\text{SO}_4$  and concentrated *in vacuo*. The crude residue was purified by flash column chromatography.

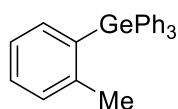


**Triphenyl(*p*-tolyl)germane 3a:**

Synthesized according to the general procedure using 4-fluorotoluene (13.2 mg, 0.12 mmol), triphenylgermanium hydride (30.5 mg, 0.1 mmol), sodium *tert*-butanolate (19.2 mg, 0.2 mmol) and DMSO (1 mL). Purification by flash chromatography (SiO<sub>2</sub>, 2:98 DCM:pentane) afforded the title compound as a colorless solid. (28.3 mg, 72%). **IR (neat)**  $\nu_{\text{max}}/\text{cm}^{-1}$  3064, 3041, 2922, 2853, 1960, 1914, 1596, 1484, 1447, 1091, 803, 738, 698, 492. **<sup>1</sup>H NMR** (CDCl<sub>3</sub>, 300 MHz):  $\delta_{\text{H}}$  7.59 – 7.51 (m, 6H), 7.45 (d,  $J$  = 7.9 Hz, 2H), 7.43 – 7.34 (m, 9H), 7.22 (d,  $J$  = 7.5 Hz, 2H), 2.39 (s, 3H). **<sup>13</sup>C{<sup>1</sup>H} NMR** (CDCl<sub>3</sub>, 75 MHz):  $\delta_{\text{C}}$  139.1, 136.5, 135.5, 132.5, 129.3, 129.2, 128.4, 21.6. **HRMS (DCI-CH<sub>4</sub>)**:  $m/z$  calc'd for C<sub>25</sub>H<sub>22</sub><sup>70</sup>Ge [M]<sup>+</sup> = 392.0964, found 392.0969.

**Triphenyl(*m*-tolyl)germane 3b:**

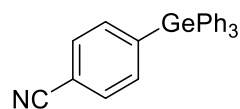
Synthesized according to the general procedure using 3-fluorotoluene (13.2 mg, 0.12 mmol), triphenylgermanium hydride (30.5 mg, 0.1 mmol), sodium *tert*-butanolate (19.2 mg, 0.2 mmol) and DMSO (1 mL). Purification by flash chromatography (SiO<sub>2</sub>, 2:98 DCM:pentane) afforded the title compound as a colorless solid. (33.0 mg, 84%). **IR (neat)**  $\nu_{\text{max}}/\text{cm}^{-1}$  3136, 3064, 3043, 2922, 2851, 1960, 1886, 1824, 1592, 1483, 1429, 1090, 736, 698, 463. **<sup>1</sup>H NMR** (CDCl<sub>3</sub>, 300 MHz):  $\delta_{\text{H}}$  7.56 – 7.51 (m, 6H), 7.43 – 7.27 (m, 12H), 7.24 – 7.21 (m, 1H), 2.32 (s, 3H). **<sup>13</sup>C{<sup>1</sup>H} NMR** (CDCl<sub>3</sub>, 75 MHz):  $\delta_{\text{C}}$  137.9, 136.4, 136.0, 136.0, 135.6, 132.6, 130.1, 129.2, 128.4, 128.2, 21.7. **HRMS (DCI-CH<sub>4</sub>)**:  $m/z$  calc'd for C<sub>25</sub>H<sub>22</sub><sup>70</sup>Ge [M]<sup>+</sup> = 392.0964, found 392.0978.

**Triphenyl(*o*-tolyl)germane 3c:**

Synthesized according to the general procedure using 2-fluorotoluene (13.2 mg, 0.12 mmol), triphenylgermanium hydride (30.5 mg, 0.1 mmol), sodium *tert*-butanolate (19.2 mg, 0.2 mmol) and DMSO (1 mL). Purification by flash chromatography (SiO<sub>2</sub>, 2:98 DCM:pentane) afforded the title compound as a colorless solid. (25.0 mg, 63%). **IR (neat)**  $\nu_{\text{max}}/\text{cm}^{-1}$  3064, 2995, 2925, 2854, 1483, 1430, 1089, 1026, 998, 755, 739, 700, 475. **<sup>1</sup>H NMR** (CDCl<sub>3</sub>, 300 MHz):  $\delta_{\text{H}}$  7.59 – 7.52 (m, 6H), 7.43 – 7.23 (m, 12H), 7.15 (td,  $J$  = 7.4, 1.4 Hz, 1H), 2.16 (s, 3H). **<sup>13</sup>C{<sup>1</sup>H} NMR** (CDCl<sub>3</sub>, 75 MHz):  $\delta_{\text{C}}$  144.3, 136.9, 136.7, 135.4,

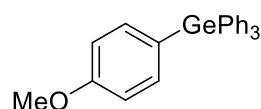
134.8, 130.3, 129.7, 129.1, 128.4, 125.5, 24.1. **HRMS (DCI-CH<sub>4</sub>):**  $m/z$  calc'd for C<sub>25</sub>H<sub>22</sub><sup>70</sup>Ge [M]<sup>+</sup> = 392.0964, found 392.0961.

#### **4-(triphenylgermyl)benzonitrile 3d:**



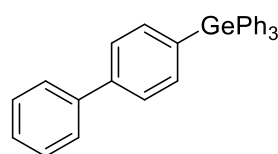
Synthesized according to the general procedure using 4-fluorobenzonitrile (14.5 mg, 0.12 mmol), triphenylgermanium hydride (30.5 mg, 0.1 mmol), sodium *tert*-butanolate (19.2 mg, 0.2 mmol) and DMSO (1 mL). Purification by flash chromatography (SiO<sub>2</sub>, 2:98 Et<sub>2</sub>O:pentane) afforded the title compound as a colourless solid. (18.0 mg, 44%). **IR (neat)**  $\nu_{\max}/\text{cm}^{-1}$  3068, 2961, 2922, 2852, 2229, 1430, 1260, 1090, 1020, 797, 734, 697, 552, 462. **<sup>1</sup>H NMR** (CDCl<sub>3</sub>, 300 MHz):  $\delta_{\text{H}}$  7.65 (s, 4H), 7.53 – 7.47 (m, 6H), 7.46 – 7.37 (m, 9H). **<sup>13</sup>C{<sup>1</sup>H} NMR** (CDCl<sub>3</sub>, 75 MHz):  $\delta_{\text{C}}$  143.9, 136.0, 135.4, 134.8, 131.5, 129.7, 128.7, 119.0, 113.0. **HRMS (DCI-CH<sub>4</sub>):**  $m/z$  calc'd for C<sub>25</sub>H<sub>19</sub><sup>70</sup>GeN [M]<sup>+</sup> = 403.0760, found 403.0779.

#### **(4-methoxyphenyl)triphenylgermane 3e:**



Synthesized according to the general procedure using 4-fluoroanisole (15.1 mg, 0.12 mmol), triphenylgermanium hydride (30.5 mg, 0.1 mmol), sodium *tert*-butanolate (19.2 mg, 0.2 mmol) and DMSO (1 mL). Purification by flash chromatography (SiO<sub>2</sub>, 2:98 DCM:pentane) afforded the title compound as a colourless solid. (33.7 mg, 82%). **IR (neat)**  $\nu_{\max}/\text{cm}^{-1}$  3066, 3011, 2995, 2958, 2928, 2834, 1898, 1592, 1500, 1429, 1283, 1249, 1182, 1090, 1029, 821, 736, 698, 523. **<sup>1</sup>H NMR** (CDCl<sub>3</sub>, 300 MHz):  $\delta_{\text{H}}$  7.61 – 7.51 (m, 6H), 7.47 (d,  $J$  = 8.6 Hz, 2H), 7.43 – 7.34 (m, 9H), 6.96 (d,  $J$  = 8.6 Hz, 2H), 3.83 (s, 3H). **<sup>13</sup>C{<sup>1</sup>H} NMR** (CDCl<sub>3</sub>, 75 MHz):  $\delta_{\text{C}}$  160.6, 136.8, 136.6, 135.5, 129.2, 128.4, 126.8, 114.2, 55.2. **HRMS (DCI-CH<sub>4</sub>):**  $m/z$  calc'd for C<sub>25</sub>H<sub>22</sub><sup>70</sup>GeO [M]<sup>+</sup> = 403.0779, found 403.0760.

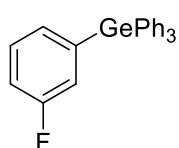
#### **[1,1'-biphenyl]-4-yltriphenylgermane 3f:**



Synthesized according to the general procedure using 4-fluorobiphenyl (20.7 mg, 0.12 mmol), triphenylgermanium hydride (30.5 mg, 0.1 mmol), sodium *tert*-butanolate (19.2 mg, 0.2 mmol), DMSO (1 mL) and was irradiated for 15 hours. Purification by flash chromatography (SiO<sub>2</sub>, 5:95 DCM:pentane) afforded the title compound as a colourless solid. (24.6 mg, 54%). **IR (neat)**  $\nu_{\max}/\text{cm}^{-1}$  3065, 3050, 3022, 2982, 2924, 1958, 1888, 1827, 1546, 1483, 1429, 1386,

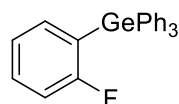
1092, 832, 738, 724, 699, 459. **<sup>1</sup>H NMR** (CDCl<sub>3</sub>, 300 MHz): δ<sub>H</sub> 7.67 – 7.54 (m, 12H), 7.51 – 7.31 (m, 12H). **<sup>13</sup>C{<sup>1</sup>H} NMR** (CDCl<sub>3</sub>, 75 MHz): δ<sub>C</sub> 142.0, 141.1, 136.2, 136.0, 135.6, 135.1, 129.3, 128.9, 128.5, 127.6, 127.3, 127.1. **HRMS (DCI-CH<sub>4</sub>)**: m/z calc'd for C<sub>30</sub>H<sub>24</sub><sup>70</sup>Ge [M]<sup>+</sup> = 454.1121, found 454.1118.

### **(3-fluorophenyl)triphenylgermane 3g:**



Synthesized according to the general procedure using 1,3-difluorobenzene (27.4 mg, 0.24 mmol), triphenylgermanium hydride (30.5 mg, 0.1 mmol), sodium *tert*-butanolate (19.2 mg, 0.2 mmol) and DMSO (1 mL). Purification by flash chromatography (SiO<sub>2</sub>, 2:98 DCM:pentane) afforded the title compound as a colourless solid. (19.0 mg, 48%). **IR (neat)** ν<sub>max</sub>/cm<sup>-1</sup> 3065, 3041, 3011, 2995, 2921, 2851, 1961, 1884, 1821, 1573, 1483, 1472, 1428, 1260, 1212, 1089, 736, 697, 459. **<sup>1</sup>H NMR** (CDCl<sub>3</sub>, 300 MHz): δ<sub>H</sub> 7.57 – 7.49 (m, 6H), 7.46 – 7.34 (m, 10H), 7.34 – 7.29 (m, 1H), 7.26 – 7.19 (m, 1H), 7.10 (dddd, *J* = 9.2, 7.8, 2.7, 1.4 Hz, 1H). **<sup>13</sup>C{<sup>1</sup>H} NMR** (CDCl<sub>3</sub>, 75 MHz): δ<sub>C</sub> 162.9 (d, *J* = 249.3 Hz), 139.3 (d, *J* = 4.0 Hz), 135.6, 135.5, 131.1 (d, *J* = 3.1 Hz), 130.0 (d, *J* = 6.9 Hz), 129.5, 128.5, 121.9 (d, *J* = 19.2 Hz), 116.3 (d, *J* = 21.0 Hz). **<sup>19</sup>F{<sup>1</sup>H} NMR** (CDCl<sub>3</sub>, 282 MHz): δ<sub>F</sub> -112.84. **HRMS (DCI-CH<sub>4</sub>)**: m/z calc'd for C<sub>24</sub>H<sub>19</sub>F<sup>70</sup>Ge [M]<sup>+</sup> = 396.0713, found 396.0717.

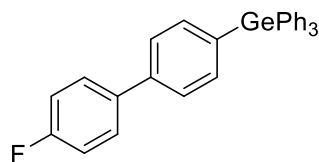
### **(2-fluorophenyl)triphenylgermane 3h:**



Synthesized according to the general procedure using 1,2-difluorobenzene (27.4 mg, 0.24 mmol), triphenylgermanium hydride (30.5 mg, 0.1 mmol), sodium *tert*-butanolate (19.2 mg, 0.2 mmol) and DMSO (1 mL). Purification by flash chromatography (SiO<sub>2</sub>, 2:98 DCM:pentane) afforded the title compound as a colourless solid. (18.9 mg, 47%). **IR (neat)** ν<sub>max</sub>/cm<sup>-1</sup> 3067, 3012, 2996, 2924, 2853, 1962, 1885, 1829, 1654, 1595, 1484, 1466, 1438, 1091, 736, 697, 475. **<sup>1</sup>H NMR** (CDCl<sub>3</sub>, 300 MHz): δ<sub>H</sub> 7.59 – 7.50 (m, 6H), 7.44 – 7.36 (m, 10H), 7.29 (ddd, *J* = 7.0, 5.2, 1.9 Hz, 1H), 7.16 – 7.06 (m, 2H). **<sup>13</sup>C{<sup>1</sup>H} NMR** (CDCl<sub>3</sub>, 75 MHz): δ<sub>C</sub> 166.5 (d, *J* = 241.4 Hz), 137.2 (d, *J* = 10.3 Hz), 135.6, 135.4 (d, *J* = 0.9 Hz), 131.9 (d, *J* = 7.9 Hz), 129.4, 128.4, 124.4 (d, *J* = 2.9 Hz), 122.6 (d, *J* =

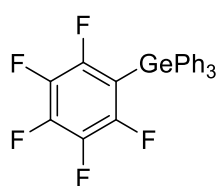
32.3 Hz), 115.4 (d,  $J = 25.4$  Hz).  $^{19}\text{F}\{^1\text{H}\}$  NMR ( $\text{CDCl}_3$ , 282 MHz):  $\delta_{\text{F}}$  -95.33. **HRMS (DCI-CH<sub>4</sub>)**:  $m/z$  calc'd for  $\text{C}_{24}\text{H}_{19}\text{F}^{70}\text{Ge}$   $[\text{M}]^+$  = 396.0713, found 396.0730.

**(4'-fluoro-[1,1'-biphenyl]-4-yl)triphenylgermane 3i:**



Synthesized according to the general procedure using 4,4'-difluorobiphenyl (45.6 mg, 0.24 mmol), triphenylgermanium hydride (30.5 mg, 0.1 mmol), sodium *tert*-butanolate (19.2 mg, 0.2 mmol), DMSO (1 mL) and was irradiated for 15 hours. Purification by flash chromatography ( $\text{SiO}_2$ , 5:95 DCM:pentane) afforded the title compound as a colourless solid. (25.1 mg, 53%). **IR (neat)**  $\nu_{\text{max}}/\text{cm}^{-1}$  3140, 3070, 3051, 2924, 2853, 1954, 1884, 1823, 1764, 1655, 1595, 1489, 1430, 1092, 812, 736, 698.  $^1\text{H}$  NMR ( $\text{CDCl}_3$ , 300 MHz):  $\delta_{\text{H}}$  7.66 – 7.51 (m, 12H), 7.47 – 7.36 (m, 9H), 7.14 (t,  $J = 8.7$  Hz, 2H).  $^{13}\text{C}\{^1\text{H}\}$  NMR ( $\text{CDCl}_3$ , 75 MHz):  $\delta_{\text{C}}$  162.7 (d,  $J = 246.6$  Hz), 141.0, 137.2 (d,  $J = 3.2$  Hz), 136.1, 136.0, 135.5, 135.2, 129.3, 128.8 (d,  $J = 8.0$  Hz), 128.5, 127.0, 115.8 (d,  $J = 21.4$  Hz).  $^{19}\text{F}\{^1\text{H}\}$  NMR ( $\text{CDCl}_3$ , 282 MHz)  $\delta_{\text{F}}$  -115.53. **HRMS (DCI-CH<sub>4</sub>)**:  $m/z$  calc'd for  $\text{C}_{30}\text{H}_{23}\text{F}^{70}\text{Ge}$   $[\text{M}]^+$  = 472.1026, found 472.1044. **Xrays**: The compound was solubilized in dichloromethane before being layered with pentane and left to diffuse slowly, providing crystals suitable for Xray diffraction.

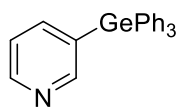
**(perfluorophenyl)triphenylgermane 3j:**



Synthesized according to the general procedure using hexafluorobenzene (93.1 mg, 0.50 mmol), triphenylgermanium hydride (30.5 mg, 0.1 mmol), sodium *tert*-butanolate (19.2 mg, 0.2 mmol) and DMSO (1 mL). Purification by flash chromatography ( $\text{SiO}_2$ , 2:98 DCM:pentane) afforded the title compound as a colourless solid. (20.0 mg, 43%). **IR (neat)**  $\nu_{\text{max}}/\text{cm}^{-1}$  3065, 3013, 2920, 2851, 1642, 1514, 1485, 1473, 1431, 1379, 1092, 1080, 971, 738, 697, 462.  $^1\text{H}$  NMR ( $\text{CDCl}_3$ , 300 MHz):  $\delta_{\text{H}}$  7.56 – 7.53 (m, 6H), 7.48 – 7.38 (m, 9H).  $^{13}\text{C}\{^1\text{H}\}$  NMR ( $\text{CDCl}_3$ , 75 MHz (except  $\text{C}_6\text{F}_5$  moiety)):  $\delta_{\text{C}}$  134.8, 134.3, 129.8, 128.5.  $^{19}\text{F}$  NMR (282 MHz, Chloroform-*d*)  $\delta_{\text{F}}$  -121.91 (ddd,  $J = 23.2, 8.6, 3.6$  Hz), -150.51 (tt,  $J = 20.4, 3.4$  Hz), -160.07 (ddt,  $J = 27.8, 13.2, 6.7$  Hz).  $^{19}\text{F}\{^1\text{H}\}$  NMR ( $\text{CDCl}_3$ , 282 MHz):  $\delta_{\text{F}}$  -121.91 (ddd,  $J = 23.2, 8.6, 3.6$  Hz), -150.51 (tt,  $J = 20.4,$

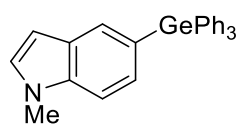
3.4 Hz), -160.07 (ddt,  $J = 27.8, 13.2, 6.7$  Hz). **HRMS (DCI-CH<sub>4</sub>)**:  $m/z$  calc'd for C<sub>24</sub>H<sub>15</sub>F<sup>70</sup>Ge [M]<sup>+</sup> = 468.0336, found 468.0344.

### 3-(triphenylgermyl)pyridine 3k:



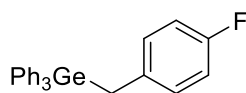
Synthesized according to the general procedure using 3-fluoropyridine (11.7 mg, 0.12 mmol), triphenylgermanium hydride (30.5 mg, 0.1 mmol), sodium *tert*-butanolate (19.2 mg, 0.2 mmol) and DMSO (1 mL). Purification by flash chromatography (SiO<sub>2</sub>, 2:98 to 20:80 Et<sub>2</sub>O:pentane) afforded the title compound as a colourless solid. (17.0 mg, 45%). **IR (neat)**  $\nu_{\max}/\text{cm}^{-1}$  3067, 3043, 2995, 2922, 2851, 1484, 1432, 1091, 739, 698, 475. **<sup>1</sup>H NMR** (CDCl<sub>3</sub>, 300 MHz):  $\delta_{\text{H}}$  8.72 (s, 1H), 8.64 (d,  $J = 3.2$  Hz, 1H), 7.81 (dt,  $J = 7.5, 1.8$  Hz, 1H), 7.54 – 7.50 (dd,  $J = 7.4, 2.0$  Hz, 6H), 7.47 – 7.35 (m, 9H), 7.32 – 7.27 (s, 1H). **<sup>13</sup>C{<sup>1</sup>H} NMR** (CDCl<sub>3</sub>, 75 MHz):  $\delta_{\text{C}}$  155.6, 150.4, 143.2, 135.4, 135.0, 132.1, 129.6, 128.6, 123.9. **HRMS (DCI-CH<sub>4</sub>)**:  $m/z$  calc'd for C<sub>23</sub>H<sub>19</sub><sup>70</sup>GeN [M]<sup>+</sup> = 379.0760, found 379.0771.

### 1-methyl-5-(triphenylgermyl)-1H-indole 3l:



Synthesized according to the general procedure using 5-fluoro-1-methyl-1H-indole (14.9 mg, 0.10 mmol), triphenylgermanium hydride (61.0 mg, 0.2 mmol), sodium *tert*-butanolate (38.4 mg, 0.4 mmol) and DMSO (1 mL). Purification by flash chromatography (SiO<sub>2</sub>, 20:80 DCM:pentane) afforded the title compound as a colourless solid. (11.8 mg, 27%). **IR (neat)**  $\nu_{\max}/\text{cm}^{-1}$  3013, 3066, 3049, 2924, 2852, 1961, 1886, 1829, 1685, 1584, 1512, 1483, 1429, 1110, 733, 698. **<sup>1</sup>H NMR** (CDCl<sub>3</sub>, 300 MHz):  $\delta_{\text{H}}$  7.79 (t,  $J = 0.9$  Hz, 1H), 7.60 – 7.57 (m, 6H), 7.40 – 7.35 (m, 11H), 7.05 (d,  $J = 3.1$  Hz, 1H), 6.45 (d,  $J = 3.1$  Hz, 1H), 3.81 (s, 3H). **<sup>13</sup>C{<sup>1</sup>H} NMR** (CDCl<sub>3</sub>, 75 MHz):  $\delta_{\text{C}}$  137.4, 137.2, 135.7, 135.6, 129.0, 128.9, 128.8, 128.3, 128.1, 124.7, 109.4, 101.2, 32.9. **HRMS (DCI-CH<sub>4</sub>)**:  $m/z$  calc'd for C<sub>27</sub>H<sub>23</sub><sup>70</sup>GeN [M]<sup>+</sup> = 431.1073, found 431.1064.

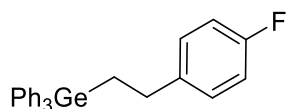
### (4-fluorobenzyl)triphenylgermane 4a:



Synthesized according to the general procedure using 4-fluorobenzotrifluoride (19.7 mg, 0.12 mmol), triphenylgermanium hydride (30.5 mg, 0.1 mmol), sodium *tert*-butanolate (19.2 mg, 0.2 mmol) and DMSO (1 mL) and was irradiated for 15 hours. Purification by flash chromatography (SiO<sub>2</sub>, 2:98 DCM:pentane) afforded the title compound as a colourless solid. (13.5 mg, 33%). **IR (neat)**  $\nu_{\max}/\text{cm}^{-1}$  3067, 3050, 2922, 2852, 1596, 1507, 1430, 1221, 1092, 908, 837, 735, 701,

465.  **$^1\text{H}$  NMR** ( $\text{CDCl}_3$ , 500 MHz)  $\delta_{\text{H}}$  7.44 – 7.30 (m, 15H), 6.83 (dd,  $J = 8.6, 5.5$  Hz, 2H), 6.76 (t,  $J = 8.7$  Hz, 2H), 2.96 (s, 2H).  **$^{13}\text{C}\{^1\text{H}\}$  NMR** ( $\text{CDCl}_3$ , 126 MHz)  $\delta_{\text{C}}$  160.7 (d,  $J = 242.2$  Hz), 136.1, 135.2, 134.7 (d,  $J = 3.2$  Hz), 130.0 (d,  $J = 7.7$  Hz), 129.2, 128.3, 114.9 (d,  $J = 21.1$  Hz), 22.7.  **$^{19}\text{F}\{^1\text{H}\}$  NMR** ( $\text{CDCl}_3$ , 282 MHz)  $\delta_{\text{F}}$  -119.36. **HRMS (DCI- $\text{CH}_4$ )**:  $m/z$  calc'd for  $\text{C}_{25}\text{H}_{21}\text{F}^{70}\text{Ge}$   $[\text{M}]^+$  = 410.0870, found 410.0873. **Xrays**: The compound was solubilized in cyclohexane and left to evaporate slowly, providing crystals suitable for Xray diffraction.

**(4-fluorophenethyl)triphenylgermane 4b:**



Synthesized according to the general procedure using 4-fluorostyrene (14.7 mg, 0.12 mmol), triphenylgermanium hydride (30.5 mg, 0.1 mmol), sodium *tert*-butanolate (19.2 mg, 0.2 mmol) and DMSO (1 mL). Purification by flash chromatography ( $\text{SiO}_2$ , 1:99 DCM:pentane) afforded the title compound as a colourless solid. (39.3 mg, 92%). **IR (neat)**  $\nu_{\text{max}}/\text{cm}^{-1}$  3064, 2927, 2854, 1508, 1484, 1430, 1220, 1091, 739, 698.  **$^1\text{H}$  NMR** ( $\text{CDCl}_3$ , 300 MHz):  $\delta_{\text{H}}$  7.59 – 7.46 (m, 6H), 7.46 – 7.33 (m, 9H), 7.13 (dd,  $J = 8.5, 5.6$  Hz, 2H), 6.95 (t,  $J = 8.8$  Hz, 2H), 2.88 – 2.77 (m, 2H), 1.92 – 1.80 (m, 2H).  **$^{13}\text{C}\{^1\text{H}\}$  NMR** ( $\text{CDCl}_3$ , 75 MHz):  $\delta_{\text{C}}$  161.3 (d,  $J = 243.2$  Hz), 140.3 (d,  $J = 3.2$  Hz), 136.9, 135.1, 129.3 (d,  $J = 7.8$  Hz), 129.2, 128.4, 115.2 (d,  $J = 21.1$  Hz), 30.5, 16.3.  **$^{19}\text{F}\{^1\text{H}\}$  NMR** ( $\text{CDCl}_3$ , 282 MHz)  $\delta_{\text{F}}$  -117.85. **HRMS (DCI- $\text{CH}_4$ )**:  $m/z$  calc'd for  $\text{C}_{26}\text{H}_{23}\text{F}^{70}\text{Ge}$   $[\text{M}]^+$  = 424.1026, found 424.1025. **Xrays**: The compound was solubilized in cyclohexane and left to evaporate slowly, providing crystals suitable for Xray diffraction.

**(triphenylgermyl)lithium 5:**

$\text{Ph}_3\text{Ge}-\text{Li}(\text{THF})_3$  Triphenylgermanium hydride (153 mg, 0.5 mmol) was weighted in an oven dried Schlenk and capped with a rubber septum before evacuating and replacing the atmosphere with argon thrice. Dried and degassed THF (5 mL) was added providing a colorless solution. *n*-Butyllithium (330  $\mu\text{L}$ , 1.6M in hexanes, 0.525 mmol) was subsequently added and the clear yellow solution was stirred for 2 hours before evaporation of the solvent *in vacuo*. 1 mL of THF and 2 mL of dry pentane were then added providing a cloudy solution. After a gentle warming allowing the solids to solubilize, the solution was left to cool slowly, providing crystals suitable for Xray diffraction.

EDA complex investigations:

To investigate whether an EDA complex is involved in the mechanism, UV spectra of  $\text{Ph}_3\text{GeNa}$  solutions were recorded with and without 4-fluorotoluene.

Protocol:

In an argon filled glove-box,  $\text{Ph}_3\text{GeH}$  (15.3 mg, 0.05 mmol) and  $\text{tBuONa}$  (9.6 mg, 0.1 mmol), were weighted in a 5 mL volumetric flask and filled with dry and degassed DMSO, thus preparing a  $10^{-2}$  M solution of  $\text{Ph}_3\text{GeNa}$ . Separately, 4-fluorotoluene (13.2 mg, 0.06 mmol) was weighted in another 5 mL volumetric flask and diluted with DMSO, thus preparing a  $1.2 \cdot 10^{-2}$  M solution.

In one hand, the  $\text{Ph}_3\text{GeNa}$  solution was diluted by a 10-fold, on another hand, 0.5 mL of the  $\text{Ph}_3\text{GeNa}$  solution and 0.5 mL of the 4-fluorotoluene solution were mixed in a 5 mL volumetric flask and diluted with DMSO to  $10^{-3}$  M for the  $\text{Ph}_3\text{GeNa}$ . Both solutions were transferred in UV-cuvettes, sealed using a Teflon cap and wrapped with parafilm and aluminum foil, before being removed from the glove-box and studied.

Similarly, the fluorescence spectrum of  $\text{Ph}_3\text{GeNa}$  was recorded.

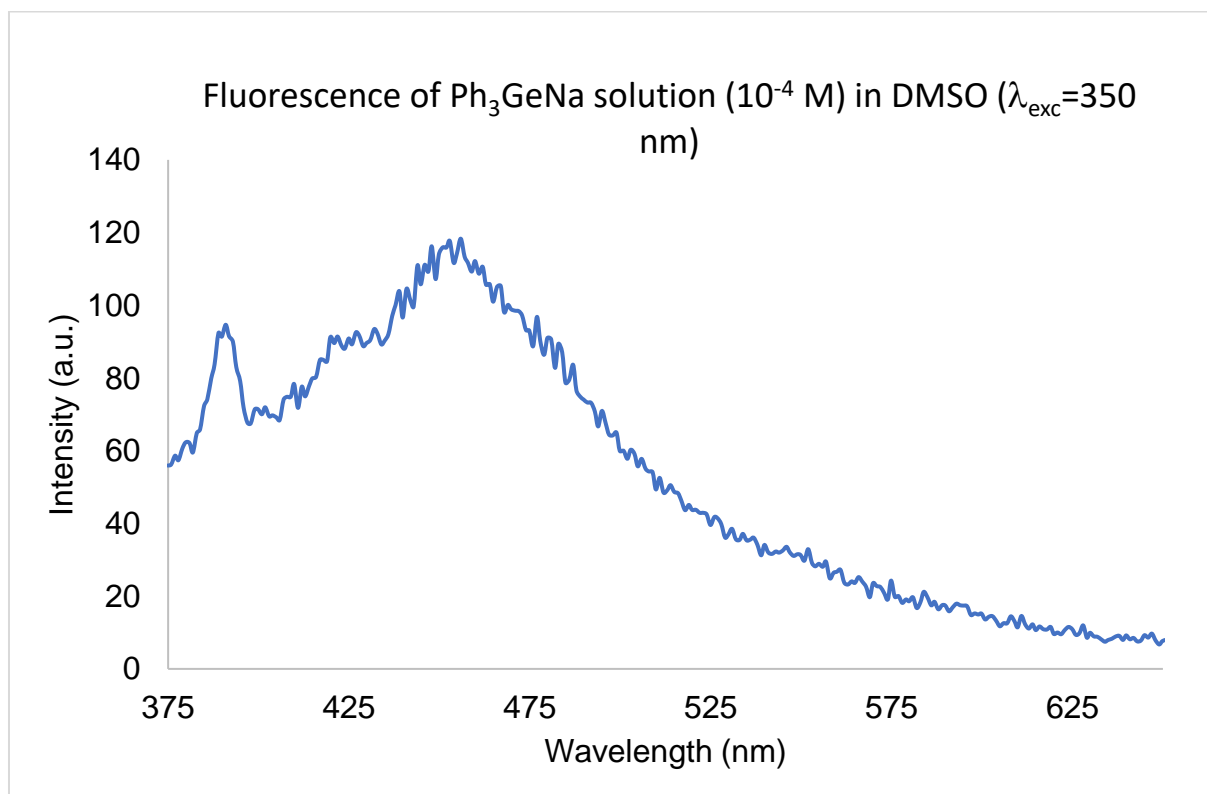


Figure IV-23: Emission spectrum of the germyl anion in DMSO at  $10^{-4}$  M.

### Crystallographic data collection and structure determination

The data were collected at low temperature (193 K) on a Bruker-AXS APEX II CCD Quazar diffractometer equipped with a 30 W air-cooled microfocus source (**3i**, **4a** and **4b**), or on a Bruker-AXS D8-Venture equipped with a Photon III-C14 detector (**5**), using MoK $\alpha$  radiation ( $\lambda = 0.71073\text{\AA}$ ). Phi- and omega- scans were used. The data were integrated with SAINT (S<sup>i</sup>) and an empirical absorption correction with SADABS was applied (S<sup>ii</sup>). The structures were solved using an intrinsic phasing method (SHELXT) (S<sup>iii</sup>) and refined using a least-squares method on  $F^2$  (S<sup>iv</sup>). All non-H atoms were refined with anisotropic displacement parameters. Hydrogen atoms were refined isotropically at calculated positions using a riding model with their isotropic displacement parameters constrained to be equal to 1.5 times the equivalent isotropic displacement parameters of their pivot atoms for terminal sp<sup>3</sup> carbon and 1.2 times for all other carbon atoms. Structures **4a** and **4b** were disordered. Several restraints (SAME, SADI, SIMU, DELU), equal xyz and Uij constraints (EXYZ and EADP) were applied to refine some moieties of the molecules and to avoid the collapse of the structures during the least-squares refinement by the large anisotropic displacement parameters.

CCDC-2152443 (**3i**), CCDC-2152444 (**4a**), CCDC-2239126 (**4b**) and CCDC-2152441 (**5**) contain the supplementary crystallographic data for this paper. These data can be obtained free of charge from the Cambridge Crystallographic Data Centre via <https://www.ccdc.cam.ac.uk/structures/>.

S<sup>i</sup> SAINT, Program for data reduction, Bruker-AXS.

S<sup>ii</sup> SADABS, Program for data correction, Bruker-AXS.

S<sup>iii</sup> SHELXT, G. M. Sheldrick, *Acta Crystallogr. Sect. A*, **2015**, 71, 3-8.

S<sup>iv</sup> SHELXL, G. M. Sheldrick, *Acta Crystallogr. Sect. C*, **2015**, 71, 3-8.



	<b>3i</b>	<b>4a</b>	<b>4b</b>	<b>5</b>
Empirical formula	C <sub>30</sub> H <sub>23</sub> FGe	C <sub>25</sub> H <sub>21</sub> FGe, CHCl <sub>3</sub>	C <sub>26</sub> H <sub>23</sub> FGe	C <sub>30</sub> H <sub>39</sub> GeLiO <sub>3</sub>
Molecular weight (g mol <sup>-1</sup> )	475.07	532.37	427.03	527.14
Temperature	193(2) K	193(2) K	193(2) K	193(2) K
Crystal system	Triclinic	Triclinic	Orthorhombic	Orthorhombic
Space group	<i>P</i> 1	<i>P</i> 1	<i>Iba</i> 2	<i>Fdd</i> 2
a (Å)	6.9795(15)	9.6434(6)	16.3617(19)	23.5400(13)
b (Å)	9.4475(18)	10.1516(7)	35.827(4)	24.7152(14)
c (Å)	18.696(4)	13.7789(10)	7.2626(7)	19.5554(9)
α (°)	98.341(6)	80.343(2)	90	90
β (°)	90.388(7)	77.542(2)	90	90
γ (°)	110.810(6)	68.819(2)	90	90
Volume (Å <sup>3</sup> )	1137.9(4)	1222.17(15)	4257.3(8)	11377.2(10)
Z	2	2	8	16
Density (g cm <sup>-3</sup> )	1.387	1.447	1.333	1.231
Crystal size (mm <sup>3</sup> )	0.25 × 0.04 × 0.02	0.30 × 0.20 × 0.15	0.40 × 0.18 × 0.10	0.40 × 0.22 × 0.15
Reflections collected	27828	37342	71154	92505
Independent reflections	3998 [R(int) = 0.1443]	6146 [R(int) = 0.0240]	4324 [R(int) = 0.0741]	6800 [R(int) = 0.0358]
Restraints / parameters	0 / 290	105 / 317	538 / 342	1 / 316
Final R indices [I > 2σ(I)]	R1 = 0.0553 wR2 = 0.1020	R1 = 0.0313 wR2 = 0.0827	R1 = 0.0515 wR2 = 0.1192	R1 = 0.0227 wR2 = 0.0565
R indices (all data)	R1 = 0.1095 wR2 = 0.1255	R1 = 0.0359 wR2 = 0.0866	R1 = 0.0868 wR2 = 0.1412	R1 = 0.0260 wR2 = 0.0581
Goodness-of-fit on F <sup>2</sup>	1.024	1.025	1.041	1.042
Largest diff. peak and hole (e.Å <sup>-3</sup> )	0.438 and -0.693	0.923 and -0.797	0.695 and -0.918	0.310 and -0.284
CCDC number	2152443	2152444	2239126	2152441

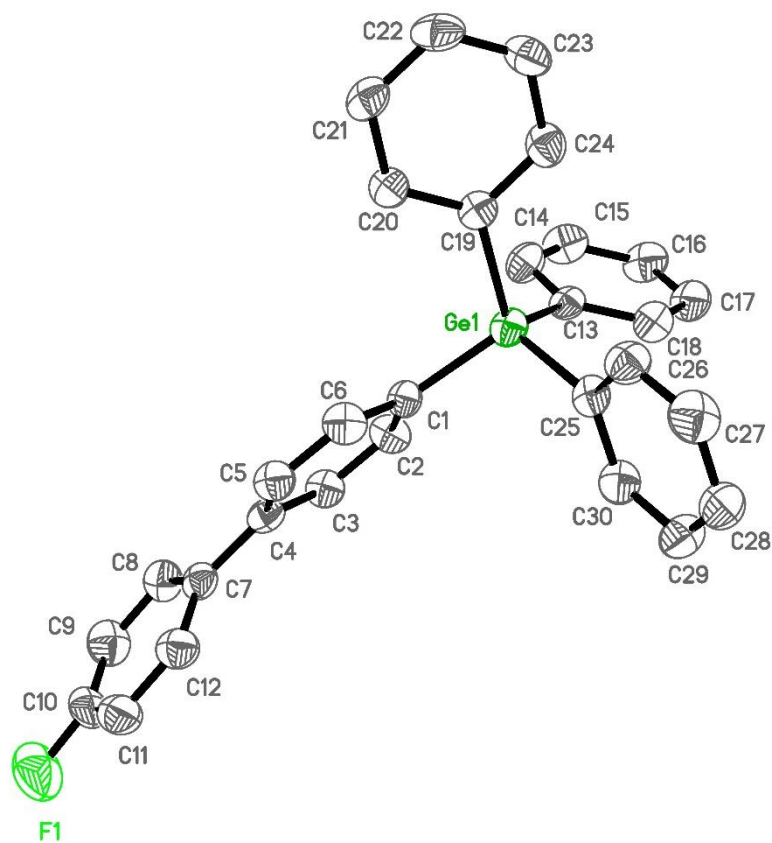


Figure IV-24: Molecular structure of **3i**. Thermal ellipsoids represent 50 % probability. H atoms are omitted for clarity.

Selected bond lengths [ $\text{\AA}$ ] and angles [ $^\circ$ ]:

Ge1-C25 1.940(5), Ge1-C13 1.948(5), Ge1-C1 1.948(5), Ge1-C19 1.965(5), F1-C10 1.357(6),  
C25-Ge1-C13 108.9(2), C25-Ge1-C1 107.9(2), C13-Ge1-C1 110.9(2), C25-Ge1-C19  
109.9(2), C13-Ge1-C19 107.8(2), C1-Ge1-C19 111.5(2).

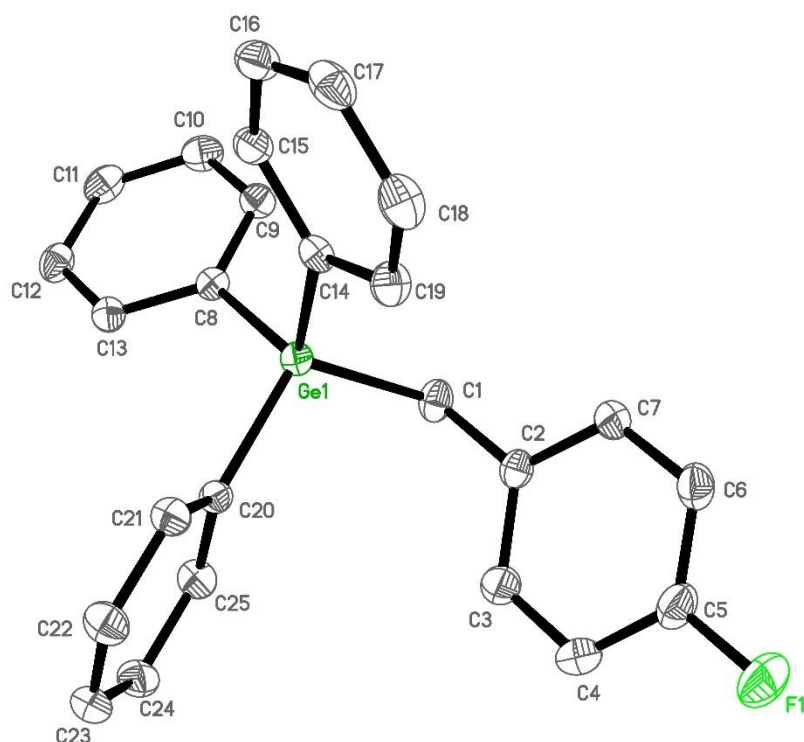


Figure IV-25: Molecular structure of **4a**. Thermal ellipsoids represent 30 % probability. H and solvent molecule are omitted for clarity.

Selected bond lengths [Å] and angles [°]:

Ge1-C8 1.946(2), Ge1-C20 1.948(2), Ge1-C14 1.954(2), Ge1-C1 1.969(2), F1-C5 1.366(2), C1-C2 1.504(3), C8-Ge1-C20 109.7(1), C8-Ge1-C14 108.9(1), C20-Ge1-C14 108.7(1), C8-Ge1-C1 107.1(1), C20-Ge1-C1 109.1(1), C14-Ge1-C1 113.3(1), C2-C1-Ge1 114.2(1).

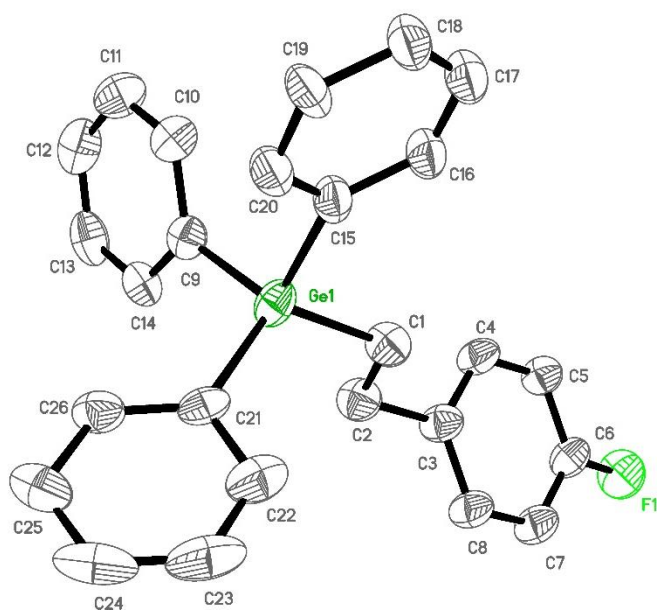


Figure IV-26: Molecular structure of **4b**. Thermal ellipsoids represent 50 % probability. H atoms are omitted for clarity.

Selected bond lengths [Å] and angles [°]:

Ge(1)-C(9) 1.945(8), Ge(1)-C(15) 1.944(9), Ge(1)-C(21) 1.947(9), Ge(1)-C(1) 1.980(13),  
 C(6)-F(1) 1.327(12), C(1)-C(2) 1.478(17), C(2)-C(3) 1.544(13), C(9)-Ge(1)-C(21)  
 110.1(3), C(15)-Ge(1)-C(9) 105.9(8), C(15)-Ge(1)-C(21) 110.4(7), C(9)-Ge(1)-C(1)  
 111.1(5), C(21)-Ge(1)-C(1) 117.2(5), C(15)-Ge(1)-C(1) 101.3(8), C(2)-C(1)-Ge(1)  
 111.6(10), C(1)-C(2)-C(3) 109.5(10).

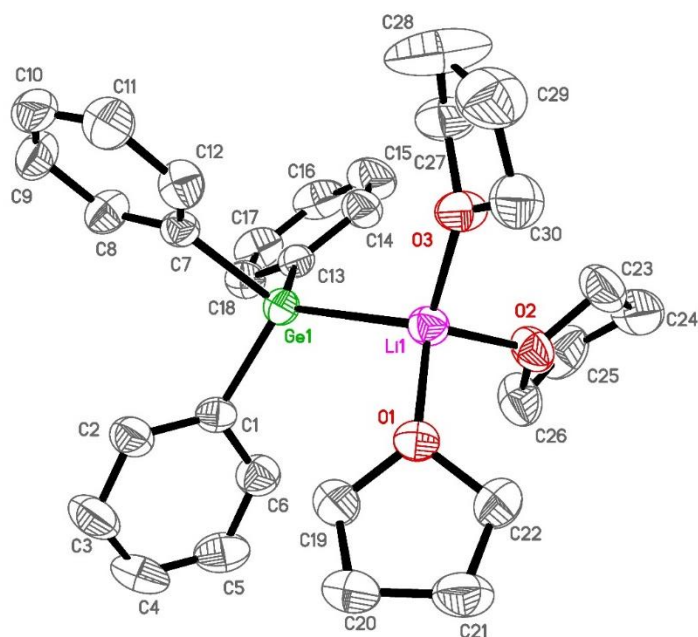


Figure IV-27: Molecular structure of **5**. Thermal ellipsoids represent 50 % probability. H atoms are omitted for clarity.

Selected bond lengths [Å] and angles [°]:

Ge1-Li1 2.667(5), Ge1-C1 2.008(2), Ge1-C7 2.005(2), Ge1-C13 2.014(2), Li1-O1 1.978(4),  
 Li1-O2 1.969(4), Li1-O3 1.965(4), Ge1-Li1-O1 108.9(2), Ge1-Li1-O2 111.9(2), Ge1-Li1-  
 O1 108.9(2), C7-Ge1-C1 100.2(1), C7-Ge1-C13 99.4(1), C1-Ge1-C13 98.8(1), C7-Ge1-  
 Li1 118.8(1),  
 C1-Ge1-Li1 116.7(1), C13-Ge1-Li1 119.2(1), O3-Li1-O2 105.4(2), O3-Li1-O1 113.0(2), O2-  
 Li1-O1 105.0(2).

## 5. References

- (1) Fricke, C.; Schoenebeck, F. Organogermanes as Orthogonal Coupling Partners in Synthesis and Catalysis. *Acc. Chem. Res.* **2020**, *53* (11), 2715–2725. <https://doi.org/10.1021/acs.accounts.0c00527>.
- (2) Langle, S.; David-Quillot, F.; Balland, A.; Abarbri, M.; Duchêne, A. General Access to Para-Substituted Styrenes. *J. Organomet. Chem.* **2003**, *671* (1–2), 113–119. [https://doi.org/10.1016/S0022-328X\(03\)00053-6](https://doi.org/10.1016/S0022-328X(03)00053-6).
- (3) Azarian, D.; Dua, S. S.; Eaborn, C.; Walton, D. R. M. Reactions of Organic Halides with R<sub>3</sub>MMR<sub>3</sub> Compounds (M = Si, Ge, Sn) in the Presence of Tetrakis(Triarylphosphine)Palladium. *J. Organomet. Chem.* **1976**, *117* (3), 55–57. [https://doi.org/10.1016/S0022-328X\(00\)91902-8](https://doi.org/10.1016/S0022-328X(00)91902-8).
- (4) Nakamura, T.; Kinoshita, H.; Shinokubo, H.; Oshima, K. Biaryl Synthesis from Two Different Aryl Halides with Tri(2-Furyl)Germane. *Org. Lett.* **2002**, *4* (18), 3165–3167. <https://doi.org/10.1021/ol026613t>.
- (5) Kanyiva, K. S.; Kuninobu, Y.; Kanai, M. Palladium-Catalyzed Direct C-H Silylation and Germanylation of Benzamides and Carboxamides. *Org. Lett.* **2014**, *16* (7), 1968–1971. <https://doi.org/10.1021/ol500519y>.
- (6) Chen, C.; Guan, M.; Zhang, J.; Wen, Z.; Zhao, Y. Palladium-Catalyzed Oxalyl Amide Directed Silylation and Germanylation of Amine Derivatives. *Org. Lett.* **2015**, *17* (15), 3646–3649. <https://doi.org/10.1021/acs.orglett.5b01393>.
- (7) Modak, A.; Patra, T.; Chowdhury, R.; Raul, S.; Maiti, D. Palladium-Catalyzed Remote Meta-Selective C-H Bond Silylation and Germanylation. *Organometallics* **2017**, *36* (13), 2418–2423. <https://doi.org/10.1021/acs.organomet.7b00309>.
- (8) Elsby, M. R.; Liu, J.; Zhu, S.; Hu, L.; Huang, G.; Johnson, S. A. Influence of N-Heterocyclic Carbene Steric Bulk on Selectivity in Nickel Catalyzed C-H Bond Silylation, Germylation, and Stannylation. *Organometallics* **2019**, *38* (2), 436–450. <https://doi.org/10.1021/acs.organomet.8b00786>.
- (9) Selmani, A.; Gevondian, A. G.; Schoenebeck, F. Germylation of Arenes via Pd(I) Dimer Enabled Sulfonium Salt Functionalization. *Org. Lett.* **2020**, *22* (12), 4802–4805. <https://doi.org/10.1021/acs.orglett.0c01609>.
- (10) Selmani, A.; Schoenebeck, F. Transition-Metal-Free, Formal C-H Germylation of

- Arenes and Styrenes via Dibenzothiophenium Salts. *Org. Lett.* **2021**, 23 (12), 4779–4784. <https://doi.org/10.1021/acs.orglett.1c01505>.
- (11) Mochida, K.; Matsushige, N. Reactions of Aryl Halides with Triethylgermyl Anions. *J. Organomet. Chem.* **1982**, 229 (1), 11–20. [https://doi.org/10.1016/S0022-328X\(00\)89112-3](https://doi.org/10.1016/S0022-328X(00)89112-3).
- (12) Fricke, C.; Sherborne, G. J.; Funes-Ardoiz, I.; Senol, E.; Guven, S.; Schoenebeck, F. Orthogonal Nanoparticle Catalysis with Organogermanes. *Angew. Chemie - Int. Ed.* **2019**, 58 (49), 17788–17795. <https://doi.org/10.1002/anie.201910060>.
- (13) Fricke, C.; Dahiya, A.; Reid, W. B.; Schoenebeck, F. Gold-Catalyzed C-H Functionalization with Aryl Germanes. *ACS Catal.* **2019**, 9 (10), 9231–9236. <https://doi.org/10.1021/acscatal.9b02841>.
- (14) Sherborne, G. J.; Gevondian, A. G.; Funes-Ardoiz, I.; Dahiya, A.; Fricke, C.; Schoenebeck, F. Modular and Selective Arylation of Aryl Germanes (C–GeEt<sub>3</sub>) over C–Bpin, C–SiR<sub>3</sub> and Halogens Enabled by Light-Activated Gold Catalysis. *Angew. Chemie - Int. Ed.* **2020**, 59 (36), 15543–15548. <https://doi.org/10.1002/anie.202005066>.
- (15) Sakamoto, K.; Nagashima, Y.; Wang, C.; Miyamoto, K.; Tanaka, K.; Uchiyama, M. Illuminating Stannylation. *J. Am. Chem. Soc.* **2021**, 143 (15), 5629–5635. <https://doi.org/10.1021/jacs.1c00887>.
- (16) Bunnett, J. F. Aromatic Substitution by the SRN1 Mechanism. *Acc. Chem. Res.* **1978**, 11 (11), 413–420. <https://doi.org/10.1021/ar50131a003>.
- (17) Saveant, J. M. Catalysis of Chemical Reactions by Electrodes. *Acc. Chem. Res.* **1980**, 13 (9), 323–329. <https://doi.org/10.1021/ar50153a005>.
- (18) Savéant, J. M. Mechanisms and Reactivity in Electron Transfer Induced Aromatic Nucleophilic Substitution. Recent Advances. *Tetrahedron* **1994**, 50 (34), 10117–10165. [https://doi.org/10.1016/S0040-4020\(01\)81748-8](https://doi.org/10.1016/S0040-4020(01)81748-8).
- (19) Shilov, A. E.; Shul'pin, G. B. Activation of Carbon-Fluorine Bonds by Metal Complexes. *Chem. Rev.* **1994**, 94, 373–431. <https://doi.org/10.1021/cr9411886>.
- (20) Glaser, F.; Kerzig, C.; Wenger, O. S. Multi-Photon Excitation in Photoredox Catalysis: Concepts, Applications, Methods. *Angew. Chemie - Int. Ed.* **2020**, 59 (26), 10266–10284. <https://doi.org/10.1002/anie.201915762>.
- (21) Wu, S.; Kaur, J.; Karl, T. A.; Tian, X.; Barham, J. P. Synthetic Molecular

- Photoelectrochemistry: New Frontiers in Synthetic Applications, Mechanistic Insights and Scalability. *Angew. Chemie - Int. Ed.* **2022**, *61* (12). <https://doi.org/10.1002/anie.202107811>.
- (22) Glaser, F.; Larsen, C. B.; Kerzig, C.; Wenger, O. S. Aryl Dechlorination and Defluorination with an Organic Super-Photoreductant. *Photochem. Photobiol. Sci.* **2020**, *19* (8), 1035–1041. <https://doi.org/10.1039/d0pp00127a>.





# ***Chapter V:***

## ***GENERAL CONCLUSION***

The development of photochemical reactions has received significant attention over the past century. This interest is attributable to the capacity of excited state molecules and radical species to react in a completely different fashion than intermediates of polar chemistry. However, because high energy UV-irradiation was typically employed in photochemical reactions, photodecomposition is usually observed when complex structures are employed along with byproducts formation due to the ability of short wavelength ultraviolet light to interact with most organic molecules.

More recently, there has been a renaissance in the field of organic photochemistry enabled by the use of readily available organometallic and organic dyes that absorb low-energy visible light. By employing this practically simple technology, the synthesis of a large variety of molecules, including complex ones, is now possible under mild conditions. The concept of photoredox catalysis becomes also popular in industry and many companies employ now photocatalytic transformations for the synthesis of drugs or medicines.

Despite the remarkable development of visible-light mediated organic transformations, there are still many challenges to be addressed, among them are: *i*) the activation of strong chemical bonds (C–X) where the energy of blue photon is not enough to homolyze (C–X), and *ii*) the compatibility of photochemical reactions with highly sensitive molecules. In this work, we employed experimental and theoretical physical organic tools to gain insights into these two synthetic challenges.

After a general introduction about visible light, we have presented the unprecedented synthesis of phosphiranium ylides by the reaction of 1-mesitylphosphirane with blue-light generated electrophilic carbenes. This ylide was indirectly confirmed by its protonation towards the phosphiranium salt and obtention of XRD suitable crystals. Subjecting phosphiranium ylide to carboxylic acids allowed for the regioselective C-centered ring opening in high yields. We could benefit from the Brønsted basic character of the ylide to generate nucleophilic anions after deprotonation that could not attack on the phosphorus atom because of the steric hindrance previously incorporated around it. These results were supported by DFT calculations that supported the plausible mechanism proposed. This new strategy opens new avenues in the activation of phosphiranes and related structures, where photochemically generated carbenes could be used to form highly reactive phosphiraniums that can react regioselectively with a large panel of nucleophiles.

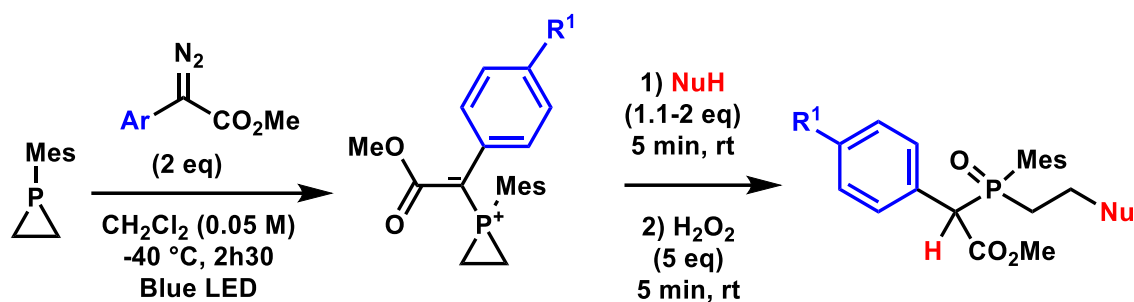


Figure V-1 : Methodology developed in chapter III

In chapter III, we have discussed two methodologies to unlock access to the difficult aryl chloride reduction: ConPET and e-PC. We have electrochemically generated the radical anion of several D-A cyanoarenes in a clean fashion and studied their photophysical properties. The excited state of these radical anions was showed to be non-trivial with the presence of several species in solution. The irradiated solution of radical anions was quenched by chlorobenzene.

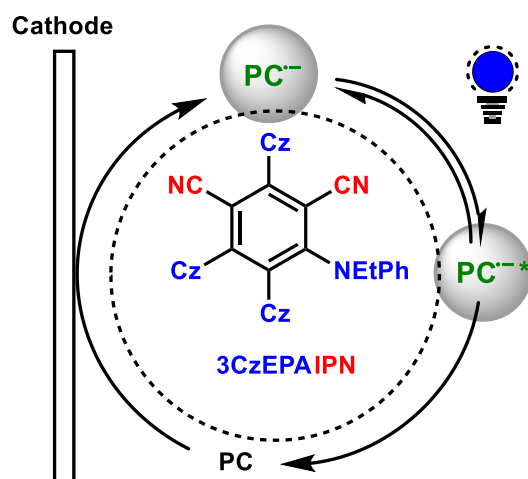
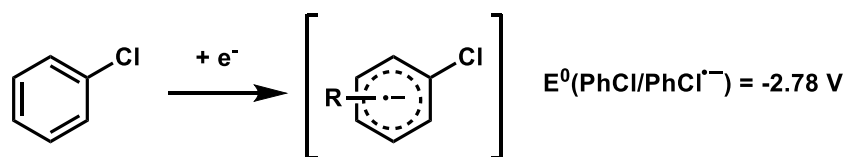


Figure V-2 : Study of the radical anions of donor-acceptor cyanoarenes both in ground and excited states in chapter III

We have furthermore investigated the effect of a strong Lewis acid on the electrochemical and photophysical properties of cyanoarenes. In this context different cyanoarenes/BCF complexes were synthesized and characterized and their behavior compared to the parent molecules was discussed.

A similar challenge lies in the reduction of aryl fluorides which are more difficult to reduce than their chloride equivalents.



$$E^0(\text{PhF}/\text{PhF}^{\bullet-}) = -2.97 \text{ V vs SCE} > E^0(\text{PhCl}/\text{PhCl}^{\bullet-}) = -2.78 \text{ V vs SCE}$$

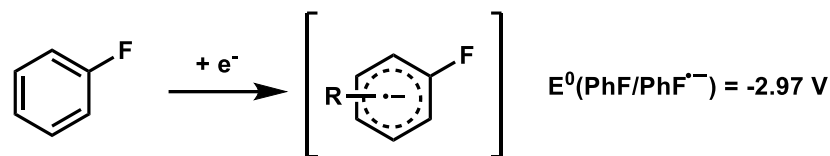


Figure V-3 : Reduction potentials of both chloro and fluorobenzene. Potentials given vs SCE in DMF.

In chapter IV, we have discussed the discovery of the triphenylgermanyl anion's excited state super-reducing properties applied in the reduction of aryl fluorides to provide a new synthetic route to arylgermanes.

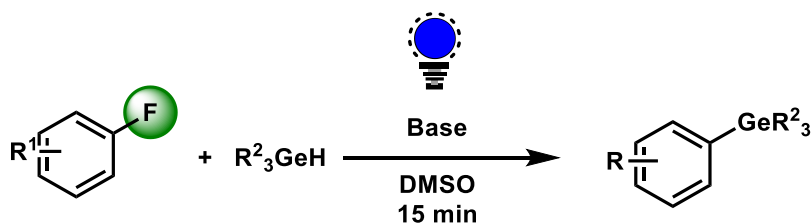


Figure V-4 : Work described in chapter IV, reduction of aryl fluorides with the triphenylgermanyl anion under blue light irradiation.

By simply combining readily available fluoro-arenes with germanes in the presence of a base and under blue irradiation, tetraarylgermanes can be synthesized in reasonable to good yield. Here again, experimental and theoretical investigations have been undertaken and a reasonable reaction mechanism is discussed. The ability of light to interact with anion forming highly reducing excited states is undoubtedly a very attractive approach to activate strong chemical bonds. However, the reaction of these highly nucleophilic and Lewis basic nucleophiles with aryl halides in the ground state might be considered to avoid background reactions.

*In fine*, we showed throughout this manuscript the potential of combining physical organic chemistry with organic synthesis to understand, but also to design new visible-light-mediated reactions. We are well aware that some of the results presented herein, in particular in Chapter III, raise more questions than answers about the reactivity of the cyanoarenes derived radical anions with arene halides, and the reactive species involved in that mechanism. We believe, however, that the insights presented and discussed in the chapter will be highly useful for researchers active in the field of physical organic photochemistry and beyond.

### Résumé détaillé en Français

Ce manuscrit est intitulé « Formation et rupture de liaisons chimiques par action de la lumière visible : Synthèse et études mécanistiques ». Il est divisé en cinq chapitres. Le premier est une introduction générale portant sur la définition de la lumière visible, dont l'usage lie les divers chapitres de cette thèse. Il y est rappelé l'importance fondamentale de la lumière visible pour le maintien de la vie sur Terre au travers notamment de la photosynthèse et du mécanisme de la vision. Une brève histoire de l'utilisation de la lumière visible en chimie est ensuite fournie. Elle est suivie d'une description générale des mécanismes photophysiques liés à l'absorption d'un photon par une molécule (par exemple : diagramme de Jablonski) et des mécanismes photochimiques portant sur l'étude des réactions chimiques ayant lieu après cette absorption (par exemple : transfert d'électron).

Le chapitre II présente les progrès effectués dans la quaternarisation des phosphiranes et de l'ouverture de cycle C-centrée des sels de phosphiranium.

L'introduction de ce chapitre fait un état de l'art sur les phosphiranes, cycles à trois chaînons contenant deux atomes de carbone et un atome de phosphore. Leurs équivalents oxygénés sont les oxiranes (ou époxydes) et leurs équivalents azotés sont les aziridines.



*Figure 1 : Cycles à chaînons oxygéné, azoté et phosphoré*

Ces derniers sont notamment largement utilisés grâce à leur capacité à subir une ouverture de cycle sélective centrée sur l'atome de carbone. Cependant, en comparaison, les phosphiranes n'ont été que très peu étudiés jusqu'à aujourd'hui. Leur faible stabilité a participé à retenir la communauté scientifique d'effectuer des progrès significatifs dans leur compréhension et leur usage en synthèse. Les travaux de Mathey et Marinetti, pionniers en la matière, ont consisté en la stabilisation des phosphiranes dans la sphère de coordination d'un complexe de tungstène pentacoordiné par du monoxyde de carbone. L'étude et la réactivité des phosphiranes dits « libres », ne couvre pas ces développements et est le point d'intérêt particulier de ce chapitre, notamment au travers de l'exemple du 1-mésitylphosphirane.

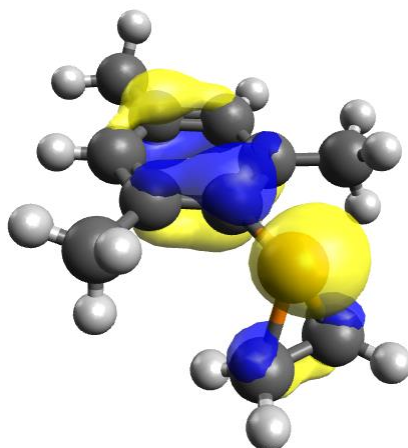


Figure 2 : Orbitale moléculaire la plus haute occupée (HO) du 1-mésitylphosphirane. La distribution électronique est majoritaire au niveau de l'atome de phosphore mais aussi diffuse sur le cycle à trois chaînons ainsi que le cycle aromatique.

Après avoir présenté plusieurs voies de synthèse des phosphiranes « libres », le bilan des connaissances de leur réactivité est effectué sous quatre angles différents : leur coordination à un centre métallique, leur quaternarisation en sels de phosphiranium, la formation de phosphinidènes par irradiation avec des rayonnements ultra-violet, et leur ouverture de cycle par attaque d'un nucléophile.

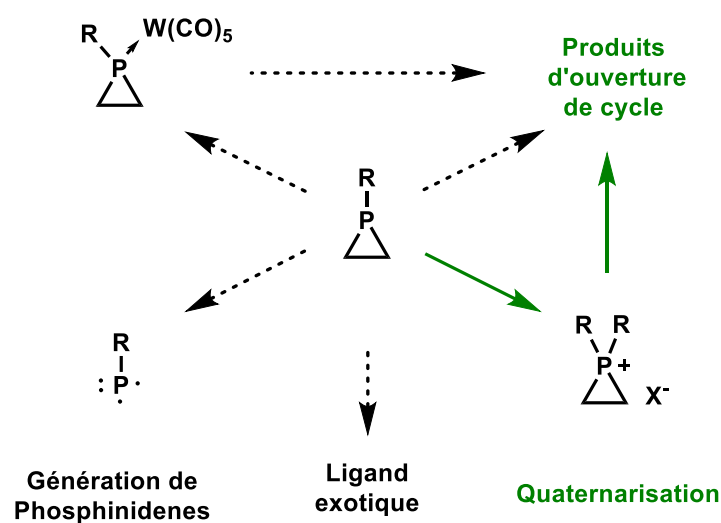
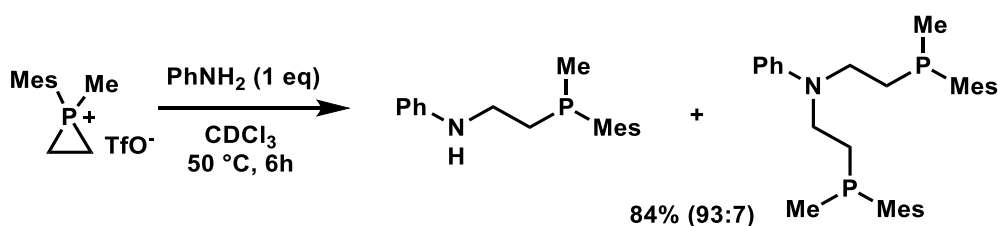


Figure 3 : Applications liées aux phosphiranes. En vert : les voies explorées dans ce chapitre de thèse.

Les travaux de ce chapitre adressent deux de ces quatre points : la quaternarisation en sels de phosphiranium et l'ouverture de cycle sélective centrée sur l'atome de carbone. Ces deux étapes sont difficiles à réaliser, et la connaissance de la réactivité du cycle phosphoré à trois chaînons, à savoir les phosphiranes et les sels de phosphiranium, est actuellement limitée. Pour les difficultés liées à la quaternarisation (majoritairement effectuée en présence de dérivés de triflates), la faible nucléophilie et la faible basicité de Lewis du phosphirane sont utilisées

comme justification dans la littérature. Concernant l'ouverture de cycle des phosphirane, celle-ci est facilitée lorsqu'ils sont quaternarisés en sels de phosphiranium. Cependant, même ainsi, la sélectivité est majoritairement centrée sur l'atome de phosphore. Un exemple récent de la littérature a montré qu'en jouant sur une combinaison d'effets stériques et électroniques il était possible d'orienter favorablement l'ouverture sur l'atome de carbone en sélectionnant aussi un partenaire nucléophile approprié, des dérivés d'aniline, dont quelques exemples sont présentés ci-dessous. Il est remarqué que la présence d'un groupe électroattracteur proche de l'atome de phosphore permet la diminution de la température de réaction de 50 °C à température ambiante (T.A.), accompagné d'une baisse de rendement à 27% attribuée à une moins bonne sélectivité. L'accroissement de l'encombrement stérique du nucléophile permet une meilleure sélectivité au coût d'une baisse de réactivité.

#### Exemple récent d'ouverture de cycle de phosphiranium C-centrée



#### Exemples sélectionnés

(Durée, Température, Rendement, Ratio des produits mono et di-substitués)

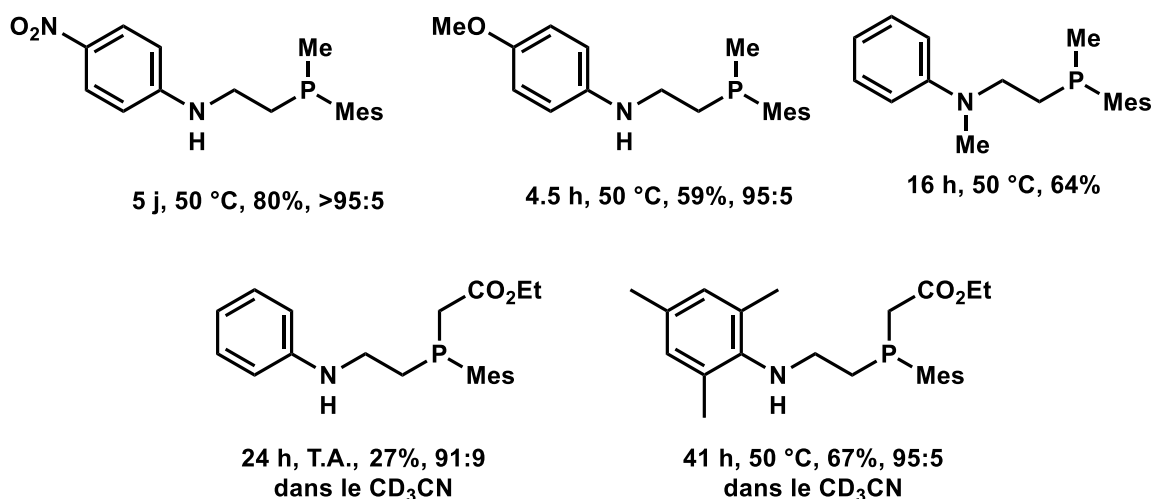


Figure 4 : Seule réaction connue d'ouverture C-centrée spécifique de sels de phosphiranium. Une partie des partenaires réactionnels et les conditions de réaction sont présentés ici.



Afin de surmonter ces deux difficultés et d'étendre les possibilités d'ouverture sélective C-centrée du cycle phosphoré à trois chaînons, la nucléophilie et la basicité de Lewis du 1-mésitylphosphirane ont d'abord été estimées sur l'échelle de Mayr. Cette estimation a permis de situer le 1-mésitylphosphirane parmi les phosphines les moins nucléophiles et les moins basiques selon Lewis. Confortés par ces résultats, en accord avec les observations précédentes, nous avons rationnellement décidé d'explorer la réactivité du 1-mésitylphosphirane en présence d'acides de Lewis forts, les carbènes électrophiles libres, afin de rendre la réaction de quaternarisation du phosphirane irréversible. De plus, la présence d'un groupe ester devrait rationnellement faciliter l'ouverture de cycle, et la présence du groupement phényle devrait quant à elle accroître l'encombrement stérique autour de l'atome de phosphore afin de diminuer les attaques P-centrées.

Dans ce chapitre, nous présentons que la réaction entre des carbènes électrophiles libres (générés par irradiation de leurs équivalents « diazo » par la lumière visible) avec le 1-mésitylphosphirane produit des ylures de phosphiranium.

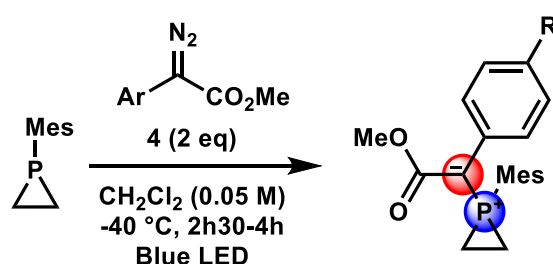


Figure 5 : Travaux de ce chapitre de thèse : Formation d'ylures de phosphiranium à partir de phosphirane et d'aryle diazoacétate sous irradiation par la lumière visible.

L'ylure de phosphiranium a été protoné avec succès par l'acide tétrafluoroborique afin de fournir le sel de phosphiranium correspondant dont la structure par diffraction des rayons X sur monocristaux a été obtenue.

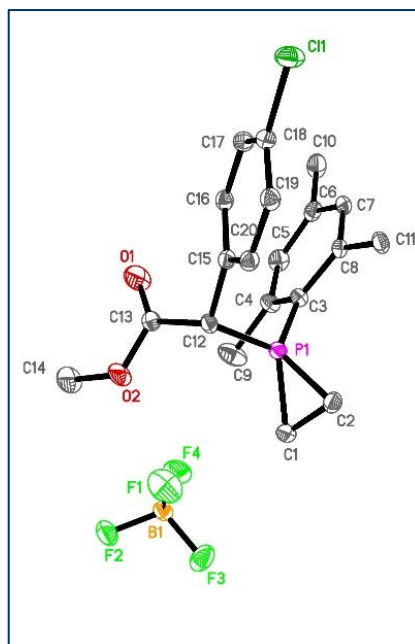


Figure : Conditions : 1-mesitylphosphirane (1 eq, 0.05 mmol), aryldiazoacetate (2 eq, 0.1 mmol) at - 40 °C for 2h30 to 4h00 in  $\text{CH}_2\text{Cl}_2$

La réactivité des ylures de phosphiranium, jusqu'ici inconnus, est ensuite explorée en présence de nucléophiles protiques qui, après déprotonation par le carbone de l'ylure, s'engagent dans une ouverture C-centrée du sel de phosphiranium généré.

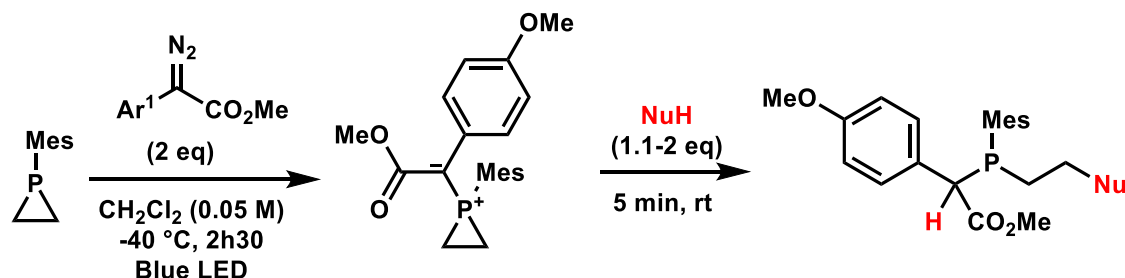


Figure 7 : Formation d'un ylure de phosphiranium et réaction d'ouverture de cycle en présence d'un nucléophile protique.

Les thiophénols ont d'abord été utilisés avec succès afin de fournir les phosphines issues de l'ouverture de cycle dont l'étendue des partenaires réactionnels compatibles testés est présentée dans la Figure 8. Les résultats sont homogènes et relativement peu sensibles aux modifications stériques ou électroniques du nucléophile.

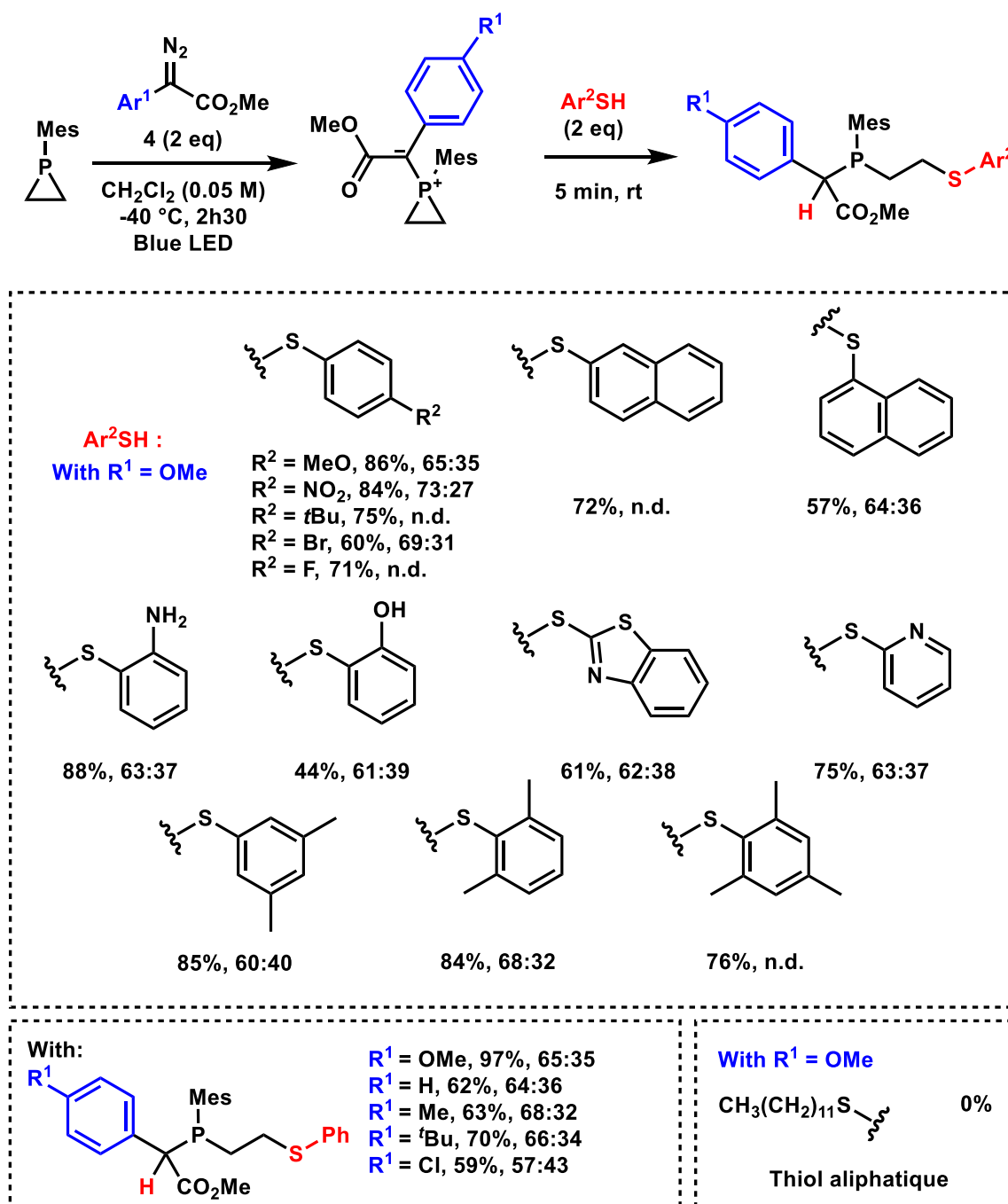


Figure 8 : Conditions : 1-mésitylphosphirane (1 eq, 0.05 mmol), aryle diazoacetate (2 eq, 0.1 mmol) à  $-40^\circ\text{C}$  pendant 2h30 à 4h00 dans le  $\text{CH}_2\text{Cl}_2$  (0.05 M, 1 mL) puis addition de thiophénole (2 eq, 0.1 mmol) à température ambiante, 5 min. Les rendements donnés sont des rendements RMN obtenus avec une référence interne, le 1,3,5-trimethoxybenzene. Les rapports diastéréomériques sont donnés après le rendement. n.d. : non déterminé.

Les acides carboxyliques ont ensuite été utilisés avec succès en tant que partenaires réactionnels et ont démontré l'applicabilité de la méthode par un scope important, de bons rendements, et des diastéréosélectivités modérées.

La méthodologie expérimentale a été optimisée pour permettre l'isolement et la caractérisation des produits par oxydation des phosphines résultant de l'ouverture de cycle en oxydes de

phosphine. Cette méthodologie a été appliquée à une grande variété de substrats dans un travail collaboratif avec Avisek Ghosh, doctorant au sein de la même équipe. Cette réaction est une première dans ce domaine d'étude pour plusieurs raisons : Les réactifs oxygénés avaient jusqu'à aujourd'hui réagit uniquement sur l'atome de phosphore (connu pour être oxophile) de substrats similaires. De plus, la réaction est très rapide à température ambiante (moins de cinq minutes) alors que les exemples précédents nécessitaient un chauffage et des temps de réaction prolongés allant jusqu'à plusieurs jours. Enfin, cette réaction, impliquant un réactif relativement instable aux multiples voies de décomposition, fournit des rendements isolés stables aux environs de 70-80% de manière quasi-indépendante de la nature des substituants du réactif nucléophile (aliphatiques, aromatiques, riches ou pauvres en électrons...).

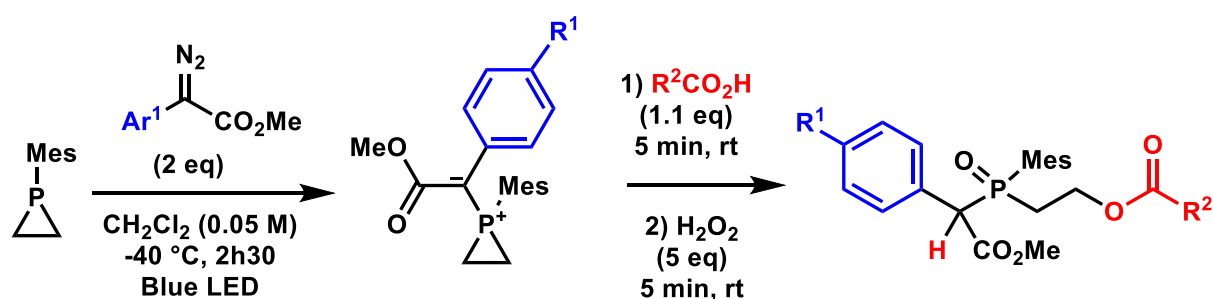


Figure 9 : Formation d'un ylure de phosphiranium et réaction d'ouverture de cycle en présence d'acide carboxylique (suite page suivante)

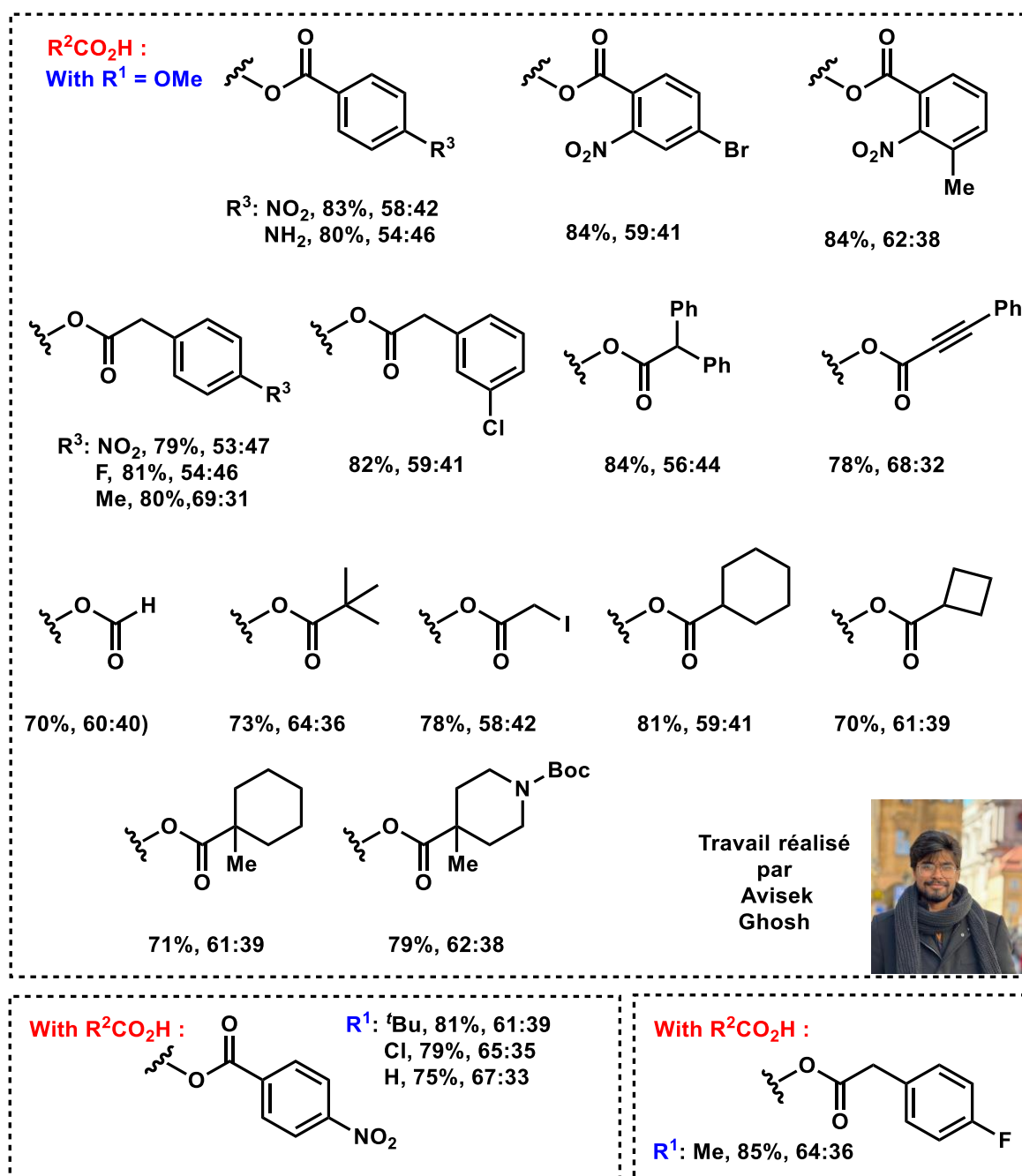


Figure 9 suite : Conditions : 1-mésitylphosphirane (1 eq, 0.1 mmol), aryle diazoacetate (2 eq, 0.2 mmol) à - 40 °C pendant 2h30 à 4h00 dans le CH<sub>2</sub>Cl<sub>2</sub> (0.05 M, 2 mL) puis addition de l'acide carboxylique (1.1 eq, 0.11 mmol) à température ambiante, 5 min, suivi de l'addition d'H<sub>2</sub>O<sub>2</sub> à température ambiante et agitation pendant au moins 5 minutes. Rendements isolés donnés suivi du rapport diastéréomérique. Boc : tert-butyloxycarbonyl

Cette étude est finalement complétée par des calculs DFT afin de soutenir un mécanisme raisonnable. Ces calculs ont été effectués sous la direction d'Isabelle Dixon au Laboratoire de Chimie Physique Quantiques à Toulouse. Un chemin réactionnel en bonne adéquation avec les observations expérimentales a été calculé et a montré l'importance déterminante du relâchement de la tension de cycle.

Le raisonnement menant au choix et à l'optimisation d'une méthodologie robuste est détaillé. Un point crucial est l'utilisation du programme CREST développé par Grimme et ses collaborateurs, afin d'étudier les myriades de conformères accessibles aux molécules étudiées, ce qui s'est montré indispensable dans notre cas pour éviter une vision trop statique de ces systèmes en réalité très flexibles.

La formation de l'ylure de phosphiranium à partir de l'irradiation de l'aryle diazoacétate de méthyle correspondant en présence de 1-mésitylphosphirane a été étudiée dans un premier temps. L'addition du 1-mésitylphosphirane sur le carbène électrophile libre formé *in-situ* a été calculée sans barrière d'activation, montrant ainsi son caractère favorable. L'ylure de phosphiranium résultant se trouve 37.4 kcal/mol plus bas en énergie libre de Gibbs que les réactifs au départ de la réaction, ce qui est cohérent avec les observations expérimentales. Cette partie détaille aussi une étude des carbènes dans leur état singulet et triplet afin de compléter une étude précédente de la littérature, ainsi que l'étude des conformères de l'ylure de phosphiranium afin de proposer une explication aux deux signaux observés en résonance magnétique nucléaire du phosphore dans un rapport d'environ deux pour un.

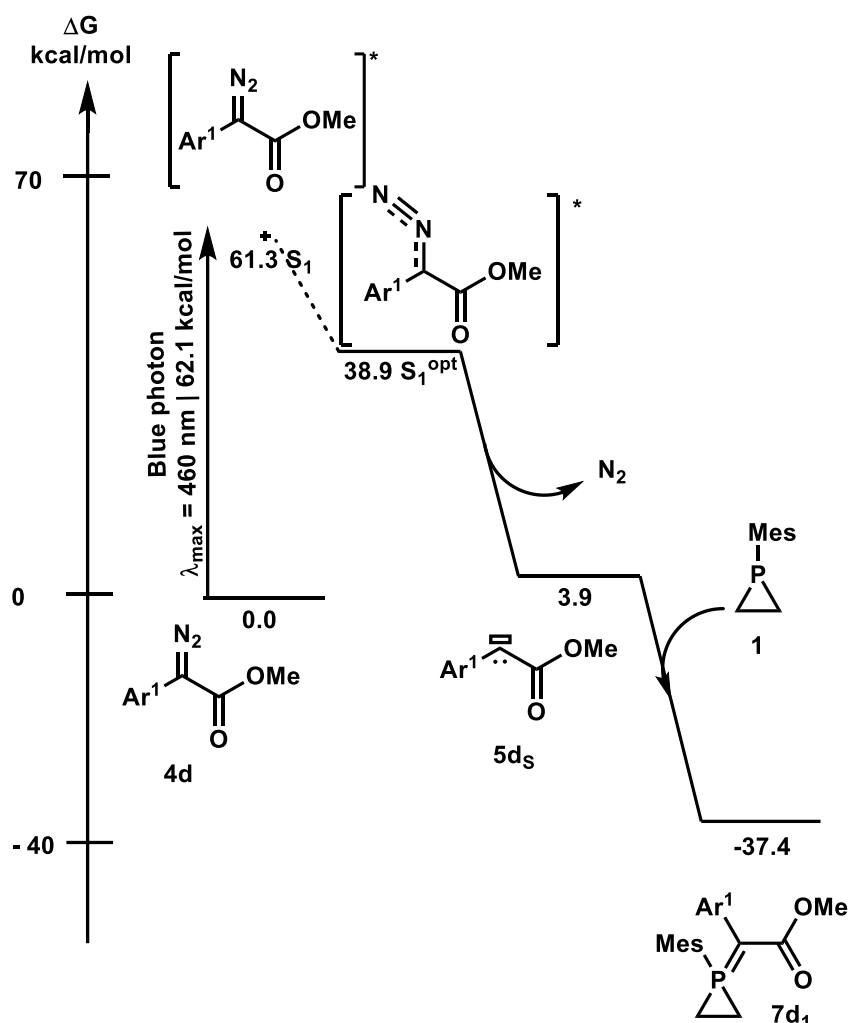


Figure 10 : profil d'énergie libre de Gibbs pour la formation d'un ylure de phosphiranium calculé par DFT.

Ensuite, le profil énergétique menant de l'ylure de phosphiranium au produit d'ouverture oxydé en présence de l'acide 4-nitrobenzoïque a été calculé. Une comparaison systématique avec les observations expérimentales est effectuée au fil de la discussion, et le passage par un sel de phosphiranium intermédiaire après déprotonation de l'acide carboxylique par l'ylure de phosphiranium est proposé. La paire d'ions sel de phosphiranium – carboxylate résultante interagit ensuite par une ouverture du cycle C-centrée du sel de phosphiranium par l'oxygène du carboxylate pour fournir une phosphine, reposant 17.2 kcal/mol plus bas que les réactifs initiaux, présente dans le milieu sous la forme de deux diastéréoisomères. Enfin l'oxydation par l'eau oxygénée permet d'oxyder la phosphine en oxyde de phosphine, produit beaucoup plus bas en énergie que la phosphine (environ 100 kcal/mol) et permet ainsi son isolement expérimental après purification sur gel de silice.

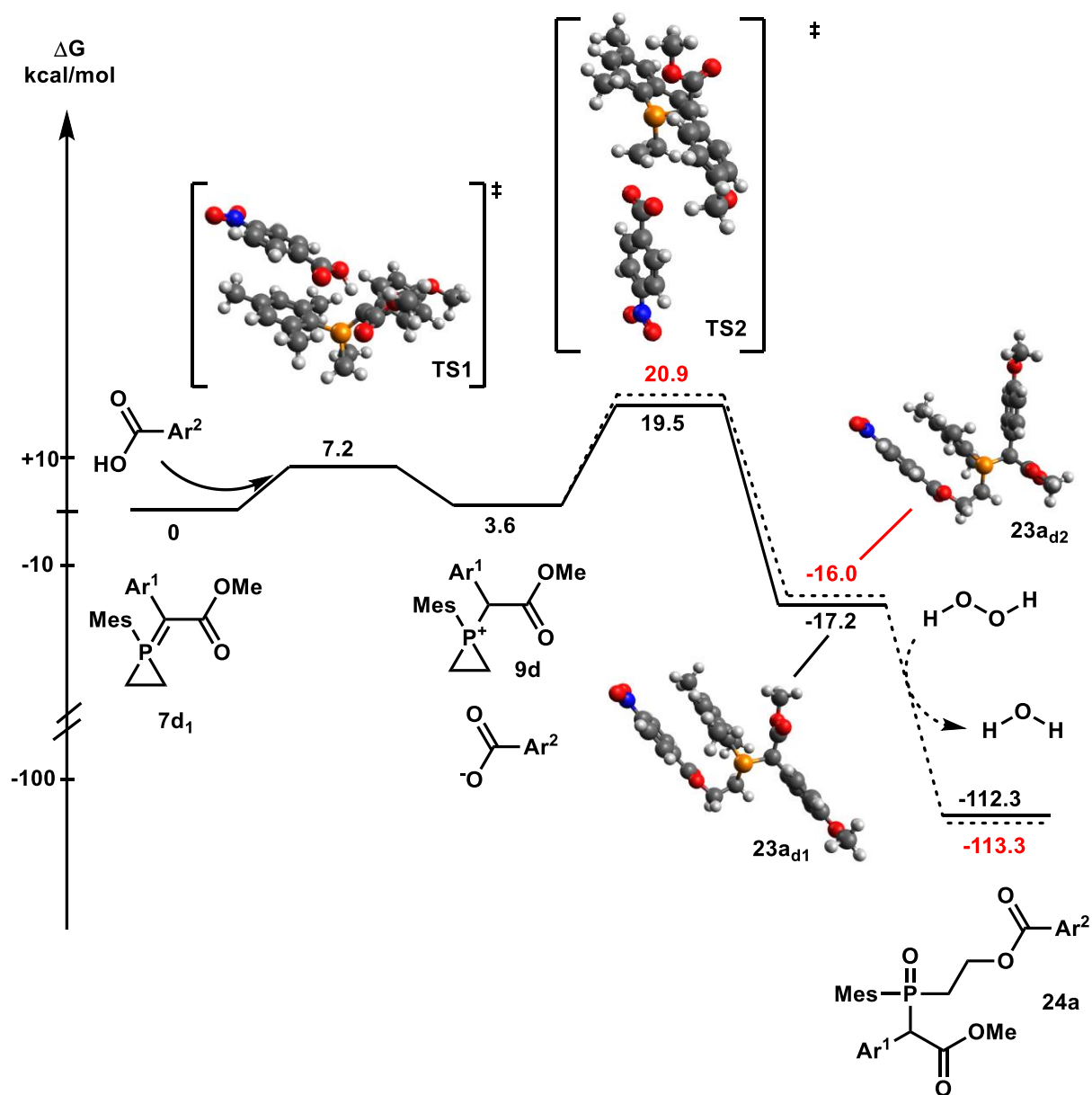


Figure 11 : profil d'énergie libre de Gibbs pour l'ouverture de cycle d'un ylure de phosphiranium par l'acide 4-nitrobenzoïque calculé par DFT.



Le chapitre III se concentre sur les cyanoarènes donneur-accepteur, largement utilisés à ce jour en tant que photocatalyseurs en catalyse photoredox. Le plus connu de cette classe de molécules est le 1,2,3,5-Tetrakis(carbazol-9-yl)-4,6-dicyanobenzène (4CzIPN) présenté dans la figure ci-dessous (Figure 12).

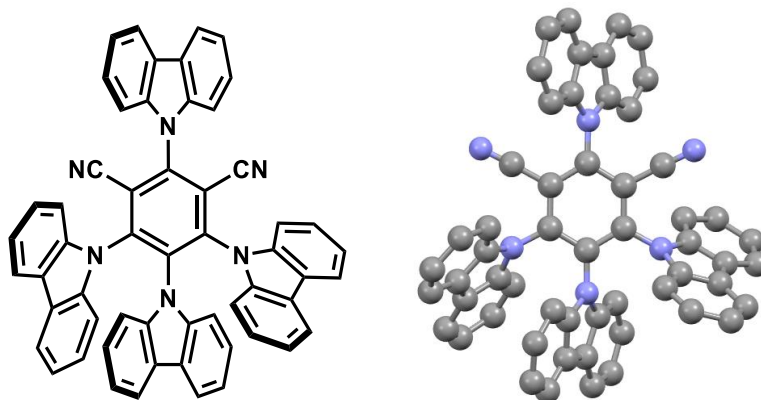


Figure 12 : Structure du 4CzIPN (chemdraw, à gauche et structure obtenue par diffraction des rayons X à droite)

L'introduction de ce chapitre remonte aux origines de telles molécules, attribuées au 4-(N,N-diméthyle)aminobenzonitrile dont la fluorescence duelle a éveillé la curiosité et maintenu l'intérêt des chercheurs depuis 1961. L'état de l'art du 4CzIPN et ses équivalents, synthétisés pour la première fois en 2012 par Adachi et ses collaborateurs, est effectué en couvrant plusieurs domaines incluant la science des matériaux avec leur utilisation dans les diodes électroluminescentes organiques (DELO ou OLED), la chimie médicinale avec les applications en thérapie photodynamique dans le traitement de cancers, et plus particulièrement la photochimie avec leur usage en tant que photocatalyseurs. Les mécanismes photophysiques et photochimiques mis en jeu sont détaillés, en particulier leur capacité à effectuer de la fluorescence retardée activée thermiquement et celle à s'engager dans des réactions de transfert d'électrons et de transferts d'énergie.

Un intérêt particulier est dédié à l'explication du lien entre leur structure et leurs propriétés, notamment la disposition spatiale des orbitales moléculaires frontières, très particulière, dont la plus basse vacante (BV) et la plus haute occupée (HO) sont clairement séparées dans l'espace respectivement sur les squelettes accepteur (cyanobenzène) et donneur (amines).

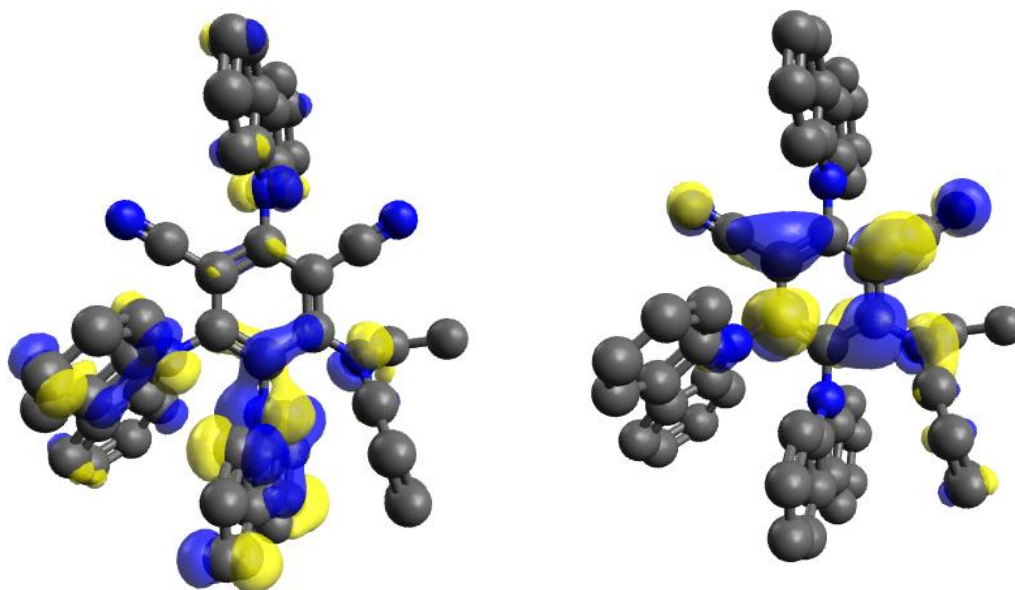


Figure 13 : Orbitales moléculaires frontières du 2,4,5-Tri(9H-carbazol-9-yl)-6-(éthyl(phényl)amino)isophthalonitrile (3CzEPAIPN), HO à gauche et BV à droite.

Leurs potentiels redox sont aussi discutés, notamment la facilité avec laquelle ils peuvent être modulés à partir d'une modification des substituants, en lien direct avec la séparation des orbitales moléculaires frontières. Une partie importante de cette introduction concerne la clarification de la nomenclature des potentiels redox utilisée couramment par la communauté scientifique. La proposition effectuée est présentée dans les cycles photocatalytiques en Figure 14, où l'espèce la plus réduite est indiquée à droite et la plus oxydée à gauche dans la parenthèse du potentiel en question, comme seul formalisme.

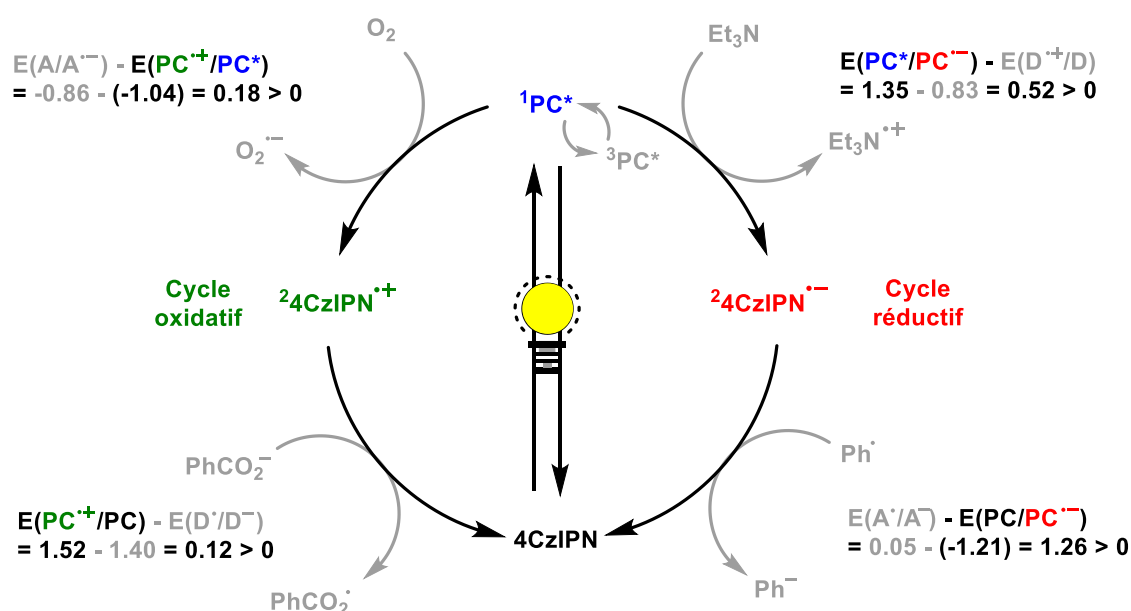


Figure 14 : Exemples de transferts d'électrons et calcul associés à partir des potentiels redox des espèces en présence dans des cycles photocatalytiques du 4CzIPN.

Leur utilisation en tant que photocatalyseurs est détaillée à partir de la famille des cyanoarènes sans substituants donneurs d'électrons afin de fournir une meilleure compréhension des avantages de leur ajout dans les cyanoarènes donneur-accepteur. Ce passage présente leur intérêt synthétique à partir d'exemples de synthèse en chimie organique dans une grande variété d'utilisations.

L'application la plus importante pour ce chapitre de thèse est leur utilisation en électrophotocatalyse, qui consiste à réduire l'état fondamental du cyanoarène donneur-accepteur par voie électrochimique en son radical anion, suivi d'une irradiation par la lumière visible avec de générer l'état excité du radical anion. Il s'agit ici d'un état excité d'état de spin doublet, dont le comportement est bien moins connu que les états de spin singulet et triplet. Des résultats récents ont montré la capacité de l'état excité de leur radicaux anions à réduire les chlorures d'aryles. Cependant, un débat anime actuellement la communauté scientifique sur cette affirmation. Des exemples utilisent une amine sacrificielle en tant que donneur d'électron, ce qui n'est pas chimiquement innocent. Les travaux présentés dans ce chapitre, effectués au Département de Chimie Moléculaire (DCM, Grenoble) sous la direction de Pr. Cyrille Costentin, cherchent à apporter une contribution à ce domaine qui nécessite de plus amples études.

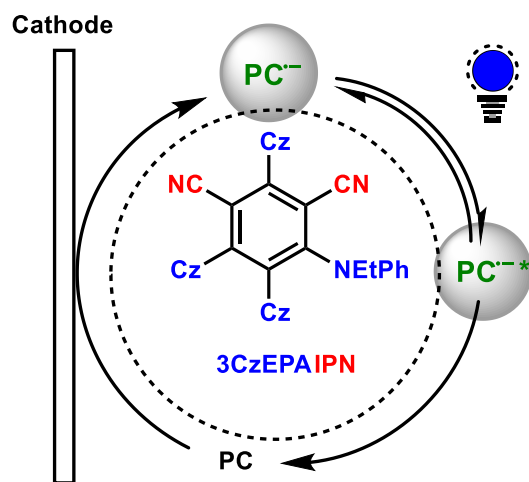


Figure 15 : Schéma présentant les étapes de l'électrophotocatalyse avec le 3CzEPAIPN.

Nous montrons que la génération électrochimique des radicaux anions des cyanoarènes donneur-accepteur est une méthode efficace. La stabilité du radical anion du 2,4,5-Tri(9H-carbazol-9-yl)-6-(éthyl(phényl)amino)isophthalonitrile (3CzEPAIPN) est remarquable, de

plusieurs heures à température ambiante sous atmosphère inerte. Sa génération dans des conditions électrochimiques a permis l'obtention de son spectre d'absorption sans ambiguïté.

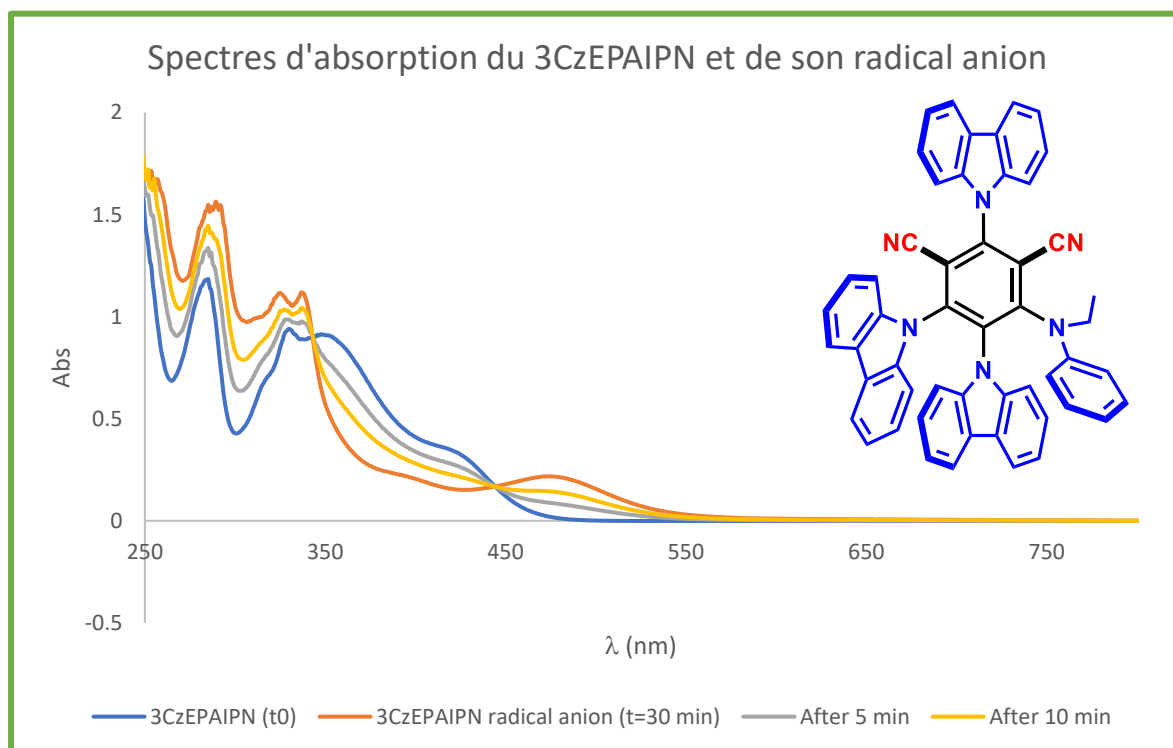


Figure 16 : Evolution du spectre d'absorption d'une solution de 3CzEPAIPN au cours du temps pendant une électrolyse à un potentiel permettant sa réduction monoélectronique. Le spectre du 3CzEPAIPN est en bleu et celui de son radical anion est en orange.

L'étude de ses propriétés a été effectuée par voltampérométrie cyclique, spectroscopie d'absorption et de fluorescence, résonance paramagnétique électronique, et enfin par comptage de photons uniques corrélé en temps (TCSPC).

Le spectre de fluorescence de la solution du radical anion a présenté un profil particulier avec une irradiation à 409 nm, avec trois bandes émissives distinctes.

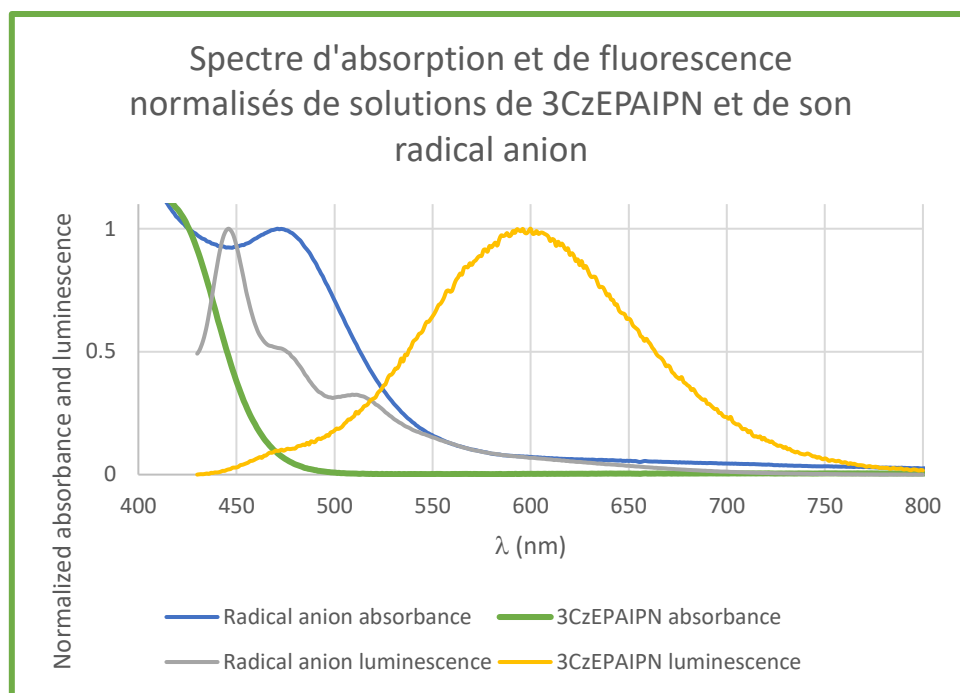


Figure 17 : Profils superposés d'absorption et de fluorescence du 3CzEPAIPN et de son radical anion.

L'analyse TCSPC a été effectuée en présence et absence de chlorobenzène et a fourni des résultats différents de la littérature précédente. Cela ajoute de nouvelles données au débat sur la capacité des radicaux anions à agir en tant que super-réducteurs. Il s'avère, d'après nos résultats, que les mécanismes mis en jeu lors de la réduction de chlorures d'aryles par l'état excité du radical anion sont plus compliqués que ce qui est supposé actuellement. Notamment, plusieurs durées de vie d'états excités sont obtenues pour la solution du radical anion du 3CzEPAIPN, dont l'une qui dépasse les 30 ns et se trouve diminuée de manière cohérente avec un accroissement de la concentration en chlorobenzène. Cette valeur, remarquablement élevée si elle devait être attribuée au radical anion, semble donc pourtant corrélée à la réduction du chlorobenzène.

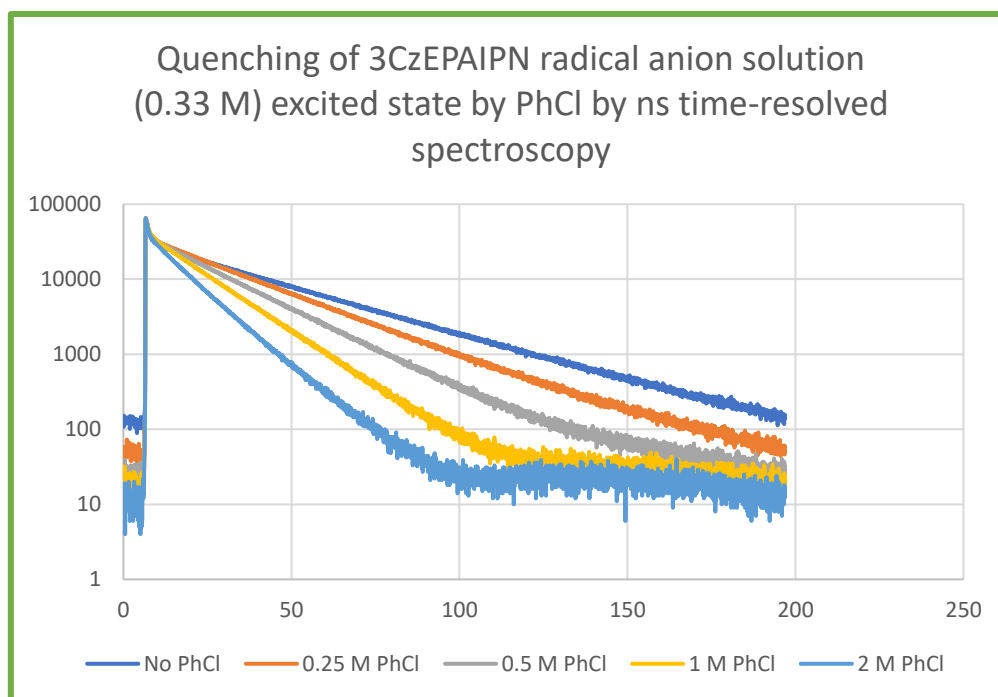


Figure 18 : Déclin au cours du temps de l'émission de photons par une solution du radical anion du 3CzEPAIPN en présence de différentes concentrations de chlorobenzène.

Ces études ont aussi été menées entièrement sur le 4CzIPN ainsi que partiellement sur d'autres cyanoarènes donneur-accepteur. La complexité et la diversité des résultats obtenus indiquent un comportement variable suivant la structure du cyanoarène donneur-accepteur considéré, mettant en avant le caractère particulier du 3CzEPAIPN pour des raisons qui restent aujourd'hui à approfondir. Ces travaux ouvrent la voie à des études complémentaires pour affiner la compréhension de ces systèmes et développer leur utilisation en électrophotocatalyse.

Une partie de ce chapitre est dédiée à l'étude de l'interaction entre les cyanoarènes donneur-accepteur et l'acide de Lewis  $B(C_6F_5)_3$  (BCF).

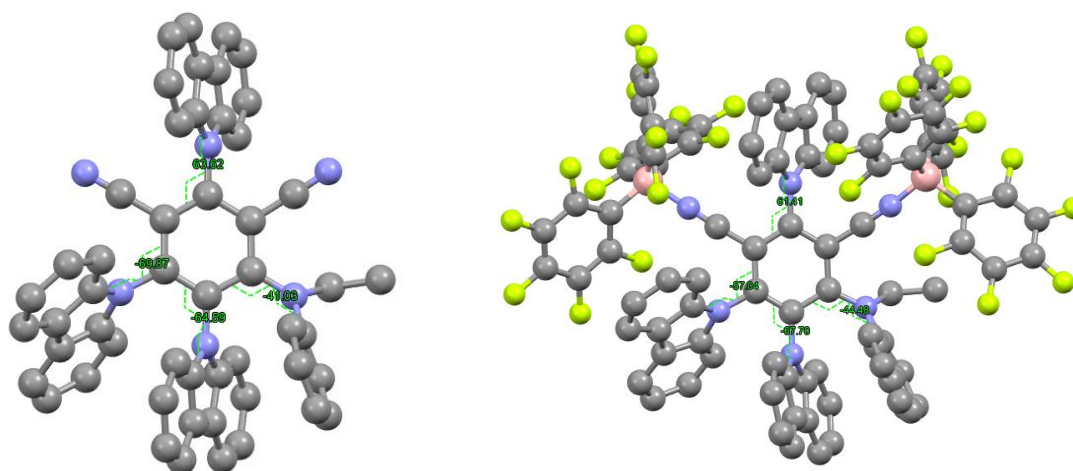


Figure 19 : Structures obtenues par diffraction des rayons X du 3CzEPAIPN (gauche) et du 3CzEPAIPN di-coordinés par des BCF (droite).

Leur coordination induit d'importants changements structuraux et photophysiques, en particulier des torsions d'angles dièdres entre certains groupements amines donneurs et le cycle aromatique central ainsi que leur absorbance qui subit un important déplacement bathochrome.

Une étude électrochimique approfondie montre que le 3CzEPAIPN dans son état fondamental en présence de BCF existe sous la forme d'un mélange d'équilibres entre l'espèce non coordonnée 3CzEPAIPN, l'espèce mono-coordonnée 3CzEPAIPN.BCF, et des traces de l'espèce di-coordonnée 3CzEPAIPN.BCF<sub>2</sub>. Ces proportions varient en fonction de la concentration en 3CzEPAIPN ainsi que du nombre d'équivalents de BCF. Dans les conditions utilisées dans ces travaux, le 3CzEPAIPN en présence de deux équivalents de BCF existe favorablement sous la forme non coordonnée. En revanche, l'accroissement du nombre d'équivalents de BCF indique une mono-coordination favorable, la di-coordination n'étant quasiment pas observée. Une fois réduit électrochimiquement, le 3CzEPAIPN sous sa forme radical anion se coordine favorablement au BCF pour former presque instantanément le complexe radical anion mono-coordonné. Une modification de la vitesse de balayage par voltampérométrie cyclique a permis de montrer que cette espèce évolue au cours du temps vers la forme di-coordonnée 3CzEPAIPN.BCF<sub>2</sub><sup>•-</sup>. Cependant, l'adduit ainsi formé est instable et conduit à la récupération du 3CzEPAIPN ainsi que la décomposition de l'acide de Lewis.

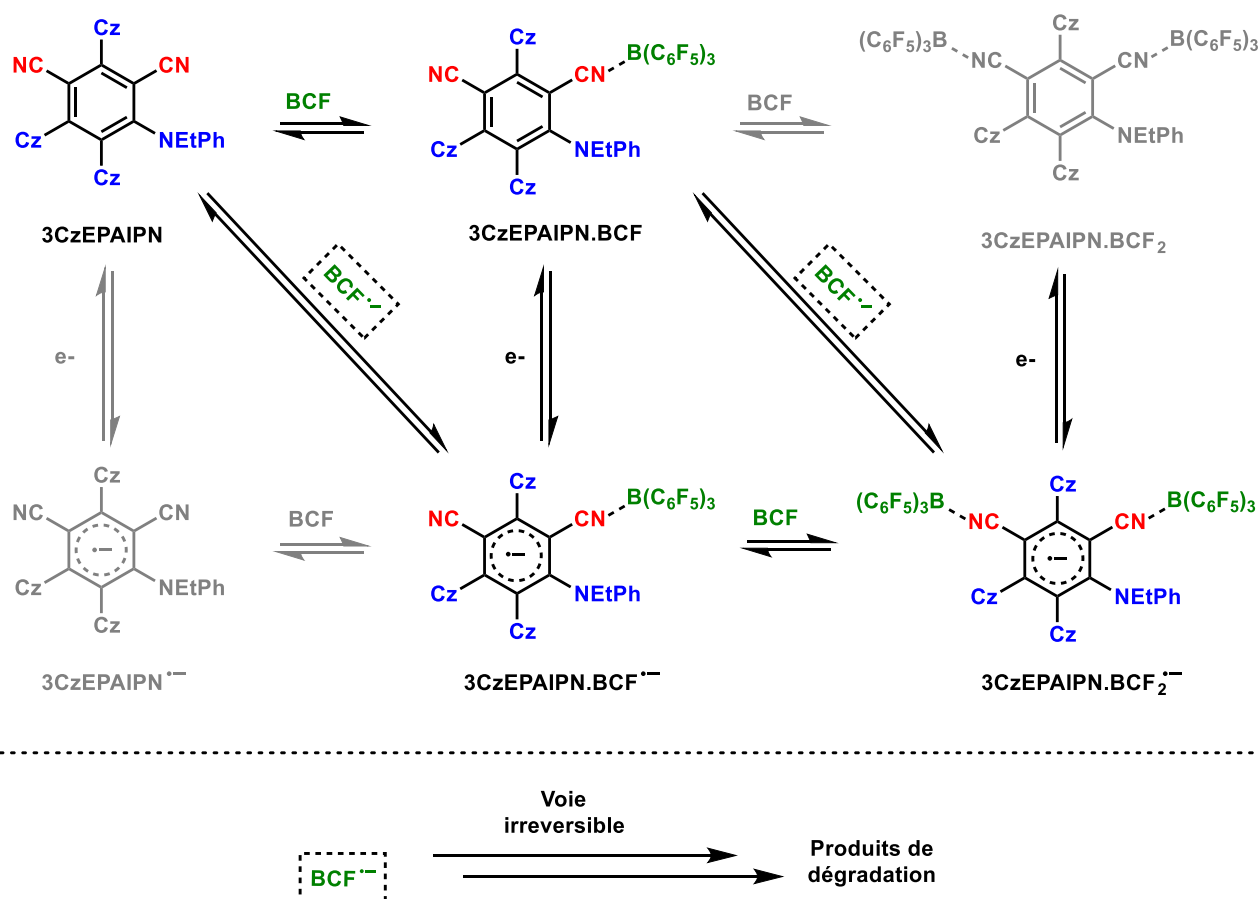


Figure 20 : Schéma proposant les espèces majoritaires en présence avant et après électrolyse d'une solution de 3CzEPAIPN en présence de BCF.

Nous supposons que l'électron supplémentaire est éjecté du système avec le départ d'un  $\text{BCF}^{\bullet-}$  qui se dégrade de manière incontrôlée.

Le chapitre IV présente la découverte de propriétés super-réductrices de l'état excité de l'anion du triphénylgermane appliquées à la germanylation de fluorures d'aryle.

L'introduction de ce chapitre rappelle les voies de synthèse connues pour accéder aux phényle germanes. Notamment, les travaux récents du groupe de Schoenebeck dévoilant l'intérêt particulier des phényle germanes comme partenaires robustes dans les réactions de couplage croisé catalysées par les métaux de transition est détaillé. Cette introduction se termine sur des travaux récents montrant l'activation par la lumière visible d'anions stannylés, qui ont inspiré les travaux décrits ci-après à partir de l'anion du triphénylgermane.

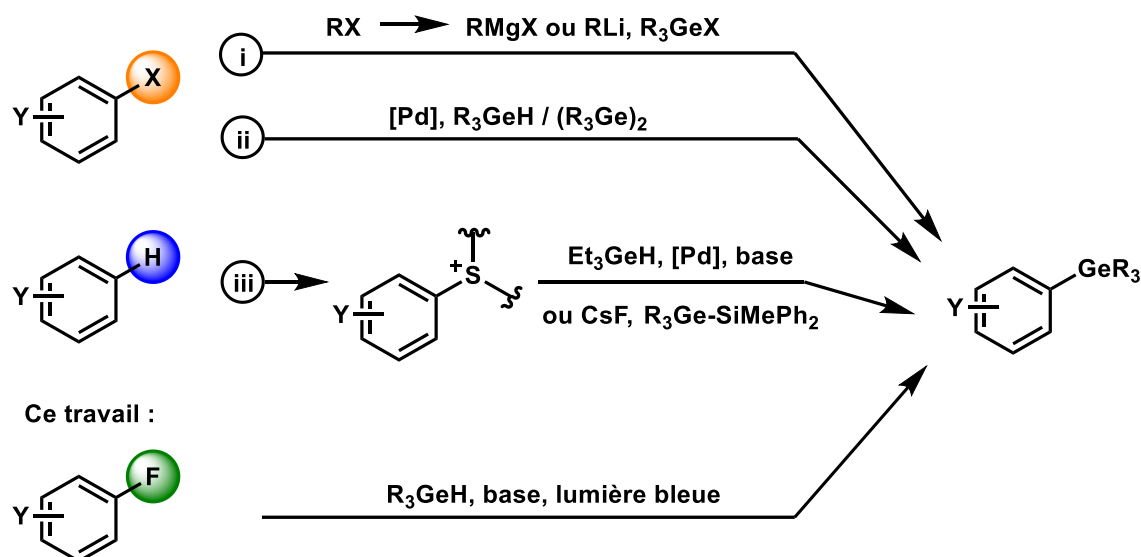


Figure 21 : Germanylation de différents aryles connues dans la littérature.

Les conditions de réaction générales pour la germanylation photoinduite de différents fluorures d'aryle présentée au travers de ces travaux sont données dans la figure suivante (Figure 22).

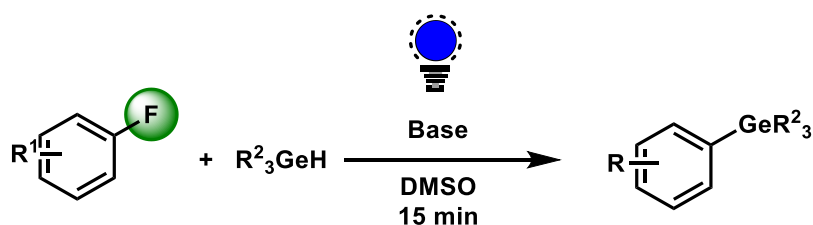


Figure 22 : Germanylation de fluorures d'aryle par voie photochimique



La déprotonation du triphénylgermane par le *tert*-butanoate de sodium dans le DMSO produit l'anion du triphénylgermane. Celui-ci est capable sous irradiation par la lumière visible de fournir les aryles germanylés suivants (Figure 23). La tolérance de la réaction se limite à des substrats aprotiques ne portant pas de fonction électrophile en raison de la puissante nucléophilie de l'anion du triphénylgermane dans son état fondamental.

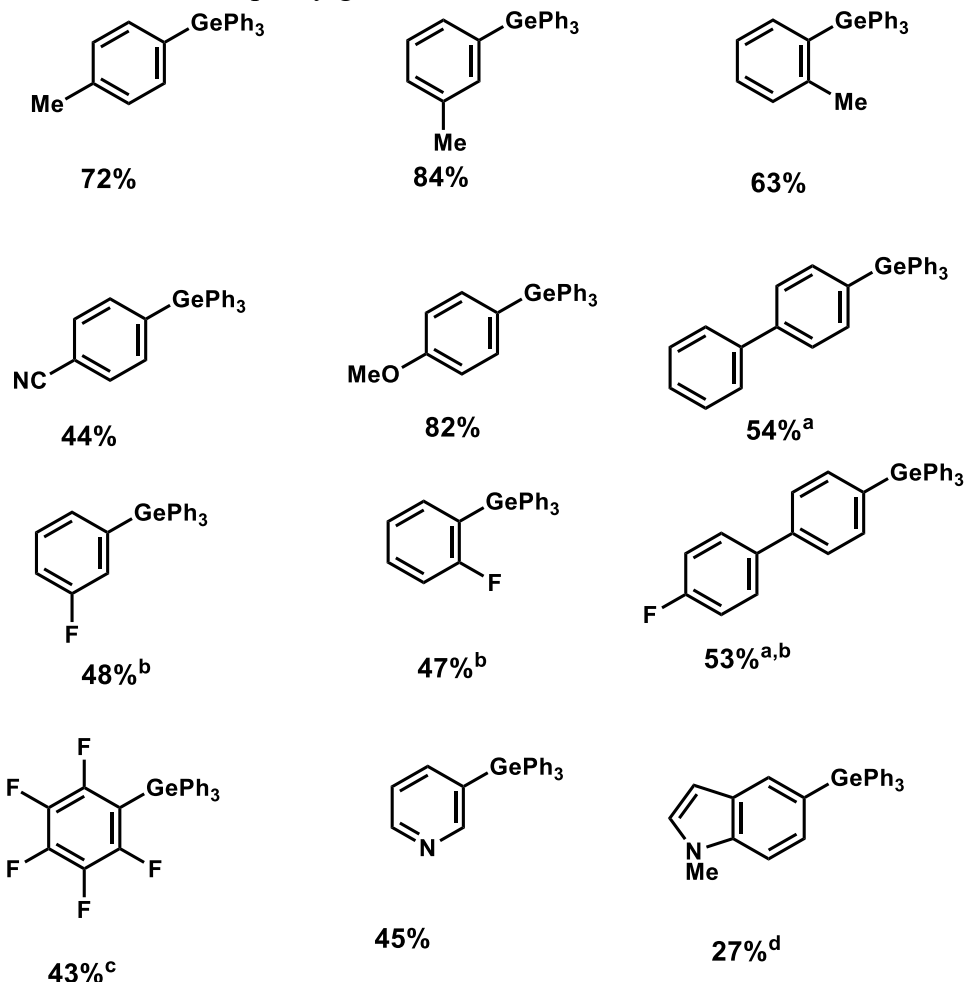


Figure 23 : Etendue de la réaction photoinduite de germanylation de fluorures d'aryles. Réactifs et conditions: Fluoro(hetero)arene (1.2 eq), Ph<sub>3</sub>GeH (1 eq), *t*BuONa (2.0 eq), 15 min. <sup>a</sup>Durée de réaction : 15 h. <sup>b</sup>Fluoro(hetero)arene (2.4 eq). <sup>c</sup>Fluoro(hetero)arene (5 eq). <sup>d</sup>Fluoro(hetero)arene (1.0 eq), Ph<sub>3</sub>GeH (2.0 equiv), *t*BuONa (4.0 equiv).

Concernant le mécanisme, supporté par des calculs DFT, un transfert d'électron depuis l'état excité de l'anion du triphénylgermane vers le fluorure d'aryle conduit à la rupture de la liaison carbone-fluor et fournit un anion fluorure et un radical aryle. Ce radical aryle se recombine avec le radical du triphénylgermane pour fournir les aryles germanylés d'intérêt (Figure 24).

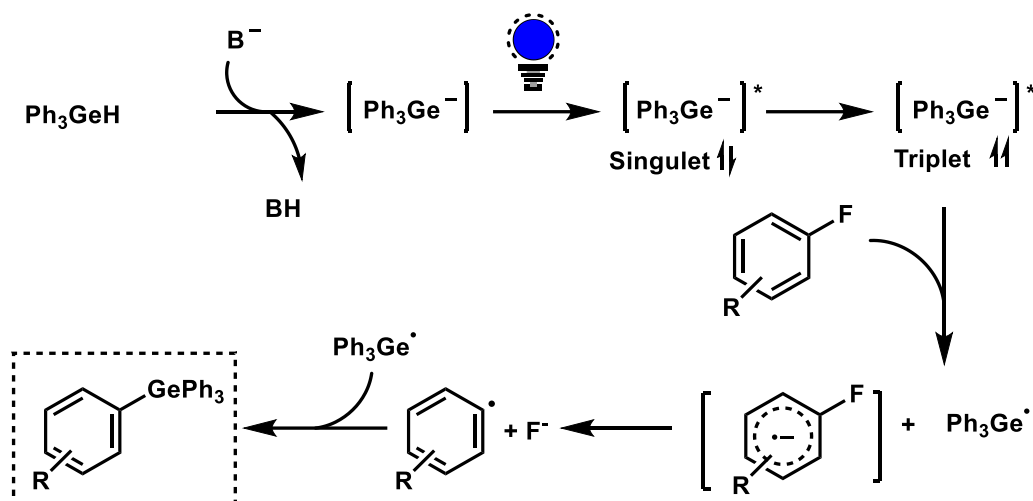


Figure 24 : Proposition de mécanisme supporté par des calculs DFT de la germanylation de fluorures d'aryles sous irradiation par la lumière visible.

Enfin, le chapitre V fournit une conclusion générale au manuscrit en résumant les différents résultats obtenus ainsi que les perspectives de chaque chapitre, afin d'ouvrir vers les poursuites des travaux. *In fine*, nous montrons à travers ce manuscrit le potentiel de la combinaison de la chimie physique organique avec la synthèse organique afin de comprendre et mettre au point de nouvelles réactions assistées par la lumière visible. Nous sommes bien conscients que certains résultats présentés, notamment ceux du chapitre III, soulèvent plus questions qu'ils n'apportent de réponses à propos de la réactivité des radicaux anions des cyanoarènes donneur-accepteur sous irradiation lumineuse en présence d'halogénures d'aryle. Nous pensons, cependant, que les aperçus présentés et discutés dans ce chapitre, et plus généralement dans ce manuscrit, seront d'un intérêt important pour les chercheurs actifs dans le milieu de la photochimie et la photophysique organiques.